NASA Conference Publication 3003—Vol. 1

Lewis Structures Technology—1988

Volume 1—Structural Dynamics

(NASA-CP-3003-Vol-1) LEWIS STRUCTURES TECHNOLOGY, 1988. VOLUME 1: STRUCTURAL DYNAMICS (NASA) 463 p CSCL 20K

N88-23226
--THRU--
N88-23259
Unclas
H1/39 0140059

Proceedings of an exposition and
symposium of structures technology
developed under the auspices of
NASA Lewis Research Center's
Structures Division
Cleveland, Ohio
May 24-25, 1988

NASA Conference Publication 3003—Vol. 1

Lewis Structures Technology—1988

Volume 1—Structural Dynamics

Proceedings of an exposition and
symposium of structures technology
developed under the auspices of
NASA Lewis Research Center's
Structures Division
Cleveland, Ohio
May 24-25, 1988

NASA

National Aeronautics and
Space Administration

Scientific and Technical
Information Branch

1988

PREFACE

Aeronautical and space propulsion systems structures technology has been the mission of the Structures Division at the NASA Lewis Research Center for many years. We have carried out both fundamental and applied research projects in pursuit of that mission. We have worked cooperatively with members of the industrial and academic communities in order to strengthen our ties to both the discipline rigors found in university research and the needs of industrial design engineers. It is from this perspective that we have prepared the material for this symposium. And we hope to transfer our technology beyond our usual industrial partners.

The technology required for the reliable, high-performance, lightweight structures needed for aerospace propulsion is among the most complex and challenging facing the design engineer. We provide a comprehensive review of the status of the technology, a review of our recent contributions, and a flavor of the directions for the future. The symposium is meant to be as informative as possible, with the intent to establish new and broader lines for technology transfer. We encourage continued interaction and the chance to exchange information, ideas, and problems with the intention of improving the capability of aerospace propulsion systems.

Our two-day symposium and exposition, LST '88, is expected to attract 300 technologists from all walks of structurally related engineering. The 83 technical contributions have been created by over 100 authors who are respected authorities in their fields. Fifty percent of these are NASA civil servants, and twenty-five percent are on-site contractors and grantees, National Research Council associates, Institute for Computational Mechanics in Propulsion (ICOMP) associates, and U.S. Army Aviation Research and Technology Activity (AVSCOM) personnel. The balance are from industry and academia.

It is a well-rounded symposium, and the proceedings should be a valuable resource for several years to come. The format is easy to access and extract information from. Each topic within a presentation is self-contained on a single page. The topic title appears at the top of the page followed by an extended figure caption, and the figure is located at the bottom of the page. Considerable effort has been expended in streamlining the presentations and freeing them of extraneous information so as to make them clear to the potential user - YOU. References are cited for more detailed followup of a particular topic. On-site personnel are also willing to lend assistance in answering questions and resolving problems that need clarification.

Lester D. Nichols
Chief, Structures Division
NASA Lewis Research Center

PRECEDING PAGE BLANK NOT FILMED

CONTENTS TO VOLUME 1

VIBRATION CONTROL

Session Overview 1-1
Louis J. Kiraly, NASA Lewis Research Center
Survey of Impact Damper Performance 1-3
Gerald V. Brown, NASA Lewis Research Center
Periodic Response of Nonlinear Systems 1-13
C. Nataraj, Trumpler Associates, Inc., and H.D. Nelson, Arizona State University
Piezoelectric Pushers for Active Vibration Control of Rotating Machinery 1-29
Alan B. Palazzolo, Texas A&M University, and Albert F. Kascak, U.S. Army Aviation Research and Technology Activity - AVSCOM
Active Control and System Identification of Rotordynamic Structures . . 1-47
M.L. Adams, Case Western Reserve University
Electromagnetic Dampers for Cryogenic Applications 1-53
Gerald V. Brown and Eliseo DiRusso, NASA Lewis Research Center

PARALLEL COMPUTING

Session Overview 1-65
Louis J. Kiraly, NASA Lewis Research Center
Multigrid for Structures Analysis 1-67
Albert F. Kascak, U.S. Army Aviation Research and Technology Activity - AVSCOM
Parallel Computer Methods for Eigenvalue Extraction 1-91
Fred Akl, Ohio University
Adapting High-Level Language Programs for Parallel Processing Using Data Flow 1-103
Hilda M. Standley, University of Toledo
Iterative Finite Element Solver on Transputer Networks 1-113
Albert Danial and James Watson, Sparta, Inc.
Multiprocessor Graphics Computation and Display Using Transputers . . . 1-125
Graham K. Ellis, Institute for Computational Mechanics in Propulsion

DYNAMIC SYSTEMS

Session Overview 1-141
Louis J. Kiraly, NASA Lewis Research Center
Microgravity Mechanisms and Robotics Program 1-143
Douglas A. Rohn, NASA Lewis Research Center
Base Reaction Optimization of Manipulators with Redundant Kinematics 1-157
C.L. Chung and S. Desa, Carnegie Mellon University

PRECEDING PAGE BLANK NOT FILMED

Evaluation of a High-Torque Backlash-Free Roller Actuator 1-175
Bruce M. Steinetz, NASA Lewis Research Center
Low-Cost Optical Data Acquisition System for Blade Vibration Measurement 1-191
Stephen J. Posta, NASA Lewis Research Center
Roller Drive Materials Performance 1-203
Douglas A. Rohn, NASA Lewis Research Center
Microgravity Manipulator Demonstration 1-217
Andrew S. Brush, Sverdrup Technology, Inc., Lewis Research Center Group
Accurate Positioning of Long, Flexible ARM's 1-229
Michael J. Malachowski, CCE - Robotics

AEROELASTICITY

Session Overview 1-245
Louis J. Kiraly, NASA Lewis Research Center
Development of Aeroelastic Analysis Methods for Turborotors and Propfans - Including Mistuning 1-247
Krishna Rao V. Kaza, NASA Lewis Research Center
2-D and 3-D Time Marching Transonic Potential Flow Method for Propfans 1-263
Marc H. Williams, Purdue University
Propfan Model Wind Tunnel Aeroelastic Research Results 1-273
Oral Mehmed, NASA Lewis Research Center
Aeroelastic Forced Response Analysis of Turbomachinery 1-287
Todd E. Smith, Sverdrup Technology, Inc., Lewis Research Center Group
Reduced Order Models for Nonlinear Aerodynamics 1-299
Aparajit J. Mahajan, Earl H. Dowell, and Donald B. Bliss, Duke University
Application of Navier-Stokes Analysis to Stall Flutter 1-309
J.C. Wu, R. Srivastava, and L.N. Sanker, Georgia Institute of Technology

COMPUTATIONAL METHODS FOR DYNAMICS

Session Overview 1-321
Louis J. Kiraly, NASA Lewis Research Center
A Computational Procedure for Automated Flutter Analysis 1-323
Durbha V. Murthy, University of Toledo
Characterization of Structural Connections for Multicomponent Systems 1-337
Charles Lawrence, NASA Lewis Research Center, and
Arthur A. Huckelbridge, Case Western Reserve University
Mixed Finite Element Formulation Applied to Shape Optimization 1-353
Helder Rodrigues, John E. Taylor, and Noboru Kikuchi, The University of Michigan
Modal Forced Response of Propfans in Yawed Flow 1-367
G.V. Narayanan, Sverdrup Technology, Inc., Lewis Research Center Group

STRUCTURAL DYNAMICS CODE APPLICATIONS

Session Overview 1-377
Krishna Rao V. Kaza, NASA Lewis Research Center
Vibration and Flutter Analysis of the SR-7L Large-Scale Propfan 1-379
Richard August, Sverdrup Technology, Inc., Lewis Research Center Group
Supersonic Axial-Flow Fan Flutter 1-393
John K. Ramsey, NASA Lewis Research Center
Stall Flutter Analysis of Propfans 1-405
T.S.R. Reddy, University of Toledo
SSME Single-Crystal Turbine Blade Dynamics 1-421
Larry A. Moss, Sverdrup Technology, Inc., Lewis Research Center Group
PARAFRASE Restructuring of FORTRAN Code for Parallel Processing 1-431
Atul Wadhwa, Sverdrup Technology, Inc., Lewis Research Center Group
Analysis of Rotating Flexible Blades Using MSC/NASTRAN 1-449
Michael A. Ernst, NASA Lewis Research Center

APPENDIX

Contents to Volume 2 1-466
Contents to Volume 3 1-468

VIBRATION CONTROL

SESSION OVERVIEW

Louis J. Kiraly
Structural Dynamics Branch
NASA Lewis Research Center

We require that turbomachinery be as light in weight as possible in order to maximize flight system performance. The structural members are necessarily flexible in nature, which means that they can vibrate in complex ways during normal mission cycles. If a component is designed to be too flexible, vibration levels can be damaging unless the vibrations can be controlled in some way. In effect, vibration control methods allow designers to trade off weight and stiffness aspects of turbomachinery components with various vibration control strategies to optimize overall system performance.

With turbomachinery, large rotational kinetic energies can couple with vibration modes and result in large vibrations or dynamic instabilities. This is also true for dynamic unbalancing and aero coupled blade vibrations. The rotating components can contribute as much as 50 percent to a propulsion systems weight; the induced vibrations can be very large.

Traditional vibration control methods have involved passive devices such as squeeze films to minimize rotor-shaft vibrations and frictional or aerodynamic damping to control blade vibrations. This session presents some newer, potentially better methods. Our session begins with a discussion of nonlinear impact dampers which can be designed to control blade vibrations. Other blade vibration control methods involving aerodynamic damping are discussed in the aeroelasticity session. We proceed with a discussion of the nonlinear vibrations of rotor-shaft systems. The session concludes with discussions of actively controlled vibrations for rotor systems for both steady-state and transient rotor vibrations. Our poster session describes a passive electromagnetic damper for controlling shaft vibrations which can be readily extended to be an active device.

Active methods for controlling rotor vibrations will result in substantial system weight and performance improvements. One early estimate predicts weight decreases of over 10 percent coupled with performance increases of over 5 percent when active methods are used for design of new propulsion systems. Careful tradeoffs between system weight and control system complexity will be required as these new methods become available.

VIBRATION CONTROL

SESSION 1(A)

SESSION OVERVIEW
- L.J. KIRALY, CHIEF, STRUCTURAL DYNAMICS BRANCH, NASA

SURVEY OF IMPACT DAMPER PERFORMANCE
- G.V. BROWN, STRUCTURAL DYNAMICS BRANCH, NASA

PERIODIC RESPONSE OF NONLINEAR SYSTEMS
- C. NATARAJ, TRUMPLER ASSOCIATES, INC., WESTCHESTER, PA
- H.D. NELSON, ARIZONA STATE UNIVERSITY, TEMPE, AZ

SESSION 1(B)

PIEZOELECTRIC PUSHERS FOR ACTIVE VIBRATION CONTROL OF ROTATING MACHINERY
- A.B. PALAZZOLO, TEXAS A&M UNIVERSITY, COLLEGE STATION, TX
- A.F. KASCAK, U.S. ARMY AVSCOM/STRUCTURAL DYNAMICS BRANCH, NASA

ACTIVE CONTROL AND SYSTEM IDENTIFICATION OF ROTORDYNAMIC STRUCTURES
- M.L. ADAMS, CASE WESTERN RESERVE UNIVERSITY, CLEVELAND, OH

ELECTROMAGNETIC DAMPERS FOR CRYOGENIC APPLICATIONS (POSTER)
- G.V. BROWN AND E. DiRUSSO, STRUCTURAL DYNAMICS BRANCH, NASA

CD-88-32629

EVOLUTION OF TURBINE SHAFT SUPPORT SYSTEMS

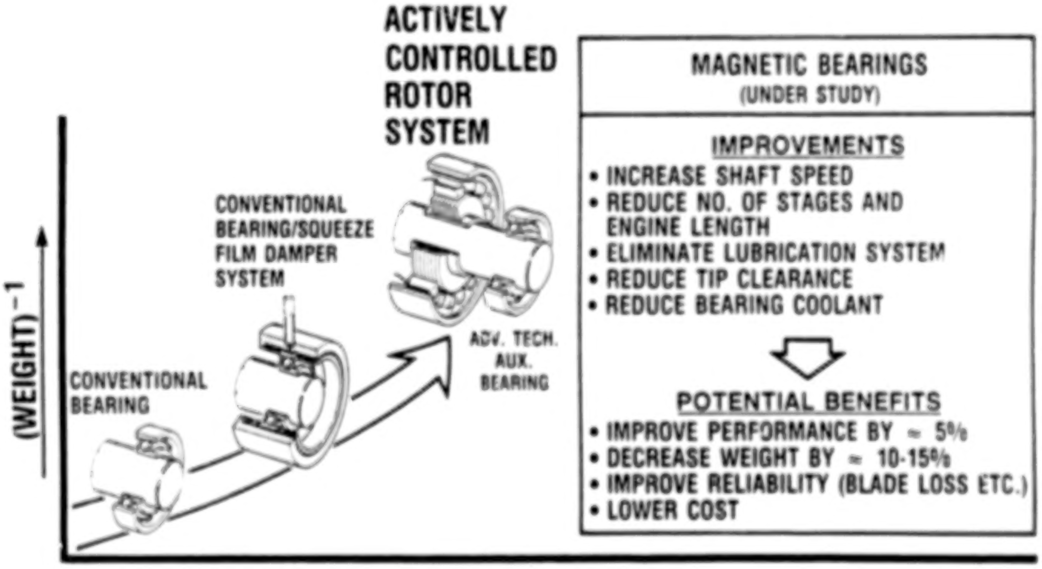
ACTIVELY CONTROLLED ROTOR SYSTEM
CONVENTIONAL BEARING/SQUEEZE FILM DAMPER SYSTEM
CONVENTIONAL BEARING
ADV. TECH. AUX. BEARING
(WEIGHT)$^{-1}$
TECHNOLOGY

MAGNETIC BEARINGS
(UNDER STUDY)

IMPROVEMENTS
- INCREASE SHAFT SPEED
- REDUCE NO. OF STAGES AND ENGINE LENGTH
- ELIMINATE LUBRICATION SYSTEM
- REDUCE TIP CLEARANCE
- REDUCE BEARING COOLANT

⇩

POTENTIAL BENEFITS
- IMPROVE PERFORMANCE BY ≈ 5%
- DECREASE WEIGHT BY ≈ 10-15%
- IMPROVE RELIABILITY (BLADE LOSS ETC.)
- LOWER COST

CD-88-33193

N88-23227

SURVEY OF IMPACT DAMPER PERFORMANCE

Gerald V. Brown
Structural Dynamics Branch
NASA Lewis Research Center

ABSTRACT

The impact damper is a simple device in which inelastic collisions can produce high damping in vibrating systems over a wide range of frequencies. But it is hard to analyze because the inelastic impacts make the system nonlinear. Fifty years of study of special cases have failed to produce an overall picture of the complex behavior of this physically simple system. Previous predictions of its damping have been limited to narrow regimes of behavior.

The present study obtains an overall picture by utilizing time-history solutions of the system motion for the oscillator in free decay. The impactor behavior depends very strongly on oscillator amplitude, and free decay can sample the full range of behavior from an infinite number of impacts per cycle at high amplitude to no impacts at low amplitude. This overall picture cannot be obtained by analysis of steady-state forced response. Yet the predictions are relevant to forced response behavior when the damping is relatively light.

Three major regimes of impactor behavior are shown to exist: (1) a low amplitude range, with less than one impact per cycle and very low impact damping, (2) a useful middle amplitude range with at least one, but a finite number, of impacts per half cycle and good impact damping, and (3) a high amplitude range with progressively decreasing damping and an infinite number of impacts in each half cycle. For light damping the impact contribution to the damping in the middle range is (1) proportional to the impactor mass, (2) additive to the proportional damping of the oscillator, (3) a strong but unique function of the vibration amplitude, (4) proportional to $1 - \varepsilon$, where ε is the coefficient of restitution, and (5) very roughly inversely proportional to the amplitude. The system exhibits jump phenomena and period doublings which may be precursors of chaotic states. An impactor with 2 percent of the mass of the oscillator can produce a loss factor near 0.1, a very substantial level of damping for aerospace systems.

SYSTEM SCHEMATIC AND DECAY RATE

A harmonic oscillator containing a loose particle, or impactor, is represented below. Collisions at either wall are described by a coefficient of restitution model. External proportional damping is included in the analysis.

When the oscillator is released from rest at an initial displacement (measured in units of the impactor gap), the amplitude of oscillation decays as shown in the right-hand figure. The decay is not exponential, but instead approximates the linear decay of a dry friction damped system. Decay curves for three values of the impactor mass μ (expressed as a fraction of the oscillator's mass) are shown. The damping fraction of the oscillator is ζ. The behavior of the impactor at six values of amplitude is shown on the following pages.

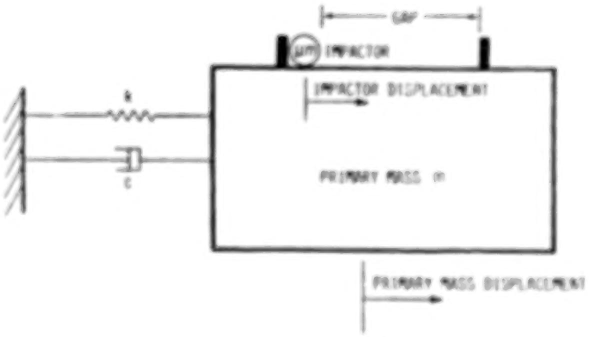

CD-80-[illegible]

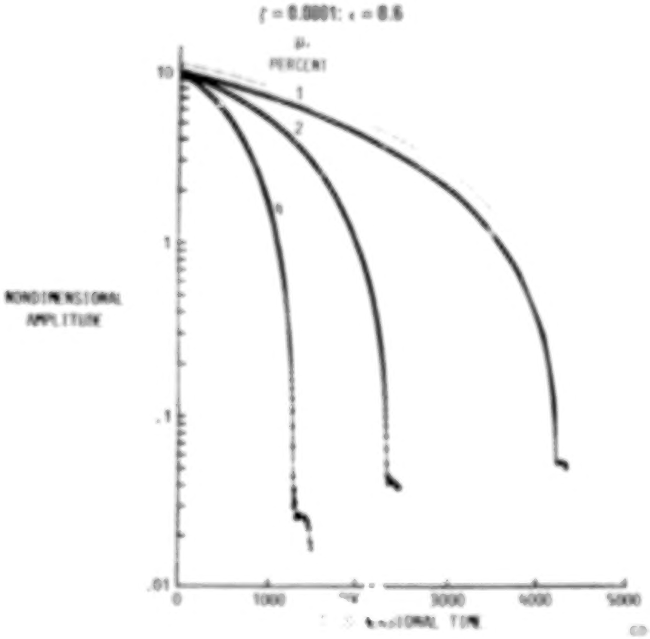

CD-80-[illegible]

IMPACTOR BEHAVIOR FOR AMPLITUDE GREATER THAN THE IMPACT GAP

At high amplitudes the impactor bounces an infinite number of times on one side of its cavity (like a ball bouncing to rest) before crossing to the other side. This is shown at the left where the impactor position is measured relative to the cavity walls. Time is measured in nondimensional units. When the amplitude decreases sufficiently, a finite number of impacts occurs in each half cycle (below a nondimensional amplitude of about 5 for the parameters used). An example with three impacts per side is displayed in the figure on the right. The number of impacts may be even on one side and odd on the other, as shown in the bottom figure.

AMPLITUDE, ~ 5.6; INFINITE NUMBER OF IMPACTS EACH HALF CYCLE

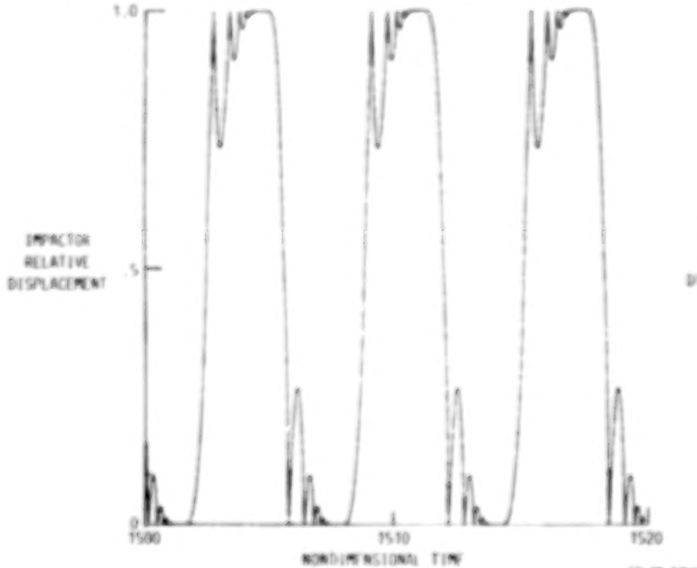

CD-88-32645

AMPLITUDE, ~ 2.6; THREE IMPACTS EACH HALF CYCLE

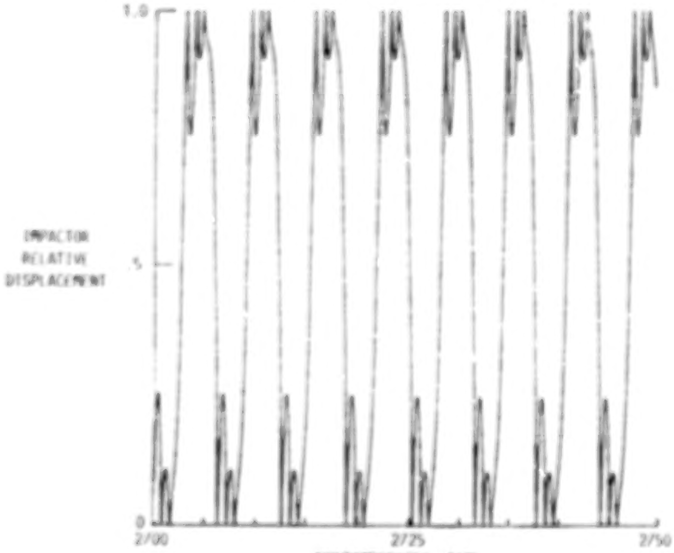

CD-88-32646

AMPLITUDE, ~ 0.6; ONE IMPACT PER HALF CYCLE ALTERNATING WITH TWO

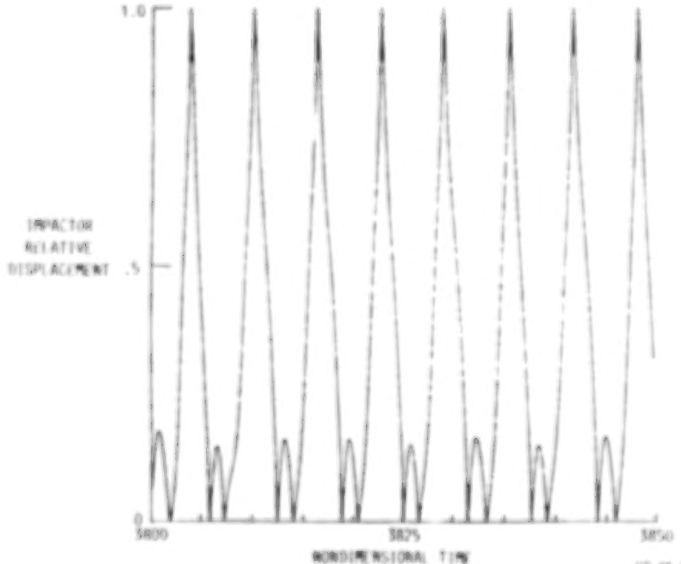

CD-88-32647

CD-87

IMPACTOR BEHAVIOR AT AMPLITUDES BELOW ONE

When the amplitude becomes small enough that only one impact occurs in each half cycle, very good damping is obtained. Rather surprisingly, the impacts need not be equally spaced in time, as shown in the figure on the left. The plots show the absolute displacement of the impactor and of both walls in order to clearly reveal the asymmetrical behavior. At somewhat smaller amplitude, the system locks into a symmetrical pattern of equally spaced impacts and produces its best damping (figure at right). At still lower amplitude, impacts in each half cycle become impossible (bottom figure), and the damping falls abruptly.

AMPLITUDE, ~0.4; TWO UNEQUALLY SPACED IMPACTS PER CYCLE

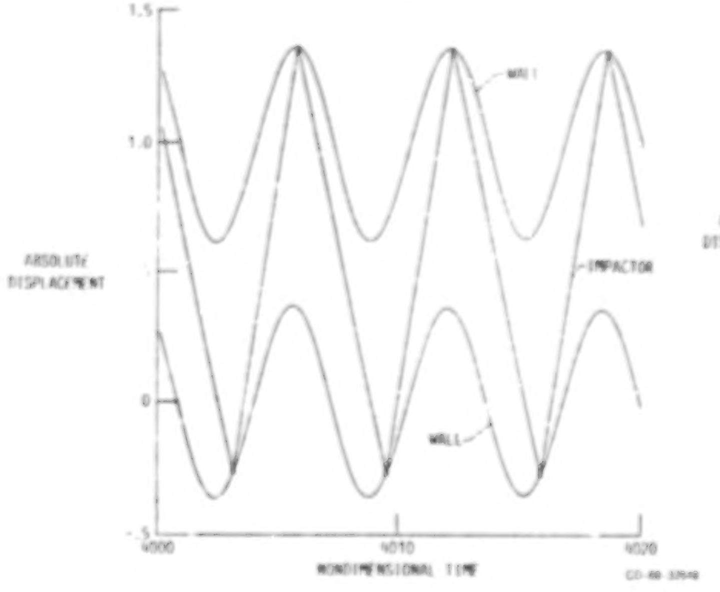

AMPLITUDE, ~0.2; TWO EQUALLY SPACED IMPACTS PER CYCLE

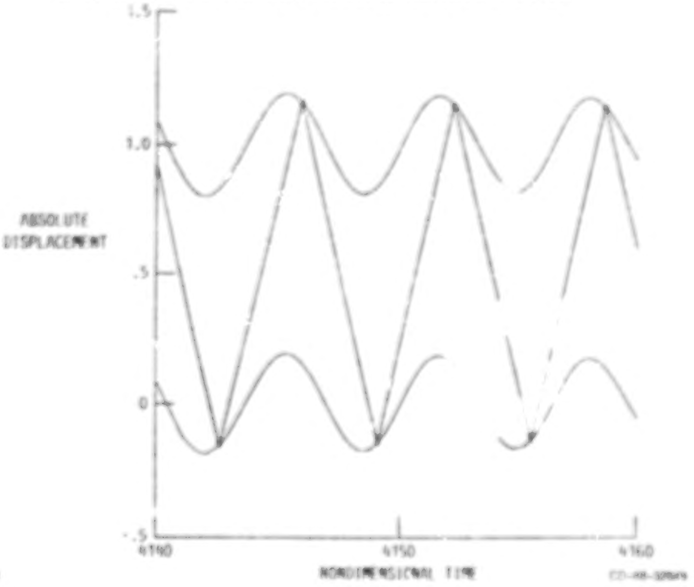

AMPLITUDE, ~0.055; BEGINNING OF IMPACT FAILURE

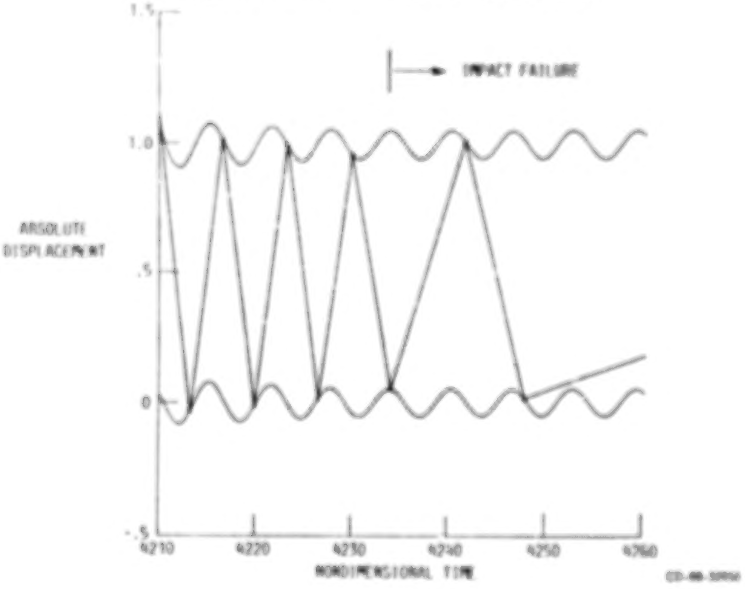

LOSS FACTOR AND ITS PROPORTIONALITY TO IMPACTOR MASS

The loss factor (the fraction of oscillator energy dissipated per radian) is plotted as a function of amplitude for three values of impactor mass fraction in the left-hand figure. Note that at the amplitude where the best damping occurs, an impactor with only 2 percent of the mass of the oscillator can dissipate nearly 10 percent of the oscillator's energy per radian, or about 50 percent of the energy in one cycle. This level of damping is substantial compared to that normally encountered in many aerospace systems and could, therefore, have a major effect in suppressing resonant vibrations and vibration instabilities. If the loss factor is divided by the impactor mass fraction and plotted as a function of amplitude, as in the right-hand figure, it can be seen that damping is rather closely proportional to impactor mass fraction.

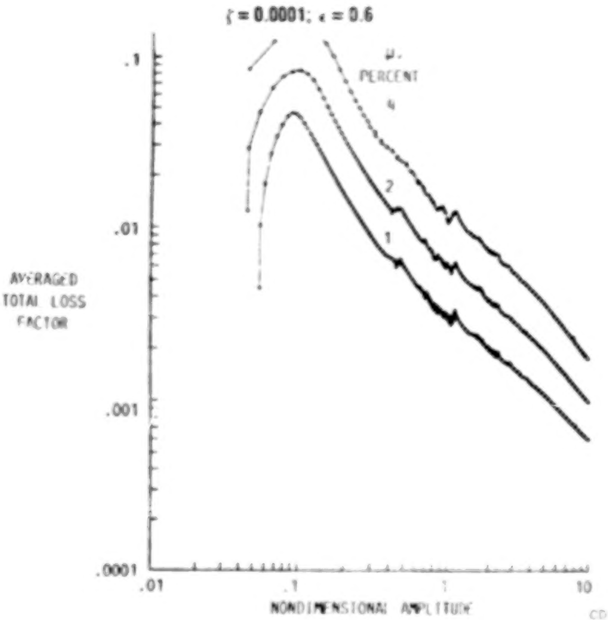

CD-88-32088

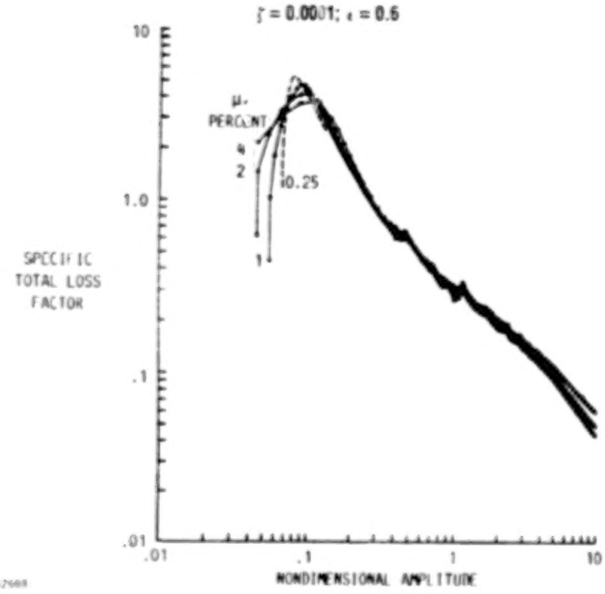

CD-88-32089

ADDITIVITY OF IMPACT DAMPING AND PROPORTIONAL DAMPING

Whether the contributions of impact damping and proportional damping are simply additive should be questioned in a nonlinear system. However, for the light to moderate damping regime explored herein, these contributions are additive, as shown below. The loss factor is shown at the left for several values of the proportional damping of the oscillator. On the right, the loss factor corresponding to proportional damping has been subtracted from each curve to yield the contribution due to the impactor alone, and a single curve results, proving additivity.

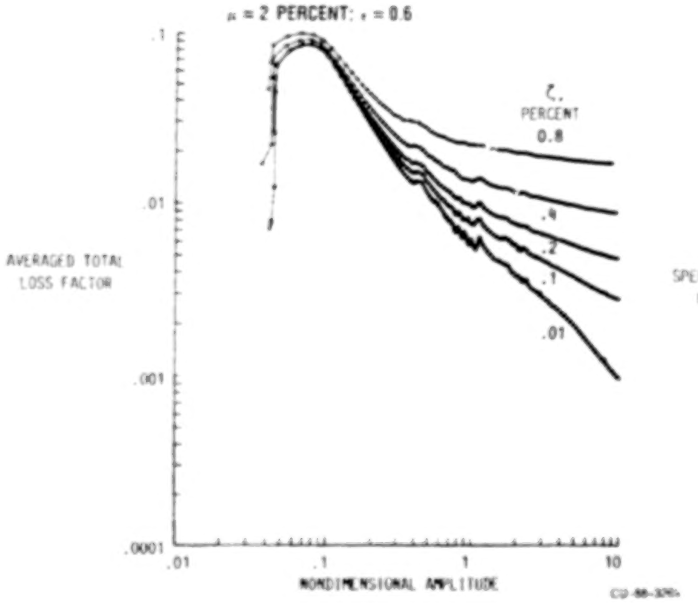

μ = 2 PERCENT; ϵ = 0.6

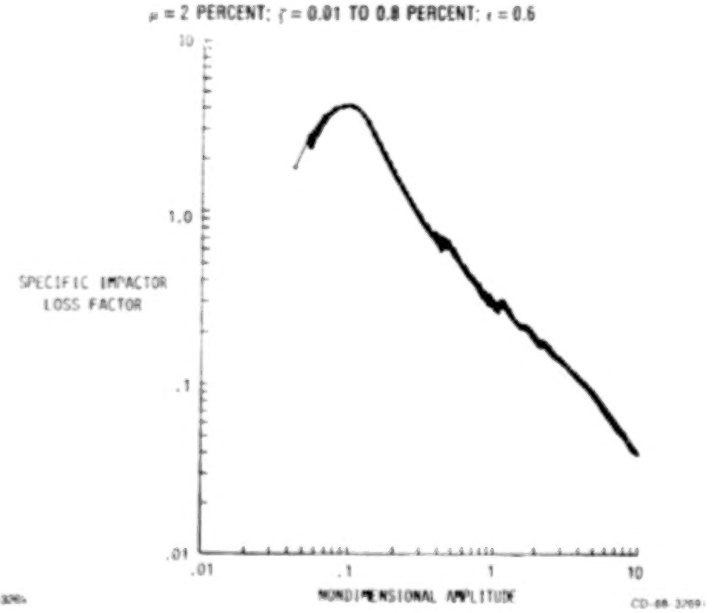

μ = 2 PERCENT; ζ = 0.01 TO 0.8 PERCENT; ϵ = 0.6

ORIGINAL PAGE IS
OF POOR QUALITY

DAMPING DEPENDENCE ON AMPLITUDE AND RESTITUTION COEFFICIENT

It has been known that the loss factor due to impact damping, like that of dry friction damping, is roughly inversely proportional to amplitude. The plot on the left shows the degree of deviation from that dependence. The ordinate variable is amplitude times the specific loss factor, which for exact inverse proportionality would plot as a horizontal straight line. For the amplitude range between 0.1 and 10, the ordinate lies within about 30 percent of its mean value. A similar plot on the right shows the dependence on the restitution coefficient, and the replot at the bottom shows that damping is reasonably proportional to one minus the restitution coefficient.

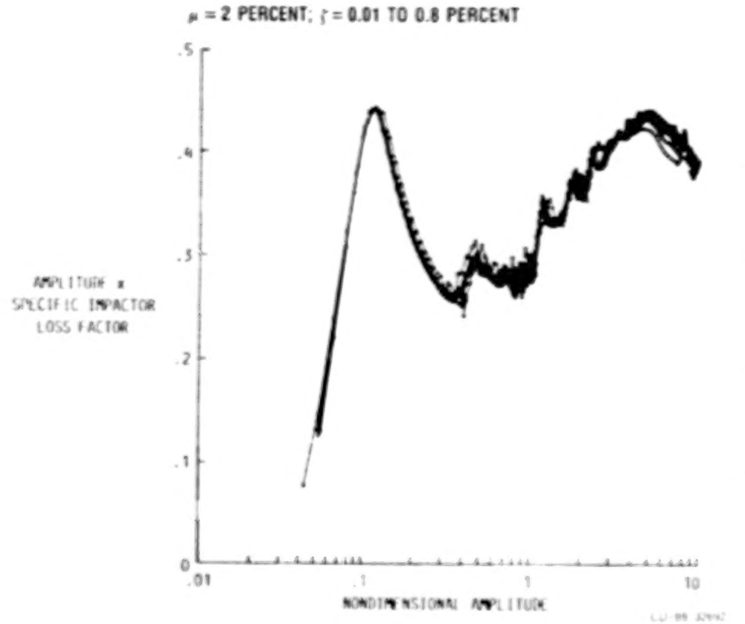

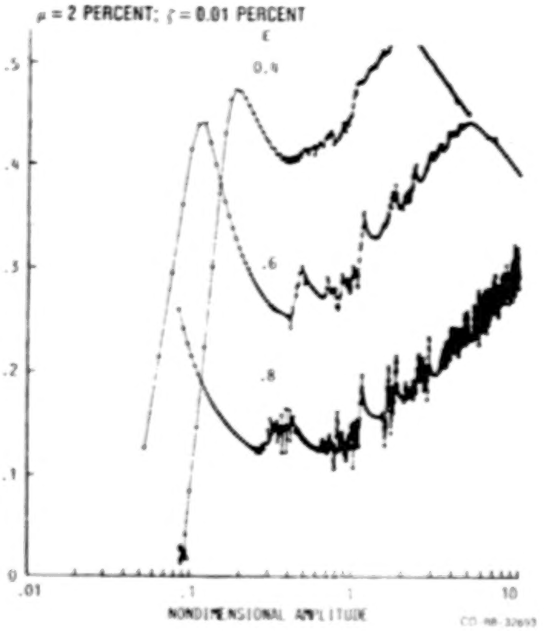

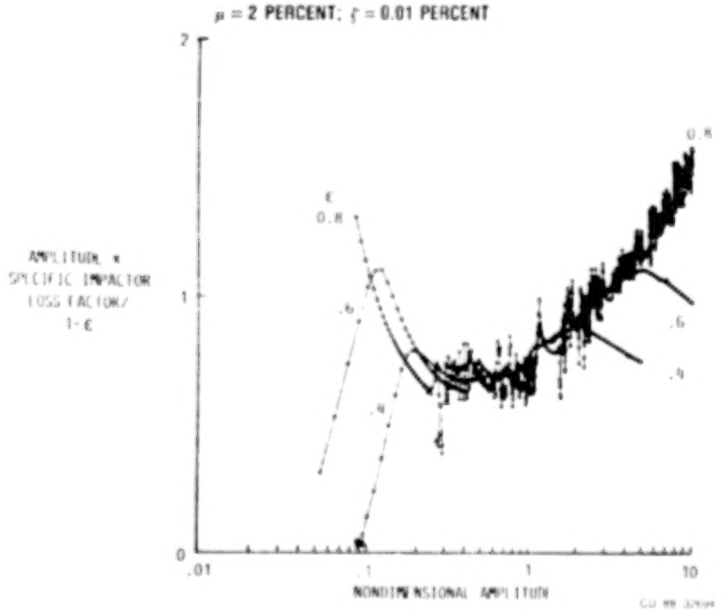

IMPACT PHASE, JUMP PHENOMENA, AND CHAOS

The figure at the upper left shows, for a very slow decay, exactly when impact occurs during each half cycle as a function of amplitude. At some amplitudes the impacts appear to be random; at others they are so regular that the circles representing their impact times merge to produce smooth continuous lines in the plot. In several places such a line splits into two (moving in the direction of increasing amplitude), and a period doubling occurs, suggesting that the random-looking regions are chaotic. A comparison of the upper right and lower left figures, in which the same amplitude range is traversed very slowly in opposite directions, reveals a type of jump phenomenon. The lower right figure shows impact phase angle for an impactor of useful mass over a large amplitude range which includes the infinite-bounce region.

$\mu = 0.001$ PERCENT; $\zeta = 0.025$ PERCENT; $\epsilon = 0.6$

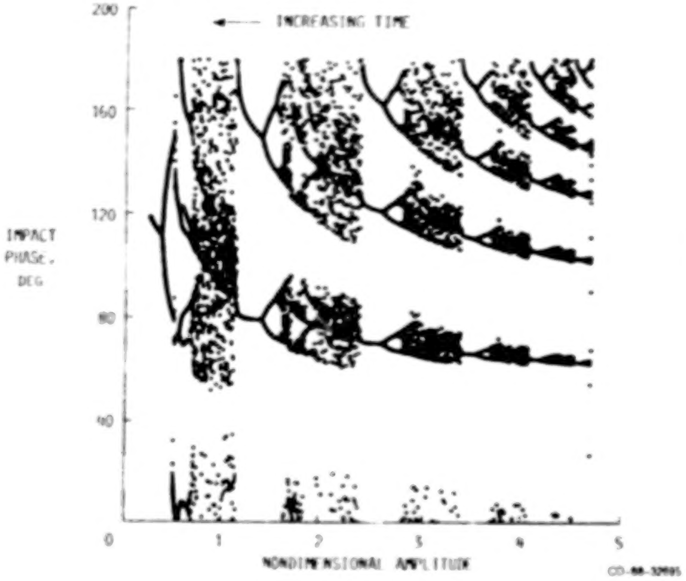

DURING DECAY $\mu = 0.001$ PERCENT; $\zeta = 0.02$ PERCENT; $\epsilon = 0.6$

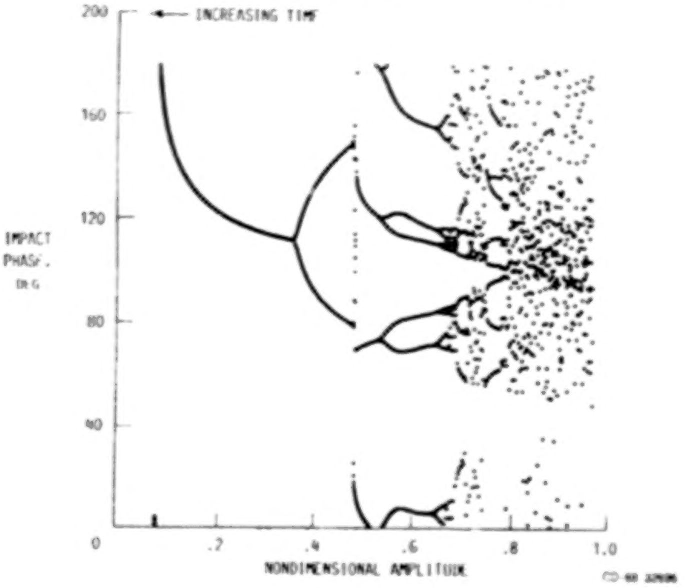

DURING GROWTH $\mu = 0.001$ PERCENT; $\zeta = 0.02$ PERCENT; $\epsilon = 0.6$

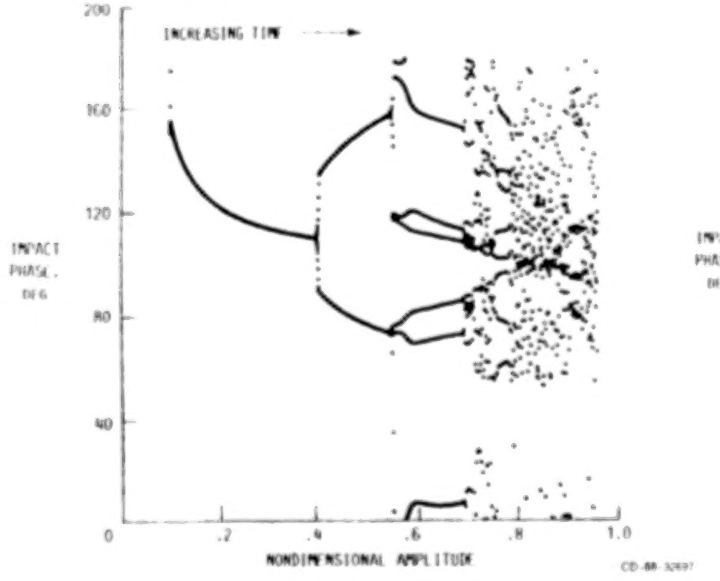

$\mu = 0.2$ PERCENT; $\zeta = 0.01$ PERCENT; $\epsilon = 0.6$

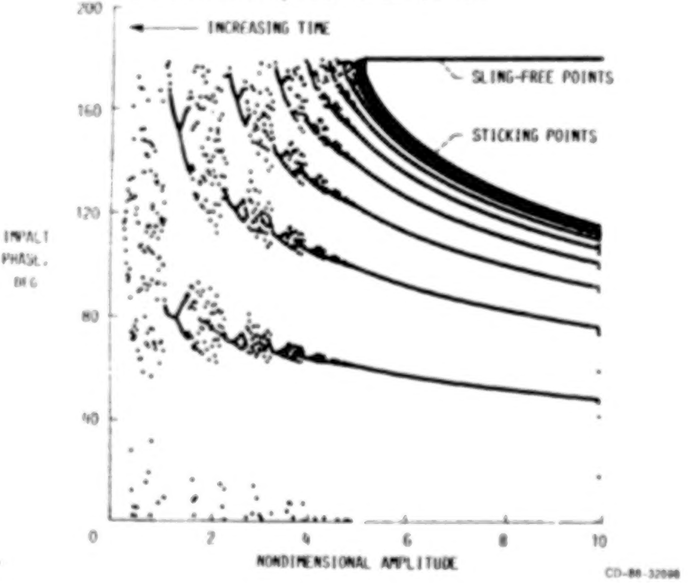

ORIGINAL PAGE IS
OF POOR QUALITY

CONCLUSIONS

Designed to operate near the most favorable amplitude, the impact damper provides very substantial damping per unit mass. An impactor with 2 percent of the mass of the oscillator can provide a loss factor of nearly 10 percent, a very high level for aerospace systems.

The free decay study provides a comprehensive picture of the extremely varied behavior exhibited by the impact damper. This behavior ranges from periodic motion to period doubling, jump phenomena, and chaos.

The damping provided is approximately predictable, since the free decay study has shown that the loss factor is proportional to the impactor mass fraction and to $1 - \varepsilon$ (where ε is the coefficient of restitution), and is roughly inversely proportional to the nondimensional amplitude.

CONCLUSIONS

- EXCELLENT DAMPING PER UNIT MASS
- FREE DECAY PROVIDES COMPREHENSIVE PICTURE
- DAMPING IS PROPORTIONAL TO
  - IMPACTOR MASS
  - $1 - \varepsilon$
  - 1/AMPLITUDE
- SYSTEM EXHIBITS
  - PERIODIC BEHAVIOR
  - PERIOD DOUBLING
  - JUMP PHENOMENA
  - CHAOS

CD-88-32699

BIBLIOGRAPHY

Bapat, C.N., Popplewell, N., and McLachlan, K., 1983, "Stable Periodic Motions of an Impact-Pair," Journal of Sound and Vibration, Vol. 87, No. 1. pp. 19-40.

Bapat, C.N. and Sankar, S., 1985, "Single Unit Impact Damper in Free and Forced Vibration," Journal of Sound and Vibration, Vol. 99, No. 1, pp. 85-94.

Brown, G.V., 1987, "The Impact Damped Harmonic Oscillator in Free Decay," NASA TM-89897.

Fedosenko, Iu.S. and Feigin, M.I., 1971, "Periodic Motions of a Vibrating Striker Including a Slippage Region," PMM: Journal of Applied Mathematics and Mechanics, Vol. 35, No. 5, pp. 844-850.

Higdon, A. and Stiles, W.B., 1955, Engineering Mechanics, Second Ed., Prentice-Hall, New York, p. 509.

Masri, S.F., 1970, "General Motion of Impact Dampers," Journal of the Acoustical Society of America, Vol. 47, No. 1, Pt. 2, pp. 229-237.

Popplewell, N., Bapat, C.N., and McLachlan, K., 1983, "Stable Periodic Vibroimpacts of an Oscillator," Journal of Sound and Vibration, Vol. 87, No. 1, pp. 41-59.

Shaw, S.W., 1985, "The Dynamics of a Harmonically Excited System Having Rigid Amplitude Constraints, Part I: Subharmonic Motions and Local Bifurcation, Part II: Chaotic Motions and Global Bifurcations," Journal of Applied Mechanics, Vol. 52, No. 2, pp. 453-464.

Sollar, P.J., 1985, "The Development of a Computer Model as an Aid to the Solution of the Problem of Impact Damping," MA Thesis, Rose-Hulman Institute of Technology, Terra Haute, IN.

Veluswami, M.A., Crossley, F.R.E., and Horvay, G., 1975, "Multiple Impacts of a Ball Between Two Plates, Part II: Mathematical Modeling," Journal of Engineering for Industry, Vol. 97, No. 3, pp. 828-835.

N88-23228

Periodic Response of Nonlinear Systems

C. Nataraj, Ph.D
Trumpler Associates, Inc.
Westchester, PA 19380

H. D. Nelson, Ph.D
Mechanical and Aerospace Engineering
Arizona State University
Tempe, AZ 85287-6106

ABSTRACT

A procedure is developed to determine approximate periodic solutions of autonomous and non-autonomous systems. The trignometic collocation method (TCM) is formalized to allow for the analysis analysis of relatively small order systems directly in physical coordinates. The TCM is extended to large order systems by utilizing modal analysis in a component mode synthesis strategy. The procedure was coded and verified by several check cases. Numerical results for two small order mechanical systems and one large order rotor dynamic system are presented. The method allows for the possibility of approximating periodic responses for large order forced and self excited nonlinear systems.

NOMENCLATURE

$\mathbf{a}_0$	Fourier static coef. vector
$\mathbf{a}_i, \mathbf{b}_j$	Fourier cosine, sine coef. vector
$\underline{A}, \underline{B}$	state matrices
$\mathbf{c}$	vector of Fourier coef.
$\underline{C}$	matrix of collocation values
$\underline{D}$	tridiagonal matrix
$\mathbf{f}$	state function vector
$\mathbf{F}$	state force vector
$\underline{G}$	damping matrix
$\underline{K}$	stiffness matrix
$\underline{M}$	mass matrix
m	no. of harmonics
N	no. of collocation points
n	no. of modes
$\hat{n}$	truncated no. of modes
$\mathbf{q}$	physical coordinate vector
$\mathbf{q}^b$	nonlinear subvector of $\mathbf{q}$
$\mathbf{Q}^s$	linear system force vector
$\mathbf{Q}^b$	nonlinear force vector
R	norm
$\mathbf{r}, \mathbf{l}$	right, left displacement vectors
$\underline{r}$	right modal matrix
$\underline{S}$	connectivity matrix
t	time
T	fundamental period

$\mathbf{T}$	transformation matrix
$\mathbf{x}$	state vector
$\mathbf{y},\mathbf{z}$	state right, left vectors

GREEK

δ_{ij}	Kronecker delta
λ	eigenvalue
η	modal coordinate
ω	fundamental frequency

SUPERSCRIPT

o	collocation values
•	d/dt
T	transpose

INTRODUCTION

Nonlinear phenomena of many forms are clearly present in all complicated machinery. The future development and advancements in these machines depends strongly on our ability to identify, understand, model, analyze and design with these various nonlinear mechanisms present. Transient and steady state analysis capabilities are required with direct numerical integration, presently the most popular tool. This work presents a method based on trignometric collocation for approximating periodic solutions of forced systems and for locating limit cycles of self excited systems. The use of modal analysis allows the method to be extended to large order systems.

Previous work on the steady state response of systems which include nonlinear components is limited except by direct numerical integration. This can be very time consuming, especially for large order systems, and is not particularly economical in parametric design applications. It is really the only option available for transient analysis, however, and also serves as a useful means for verifying final designs.

Some quantitative methods for steady state analysis of nonlinear systems include perturbation techniques, describing function procedures, harmonic balance procedures, and methods of weighted residuals. Perturbation techniques (Nayfeh, 1981) have a limited range of applicability due primarily to high algebraic complexity for large order systems. They also require the introduction of a small parameter, thus restricting the solution validity to systems with weak nonlinearities. Describing function methods (Atherton, 1982) are a good choice for many problems since they can accommodate non-analytic nonlinearities. They can be used, however, only when higher harmonics are small compared to the fundamental component.

The harmonic balance method, (Hagedorn, 1982), has been recently applied to the analysis of engineering systems (Yamauchi, 1983; Saito, 1985) and the preliminary results indicate that the method may be quite effective. An alternate approach is the use of methods of weighted residuals which have been used quite extensively in the past to solve nonlinear boundary value problems. Some of these methods, which have been extended to the problem of determining periodic response, include Galerkin's method (Urabe, 1965; Urabe and Reiter, 1966; Stokes, 1972) and the Trignometric Collocation method (Samoilenko and Ronto, 1979).

The primary objective of this work is to formulate the mathematical procedures for the analysis of periodic motion in nonlinear systems. The proposed procedure involves a coupling of the Trignometric Collocation method (TCM) with modal analysis techniques, thereby effecting a substantial reduction in the number of unknown quantities in the iterative part of the solution process.

MATHEMATICAL DEVELOPMENT

The focus of this research is on the TCM that was developed and formalized by Ronto (Samoilenko and Ronto, 1979) with applicability to small order systems. Described below are the essential features of the procedure for both non-autonomous and autonomous systems.

Trignometric Collocation Method

Many engineering systems can be modelled by a set of n nonlinear ordinary differential equations of the non-autonomous form

$$\dot{\mathbf{x}} = \mathbf{f}(\mathbf{x}, t) \tag{1}$$

where the RHS is continuous and periodic with a period T. It is required to determine a periodic solution $\mathbf{x}(t)$ of Eq. (1). It is assumed that the required solution can be approximated by a finite trigonometric series:

$$\mathbf{x} = \mathbf{a}_0 + \sum_{j=1}^{m} \left[\mathbf{a}_j \cos(j\omega t) + \mathbf{b}_j \sin(j\omega x) \right] \tag{2}$$

where ω is is the fundamental frequency. The unknown coefficients of the above series can be ordered into a vector,

$$\mathbf{c}_i = (a_0, a_1, b_1, a_2, b_2, \dots .\, a_m, b_m)^T \tag{3}$$

corresponding to each variable x_i.

The collocation method essentially consists of substituting the assumed solution form, Eq. (2), into the system state, Eq. (1), and requiring that the equations be identically satisfied at a specified number of points, N. This gives rise to N•n nonlinear algebraic equations which must be solved to obtain the unknown coefficients. For a unique solution, the following inequality must be satisfied

$$N \geq (2m + 1) \tag{4}$$

Rigorous investigations of the applicability and foundation of the TCM have been carried out by Ronto (Samoilenko and Ronto, 1979), and only the formalism of the procedure is presented here.

The state variables can be evaluated at the collocation points in terms of the unknown coefficients leading to the form:

$$\overset{o}{\dot{\mathbf{x}}}_i = \underline{T}\, \mathbf{c}_i \tag{5}$$

where,

$$\overset{0}{\dot{\mathbf{x}}}_j = \left(x_i(t_o), x_i(t_1), \dots\dots, x_i(t_N) \right)^T \tag{6}$$

is a vector of values of the trignometric polynomial at the collocation points. The array $\underline{T}$ is an N * (2m + 1) transformation matrix whose elements are defined as:

$$T_{ij} \begin{cases} 1 & j = 1 \\ \cos[\,(i-1)\,j\pi / N\,] & j = 2, 4, \ldots \\ \sin[\,(i-1)\,(j-1)\,\pi / N\,] & j = 3, 5, \ldots \end{cases} \tag{7}$$

The derivative of each state variable can be expressed in a trignometric series and is obtained by differentiation of Eq. (2). Hence, the following relation, which is similar to Eq. (5), is obtained:

$$\overset{\circ}{\dot{\mathbf{x}}}_i = \omega\,\underline{T}\;\underline{D}\;\mathbf{c}_i \tag{8}$$

The array D is a (2m + 1) square tridiagonal matrix of the form:

$$\begin{bmatrix} 0 & & & & & & & \\ & 0 & +1 & & & & & \\ & -1 & 0 & & & & & \\ & & & 0 & +2 & & & \\ & & & -2 & 0 & & & \\ & & & & & \ddots & & \\ & & & & & & 0 & +m \\ & & & & & & -m & 0 \end{bmatrix} \tag{9}$$

and the elements are given by,

$$D_{i,i+1} = -D_{i+1,i} = i/2, \qquad i = 2, 3, \ldots\ldots, (2m)$$

The requirement that the set of system state equations, Eq. (1), be satisfied exactly at N collocation points leads to N algebraic equations of the form:

$$\omega\,\underline{T}\;\underline{D}\;\mathbf{c}_i = \mathbf{f}_i(\,\underline{T}\;\mathbf{c}_i\,,\,t_k\,) \tag{10}$$

where $\mathbf{f}_i$ is the vector of the ith function evaluated at the N collocation time points. Hence, the collocation process yields N*n nonlinear algebraic equations in the (2m + 1) * n unknown coefficients. These equations are then solved using a secant method from standard subroutine packages of IMSL.

If the system state equations are autonomous, then Eq. (1) may be written as

$$\dot{\mathbf{x}} = \mathbf{f}(\,\mathbf{x}\,) \tag{11}$$

The frequency or frequencies of self-oscillation for such systems are unknown *a priori*. The analysis procedure is essentially the same as in the non-autonomous systems and leads to a set of nonlinear algebraic equations,

$$\omega \underline{T}\ \underline{D}\ \mathbf{c}_i = \mathbf{f}_i(\underline{T}\ \mathbf{c}_i) \qquad (12)$$

The number of unknown quantities is increased by one, the unknown frequency, to [(2m+1)*n + 1], and the number of collocation points must satisfy the following inequality to assure a unique solution

$$N \geq (2m+1) + 1 \qquad (13)$$

Hence, this situation is a case of non-linear least squares and cannot be solved by the secant method used for non-autonomous systems. An IMSL developed procedure, however, based on the Levinberg-Marquardt algorithm for nonliunear curve-fitting can be applied to the autonomous problem and has succesfully yielded satisfactory results, for several problems.

Rotor System Equations

The equations of motion for a typical multi-shaft flexible rotor system can be written in the second order form

$$\underline{M}\,\ddot{\mathbf{q}} + \underline{G}\,\dot{\mathbf{q}} + \underline{K}\,\mathbf{q} = \mathbf{Q}^s + \mathbf{Q}^b(\dot{\mathbf{q}}^b, \mathbf{q}^b) \qquad (13)$$

or equivalently in the first order form

$$\underline{A}\,\dot{\mathbf{x}} + \underline{B}\,\mathbf{x} = \mathbf{F} \qquad (14)$$

where

$$\mathbf{x} = \begin{Bmatrix} \dot{\mathbf{q}} \\ \mathbf{q} \end{Bmatrix}, \qquad \mathbf{F} = \begin{Bmatrix} \mathbf{Q}^s \\ \mathbf{Q}^b \end{Bmatrix}$$

and

$$\underline{A} = \begin{bmatrix} \underline{O} & \underline{M} \\ \underline{M} & \underline{G} \end{bmatrix}, \qquad \underline{B} = \begin{bmatrix} -\underline{M} & \underline{O} \\ \underline{O} & \underline{K} \end{bmatrix} \qquad (15)$$

The linear forces of the system are included in the vector **Q** and the nonlinear component forces are included in the sparse vector $\mathbf{Q}^b$. A direct application of the TCM to a large order system such as Eq. (14) would almost always be computationally untenable. Thus, to obtain a mathematical model that is sufficiently small for the TCM to be effective, it is necessary to reduce the order of the original model.

It is propsosed here to develop a procedure to analyze the periodic motion of large order structural systems with nonlinear supports or pseudo supports by using the TCM in conjunction with modal analysis. This algorithm will reduce the original problem to a set of nonlinear algebraic equations involving only the physical coordinates which are associated with the nonlinear supports. This would normally result in a susbstantial reduction in order hopefully rendering the TCM computationally tenable.

The connectivity between the nonlinear coordinates and the system displacement is specified by the connecticity matrix $\underline{S}$ and can be written as

$$\mathbf{q}^b(t) = \underline{S}\,\mathbf{q}(t) \tag{16}$$

where $\mathbf{q}^b$ is the displacement vector associated with the coordinates of the nonlinear supports. The connectivity matrix S is a sparse matrix consisting mostly of zero elements and a few unity elements that ensure that the displacements in the nonlinear supports are identical with the displacements at the corresponding connection points of the linear system. Hence, Eq. (16) is a statement of geometric displacement compatibility for the system.

Modal Analysis

The $\underline{A}$ and $\underline{B}$ arrays of Eq. (14) are not generally symmetric, thus both the right eigenvectors $\mathbf{y}_i$ and adjoint left eigenvectors $\mathbf{z}_j$ must be evaluated for use in a modal expansion. These two sets of vectors satisfy the biorthoganality conditions

$$\begin{aligned} \mathbf{z}_j^T\,\underline{A}\,\mathbf{y}_i &= R_i\,\delta_{ij} && \text{a)} \\ \mathbf{z}_j^T\,\underline{B}\,\mathbf{y}_i &= -\lambda_i\,R_i\,\delta_{ij} && \text{b)} \end{aligned} \tag{17}$$

where R_i is the system norm associated with the eigenvalue λ_i.

With the state vector defined in Eqs. (15), the system eigenvectors are of the form

$$\mathbf{y}_i = \begin{Bmatrix} \lambda_i\,\mathbf{r}_i \\ \mathbf{r}_i \end{Bmatrix} \quad , \quad \mathbf{z}_i = \begin{Bmatrix} \lambda_i\,\mathbf{l}_i \\ \mathbf{l}_i \end{Bmatrix} \tag{18}$$

where $\mathbf{r}_i$ and $\mathbf{l}_i$ are the right and left displacement eigenvectors associated with the physical coordinate vector $\mathbf{q}$. The state response of Eq. (14) is represented by the modal expansion

$$\mathbf{x} = \sum_{i=1}^{2n} \mathbf{y}_i\,\eta_i \tag{19}$$

where η_i is the ith modal coordinate. Substitution of Eq. (19) into Eq. (14) and premultiplication by $\mathbf{z}_i^T$, using the biorthogonality conditions of Eq. (17), yield the 2n equations

$$\dot{\eta}_i - \lambda_i\,\eta_i = \frac{1}{R_i}\,\mathbf{l}_i^T\,(\mathbf{Q}^s + \mathbf{Q}^b) \qquad i = 1, 2, ..., 2n \tag{20}$$

These equations are still coupled due to the nonlinear force vector $\mathbf{Q}^b$. For a large order system, it is not normally necessary nor is it feasible to retain all the modal information when determining the system steady state response. Usually only n lower modes are retained in the modal expansion of Eq. (19), thus there are correspondingly $\hat{n}$ equations in Eq. (20).

SOLUTION PROCEDURE

Following the TCM procedure, periodic solution forms are assumed for the system physical coordinates, the nonlinear subset of the system physical coordinates, and the generalized coordinates in the modal expansion. i.e.,

$$\mathbf{q} = \mathbf{a}_0 + \sum_{j=1}^{m} \left[\mathbf{a}_j \cos(\omega_j t) + \mathbf{b}_j \sin(\omega_j t) \right] \qquad \text{a)}$$

$$\mathbf{q}^b = \mathbf{a}_0^b + \sum_{j=1}^{m} \left[\mathbf{a}_j^b \cos(\omega_j t) + \mathbf{b}_j^b \sin(\omega_j t) \right] \qquad \text{b)} \qquad (21)$$

$$\boldsymbol{\eta} = \mathbf{a}_0^\eta + \sum_{j=1}^{m} \left[\mathbf{a}_j^\eta \cos(\omega_j t) + \mathbf{b}_j^\eta \sin(\omega_j t) \right] \qquad \text{c)}$$

By choosing N equally spaced collocation points and evaluating the variables of Eq. (21) at these time points, the following set of relations is obtained

$$^{o}\underline{q} = \underline{T}\,\underline{C} \qquad \text{a)}$$

$$^{o}\underline{q}^{b} = \underline{T}\,\underline{C}^{b} \qquad \text{b)} \qquad (22)$$

$$^{o}\underline{\eta} = \underline{T}\,\underline{C}^{\eta} \qquad \text{c)}$$

where the ith column of $\underline{C}$ corresponds to the variable q_i (t) evaluated at each of the N collocation points. The ith typical column of $\underline{C}$ is defined by Eq. (3). Similar definitions apply for the arrays of Eqs. (22 b,c).

The unknown coefficient arrays ($\underline{C}, \underline{C}^b, \underline{C}^\eta$) are dependent and are related through the geometric displacement relation of Eq. (16) and the modal expansion of Eq. (19). From Eqs. (22 a,b) and (16),

$$\underline{T}\,\underline{C}^{b} = \underline{T}\,\underline{C}\,\underline{S}^{T} \qquad (23)$$

and by utilizing the form of the system right vectors, Eq. (18), the modal expansion for the system physical coordinates may be written as

$$\mathbf{q} = \sum_{i=1}^{\hat{n}} \mathbf{r}_i \eta_i = \mathbf{r}\,\boldsymbol{\eta} \qquad (24)$$

Thus, from Eq. (22a) and (24) the following relation between physical coordinate and normal coordinate Fourier coefficients is obtained:

$$\underline{T}\,\underline{C} = \underline{T}\,\underline{C}^{\eta}\,\underline{r}^{T} \qquad (25)$$

The substitution of this constraint relation into Eq. (23) gives

$$\underline{C}^b = \underline{C}^\eta \underline{T}^T \underline{S}^T \tag{26}$$

The next step in establishing the solution is to apply the TCM procedure to the set of pseudo modal equations, Eq. (20). Utilizing the equivalent form of Eqs. (5) and (8), Eq. (20) may be written as

$$\omega \underline{T} \underline{D} \mathbf{c}_i^\eta - \lambda_i \underline{T} \mathbf{c}_i^\eta = {}^o\mathbf{f}_i \tag{27}$$

where:

$${}^o\mathbf{f}_i = \frac{1}{R_i} \begin{bmatrix} \mathbf{l}_i^T (\mathbf{Q}^s (t_1) + \mathbf{Q}^b (t_1)) \\ \cdot \\ \cdot \\ \cdot \\ \mathbf{l}_i^T (\mathbf{Q} (t_N) + \mathbf{Q}^b (t_N)) \end{bmatrix} \tag{28}$$

The elements of the ${}^o\mathbf{f}_i$ vector are the RHS values of Eq. (20) evaluated at the collocation points, and are functions of the nonlinear displacements $\mathbf{q}^b$ and velocities $\mathbf{q}^b$.

Equation (27) can be rearranged to the form

$$\mathbf{c}_i^\eta = [(\omega\underline{D} - \lambda_i \underline{I})^{-1} (\underline{T}^T \underline{T})^{-1}] \underline{T}^T \, {}^o\mathbf{f}_i \tag{29}$$

$$i = 1, 2, ..., n$$

which is a typical column of the array of modal coordinate Fourier coefficients, $\underline{C}^\eta$. The combination of relations (29) with Eq. (26) results in a set of nonlinear algebraic equations in terms of Fourier coefficients for the physical coordinate subset $\mathbf{q}^b$.Thus, the size of the problem has been substantitally reduced and the location of a solution is computationally more feasible.

The iterative procedure for estimating the Fourier coefficients $\underline{C}^b$ can be summarized in the following steps:

1. Choose a starting value for $\underline{C}^b$.
2. Compute ${}^o\mathbf{q}^b$ using Eq. (22 b).
3. Compute $\underline{C}^\eta$ using Eqs. (19).
4. Evaluate and update the value for $\underline{C}^b$ using Eq. (26).
5. Check convergence between steps 1. and 4.

The procedure involves the solution of a set of nonlinear equations and its success depends upon the effectiveness of the numerical routine utilized. The optimization routine based on the secant method from the IMSL subroutine library proved to be very effective with convergence being achieved for a wide variety of starting points. The error norm in the algebraic equations appears to be a reasonable measure of the solution accuracy.

NUMERICAL EXAMPLES

The results of analyzing three example systems are presented below. The first two are relatively small order systems and are analyzed directly in terms of physical coordinates. The third example is a larger order dual shaft rotor system that utilizes modal analysis in conjunction with the TCM.

Journal - Hydrodynamic Bearing System

Consider a single rotating journal on a hydrodynamic bearing as illustrated in Fig. 1. With reference to this figure, O is the bearing center, C is the geometric center of the journal, and c represents the radial bearing clearance. The mass center of the journal is assumed to be displaced from the geometric center by the cg offset e. During rotation this offset gives rise to a rotating unbalance force which is synchronous with journal spin frequency. The converging wedge that arises due to the eccentricity of the journal gives rise to a pressure field in the fluid film that supports the load.

The nondimensionalized equations of motion of the journal assume the form:

$$\begin{aligned} \ddot{v} &= F_r \cos\phi + F_t \sin\phi + u \cos(t+\beta) + g \\ \ddot{w} &= F_r \sin\phi - F_t \cos\phi + u \sin(t+\beta) \end{aligned} \tag{30}$$

In these equations, v and w represent the nondimensional displacement coordinates of the journal center with respect to a fixed reference frame. The quantities g and u represent the gravity and unbalance parameters, and F_r and F_t represent the radial and tangential fluid film force components acting on the journal.

Using short bearing theory, Reynolds equation can be integrated to obtain closed form expressions for the plain journal bearing force components, e.g. (Holmes, 1960). Thus,

$$F_r = -B \left[\frac{\pi(1+2\varepsilon^2)\dot{\varepsilon}}{(1-\varepsilon^2)^{5/2}} + \frac{2\varepsilon^2(1-2\dot{\phi})}{(1-\varepsilon^2)^2} \right]$$

$$F_t = +B \left[\frac{4\varepsilon\dot{\varepsilon}}{(1-\varepsilon^2)^2} + \frac{\pi\varepsilon(1-2\dot{\phi})}{2(1-\varepsilon^2)^{5/2}} \right] \tag{31}$$

where, $\varepsilon = (v^2 + w^2)^{1/2}$, $\phi = \arctan(w/v)$
and B is a bearing parameter that is dependent on the fluid viscosity, and geometry of the bearing.

Clearly F_r and F_t are highly nonlinear functions of the response variables. Typically, the journal equations, Eqs. (30) are linearized about the static equilibrium position. The resulting linear response corresponds to an elliptical orbit centered at the equilibrium position. Application of the TCM to this problem can yield an orbit which is quite different the linearized response as displayed in Fig. 2.

An interesting fact revealed by the TCM is that the higher harmonics in the response of the journal may not be negligible as contrasted with many nonlinear problems. In the results presented, at least 8 harmonics were required to obtain close agreement between the TCM and numerical integration. In this case, many analytical procedures, such as the Describing Function Method, which neglect harmonics above the fundamental would not adequately describe the dynamics of the journal.

Flow Induced Vibration

Consider the problem of quasi-steady analysis of the transverse galloping of a long prism of square cross-section (Blevins, 1977; Parkinson and Smith, 1964).The equation of motion for the single degree-of-freedom oscillator is

$$y'' + 2\zeta y' + y = n U^2 c_f \qquad (32)$$

where U is the non-dimensional velocity of wind and y is the non-dimensional vibration displacement. The non-dimensional aerodynamic force coefficient c_f is obtained by experimental measurements in a wind tunnel and can be approximated by a polynomial in α, the angle of attack, or equivalently (y'/U).

$$c_f = n\left[A U y' - \frac{B}{U}(y')^3 + \frac{C}{U^3}(y')^5 - \frac{D}{U^5}(y')^7 \right] \qquad (33)$$

From a curve-fit to experimental values, A = 2.69, B = 168, C = 6270, D = 59,900 (for a Reynolds number = 22,300) ; n is a mass parameter, which is a function of the prism dimensions and the density of air; ζ is the linear viscous damping coefficient.

The second-order nonlinear autonomous equation (32) has been shown to exhibit self-excited oscillations and an analysis by the method of averaging was carried out by (Parkinson, 1964). It was found that the amplitude (A_1) vs wind velocity curves for various values of the damping coefficient collapse into a single curve if normalized by $nA_1 / 2\zeta$.

The first harmonic amplitudes obtained by the application of TCM are shown in Fig. 3. As is evident from the figure, the response exhibits a hysteresis loop. A choice of different initial guesses helped the procedure converge to the multiple solution points. It is identical to the figure in Parkinson and Smith (1964) and indicates that the collocation procedure developed here is valid for problems with multiple solution points.

Dual Shaft Rotor System

The dual-shaft rotor system with configuration shown in Fig. 4 includes a nonlinear bearing at station 6 and excited by rotating unbalance in shaft 1 and a static side load at station 6. Rotor (1,2) is modelled as a (6,4) station, (24,16) degree - of - freedom, (5,3) element assembly with stations as indicated in Fig. 4. Detailed rotor configuration data is provided in (Nelson and Alam, 1983). The rotating assemblies are connected to a rigid foundation by linear bearings at stations 1 and 7 and are interconnected by a linear bearing between stations 4 and 10. A nonlinear bearing with cubic stiffness variation and linear viscous damping connects shaft 1 to the rigid foundation at station 6. The nonlinear bearing force components are given by the relations:

$$\begin{aligned} F_Y &= -(k_1 r + k_3 r^3)\frac{v}{r} - c_v \dot{v} \\ F_Z &= -(k_1 r + k_3 r^3)\frac{w}{r} - c_w \dot{w} \end{aligned} \qquad (34)$$

where $r = (v^2 + w^2)^{1/2}$, and $k_1 = 50{,}000$ lbf/in, $k_3 = 50 * 10^9$ lbf / in^3, and $c_v = c_w = 20$ lbf-s/in.

The unbalance distribution of the rotating assembly consists of a single concentrated unbalance at station 2 with a cg eccentricity of 0.95 mils. In addition, a static side load acts on the system at station 6. Shaft 1 spins at 80,000 Rpm and shaft 2 co-rotates at 120,000 Rpm.

It should be noted that the linear subsystem is not totally constrained. Thus, an "artificial support" is added at station 6 to eliminate a singularity. This influence is then subsequently removed from the model by subtracting its influence in the nonlinear forces. A value of 10,000 lbf / in at station 6 was arbitrarily selected for this system. The nonlinear radial force versus displacement is shown in Fig. 5. The linear bearing stiffnesses are 150,000, 50,000, and 100,000 lbf / in at station 1, 4-10, and 7 respectively.

Displacement orbits, as determined using the TCM procedure, for this system are plotted in Fig. 6 for two stations and a side load of 100 lbf acting in the negative z direction. The orbit distortion clearly indicates the presence of higher harmonics in the response.

CONCLUSIONS

A numeric-analytic procedure based on the trignometric collocation method has been developed and implemented for estimating the periodic response of engineering systems. The procedure allows for estimating periodic forced response and for locating limit cycles of self-excited systems. A component mode synthesis strategy coupled with the TCM extends the method to large order system application.

Three example analyses are presented. Two of small order in physical coordinates and the third on larger order using the modal strategy. Preliminary indications are that this method may be very effective in estimating the periodic response of both small and large order systems. Additional work is required to further test its generality, to handle systems with subharmonic response and, to ascertain the stability of the located periodic responses. Study on the speed and accuracy of the necessary computational work should also lead to improvement in the utility of the approach.

REFERENCES

Atherton, D. F., 1982, *Nonlinear Control Engineering*, Van Nostrand Reinhold: London.

Blevins, R. D., 1977, "Flow Induced Vibration," Van Nostrand Reinhold, New York.

Hagedorn P., 1982, *Nonlinear Oscillations*, Clarendon Press: Oxford.

Holmes, R., 1960, "Vibration of a Rigid Shaft on Short Sleeve Bearings," J. Mech. Engr. Sciences, Vol. 2, No. 4m pp. 337-341

Nataraj,C., Nelson, H. D. and Arakere, N., 1985, "Effect of Coulomb Spline on Rotor Dynamic Response," *Instability in Rotating Machinery*, NASA CP 2409, pp. 225-233.

Nayfeh, A. H., 1981, *Introduction to Perturbation Techniques*, John Wiley & Sons: New York.

Nelson, H. D., and Alam, M., 1983, "Transient Response of Rotor Bearing Systems using Component Mode Synthesis: Part VI Blade Loss Response Spectrum," NASA Grant NAG3-6 Report.

Parkinson, G. V. and Smith, J. D., 1964, "The Square Prism as an Aeroelastic Nonlinear Oscillator," Quart. J. Mech. & App. Math., Vol. 17, pt. 2, pp. 225-239.

Saito, S., 1985, "Calculation of Nonlinear Unbalance Response of Horizontal Jeffcott Rotors Supported by Ball Bearings with Radial Clearances," *ASME J. of Vibration, Accoustics, Stress and Reliability in Design*, Vol. 107, pp. 416-420.

Samoilenko, A, M, and Ronto, N. I., 1979, *Numerical-Analytical Methods of Investigating Periodic Solutions*, Mir. Publishers: Moscow.

Stokes, A., 1972, "On the Approximation of Nonlinear Oscillations," *J. Differential Equations*, Vol. 12, pp. 535-558.

Urabe, M., 1965, "Galerkin's Procedure for Nonlinear Periodic Systems," Archives of Rational Analysis, Vol. 20, pp. 120-152.

Urabe, M. and Reiter, N., 1966, "Numerical Computation of Nonlinear Forced Oscillations by Galerkin's Procedure," J. Mathematical Analysis Applications, Vol. 14, pp. 107-140.

Yamauchi, S. 1983, "The Nonlinear Vibration of Flexible Rotors: First Report, Development of a New Analysis Technique," J. ASME, Vol. 49, No. 446, Series C, pp. 1862-1868.

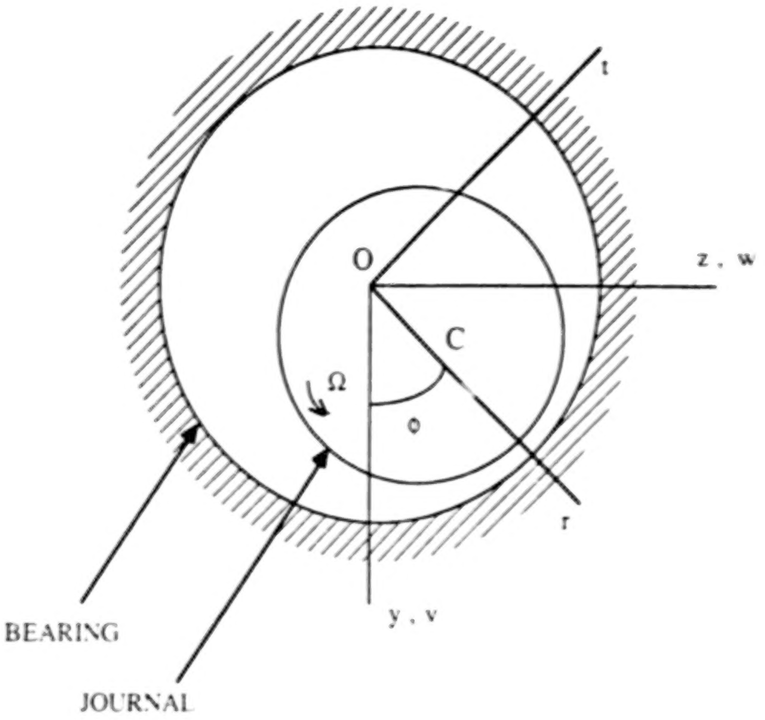
t
O
z , w
C
Ω
φ
r
y , v
BEARING
JOURNAL

Fig. 1 Journal Bearing Configuration

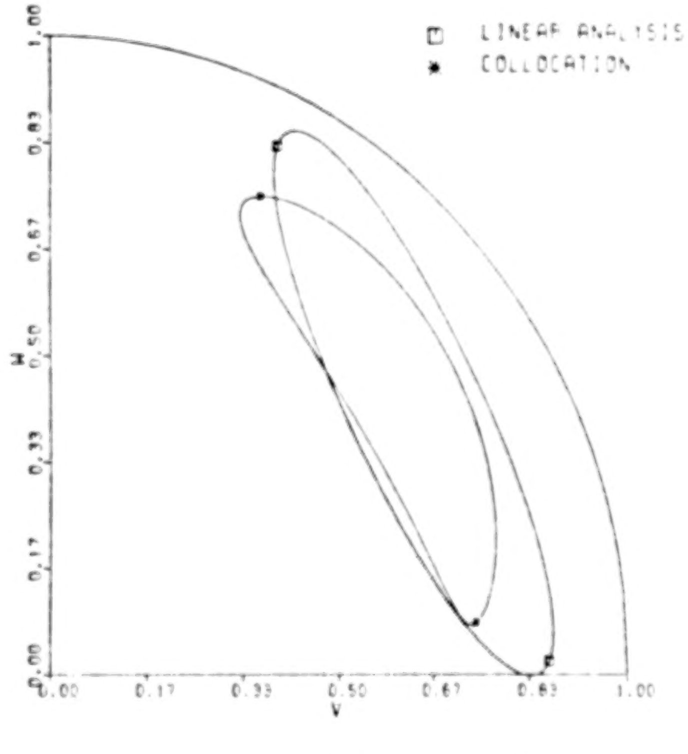

Fig. 2 Linearized and Collocation Solutions

ORIGINAL PAGE IS
OF POOR QUALITY

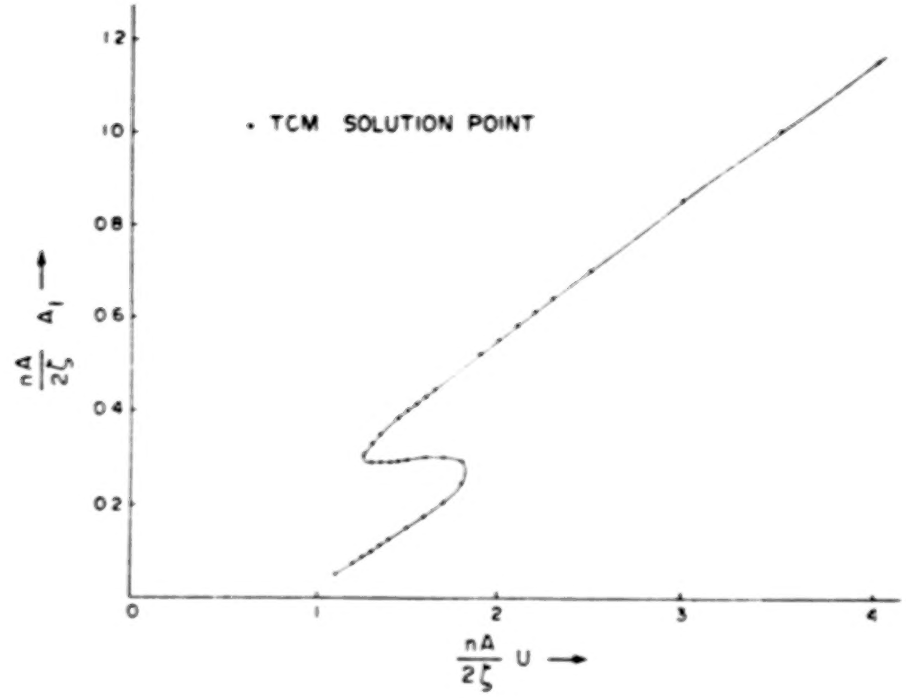

Fig. 3 First Harmonic Amplitude vs. Wind Velocity

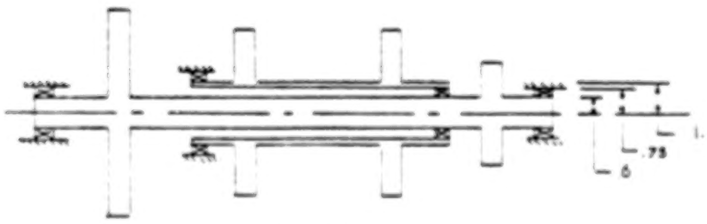

a) Physical System

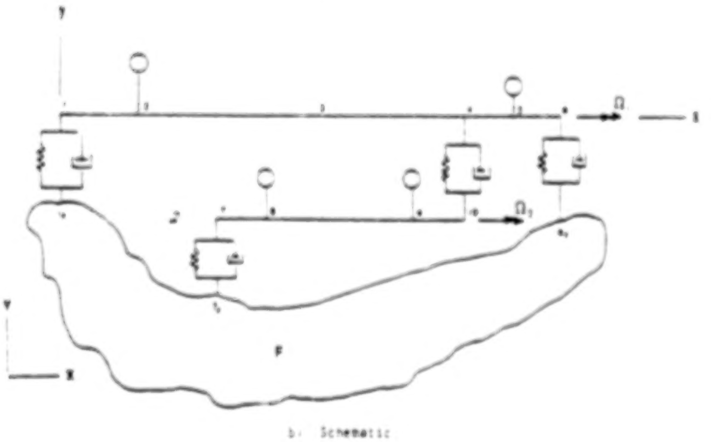

b) Schematic

Fig. 4 Dual Rotor Schematic and Model

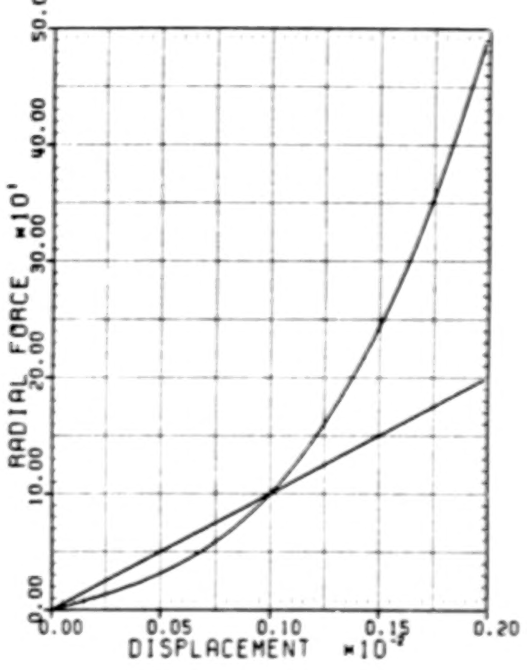

Fig. 5 Nonlinear Force-Displacement Relation

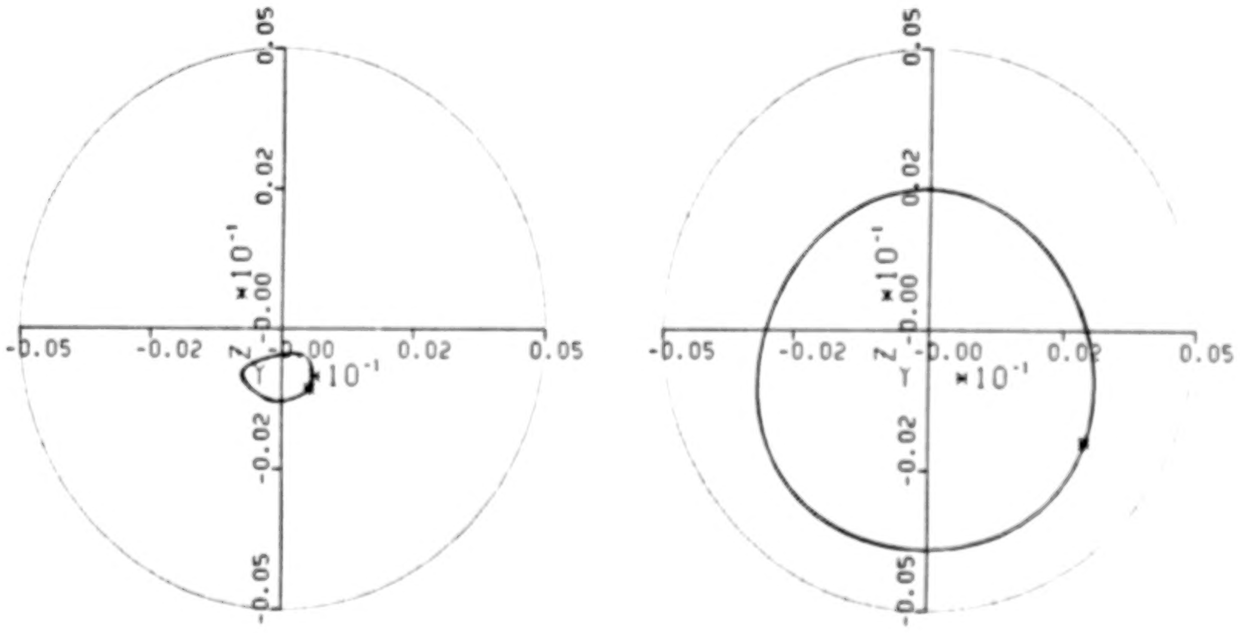

(a) Station 6

(b) Station 10

Fig. 6 Rotor Station Orbits

N88-23229

PIEZOELECTRIC PUSHERS FOR ACTIVE VIBRATION CONTROL OF ROTATING MACHINERY

Alan B. Palazzolo* and Albert F. Kascak
U.S. Army Aviation Research and Technology Activity - AVSCOM
Structural Dynamics Branch
NASA Lewis Research Center

ABSTRACT

The active control of rotordynamic vibrations and stability by magnetic bearings and electromagnetic shakers has been discussed extensively in the literature. These devices, though effective, are usually large in volume and add significant weight to the stator. The use of piezoelectric pushers may provide similar degrees of effectiveness in light, compact packages.

Tests are currently being conducted at the NASA Lewis Research Center with piezoelectric pusher-based active vibration control. The paper presents results from tests performed on the NASA test rig as preliminary verification of the related theory.

PRECEDING PAGE BLANK NOT FILMED

---

*Texas A&M University, College Station, Texas.

MODEL OF PIEZOELECTRIC PUSHER

A piezoelectric pusher consists of a stack of piezoelectric ceramic disks that expands in response to an applied voltage. The extension and force of the pusher depends on the number and thickness of the disks and on the cross sectional area of the disks, respectively.

The ideal model consists of a prescribed displacement α, which is proportional to the input voltage, and a spring representing the stiffness of the stack.

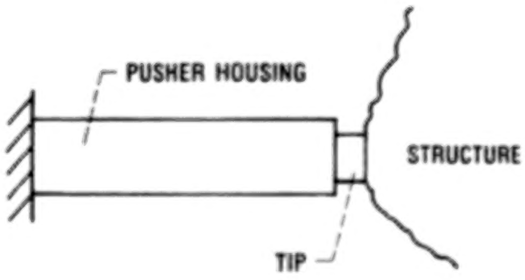
PUSHER HOUSING
STRUCTURE
TIP

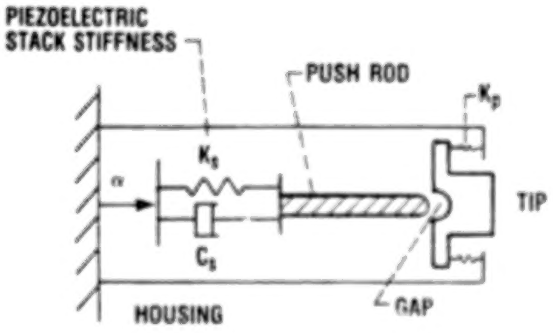
PIEZOELECTRIC STACK STIFFNESS
PUSH ROD
K_p
K_s
α
C_s
TIP
HOUSING
GAP

CD-88-32659

DEFLECTION VERSUS INPUT VOLTAGE

The figure shows a typical voltage versus tip displacement plot for the pusher in the previous figure. The curve in this plot provides an approximate description of the internal displacement α versus voltage relation, since the tip is unloaded and since the preload spring in the previous figure is very light (114 lb/in.). Therefore, it is assumed that the voltage sensitivity for α is $S_A = -1448$ V/in.

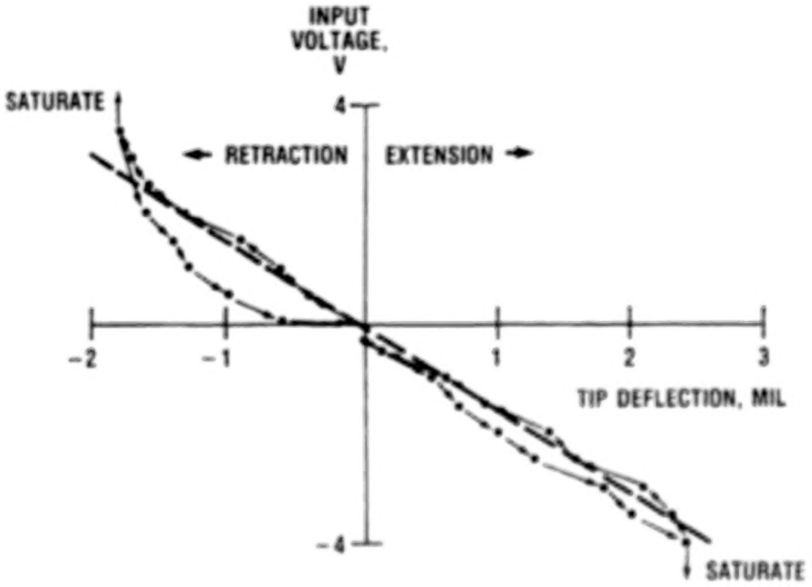

CD-88-32880

DEFLECTION VERSUS LOAD

Load deflection characteristics of the pushers, were obtained by securing each one in a solid cylinder, applying the load W, which produces reaction R on the protruding tip of the pusher, and then measuring the tip deflection. Repeated tests with three separate pushers yielded an average stiffness of approximately 20 000 lb/in.

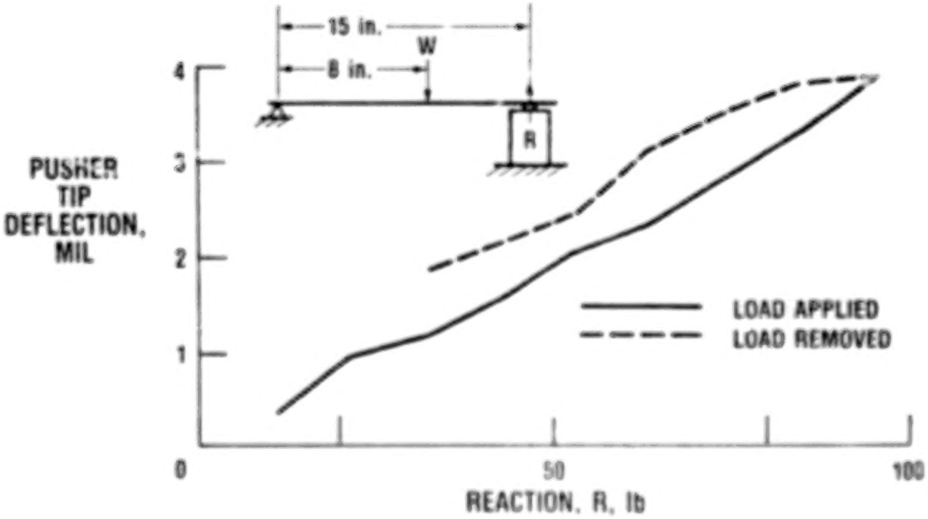

CD-88-32861

TEST RIG

This figure shows a simple sketch of the test rig, which consists of a 1-in.-diameter shaft, a 24-in.-long, 5.1-in. diameter, 3.15-lb overhung disk, and two squirrel-cage-mounted ball bearings. The outboard bearing is externally forced by an orthogonal pair of piezoelectric pushers, which are, in turn, positioned opposite the two eddy-current displacement probes d_3 and d_4. The uncoupled, velocity feedback control law used is

$$\alpha_{hor} = -G'_{hor}\,\dot{d}_4$$

$$\alpha_{ver} = -G'_{ver}\,\dot{d}_3$$

where G' represents a gain factor.

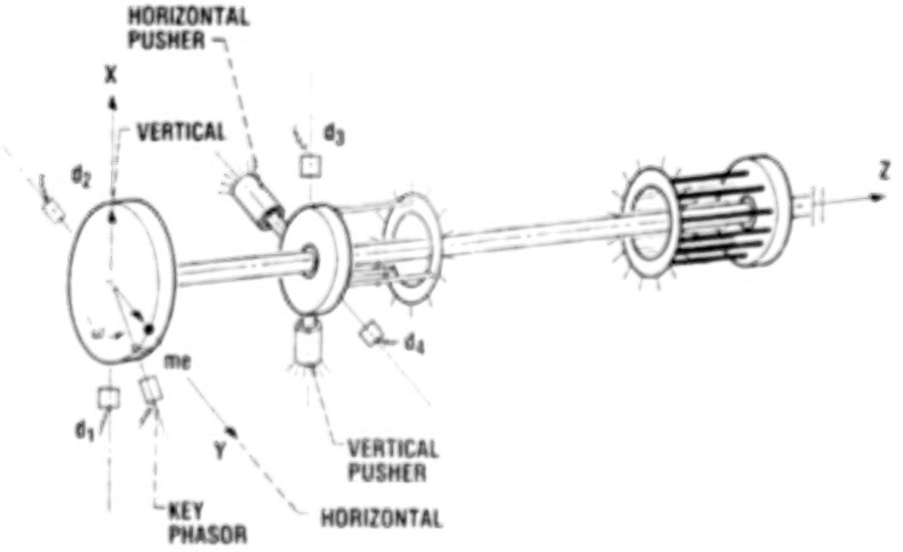
HORIZONTAL PUSHER
X
VERTICAL
d_3
d_2
Z
ω
me
d_4
d_1
Y
VERTICAL PUSHER
KEY PHASOR
HORIZONTAL

CD-88-32862

FEEDBACK CIRCUIT

This figure outlines how effective damping can be calculated once the probe and actuator sensitivities and actuator stiffness are known. The horizontal and vertical active damping were set equal in this arrangement, that is, $C_A = 1.57G$ lb sec/in., where G is the amplifier gain.

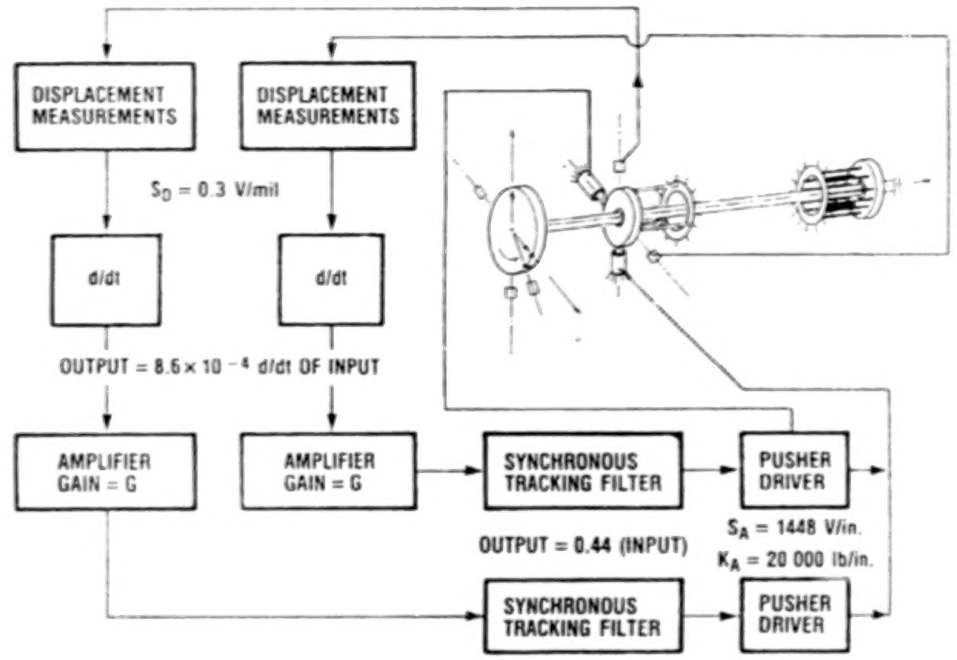
DISPLACEMENT MEASUREMENTS
DISPLACEMENT MEASUREMENTS
$S_D = 0.3$ V/mil
d/dt
d/dt
OUTPUT = 8.6×10^{-4} d/dt OF INPUT
AMPLIFIER GAIN = G
AMPLIFIER GAIN = G
SYNCHRONOUS TRACKING FILTER
PUSHER DRIVER
$S_A = 1448$ V/in.
$K_A = 20\ 000$ lb/in.
OUTPUT = 0.44 (INPUT)
SYNCHRONOUS TRACKING FILTER
PUSHER DRIVER

CD-88-32863

UNCOUPLED VELOCITY FEEDBACK $\alpha = G'\dot{d}$

ACTIVE DAMPING $C_A = K_A G'$

ACTUATOR INPUT VOLTAGE FOR α DISPLACEMENT, V_A

$V_A = S_A \alpha$

SUBSTITUTING THE DATA $V_A = S_A G'\dot{d} = 0.44\, S_D(8.6 \times 10^{-4}\dot{d})G$

RESULTS IN

$$S_A \frac{C_A}{K_A}\dot{d} = S_D \times G(3.8 \times 10^{-4})\dot{d}$$

OR

$$C_A = 3.8 \times 10^{-4}\frac{S_D}{S_A} \times G \times K_A = 1.57 \times G \text{ lb sec/in.}$$

CD-88-32864

TEST VIBRATION AMPLITUDES FOR PROBES d_1 AND d_2

The rotor was carefully balanced and then intentionally unbalanced by a known amount (0.14 oz in.), in order to compare the test results with those predicted by an unbalance response computer program. The top figure shows the test vibration amplitudes versus speed plots for the disk probe d_1. The family of curves is generated by switching amplifier gains in the feedback circuit and calculating effective damping according to the feedback relationships. The bottom figure shows the test vibration amplitudes for disk probe d_2.

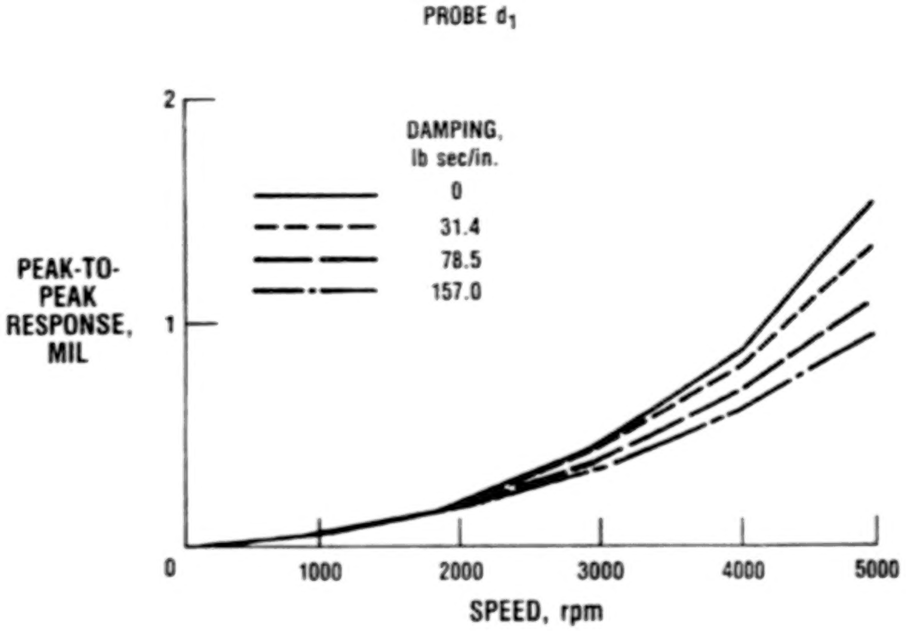

CD-88-32865

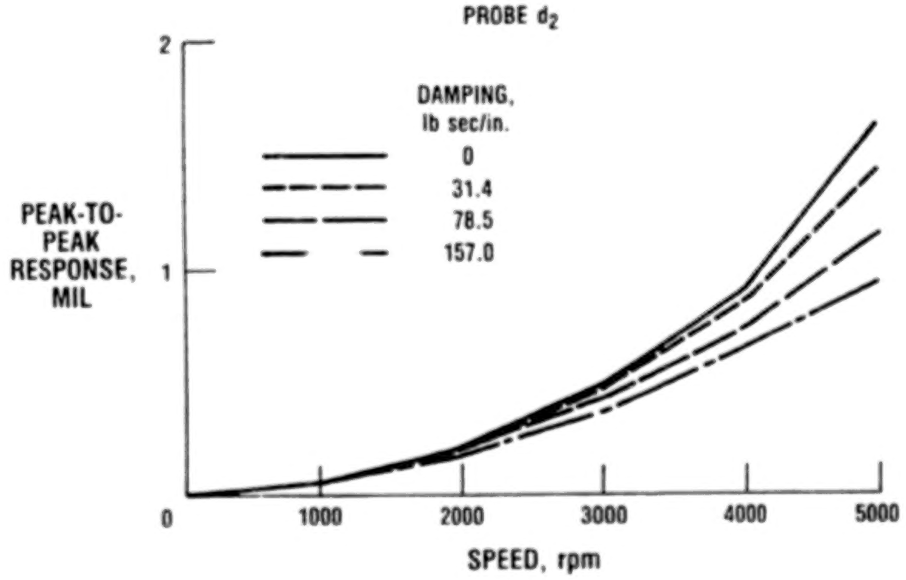

CD-88-32866

COMPUTED VIBRATION AMPLITUDES FOR PROBE d_1 OR d_2

This figure shows the computer simulation results for either probe d_1 or d_2. Although the test results show less damping than the predicted results exhibit, the trends are very similar, and the test damping is still approximately (57 lb sec/in.).

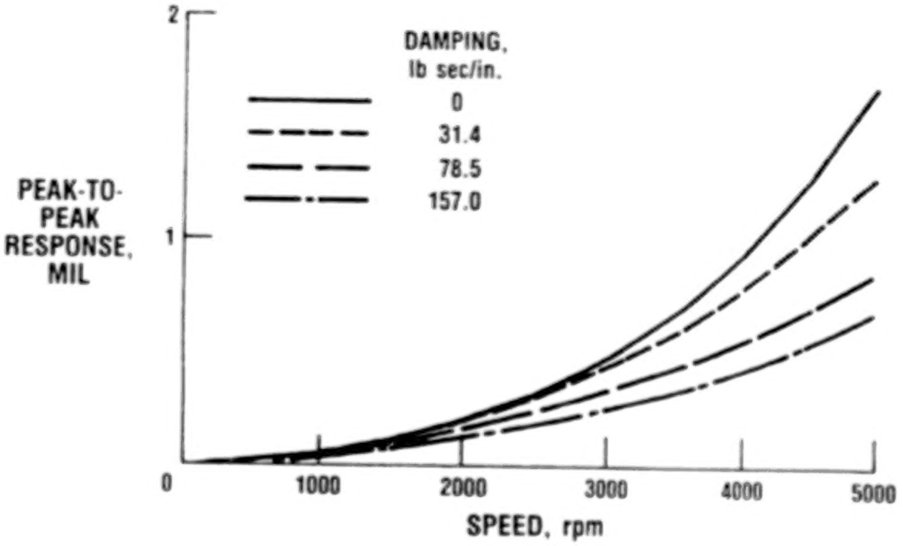

CD-88-32867

TEST VIBRATION AMPLITUDES FOR PROBES d_3 AND d_4

The top figure shows the test vibration amplitudes for the bearing housing probe d_3. The bottom figure shows the test vibration amplitudes for the bearing housing probe d_4.

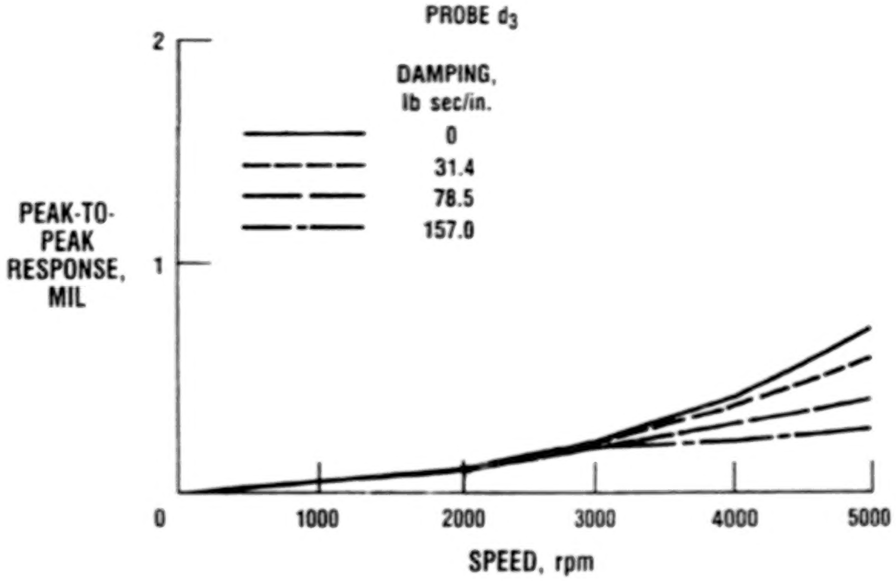

CD-88-32868

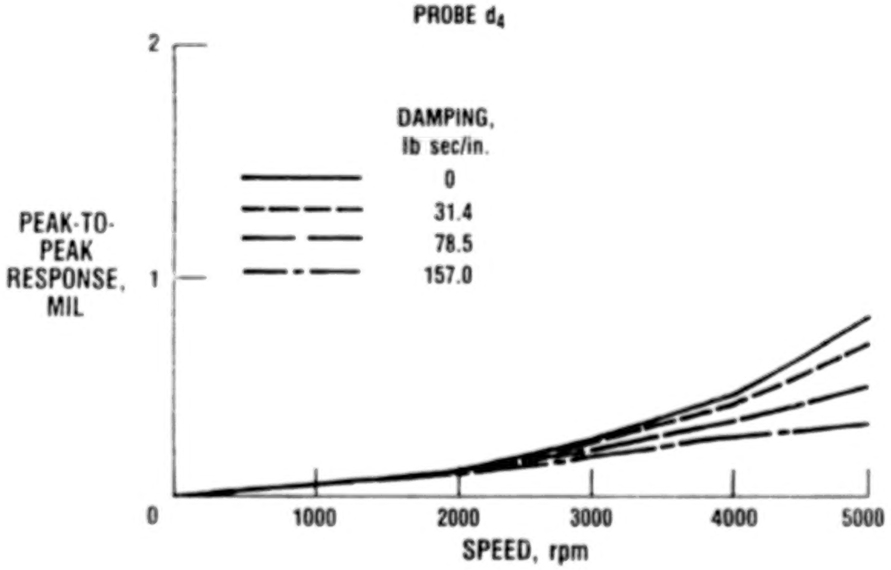

CD-88-32869

COMPUTED VIBRATION AMPLITUDES FOR PROBE d_3 OR d_4

This figure shows the computer simulation results for either probe d_3 or d_4. The results again indicate that the equation in the feedback circuit overpredicts the active damping. However, the pushers do provide approximately (80.0 lb sec/in.) damping at the highest amplifier gain setting.

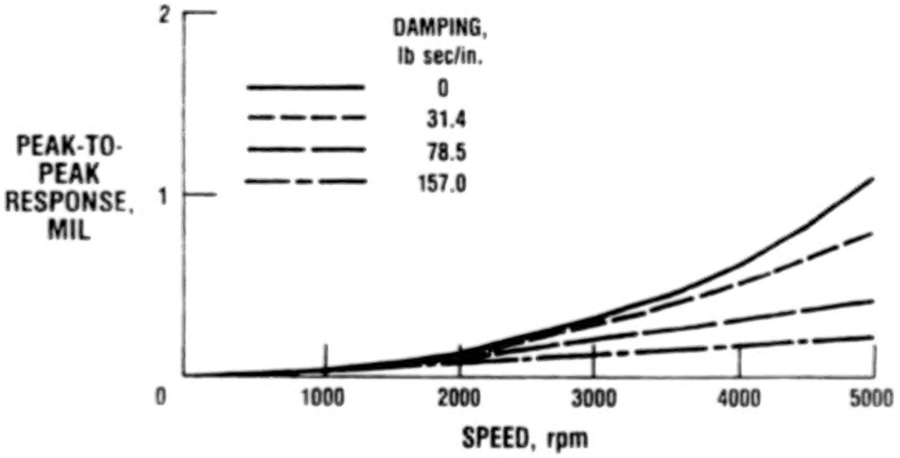

CD-88-32870

AIRCRAFT TURBINE ENGINE (T-64)

Computer simulations were performed to estimate the pusher stroke and force requirements for providing useful levels of damping in actual turbomachinery. The engine in this figure consists of a power turbine drive shaft supported by two rolling-element bearings which rotate concentrically inside a hollow gas-generator drive up to 17 000 rpm. There are four rolling-element bearings associated with the gas-generator turbine that runs between 10 500 to 18 230 rpm. The power turbine drive shaft has a span of 55.5 in. and weighs 91.5 lb. The gas-generator driveshaft is 44.2 in. long and weighs 112 lb.

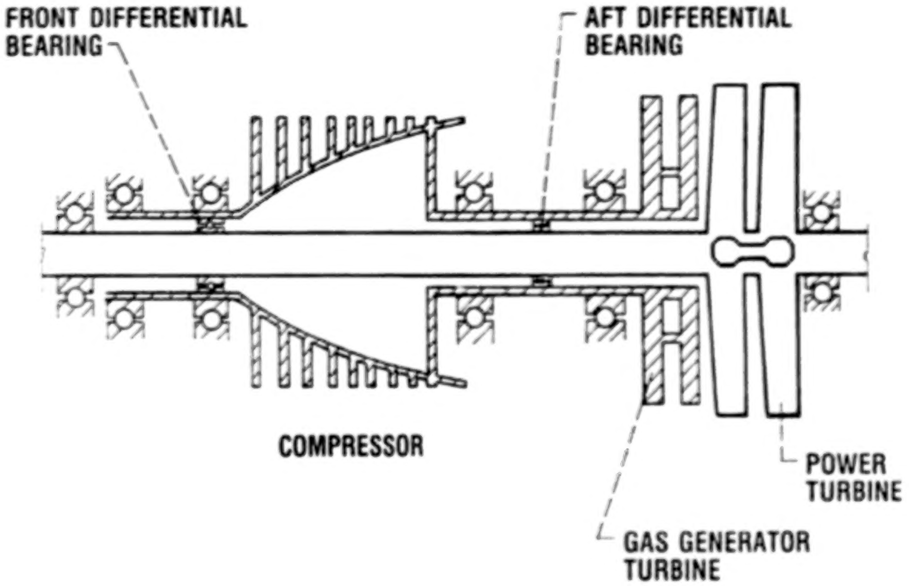
FRONT DIFFERENTIAL BEARING
AFT DIFFERENTIAL BEARING
COMPRESSOR
POWER TURBINE
GAS GENERATOR TURBINE

CD-88-32871

FINITE-ELEMENT MODEL

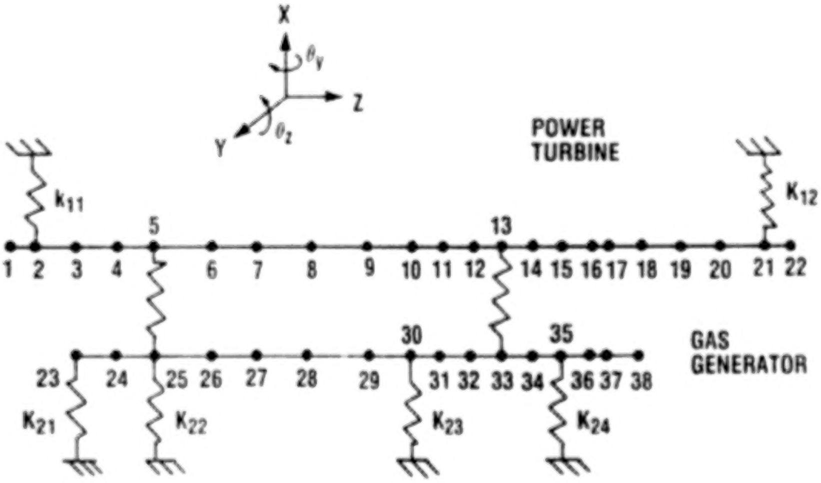
X
θy
Z
Y
θz
POWER TURBINE
K11
K12
1 2 3 4 5 6 7 8 9 10 11 12 13 14 15 16 17 18 19 20 21 22
30
35
GAS GENERATOR
23 24 25 26 27 28 29 31 32 33 34 36 37 38
K21
K22
K23
K24

CD-88-32872

MODE SHAPE PLOTS

The plots below show the lowest, undamped forward mode, the lowest, undamped backward whirl mode, and the second, forward whirl mode for the finite-element model of each set. The upper plot is the power turbine, and the lower is the gas generator. The gas generator participation in the first, forward whirl mode is very small, but it predominates in the first, backward whirl mode. The plot for second, forward whirl mode shows participation of both power turbine and gas generator motion.

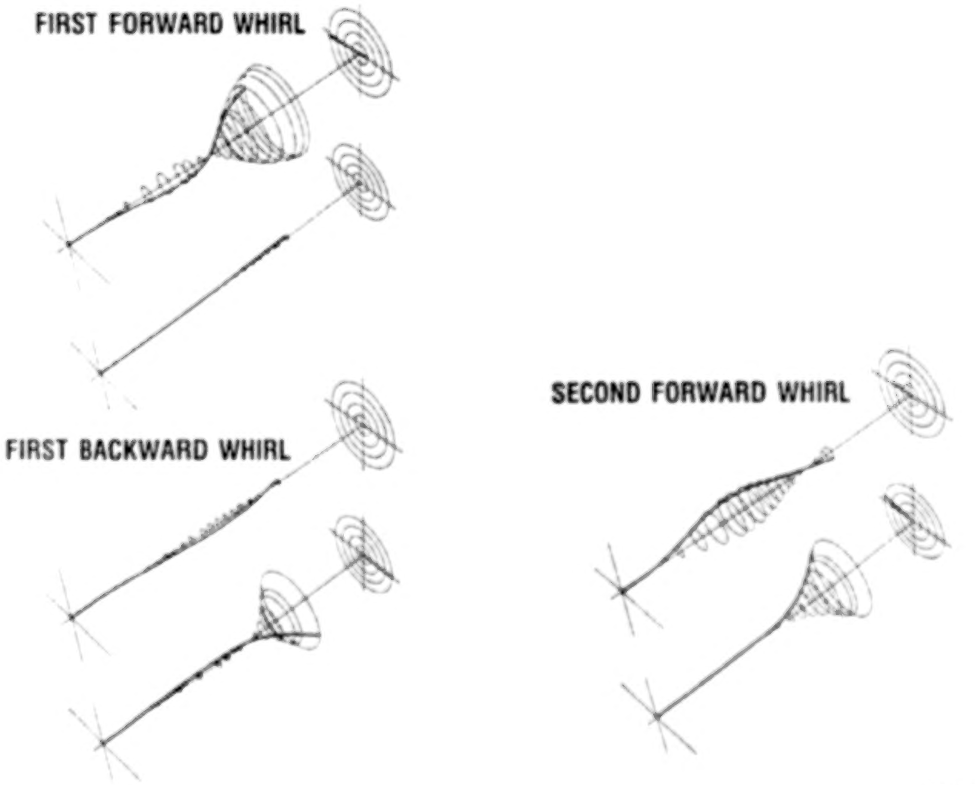
FIRST FORWARD WHIRL
FIRST BACKWARD WHIRL
SECOND FORWARD WHIRL

CD-88-32873

POWER TURBINE STEADY RESPONSE

This figure shows an unbalance response plot at the outboard end of the gas generator (node 36). The system is excited by out-of-phase unbalances of 0.25 oz in. at nodes 8 and 20. The damper is located at the right bearing of the power turbine (node 21). The results show that a 100 lb sec/in. damping value can significantly attenuate vibration at all critical speeds.

POWER TURBINE UNBALANCE, 0.25 oz in.; NODES 8 & 20; GAS GENERATOR SPEED, 15 000 rpm; DAMPER AT NODE 21

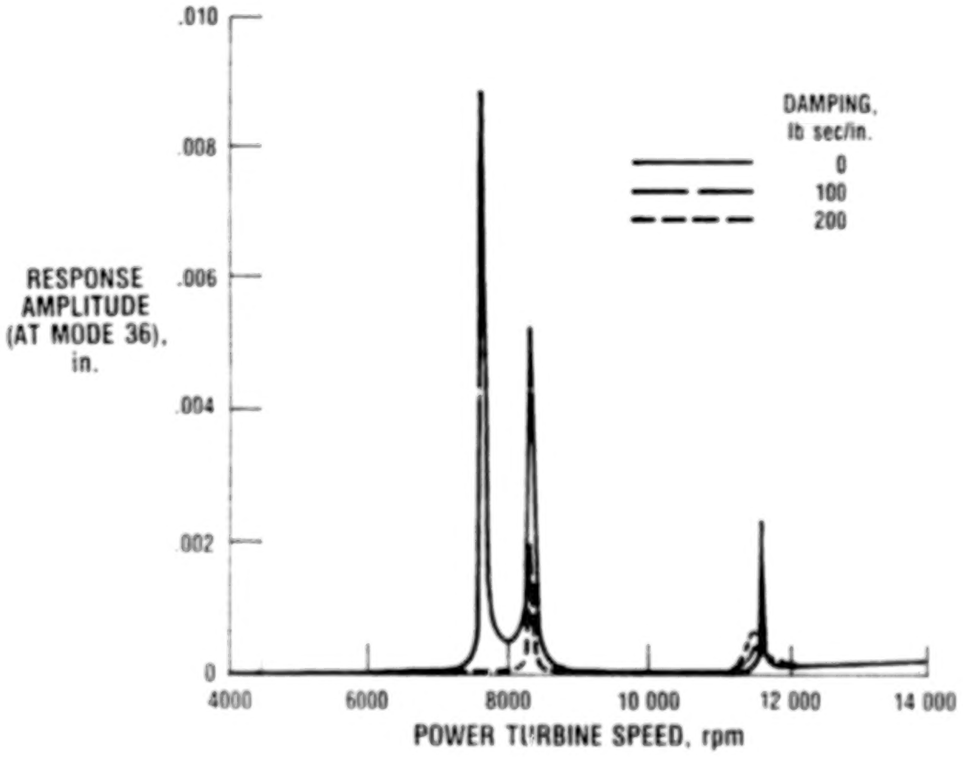

CD-88-32874

PRESCRIBED PUSHER DISPLACEMENT

This figure shows the internal displacement α of the pusher damper for the previous unbalance response run. These results are based on $\alpha = -C\dot{Z}/K$, where C is the active damping value, $\dot{Z}$ is the velocity of the pusher attachment point (node 21), and K, the assumed pusher stiffness, is 25 000 lb/in. Note that the maximum internal displacement of the pusher with $C = 100$ is about 4 mils.

POWER TURBINE UNBALANCE, 0.25 oz in.; NODES 8 & 20; GAS GENERATOR SPEED, 15 000 rpm; DAMPER AT NODE 21; PUSHER STIFFNESS, 25 000 lb/in.

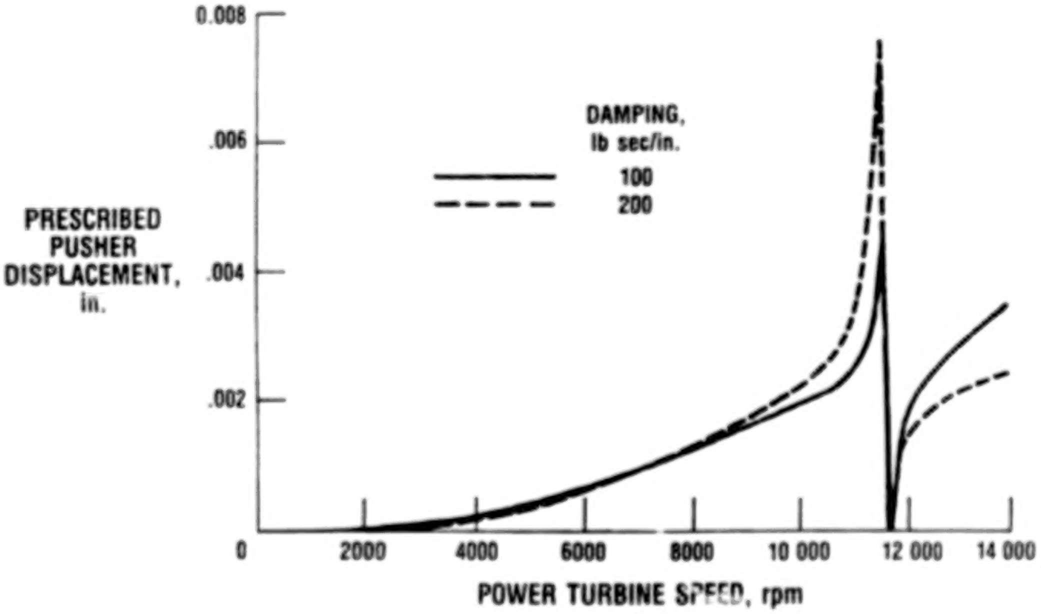

CD-88-32875

REQUIRED PUSHER FORCE VERSUS SPEED

The plot shows pusher force (pusher stiffness times (Z - α) versus speed) for the previous unbalance response run. The maximum pusher force with C = 100 is approximately 100 lb.

POWER TURBINE UNBALANCE, 0.25 oz in.; NODES 8 & 20; GAS GENERATOR SPEED, 15 000 rpm; DAMPER AT NODE 21; PUSHER STIFFNESS, 25 000 lb/in.

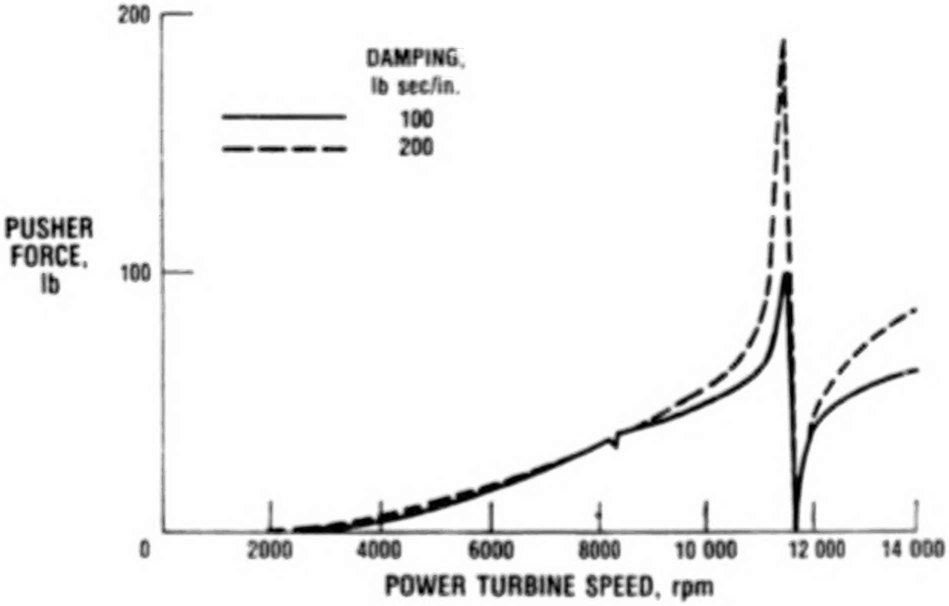

CD-88-32876

POWER TURBINE STEADY RESPONSE

This figure shows the same response as in the previous case. However, the damper is now located at the outboard bearing of the gas generator, that is, at node 36. At this location the damper is ineffective in controlling the lowest mode. This results because the gas generator does not participate in this mode, as shown in the mode shape plots.

POWER TURBINE UNBALANCE, 0.25 oz in.; NODES 8 & 20; GAS GENERATOR SPEED, 15 000 rpm; DAMPER AT NODE 36; PUSHER STIFFNESS, 25 000 lb/in.

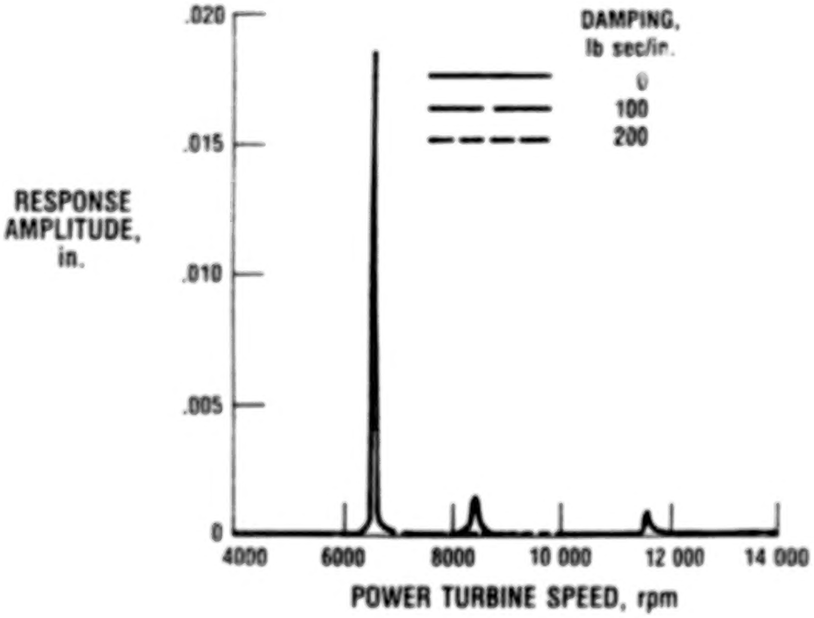

CD-88-32877

VARIATION OF REAL PART VERSUS CROSS-COUPLED STIFFNESS

This rotor-bearing system is unstable if the damper is removed and an Alford type cross couple stiffness of 1000 lb/in. is applied at node 37. The unstable eigenvalue is 3.3 sec^{-1} at 12 390 rpm. This figure shows the real part of the same eigenvalue when a 100-lb sec/in.-damper is installed at node 35. The previously unstable mode is seen to be stable even with a cross-coupled stiffness of 10 000 lb/in.

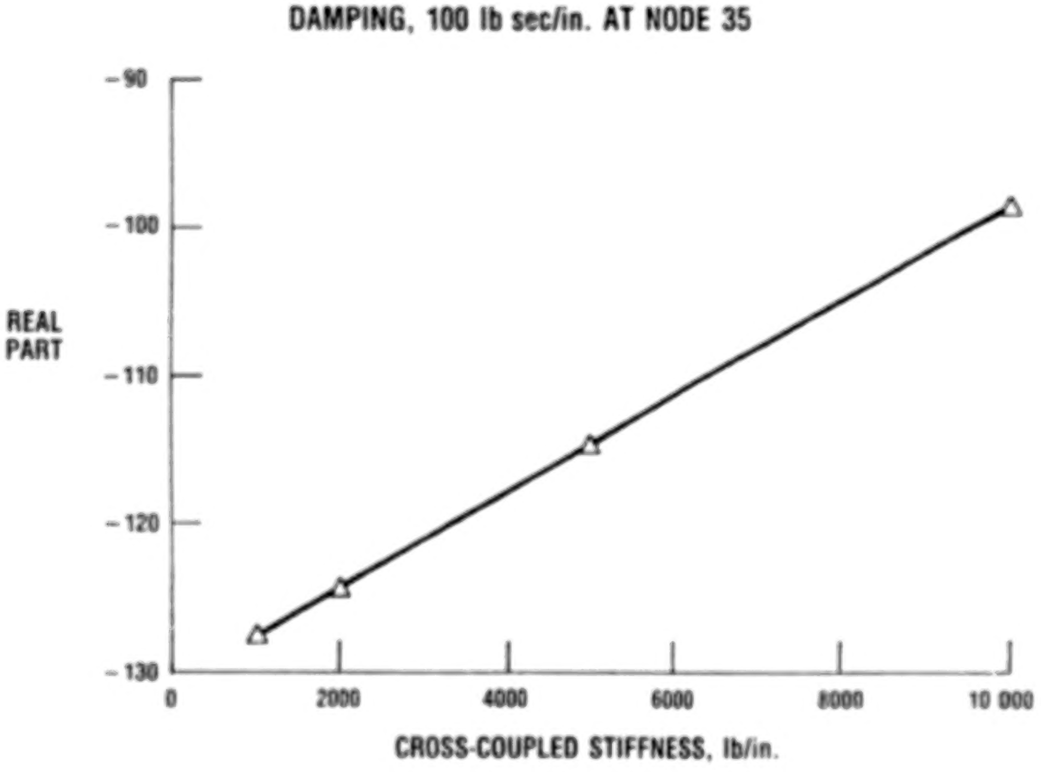

CD-88-32878

SUMMARY

This presentation has examined the potential use of piezoelectric pushers for active control of rotor-bearing system vibrations. The results showed significant levels of active damping contributed by the pushers (50 to 80 lb sec/in.) and very good agreement between vibration response trends predicted by theory and measured on the rig. Finite-element computer simulations showed that significant improvements in rotor stability and unbalance response could be achieved with an active damping of 100 lb sec/in., which requires a pusher with displacement of about 4 mils, force of 100 lb, and a stiffness of 25 000 lb/in.

- **PIEZOELECTRIC PUSHERS APPLIED TO ACTIVE CONTROL OF ROTOR-BEARING SYSTEM VIBRATIONS**
- **TESTING CONDUCTED AT NASA LEWIS SHOWED SIGNIFICANT LEVELS OF ACTIVE DAMPING**
- **COMPUTER SIMULATIONS SHOWED PIEZOELECTRIC PUSHERS EFFECTIVELY CONTROLLED VIBRATION IN ENGINES.**

CD-88-32879

N88-23230

ACTIVE CONTROL AND SYSTEM IDENTIFICATION OF ROTORDYNAMIC STRUCTURE

M. L. Adams
Department of Mechanical and Aerospace Engineering
Case Western Reserve University
Cleveland, Ohio

ABSTRACT

Two general topics are currently at the forefront of investigations by presently active researchers working on problems in the dynamics of rotating machinery. These two topics are Active Control and System Identification, both of which are being actively researched at Case Western Reserve University (CWRU). Four current CWRU research projects are summarized in this paper: (1) Active control of rotor system dynamics, this work being performed on site at NASA Lewis by the CWRU rotordynamics research team, (2) Attenuation of rotor vibration using controlled-pressure hydrostatic bearings, (3) A new seal test facility at CWRU for measuring isotropic and anisotropic linear rotordynamic characteristics, and (4) The use of rotordynamic instability thresholds to accurately measure bearing rotordynamic characteristics.

ACTIVE CONTROL RIG

This test rig has been recently installed at NASA Lewis Research Center to perform a wide variety of experimental studies on techniques for actively controlling rotor system dynamics. The rig is shown here with four independently controllable electromagnetic shakers. Other types of servomechanisms are also presently being designed for use in this rig, including a magnetic bearing. This test facility is fully operational except for establishing the best type of servomechanism for delivering the controlled input forces.

In parallel with perfecting this general purpose test facility, we are also developing mathematical and conputational approaches for the controller. Published work in recent years have focused on control approaches based upon detailed a priori dynamic characteristics of the rotor system and these approaches has been successfully demonstrated in laboratory test setups. The approaches being researched at CWRU are focused on optimization (i.e., minimization) methods, not requiring a priori dynamic characteristics and thus are potentially much more robust and automatically adaptable to system changes and uncertainties in applications outside the laboratory.

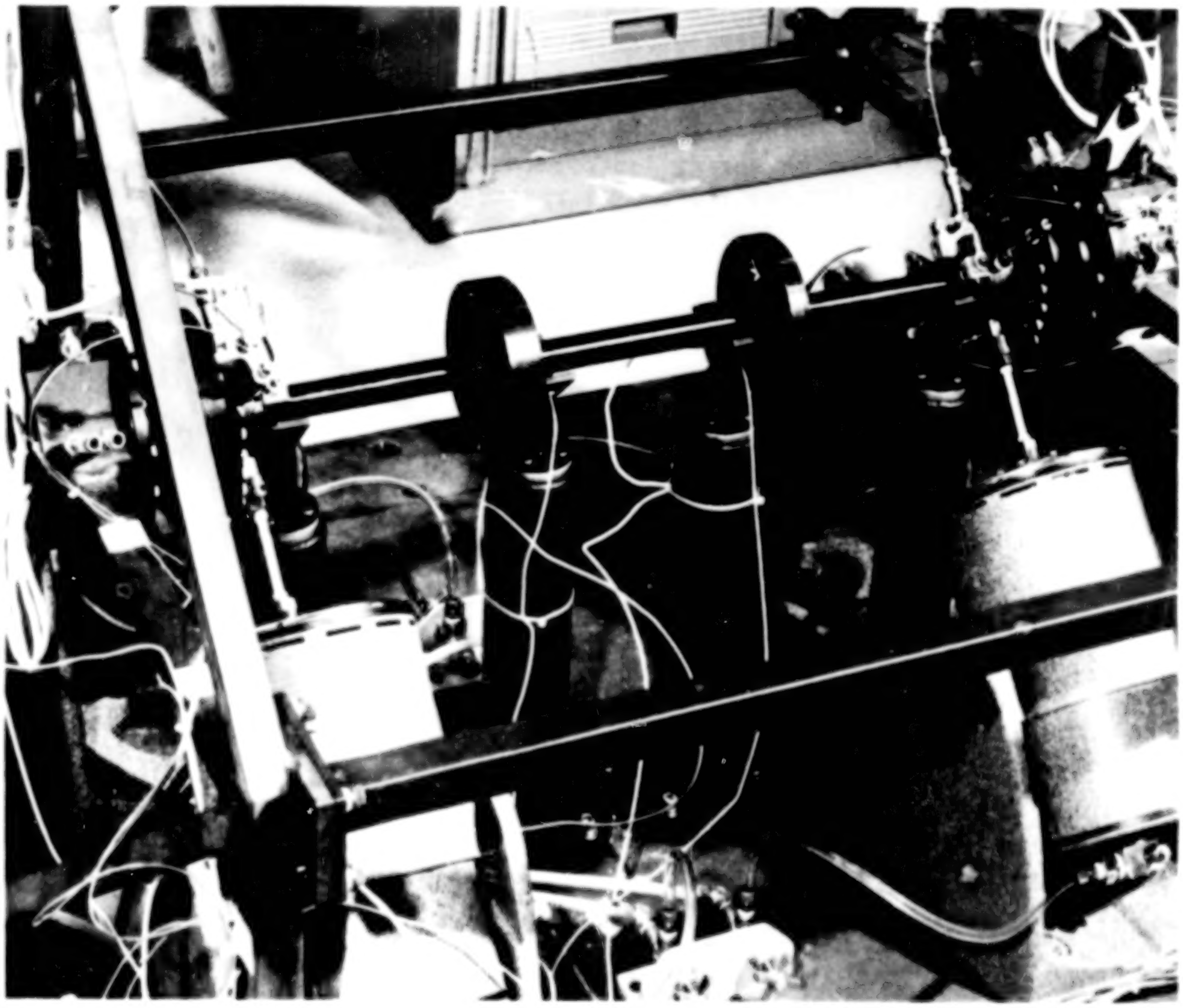

ORIGINAL PAGE IS
OF POOR QUALITY

ATTENUATION OF ROTOR VIBRATION USING CONTROLLED-PRESSURE HYDROSTATIC SQUEEZE-FILM DAMPERS

The use of fluid-film hydrostatic bearings to minimize flexible rotor vibration is a practical design approach with potential advantages. Computational results of the first phase of this work has been recently published by Adams and Zahloul (1987) and are summarized in the illustrations here. Essentially, the results demonstrate the degree of system controlled variability which could typically be provided on a variety of rotating machinery through the use of controlled-pressure hydrostatic bearings. The case shown below is based on a single controlled supply pressure, common to all hydrostatic bearing pockets. More elaborate scenarios would provide even more controllability.

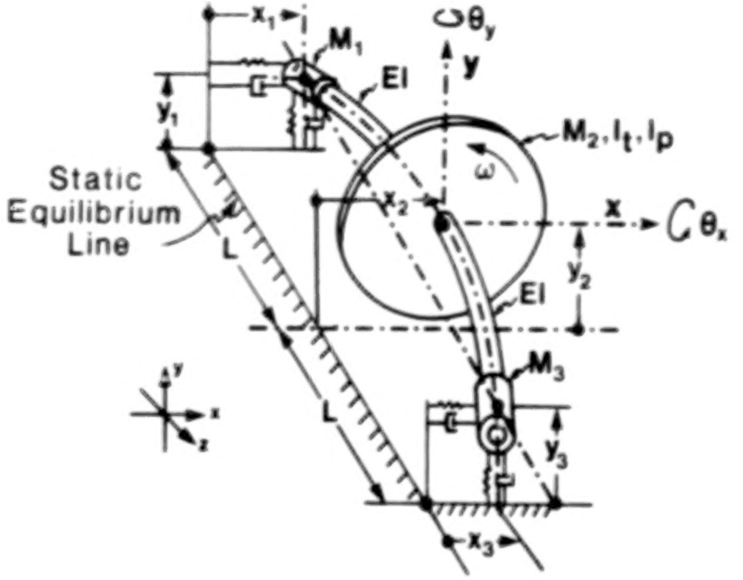

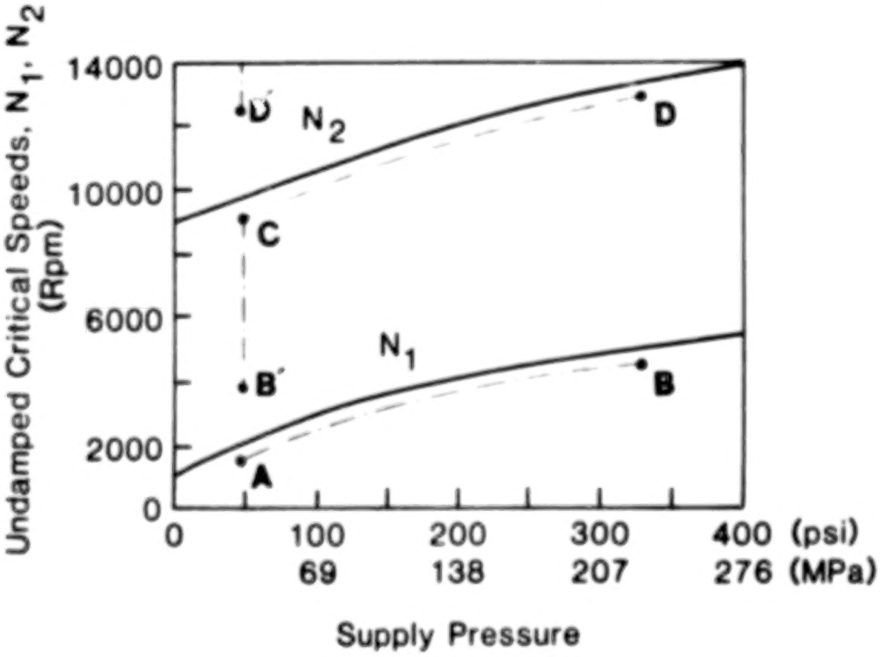

NEW GENERAL PURPOSE TEST FACILITY AT CWRU FOR MEASURING SEAL AND BEARING ROTORDYNAMIC CHARACTERISTICS

The illustration below is a schematic of a new test facility at CWRU for system identification research pertaining to both seals and bearings. The design of the apparatus is quite unique and the most advanced in its field, see Adams and Makay (1983). A controlled rotor vibration circular orbit is provided using the double-spool shaft configuration shown. The spindle is designed with an adjustable eccentricity (0-60 mils) between the inner and outer spindle centerlines. This provides independent control over spin speed and vibration orbit using two variable speed drives, and permits experimental studies in both linear and nonlinear regimes of any seal or bearing tested. This facility also contains an eighteen stage centrifugal pump with a design output of 50 gpm at 450 psi. This pump is used to subject tested seals to actual pressure/flow conditions of the intended application.

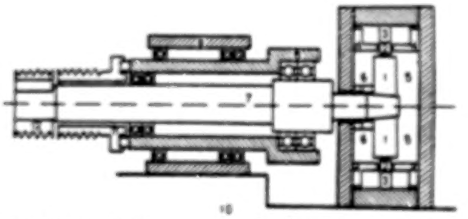

1 - Test rotating element
2 - Test annulus ring
3 - Piezoelectric load cells
4 - Hydrostatic axial ring supports
5 - High-pressure compartment
6 - Low-pressure compartment

7 - Inner spindle rotor
8 - Outer spindle rotor
9 - Spindle housing
10 - Support base
11 - V-belt pulley
12 - V-belt pulley

Conceptual Sketch of Rotor Support Component Test Apparatus

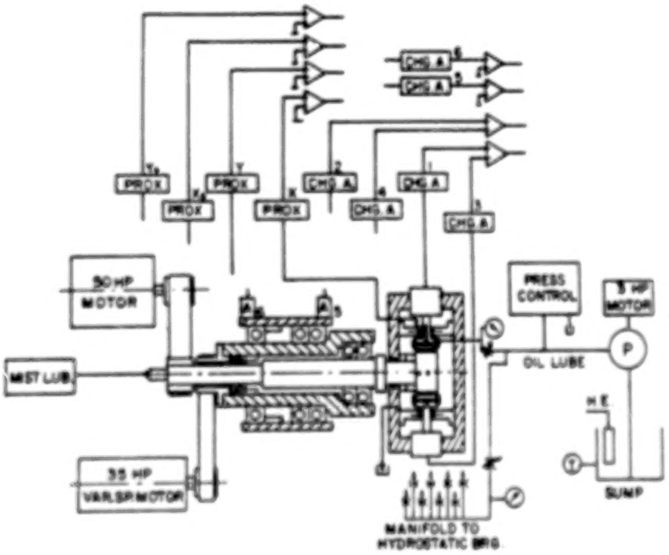
PROX
PROX
PROX
PROX
CHG A
CHG A
CHG A
CHG A
CHG A
CHG A
30 HP MOTOR
MIST LUB
35 HP VAR.SP.MOTOR
PRESS CONTROL
5 HP MOTOR
P
OIL LUBE
H.E.
SUMP
MANIFOLD TO HYDROSTATIC BRG.

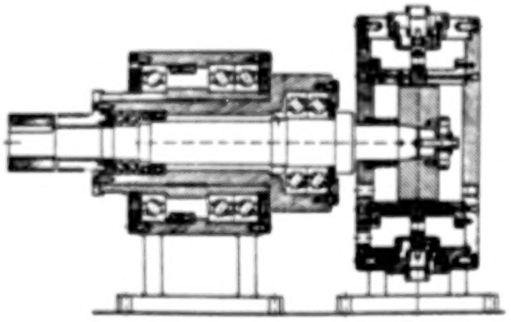

Assembly Layout of Rotor Support Component Test Apparatus

④

THE USE OF ROTORDYNAMIC INSTABILITY THRESHOLDS TO ACCURATELY MEASURE BEARING ROTORDYNAMIC CHARACTERISTICS

A re-examination of rotor-bearing dynanic instability has led to a fresh approach that has been shown to significantly improve the measurement accuracy of journal bearing rotordynamic coefficients. The approach uses a two-degree-of-freedom system and has two major parts. First, bearing stiffness coefficients are measured using static loading. Second, measured orbital motion at an adjustable threshold speed is used to extract the bearing damping coefficients by inverting the associated Eigen problem. Below is shown the test rig design for this new experimental method. Detailed treatment is given by Adams and Rashidi (1985) and Rashidi and Adams (1988).

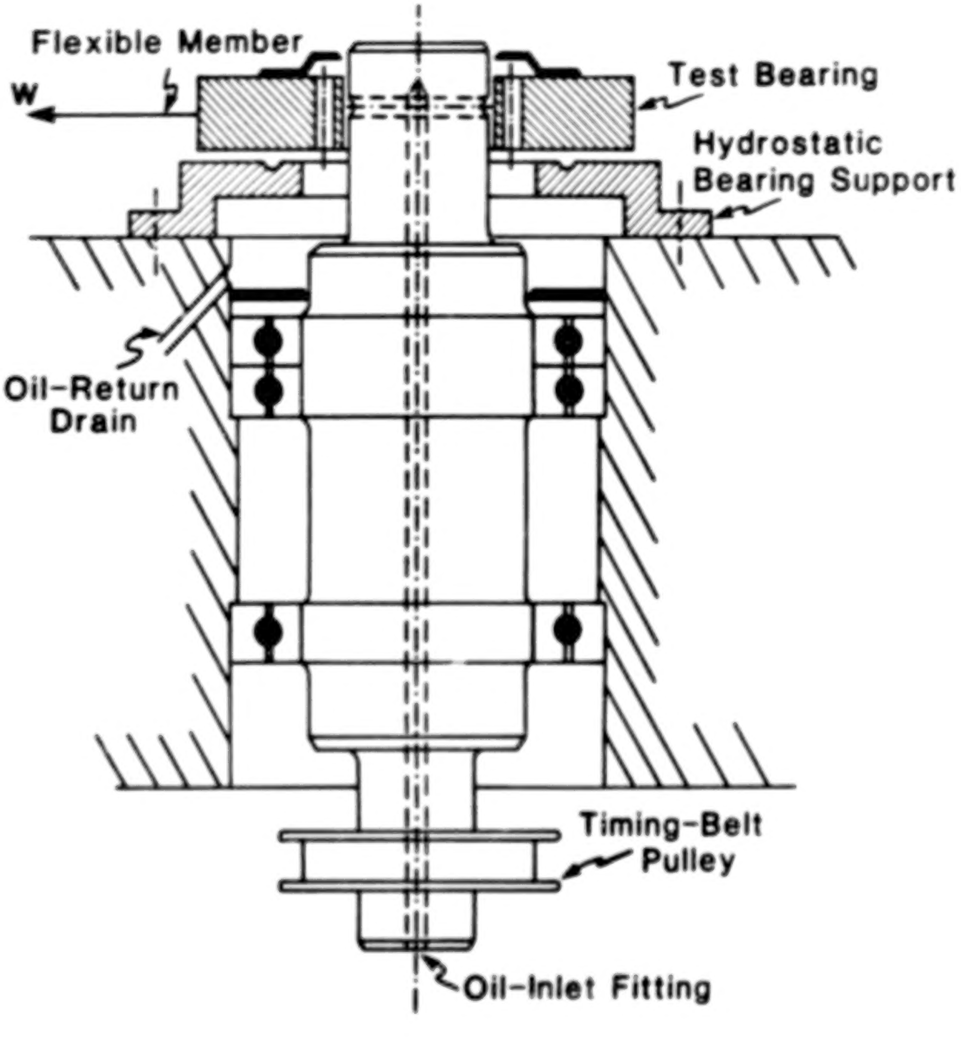
Flexible Member
W
Test Bearing
Hydrostatic Bearing Support
Oil-Return Drain
Timing-Belt Pulley
Oil-Inlet Fitting

④

REFERENCES

Adams, M.L., and Makay, E., 1983, "Development of Advanced Rotor-Bearing Systems for Feedwater Pumps - Phase 3: Hardware Design and Fabrication," Electric Power Research Institute, EPRI-CS-3203.

Adams, M.L., and Rashidi, M., 1985, "On the Use of Rotor-Bearing Instability Thresholds to Accurately Measure Bearing Rotordynamic Properties," Trans. ASME, Journal of Vibration, Stress and Reliability in Design, Vol. 107 (4).

Adams, M.L., and Zahloul, 1987, "Attenuation of Rotor Vibration Using Controlled Pressure Hydrostatic Squeeze-Film Dampers," Proceedings of Rotor Dynamics Papers, ASME Vibration Conference, Boston

Rashidi, M., and Adams, M.L., 1988, "Accurate Prediction of Rotordynamic Stability Limits Using Bearing Dynamic Properties Extracted From a Controlled Instability Threshold Experiment," submitted for publication, 4th International Conference on Vibrations in Rotating Machinery,

N88-23231

ELECTROMAGNETIC DAMPERS FOR CRYOGENIC APPLICATIONS

Gerald V. Brown and Eliseo DiRusso
Structural Dynamics Branch
NASA Lewis Research Center

ABSTRACT

Cryogenic turbomachinery of the type used to pump high-pressure liquid hydrogen at -423 °F and liquid oxygen at -297 °F to the main engines of the space shuttle are subjected to lateral rotor vibrations from unbalance forces and transient loads. Conventional dampers which utilize viscous fluids such as bearing lubricating oil cannot be used in turbopumps because the bearing compartments are filled with either liquid hydrogen or liquid oxygen. Liquid oxygen and liquid hydrogen have a viscosity comparable to air and, therefore, are not effective in viscous dampers.

Electromagnetic dampers are currently being explored at Lewis Research Center as a means of providing damping in cryogenic turbopumps because their damping effectiveness increases as temperature decreases and because they are compatible with the liquid hydrogen or liquid oxygen in the turbopumps. Therefore, these dampers make effective use of the cold environment inherent in cryogenic turbopumps.

OVERVIEW

ELECTROMAGNETIC DAMPER

Electromagnetic dampers are being explored at the Lewis Research Center as a means of damping rotor vibrations in cryogenic turbopumps. Use of this damper in turbopumps can extend bearing life and can lead to more reliable, less costly turbopumps.

- **DAMPING IS ACHIEVED BY GENERATING AN ELECTRICAL CURRENT AND DISSIPATING THE ENERGY AS HEAT.**
- **APPLICATION—SPACE SHUTTLE MAIN ENGINE TURBOPUMPS**
- **BENEFITS**
  - **CAN TOLERATE LESS ACCURATE ROTOR BALANCE**
  - **INCREASES BEARING LIFE**
  - **PROVIDES MORE LATITUDE IN ROTOR DESIGN**

CD-88-31902

WHY USE ELECTROMAGNETIC DAMPERS IN TURBOPUMPS?

Choices of damping methods for cryogenic turbopumps are limited because of the cold temperatures and the very low viscosity of cryogenic fluids. Electromagnetic dampers are very desirable for turbopump applications because they are compatible with cryogenic fluids and because their effectiveness is enhanced at the low cryogenic temperatures.

- VISCOUS DAMPERS REQUIRE HIGH VISCOSITY FLUIDS (INCOMPATIBLE WITH TURBOPUMP FLUIDS).
- FLUIDS FOUND IN TURBOPUMPS HAVE VERY LOW VISCOSITY (COMPARABLE TO AIR).
- ELECTROMAGNETIC DAMPER EFFECTIVENESS IS GREATLY ENHANCED AT CRYOGENIC TEMPERATURES.
- ELECTROMAGNETIC DAMPERS ARE COMPATIBLE WITH TURBOPUMP FLUIDS.

CD-88-31903

HIGH-PRESSURE OXYGEN TURBOPUMP

Shown in the figure is a typical turbopump used in the space shuttle main engines to pump liquid hydrogen and liquid oxygen to the space shuttle main engines. These pumps have been plagued with rotor vibration problems and short bearing life. Electromagnetic dampers are being explored at Lewis Research Center to help solve these problems.

ORIGINAL PAGE IS
OF POOR QUALITY

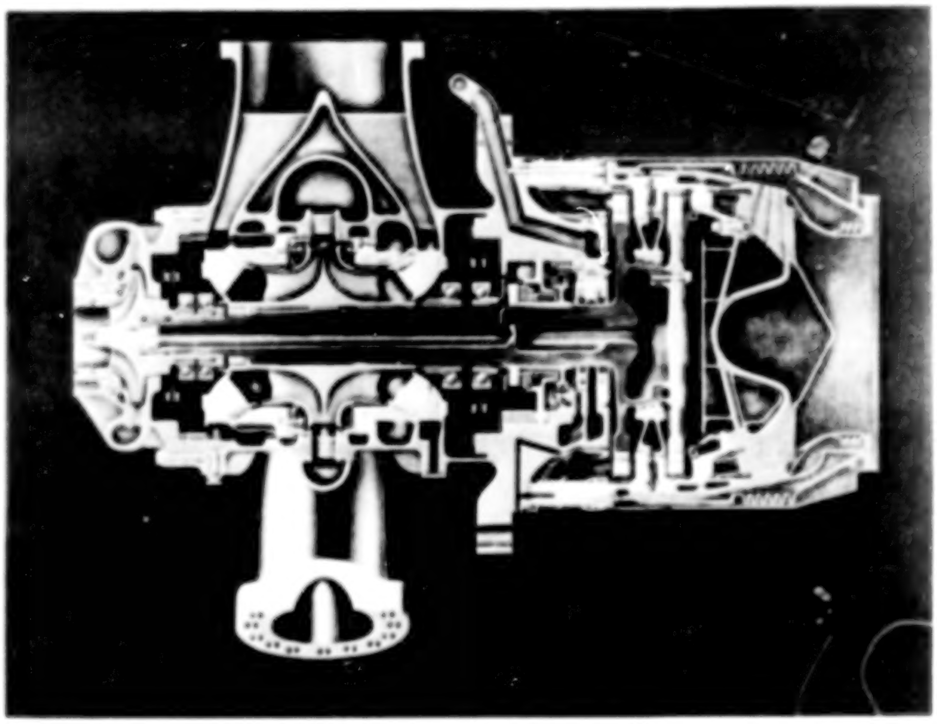

CD-88-31904

ELECTROMAGNETIC DAMPER SCHEMATIC

This figure shows a schematic of an electromagnetic damper. This type of damper converts energy from an unwanted mechanical vibration to an electrical current and dissipates the energy as heat. It is particularly well suited to the cold environment found in turbopumps because their damping effectiveness increases at low temperatures.

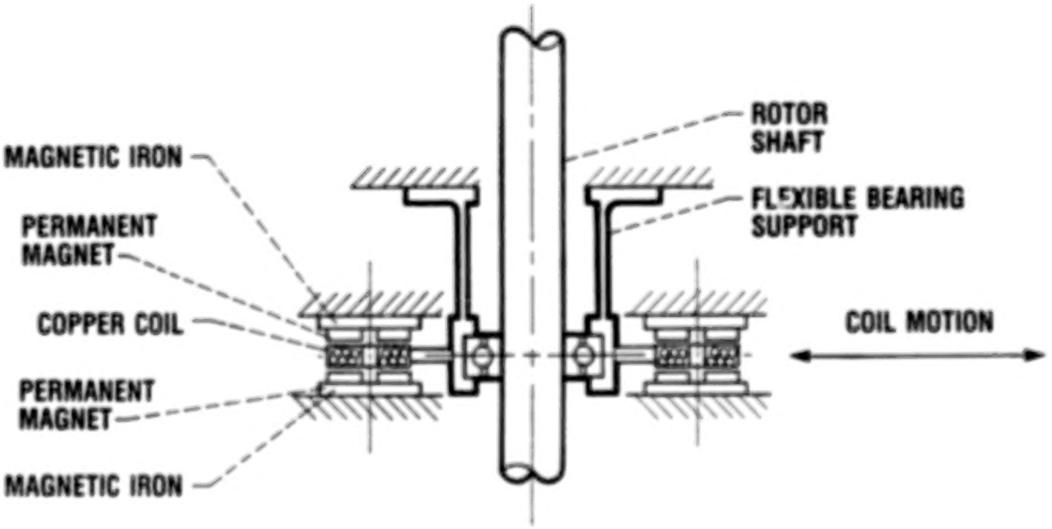
ROTOR SHAFT
MAGNETIC IRON
FLEXIBLE BEARING SUPPORT
PERMANENT MAGNET
COPPER COIL
COIL MOTION
PERMANENT MAGNET
MAGNETIC IRON

CD-88-31905

ORIGINAL PAGE IS
OF POOR QUALITY

POSTER PRESENTATION

HIGH-PRESSURE OXYGEN TURBOPUMP

This picture shows a high-pressure liquid oxygen turbopump of the type used in the space shuttle main engines. These pumps have rigidly mounted bearings which are submerged in liquid oxygen; hence conventional viscous dampers using lubricating oils cannot be used for damping purposes. Electromagnetic dampers are being explored as a means of providing damping in these pumps. Use of electromagnetic dampers in these pumps could provide greater flexibility in the design of turbopump rotors and also could permit less precision in balancing the rotor.

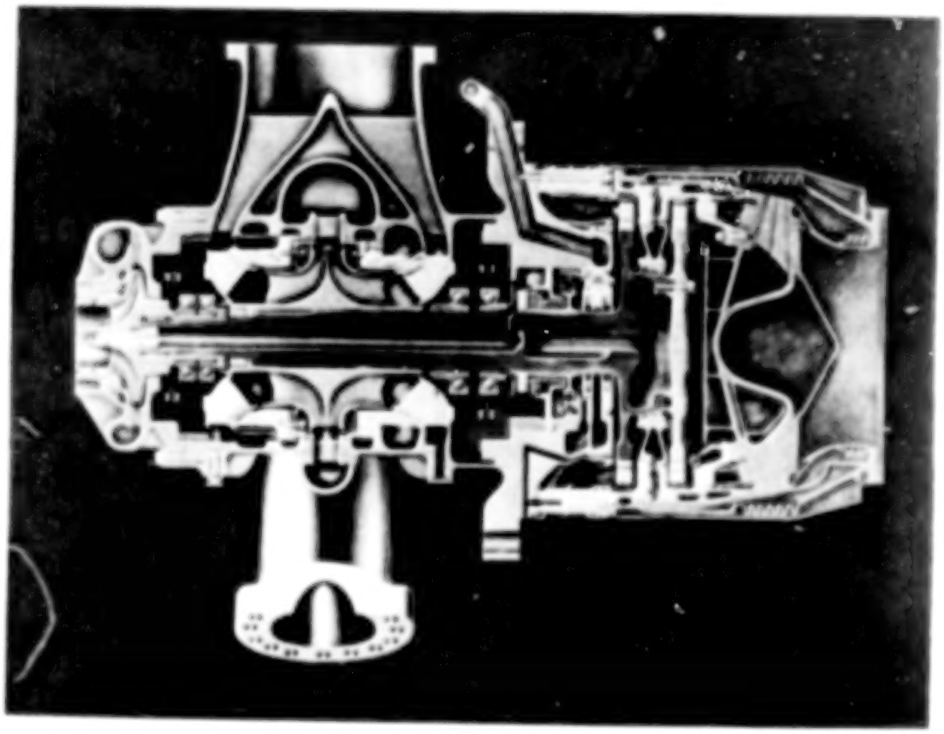

CD-86-31904

ELECTROMAGNETIC DAMPER SCHEMATIC

This figure shows a typical schematic of an electromagnetic damper. The principle elements of the damper are permanent magnets, copper coil, and magnetic iron. The coil (nonrotating) is rigidly attached to the bearing housing. Lateral vibration of the bearing housing produces a coil motion, as shown in the figure. This motion causes the coil conductors to cut the flux lines of the permanent magnets, thereby generating a current in the coil. The current flowing in the coil causes the coil to heat up. This heat is dissipated in the liquid oxygen, thereby providing damping for the vibrating bearing housing.

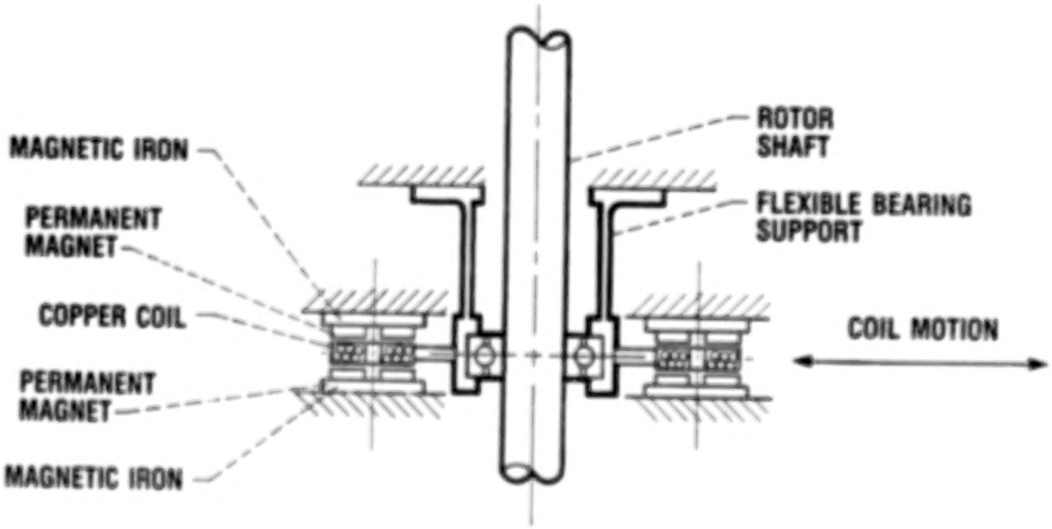
MAGNETIC IRON
PERMANENT MAGNET
COPPER COIL
PERMANENT MAGNET
MAGNETIC IRON
ROTOR SHAFT
FLEXIBLE BEARING SUPPORT
COIL MOTION

CD-88-31905

TUNED ELECTRICAL CIRCUIT SCHEMATIC

In order to maximize the current generated in the coil, a capacitor is placed in series with the coil. This forms a series circuit with resistance, capacitance, and inductances, as shown in the figure. The resistance is the coil resistance, and the inductance is the coil inductance. This circuit can be tuned such that the current flowing in the coil is maximized at the frequency of the vibrating shaft. The tuning is accomplished by selecting the capacitance such that the electronic circuit has a resonant frequency equal to the mechanical shaft vibration. Tuning the electronic circuit to the mechanical vibration frequency thus maximizes the effectiveness of the damper.

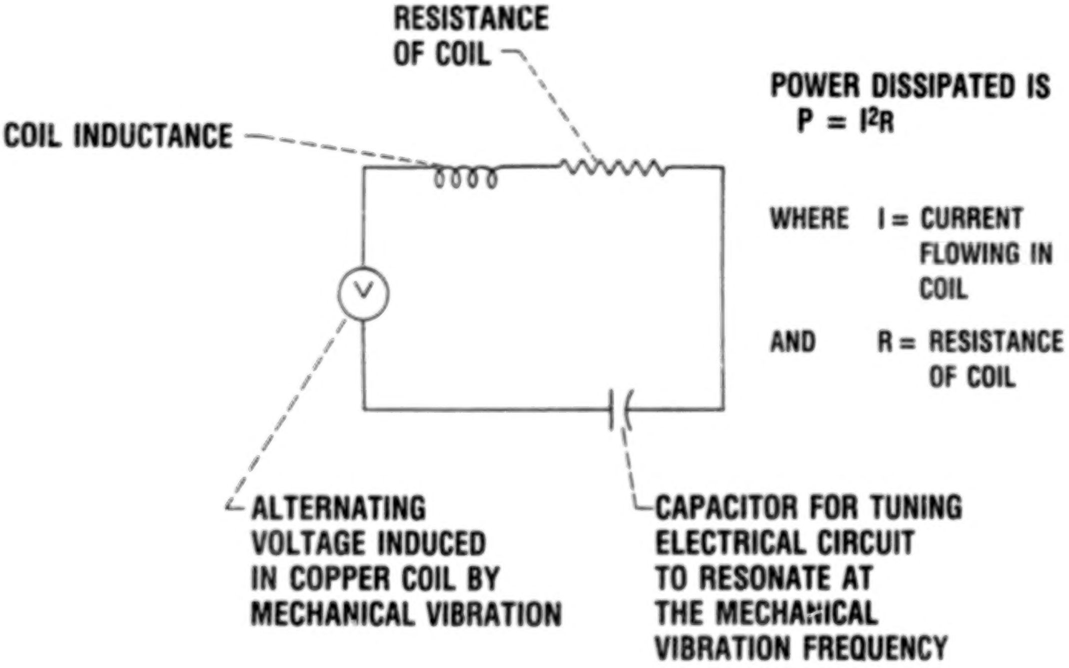
RESISTANCE OF COIL
COIL INDUCTANCE
V
POWER DISSIPATED IS $P = I^2R$
WHERE I = CURRENT FLOWING IN COIL
AND R = RESISTANCE OF COIL
ALTERNATING VOLTAGE INDUCED IN COPPER COIL BY MECHANICAL VIBRATION
CAPACITOR FOR TUNING ELECTRICAL CIRCUIT TO RESONATE AT THE MECHANICAL VIBRATION FREQUENCY

CD-88-31906

CURRENT INDUCED IN COIL VERSUS FREQUENCY - ROOM TEMPERATURE

This figure shows the current generated versus frequency for typical tuned and untuned circuits at room temperature. This illustrates that at room temperature there is a negligible difference between the tuned and untuned circuits. Also, the current is low.

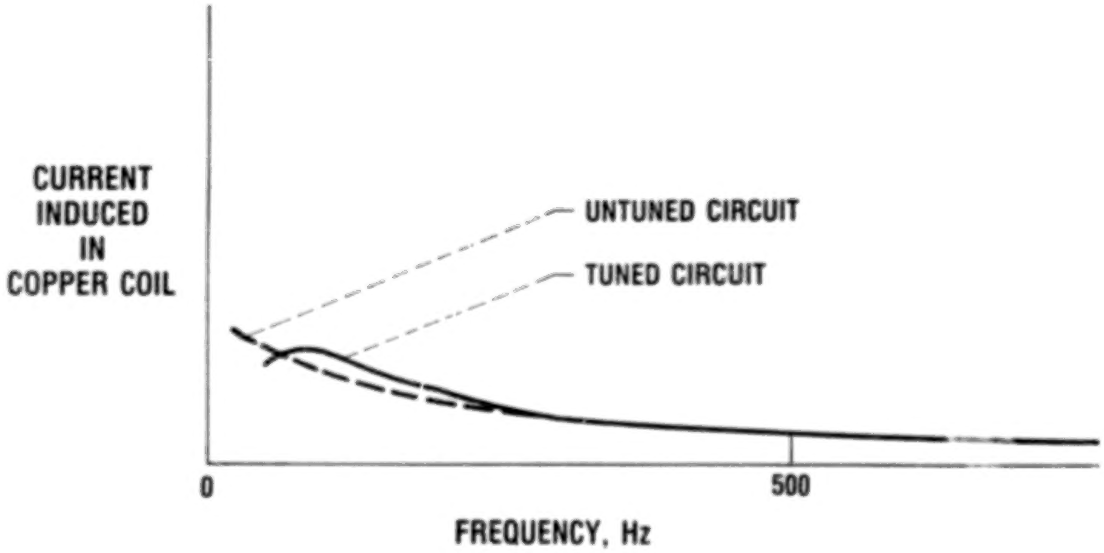

CD-88-31907

CURRENT INDUCED IN COIL VERSUS FREQUENCY - LIQUID NITROGEN LOW TEMPERATURE

This figure shows the current generated versus frequency for tuned and untuned circuits at liquid nitrogen temperature (-321 °F). At the tuned frequency, the current output is much higher for the tuned circuit than for the untuned circuit. This illustrates the effectiveness of the damper at cryogenic temperatures.

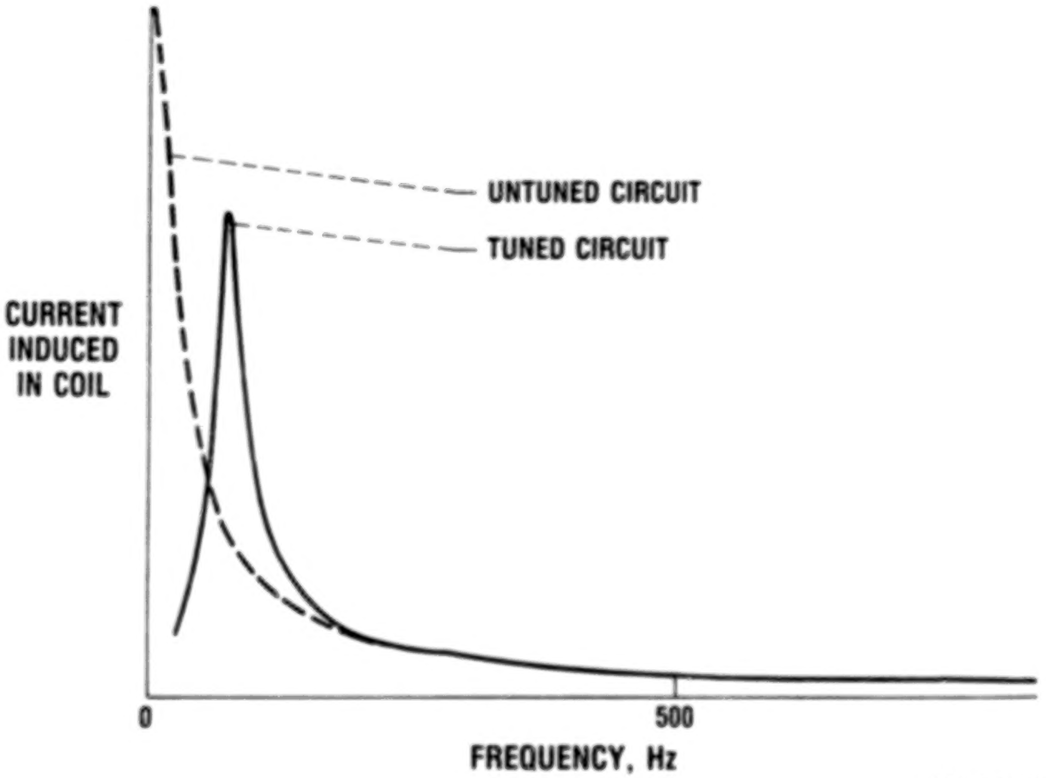

CD-88-31908

ORIGINAL PAGE IS
OF POOR QUALITY

ELECTROMAGNETIC DAMPER TEST APPARATUS - LIQUID NITROGEN

This figure shows a rig which is used for conducting electromagnetic damper experiments in simulated cryogenic turbopump conditions. The electromagnetic damper is submerged in liquid nitrogen at -321 °F. Vibration of the lower bearing housing is induced by unbalancing the rotor disk. Damper performance is evaluated by measuring lateral shaft displacements (shaft orbits) and processing these data in a computer to get synchronous rotor response and damping ratio.

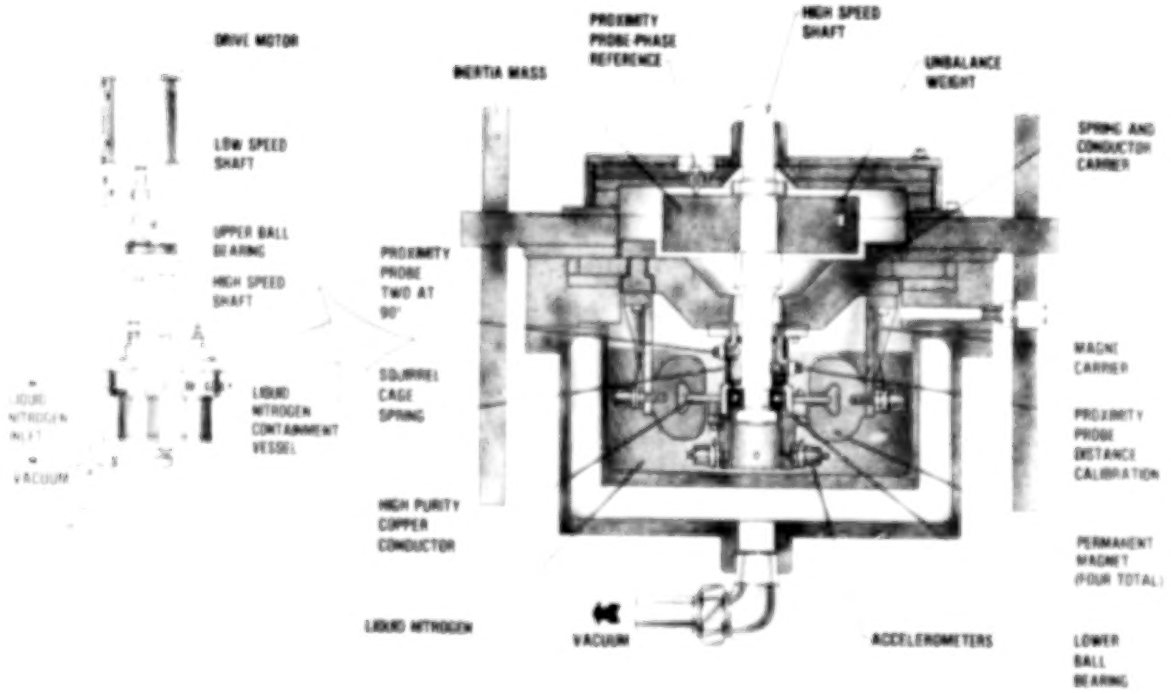
DRIVE MOTOR
LOW SPEED SHAFT
UPPER BALL BEARING
HIGH SPEED SHAFT
LIQUID NITROGEN INLET
VACUUM
LIQUID NITROGEN CONTAINMENT VESSEL
INERTIA MASS
PROXIMITY PROBE-PHASE REFERENCE
HIGH SPEED SHAFT
UNBALANCE WEIGHT
SPRING AND CONDUCTOR CARRIER
PROXIMITY PROBE TWO AT 90°
SQUIRREL CAGE SPRING
MAGNE CARRIER
PROXIMITY PROBE DISTANCE CALIBRATION
HIGH PURITY COPPER CONDUCTOR
PERMANENT MAGNET (FOUR TOTAL)
LIQUID NITROGEN
VACUUM
ACCELEROMETERS
LOWER BALL BEARING

CD-88-31909

SUMMARY

Research on electromagnetic damping for cryogenic applications is being explored at Lewis Research Center. The program is oriented towards providing new damping methods for cryogenic turbopump rotors of the type used in the space shuttle main engines. Research to date has shown that this type of damper must be electronically tuned to the frequency of the mechanical vibration in order to be effective as a damper. This is accomplished by forming a series "resistive, inductive, capacitive circuit" and selecting the capacitance such that the circuit is tuned to the frequency of the mechanical vibration. Research testing of the tuned cryogenic electromagnetic damper is planned for the near future.

PARALLEL COMPUTING

SESSION OVERVIEW

Louis J. Kiraly
Structural Dynamics Branch
NASA Lewis Research Center

Our knowledge of the physical processes that interplay within the complex dynamic environs of modern turbomachinery exceeds our ability to compute their overall effect. We can analyze aspects of most of the important processes effects, but we cannot readily compute their overall impact on system response.

We cannot design an engine mathematically today - we need experimental versions to "adjust" our mathematical models. There are several reasons for this. First of all, we do not always understand the physical interactions between processes such as those between thermal effects on basic material properties, the coupled aero-structural response of blades made from such materials, and the coupling of such blade vibrations with net rotor-shaft system response. Understanding of physical process interactions like these requires further study. Secondly, we are unable to adequately numerically simulate many fundamental processes. Much of this conference addresses these first two problems with development of numerical simulations of the most significant engine phenomena. The third and final problem is one of even being able to compute those processes which we understand and which we can reasonably simulate. The computing problem can rapidly exceed the capacity of today's computers. These complex problems become so large that they will only be solved by breaking them into parts which can be simultaneously solved in parallel computer systems. This session deals with some initial work to develop needed parallel computing methods for structures.

Generally, there are three areas of interest. First, there may be fundamentally new approaches for solving traditional problems which "map" well onto parallel computers - with great increases in computing speed and efficiency. The talks on multigrid analysis and parallel eigenvalue extraction are in this first category. Secondly, tools are needed to help formulate and construct parallel computing programs which, by their very nature, can be exceedingly complex and difficult to manage. The presentation on adapting high-level language programs using data flow and the poster session for doing graphical computations in parallel are in this second category. The third area of interest involves making use of our current huge investment in existing single-processor mathematical methods and models (such as finite-element models) and our need to adapt these models to the parallel processing. The presentation of iterative finite-element solvers is in this category.

These are only the first steps toward the eventual coupling of complex physical system models which will enable "mathematical" engine system design as well as the detailed study of various interactions within engine systems.

PARALLEL COMPUTING

SESSION OVERVIEW
- L.J. KIRALY, CHIEF, STRUCTURAL DYNAMICS BRANCH, NASA

MULTIGRID FOR STRUCTURES ANALYSIS
- A.F. KASCAK, U.S. ARMY AVSCOM/STRUCTURAL DYNAMICS BRANCH, NASA

PARALLEL COMPUTER METHODS FOR EIGENVALUE EXTRACTION
- F. AKL, OHIO UNIVERSITY, ATHENS, OH

ADAPTING HIGH-LEVEL LANGUAGE PROGRAMS FOR PARALLEL PROCESSING USING DATA FLOW
- H.M. STANDLEY, UNIVERSITY OF TOLEDO, TOLEDO, OH

ITERATIVE FINITE-ELEMENT SOLVER ON TRANSPUTER NETWORKS
- A. DANIAL AND J. WATSON, SPARTA, INC., HUNTSVILLE, AL

MULTIPROCESSOR GRAPHICS COMPUTATION AND DISPLAY USING TRANSPUTERS (POSTER)
- G.K. ELLIS, STRUCTURAL DYNAMICS BRANCH, ICOMP

CD-88-32608

N88-23232

MULTIGRID FOR STRUCTURES ANALYSIS

Albert F. Kascak
U.S. Army Aviation Research and Technology Activity - AVSCOM
Structural Dynamics Branch
NASA Lewis Research Center

ABSTRACT

In structural analysis the amount of computational time necessary for a solution is proportional to the number of degrees of freedom times the bandwidth squared. In implicit time analysis, this solution must be calculated at each discrete point in time. If, in addition, the problem is nonlinear, then this solution must be iterated at each point in time. If the bandwidth is large, the size of the problem that can be analyzed is severely limited.

The multigrid method is a possible algorithm that can make this solution much more computationally efficient. This method has been used for years in computational fluid mechanics. It works on the fact that relaxation is very efficient on the high-frequency components of the solution (nearest-neighbor interactions) but is not very efficient on the low-frequency components of the solution (far interactions). The multigrid method relaxes the solution on a particular model until the residual stops changing, which indicates that the solution contains the higher frequency components. A coarse model is then generated and relaxed for the lower frequency components of the solution. These lower frequency components are then interpolated to the fine model.

In computational fluid mechanics the equations are usually expressed as finite differences. A coarse model is generated by just doubling the grid size and using a Green's integral theorem to obtain the forcing function on the coarse grid. Linear interpolation is used to transfer the lower frequency solution back to the fine grid.

In structural dynamics the equations are usually expressed as finite elements. Neighbor elements need not be connected. The process of condensing a fine model into a coarse model and interpolating the low-frequency solution to the fine model will be studied in this work.

OBJECTIVE

The objective of this work is to use an implicit time march solution to study nonlinear structural dynamics. The work will be done in three phases. The first phase, a beam structure, will have application in a multishaft, combined lateral, torsional, and axial rotordynamic analysis. The second phase, a plate structure, will have application in bladed disk vibration with coulomb damping. The third phase, a full three-dimensional structure, will have application in space structures.

To aid the reader, a symbols list has been included in the appendix.

IMPLICIT TIME MARCH SOLUTION OF NONLINEAR STRUCTURAL DYNAMICS

- **BEAM—MULTISHAFT, COMBINED LATERAL, TORSIONAL, AND AXIAL ANALYSIS**
- **PLATE—BLADE VIBRATION WITH COULOMB DAMPING**
- **THREE-DIMENSIONAL SPACE STRUCTURES ANALYSIS**

CD-88-32936

NUMERICAL INTEGRATION

The numerical integration method is based on a Nordsieck-like method. The displacement, velocity, and acceleration are defined at an initial time. A modified Taylor series is used to calculate the displacement, velocity, and acceleration at the advanced time. The Lagrange remainder term, the time derivative of the acceleration, is calculated from the equations of motion at the advanced time. The constants α and β are determined so that the method is stable as time approaches infinity.

This method of integration for a first-order differential equation is Gear's method (Gear, 1971). Zeleznik showed that this method could be used on higher order equations (private communication with F.J. Zeleznik at NASA Lewis Research Center in 1979). Kascak (1980) showed that for a third-order integrator used on a linear second-order differential equation the method is unconditionally stable.

LET $R(t)$ BE AN n ELEMENT VECTOR OF NODAL DISPLACEMENTS AND

$$V(t) = \dot{R} \qquad A(t) = \dot{V}$$

MODIFIED TAYLOR SERIES

$$R(t) = R(0) + V(0)t + \frac{1}{2} A(0)t^2 + \frac{1}{6} \alpha \dot{A}(\xi)t^3$$

$$V(t) = V(0) + A(0)t + \frac{1}{2} \beta \dot{A}(\xi)t^2$$

$$A(t) = A(0) + \dot{A}(\xi)t$$

WHERE

$$0 \leq \xi \leq t$$

AND α AND β ARE DETERMINED SO THAT THE METHOD IS NUMERICALLY STABLE AS $t \to \infty$

CD-88-32937

NUMERICAL STABILITY

The numerical stability of the integration method can be examined by substituting the displacement, velocity, and acceleration into the linear equations of motion, and solving for the time derivative of the acceleration. As time approaches infinity the dominate term on each side of the equation has the stiffness matrix as a premultiplier. The time derivative of the acceleration is proportional to the initial acceleration divided by the time. If the time derivative is substituted into the modified Taylor series and if α is set to 3 and β is set to 2, then the acceleration is zero and the velocity is constant. The eigenvalues become zero and one.

$$MA + CV + KR = F$$

$$\left(tM + \frac{1}{2}\beta t^2 C + \frac{1}{6}\alpha t^3 K\right)\dot{A}(\xi) = F - \left(M + tC + \frac{1}{2}t^2 K\right)A(0) - (C + tK)V(0) - KR(0)$$

AS $t \to \infty$

$$\dot{A}(\xi) \approx -\left(\frac{3}{\alpha t}\right)A(0)$$

$$R = R(0) + V(0)t$$

$$V = V(0) + \left(1 - \frac{3}{2}\left(\frac{\beta}{\alpha}\right)\right)A(0)t$$

$$A = \left(1 - \left(\frac{3}{\alpha}\right)\right)A(0)$$

LET $\alpha = 3$ AND $\beta = 2$

$$\therefore R = R(0) + V(0)t \qquad V = V(0) \qquad A = 0$$

CD-86-32938

ITERATIVE SOLUTION

If the initial displacement, velocity, and acceleration, and an initial estimate of the time derivative of the acceleration are given, then estimates of the advanced displacement, velocity, and acceleration are given by using the modified Taylor series. If a correction to the estimate of the time derivative of the acceleration is given, then new estimates of the displacement, velocity, and acceleration are given by the modified Taylor series. The correction to the time derivative of the acceleration can be found from the equations of motion.

GIVEN $R(0), V(0), A(0)$, AND $\dot{A}(\xi) \sim \dot{A}^{(0)}$

THEN $R^{(0)} = R(0) + V(0)t + \frac{1}{2}A(0)t^2 + \frac{1}{2}\alpha\dot{A}^{(0)}t^3$

$V^{(0)} = V(0) + A(0)t + \frac{1}{2}\beta\dot{A}^{(0)}t^2$

$A^{(0)} = A(0) + \dot{A}^{(0)}t$

LET $\dot{A}(\xi) = \dot{A}^{(0)} + \Delta\dot{A}$

THEN $R(t) = R^{(0)} + \frac{1}{6}\alpha\Delta\dot{A}t^3$

$V(t) = V^{(0)} + \frac{1}{2}\beta\Delta\dot{A}t^2$

$A(t) = A^{(0)} + \Delta\dot{A}t$

CD-88-32939

NONLINEAR EQUATIONS OF MOTION

The nonlinear equations of motion are the sum of both the static and dynamic forces for each element. As such, the equations are functions of the displacement, velocity, acceleration, and time. If the modified Taylor series is substituted into the equations of motion using the iterative form, then the equations of motion become a function of the correction to the time derivative of the acceleration.

$$0 = F(R, V, A, t)$$

WHERE F IS AN n ELEMENT VECTOR SUM OF THE STATIC AND DYNAMIC FORCES

THEN

$$0 = F\left(R^{(0)} + \frac{1}{6}\alpha\Delta\dot{A}t^3,\ V^{(0)} + \frac{1}{2}\beta\Delta\dot{A}t^2,\ A^{(0)} + \Delta\dot{A}t,\ t\right)$$

OR

$$0 = F(\Delta\dot{A})$$

CD-88-32940

LINEARIZED EQUATIONS OF MOTION

To solve for the correction, the equations of motion are linearized about the estimated values. The instantaneous stiffness, damping, and mass are defined by the various partial derivatives with respect to displacement, velocity, and acceleration. If the linearization is done numerically, the stiffness, damping, and mass do not have to be calculated. The numerical differentiation of the correction to the time derivative of the acceleration is all that is needed.

This solution procedure is equivalent to the Newton-Raphson technique. The numerical differentiation and the solution of the linearized equations of motion are computationally time consuming, although straight forward. The multigrid technique could be potentially orders of magnitudes faster. The linearized equations of motion will be the basis for generating a coarse model from a fine model.

$$0 = F^{(0)} - B\Delta\dot{A}$$

WHERE

$$F^{(0)} = F(R^{(0)}, V^{(0)}, A^{(0)}, t)$$

$$B = \frac{1}{6}\alpha t^3 K + \frac{1}{2}\beta t^2 C + tM$$

$$K = -\frac{\partial F}{\partial R}, \quad C = -\frac{\partial F}{\partial V}, \quad M = -\frac{\partial F}{\partial A}$$

$$\therefore \; B\Delta\dot{A} = F^{(0)}$$

CD-88-32941

STRUCTURAL CONDENSATION

If the linearized equation set is partitioned into nodes belonging to a coarse model (upper partition) and the nodes that are eliminated from the fine model (lower partition), then structural condensation can be used to solve for the coarse model. In addition, the structural condensation process can be used to interpolate the solution from the coarse model to the fine model. If the higher frequency part of the solution is found on the fine model and the lower frequency part of the solution is found on the coarse model, then the resultant forces must be zero. Thus the solution for the nodes eliminated from the fine model can be found.

$$\left[\begin{array}{c:c} B_{11} & B_{12} \\ \hdashline B_{21} & B_{22} \end{array}\right]\left[\begin{array}{c} \Delta\dot{A}_1 \\ \hdashline \Delta\dot{A}_2 \end{array}\right] = \left[\begin{array}{c} F_1^{(f)} \\ \hdashline F_2^{(f)} \end{array}\right]$$

$$\left(B_{11} - B_{12}B_{22}^{-1}B_{21}\right)\Delta\dot{A}_1 = F_1^{(f)} - B_{12}B_{22}^{-1}F_2^{(f)}$$

$$\Delta\dot{A}_2 = B_{22}^{-1}\left(F_2^{(f)} - B_{21}\Delta\dot{A}_1\right)$$

$$\text{LET } B^{(c)} = B_{11} - B_{12}B_{22}^{-1}B_{21}, \; F^{(c)} = F_1^{(f)} - B_{12}B_{22}^{-1}F_2^{(f)}$$

$$\therefore B^{(c)}\Delta\dot{A}_1 = F^{(c)}$$

$$\text{IF } F_2^{(f)} = 0 \Rightarrow \Delta\dot{A}_2 = -B_{22}^{-1}B_{21}\Delta\dot{A}_1 \text{ (INTERPOLATOR)}$$

CD-88-32942

FINE-TO-COARSE AND COARSE-TO-FINE MODEL TRANSFORMATIONS

The fine-to-coarse model transformation is a rectangular matrix that averages the force from the fine model to the coarse model. The upper partition is an identity matrix, and the lower partition is defined in the structural condensation process. The coarse-to-fine transformation interpolates the correction of the time derivative of the acceleration from the coarse to fine model. In the symmetric case, the fine-to-coarse transformation is the transpose of the coarse-to-fine transformation.

FINE-TO-COARSE MODEL TRANSFORMATION

$$\Phi = \begin{bmatrix} I \\ \hline -B_{22}B_{21} \end{bmatrix} \Rightarrow \Delta\dot{A} = \Phi\Delta\dot{A}_1$$

COARSE-TO-FINE MODEL TRANSFORMATION

$$\theta = \left[I \;\vdots\; -B_{12}B_{22}^{-1} \right] \Rightarrow F^{(c)} = \theta F^{(f)}$$

$$\therefore B\,\Delta\dot{A} = F^{(f)} \Rightarrow \theta B\Phi\Delta\dot{A}_1 = \theta F^{(f)}$$

OR

$$B^{(c)}\Delta\dot{A}_1 = F^{(c)}$$

CD-88-32943

NONLINEAR CONDENSATION

The nonlinear condensation process transforms the independent variables from the coarse model to the fine model and the dependent variables from the fine to coarse model. Thus the resultant forces are relaxed on the coarse model. This would only require the inversion of a diagonal matrix. The corrections on the coarse model are then interpolated to the fine model. The linearization of the equations of motion are not needed in the solution process, but are needed only to define the transformations.

$$0 = F(\Delta\dot{A}) \Rightarrow 0 = \theta F(\Phi\Delta\dot{A}_1)$$

RELAXATION

$$0 = \theta F^{(f)} - D\Delta\dot{A}_1 \Rightarrow \Delta\dot{A}_1 = D^{-1}F^{(c)}$$

CD-88-32944

LOCAL STRUCTURAL CONDENSATION

The linearization of the equations of motion and the structural condensation process requires a considerable amount of computational time. Multigrid via relaxation is most efficient on nearest neighbor interactions. Thus only a partial linearization of the equations of motion is necessary. The equations of motion have to be linearized only with respect to the node under consideration and its nearest neighbors. Applying condensation to this local interaction model results in local structural condensation. In the case of a beam, this linearization results in a block tridiagonal matrix and the structural condensation results in a coarse model in which every other node is removed from the fine model.

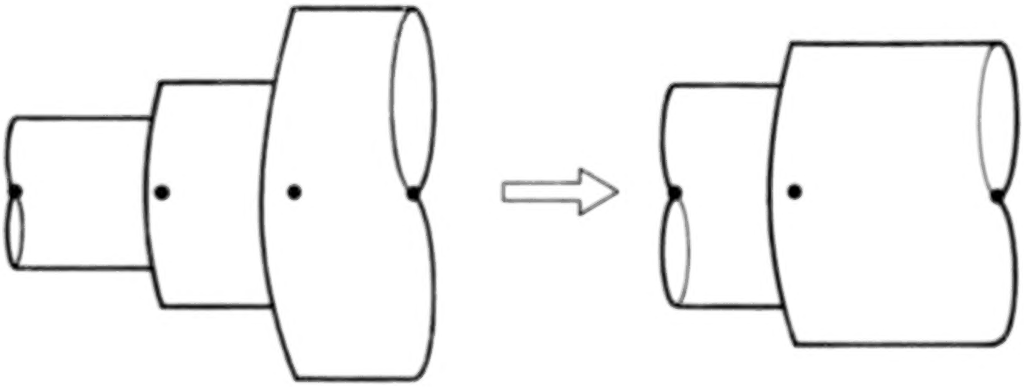

B IS BLOCK TRIDIAGONAL—INCLUDES NEAREST NEIGHBOR INTERACTION, NEGLECTS FAR INTERACTION

CD-88-32945

BEAM EXAMPLE

If the tridiagonal equation set is reordered so that the even numbers are in the upper partition for both the fine and coarse model and the odd numbers are in the lower partition for the fine model, then the structural condensation has a simple form. In the reordered equation set, the block matrices on the diagonal of the partitions are diagonal. The inversions of these block matrices are trivial.

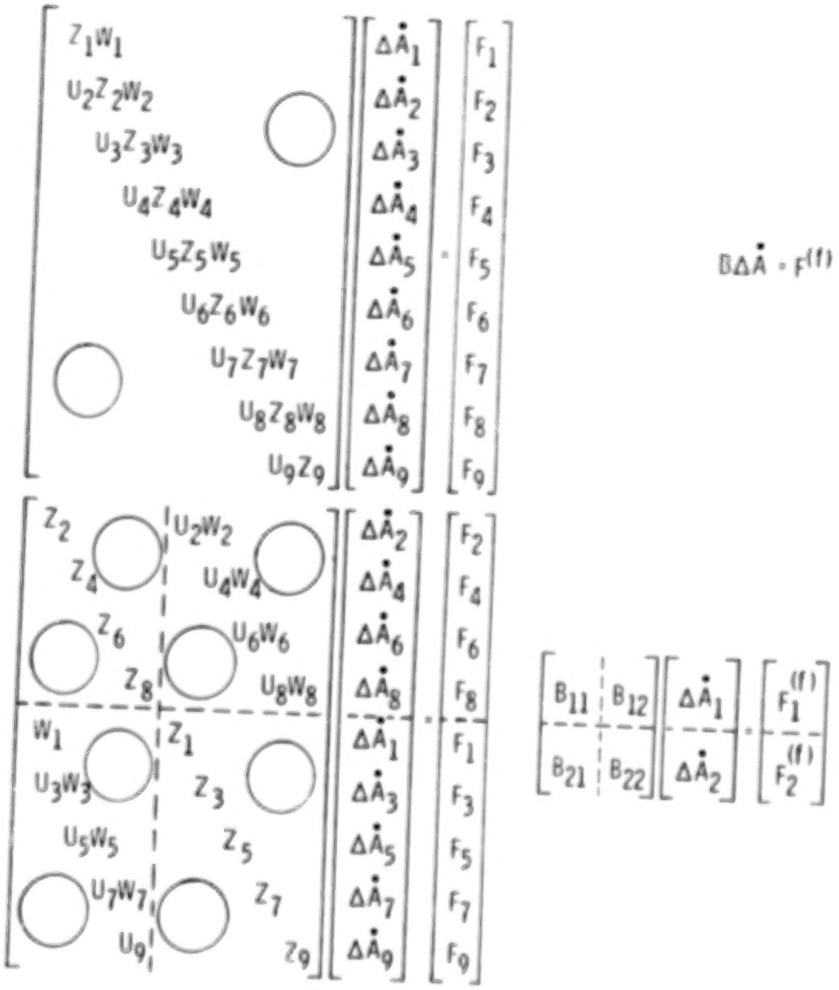

$$\begin{bmatrix} Z_1 & W_1 & & & & & & & \\ U_2 & Z_2 & W_2 & & & & & & \\ & U_3 & Z_3 & W_3 & & & & & \\ & & U_4 & Z_4 & W_4 & & & & \\ & & & U_5 & Z_5 & W_5 & & & \\ & & & & U_6 & Z_6 & W_6 & & \\ & & & & & U_7 & Z_7 & W_7 & \\ & & & & & & U_8 & Z_8 & W_8 \\ & & & & & & & U_9 & Z_9 \end{bmatrix} \begin{bmatrix} \Delta\dot{A}_1 \\ \Delta\dot{A}_2 \\ \Delta\dot{A}_3 \\ \Delta\dot{A}_4 \\ \Delta\dot{A}_5 \\ \Delta\dot{A}_6 \\ \Delta\dot{A}_7 \\ \Delta\dot{A}_8 \\ \Delta\dot{A}_9 \end{bmatrix} = \begin{bmatrix} F_1 \\ F_2 \\ F_3 \\ F_4 \\ F_5 \\ F_6 \\ F_7 \\ F_8 \\ F_9 \end{bmatrix} \qquad B\Delta\dot{A} = F^{(f)}$$

$$\left[\begin{array}{cccc|ccccc} Z_2 & & & & U_2 & W_2 & & & \\ & Z_4 & & & & U_4 & W_4 & & \\ & & Z_6 & & & & U_6 & W_6 & \\ & & & Z_8 & & & & U_8 & W_8 \\ \hline W_1 & & & & Z_1 & & & & \\ U_3 & W_3 & & & & Z_3 & & & \\ & U_5 & W_5 & & & & Z_5 & & \\ & & U_7 & W_7 & & & & Z_7 & \\ & & & U_9 & & & & & Z_9 \end{array}\right] \left[\begin{array}{c} \Delta\dot{A}_2 \\ \Delta\dot{A}_4 \\ \Delta\dot{A}_6 \\ \Delta\dot{A}_8 \\ \hline \Delta\dot{A}_1 \\ \Delta\dot{A}_3 \\ \Delta\dot{A}_5 \\ \Delta\dot{A}_7 \\ \Delta\dot{A}_9 \end{array}\right] = \left[\begin{array}{c} F_2 \\ F_4 \\ F_6 \\ F_8 \\ \hline F_1 \\ F_3 \\ F_5 \\ F_7 \\ F_9 \end{array}\right] \qquad \left[\begin{array}{c|c} B_{11} & B_{12} \\ \hline B_{21} & B_{22} \end{array}\right] \left[\begin{array}{c} \Delta\dot{A}_1 \\ \hline \Delta\dot{A}_2 \end{array}\right] = \left[\begin{array}{c} F_1^{(f)} \\ \hline F_2^{(f)} \end{array}\right]$$

CD-88-32946

SOLUTION OF BEAM EXAMPLE

The solution for the nonidentity partition of both transformations is tridiagonal. For the fine-to-coarse transformation, the nonidentity partition is also lower triangular. For the coarse-to-fine transformation, the nonidentity partition is also upper triangular.

$$-B_{22}^{-1}B_{21} = \begin{bmatrix} T_1 & & \bigcirc & \\ S_2 & T_2 & & \\ & S_3 & T_3 & \\ & & S_4 & T_4 \\ \bigcirc & & & S_5 \end{bmatrix} \qquad \begin{aligned} T_L &= -Z_{2L-1}^{-1}W_{2L-1} \\ S_L &= -Z_{2L-1}^{-1}U_{2L-1} \end{aligned}$$

$$-B_{12}B_{22}^{-1} = \begin{bmatrix} X_1 & Y_1 & & \bigcirc & \\ & X_2 & Y_2 & & \\ & & X_3 & Y_3 & \\ \bigcirc & & & X_4 & Y_4 \end{bmatrix} \qquad \begin{aligned} X_L &= -U_{2L}Z_{2L-1}^{-1} \\ Y_L &= -W_{2L}Z_{2L+1}^{-1} \end{aligned}$$

$$B_{11} - B_{12}B_{22}^{-1}B_{21} = \begin{bmatrix} Z_1^{(c)} & W_1^{(c)} & & \bigcirc \\ U_2^{(c)} & Z_2^{(c)} & W_2^{(c)} & \\ & U_3^{(c)} & Z_3^{(c)} & W_3^{(c)} \\ \bigcirc & & U_4^{(c)} & Z_4^{(c)} \end{bmatrix} \qquad \begin{aligned} Z_L^{(c)} &= Z_{2L} + X_L W_{2L-1} + Y_L U_{2L+1} \\ U_L^{(c)} &= X_L U_{2L-1} \\ W_L^{(c)} &= Y_L W_{2L+1} \end{aligned}$$

$$\Delta\dot{A}_{2L} = \Delta\dot{A}_L^{(c)} \qquad \Delta\dot{A}_{2L-1} = S_L \Delta\dot{A}_{L-1}^{(c)} + T_L \Delta\dot{A}_L^{(c)}$$

$$F_L^{(c)} = F_{2L} + X_L F_{2L-1} + Y_L F_{2L+1}$$

CD-88-32947

ACCELERATION PARAMETER

Normally the relaxation technique can be improved by using a weighted average of the previous and present calculated values of the corrections to the solution (overrelaxation). The rate of convergence of the high-frequency components can be improved at the expense of the low-frequency components. For this improvement, an estimate of the highest frequency eigenvalue is needed. The Rayleigh quotient is a good method to estimate the highest eigenvalue (at least in the symmetric case). In addition the highest eigenvalue should be a strong function of the nearest neighbors, therefore local linearization could be used in the Rayleigh quotient.

$\epsilon(\lambda)$ IS BASED ON LOCAL COEFFICIENTS

$$\lambda = \frac{(\Delta \dot{\vec{A}})^T D (\Delta \dot{\vec{A}})}{(\Delta \dot{\vec{A}})^T (\Delta \dot{\vec{A}})}$$

THIS IS THE RAYLEIGH QUOTIENT

CD-88-32948

MULTIGRID METHOD

In summary, the multigrid method for structural dynamics is performed as follows. First relax the equations of motion on the fine grid to obtain the high-frequency components of the solution. Then calculate the norm of the residual on the fine model. Next check to see that the norm is small enough for a solution. If not, check to see if the norm has changed significantly from the previous iteration. If the norm has changed, then relax the solution until the norm stops changing. This indicates that the high-frequency components on this model have been found.

To find the lower frequency components of the solution, use the local structural condensation to generate a coarse model. On the coarse model, use relaxation to generate the lower frequency components of the solution. These lower frequency components are interpolated to the fine grid where the norm of the residual is calculated. Based on this norm, either a solution is found, more relaxation is needed, or a coarser model is needed. The process is repeated until a solution is found.

- **RELAX ON FINE GRID TO GET HIGH-FREQUENCY COMPONENT**
- **CALCULATE RESIDUAL ON FINE GRID**
- **CHECK RESIDUAL FOR SOLUTION**
- **CHECK CHANGE IN RESIDUAL FOR CHANGE IN GRID**
- **STATIC CONDENSE TO COARSE GRID**
- **RELAX ON COARSE GRID TO GET LOW-FREQUENCY COMPONENT**
- **INTERPOLATE LOW-FREQUENCY TO FINE GRID**

CD-88-32950

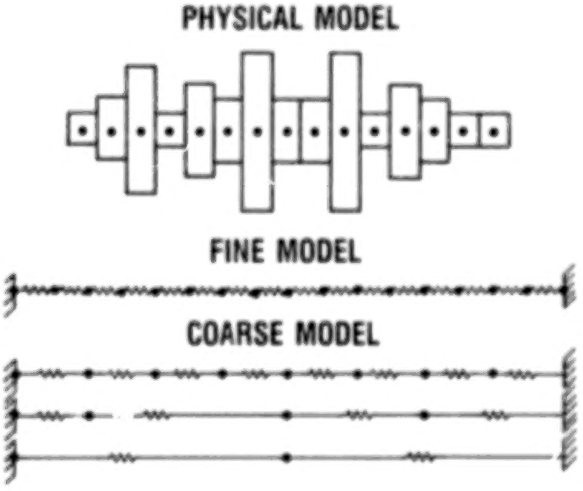

CD-88-32949

MULTIGRID ANALYSIS APPLIED TO TRANSMISSION DYNAMICS

Complete transmission dynamic analyses are rare in the open literature. David and Mitchell (1986) have used a modal balance technique. The problem with modal techniques is that the nonlinearities cause the set of modes not to be closed. This results in side bands around the tooth passing frequency. Therefore, the solutions may not always include all of the important modes. Also, superfluous modes tend to overwhelm the solution technique. The time march multigrid method should eliminate these problems.

TRANSMISSION DYNAMIC ANALYSIS

Transmission dynamics is a case of nonlinear structural dynamics. Physically a transmission is composed of gears, shafts, bearings, seals, and a case. The case and the shafts can be modeled by finite element methods. The bearings and seals are modeled by special programs developed in tribology and other areas. Gear interactions are developed for some kinds of gears, but not for others. Thus a transmission can be modeled by a number of linear and nonlinear finite elements. As a first approximation, a transmission can be modeled as a beam structure. The transmission can be analyzed as a multishaft, combined lateral, torsional, and axial rotordynamic system.

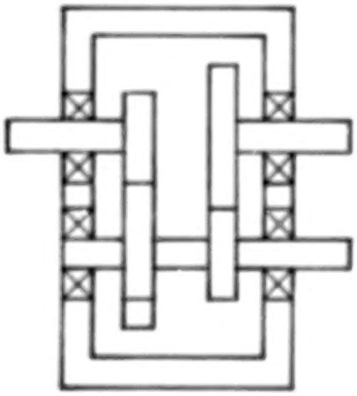

PHYSICAL MODEL

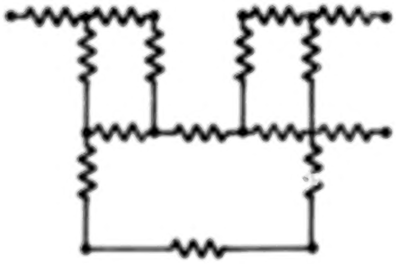

NONLINEAR FINITE ELEMENT MODEL

CD-88-32952

SPECIAL FEATURES

Special features complicate the dynamic analysis of transmissions. Gyroscopic and gear forces cause nonlinear lateral and torsional coupling. Gear-tooth passing frequencies are high-frequency forcing functions and, therefore, imply a need for a fine structural model. Gear-gear interactions cause the system to have a wide bandwidth.

- GYROSCOPIC AND GEAR FORCES CAUSE NONLINEAR LATERAL AND TORSIONAL COUPLING
- GEAR-TOOTH PASSING FREQUENCIES ARE HIGH-FREQUENCY FORCING FUNCTIONS—IMPLIES NEED FOR FINE STRUCTURAL MODEL
- GEAR-GEAR INTERACTIONS CAUSE WIDE BAND WIDTH

CD-88-32953

GEAR TOOTH INTERACTION

Consider gear tooth interaction. For any gear set, the line of force does not pass through the gear centers. In the case of spur gears any perturbation of the radial force will result in a perturbation of the tangential force and vice versa. In the case of helical or spiral gears any perturbation of the radial force will result in perturbations of both the axial and tangential force. These perturbations result in a nonlinear coupling between the axial, tangential, and radial directions.

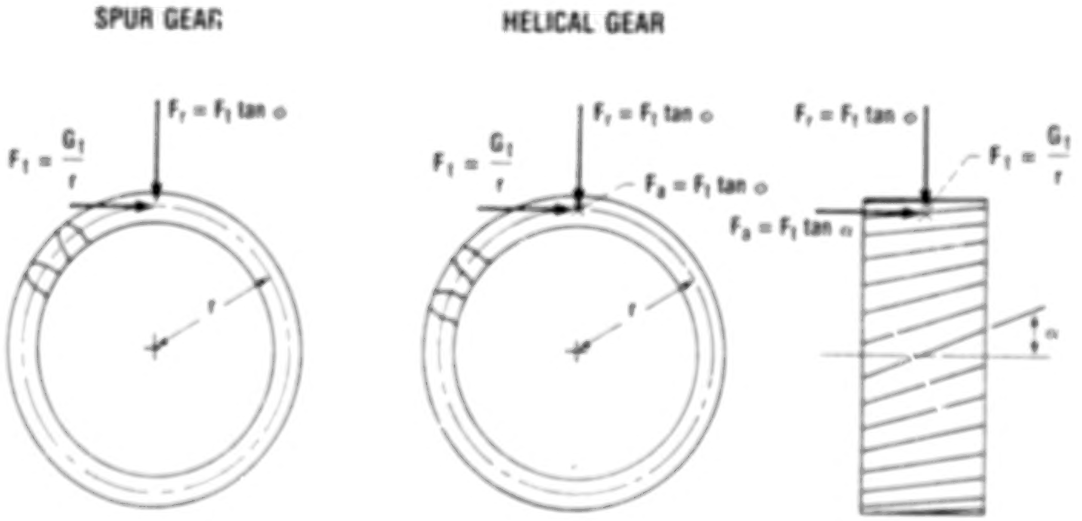
SPUR GEAR
HELICAL GEAR
$F_r = F_t \tan \phi$
$F_t = \frac{G_t}{r}$
r
$F_r = F_t \tan \phi$
$F_t = \frac{G_t}{r}$
$F_a = F_t \tan \alpha$
r
$F_r = F_t \tan \phi$
$F_t = \frac{G_t}{r}$
$F_a = F_t \tan \alpha$
α

CD-88-32954

GEAR TOOTH MODEL

Consider the gear tooth interactions of a spur gear set. The contact point varies as the angle of the gear set varies. Machining errors cause the contact point to move. High torque can cause the teeth to bend. The number of teeth in contact varies as the torque varies. Negative torque can result in backlash. The force must be transmitted through the contact point. All these effects cause nonlinear time varying interactions between the spur gears set. For the other kind of gears the interaction is more complicated. Thus, gear tooth interactions cause high-frequency forcing functions on the structure.

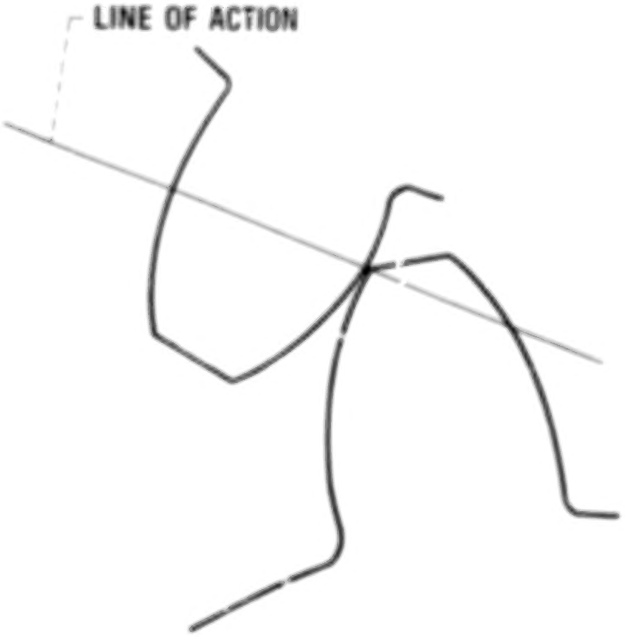

CD-88-32955

TYPICAL TRANSMISSION

In a typical transmission there are many gear sets. Each of these gear sets causes one location on the structure to interact with another point on the structure. Thus, far interactions are important and the structural model has a wide bandwidth.

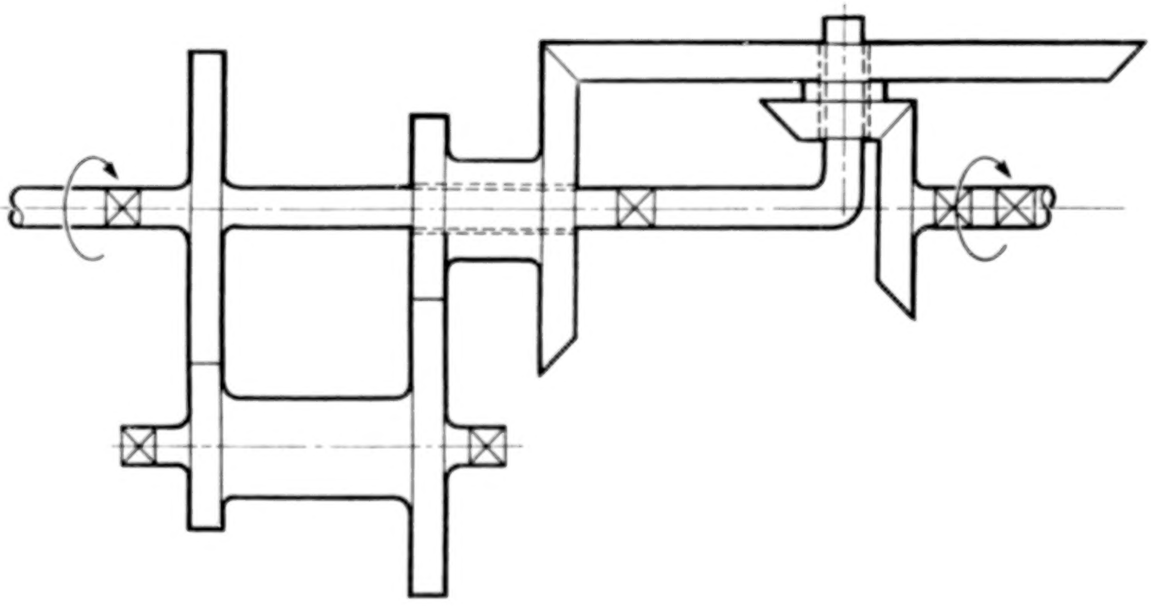

CD-88-32956

POTENTIAL IMPACT

The multigrid method, although used for years in fluid dynamics, now offers a new approach to nonlinear structural dynamics. The computing time does not depend on the cube of the number of degrees of freedom. Thus, dramatic reductions in computing time are possible. In addition, the relaxation process is applicable to parallel computation. Thus, the method is very attractive for future computers.

- **NEW APPROACH TO NONLINEAR STRUCTURAL DYNAMIC SIMULATION**
- **DRAMATIC REDUCTION IN COMPUTING TIME**
- **APPLICABLE TO PARALLEL COMPUTERS**

CD-88-32957

APPENDIX - SYMBOLS

A	acceleration vector
B	linearized coefficient matrix
C	damping matrix
D	diagonal matrix
F	force vector
G	gear torque
K	stiffness matrix
M	mass matrix
n	number of degrees of freedom
R	displacement vector
r	pitch radius of gear
S	block matrix used in Φ (beam solution)
T	block matrix used in Φ (beam solution)
t	time
L	block matrix on lower diagonal of B
V	velocity vector
W	block matrix on upper diagonal of B
X	block matrix used in Θ (beam solution)
Y	block matrix used in Θ (beam solution)
Z	block matrix on diagonal of B
α	constant, modifying Taylor series
β	constant, modifying Taylor series
ε	weighting factor used in overrelaxation
Θ	coarse-to-fine transformation
θ	helical gear angle
λ	highest eigenvalue
ξ	value between 0 and t

Φ	fine-to-coarse transformation
ϕ	pressure angle

Subscripts:

a	axial
L	node number
r	radial
t	tangential

Superscripts:

c	coarse model
f	fine model
T	transpose
•	time derivative
(0)	estimated value

REFERENCES

David, J.W., and Mitchell, L.D., 1986, "Linear Dynamic Coupling in Geared Rotor Systems," Transactions of the ASME, Journal of Vibration, Acoustics, Stress, and Reliability in Design, Vol. 108, pp. 171-176.

Gear, C.W., 1971, "Numerical Initial Value Problems in Ordinary Differential Equations," Prentice-Hall Inc.

Kascak, A.F., 1980, "The Response of Turbine Engine Rotors to Interferences Rubs," NASA TM-81518.

N88-23233

PARALLEL COMPUTER METHODS FOR EIGENVALUE EXTRACTION

Fred Akl*
Department of Civil Engineering
Ohio University
Athens, Ohio

ABSTRACT

This paper presents a new numerical algorithm for the solution of large-order eigenproblems typically encountered in linear elastic finite element systems. The architecture of parallel processing is used in the algorithm to achieve increased speed and efficiency of calculations. The algorithm is based on the frontal technique for the solution of linear simultaneous equations and the modified subspace eigenanalysis method for the solution of the eigenproblem. Assembly, elimination, and back-substitution of degrees-of-freedom are performed concurrently by using a number of fronts. All fronts converge to and diverge from a predefined global front during elimination and back-substitution, respectively. In the meantime, reduction of the stiffness and mass matrices required by the modified subspace method can be completed during the convergence/divergence cycle, and an estimate of the required eigenpairs can be obtained. Successive cycles of convergence and divergence are repeated until the desired accuracy of calculations is achieved. The advantages of this new algorithm in parallel computer architecture are discussed.

---

*NASA Resident Research Associate. Work funded by NASA grant NAG3-762 (monitor: L.J. Kiraly) and performed on-site at the Lewis Research Center for the Structural Dynamics Branch.

GENERALIZED EIGENPROBLEM

- New parallel algorithm for the solution of large-scale eigenproblems in finite element applications

- Assumptions

  (1) Linear elastic finite element models

  (2) n lower order eigenpairs are required, i.e., $\omega_1^2 \leq \omega_2^2 \leq \ \ldots \omega_n^2$

  (3) [K] is positive-definite

  (4) [M] is semipositive definite

$[K]\,[\Phi] = [M]\,[\Phi]\,[\Omega]$

N – DEGREES OF FREEDOM

REQUIRED n EIGENPAIRS, $n \leq N$

[K] POSITIVE-DEFINITE

CD-88-31668

PARALLEL ARCHITECTURE

- Consider a parallel computer with (m+1) processors (tasks).
- Designate the first processor as a global processor (task).
- Designate the remaining m-processors as domain processors (tasks).
- A finite element model can be divided into a number of domains equal to m.
- A star architecture (or tree) is the first to be investigated.

FINITE ELEMENT MODEL SUBDIVIDED INTO m DOMAINS

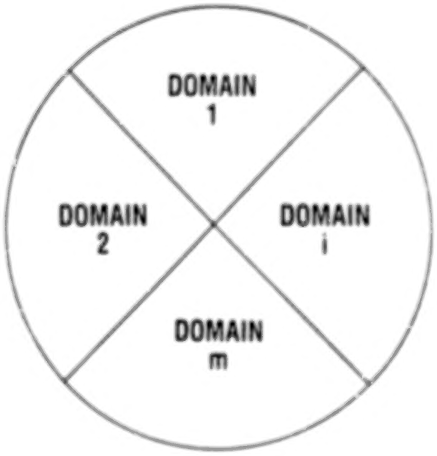
DOMAIN 1
DOMAIN 2
DOMAIN i
DOMAIN m

STAR ARCHITECTURE

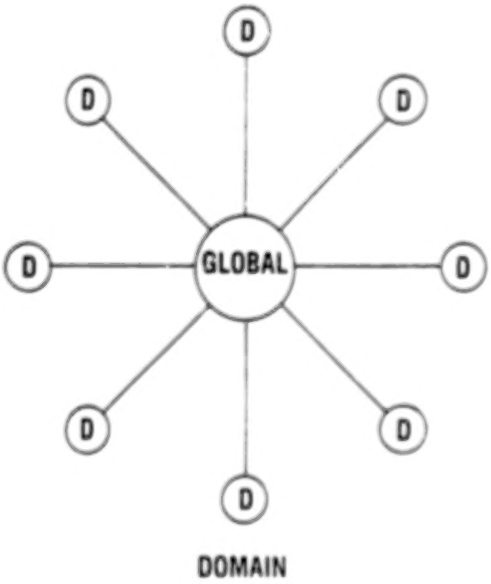
D
D
D
D
GLOBAL
D
D
D
D
DOMAIN

CD-88-31669

MAJOR COMPUTATIONAL TASKS

Three major steps of large computational requirements

(1) Creation of element stiffness and mass matrices

(2) Extraction of a set of eigenpairs

(3) Solution of a set of simultaneous linear equations

The merits of selecting the modified subspace method for step 2 and the frontal solution for step 3 are discussed in the next viewgraphs.

$$[K]\,[\Phi] = [M]\,[\Phi]\,[\Omega]$$

(1) CREATION OF K^e AND M^e

(2) EIGENSOLUTION (MODIFIED SUBSPACE)

(3) EQUATION SOLVER (FRONTAL SOLUTION)

CD-88-31670

MODIFIED SUBSPACE METHOD

The Modified Subspace Method iterates simultaneously for a subset of eigenpairs $[\phi,\omega^2]$ of the generalized eigenproblem:

(1) Let $[V]_1$ be n starting eigenvectors.

(2) Operate on each $[V]_\ell$ as follows:

$$[V]^*_{\ell+1} = [K]^{-1}[M][V]_\ell = [K]^{-1}[B]_\ell, \quad \ell = 1,2,3, \ldots$$

(3) Modify $[V]^*_{\ell+1}$ to increase convergence rate by one third on average

$$[V]^*_{\ell+1} \leftarrow [V]^*_{\ell+1} - \beta_\ell [V]_\ell$$

where $\beta_\ell = 0$ for $\ell = 1$ and $\ell > 11$

$$\beta_\ell = 0.5\,(1+r_{\ell-1})/\omega_n^2 \quad 1 < \ell \leq 11$$

$r_{\ell-1}$ are the interval points of the 11th order Labatoo rule [-1, 1]

(4) Project K and M onto the required subspace.

(5) Solve the auxiliary eigenproblem to obtain $[Q]_{\ell+1}$ and $[\Omega]_{\ell+1}$.

(6) An improved set of eigenvectors $[V]_{\ell+1}$ can be obtained.

(7) Test for convergence on ω_n^2. Repeat steps 2 to 6 until desired accuracy is achieved.

$$[K]^*_{\ell+1} = \sum_e [V]^{*T}_{\ell+1}[K][V]^*_{\ell+1}$$

$$[M]^*_{\ell+1} = \sum_e [V]^{*T}_{\ell+1}[M][V]^*_{\ell+1}$$

AUXILIARY EIGENPROBLEM

$$[K]^*_{\ell+1}[Q]_{\ell+1} = [M]^*_{\ell+1}[Q]_{\ell+1}[\Omega]_{\ell+1}$$

IMPROVED EIGENVECTORS

$$[V]^e_{\ell+1} = [V]^{*e}_{\ell+1}[Q]_{\ell+1}$$

CD-86-21671

RATE OF CONVERGENCE

Rate of convergence of the modified subspace is 33 percent faster on average compared to the classical subspace method.

The figure shows typical behavior.

Most computations are performed on an element-by-element basis.

BASIC SUBSPACE $\leq \dfrac{\omega_i^2}{\omega_{n+1}^2}$

MODIFIED SUBSPACE $\leq \dfrac{\omega_i^2}{\omega_{n+1}^2} \quad \dfrac{1-\beta_i\omega_{n+1}^2}{1-\beta_i\omega_i^2}$

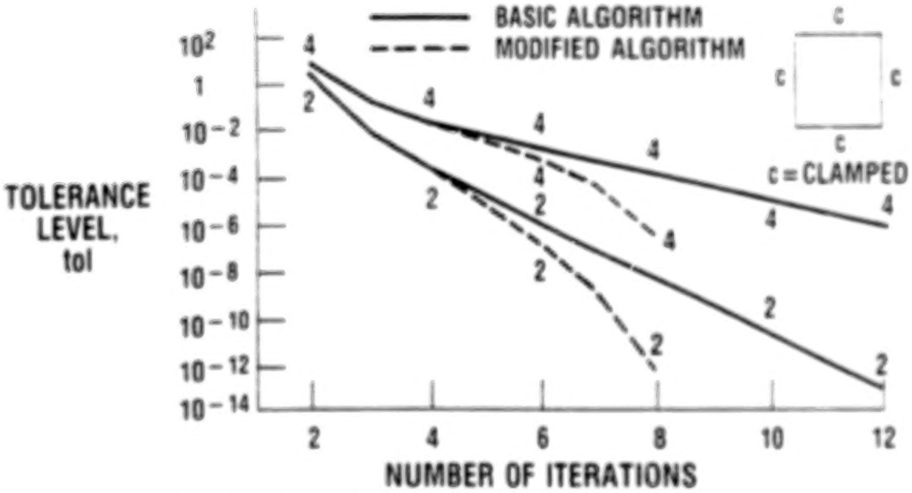

CONVERGENCE OF λ_2 AND λ_4 FOR SQUARE PLATE

CD-88-31672

FRONTAL SOLUTION

(1) Gauss elimination technique

(2) Underlying philosophy based on processing of elements one by one

(3) Simultaneous assembly and elimination of variables

(4) The optimum frontal width at most equal to the optimum bandwidth

(5) Numbering of nodes - no impact on optimality; numbering of elements - important to minimize the frontal width

(6) More efficient for solid elements and elements with midside nodes

(7) Requires a prefront to determine last appearance of each node

(8) Lends itself to parallel solutions

WITHIN EACH DOMAIN

$$k_{ij} = k_{ij} - \sum \left[\frac{k_{is} k_{sj}}{k_{ss}} \right]$$

$$b_{iq} = b_{iq} - \sum \left[\frac{k_{is} b_{sq}}{k_{ss}} \right]$$

CD-88-31673

DOMAIN PROCESSING

Multitasking on the Cray supercomputer provides tools for implementing the frontal solution concurrently within a number of domains. Assembly and elimination for the i-th domain is assigned to a task (processor). Simultaneous assembly and elimination of variables within the domains is performed in parallel tasks until the domain fronts reach their respective global fronts. However, it is instructive to analyze the set of simultaneous equations for the i-th domain assuming that the domain stiffness matrix and right-hand sides are fully assembled before Gauss elimination is performed.

For domain i

$$[K][V]^*_{\ell+1} = [B]_\ell \qquad \text{at iteration } \ell$$

Elimination gives

$$U_d V^*_d + K_d V^*_F = B_d$$

$$K_F \, V^*_F = B_F$$

where U_d upper Δ matrix for domain i

V^*_d variables within domain i

V^*_F variables along global front of domain i

B_d and B_F are right-hand sides for domain variables and global fronts, respectively.

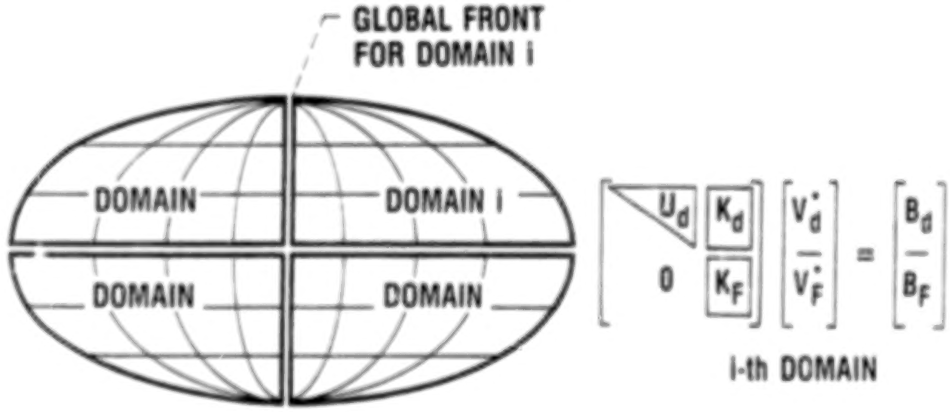

$$U_d \, V^*_d + K_d \, V^*_F = B_d$$

$$K_F \, V^*_F = B_F$$

CD-88-31674

GLOBAL FRONTS

$$K_{FF} = \sum^{m} K_F$$

$$B_{FF} = \sum^{m} B_F$$

where m = total numbers of domains

$$K_{FF} V_{FF} = B_{FF}$$

Solution for V_{FF} is then obtained by using the frontal solution on the global fronts. Since V_{FF} is a superset of all V_F^*, back-substitution for V_d^* follows concurrently within the domains.

$$K_{FF} = \sum^{m} K_F$$

$$B_{FF} = \sum^{m} B_F$$

WHERE m = TOTAL NUMBER OF DOMAINS

$$K_{FF} V_{FF} = B_{FF}$$

CD-88-31675

IMPLEMENTATION

Successful implementation of the new parallel algorithm depends on

(1) Maximizing the efficiency of communication links between the global task and the domains

(2) Minimizing sequential computational steps

(3) Multithreaded I/O

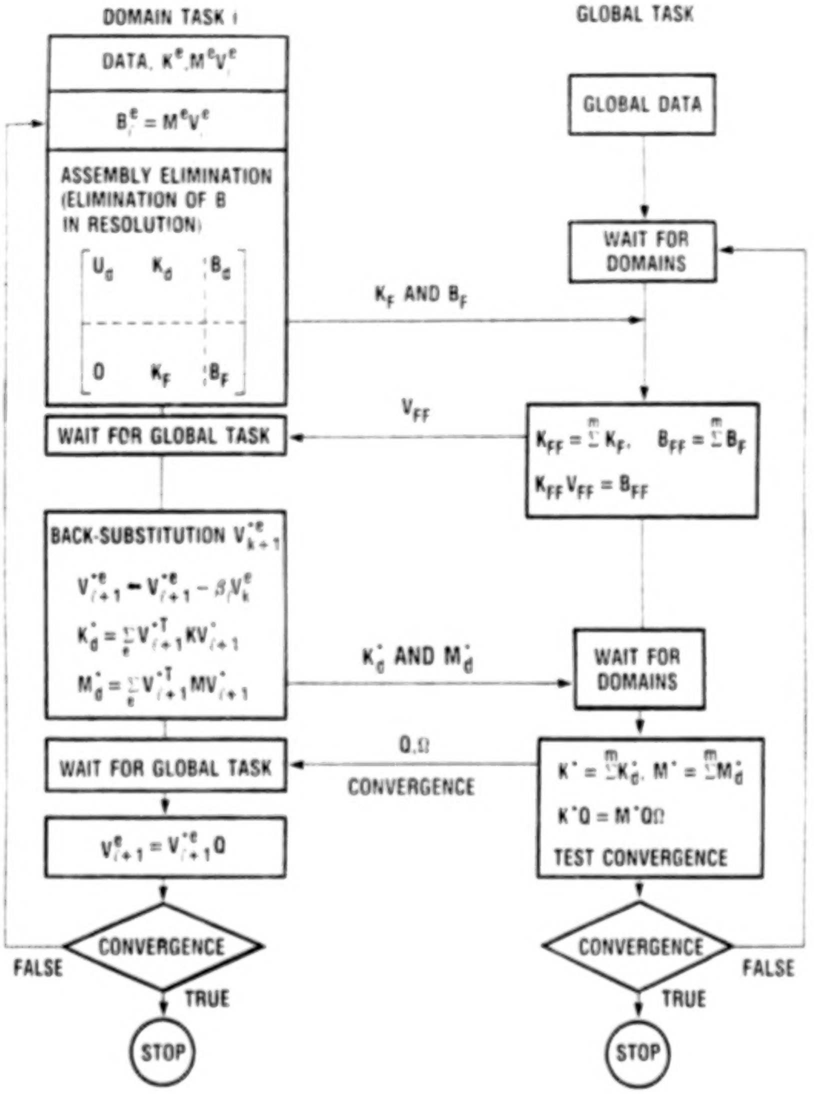
DOMAIN TASK i
GLOBAL TASK
DATA, $K^e, M^e V^e_i$
$B^e_i = M^e V^e_i$
ASSEMBLY ELIMINATION (ELIMINATION OF B IN RESOLUTION)
$\left[\begin{array}{cc|c} U_d & K_d & B_d \\ \hline 0 & K_F & B_F \end{array}\right]$
GLOBAL DATA
WAIT FOR DOMAINS
K_F AND B_F
V_{FF}
WAIT FOR GLOBAL TASK
$K_{FF} = \sum^m K_F, \quad B_{FF} = \sum^m B_F$
$K_{FF} V_{FF} = B_{FF}$
BACK-SUBSTITUTION V^{*e}_{k+1}
$V^{*e}_{i+1} \leftarrow V^{*e}_{i+1} - \beta_i V^e_k$
$K^*_d = \sum_e V^{*T}_{i+1} K V^*_{i+1}$
$M^*_d = \sum_e V^{*T}_{i+1} M V^*_{i+1}$
K^*_d AND M^*_d
WAIT FOR DOMAINS
Q, Ω
CONVERGENCE
WAIT FOR GLOBAL TASK
$K^* = \sum^m K^*_d, \; M^* = \sum^m M^*_d$
$K^* Q = M^* Q \Omega$
TEST CONVERGENCE
$V^e_{i+1} = V^{*e}_{i+1} Q$
CONVERGENCE
FALSE
TRUE
STOP
CONVERGENCE
FALSE
TRUE
STOP

CONCLUSIONS

Parallel solution method for eigenvalue extraction for linear elastic finite element models has been successfully implemented on the Cray supercomputer by using the multitasking environment. Preliminary results are encouraging and extensive testing of the new algorithm is currently progressing. The new algorithm enhances the speed-up of similar sequential solution methods. Both the frontal method for the solution of the set of simultaneous equations arising in finite element problems and the modified subspace method for the solution of a subset of eigenpairs offer a new algorithm which has been efficiently parallelized. The parallel tasks are associated with recognizable finite element domains rather than dissected blocks of abstract equations. Moreover, the complexity of data management and data flow normally associated with parallel solution methods is avoided in this new algorithm.

REFERENCES

Adams, L., and Ortega, J., 1982, "A Multi-Color SOR Method for Parallel Computation," Proceedings of the 1982 International Conference on Parallel Processing, IEEE, New York, pp. 53-56.

Akl, F.A. and Hackett, R.M., 1986, "A Multi-Frontal Algorithm for Parallel Processing of Large Eigenproblems," AIAA 27th Structures, Structural Dynamics, and Materials Conference, Part 2, AIAA, New York, pp. 395-399.

Baudet, G., 1978, "Asynchronous Iterative Methods for Multiprocessors," Journal of the Association for Computing Machinery, Vol. 25, pp. 226-244.

Bostic, S.W. and Fulton, R.E., 1986, "Implementation of the Lanczos Method for Structural Vibration Analysis on a Parallel Computer," AIAA 27th Structures, Structural Dynamics, and Materials Conference, Part 2, AIAA, New York, pp. 400-410.

Bostic, S.W. and Fulton, R.E., 1985, "A Concurrent Processing Implementation for Structural Vibration Analysis," AIAA 26th Structures, Structural Dynamics, and Materials Conference, Part 2, AIAA, New York, pp. 566-572.

Crockett, T.W. and Knott, J.D., 1985, "System Software for the Finite Element Machine," NASA CR-3870.

Darbhamulla, S.P., Razzaq, Z., and Storaasli, O.O., 1986, "Concurrent Processing in Nonlinear Structural Stability," AIAA 27th Structures, Structural Dynamics, and Materials Conference, Part 1, AIAA, New York, pp. 545-550.

Gannon, D., 1980, "A Note on Pipelining a Mesh Connected Multiprocessor for Finite Element Problems by Nested Dissection," Proceedings of the 1980 International Conference on Parallel Processing, IEEE, New York, pp. 197-204.

Rheinboldt, W.C. (Panel Chairman), 1985, "Report of the Panel on Future Directions in Computational Mathematics, Algorithms, and Scientific Software," Society of Industrial and Applied Mathematics, New York.

Salama, M., Utku, S. and Melosh R., 1983, Parallel Solution of Finite Element Equations," Proceedings of the 8th Conference on Electronic Computation, American Society of Civil Engineers, Houston, Texas, pp. 526-539.

Schendel, U., 1984, Introduction to Numerical Methods for Parallel Computers, Trans. by B.W. Conolly, Ellis Horwood Limited, New York.

Silbar, M.L., 1985, "The Pursuit of Parallelism," MOSAIC, National Science Foundation, Vol. 16, No. 3, pp. 8-17.

Storaasli, O.O., and Bergan, P., 1986, "A Nonlinear Substructuring Method for Concurrent Processing Computers," AIAA 27th Structures, Structural Dynamics, and Materials Conference, Part 2, AIAA, New York, pp. 13-20.

Storaasli, O.O., Peebles, S.W., Crockett, T.W., Knott, J.D. and Adams, L., 1982, "The Finite Element Machine: An Experiment in Parallel Processing," NASA-TM 84514.

N88-23234

ADAPTING HIGH-LEVEL LANGUAGE PROGRAMS FOR PARALLEL PROCESSING USING DATA FLOW

Hilda M. Standley
Department of Computer Science and Engineering
Toledo, Ohio

ABSTRACT

EASY-FLOW, a very high-level data flow language, is introduced for the purpose of adapting programs written in a conventional high-level language to a parallel environment. The level of parallelism provided is of the large-grained variety in which parallel activities take place between subprograms or processes. A program written in EASY-FLOW is a set of subprogram calls as units, structured by iteration, branching, and distribution constructs. A data flow graph may be deduced from an EASY-FLOW program. All permissible schedulings of executions within the graph are dictated by the data dependencies between units.

NASA Lewis Research Center Grant # NAG 3-699.
Technical Monitor: L. J. Kiraly

SOFTWARE TO FACILITATE PARALLELISM

Parallel software technology continues to lag behind parallel hardware technology. Synchronization and communication problems have been solved at the hardware level to the degree to enable several multiprocessor systems to be offered commercially. Software is required to provide for the efficient utilization of these multiprocessor systems. Three areas must be addressed in a parallel software solution: (1) the determination of potential parallelism, (2) partitioning the programs into processes or tasks, each of which may be assigned to a single processor, and (3) scheduling the program partitions to execute in a cooperative fashion.

(1) DETERMINE POTENTIAL PARALLELISM

(2) PARTITION A PROGRAM

(3) SCHEDULE PROGRAM PARTITIONS

DATA FLOW

The data flow schema of parallel computation (Agerwala, 1982) offers at the same time a model of software and hardware. Data values flow between nodes representing operations in a data flow graph. Data flowing into operations serve as operands. Input data values are consumed by an operation and result values output and directed to other operations for which they serve as operands. Execution is completely data driven. The presence of all data values required as operands triggers the execution of an operation. A single "operation" may be low-level (for example, an addition) or high-level (for example, the execution of a subprogram) (Babb, 1984).

$$P := (Q + R) * (Z - W)$$

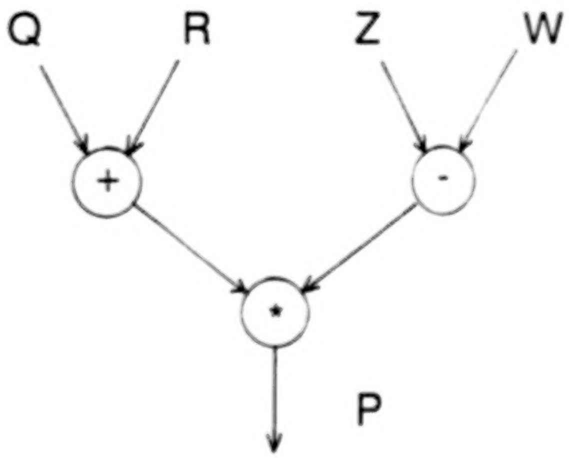

LANGUAGE DESIGN PROJECT GOALS

The language design project, resulting in EASY-FLOW (Standley, 1987), has three goals: to develop a language (1) to expose potential parallelism both implicitly and explicitly, at the large-grained level or below (referred to as "variable resolution"), (2) to provide for the continued use of the magnitude of software in existence with only minor modifications, and (3) to require very little retraining of conventional language programmers.

- TO EXPOSE PARALLELISM
- TO USE CURRENT SOFTWARE WITH
  ONLY MINOR
  MODIFICATIONS
- TO NECESSITATE VERY LITTLE
  RETRAINING OF
  CONVENTIONAL LANGUAGE
  PROGRAMMERS

STRUCTURING UNITS WITHIN AN EASY-FLOW PROGRAM

An EASY-FLOW program is specified as a hierarchy of units. Each unit consists of a substructure of units, a reference to an external unit, or it is atomic. An atomic unit is a call to a subprogram expressed in a conventional, high-level language such as FORTRAN or C.

Constructs in the EASY-FLOW language are used to specify the subunits (if any) in a unit and the relationships between them. Lists of "input values" and "output values" associated with each unit may be used to determine the data dependencies between units and can consequently be used in establishing the proper scheduling of unit executions.

EASY-FLOW offers the minimal set of language constructs required for the flow of control: sequencing (SUBPROGRAM call), branching (IF-THEN-ELSE), and looping (ITER for iteration). One additional construct, DISTRIBUTE, provides an explicit notation for parallelism.

- SUBPROGRAM CALL
- IF-THEN-ELSE
- ITER
- DISTRIBUTE

THE EASY-FLOW PROGRAM

The language constructs provide a framework within which one or more units may be placed. Multiple units appearing within a structure are termed a "unit set." Each unit is enclosed within an input list and an output list pair, stating the names of the data values required as "operands" and produced as results, respectively. A data flow graph may be constructed by the EASY-FLOW language processor from the data dependencies determined by these input/output pairs.

```
MAIN PROGRAM:

DECLARATIONS:

UNIT

ENDUNIT

UNIT
      IF

      THEN

      ELSE

ENDUNIT

UNIT

ENDUNIT
```

EXAMPLE PROGRAM, MAXTWO

The example program, MAXTWO, calculates the maximum of the values of the two functions, f and g, at a point X. Four names for data values are declared having type "real." The program consists of one unit, called MAIN, with one input value, X, and one output value, RESULT. The body of the MAIN unit is a unit set consisting of three units, each having a call to a subprogram as its body, for calculating functions f(X), g(X), and max(f(X),g(X)). These three units may appear in any order. Three subprograms F, G, and MAX (assumed to be written in a conventional language) must be supplied in order to complete the program.

```
MAXTWO:
    declare: real X,FX,GX,RESULT
    unit MAIN:
        input: X
            unit CALCF:
                into: X => X
                subprogram F(X,FX)
                outof:FX => FX
            endunit CALCF
            unit CALCG:
                into: X => X
                subprogram G(X,GX)
                outof:GX => GX
            endunit CALCG
            unit FINDMAX:
                into: FX => FX
                      GX => GX
                subprogram MAX(FX,GX,
                                RESULT)
                outof:RESULT=>RESULT
            endunit FINDMAX
        output: RESULT
    endunit MAIN
```

THE EASY-FLOW LANGUAGE PROCESSOR

The EASY-FLOW language processing system constructs a data flow graph from the program and partitions and assigns code for execution based upon the nature of the target machine. If the target machine is a uniprocessor, a topological sort on the nodes in the data flow graph determines an appropriate, although not necessarily unique, unit execution sequence. For a multiprocessor system, the partitioning and assignment may be directed by the data flow graph. The language processing system must also provide for the "sanitizing" of the traditional language subprograms, removing references to global variables, for example.

EASY-FLOW LANGUAGE PROCESSOR

- CONSTRUCTS DATA-FLOW GRAPH
- PARTITIONS AND ALLOCATES UNIT EXECUTION BASED UPON TARGET ARCHITECTURE
- "SANITIZES" TRADITIONAL LANGUAGE SUBPROGRAMS

BIBLIOGRAPHY

Agerwala, T., and Arvind, 1982, "Data Flow Systems--Guest Editors' Introduction," computer Vol. 15, No. 2, pp. 10-13.

Babb II, R., 1984, "Parallel Processing with Large-Grained Data Flow Techniques," Computer, Vol. 17, No. 7, pp. 55-61.

Standley, H., 1987, "A Very High Level Language for Large-Grained Data Flow," 1987 ACM Computer Science Conference Proceedings, St. Louis, Mo.

N88-23235

ITERATIVE FINITE ELEMENT SOLVER ON TRANSPUTER NETWORKS*

Albert Danial and James Watson
Sparta, Inc.
Huntsville AL 35805

ABSTRACT

Iterative methods have been proven effective in obtaining solutions to large, sparse systems of linear equations such as those generated by finite element and finite difference methods. In addition to being efficient on sequential computers, iterative methods have inherent parallelism that suggests a strong potential for acceleration using parallel processing computer networks. These factors make iterative methods ideal candidates for parallel finite element/finite difference solvers. Here, we describe the parallelism inherent in the Conjugate Gradient method and discuss the initial results of a parallel implementation on a network of twelve transputers.

The high efficiencies obtained (a speed-up of 11.2 was gained with 12 processors) indicate that significant speed-up can be achieved with larger transputer arrays if communication overhead can be kept low. To this effect, we suggest a method of communication that allows large, dynamically reconfigurable transputer arrays to exchange data in $\log_4 N$ steps for N processors.

PRECEDING PAGE BLANK NOT FILMED

---

*Work done for the Sturctural Dynamics Branch under NASA Contract NAS3- ; technical monitor: Louis J. Kiraly.

Introduction

As part of a NASA innovative research grant to develop a transputer-based finite element computing engine, researchers at SPARTA have investigated techniques and computing methods which show promise for efficient parallel execution. Here, we discuss recent work done to evaluate a parallel implementation of the Conjugate Gradient (CG) method on a network of transputers. Preconditioning is implied in the context of finite element applications, but is beyond the scope of this presentation. For direct factorization methods, see [George, et al. 1986], and for polynomial preconditioning, see [Allen, 1987].

The CG method has several attributes that make it attractive for solving finite element problems. It is robust even for poorly-conditioned problems, requires less memory than direct methods since there is no matrix fill-in, and works well for widely banded problems such as those created by three dimensional models. In addition, the CG method is well suited to adaptive analysis methods which slightly modify the stiffness matrix after each solution until descretization errors are minimized. In this case, rather than completely resolving the modified system of equations, the CG method can use the most recent solution as an excellent initial guess and will consequently converge quickly. Finally, because of its heavy usage of inherently parallel matrix-vector and vector-vector operations, the CG method shows great potential for efficient concurrent processing.

Here we describe the parallelism inherent to the method, demonstrate why communication determines efficiency, discuss our transputer implementation and show how transputers can be used in massive arrays before communication becomes a problem. Using the fractional summation method described here, we predict that a 1024 transputer network rated at 1.5 gigaflops, could attain a speed-up of 929 and provide a sustained computational rate on the order of 1 gigaflop.

CG Method for Solving Finite Element Problems

- Robust for poorly conditioned problems
- Lower memory requirements than direct methods
- Ideal solution method for adaptive analysis
- Efficient for widely banded, 3-D problems
- Computations are completely parallel

Twelve Transputer Implementation

- Speed-up of 11.2 obtained; higher possible
- Efficiency depends on method of communication

CG Method + Transputers + Link Switcher = Gflop Finite Element Solver

- Dynamically reconfigurable arrays allow efficient communication
- Could attain near-linear speed-up with thousands of processors rated with Gflops of powe

Conjugate Gradient Method

The CG method can be described by 18 single operation steps. These steps, given below, use the following notation:

$[A]$ = stiffness matrix

$\{b\}$ = force vector

$\{x\}^o$ = initial guess at a displacement vector

$\{x\}$ = displacement vector (the solution)

$\{p\},\{r\},\{s\},\{t\}$ = work vectors

α, β, u, v, w = scalars

k = iteration counter

1. $k = 0$
2. $\{p\}^o = [A]\{x\}^o$ matrix-vector multiply
3. $\{r\}^o = \{b\} - \{p\}^o$ vector subtraction
4. $\{p\}^o = \{r\}^o$ vector equivalence
5. $\{s\}^k = [A]\{p\}^k$ matrix-vector multiply
6. $u^k = \{r\}^k * \{r\}^k$ vector dot product
7. $v^k = \{p\}^k * \{s\}^k$ vector dot product
8. $\alpha^k = u^k / v^k$ scalar division
9. $\{t\}^k = \alpha^k * \{p\}^k$ vector scaling
10. $\{x\}^{k+1} = \{x\}^k + \{t\}^k$ vector addition
11. Stop if $||\{t\}^k|| < \text{tolerance}$ vector comparison
12. $\{s\}^k = w^k * \{s\}^k$ vector scaling
13. $\{r\}^{k+1} = \{r\}^k - \{s\}^k$ vector subtraction
14. $v^{k+1} = \{r\}^{k+1} * \{r\}^{k+1}$ vector dot product
15. $\beta^k = v^{k+1} / u^k$ scalar division
16. $\{p\}^k = \beta^k * \{p\}^k$ vector scaling
17. $\{p\}^{k+1} = \{r\}^{k+1} + \{p\}^k$ vector addition
18. increment k
19. Go to step 5.

The following operations are performed at each iteration:

1 Matrix-vector multiplication
3 Vector dot products
3 Vector scalings
3 Vector additions
1 Vector comparison

Each one of these computations can be performed in parallel.

Parallelism in the Conjugate Gradient Method

The single most time consuming step is the matrix-vector multiply at step 5. Fortunately, it is also the operation most easily performed in parallel: each node receives a horizontal slice of the stiffness matrix and a complete copy of the {p} vector, then independently multiplies the matrix slice with the corresponding terms in {p} to obtain a partial solution for {s}. The vast majority of the remaining steps involve other vector operations, so a first glance might suggest that the algorithm is trivial to complete in parallel since the vectors can be divided up among the processors to be operated on concurrently.

This is only partially true on a local-memory processing network, however, since there are data dependencies between steps that require the processors to exchange data. After each processor computes its segment of {s} at step 5 for example, it can only perform one or two more steps before it needs a complete copy of {s} or a complete sum for v^k to perform the vector scaling at step 9. This type of data dependency (where each processor has a fraction of a value yet requires the sum of all fractions on every processor to continue), the only type encountered in the CG method, is resolved by a process called fractional summation. As its name implies, each processor simultaneously sends, receives and sums individual fractions of the value, preferably in a well-coordinated manner, until each processor has the complete sum. These communication steps can impede performance of a parallel CG solver, and must proceed as quickly as possible. The formula and graph below illustrate the effects of communicate time on speed-up.

T_c = Time spent communicating

T_p = Time spent executing parallel tasks (all compute time in CG method)

N = Number of processors

$$\text{Speed-up} = \frac{N}{N \cdot \frac{T_c}{T_p} + 1}$$

Speed-Ups for Various Ratios of Overhead

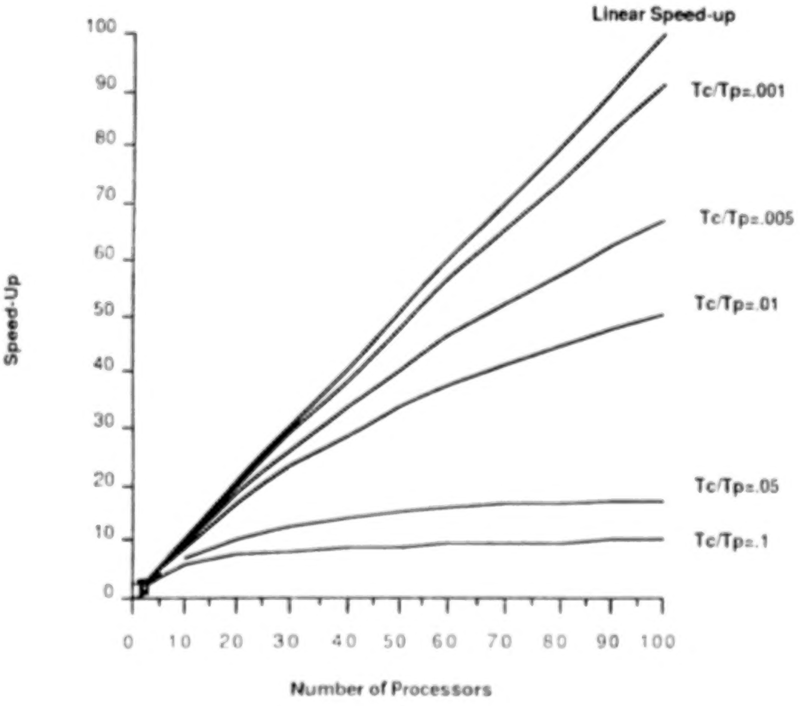

Transputer Network and Test Problem

The parallel processing network we used to implement the CG method consisted of twelve INMOS T414 transputers as shown below. Each transputer has 256 Kbytes of local RAM memory and four links capable of transferring data to other transputers at a rate of 10 Mbits/second.

A simple test problem consisted of a 2-D square plate subdivided into 81 isoparametric, four-node elements yielding 200 degrees of freedom. The lower left corner of the plate was pinned, the lower right corner constrained from vertical motion and the top right corner had a horizontal applied load.

Although the stiffness matrix was tightly banded, the implemented CG code carried all matrix and vector operations out in full, as if the matrix were dense.

TWELVE TRANSPUTER NETWORK
ARRANGED IN A DOUBLE-RING GRID

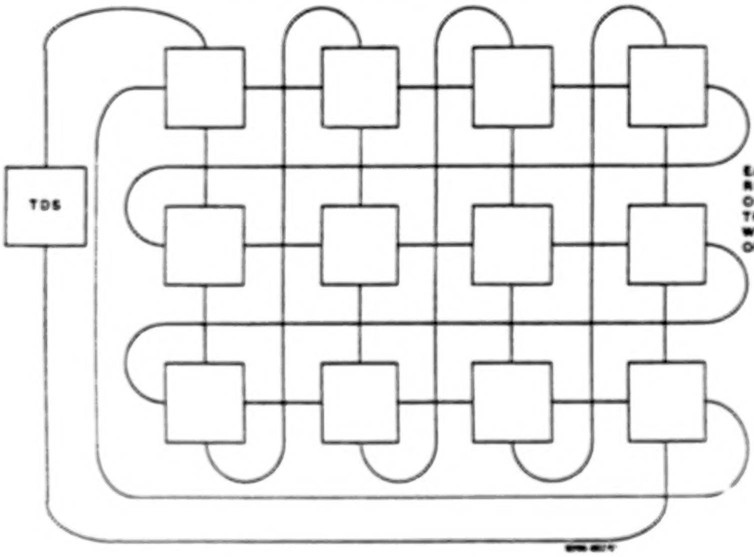

EACH BOX REPRESENTS ONE T414 TRANSPUTER WITH 256 Kbytes OF RAM

TEST PROBLEM

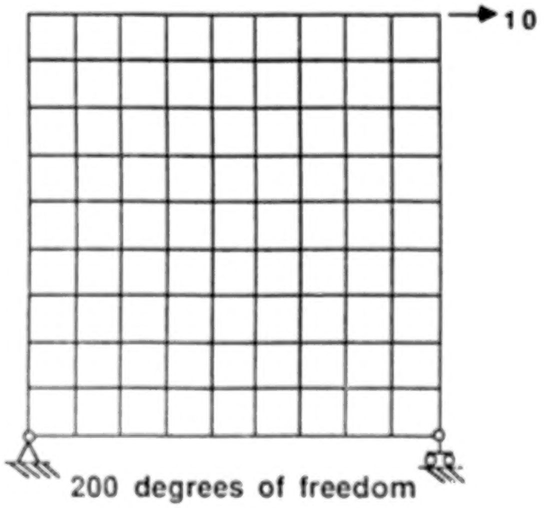

Results

Three versions of the CG method were implemented: a fully sequential version to provide a reference for performance, a parallel version written with Adnet (a high-level communications environment) and a second parallel version using direct, hardcoded communications that sent messages around a ring. The programs all stopped after 73 iterations, when changes to the displacement vector were less than a tolerance of 0.00001. The execution times are tabulated and shown graphically below.

Method: Number of Processors	Sequential	Parallel with Adnet Sec. (speed up)	Parallel without Adnet Sec. (speed up)
1	102.2		
4		26.61 (3.84)	
5		22.53 (4.54)	
6		19.60 (5.21)	
7		17.91 (5.71)	
8		16.22 (6.30)	
9		14.98 (6.82)	
10		14.14 (7.22)	
11		13.29 (7.69)	
12		12.87 (7.94)	9.13 (11.2)

Despite the impressive speed-up obtained, a timing analysis of the data exchanges showed that still higher speed-ups are possible. When done independently, the data exchanges around the processor ring take less than one-thousandth of the time calculations require, indicating that efficiencies of 0.989, or a speed-up of 11.87, should be possible on the network of twelve transputers. Further analyses of our implementation are being conducted to pinpoint the causes for the sub-optimum run times.

EXECUTION TIME AND SPEED UP VERSUS NUMBER OF PROCESSORS FOR THE TEST PROBLEM

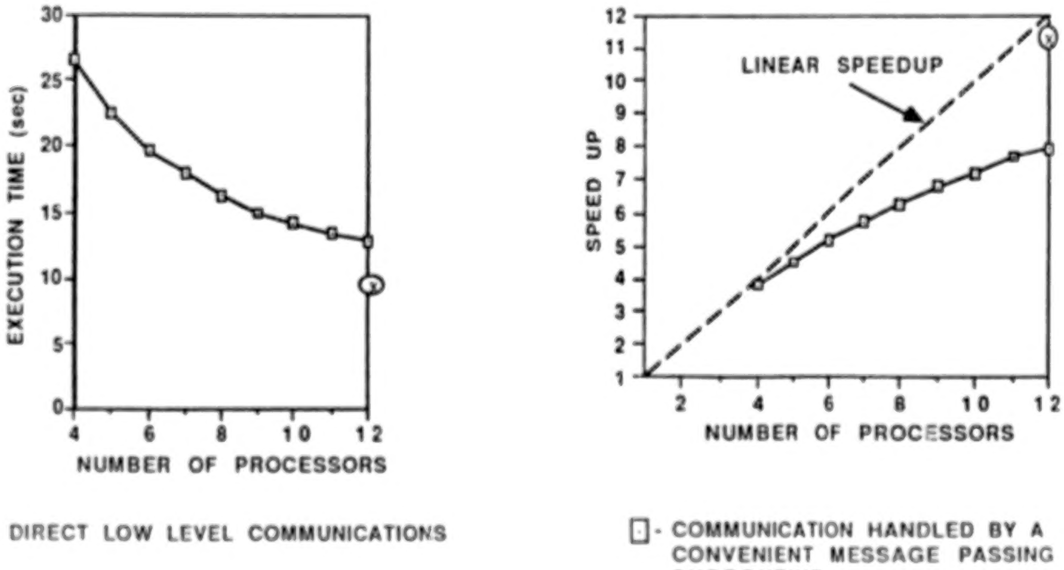

Fractional Summation on a Large, Dynamically Reconfigurable Network

If every processor in a network were directly connected to all other processors, fractional summation would be trivial -- each node would simply send its fraction out on every out-link and collect fractions from other nodes from its in-links. Few parallel processors, however, have more than 10 links, so direct connection schemes can only be used on small networks. Networks of indirectly connected processors perform fractional summation in a series of transmit and receive steps and can spend considerable amounts of time communicating. Large networks require more communication steps than small networks, making high speed-ups increasingly difficult to obtain. The table below lists the number of communication steps required to perform a fractional summation on several types of network topologies.

N = Number of processors

S = Number of steps required for fractional summation

Topology	S	Number of steps required if N = 1024
Ring	$N - 1$	1023
Double-ring grid	$2\sqrt{N}$	64
Shuffled exchange [Allen, 1987]	$2\log_2 N$	20
Hypercube	$\log_2 N$	10
Dynamically reconfigurable transputer array	$\log_4 N$	5

Example of Fractional Summation on a Dynamically Reconfigurable Network

Although transputers have only four links each, programmable link switches such as the INMOS C004 and the Unisys Switch Slice allow programs to change the network configuration during execution. Configuration changes can be made in one microsecond and can take place while the processors are busy computing, so negligible overhead is incurred. These link switches are extremely powerful devices and make possible several advanced types of network data distribution, one of which is fractional summation on a dynamically reconfigurable network. The basic idea behind this kind of fractional summation is to group together small islands of directly connected processors, allow them to exchange values, then reshuffle the processor connections so that each processor is relinked with a completely different set of processors. In this manner, the number of communication steps required will be reduced to $\log_{(1+L)} N$ where L is the number of links each processor uses to exchange data.

The example below illustrates how a network of 16 transputers connected to a programmable link switch can perform a fractional summation in two steps.

STEP 1

Network configuration: Fully connected sets of four processors. Set J contains the processors whose ID's satisfy the integer division equation

$$J = \frac{ID}{4}$$

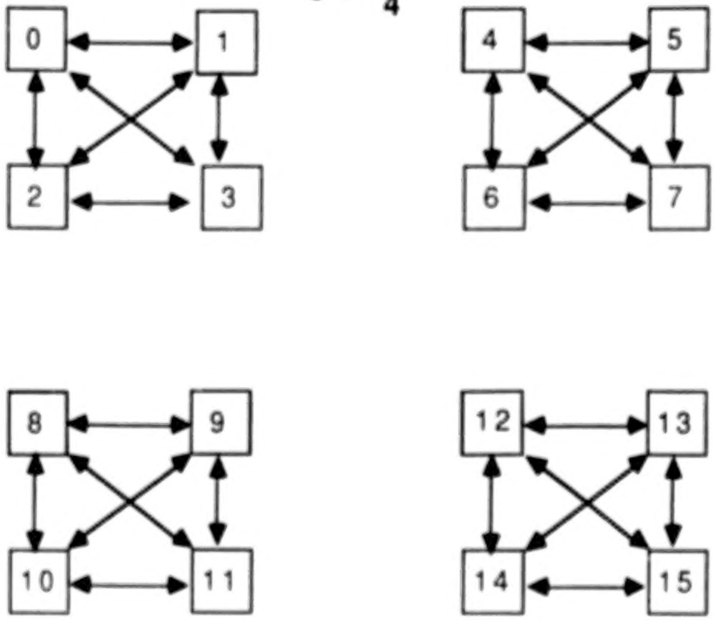

The sums on each processor will then be:

Node 0: 0+1+2+3
Node 1: 0+1+2+3
Node 2: 0+1+2+3
Node 3: 0+1+2+3
Node 4: 4+5+6+7
Node 5: 4+5+6+7
Node 6: 4+5+6+7
Node 7: 4+5+6+7
Node 8: 8+9+10+11
Node 9: 8+9+10+11
Node 10: 8+9+10+11
Node 11: 8+9+10+11
Node 12: 12+13+14+15
Node 13: 12+13+14+15
Node 14: 12+13+14+15
Node 15: 12+13+14+15

Example of Fractional Summation on a Dynamically Reconfigurable Network (Continued)

Here, only three of the four links on each transputer are being used (L=3). A free link is reserved on each node to allow the node to send control information to the link switches, or to some master transputer which controls the network configuration. If a timing scheme is used to control link switchings, all four links can be used (L=4) and the number of communication steps will be reduced to $\log_5 N$.

The methods and equipment described here can be used to assemble a massive CG solver capable of obtaining three orders of magnitude of speed-up, and sustaining on the order of one gigaflop of double precision computations. An array of 1024 T800 transputers with 1 Mbyte of RAM connected by 196 programmable link switches, should be able to run a CG algorithm with an overhead fraction (Tc/Tp) between 0.0001 and 0.001.

These overhead fractions correspond to a speed-up range from 506 to 929.

STEP 2

Network configuration: Fully connected sets of four processors. Set J contains the processors [J, J + 4, J + 2(4), J + 3(4)]

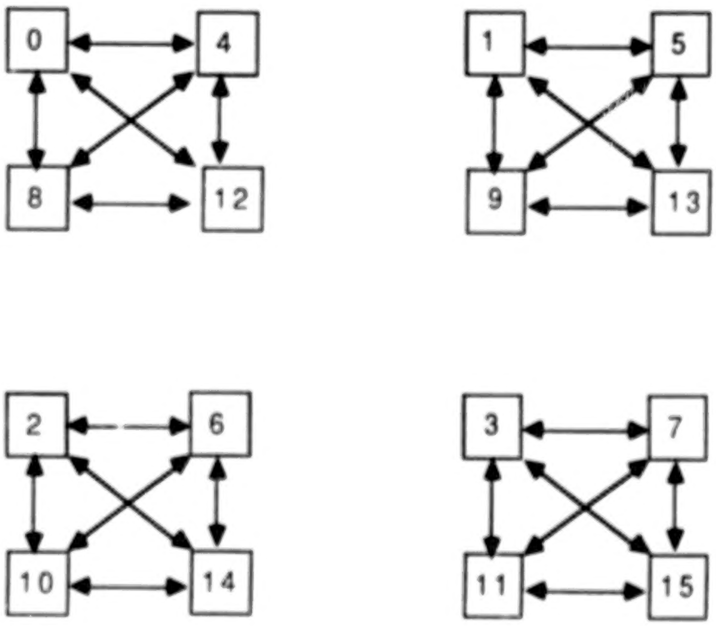

After Step 2, all of the processors will have the complete sum:

Node 0: 0+1+2+3+4+5+6+7+8+
9+10+11+12+13+14+15
Node 1: 0+1+2+3+4+5+6+7+8+
9+10+11+12+13+14+15
Node 2: 0+1+2+3+4+5+6+7+8+
9+10+11+12+13+14+15
Node 3: 0+1+2+3+4+5+6+7+8+
9+10+11+12+13+14+15
Node 4: 0+1+2+3+4+5+6+7+8+
9+10+11+12+13+14+15
•
•
•
Node 15: 0+1+2+3+4+5+6+7+8+
9+10+11+12+13+14+15

Conclusion

The parallel CG method has all the attributes of an ideal finite element solver: its computations are completely parallel enabling many processors to obtain large speed-ups; its iterative nature makes it the solution method of choice for adaptive analysis, where small refinements to the stiffness matrix only require few additional computations to obtain a new solution; and finally, the matrices can be stored in compact form since the method does not fill them in as direct methods do.

The only overhead incurred in the parallel CG method is the communication time it takes to resolve data dependencies. It was demonstrated that even inefficient ring communication schemes could attain high speed-ups - our code ran 11.2 times faster on 12 transputers than it did on one. Speed-up for the CG method is inversely proportional to the time spent communicating during fractional summation, so large networks must have efficient methods of exchanging data in order to maintain high speed-ups.

Programmable link switches, devices that permit connections between transputers to be made through software control, can be used in large transputer networks to distribute data faster than any other local-memory MIMD architecture. This permits larger networks to operate at a given communicate-to-compute ratio. This permits large networks of transputers to operate at the same overhead levels as much smaller, hardwired networks. Fractional summation on a dynamically reconfigurable network was shown to require only $\log_4 N$ communication steps - half the number a hypercube of the same size needs. The resulting reduction in communication overhead should enable more than one thousand transputers to run parallel CG code with an efficiency above 90%. At the current price of a 1 Mbyte T800 transputer rated at 1.5 megaflops, a 1 gigaflop finite element solver could be built for less than $1,000.000.

CG Method Excellent for Parallel Finite Element Solvers

- Computations are completely parallel
- Natural solution technique for adaptive analysis
- Can solve larger problems than direct methods in the same amount of RAM

Results for 12 Transputer Implementation

- Speed-up of 11.2 obtained; many improvements possible
- Demonstrated that efficiency depends on fraction of communication time to compute time

Dynamically Reconfigurable Transputer Arrays

- Reduce communication overhead
- Permit thousand-processor networks to function efficiently
- Could make possible a Gflop finite element machine for less than $1,000,000

References

1. Allen, R., 1987, "Matrix/Vector Multiplication and the Conjugate Gradient Algorithm on Transputers," presented at the Occam Users Group Meeting, September 29, 1987, Chicago, IL.

2. George, A. et al., 1986, "Sparse Cholesky Factorization on a Local Memory Multiprocessor," Oak Ridge National Laboratory TM-9962, Oak Ridge, TN.

N88-23236

MULTIPROCESSOR GRAPHICS COMPUTATION AND DISPLAY USING TRANSPUTERS

Graham K. Ellis*
Structural Dynamics Branch
Institute for Computational Mechanics in Propulsion
NASA Lewis Research Center

ABSTRACT

The transputer parallel processing lab at NASA Lewis Research Center consists of 69 processors (transputers) that can be connected into various networks for use in general purpose concurrent processing applications. The main goal of the lab is to develop concurrent scientific and engineering application programs that will take advantage of the computational speed increases available on a parallel processing system over a sequential processing system.

Because many scientific and engineering applications of interest generate large volumes of raw data, it is often convenient to display results in a graphic format. Since the analyses are performed on the transputer system, a package of graphics manipulation and display routines has been developed to also run on that system. This reduces the need for transferring data to other systems for viewing and postprocessing.

The transputer multiprocessor graphics display program uses techniques that would be of value in almost any concurrent application. Some of the topics studied in the lab include interprocessor communication time versus computation time, handling and simulation of global variables on processors with only local memory, and process synchronization.

The current implementation of the graphics program uses two processors to perform all of the graphics computations. The display processor board performs the low-level, device coordinate scan-conversion tasks and drives a CRT monitor. This low-level operating environment is normally transparent to the applications programmer although, if necessary, graphics applications can be developed using the low-level routines. The applications programmer normally interfaces with the other processor, the two-dimensional processor. At this level, all graphics operations can be performed in a two-dimensional world space. Standard two-dimensional operations such as rotation, translation, and scaling can be performed using the provided routines. Other routines allow multiple windows to be manipulated individually and allow screens and windows to be double buffered for smooth animation.

---

*Senior Research Associate (work funded under Space Act Agreement C99066G).

PRECEDING PAGE BLANK NOT FILMED

Future enhancements to the graphics system will include extensions to three-dimensional space. This would probably involve adding one or more processors to the current two in order to keep drawing speeds sufficiently fast.

OVERVIEW

WHAT IS A TRANSPUTER?

A transputer is a microcomputer with its own local memory and with links that can be used to connect it to other transputers. A transputer can be used in a single processor system, or in networks to build high-performance concurrent systems. The following figure was adapted from INMOS (1986).

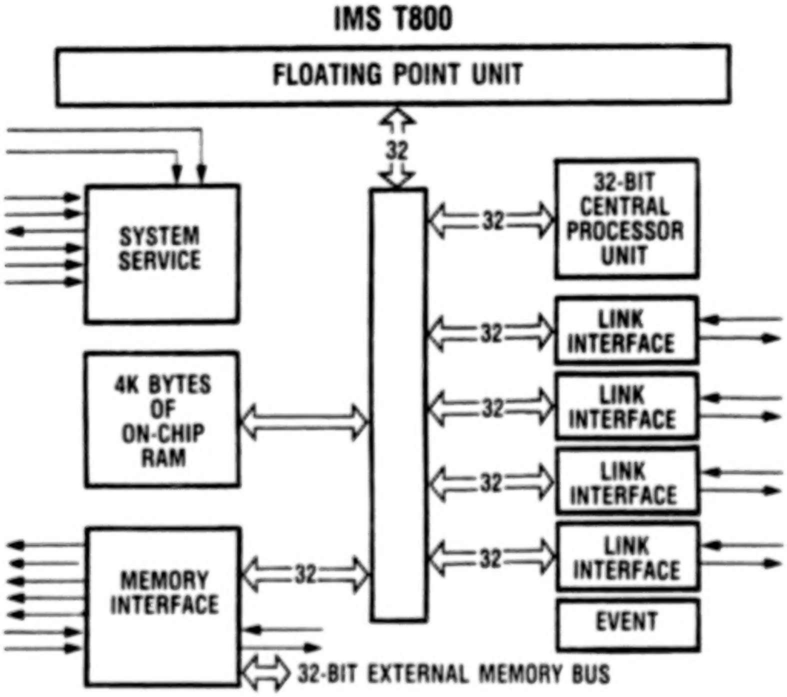
IMS T800
FLOATING POINT UNIT
32
SYSTEM SERVICE
4K BYTES OF ON-CHIP RAM
MEMORY INTERFACE
32
32-BIT CENTRAL PROCESSOR UNIT
LINK INTERFACE
LINK INTERFACE
LINK INTERFACE
LINK INTERFACE
EVENT
32
32
32
32
32
32-BIT EXTERNAL MEMORY BUS

CD-88-32004

BENEFITS OF TRANSPUTERS - FLEXIBLE CONNECTION ARCHITECTURE

Transputers can be used to build low-cost, high-speed concurrent networks. Flexible connection architecture allows optimum configuration for a wide range of problems. The following figure was adapted from INMOS (1986).

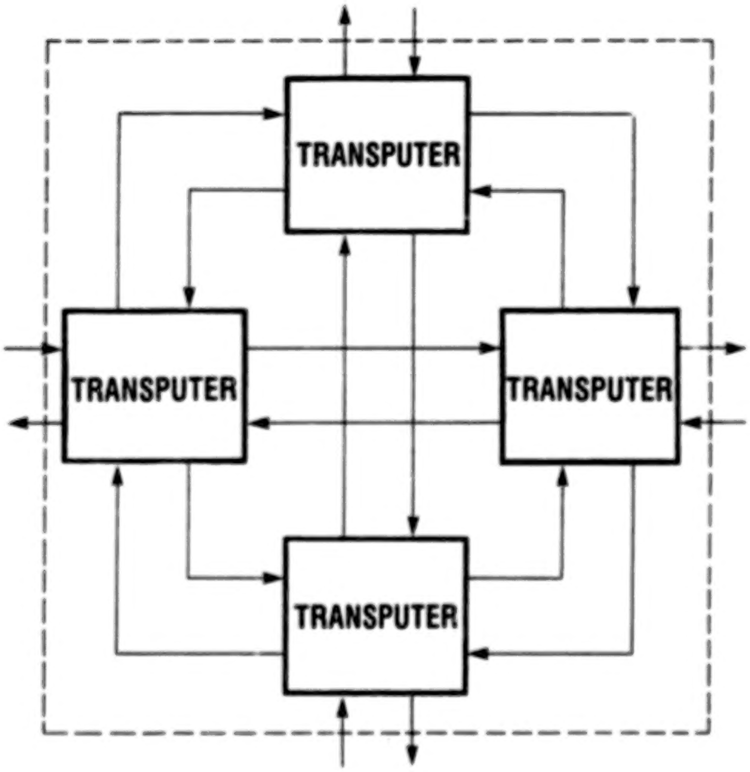
TRANSPUTER
TRANSPUTER
TRANSPUTER
TRANSPUTER

CD-88-32005

TRANSPUTER PARALLEL PROCESSING LABORATORY FACILITIES

The transputer parallel processing laboratory facilities include the following:

(1) Forty 32-bit floating point transputers with 256 KBytes memory per transputer

(2) Twenty-seven 16-bit integer processors - 24 with 8 KBytes of high-speed memory and 3 with 64 KBytes of high-speed memory

(3) One 32-bit transputer-based medium-performance graphics display board with 512 by 512 pixel resolution and capable of displaying 256 out of 262 144 colors at one time

(4) One 32-bit transputer-based development board with 2 MBytes of memory. The development board plugs into the IBM PC slot. System development software is run on this board.

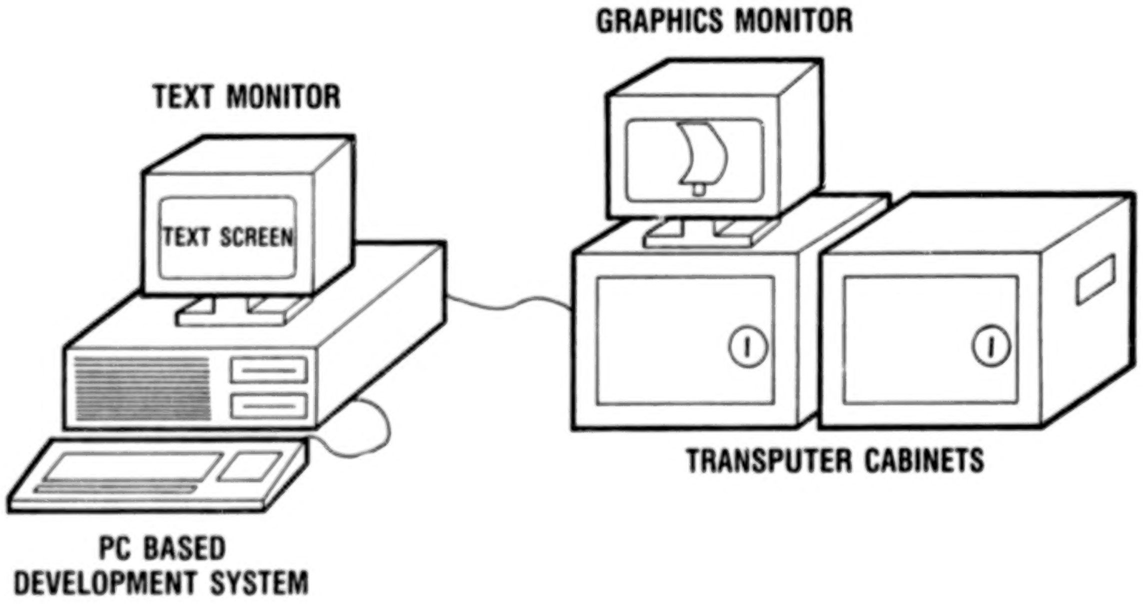
GRAPHICS MONITOR
TEXT MONITOR
TEXT SCREEN
TRANSPUTER CABINETS
PC BASED DEVELOPMENT SYSTEM

CD-88-32006

BENEFITS OF MULTIPROCESSOR GRAPHICS COMPUTATIONS

- ALLOWS ANALYSIS AND POST PROCESSING TO BE PERFORMED ON ONE SYSTEM

- USES MULTIPROCESSING TECHNIQUES FOR INCREASED PERFORMANCE

- TECHNIQUES DEVELOPED SHOW HOW CAREFUL ANALYSIS OF COMPUTATION VERSUS COMMUNICATION CAN BE USED FOR DETERMINING PERFORMANCE OF CONCURRENT ALGORITHMS

CD-88-32007

POSTER PRESENTATION

WHAT IS A TRANSPUTER?

A transputer is a microcomputer with its own local memory and with links that can be used to connect one transputer to another transputer.

A typical member of the transputer family is a single-chip very large scale integration (VLSI) device that contains a processor, memory, and serial links for point-to-point communication between transputers. A transputer can be used in a single processor system or in networks to build high-performance concurrent systems (INMOS, 1986).

Some of the transputers currently available include a 16-bit transputer with four serial links and 2K of on-chip memory; a 32-bit transputer with four serial links and 2K of on-chip memory; and a 32-bit transputer with four serial links, 4K of on-chip memory, and a built-in floating point unit. The serial links can transfer data at 10 or 20 Mbit/sec.

The block diagram of the floating point version of the transputer chip is shown below.

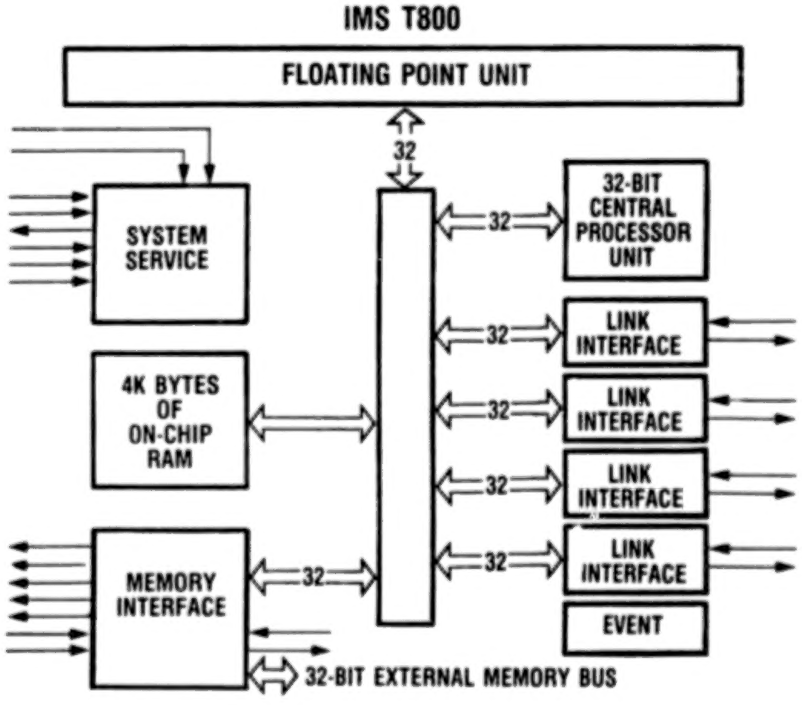
IMS T800
FLOATING POINT UNIT
32
SYSTEM SERVICE
32-BIT CENTRAL PROCESSOR UNIT
32
LINK INTERFACE
32
4K BYTES OF ON-CHIP RAM
LINK INTERFACE
32
LINK INTERFACE
32
MEMORY INTERFACE
32
LINK INTERFACE
32
EVENT
32-BIT EXTERNAL MEMORY BUS

CD-88-32004

PROGRAMMING NETWORKS OF TRANSPUTERS

Transputers can be programmed in high-level languages such as FORTRAN, C, and Pascal. To take full advantage of concurrent programming capabilities, transputers can be programmed in Occam. Occam takes advantage of the multitasking and communication features built into the transputer architecture.

The Occam software building block is the process. A system is designed as an interconnected set of processors. Each process communicates to other processes through point-to-point channels. Process-to-process communication is automatically synchronized without user intervention.

The following figure shows three processes that are running on either a single processor or a network of three processors. The Occam code fragments show how easy it is to change the mapping from a single transputer to a network of transputers.

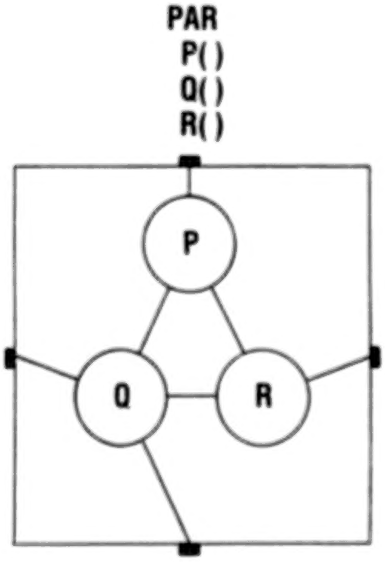

```
PAR
  P()
  Q()
  R()
```

A PROGRAM ON
A SINGLE TRANSPUTER

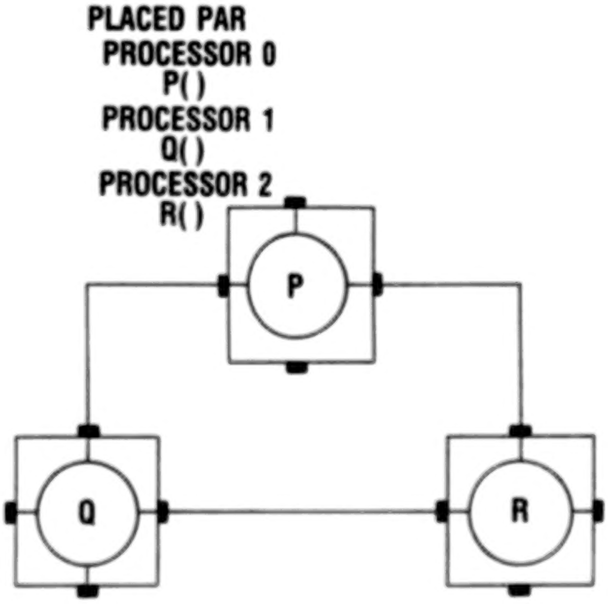

```
PLACED PAR
  PROCESSOR 0
    P()
  PROCESSOR 1
    Q()
  PROCESSOR 2
    R()
```

THE SAME PROGRAM ON
THREE TRANSPUTERS

CD-88-32008

TRANSPUTER PARALLEL PROCESSING LABORATORY FACILITIES

The transputer parallel processing laboratory facilities consist of the hardware and software described below. All of this equipment can fit on a desktop and requires no special cooling or power.

HARDWARE

- IBM AT-COMPATIBLE PC THAT ACTS AS THE SYSTEM FILM SERVER
- ONE 32-BIT TRANSPUTER DEVELOPMENT SYSTEM WITH 2M DRAM (PLUGS INTO PC SLOT)
- FORTY 32-BIT FLOATING-POINT TRANSPUTERS WITH 256K DRAM PER TRANSPUTER FOR A TOTAL OF 10M
- TWENTY-SEVEN 16-BIT TRANSPUTERS—24 WITH 8K SRAM AND 3 WITH 64K SRAM
- ONE GRAPHICS BOARD CONTAINING ONE 32-BIT TRANSPUTER, 512K PROGRAM MEMORY, 512K DUAL-PORT VIDEO MEMORY, AND A HIGH-PERFORMANCE COLOR LOOK-UP TABLE CAPABLE OF DISPLAYING 256 OUT OF 262 144 COLORS AT ONE TIME
- ONE HIGH-PERFORMANCE MULTIFREQUENCY RGB ANALOG MONITOR

SOFTWARE

- TRANSPUTER DEVELOPMENT SYSTEM (TDS) CONTAINING EDITOR, VARIOUS UTILITIES, AND AN EMBEDDED OCCAM COMPILER
- TWO VERSIONS OF PARALLEL C, AND STAND-ALONE OCCAM, C, AND FORTRAN COMPILERS

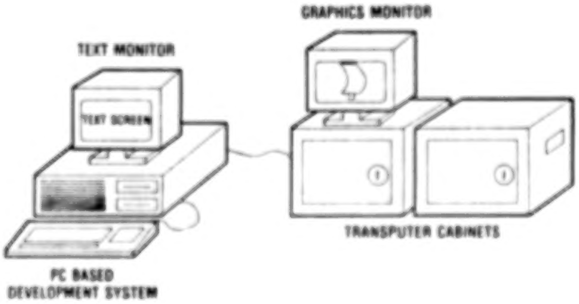

CD-88-32009

TRANSPUTER CABINETS WITH ASSOCIATED GRAPHICS DISPLAY MONITOR

The transputer cabinets are desktop size and can easily hold 80 or more transputers. Note the backplane wiring which can be changed to create various processor interconnection architectures.

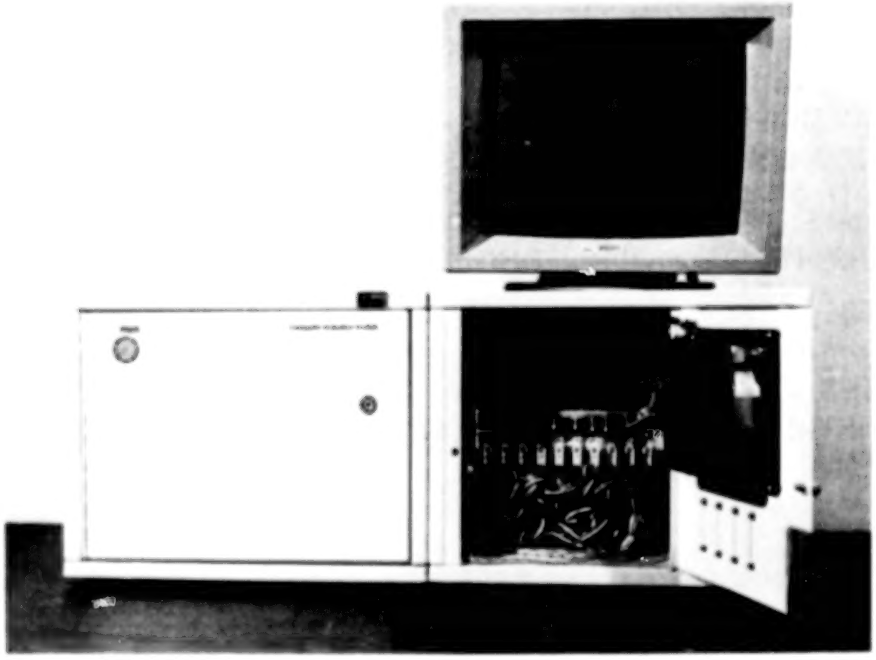

CD-88-32010

ORIGINAL PAGE IS
OF POOR QUALITY

TYPICAL TRANSPUTER BOARD

ORIGINAL PAGE IS OF POOR QUALITY

This photograph shows a typical transputer board. It contains four processors (transputers) each with 256 KBytes of memory.

inmos
IMS B003
NASA

CD-88-32011

TRANSPUTER GRAPHICS SYSTEM:
USER INTERFACE PROCEDURES

Applications programmers make calls to graphics routines provided in the package. The code is not available as a library, but the scurce code is included in any applications program. The user is insulated from any of the details of the graphics system, and only high-level graphics function calls are required.

The user defines a model in two-dimensional, real-coordinate space. Window size and placement on the screen is controlled in normalized device coordinates (screen size is from 0 to 1 on each axis). Multiple windows are allowed. The user can generate a global transformation matrix to perform scaling, rotation, and translation of the model data base.

GRAPHICS TRANSFORMATIONS	SCREEN AND WINDOW MANIPULATION	RELATIVE AND ABSOLUTE COORDINATE COMMANDS	DRAWING COMMANDS
SCALE	SET.WINDOW.2D	MOVE.REL.2D	CLIP.LINE.2D
ROTATE	SET.VIEWPORT.2D	POINT.REL.2D	CLIP.POINT.2D
TRANSLATE	ACTIVATE.VIEWPORT	LINE.REL.2D	DRAW.LINE.2D
MAKE.IDENTITY	DISPLAY.VIEWPORT	MOVE.ABS.2D	DRAW.RECTANGLE.2D
COMBINE.TRANSFORMATIONS		POINT.ABS.2D	DRAW.POLYGON.2D
TRANSFORM.POINTS		LINE.ABS.2D	DRAW.CIRCLE.2D
MAP.TO.SCREEN.COORDS			DRAW.ARC.2D

CD-88-32012

GRAPHICS DISPLAY SYSTEM ARCHITECTURE

The current implementation of the graphics display system uses two processors. The two-dimensional world processor converts the user's model from two-dimensional world space to device coordinates. The appropriate commands are sent to the graphics display board in device coordinates, and the picture is displayed on the graphics CRT.

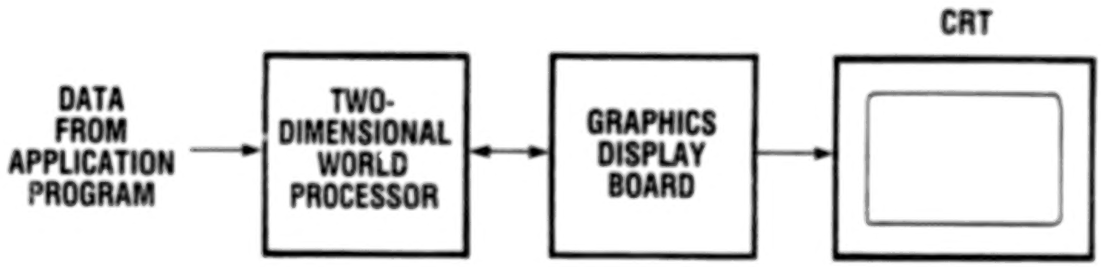
CRT
DATA FROM APPLICATION PROGRAM
TWO-DIMENSIONAL WORLD PROCESSOR
GRAPHICS DISPLAY BOARD

CD-88-32013

TWO-DIMENSIONAL WORLD PROCESSOR

The two-dimensional world processor converts the user's model from two-dimensional world space to normalized device coordinates. The user specifies all the drawing commands using two-dimensional world coordinates. Viewport sizing is performed in normalized device coordinates. The conversion to device coordinates is transparent to an application programmer. Multiple windows are allowed. Maintenance of global window parameters is transparent to the user. Copies of global window parameters are kept on both the two-dimensional world processor and the graphics board since there is no shared memory on this system.

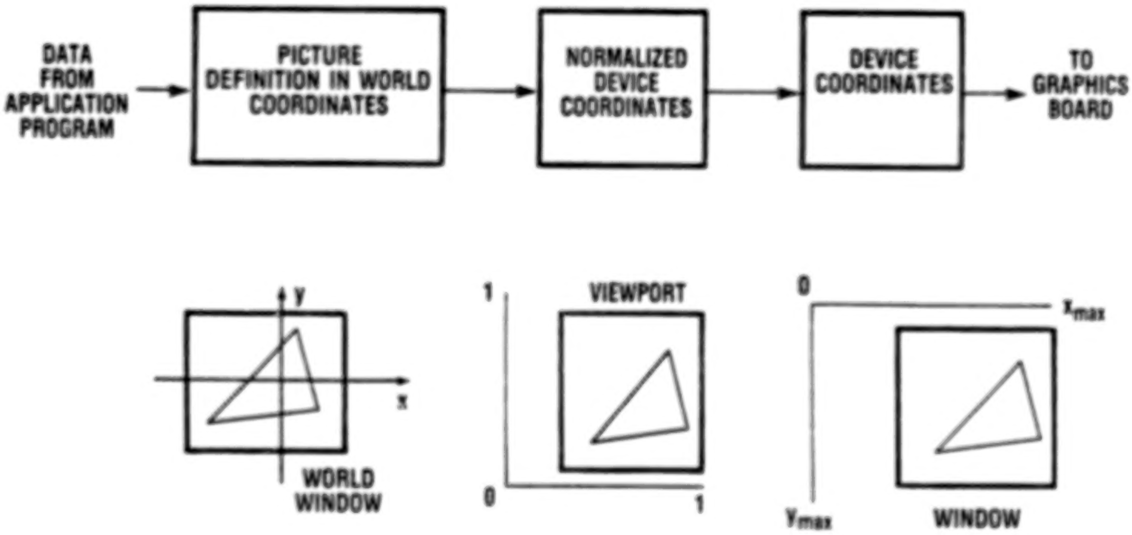
DATA FROM APPLICATION PROGRAM
PICTURE DEFINITION IN WORLD COORDINATES
NORMALIZED DEVICE COORDINATES
DEVICE COORDINATES
TO GRAPHICS BOARD
y
x
WORLD WINDOW
1
VIEWPORT
0
1
0
x_{max}
y_{max}
WINDOW

COMPUTATION AND COMMUNICATION PERFORMANCE

The architecture of the graphics display system is primarily dictated by computation versus communication times. Since there is only one transputer driving the video memory, a comparison must be made of the time to remotely (on another processor) perform a computation, communicate the computed data to the display board, and copy the result into video memory to the time to compute it on the display board and put it into video memory.

For the case of line scan conversion, the communication time dictates. For this reason, scan-conversion tasks are performed on the display board's processor. Since most drawings use multiple straight lines, a pipeline of two processors is currently being used for the graphics system.

The following table shows the actual timings* for the graphics operations.

Note that it is quicker to use the normal graphics board commands to draw a line (14 887 µsec) compared to precomputing the line on another processor and sending that data to the graphics board for display (36 399 µsec).

OPERATIONS PERFORMED	TIME,* µsec
SCAN CONVERT LINE FROM (0,0) TO (511,511)	7 933
SEND LINE DATA TO DISPLAY BOARD	12 512
SEND DATA AND DISPLAY	28 400
SCAN CONVERT, SEND DATA, AND DISPLAY	36 339
GRAPHICS BOARD DRAW LINE COMMAND	14 887
GRAPHICS BOARD FAST DRAW LINE COMMAND	3 542

*TIMINGS TYPICALLY VARY UP TO 0.1 PERCENT.

CD-88-32015

SUMMARY

A package of two-dimensional graphics routines has been developed to run on a transputer-based parallel processing system. These routines have been designed to enable applications programmers to easily generate and display results from the transputer network in a graphic format.

The graphics procedures have been designed for the lowest possible network communication overhead for increased performance. The routines have also been designed for ease of use and to present an intuitive approach to generating graphics on the transputer parallel processing system.

REFERENCES

INMOS, Oct. 1986, Transputer Reference Manual, INMOS Corporation, P.O. Box 16000, Colorado Springs, CO 80935.

DYNAMIC SYSTEMS

SESSION OVERVIEW

Louis J. Kiraly
Structural Dynamics Branch
NASA Lewis Research Center

The objectives of work performed in the Structural Dynamics Branch under the general area of dynamic systems are to analyze and verify the dynamics of interfacing systems, and to develop concepts and methods for motion control in microgravity environs. Past and present research topics and applications have included modal analysis, system identification, microgravity robotics, space mechanisms, space station power systems, blade loss transient dynamics, SP100 engine, NASP seals, and tethered satellites.

This session will include presentations on several of these subjects. Two of the formal and one poster presentation are directly related to microgravity robotics. The first outlines the current Structures Division project which deals with the mechanism and robotics technology needed to physically move payloads around in a space laboratory while not disturbing the microgravity environment. The second will highlight a unique effort to reduce the reaction forces at the base of a robot by using optimal control of redundant degrees-of-freedom of the robot. One of the poster presentations will describe the experimental hardware being set up to demonstrate the ability to reduce base reaction forces and moments on a manipulator for microgravity application. The formal presentation will describe the experimental hardware being set up to demonstrate the ability to reduce base reaction forces and moments on a manipulator for microgravity application.

One formal and one poster presentation is related to NASA Lewis research in roller drive mechanisms for space applications. The formal presentation will describe analysis and testing of one roller drive designed to take advantage of its attributes for a satellite application. The poster presentation will show the activity underway to characterize materials for use in roller drives designed to operate in space. Two other very interesting poster presentations will be included in this session.

Mr. Posta's session deals with some unique approaches for measuring blade vibrations in rotors using uniquely digital methods.

The final poster session overview is related to microgravity robotics. It has application to robot arms which are long or flexible and require accurate position control.

Several of the papers in this session stem from somewhat different sources than the aerospace propulsion system structures technology of the rest of this symposium. However, the audience will find that much of the technology is similar and that the goal of reliable, lightweight, high-performance systems for aerospace mission use is unchanged.

SESSION OVERVIEW
- L.J. KIRALY, CHIEF, STRUCTURAL DYNAMICS BRANCH, NASA

MICROGRAVITY MECHANISMS AND ROBOTICS PROGRAM
- D.A. ROHN, STRUCTURAL DYNAMICS BRANCH, NASA

BASE REACTION OPTIMIZATION OF MANIPULATORS WITH REDUNDANT KINEMATICS
- C.L. CHUNG, CARNEGIE MELLON UNIVERSITY, PITTSBURGH, PA
- S. DESA, CARNEGIE MELLON UNIVERSITY, PITTSBURGH, PA

EVALUATION OF A HIGH-TORQUE BACKLASH-FREE ROLLER ACTUATOR
- B.M. STEINETZ, STRUCTURAL DYNAMICS BRANCH, NASA

LOW-COST OPTICAL DATA ACQUISITION SYSTEM FOR BLADE VIBRATION MEASUREMENT (POSTER)
- S.J. POSTA, STRUCTURAL DYNAMICS BRANCH, NASA

ROLLER DRIVE MATERIALS PERFORMANCE (POSTER)
- D.A. ROHN, STRUCTURAL DYNAMICS BRANCH, NASA

MICROGRAVITY MANIPULATOR DEMONSTRATION (POSTER)
- A. BRUSH, SVERDRUP TECHNOLOGY, INC.

ACCURATE POSITIONING OF LONG, FLEXIBLE ARMS (POSTER)
- M.J. MALACHOWSKI, CCE-ROBOTICS, BERKELEY, CA

CD-88-33094

N88-23237

MICROGRAVITY MECHANISMS AND ROBOTICS PROGRAM

Douglas A. Rohn
Structural Dynamics Branch
NASA Lewis Research Center

ABSTRACT

NASA plans to provide the scientific community with a microgravity laboratory aboard the space station. Using and maintaining the microgravity environment will require, among other things, careful attention to experimental apparatus mechanisms and laboratory robotic manipulators. This presentation describes a technology development effort toward that end.

Since a variety of experiments that require microgravity also require or would benefit from motion or manipulation, techniques are needed to restrict these motions and motion-producing forces from disturbing the microgravity environment. The requirement is twofold: low-acceleration, smooth motion and reaction limitation. This program applies structural dynamics and unique roller traction drive technology to mitigating the problems of current mechanical motion control systems. The program objective is to develop the technology for providing acceleration control within and around space experiments by smooth, reactionless motion and manipulation. A series of subtasks have been initiated, including verifying needs and requirements, evaluating roller drives, developing reactionless mechanism technology, optimizing dynamic performance, and developing microgravity and reactionless manipulation. The products of this research will also be applicable to mechanism and robotic needs in other NASA space missions.

SPACE PLATFORMS

Current and future NASA missions involve the development and operation of complex space vehicles and platforms. Although each of these has a different purpose, they must all deal with the environment found away from Earth's surface, namely, reduced gravity, vacuum atmosphere, and increased radiation. In fact, some missions, for example the space station, will have as a primary purpose the utilization of this environment.

Furthermore many of these space vehicles and platforms include in their structural and mechanical design a large number of "moving parts" - as evidenced by the space station artist's concept showing manipulator arms, pointing antenna, solar trackers, and numerous other actuators, drives, and latches. Similarly the pressurized modules will contain numerous mechanisms. This combination of environment and moving parts requires new technology.

The microgravity mechanisms and robotics program involves mechanisms and robotic technology related to the scientific use of the microgravity environment.

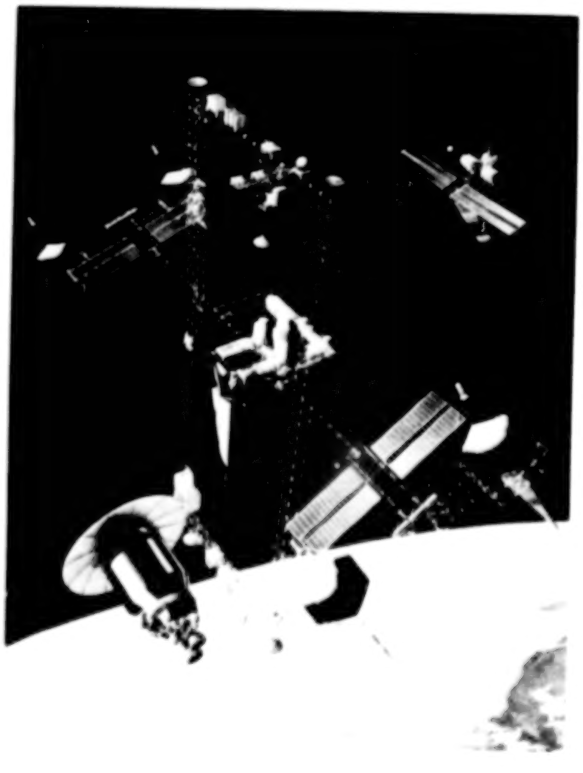

ENVIRONMENT:

- **MICROGRAVITY**
- **VACUUM**
- **RADIATION**

MOVING PARTS:

- **ROBOTS/MANIPULATORS**
- **STRUCTURAL JOINTS**
- **MECHANISMS**

CD-88-31817

ORIGINAL PAGE IS
OF POOR QUALITY

NEEDS

NASA plans to provide the scientific community with a space station microgravity laboratory. Managing the laboratory's microgravity environment will require meaningful standards and technology for conducting experiments in microgravity. Many experiments that require microgravity also involve mechanical motions. Experiments conducted external to the laboratory or on a free-flyer will require remote manipulation capabilities. Furthermore some experiments would benefit from common laboratory equipment that requires handling or scanning motions. New technology is required to ensure that these motions within experiments or the robotic manipulator motions and reaction forces do not negate the microgravity environment of the experiment itself or those of other experiments in the laboratory.

One should be aware that the term "microgravity" is generally not used literally (i.e., 10^{-6} g_o, where g_o equals the acceleration due to gravity at the Earth's surface). It refers to the fact that in low Earth orbit on a typical space platform, the gravity or acceleration field is not "zero g" but rather reduced gravity, nominally in the range 10^{-2} g_o to 10^{-7} g_o. The exact amplitude, and equally important the frequency spectrum, depend on solar pressure, atmospheric drag, the gravity gradient, astronaut motions, attitude control thrusters, rotating machinery, etc.

- **MANY MICROGRAVITY EXPERIMENTS REQUIRE INTERNAL "MOTIONS"**
- **OTHER MECHANICAL MOTIONS WILL OCCUR AROUND EXPERIMENTS**
  - **EXPERIMENT MANIPULATION**
  - **LABORATORY EQUIPMENT HANDLING**

CD-88-31818

CHALLENGE

Basically the problem breaks down into two key issues. The first is moving an item, such as a protein crystal in a vial, such that it never experiences greater than some low level of acceleration. The second involves limiting the reaction forces produced when a relatively large object is moved at relatively high acceleration rates. These reactions are transmitted to the mechanisms or robot support structure and, depending on the structure's mass, stiffness, and damping characteristics, will set up an acceleration field that might be harmful to other experiments and processes.

These issues are difficult to resolve in general since many mechanisms have problems with backlash, friction, vibration, imprecision, and lack of reaction control. Furthermore a space experimenter may not have mechanism expertise; thus the Lewis Structures Division has undertaken this program.

- **KEY MOTION CONTROL ISSUES INVOLVE MOVING AN ITEM SO THAT**
  - **IT NEVER EXPERIENCES GREATER THAN MICROGRAVITY ACCELERATIONS**
  - **ITS MOTION-PRODUCING REACTIONS DO NOT DISTURB THE SURROUNDING ACCELERATION ENVIRONMENT**

- **TECHNOLOGY ADVANCEMENT**
  - **SOLVE PROBLEMS WITH EXISTING MECHANISMS**
  - **PROVIDE MOTION CONTROL TECHNOLOGY FOR SCIENTISTS**

CD-88-31819

OBJECTIVE

The objective of the microgravity mechanisms and robotics program is to develop technology to provide acceleration control by smooth, reactionless motion and manipulation. The immediate intended use of the results is in space experiments hardware. However, the whole field of space mechanisms, robotic actuators, and precision mechanisms in general can benefit.

The program addresses the needs and problems through the application of roller drive and structural dynamics technologies. Roller drives are beneficial to mechanisms and robotic joints because of their unique zero backlash, negligible torque ripple, nonlubricated operation, high torsional stiffness, and compactness. By combining these attributes with dynamic modeling, vibration analysis, and trajectory optimization, an analytical and experimental technology base is being developed for use across the full range from experimental mechanisms to manipulators to autonomous space laboratory robots.

- **DEVELOP THE TECHNOLOGY TO PROVIDE ACCELERATION CONTROL BY SMOOTH, REACTIONLESS MOTION AND MANIPULATION THROUGH THE APPLICATION OF ROLLER DRIVE AND STRUCTURAL DYNAMICS TECHNOLOGY**
  - **ROLLER DRIVE MECHANISMS OFFER ZERO BACKLASH, NEGLIGIBLE TORQUE RIPPLE, HIGH TORSIONAL STIFFNESS, NONLUBRICATED OPERATION, AND COMPACTNESS**
  - **STRUCTURAL DYNAMICS INCLUDES DYNAMIC MODELING, TRAJECTORY OPTIMIZATION, VIBRATION ANALYSIS, AND REACTION COMPENSATION**

CD-88-31820

APPROACH

The solution to the general problem of smooth, reactionless motion is approached through a combination of analysis and experimentation. The subtasks of the project are listed here. Upon completion of these subtasks a technology base will be in place for future reactionless microgravity mechanisms and robotic systems.

- QUANTIFY AND ANALYZE REQUIREMENTS
- EVALUATE ROLLER DRIVE CONCEPTS FOR APPLICATION TO EXPERIMENT APPARATUSES
- STUDY REACTIONLESS MECHANISMS IN ORDER TO DEVELOP AND DEMONSTRATE TECHNOLOGY
- ANALYZE DYNAMICS AND KINEMATICS FOR OPTIMUM PERFORMANCE
- DEVELOP MICROGRAVITY AND REACTIONLESS MANIPULATION TECHNOLOGY ON MULTI-DOF TEST BED

CD-88-31821

IDENTIFICATION OF REQUIREMENTS

The first step has been to quantify the needs and physical requirements for reactionless microgravity mechanisms and robotic manipulators. Two need avenues are being pursued: motion and mechanism needs within space experiment apparatuses and manipulation needs within the space station laboratory module.

Analysis of experiment mechanism needs includes identifying actual mass, velocity, and distance parameters, as well as studying the transmissibility of forces and accelerations within experiment racks and the entire facility. Robot manipulation can include laboratory housekeeping functions in addition to actual experiment operation, thus offering savings in crew time and enhancing experiment productivity.

The output of this task will be a set of requirements to guide this program's technology development and future system design.

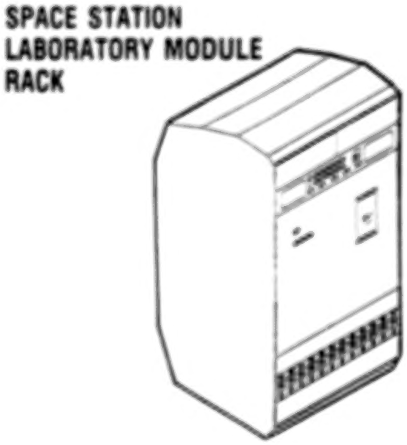

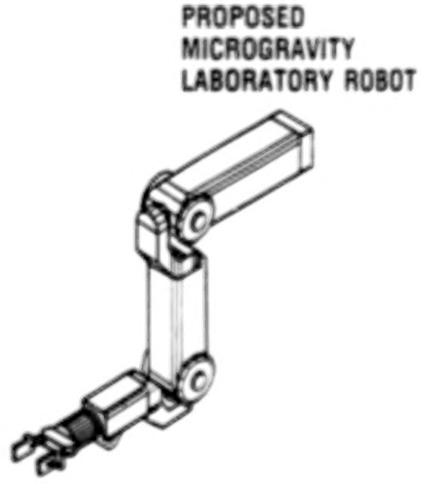

EXPERIMENT MECHANISMS

- ANALYZE EXPERIMENT APPARATUS
- IDENTIFY PHYSICAL NEEDS

ROBOTIC MANIPULATION

- ASSESS NEEDS AND BENEFITS
- DEFINE INTEGRATION AND INTERFACE REQUIREMENTS

CD-88-31822

ROLLER DRIVE EVALUATION

The use of roller traction drives in mechanisms is a key part of this investigation. Rig tests are being used to determine lubrication suitability in a vacuum, or other experimental atmospheres, contact forces required, and fineness of control. Design studies are analyzing traction drive concepts for use in the full range from individual experiment mechanisms to robotic manipulation systems. Methods that compensate for momentum and dynamic reactions, which also exploit traction drives' unique smooth operation for motion control, will be incorporated.

- **DETERMINE SUITABILITY, MEASURE PERFORMANCE, AND EXPLOIT CHARACTERISTICS**

EXPERIMENT

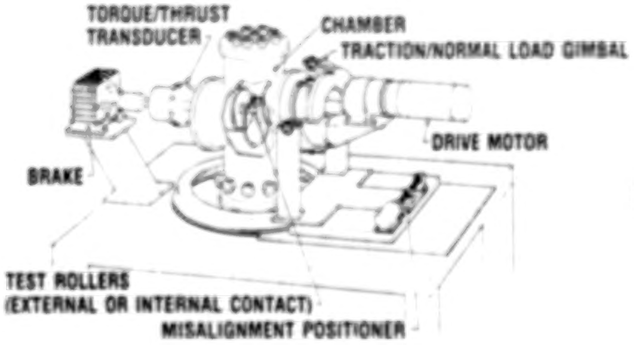
TORQUE/THRUST TRANSDUCER
CHAMBER
TRACTION/NORMAL LOAD GIMBAL
DRIVE MOTOR
BRAKE
TEST ROLLERS (EXTERNAL OR INTERNAL CONTACT)
MISALIGNMENT POSITIONER

ANALYSIS

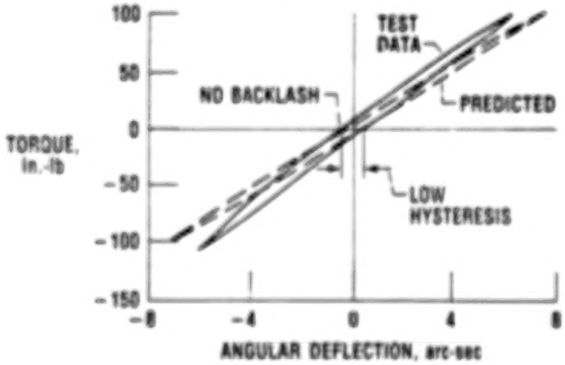

DESIGN CONCEPTS

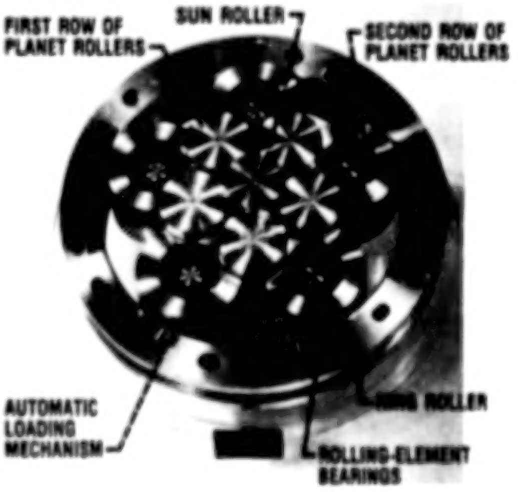
FIRST ROW OF PLANET ROLLERS
SUN ROLLER
SECOND ROW OF PLANET ROLLERS
AUTOMATIC LOADING MECHANISM
RING ROLLER
ROLLING-ELEMENT BEARINGS

CD-88-31623

ORIGINAL PAGE IS
OF POOR QUALITY

REACTIONLESS MECHANISM TECHNOLOGY

A single-degree-of-freedom roller-driven translating device is being studied as a reactionless mechanism. This mechanism is representative of linear motion devices that may be required to translate a heating element or a cooling manifold in an experiment requiring a rapid quench.

An example is the rapid solidification of molten materials, where a sample must be rapidly cooled while it remains in a microgravity environment. To pull it out of a furnace and place it in a quenching chamber would obviously cause accelerations to be placed on the sample. An alternative is to move the furnace out of the way and quickly bring a quenching block in its place while the sample is motionless. This requires a mechanism that can translate the equipment without allowing reaction forces to be transmitted back into the support structure and thus show up as accelerations.

Other reactionless concepts and techniques will be evaluated and developed for more specific applications.

- **DEVELOP TECHNIQUES FOR SMOOTH, REACTIONLESS, RAPID MOTION FOR MICROGRAVITY EXPERIMENTS REQUIRING INTERNAL MOTION**

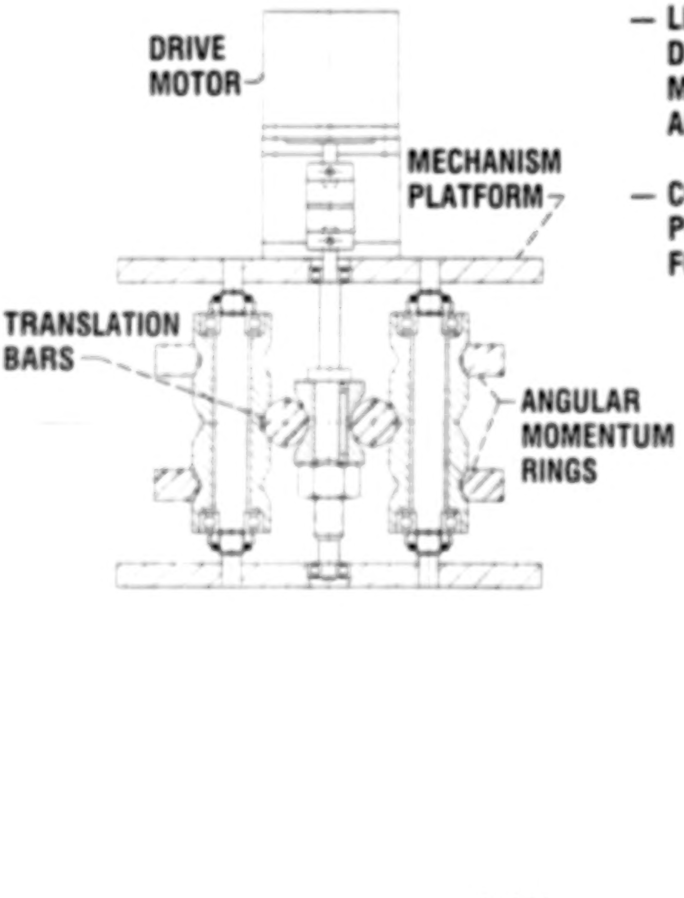

— LINEAR ROLLER DRIVE DESIGNED FOR NOMINAL MOTION (MASS, SPEED, AND DISTANCE)

— CONCEPTS, TECHNIQUES, AND PROTOTYPES WILL BE STUDIED FOR SPECIFIC APPLICATIONS

CD-86-21824

DYNAMIC ANALYSIS AND OPTIMIZATION

Kinematic and dynamic analyses are being developed to model reaction compensation techniques useful in mechanisms such as translators and multiple-degree-of-freedom systems. Emphasis has been placed on the control of reaction forces through the novel use of redundant degrees of freedom for momentum compensation and on other mechanical compensation devices.

Although much of the program involves hardware issues, we are also studying optimization techniques, reaction-force minimization strategies, and actuator controls that exploit hardware capabilities. A portion of this work will be presented separately in this symposium.

- **DEVELOP STRATEGIES FOR MINIMIZING DYNAMIC BASE REACTIONS AND END-EFFECTOR ACCELERATIONS**
  - **— KINEMATIC/DYNAMIC MODELING**
  - **— REACTION MINIMIZATION STRATEGY**
  - **— TRAJECTORY OPTIMIZATION**
  - **— JOINT ACTUATOR DYNAMICS AND CONTROL**

CD-86-21825

MULTI-DOF "MICROGRAVITY" MANIPULATION EXPERIMENTS

A multiple-degree-of-freedom (DOF) experimental test bed is being developed in order to study how structural dynamics, reaction compensation, and low-acceleration handling analyses interact with manipulator flexibility, roller joint dynamics, actuator control, and end-effector accuracy phenomena. The overall objective is to physically develop, demonstrate, and evaluate models, strategies, and mechanisms for manipulation in a microgravity laboratory. The first phase of this activity, involving reaction compensation and Oak Ridge National Laboratory (ORNL)-designed two-DOF roller-driven joints, is the subject of a poster presentation in this symposium.

Conceptual development on an advanced test bed includes consideration of low-acceleration handling, structural interactions, and actuator and end-effector research. Technology developed here and throughout the program will be channeled into future microgravity robot system definition.

- **DEVELOP, DEMONSTRATE, AND EVALUATE DRIVE MECHANISMS, OPTIMIZATION STRATEGIES, AND CONTROL MODELS FOR MANIPULATION IN A MICROGRAVITY LABORATORY**

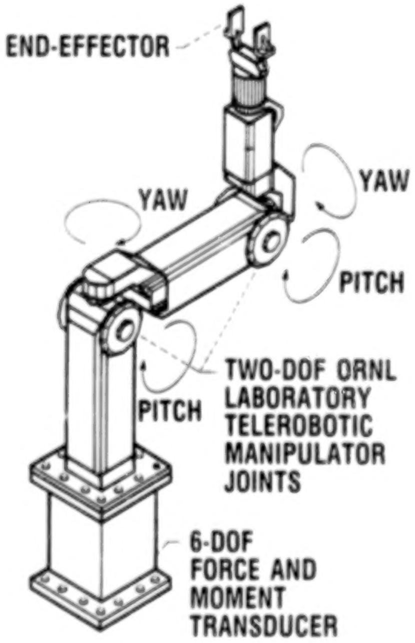
END-EFFECTOR
YAW
YAW
PITCH
TWO-DOF ORNL LABORATORY TELEROBOTIC MANIPULATOR JOINTS
PITCH
6-DOF FORCE AND MOMENT TRANSDUCER

- **REACTION COMPENSATION**
- **LOW-ACCELERATION HANDLING**
- **DYNAMIC/STRUCTURAL INTERACTIONS; VIBRATION**
- **ACTUATOR TECHNOLOGY**
- **END-EFFECTORS**
- **PRECISION AND ACCURACY**
- **MICROGRAVITY SYSTEM DEFINITION**

CD-88-31826

NASA TELEROBOTIC RESEARCH

Much of the technology developed in this program can be used in other mechanism and robotics programs, particularly the telerobotics technology research at NASA Langley and the telerobotics development for space station use at NASA Goddard. ORNL, under NASA Langley sponsorship, has developed a space telerobot concept and tested baseline joints that take advantage of the roller drive's stiffness and lack of torque ripple and particularly of its zero backlash. The pitch/yaw joint was designed by ORNL using Lewis-developed roller traction drive technology and will be used in this program's manipulation experiments.

OAK RIDGE NATIONAL LABORATORY'S SPACE TELEROBOT CONCEPT

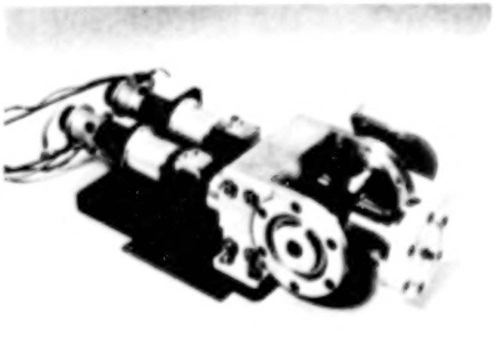

BENCH-TEST PITCH/YAW JOINT BASELINED WITH ROLLER DRIVE DIFFERENTIAL

CD-86-31827

MICROGRAVITY MECHANISMS AND ROBOTICS TECHNOLOGY

The primary goal of this program is to produce the motion control tools necessary to enhance and enable a particular NASA mission: space-laboratory-based microgravity experiments. To that end, a spectrum of technology is being and will be produced that is focused in the disciplines of precision mechanisms and robotics. This core technology will be applicable to future mechanism and robotics efforts in the Lewis Research Center's Structures Division.

RATIONALE:

- **RESPOND TO MICROGRAVITY EXPERIMENT NEEDS**

APPROACH:

- **APPLY STRUCTURAL, MECHANICAL, AND SYSTEMS TECHNOLOGIES**

GOAL:

- **DEVELOP TECHNOLOGY**

FUTURE:

- **SPIN OFF TO MECHANISM AND ROBOTIC NEEDS IN OTHER NASA SPACE MISSIONS**

FOCUS:

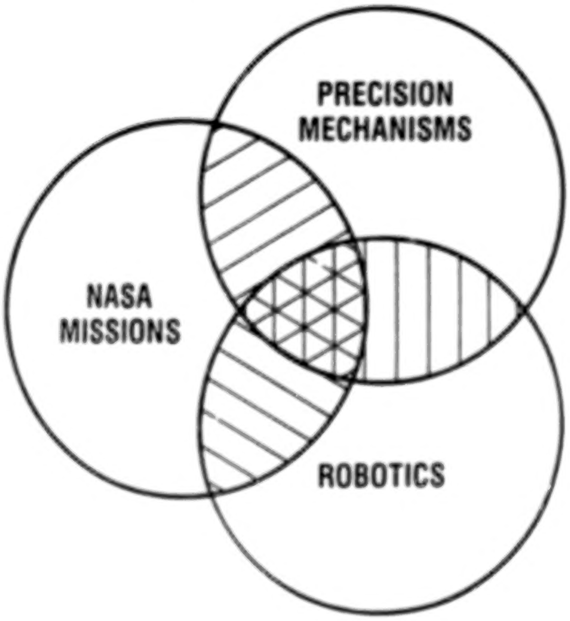

CD-88-31828

N88-23238

BASE REACTION OPTIMIZATION OF MANIPULATORS WITH REDUNDANT KINEMATICS

C.L. Chung and S. Desa
Department of Mechanical Engineering
Carnegie Mellon University
Pittsburgh, PA 15213

Abstract

Manipulators used in space applications are operated under microgravity conditions. Base reactions of space manipulator are directly exerted on the supporting space structure. It is desirable to make these reactions as small as possible in order to reduce their influence on the dynamics of the supporting space structure. Furthermore, in delicate experiments conducted in space, the test specimen would have to be moved carefully without subjecting it to excessive accelerations and jerks. It follows that minimization of base reactions and limitation of end-effector accelerations and jerks are important objectives for space manipulators.

In this presentation, a trajectory generation method for space manipulators is introduced. The approach developed employs a manipulator with redundant kinematics. The method is implemented in two steps. First, the end-effector trajectory is developed to satisfy motion requirements. Next, the joint trajectories are developed to minimize base reactions. This presentation describes the analytical development of the method, and presents an example to illustrate the method.

PRECEDING PAGE BLANK NOT FILMED

Work done under NASA Lewis grant NAG3-811.

Types of Manipulators

Manipulators can be categorized according to their degrees of freedom into two groups: nonredundant and redundant. Nonredundant manipulators have the minimum number of degrees of freedom required to follow a general trajectory. If a manipulator has more than the minimum number of degrees of freedom required to perform a task, then it is called a redundant manipulator.

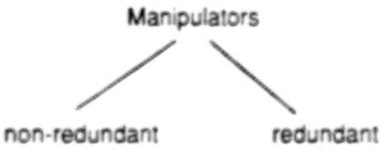
Manipulators
non-redundant
redundant

2 DOF Manipulator

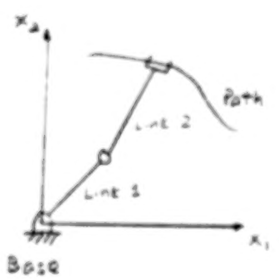
x_2
Path
Link 2
Link 1
x_1
Base

3 DOF Manipulator
(1 degree of redundancy)

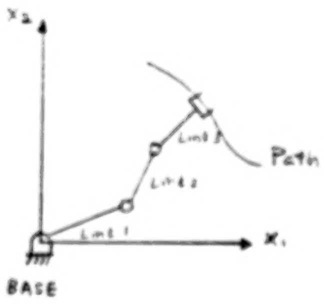
x_2
Link 3
Path
Link 2
Link 1
x_1
BASE

Space Manipulator of NASA

Manipulators used in space are operated under microgravity conditions. Base reactions of a space manipulator are directly exerted on the supporting space structure. It is desirable to make the reactions as small as possible in order to reduce their influence on the dynamics of the space structures. Besides the requirement of small base reactions, delicate experiments conducted in space require that test specimens be moved carefully without subjecting them to excessive accelerations and jerks.

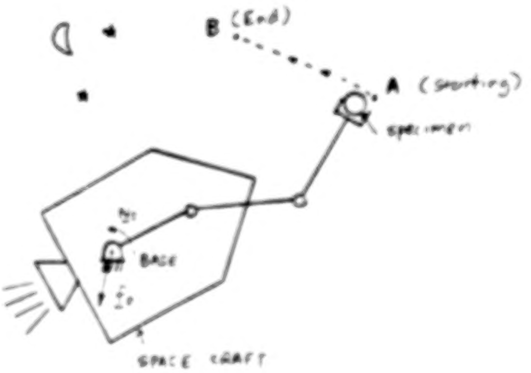

- desire to move specimens without excessive acceleration
- require base reactions ($\underline{f}_0$, $\underline{N}_0$) to be as small as possible

Problem Statement

The trajectory problem for redundant manipulators which we are going to address has two requirements: (1) to move a redundant manipulator according to task specifications; (2) to minimize base reactions ($\mathbf{N}_0$ and $\mathbf{F}_0$) transmitted by manipulators to the base during motion.

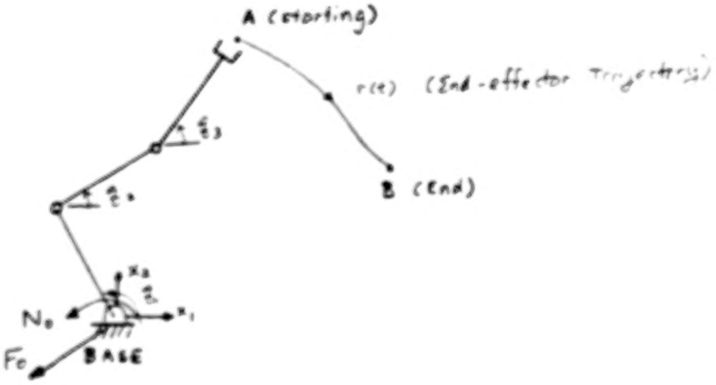
A (starting)
r(t) (End-effector Trajectory)
B (End)
ξ_3
ξ_2
ξ_1
x_2
x_1
N_0
F_0
BASE

A Planar Redundant Manipulator

- plan end-effector trajectory to satisfy acceleration constraint

- determine joint trajectories that MINIMIZE BASE REACTIONS

Proposed Approach

The trajecotry planning problem can be approached by splitting the problem into two parts. This enables us to deal with the end-effector trajectory and joint trajectories separately. The first part generates the end-effector trajectory that satisfies task specifications. The second part obtains joint space solution that minimizes base reactions.

Part 1

Determination of end-effector trajectory

Part 2

Finding joint trajectories that minimize
base reactions

Part 1: End-effector Trajectory Generation

The first part of the approach deals with the generation of end-effector trajectory, **r**(t) to satisfy certain task specifications. The task specifications of interest are total distance of the straight-line path (D_T), maximum acceleration of end-effector trajectory (a_{max}), and total time of task (T).

IDEA:

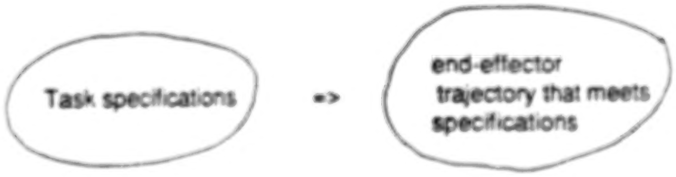
Task specifications
=>
end-effector trajectory that meets specifications

Task Specs	End-effector
1. D_T : total distance of the straight path	r(t)
2. a_{max} : max. acceleration of the path	
3. T : time to accomplish the task	

Point-to-point Motion

A point-to-point motion is considered as the motion of an end effector moving from a specified initial position to a specified final position. A simple way to execute this motion is to move the origin of a coordinate frame fixed to the end effector along a straight-line path that connects the two points.

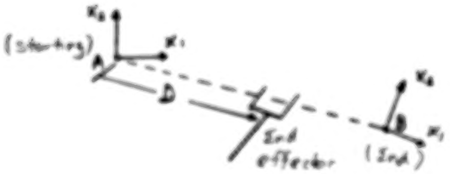

- accomplish by a straight line from A to B

$$v(t) = \frac{dD}{dt}$$ (speed along the straight path)

End-effector Trajectory Description

One of the requirements in planning end-effector trajectory is to have zero velocity at initial and final positions. Cycloid curve which satisfies this requirement can be used to describe the linear speed of the end-effector trajectory. Furthermore, it has smooth kinematics properties and can be defined by using only three constants (a, b, c).

Linear Speed:

Cycloid: $v(p) = b(1 - \cos p)$

$t(p) = a(p - c \sin p)$

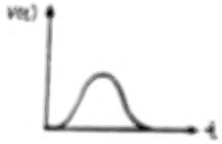

P is the parameter.

$p = 0$ (starting position)

$p = 2\pi$ (end position)

Determinaiion of a, b , and c

The three constants a, b, and c can be determined by forcing cycloid function to satisfy three motion constraints. By solving the following three equations, we can obtain the valus for the constants.

Total Time of Task : $T = 2\pi a$

Total Distance : $D_T = 2\pi a b (1 + 0.5 c)$

Max. Acceleration:

$$|a_{max}| = b / a (1 - c^2)^{-0.5}$$

From above 3 eqns. => a, b, c

Part 2: Determination of Joint Trajectories

The basic idea of proposed approach is to pose the inverse kinematics problem as an optimization problem with a cost function that measures the base reactions. The approach begins by partitioning the joint variable vector, **q** into 2 portions. Then the Jacobian matrix is partitioned into a nonsingular square Jacobian matrix and a submatrix. Using these partitioned matrices, we are able to represent the motion of all the joints in terms of an optimization parameter matrix. The unique joint space solution can be determined by finding the optimal parameter matrix for the optimization problem.

Recall

$$\dot{x} = J\,\dot{q} \qquad (1)$$

Step 1: *Partition* q & J

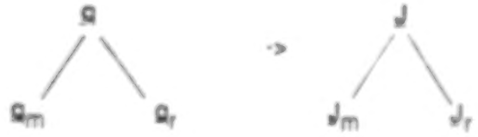

$(|J_m| \neq 0)$

Step 2. *Express* $\dot{q}_m$ & $\ddot{q}_m$ *in terms of* $\dot{q}_r$ *and* $\ddot{q}_r$

$$\dot{q}_m = g_1(\dot{q}_r) \qquad (2)$$

$$\ddot{q}_m = g_2(\dot{q}_r, \ddot{q}_r) \qquad (3)$$

Step 3: *Setup a cost function*, $J_c(\dot{q}_r, \ddot{q}_r)$

Step 4: *minimize* J_c

$$\min(J_c) \Rightarrow \quad \dot{q}_r, \ddot{q}_r \quad \xRightarrow[(2,3)]{} \quad \dot{q}_m, \ddot{q}_m$$

Part 2 Determination of Joint Trajectories (cont'd)

For the purpose of optimization,

$$\dot{\underline{q}}_r = \underline{C}\ \underline{f}(t)$$

where $\underline{f}(t) = [1, t, t^2, \ldots\ldots, t^k]^T$

$\underline{C}$ = constant coefficient matrix

For this problem:

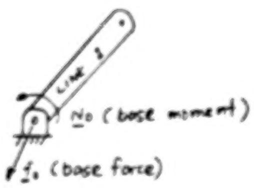
Link 1
$\underline{N}_0$ (base moment)
$\underline{f}_0$ (base force)

To minimize base reactions,

Local Cost Function : $J_c = \underline{B}^T\ \underline{\Omega}\ \ \underline{B}$

where $\underline{B} = \begin{vmatrix} \underline{f}_0 \\ \underline{N}_0 \end{vmatrix}$

$\underline{\Omega}$: positive definite weighting matrix

Algorithm of the Proposed Approach

An algorithm of the proposed approach and a computer program written in Pascal have been developed to implement this methodology. The flowchart below illustrates the basic algorithm.

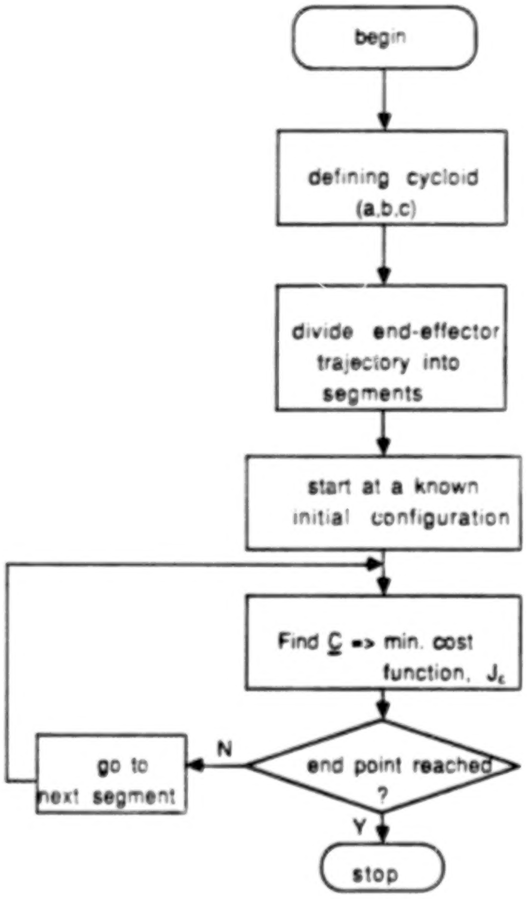
begin
defining cycloid (a,b,c)
divide end-effector trajectory into segments
start at a known initial configuration
Find C => min. cost function, J_c
end point reached ?
N
go to next segment
Y
stop

Illustrative Example

A 4 degrees of freedom spatial manipulator as shown below is studied. It has three links with lengths of l_1, l_2, and l_3 respectively. For point-to-point spatial motion, three degrees of freedom are required. Therefore, one degree of redundancy is available. The reference frame $X_bY_bZ_b$ is fixed at the base. Link 1 is mounted to the supporting structure and the other two links are each driven by a differential drive mechanism which has two outputs that rotate about orthogonal axes. For the purpose of kinematic and dynamic analyses, this mechanism can be considered as two intersecting revolute joints.

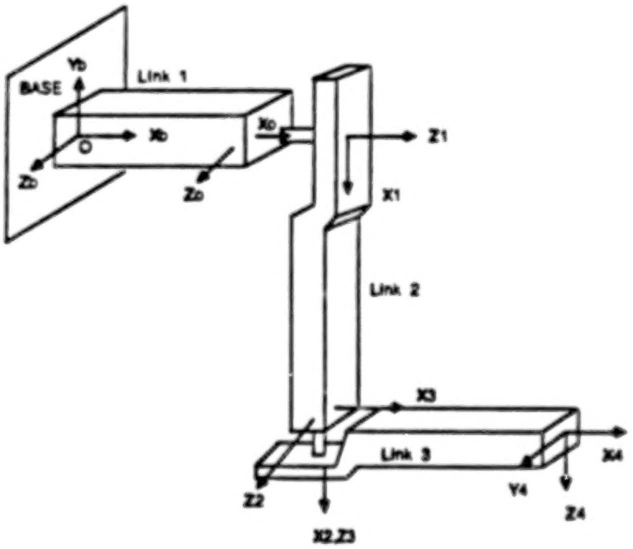

A 4 DOF Traction-Drive Manipulator

Results of Example : Optimal Cost Function

Using the algorithm developed in this research, the time history of cost function given by J = $\mathbf{R}^T\mathbf{Q}\,\mathbf{R}$ ($\mathbf{Q}$ = identity matrix) is shown in Figure 2.

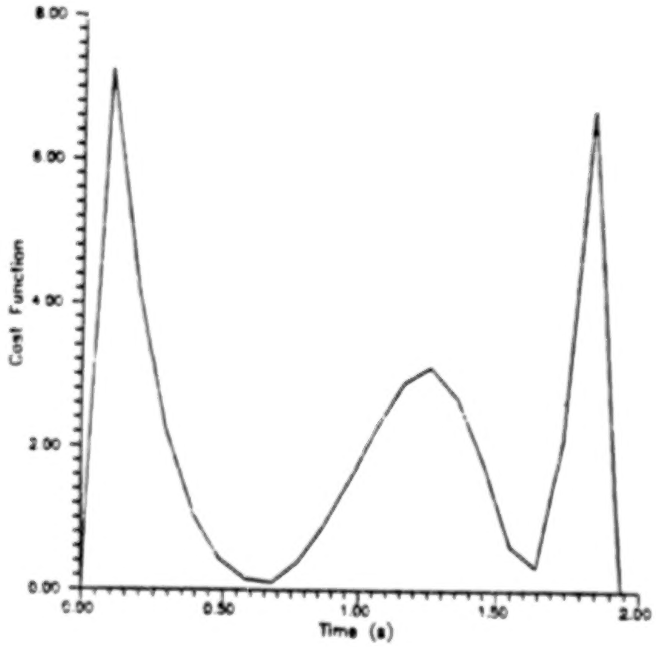

Optimal Base Reactions Cost Function

End-effector Trajectory

The end-effector trajectory defined by cycloid curve is shown in the figures below.

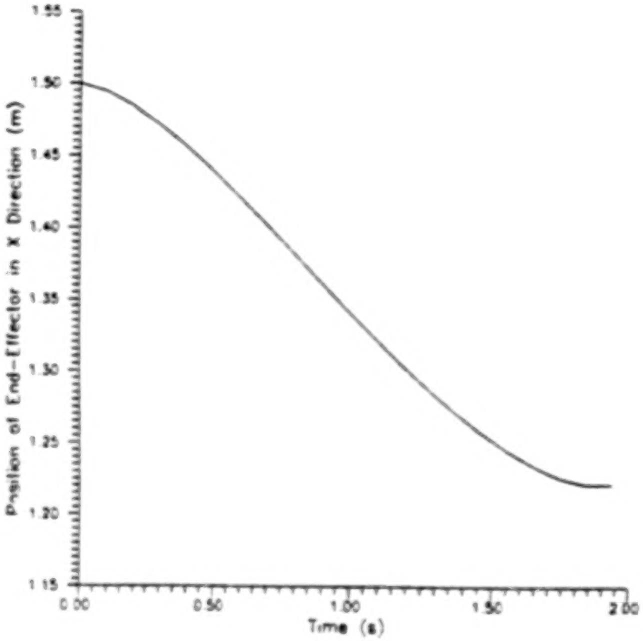

End-Effector Trajectory in X_b Direction

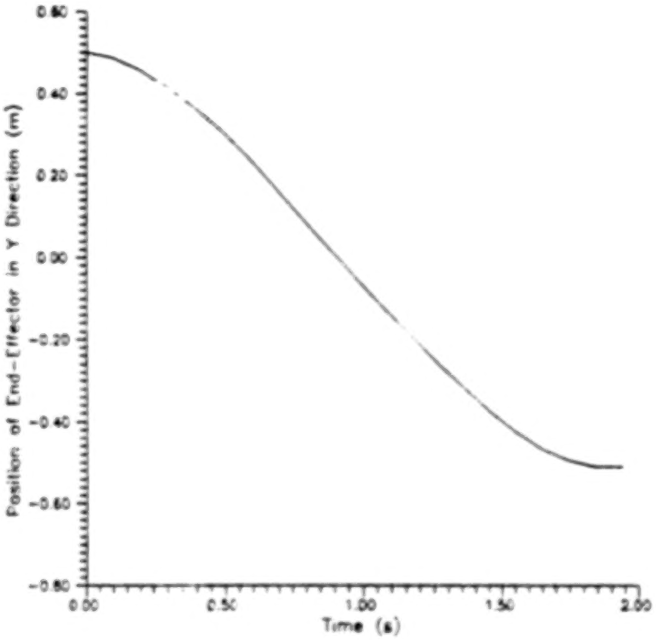

End-Efector Trajectory in Y_b Direction

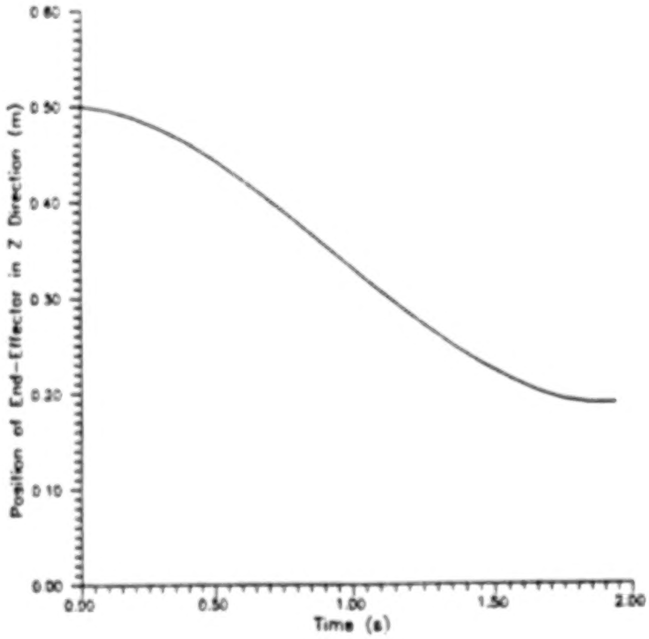

End-Effector Trajectory in Z_b Direction

Optimal Joint Trajectory

A typical joint trajectory that minimizes base reactions is shown in the figure. This figure shows that using the proposed approach, we can obtain smooth joint trajectory.

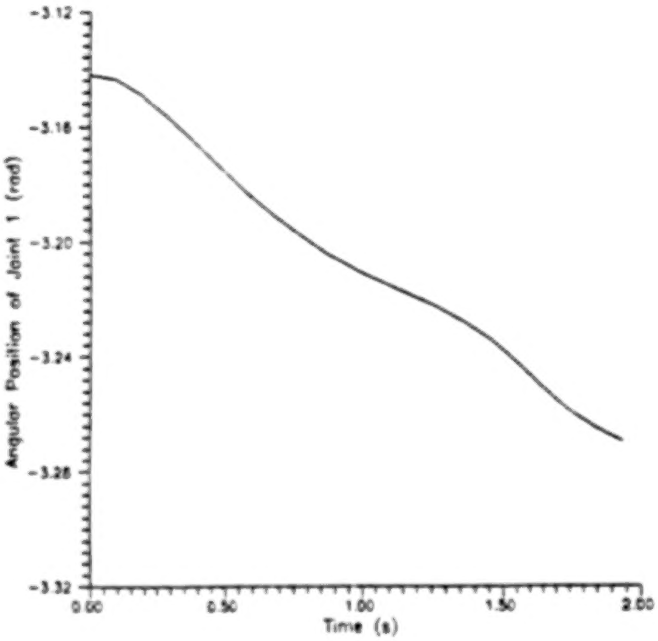

Optimal Trajectory of joint 1

Conclusions

In this presentation we have shown how kinematic redundancy can be employed in planning joint trajectories to minimize base reactions exerted by the manipulator on the supporting space structure. The results of the example show that small base reactions are exerted on the space structure. The major advantage of this approach is no special restrictions are imposed on the cost function. The disadvantage is that it is computationally intensive because an optimization routine is required to find the optimal joint trajectories.

(+) We have obtained a workable approach for this problem.

It can handle cost functions which include dynamics relatively easily.

(-) The approach is computationally intensive.

N88-23239

EVALUATION OF A HIGH-TORQUE BACKLASH-FREE ROLLER ACTUATOR

Bruce M. Steinetz
Structural Dynamics Branch
NASA Lewis Research Center

ABSTRACT

NASA Lewis Research Center recently began a research program to investigate mechanism positioning systems that would be suitable for space vehicles. High-torque-density efficient systems are required that operate smoothly without mechanical backlash and without liquid lubrication systems. Roller drives inherently have many of these required properties because power is transmitted through continuously rolling drive elements. The roller-driven mechanisms investigated range from a smooth dry-running drive designed for the Space Station alpha joint (Loewenthal and Schuller, 1986) to a backlash-free traction robot joint tested in NASA's telerobotic research program (Kuban and Williams, 1987).

This paper presents results of a test program that evaluated the stiffness, accuracy, and torque ripple of a 16:1, 320-ft-lb planetary roller drive for a potential space vehicle actuator application.

The drive's planet roller supporting structure and bearings were found to be the largest contributors to overall drive compliance (reciprocal of stiffness), accounting for more than half of the total. In comparison, the traction roller contacts contributed only 9 percent of the drive compliance based on an experimentally verified stiffness model. The drive exhibited no backlash although 8 arc sec of hysteresis deflection were recorded because of microcreep within the contact under torque load. Because of these load-dependent displacements, some form of feedback control would be required for arc-second positioning applications. Torque ripple tests showed the drive to be extremely smooth, actually providing some damping of input torsional oscillations.

PRECEDING PAGE BLANK NOT FILMED

INVESTIGATION OBJECTIVES

Under a cooperative program with industry, a 16:1, 320-ft-lb output torque roller actuator was evaluated experimentally (Steinetz et al., 1986) to determine its potential suitability as a high-torque space vehicle actuator, such as for a control moment gyro (CMG) gimbal drive. Analytical predictions of the torsional stiffness of the drive were compared with static torsional stiffness measurements, and "torsionally soft" drive components were identified. Data were also obtained on the drive's zero backlash, torque ripple, hysteresis characteristics, and positional accuracy performance.

- EVALUATE SUITABILITY OF ROLLER DRIVE TECHNOLOGY FOR POTENTIAL SPACE ACTUATOR APPLICATION
- DETERMINE DRIVE'S TORQUE RIPPLE, HYSTERESIS, POSITIONING ERROR, BACKLASH, AND CREEP CHARACTERISTICS
- ANALYTICALLY MODEL DRIVE SYSTEM TORSIONAL STIFFNESS AND EXPERIMENTALLY IDENTIFY "TORSIONALLY SOFT" COMPONENTS
- EVALUATE DRY PERFORMANCE OF GOLD ION-PLATED ROLLERS

CD-88-31899

ULTRAPRECISE TRACTION ROLLER FEED MECHANISM

Roller actuators have been used in positioning mechanisms where gear or ball screw systems could not be used as in this ultraprecise traction roller feed mechanism of the Lawrence Livermore Laboratory (Bryan, 1979). In this device a traction roller drives a translating traction bar that positions the parts to 0.2-μin. accuracy using a closed-loop laser interferometry feedback control system.

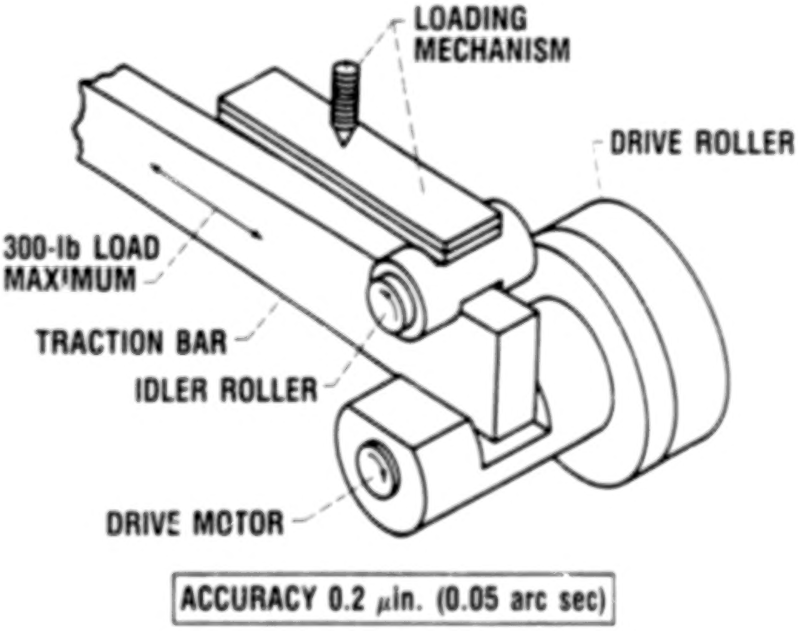
LOADING MECHANISM
DRIVE ROLLER
300-lb LOAD MAXIMUM
TRACTION BAR
IDLER ROLLER
DRIVE MOTOR
ACCURACY 0.2 μin. (0.05 arc sec)

CD-88-31637

26:1 CONTROL MOMENT GYRO ROLLER-GEAR DRIVE

An exceptional output torsional stiffness of 500 000 ft-lb/rad was demonstrated in this combined roller-gear drive designed and built for a satellite control moment gyro application (General Electric, 1972). In this drive design the rollers and gears transmit the load in parallel, combining in a compact package the excellent torsional stiffness and backlash-free behavior of traction rollers with the high-torque carrying capability of gears.

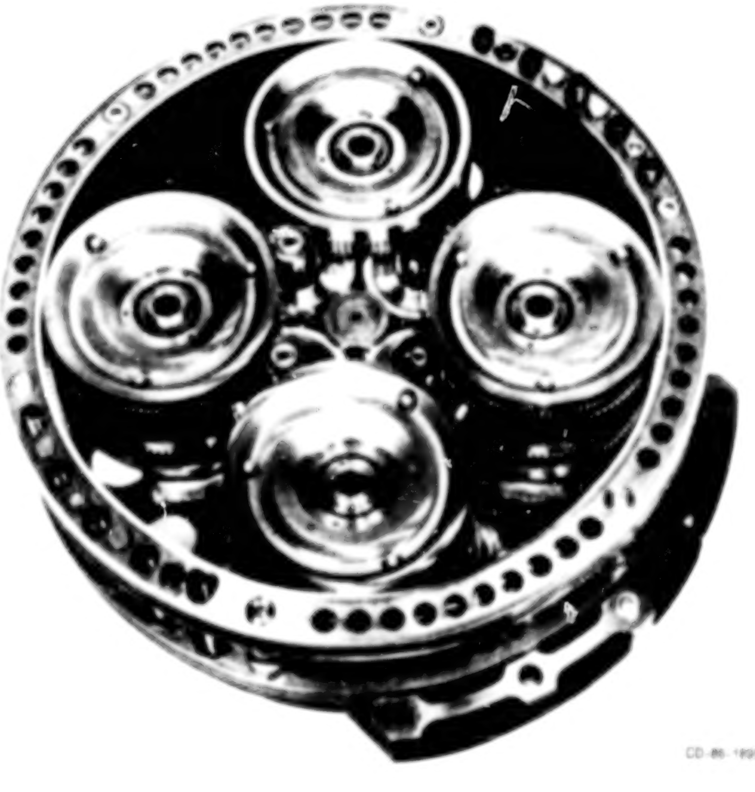

CD-86-19956

ORIGINAL PAGE IS
OF POOR QUALITY

ORIGINAL PAGE IS
OF POOR QUALITY

PROTOTYPE SPACE VEHICLE ROLLER ACTUATOR

Critical prototype drive system design requirements include a minimum drive torsional stiffness of 250 000 ft-lb/rad at the output, a low weight, and a minimum design life of 1600 hr. Maximizing the drive's torsional stiffness while minimizing the drive weight and achieving the required life were the paramount considerations guiding the design. Structural design tradeoffs and material selections were consistent with flight hardware requirements.

The drive was designed to operate without liquid lubrication with a design traction coefficient of 0.1, which is at least 20 percent below the maximum available traction coefficient of the gold-ion-plated sun rollers against their steel first-row planet rollers (Spalvins and Buzek, 1981). A layer of gold, 7.8 μin. thick, was ion plated onto the sun roller surface as a dry film lubricant to prevent the sun and first-row planet rollers from cold welding in the vacuum environment. Life limitation in this design is one of wear of the gold layer. Based on NASA sliding friction data (Spalvins, 1985), the gold thickness was determined for a minimum of 1600 hr of operation.

The drive is nominally 9.84 in. in diameter by 8.66 in. in length and weighs 22.1 lb. This compact Nasvytis planetary drive (Nasvytis, 1966) packages well in the small design envelope.

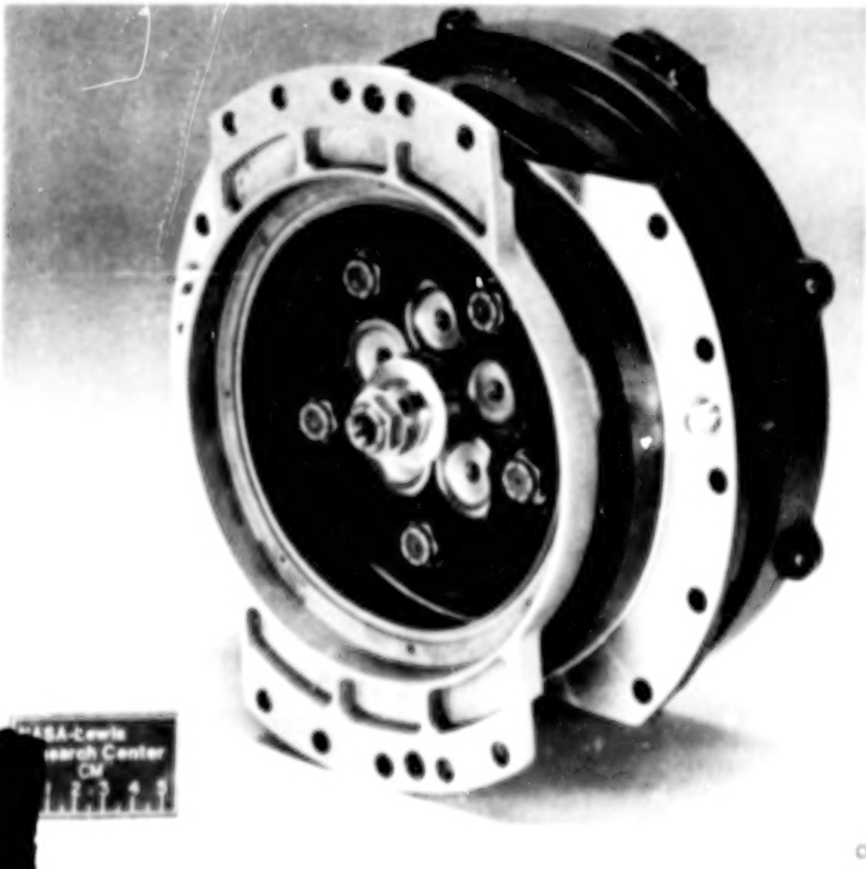

CD-88-31639

16:1 ROLLER ACTUATOR TEST UNIT

The servomotor-driven input shaft transmits torque to the two halves of the sun roller through two sets of ball-ramp loading devices. The sun roller, in turn, drives five stepped first-row planets that drive five second-row planets. These outer planets carry the torque to the ring roller attached to the output shaft. Because of the double-end geometry of the rollers, ten, twenty, and then ten parallel contact paths occur, respectively, at successive contacts. The number of planet rollers per row, number of rows, and relative step sizes are design parameters to be optimized for a given application.

The torque loading mechanism increases the normal load between the conically shaped rollers in direct proportion to the applied torque by causing inward axial motion of the sun roller halves. The potential for slip is not only eliminated by incorporating a roller loading mechanism, but also the normal loads on the rollers do not have to be set at maximum at all times, thereby extending coating wear life and minimizing frictional losses.

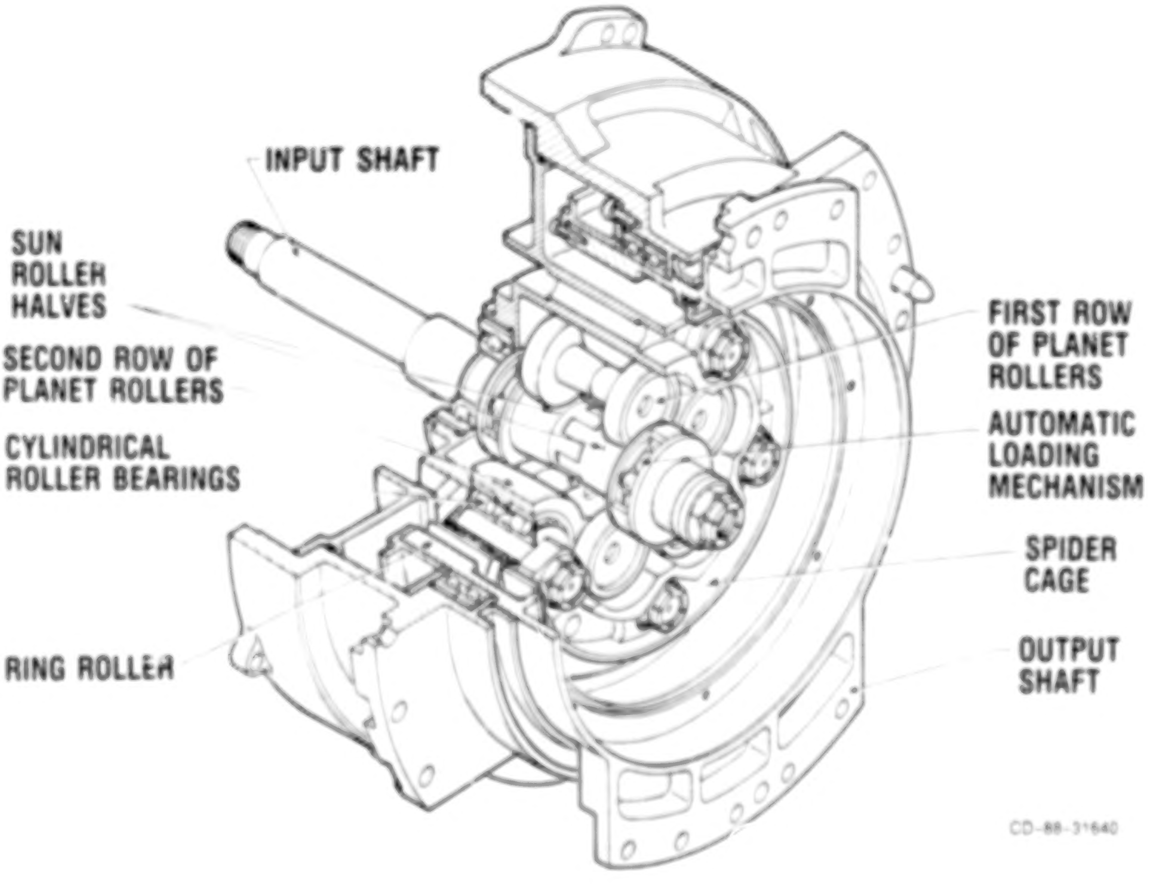
INPUT SHAFT
SUN ROLLER HALVES
SECOND ROW OF PLANET ROLLERS
CYLINDRICAL ROLLER BEARINGS
RING ROLLER
FIRST ROW OF PLANET ROLLERS
AUTOMATIC LOADING MECHANISM
SPIDER CAGE
OUTPUT SHAFT
CD-88-31640

PREDICTED DRIVE COMPLIANCE

The torsional stiffness of the drive (or its reciprocal, compliance) was analytically determined by modeling each of the drive's major components. The compliance of each element was found and is presented as a percentage of the total drive compliance. The spider cage support structure, planet bearings, and input shaft torque loader mechanism were the major contributors to the drive compliance. The traction contact compliance analyzed using a comprehensive technique developed at NASA Lewis (Rohn and Loewenthal, 1985) contributed only 9 percent to the overall drive compliance.

Adding the elemental compliances and taking the inverse resulted in an overall predicted drive torsional stiffness at the output shaft of 500 000 ft-lb/rad - twice the design target stiffness value.

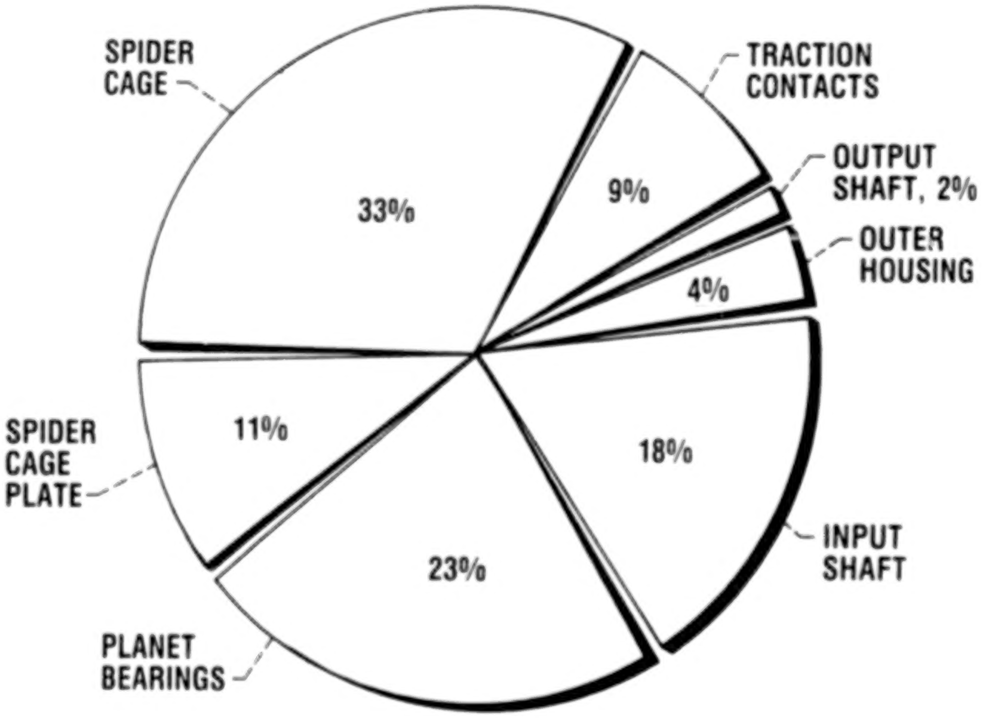

CD-88-31641

ROLLER ACTUATOR OUTPUT STIFFNESS AND HYSTERESIS

The drive's static torsional stiffness and hysteresis were measured at the output shaft. The slope of this curve reveals a torsional stiffness of 170 000 ft-lb/rad. This stiffness is just over two-thirds of the design value, or one-third of the predicted value.

Note, however, that the slope of the curve is constant across the zero torque line indicating that no backlash is present - a decided benefit for mechanism control systems that typically must position a load around a desired set point. Backlash would appear in this trace as a horizontal or "zero stiffness" line.

Inelastic displacements from contact microslip resulted in a small 8-arc-sec hysteresis loss during torque reversals. With feedback control systems, which are standard for these types of space vehicle actuators, this small hysteresis is considered acceptable.

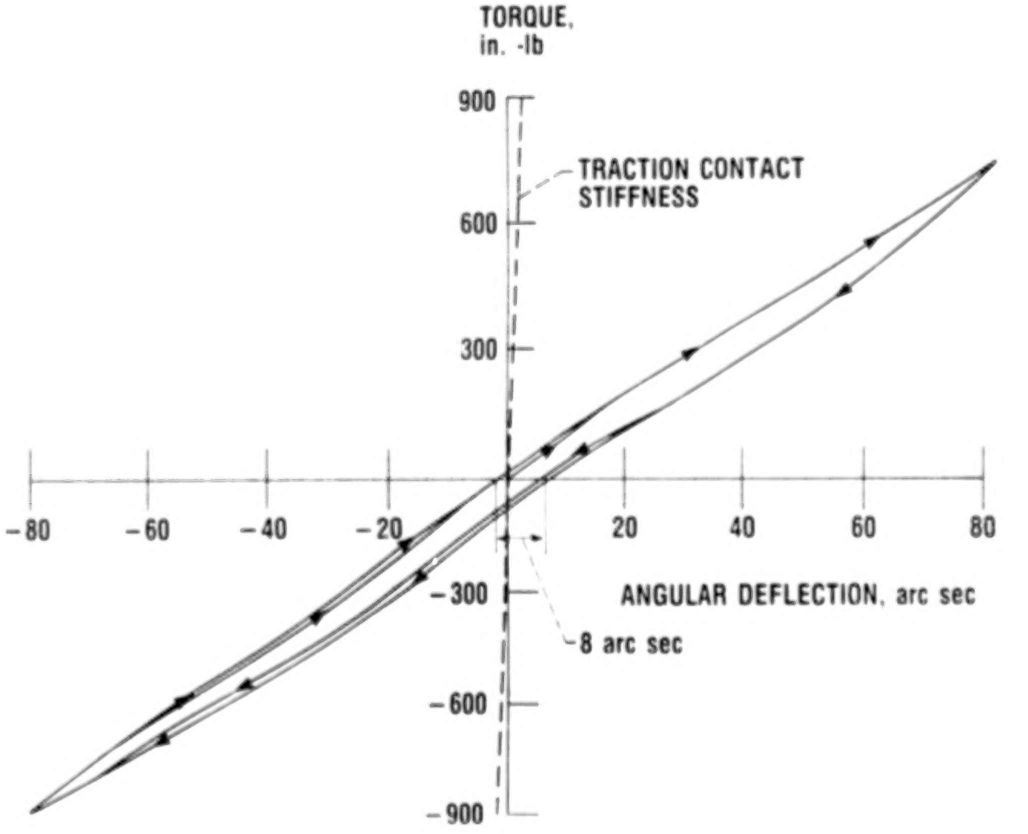

CD-88-31642

MAIN SOURCES OF STRUCTURAL COMPLIANCE

Individual stiffness measurements of key drive components were made to investigate the discrepancy between the measured and predicted drive system stiffnesses. The two largest contributors to drive compliance are the spider-cage support structure and the second-row planet support bearings. The stiffness of the spider cage was measured while installed in the drive by applying a static torque to the output shaft and measuring the angular deflection of the spider-cage about the centerline of the drive. The measured spider-cage support stiffness reflected to the output shaft was approximately half that predicted analytically using the simple beam model. Evidently, a detailed finite element model would be needed to provide better stiffness estimates for the relatively complicated spider cage.

Radial stiffness measurements of four of the drive's cylindrical roller planet bearings were made in a specially designed loading fixture with the same setup that exists in the second-row planet rollers. Near zero load, the measured radial stiffness of the cylindrical roller bearing was less than a third of that predicted by standard roller bearing theory (Harris, 1966) because of an experimentally observed settling-in phenomenon not reflected by the bearing deflection model.

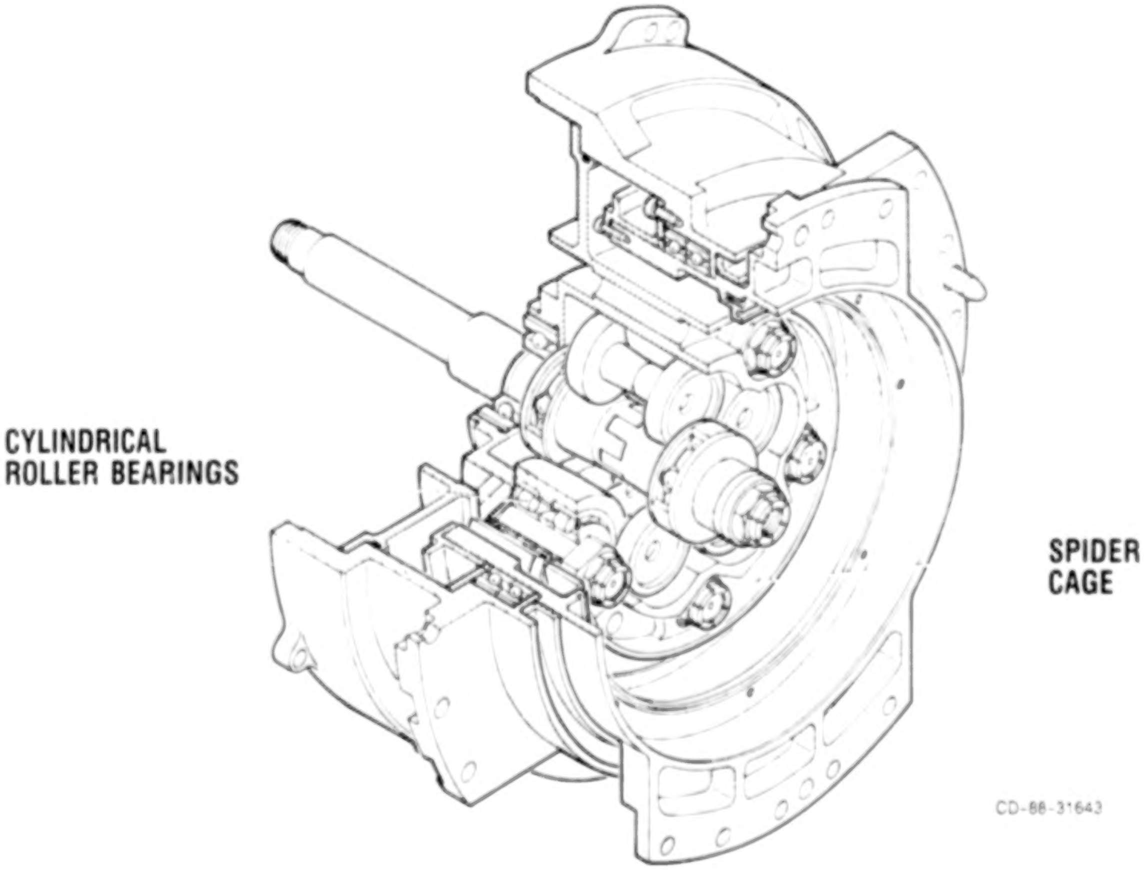

DRIVE SYSTEM STIFFNESS

The measured stiffnesses of the spider-cage support structure and the planet bearings were used in place of their original predictions (left bar shown in figure) to recalculate an overall predicted drive stiffness at zero-torque load. This stiffness of 270 000 ft-lb/rad is now 60 percent higher than that measured for the drive system.

Because of manufacturing tolerances in bearing post locations, it is possible the bearings on the test drive are out of perfect position. Thus, at initial load application only one or two of the supports may be, in fact, loaded. In view of this nonideal load sharing, a decrease in the effective planet bearing system stiffness would be expected. For instance, if it were assumed that only two of the five bearing supports were active at the initially applied torques, then the effective bearing support compliance would increase by a factor of 2.5, resulting in a recalculated drive stiffness of 170 000 ft-lb/rad (center bar shown). This stiffness agrees exactly with that measured.

Based on these results, drive stiffness improvements resulting from a redesign of the second-row planet support structure were analytically considered. Machining the spider cage from beryllium with more rigid connections for planet bearing posts would be expected to improve this component stiffness by 90 percent. Using preloaded or line-to-line fit cylindrical roller bearings would remove the initial "setting in" behavior observed, giving an appreciable higher stiffness at zero load (zero drive torque).

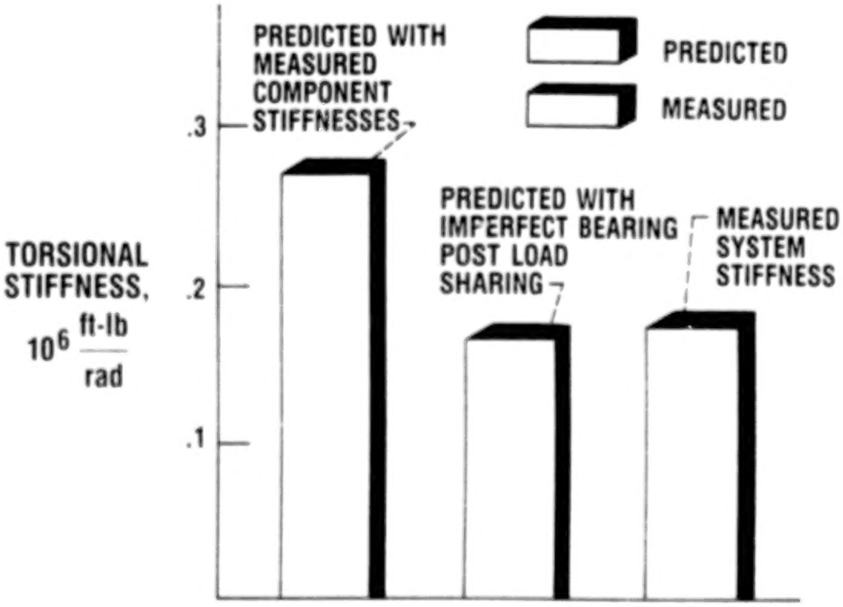

CD-88-31644

VERIFICATION OF TRACTION COMPLIANCE/HYSTERESIS MODEL

To corroborate the traction contact compliance analysis procedure, tests on a simple roller configuration were conducted at NASA Lewis. The apparatus consisted of a 3-in.-diameter crowned roller normally loaded against a flat plate. Static torque applied to the roller caused small angular displacements (resulting from tangential straining of the contact) as plotted here.

The measured and predicted contact stiffness agree well validating the analysis technique used for the overall drive. The general shapes of the curves also agree well indicating that the model accounts accurately for small inelastic microslip occurring in the contact resulting in the 0.7-arc-sec hysteresis losses shown.

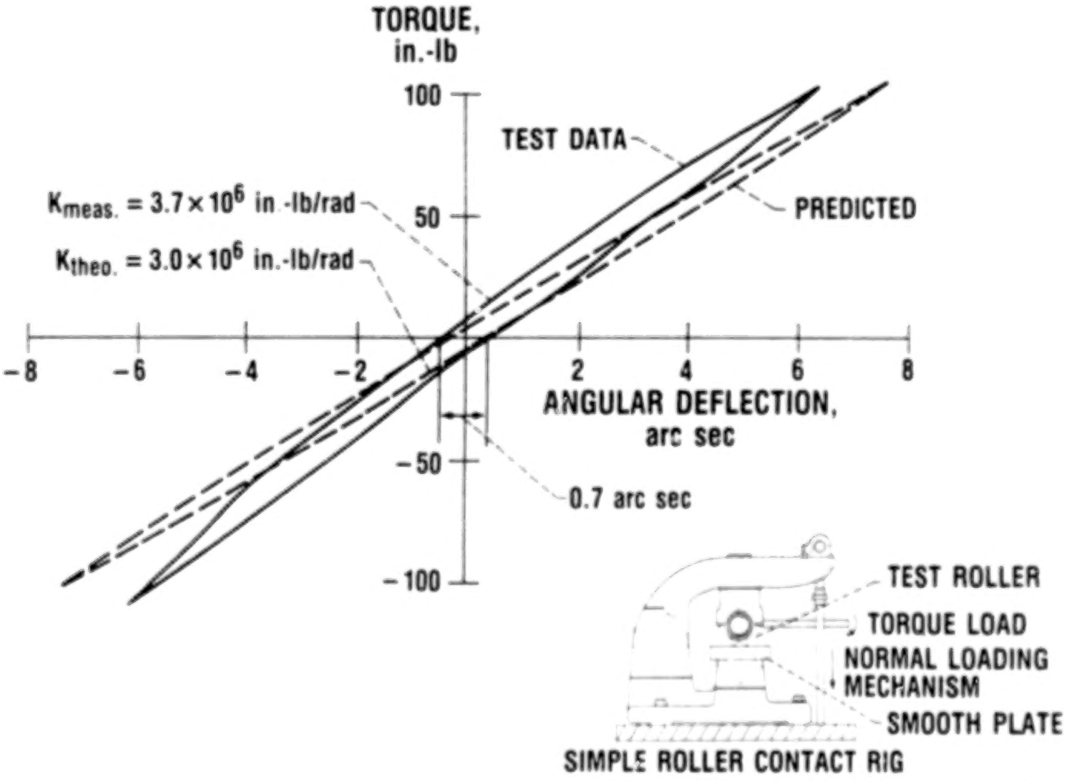

CD-88-31645

ROLLER ACTUATOR TORQUE RIPPLE

Tests were conducted to approximately determine the torsional ripple/attenuation characteristics of the roller actuator. A variable-speed dc motor drove the high-speed shaft of the actuator while steady torsional loads were applied to the output shaft.

The variations of roller actuator input and output torque signatures for one complete output shaft revolution are shown here. The actuator was driven at 10 percent of maximum speed and at three torque levels corresponding to 15, 25, and 31 percent of maximum torque at 50 percent preload. Torque ripple is shown as a percent variation (plus or minus) of the noted steady-state torque. The input torque varied approximately 7 to 8 percent while the output torque varied on the order of 0.3 percent. If no attenuation (damping) was present, then input and output torque percent fluctuations would be expected to be about the same. This suggests that the drive does not excite or amplify torsional oscillations but, in fact, helps to attenuate vibration through coulombic damping. The traces shown were taken with prerun rollers having less than perfect surface condition. Thus, these traces are considered to represent a conservative view of the smooth torque-transmitting capability of the test drive.

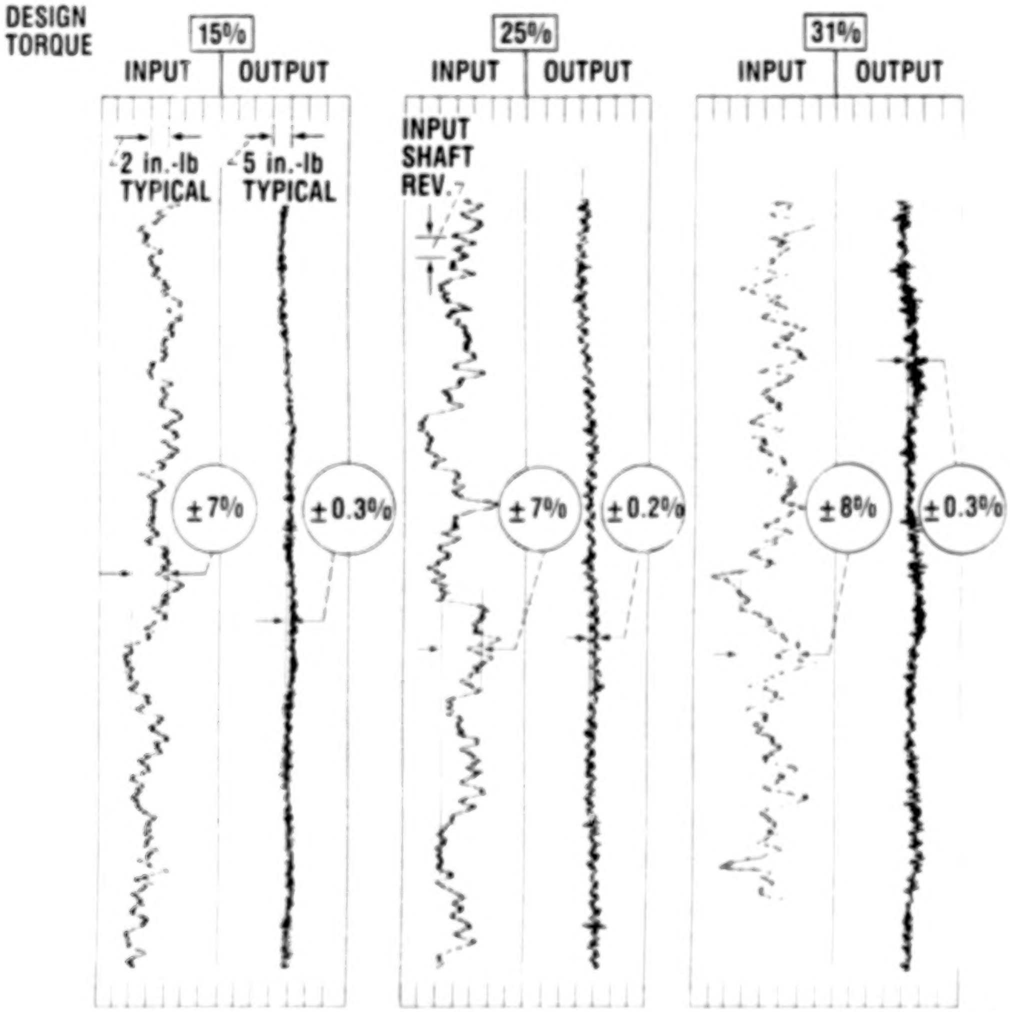

CD-88-31646

OPEN-LOOP POSITIONAL ACCURACY

A simple test was devised to determine the positional accuracy of the test drive under load in an open-loop control mode (point A to point B and back to point A). Tests were conducted by driving the input precisely 64 revolutions under four steady torque load levels at constant speed in one direction. The system was then "unwound" by rotating the input shaft back to its initial position while maintaining torque in the same direction. Dividing the difference in output shaft angular position before and after rotation by the 8 (128 input revolutions/drive ratio) total output rotations made, results in the percent angular error shown.

These small errors in reproducing commanded input position are caused by two unavoidable characteristics of roller drives. The phenomenon of rolling creep under torque loads is the major contributor to open-loop positional inaccuracy. As each pair of rollers roll over each other under a steady torque, there is a small relative speed difference which is seen at the output as lost motion. At low torques, or when the drive operates unloaded, very small kinematic errors due to imperfectly ground rollers (diameter tolerance, out-of-roundness, lobing, waviness, etc.) can be present. Hence, for critical point-to-point positioning applications the control system must be closed loop in order to feedback output position when using roller actuators. This is not uncommon for such precision positioning mechanisms.

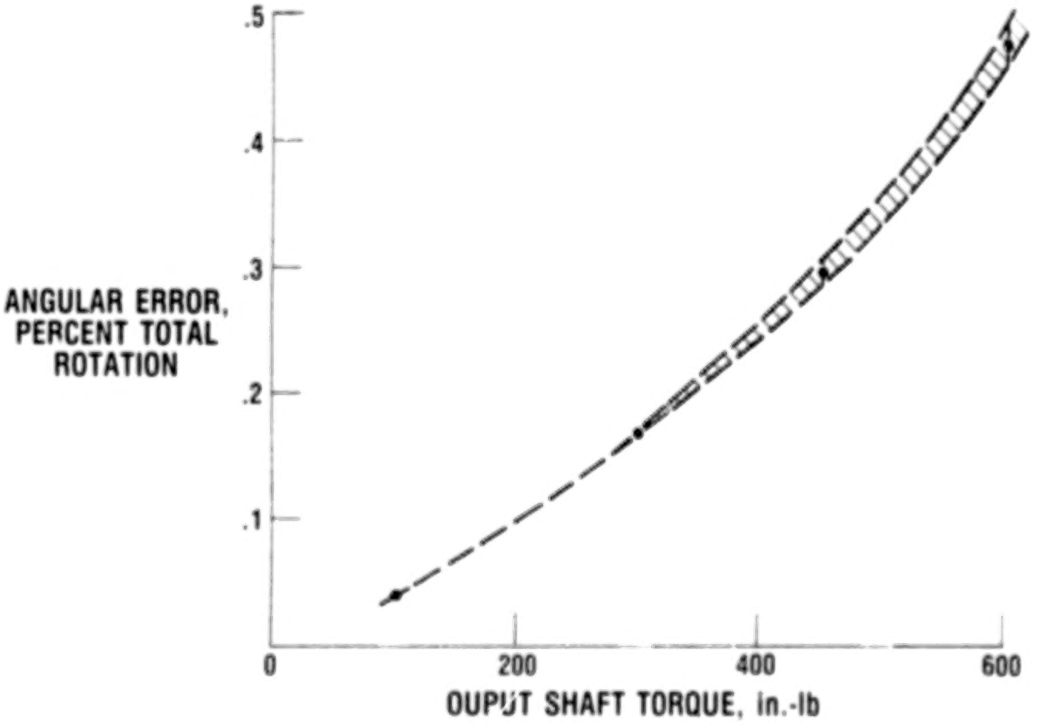

CD-88-31647

SUMMARY AND CONCLUSIONS

The suitability of roller drive technology for key space vehicle actuator needs has been shown. The drive system evaluated herein exhibited many required features of precision positioning mechanisms, including absence of mechanical backlash with minimum hysteresis, high-torque capability in a small, lightweight package, and the ability to run smoothly and operate without a liquid lubrication system.

The absence of mechanical backlash or deadband improves the resolution of the system under load-reversal conditions and simplifies the control system. The planetary drive configuration packs a high ratio in a small design envelope. The smooth running and attenuating characteristics are ideal for sensitive minimum vibration positioning applications. The traction rollers have inherently high torsional stiffness (important for high system bandwidth) since torque is transmitted through tangential shearing of the traction interface. Overall drive system stiffness, however, was compromised by support structure compliance. Operating the drive dry with only a thin gold film applied to the traction surfaces prevents cold welding of the rollers in a space vacuum environment and eliminates the need for cumbersome liquid lubrication systems that must pass difficult space qualifications tests.

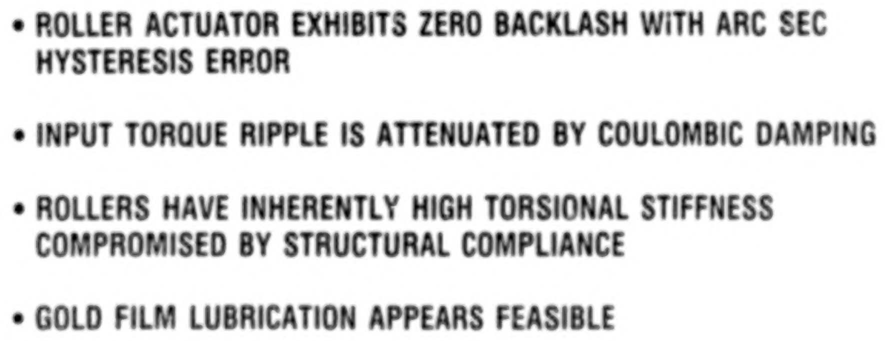

- **ROLLER ACTUATOR EXHIBITS ZERO BACKLASH WITH ARC SEC HYSTERESIS ERROR**
- **INPUT TORQUE RIPPLE IS ATTENUATED BY COULOMBIC DAMPING**
- **ROLLERS HAVE INHERENTLY HIGH TORSIONAL STIFFNESS COMPROMISED BY STRUCTURAL COMPLIANCE**
- **GOLD FILM LUBRICATION APPEARS FEASIBLE**

CD-88-31648

REFERENCES

Bryan, J.B., 1979, "Design and Construction of an Ultraprecision 84 Inch Diamond Turning Machine," Precision Engineering, Vol. 1, No. 1, pp. 13-17.

General Electric, 1972, "High Torque CMG Rotary Actuator," (ACS-10357, General Electric Co., NASA Contract NAS5-20298) NASA CR-122458, p. 2-1.

Harris, T.A., 1966, Rolling Bearing Analysis, Wiley, New York, pp. 166-171.

Kuban, D.P., and Williams, D.M., 1987, "Traction Drive, Seven-Degree-of-Freedom Telerobot Arm: A Concept for Manipulation in Space," NASA CP-2470, pp. 111-130.

Loewenthal, S.H., and Schuller, F.T., 1986, "Feasibility Study of a Discrete Bearing/Roller Drive Rotary Joint for the Space Station," NASA TM-88800.

Nasvytis, A.L., 1966, "Multiroller Planetary Friction Drive," SAE Paper 66073, October.

Rohn, D.A., and Loewenthal, S.H., 1985, "An Analysis of Traction Drive Torsional Stiffness," J. Mech. Trans. Automation Des., Vol. 107, No. 4, pp. 573-581.

Spalvins, T., and Buzek, B., 1981, "Frictional and Morphological Characteristics of Ion-Plated Soft Metallic Films," Thin Solid Films, Vol. 84, pp. 267-272.

Spalvins, T., 1985, "The Structure of Ion Plated Films in Relation to Coating Properties," NASA TM-87055.

Steinetz, B.M., Rohn, D.A., and Anderson, W.J., 1986, "Evaluation of a High-Torque Backlash-Free Roller Actuator," NASA CP-2423, pp. 205-230.

N88-23240

LOW-COST OPTICAL DATA ACQUISITION SYSTEM FOR BLADE VIBRATION MEASUREMENT

Stephen J. Posta
Structural Dynamics Branch
NASA Lewis Research Center

ABSTRACT

A low-cost optical data acquisition system was designed to measure deflection of vibrating rotor blade tips. The basic principle of the new design is to record in memory raw data (a set of blade arrival times) and to perform all processing by software after a run. This approach yields a simple and inexpensive system with much less hardware than required for an earlier design developed for this application.

Functional elements of the system were breadboarded and operated satisfactorily during rotor simulations on the bench and during a data collection run with a two-blade rotor in the Lewis spin rig.

Software was written to demonstrate the sorting and processing of data stored in the system control computer after retrieval from the data acquisition system. The demonstration produced an accurate graphical display of deflection versus time.

PRECEDING PAGE BLANK NOT FILMED

OVERVIEW

FEATURES

- MEASURES DEFLECTION OF VIBRATING ROTOR BLADE TIPS.
- FACILITATES PROCESSING AND ANALYSIS BECAUSE DATA ARE DIGITAL.
- PROVIDES COMPLETE VIBRATION RECORDS FOR EACH ROTOR BLADE.
- ELIMINATES CALIBRATION PROBLEMS INHERENT TO STRAIN GAGE SYSTEMS.

CD-88-31874

FUNCTIONAL ELEMENTS

- FIXED OPTICAL PROBES SENSE BLADE PASSAGE.
- DATA ACQUISITION BOARDS RECEIVE AND STORE NEW DATA (A SET OF BLADE ARRIVAL TIMES).
- A CONTROL COMPUTER SORTS AND PROCESSES DATA INTO USABLE FORM.
- A CONTROL BOARD PROVIDES THE INTERFACE BETWEEN DATA ACQUISITION BOARDS AND THE CONTROL COMPUTER.

CD 88 31875

OPTICAL DATA ACQUISITION SYSTEM

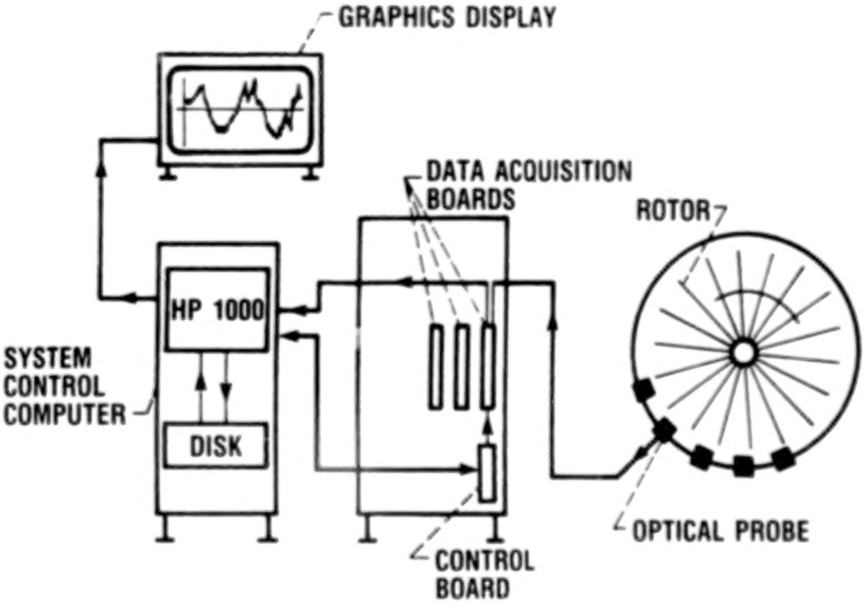
GRAPHICS DISPLAY
DATA ACQUISITION BOARDS
ROTOR
HP 1000
SYSTEM CONTROL COMPUTER
DISK
OPTICAL PROBE
CONTROL BOARD

CD 88 31876

POSTER PRESENTATION

OPTICAL DATA ACQUISITION SYSTEM

The optical data acquisition system comprises a set of fixed optical probes that sense blade passage, data acquisition boards that receive and store in memory the raw data (a set of blade arrival times), a control computer that sorts the data into a usable form after each data collection run, and a control board that provides the interface between the data acquisition boards and the control computer.

Design details for this system are reported in Posta and Brown (1986). A relatively more complex and costly earlier design was described in Brown et al. (1984) and Lawrence and Meyn (1984).

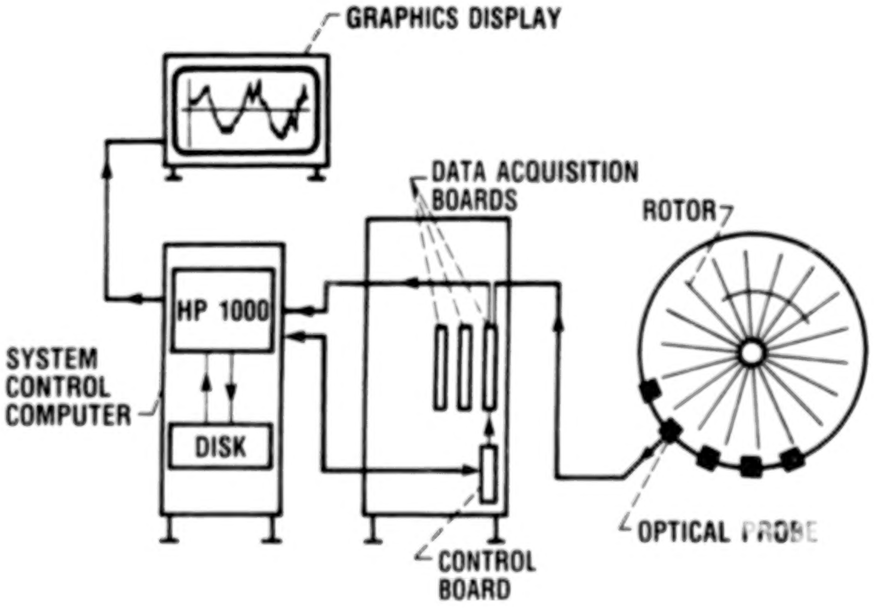
GRAPHICS DISPLAY
DATA ACQUISITION BOARDS
ROTOR
HP 1000
SYSTEM CONTROL COMPUTER
DISK
OPTICAL PROBE
CONTROL BOARD

CD 88 31876

OPTICAL PROBE

Each probe contains a high-resolution optical, reflective sensor and associated support electronics. The sensor is a focused light-emitting diode (LED) and matched photodetector in a single package. A visible light beam emitted by the LED is focused at the blade tips. As a blade edge passes by the probe at high speed, the event is detected, converted to a transistor-transitor logic (TTL)-compatible signal, and sent to a data acquisition board, where it is stored in memory.

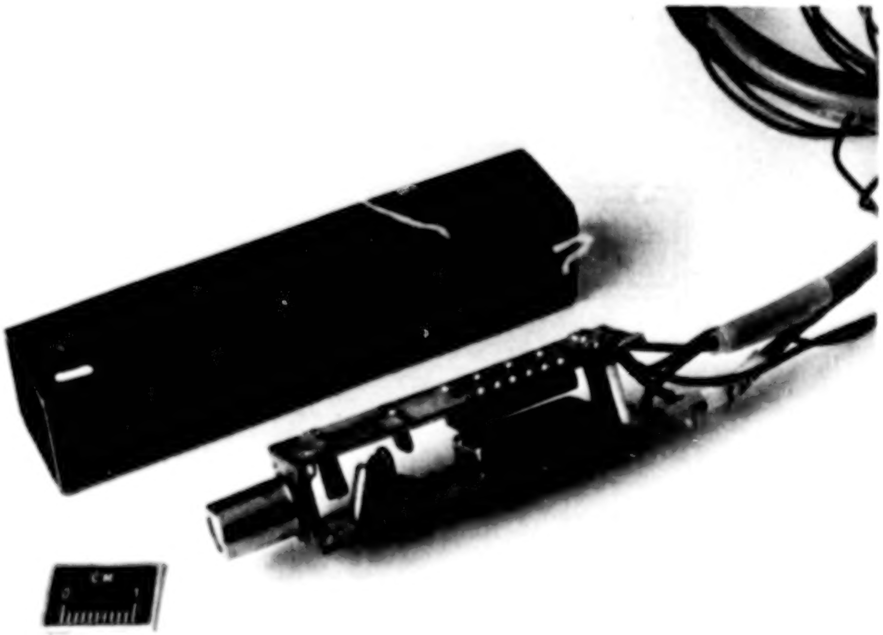

CD-88-31877

ORIGINAL PAGE IS
OF POOR QUALITY

OPTICAL PROBE INSTALLATION IN SPIN RIG

A probe assembly containing three optical probes is located at each of 16 viewing ports equally spaced around the perimeter of the spin rig case. One probe monitors the position of the blade tip leading edge, another monitors the blade tip midchord, and the third monitors the blade tip trailing edge. In this manner bending, torsion, and camber vibration modes can be identified. A single additional probe senses the start of each revolution with the passage of a timing mark on the rotor shaft.

ORIGINAL PAGE IS
OF POOR QUALITY

OPTICAL PROBE ASSEMBLY

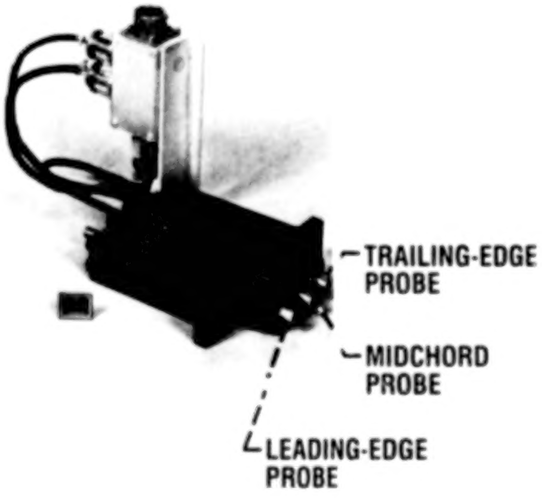
TRAILING-EDGE PROBE
MIDCHORD PROBE
LEADING-EDGE PROBE

OPTICAL PROBE INSTALLATION IN SPIN RIG

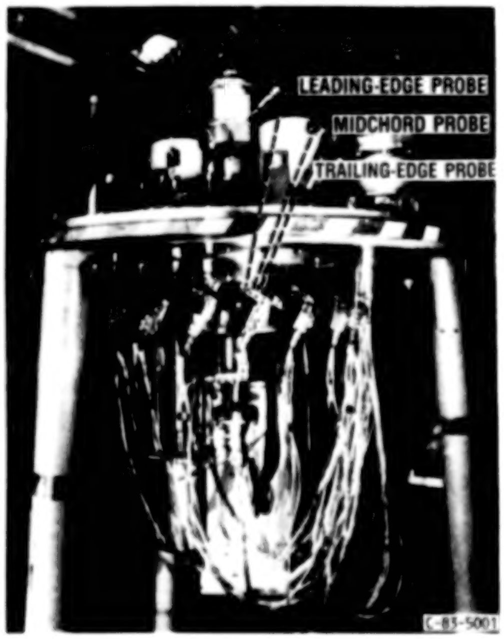
LEADING-EDGE PROBE
MIDCHORD PROBE
TRAILING-EDGE PROBE
C-83-5001

CD-88-31878

DATA ACQUISITION BOARD MEMORY LOGIC

Blade detection pulses from a probe correspond to blade arrival times measured from the start of each data collection run. These pulses latch the count from a high-speed wraparound counter located on the system control board and begin writing the count into the current memory address. In this manner the blade arrival times are "time stamped" into memory.

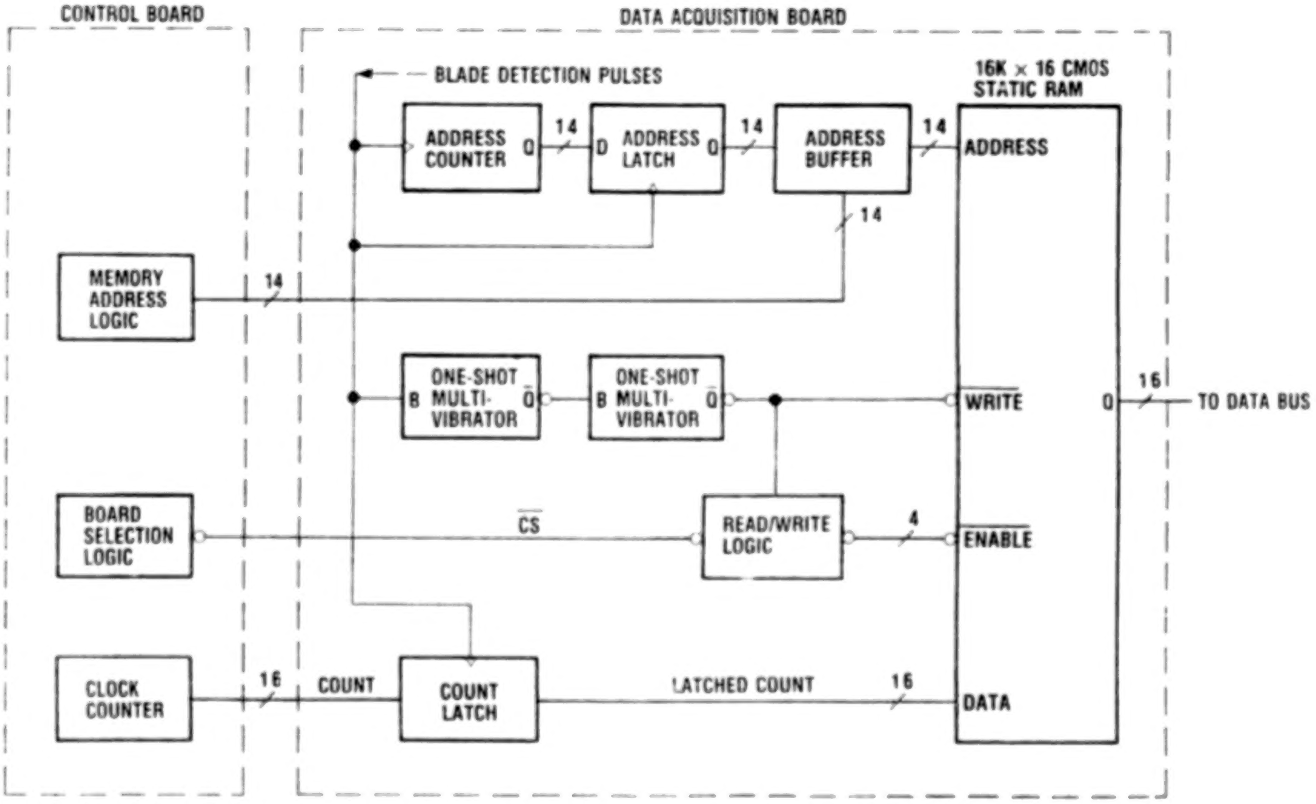

CONTROL BOARD
DATA ACQUISITION BOARD
BLADE DETECTION PULSES
16K × 16 CMOS STATIC RAM
ADDRESS COUNTER
Q
14
D
ADDRESS LATCH
Q
14
ADDRESS BUFFER
14
ADDRESS
14
MEMORY ADDRESS LOGIC
14
ONE-SHOT MULTI-VIBRATOR
B
Q̄
ONE-SHOT MULTI-VIBRATOR
B
Q̄
WRITE
Q
16
TO DATA BUS
BOARD SELECTION LOGIC
CS
READ/WRITE LOGIC
4
ENABLE
CLOCK COUNTER
16
COUNT
COUNT LATCH
LATCHED COUNT
16
DATA

CD-88-31679

DATA ACQUISITION BOARD INPUT CIRCUIT

A system with fewer data acquisition boards and fewer components can be designed if each board accepts data from more than one optical probe. This is possible because the pulses from any probe are relatively widely spaced in time, in contrast to the temporal variation of any pulse due to blade vibration. The signals from one or more other probes can be interspersed if a known ordering of the pulses is maintained. This approach does not reduce the total memory size but saves substantial duplication of other components, such as counters and latches. A board configuration having four optical probe inputs was chosen because it allows a maximum deflection of 140 mils, which exceeds the performance of the earlier designed system in this area.

One pair of probes (viewing ports 0 and 2) is separated from the other pair (viewing ports 4 and 6) by input gates G1 and G2. This allows optional delay to be added to signals from one probe pair. The signals from both probe pairs are combined at output gate G3 and appear at the output of this gate as a composite train of interspersed blade deflection pulses. Depending on the rotor configuration, delay may be required to separate probe signals that are coincident or overlap in time.

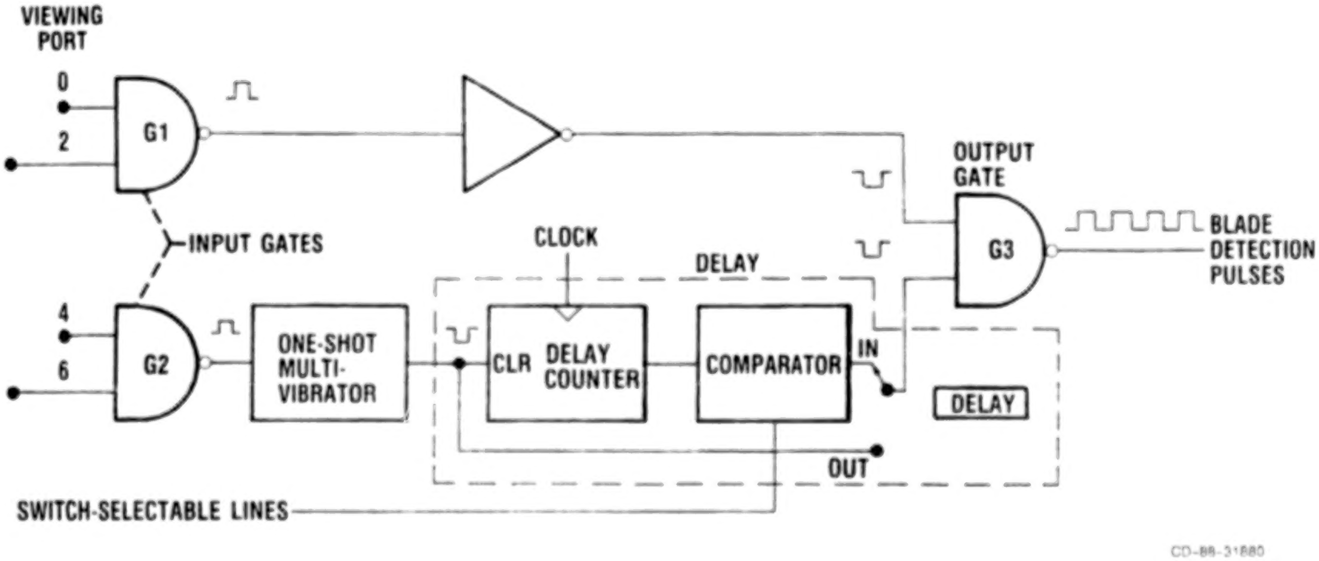
VIEWING PORT
0
2
G1
INPUT GATES
4
6
G2
ONE-SHOT MULTI-VIBRATOR
CLOCK
DELAY
CLR
DELAY COUNTER
COMPARATOR
IN
OUT
DELAY
OUTPUT GATE
G3
BLADE DETECTION PULSES
SWITCH-SELECTABLE LINES
CD-88-31880

CONTROL BOARD

The control board has control circuits for interfacing the data acquisition boards with an external computer during the acquisition, storage, and retrieval phases of a data collection run. A section of the board records the time when each rotor revolution begins, as monitored by a separate optical probe. This information is used in measuring rotor speed. The master clock and high-speed wraparound counter are also located on this board.

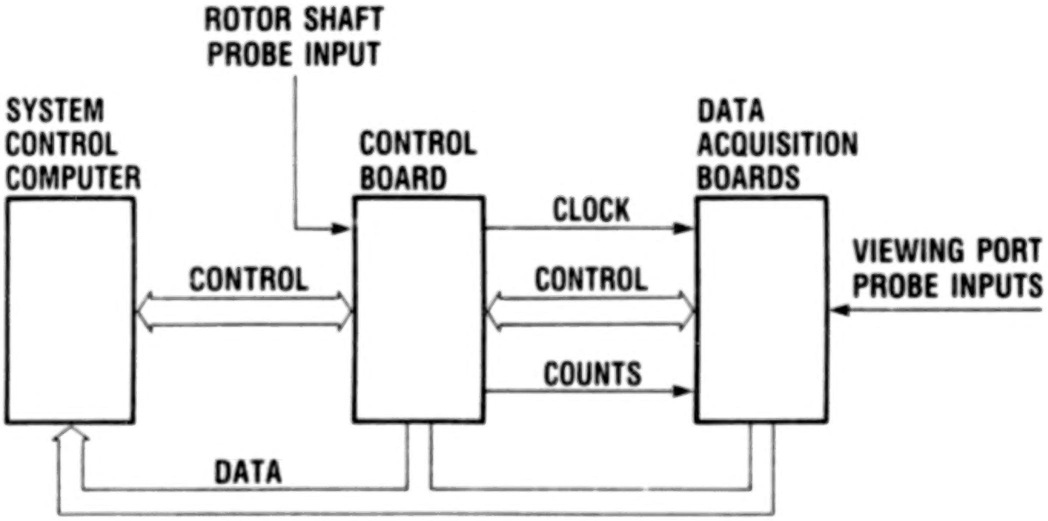
ROTOR SHAFT PROBE INPUT
SYSTEM CONTROL COMPUTER
CONTROL BOARD
DATA ACQUISITION BOARDS
CLOCK
CONTROL
CONTROL
VIEWING PORT PROBE INPUTS
COUNTS
DATA

CD 88 31881

COMPARISON OF SYSTEMS

The low-cost system retains the important performance characteristics of an earlier designed system. Maximum allowable blade tip deflection, deflection resolution, maximum (unaliased) frequency, and frequency resolution are equal to or better than those of an earlier designed system. The low-cost system requires fewer circuit boards, each with a significantly reduced component count than previous designs.

The need for frequency synthesizers is eliminated by "time stamping" the blade arrival times measured from the start of a data collection run rather than those measured from the start of each revolution.

MAXIMUM ALLOWABLE BLADE TIP DEFLECTION AND DEFLECTION RESOLUTION

ROTOR DIAMETER, 20 in.

SYSTEM	NUMBER OF ROTOR BLADES	ROTATIONAL SPEED, rpm	MAXIMUM ALLOWABLE DEFLECTION, ± mil	DEFLECTION RESOLUTION, mil
EARLIER DESIGN	ANY NUMBER	15 000 3 000	*102 TO 1257 *102 TO 1257	*0.8 TO 9.8 *0.8 TO 9.8
LOW-COST DESIGN	56	15 000 3 000	140 140	0.80 16
	2	15 000 3 000	3927 3927	80 16

*CAN BE SET OVER THIS RANGE BY SOFTWARE CHANGE OF SYNTHESIZER FREQUENCY

CD-80-31082

SYSTEM CHARACTERISTICS

56 BLADES, 15 000 rpm

SYSTEM CHARACTERISTICS	SYSTEM	
	EARLIER DESIGN	LOW-COST DESIGN
MEMORY SIZE PER BOARD	4096 8-BIT WORDS	16 384 16-BIT WORDS
NUMBER OF DATA BOARDS	16	4
SAMPLE TIME, t, μsec (TIME FOR BLADE n TO GET FROM PORT N TO PORT (N + 2))	250	250
SAMPLE RATE, f, Hz	4000	4000
MEMORY PER BLADE, $\left(\frac{\text{MEMORY SIZE} \times \text{NUMBER OF BOARDS}}{\text{NUMBER OF BLADES}}\right)$	1170 WORDS	1170 WORDS
TIME TO FILL MEMORY, T, sec, $\left(\frac{\text{MEMORY PER BLADE}}{\text{SAMPLE RATE}}\right)$	0.292	0.292
FREQUENCY RESOLUTION, 1/T, Hz	3.42	3.42
MAXIMUM UNALIASED FREQUENCY, f/2, Hz	2000	2000

CD-80-31083

HARDWARE REQUIREMENTS

REQUIREMENT	SYSTEM	
	EARLIER DESIGN	LOW-COST DESIGN
DATA ACQUISITION BOARDS		
TOTAL NUMBER OF BOARDS, $\left(\frac{\text{PORTS} \times \text{PROBES PER PORT}}{\text{PROBES PER BOARD}}\right)$	$\frac{16 \times 2}{1} = 32$	$\frac{16 \times 2}{4} = 8$
IC's PER BOARD	68	30
TOTAL IC's	2178	240
CPU	32 × 1 = 32	0
FIFO	32 × 1 = 32	0
EPROM	32 × 2 = 64	0
DRAM	^{a}32 × 8 = 256	0
SRAM	32 × 2 = 64	^{b}8 × 4 = 32
CONTROL BOARD		
NUMBER OF BOARDS	2	1
IC's PER BOARD	BOARD 1, 97, BOARD 2, 44	43
TOTAL IC's	141	43
FREQUENCY SYNTHESIZER	2	NONE

^{a}TOTAL MEMORY, 1 MEGABIT

^{b}TOTAL MEMORY, 2 MEGABITS

CD-80-31084

REFERENCES

Brown, G.V., et al., 1984, "Lewis Research Center Spin Rig and Its Use in Vibration Analysis of Rotating Systems." NASA TP-2304.

Lawrence, C., and Meyn, E.H., 1984, "The Use of an Optical Data Acquisition System for Bladed Disk Vibration Analysis." NASA TM-86891.

Posta, S.J., and Brown, G.V., 1986, "A Low-Cost Optical Data Acquisition System for Vibration Measurement." NASA TM-88907.

N88-23241

ROLLER DRIVE MATERIALS PERFORMANCE

Douglas A. Rohn
Structural Dynamics Branch
NASA Lewis Research Center

ABSTRACT

Roller drives offer several beneficial characteristics in servomechanism applications. The best use of these inherent qualities in a given design is often dependent on the performance of the materials chosen for traction rollers. This presentation outlines roller traction performance basics, a test program at Lewis to measure performance, and the need for and typical use of the information.

Smooth rollers can transmit torque when pressed together in a rolling contact. The amount of torque depends directly on the available traction coefficient and indirectly on the normal load capacity of the roller materials. Durability and life are related to both rolling element fatigue and wear. Application of roller drives to space mechanisms requires this performance data under typical traction conditions in suitable environments, for example, vacuum.

A test rig has been designed and fabricated to develop this information. Parametric conditions and specimen materials have been chosen so that the resulting data and understanding will be valuable to the design and development of advanced, roller-driven space mechanisms, from precision positioning devices to telerobot joints.

OVERVIEW

BENEFICIAL CHARACTERISTICS OF ROLLER TRACTION DRIVES

Roller drives offer several beneficial characteristics in servomechanism applications. Potential aerospace applications include antenna or solar array positioners, control moment gyro actuators, and robotic joints. In these and similar applications the zero backlash, low torque ripple, high stiffness, high efficiency, and ability to run without liquid lubrication of roller traction drives are important. Application of these inherent qualities to a given aerospace mechanism often depends on the roller material performance, in terms of available traction coefficient, load capacity, and wear rate under the design conditions.

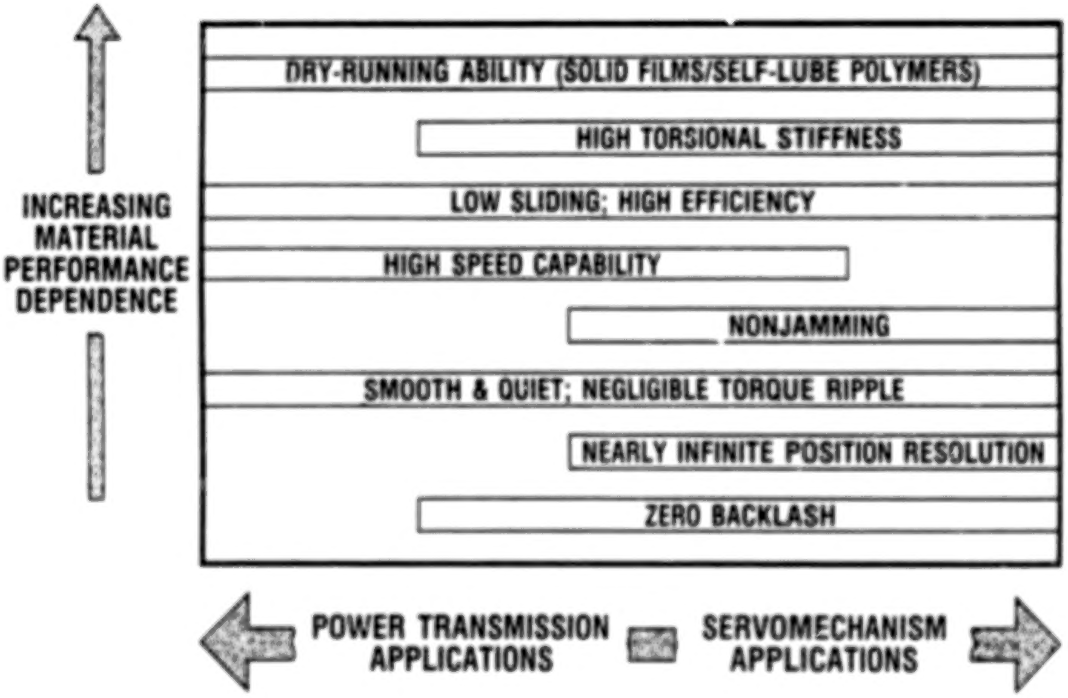
INCREASING MATERIAL PERFORMANCE DEPENDENCE
DRY-RUNNING ABILITY (SOLID FILMS/SELF-LUBE POLYMERS)
HIGH TORSIONAL STIFFNESS
LOW SLIDING; HIGH EFFICIENCY
HIGH SPEED CAPABILITY
NONJAMMING
SMOOTH & QUIET; NEGLIGIBLE TORQUE RIPPLE
NEARLY INFINITE POSITION RESOLUTION
ZERO BACKLASH
POWER TRANSMISSION APPLICATIONS
SERVOMECHANISM APPLICATIONS

CD-88-31961

FRICTION AND WEAR OF SEVERAL POLYMERS

Particularly in the case of space mechanisms, performance in the thermal-vacuum environment is critical. A large body of friction and wear data exists for sliding contact in air, as well as a fair amount for sliding in vacuum. Comparatively less information is available for rolling traction contacts (i.e., rolling and sliding) in air and very little for traction in a vacuum. Extrapolation from sliding to traction contacts is generally possible; however, exact condition data are preferred. In addition, the differences in performance in air and vacuum can be quite large.

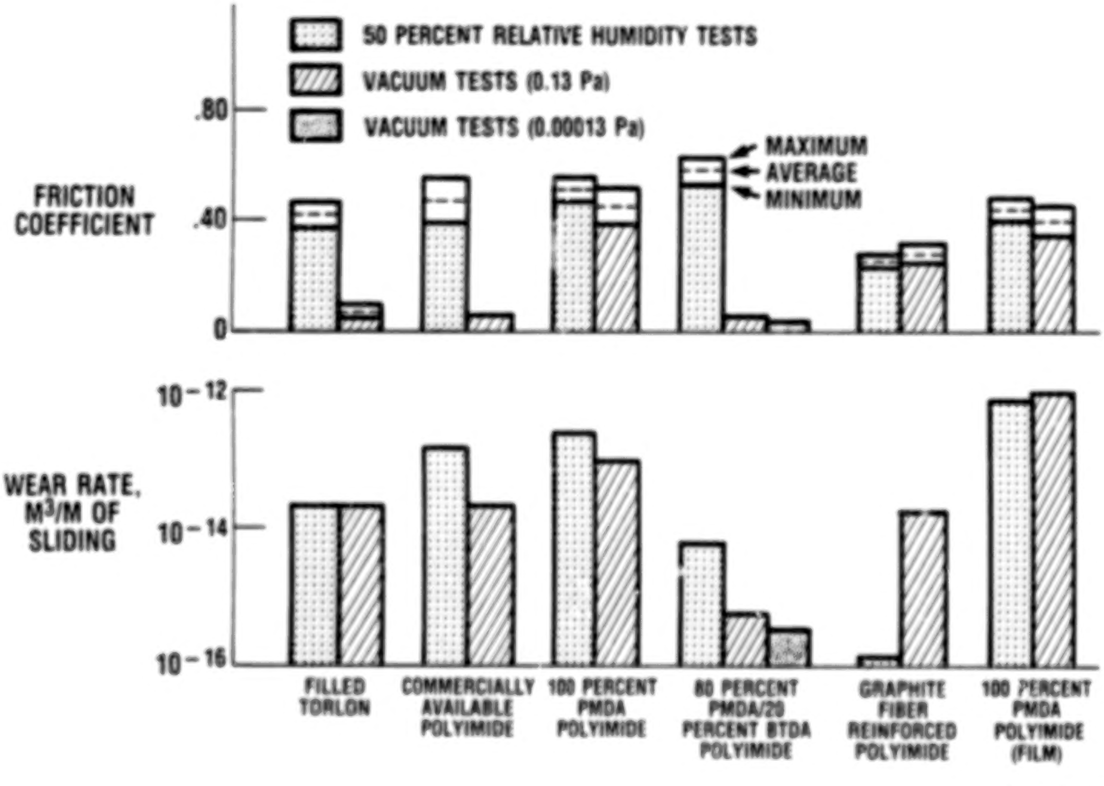

CD-88-31962

ENVIRONMENT SIMULATION ROLLER CONTACT PERFORMANCE RIG

An experimental program is under way at NASA Lewis to evaluate materials and coatings for application to roller drives in space mechanisms. Central to this effort is a test rig which properly duplicates conditions to provide valuable data for understanding rolling traction performance phenomena and to support current and future space mechanism projects.

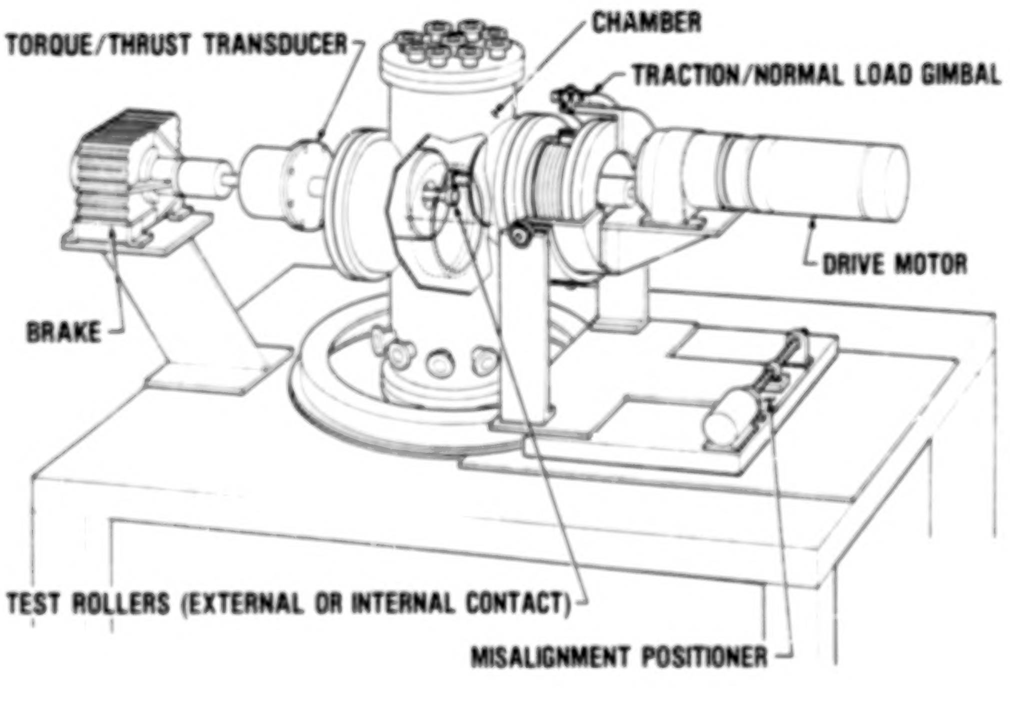
TORQUE/THRUST TRANSDUCER
CHAMBER
TRACTION/NORMAL LOAD GIMBAL
DRIVE MOTOR
BRAKE
TEST ROLLERS (EXTERNAL OR INTERNAL CONTACT)
MISALIGNMENT POSITIONER

CD-88-31963

POSTER PRESENTATION

BENEFICIAL CHARACTERISTICS OF ROLLER TRACTION DRIVES

An interesting class of mechanisms utilize traction as the means to transfer torque. Applications range from dry contacts, such as the locomotive wheel against the rail and elastomer-coated rollers in paper handling equipment, to lubricated contacts in industrial adjustable-speed traction drives (Loewenthal et al., 1983).

As power transmissions, few mechanical drives match the low noise, smooth torque transfer characteristics, high speed capability, and speed regulating accuracy of traction drives. For servo drive system applications, their ability to provide a smooth transfer of motion with relatively low hysteresis losses and high torsional stiffness while producing no detectable "backlash" upon direction reversal are obviously beneficial qualities. (Loewenthal et al., 1985).

These characteristics are inherent in the nature of roller traction drives (i.e., smooth rollers running against other smooth rollers). However, the degree to which the characteristics can be put to use depends on the performance of the roller materials.

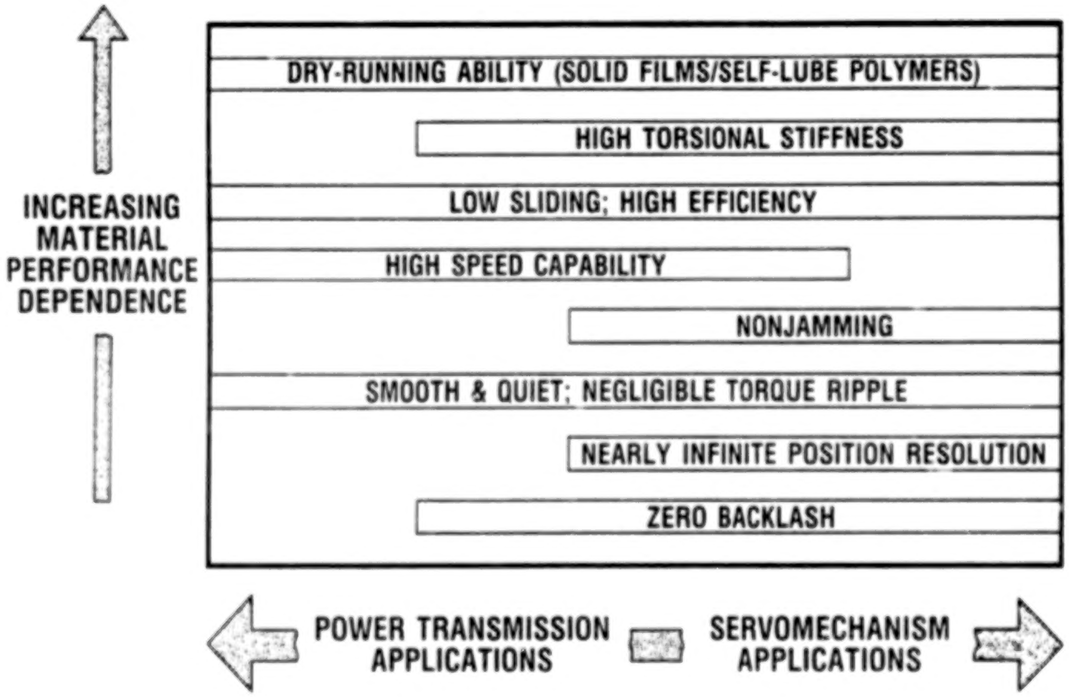
INCREASING MATERIAL PERFORMANCE DEPENDENCE
DRY-RUNNING ABILITY (SOLID FILMS/SELF-LUBE POLYMERS)
HIGH TORSIONAL STIFFNESS
LOW SLIDING; HIGH EFFICIENCY
HIGH SPEED CAPABILITY
NONJAMMING
SMOOTH & QUIET; NEGLIGIBLE TORQUE RIPPLE
NEARLY INFINITE POSITION RESOLUTION
ZERO BACKLASH
POWER TRANSMISSION APPLICATIONS
SERVOMECHANISM APPLICATIONS

CD-88-31961

TRACTION CURVE

A simple roller traction drive consists of a pair of rollers pressed together with a normal load N. The traction force T capable of being transmitted through the contact is a function of many parameters: normal load, rolling speed U, temperature, materials, and lubricants, when present. The relationship between these factors is typically shown by a set of traction curves. The speed variation between traction rollers due to torque transfer is generally referred to as creep (Loewenthal and Zaretsky, 1985). The traction coefficient is typically plotted against this value for a variety of speeds, temperatures, loads, etc. The shape of any one of the family of curves follows the range boundary lines of this figure.

Roller drives are designed to operate in the linear ascending portion of the traction curve at some point below the peak. Operating creep rates range from 0.1 to 0.2 percent for dry contacts or those lubricated with traction fluids at low speeds, to 3 or 4 percent for lightly loaded, high-speed contacts lubricated with mineral oils. This speed difference is not due to slip between driver and driven roller but is, in fact, the accumulated lost motion due to the tangential stretching and compressing motion or compliance occurring at the roller contact interface. A "locked" or "zero slip" region exists at the leading edge of the contact, and only at the peak traction point (i.e., point of impending slip) will this region completely disappear. In the case of a lubricated contact, lost motion due to viscous shear of the lubricant film in the contact is also added.

TRACTION CURVE

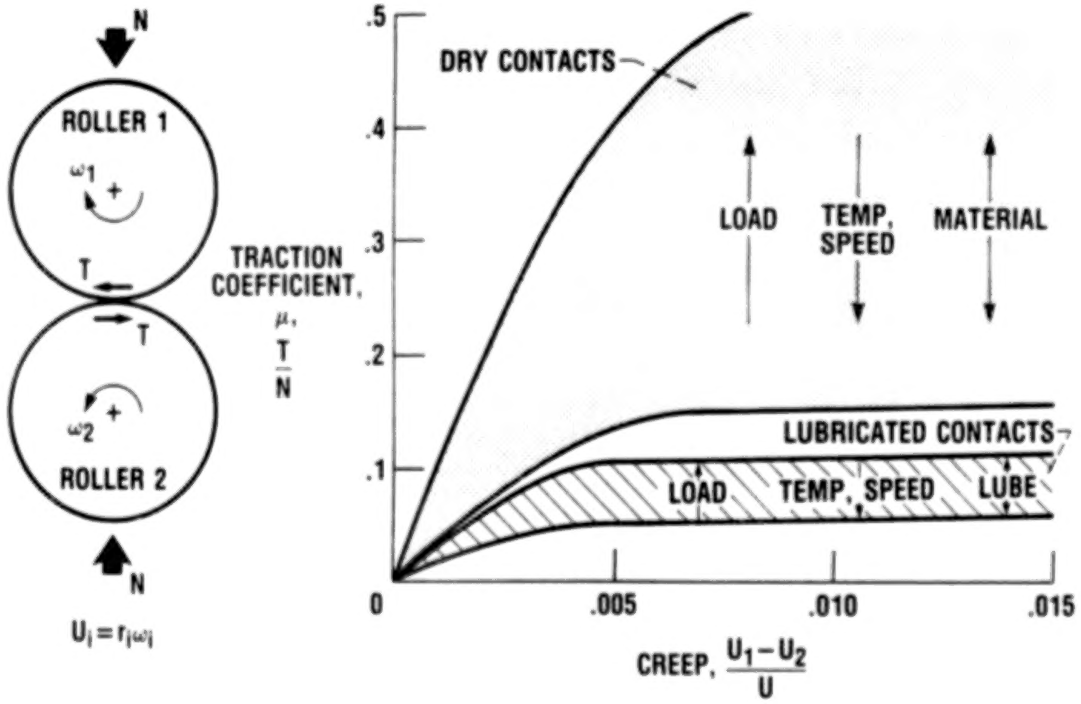

CD-88-31964

TRACTION CAPACITY OF POLYMER ROLLERS

The torque and power capacity of roller traction drive contacts are dependent on the material combination's peak available traction coefficient and the amount of normal load sustained before failure. The failure modes of lubricated roller drive contacts are very similar to those of ball and roller bearings. Rolling-element fatigue, or pitting, is the likely mode when the quality of lubrication is good. When the lubrication quality is not good, and also in the case of dry-contact roller drives, the failure mode shifts from fatigue to one that is predominantly wear.

Dry-running contacts, whether of polymer rollers or solid lubricant films, are obviously advantageous where liquid lubrication is impractical. The traction coefficient and particularly the load capacity of some commercial polymers are surprisingly high. Data shown here were generated in air, with a polymer roller running against a steel roller (Tevaarwerk, 1985).

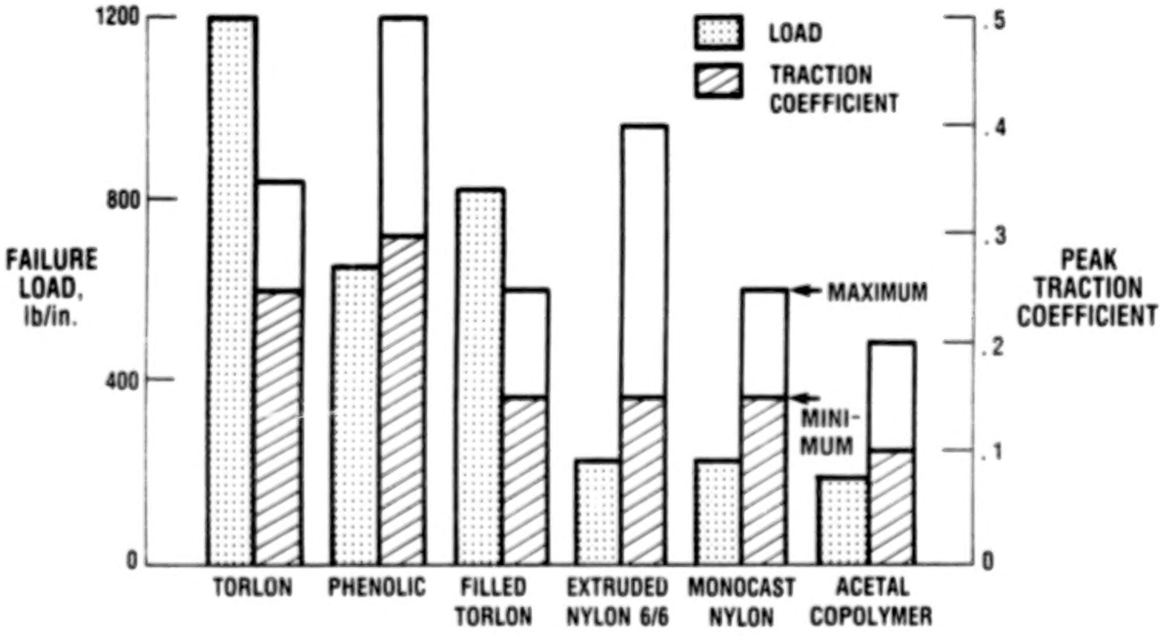

CD-88-31965

FRICTION AND WEAR OF SEVERAL POLYMERS

In order to make use of polymer rollers in space mechanism applications, their friction and wear properties must be known in representative environments. At present, data exist only for contacts undergoing full sliding. Data for several representative commercial and experimental polymers in air and vacuum are presented here (Fusaro, 1987).

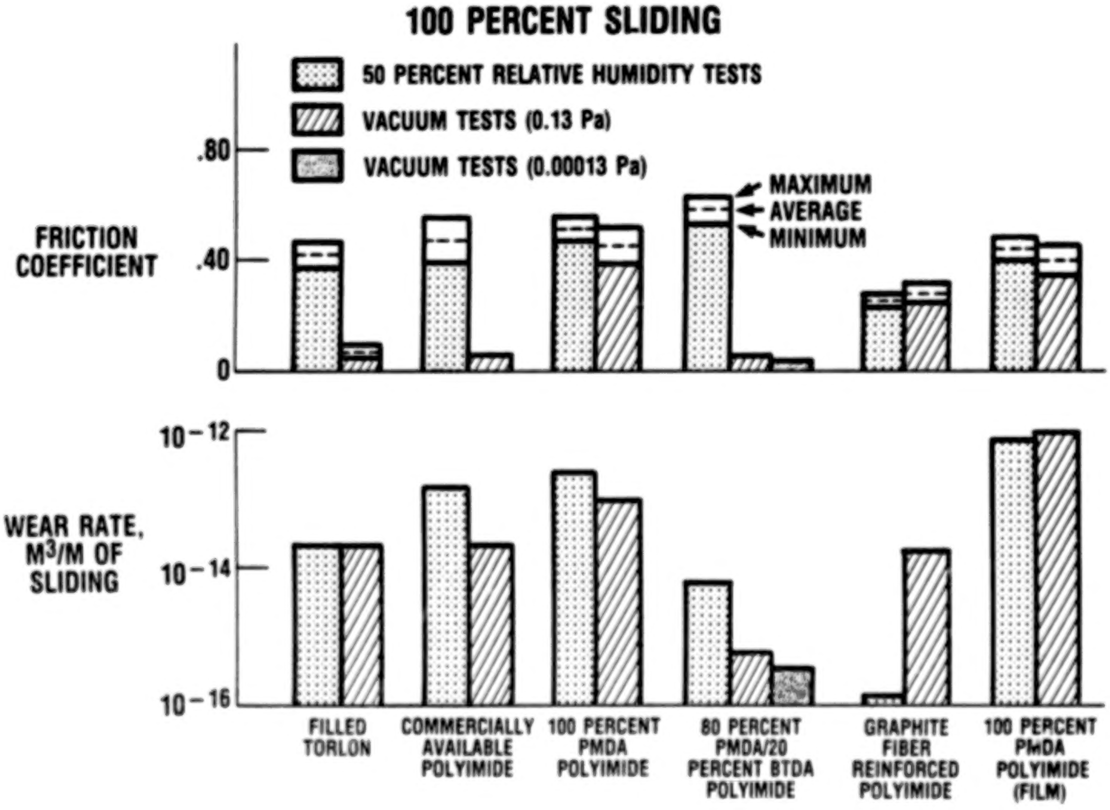

CD-88-31962

FRICTION OF GOLD-PLATED 440C

Another promising roller drive material combination is steel rollers with soft metal films (lead, silver, and gold) or hardfaced coatings (TiN and TiC). These materials serve as solid lubricants or extremely wear-resistant barriers (respectively) between the rollers which would otherwise cold weld in the nonoxidative vacuum environment. The data shown here (Spalvins, 1985) display friction as well as wear life information for gold in vacuum. Friction increases dramatically when the initial coating layer wears off and the 440C substrate is rapidly damaged.

This and the previous data charts illustrate typical available data, which are primarily for full sliding. Performance data in terms of traction coefficient, load capacity, and wear rate for all materials in a roller traction contact (combined sliding and rolling) under air, vacuum, and other environmental conditions are needed for roller drive space mechanism design.

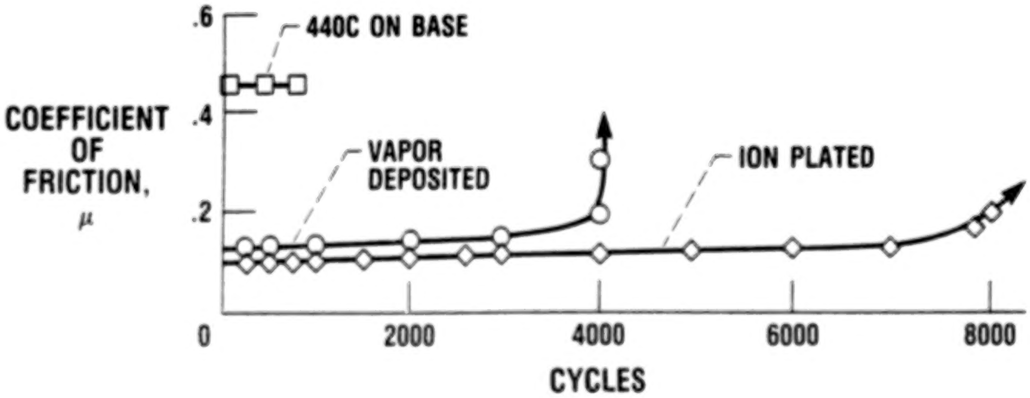

CD-88-31966

ENVIRONMENT SIMULATION ROLLER CONTACT PERFORMANCE RIG CAPABILITIES

An in-house program is under way to determine roller contact performance in nonatmospheric environments. Understanding the data and phenomena will support efforts in Lewis' Microgravity Mechanisms and Robotics Program, as well as in the space station, telerobotics research, and future space missions.

A rig has been designed and is being fabricated to satisfy the experimental criteria outlined here. Data on rolling traction contacts in a vacuum are essentially nonexistent today. Proposed specimen materials include the full range, from liquid lubricated steel, to solid film coatings, to polymers, and to ion-plated or vapor-deposited hardface materials.

PARAMETERS:

- LONGITUDINAL AND SIDE-SLIP TRACTION (ROLLING/SLIDING)
- AIR, VACUUM, GAS
- 200 lb NORMAL LOAD, 500 rpm, 600 in.-lb

OUTPUT DATA:

- TRACTION COEFFICIENT
- LOAD CAPACITY
- WEAR RATE
- EFFECTS OF MISALIGNMENT

SPECIMENS:

- SOLID ROLLERS
  - METALLIC
  - POLYMER
- COATINGS/FILMS
  - ION-PLATED METALS
  - HARDFACED LAYERS
  - POLYMERS
  - ELASTOMERS
- LIQUID LUBRICANTS

CD-88-31967

ENVIRONMENT SIMULATION ROLLER CONTACT PERFORMANCE RIG

An illustration of the rig concept is shown here. Test rollers are supported in vacuum-rated rotary feedthroughs and surrounded by a chamber which can be evacuated to 10^{-6} torr or filled with suitable gases at or below ambient pressure. A dc variable-speed motor provides rotation, and a magnetic particle brake absorbs power for longitudinal traction torque transfer testing. A more sensitive method of testing, side-slip traction (where the rollers are deliberately misaligned and the axial thrust is a measure of traction force), can also be accommodated. Misalignment is also a potential source of power loss in an actual roller drive mechanism; thus its effects on torque transfer will also be studied. Short-term, accelerated wear measurements will be possible. Presently planned future additions to the rig include the means to heat and cool the rollers to represent thermal conditions.

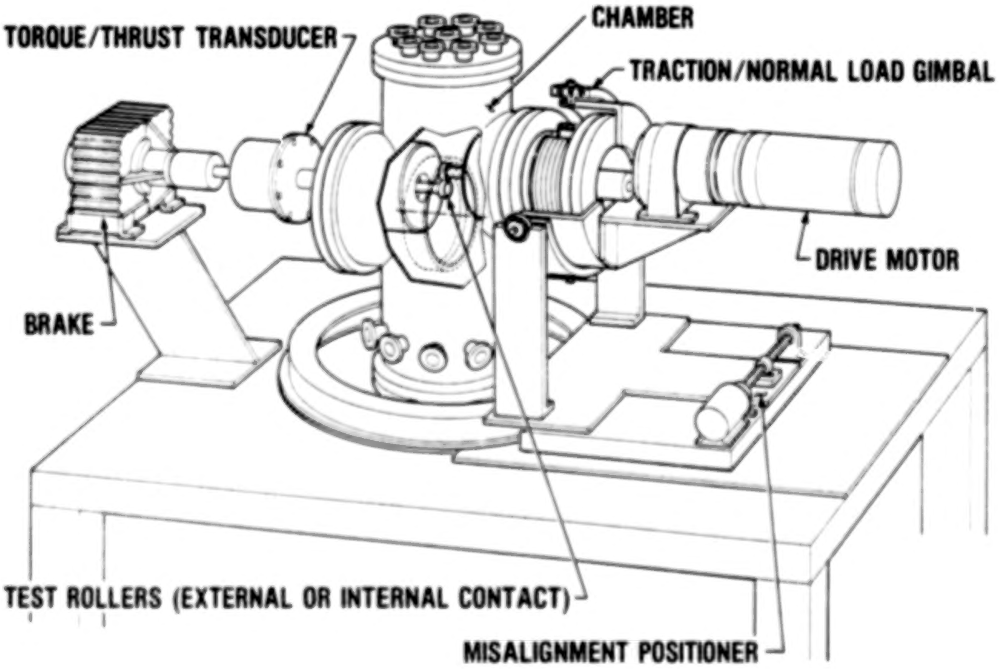
CHAMBER
TORQUE/THRUST TRANSDUCER
TRACTION/NORMAL LOAD GIMBAL
DRIVE MOTOR
BRAKE
TEST ROLLERS (EXTERNAL OR INTERNAL CONTACT)
MISALIGNMENT POSITIONER

CD-88-31963

SPACE STATION ROTARY JOINT PINCH ROLLER DRIVE CONCEPT

The data from this effort have been used to develop a concept for the space station power module alpha joint. Loewenthal and Schuller (1986) demonstrated the feasibility of a pinch roller drive. Several performance advantages relative to gears were noted, including overtorque or jamming protection, inherent acceptability to dry or self-lubricating materials, ease of manufacture, and in situ assembly and maintenance. Data to predict wear rates were extracted from plasma-nitrided steel gear data in vacuum and from pin-on-disk, 100 percent sliding data for polyimides in vacuum. While use of such data was made conservatively, actual rolling traction capacity and wear data are certainly required before committing to space flight hardware fabrication.

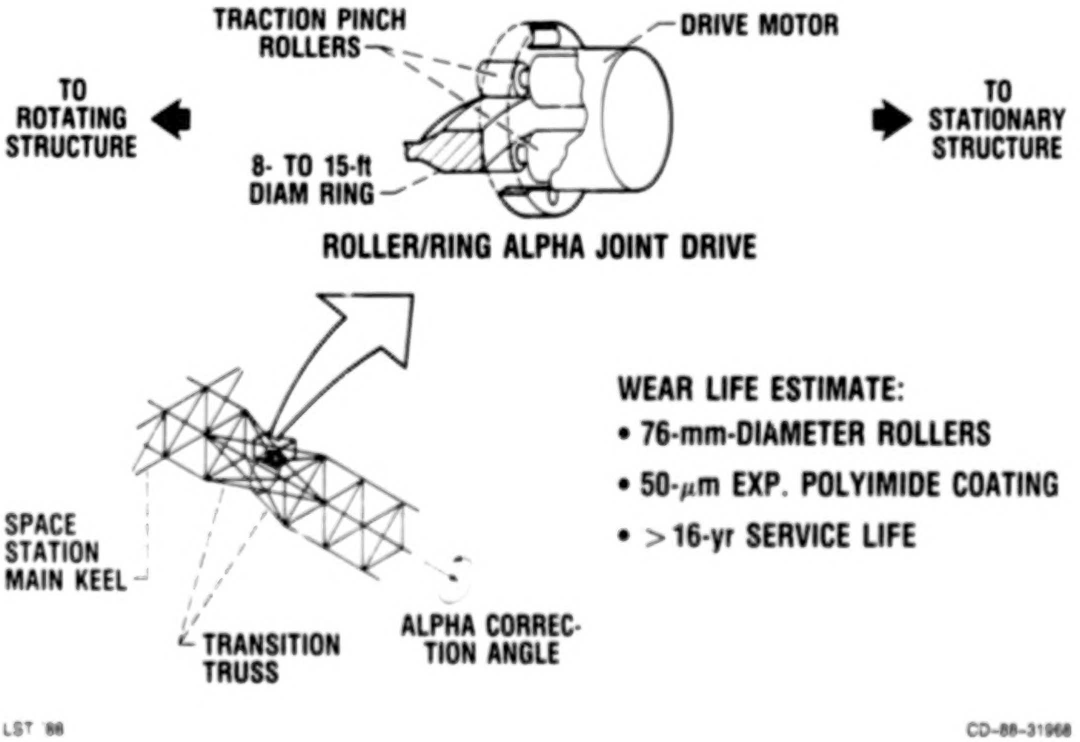
TRACTION PINCH ROLLERS
DRIVE MOTOR
TO ROTATING STRUCTURE
TO STATIONARY STRUCTURE
8- TO 15-ft DIAM RING
ROLLER/RING ALPHA JOINT DRIVE
WEAR LIFE ESTIMATE:
• 76-mm-DIAMETER ROLLERS
• 50-μm EXP. POLYIMIDE COATING
• > 16-yr SERVICE LIFE
SPACE STATION MAIN KEEL
TRANSITION TRUSS
ALPHA CORRECTION ANGLE
LST '88
CD-88-31968

ORIGINAL PAGE IS
OF POOR QUALITY

ORNL BENCH-TEST TELEROBOT JOINT WITH ROLLER DRIVE DIFFERENTIAL

Another application of advanced roller drive actuators is in robot manipulator joints. The Oak Ridge National Laboratory (ORNL) developed a design for a laboratory and ultimately a space telerobot system (Kuban and Williams, 1987). Critical to its performance is a differential pitch/yaw joint, having high torque in a compact volume, low loss, ability to operate in space, and zero backlash. A roller drive design was selected to meet these needs. High roller load capacity and reasonably high traction coefficient are both desirable to minimize the size of the joint while still carrying the required torque. Low wear is important for long life. Ion-plated gold on hardened steel was selected as the initial material combination. Data from the Roller Drive Material Performance Program are essential to this and other advanced roller drive mechanism designs.

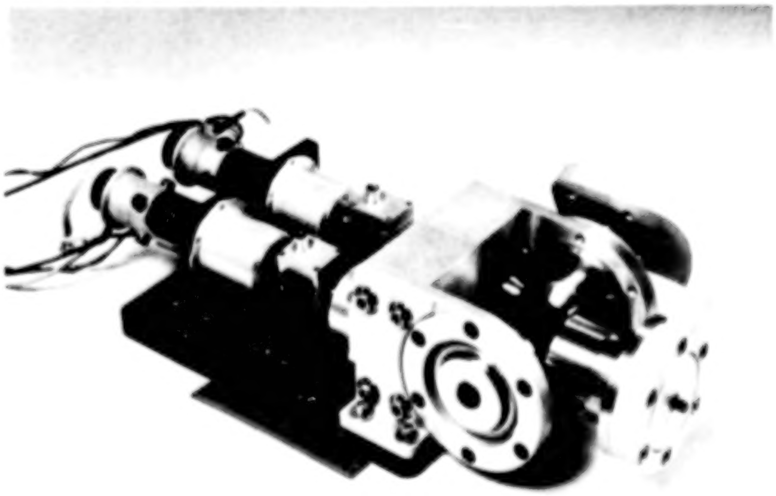

DESIGN REQUIREMENTS

- **HIGH TORQUE/ LOW LOSS**
- **DRY/VACUUM OPERATION**
- **ZERO BACKLASH**

CD-88-32530

SUMMARY

Roller drives offer several beneficial characteristics in servomechanism applications. The best use of these inherent qualities in a given design is often dependent on the performance of the materials chosen for traction rollers. Application of roller drives to space mechanisms requires this performance data under typical traction conditions in suitable environments.

An experimental program is under way to develop this information. Parametric conditions and specimen materials have been chosen so that the resulting data and understanding will be valuable to the design and development of advanced, roller space mechanisms, from precision positioning devices to telerobot joints.

REFERENCES

Fusaro, R.L., 1987, "Tribological Properties of Polymer Films and Solid Bodies in a Vacuum Environment," NASA TM-88966.

Kuban, D.P., and Williams, D.M., 1987, "Traction-Drive, Seven-Degree-of-Freedom Telerobot Arm: A Concept for Manipulation in Space," 21st Aerospace Mechanisms Symposium, NASA CP-2470, pp. 111-130.

Loewenthal, S.H., Rohn, D.A. and Anderson, N.E., 1983, "Advances in Traction Drive Technology," SAE Trans., Vol. 92, Sect. 3.

Loewenthal, S.H., and Zaretsky, E.V., 1985, "Traction Drives," Section 34, Mechanical Design and Systems Handbook, H. Rothbart, ed., McGraw-Hill Book Co., New York.

Loewenthal, S.H., and Schuller, F.T., 1986, "Feasibility Study of a Discrete Bearing/Roller Drive Rotary Joint for the Space Station," NASA TM-88800.

Spalvins, T., 1985, "The Structure of Ion Plated Films in Relation to Coating Properties," NASA TM-87055.

Tevaarwerk, J.L., 1985, "Rolling, Slip and Endurance Traction Measurements on Low Modules Materials," NASA CR-174909.

N88-23242

MICROGRAVITY MANIPULATOR DEMONSTRATION*

Andrew S. Brush
Sverdrup Technology, Inc.
(Lewis Research Center Group)
NASA Lewis Research Center

ABSTRACT

A test rig is being prepared that will be used to demonstrate and evaluate approaches to limiting manipulator base reactions in microgravity environments. The demonstration will include a 4-degrees-of-freedom (DOF) arm, control computing facilities, and a base reaction measurement system.

---

*Work performed on-site for the Structural Dynamics Branch under contract NAS3-24105 (task order 5232; monitor: Douglas A. Rohn).

OVERVIEW

REACTION FOR SPECIFIED END-EFFECTOR PATH

In order to curtail the accelerations imparted to spacecraft by space experimental activities, schemes have been developed for reducing the reactions at the bases of robotic devices used for manipulation and motion on space platforms. These call for the application of robotic joints combining smooth operation with zero backlash, to reduce vibration, and the use of path optimization strategies to control base reactions due to gross motion. Although there is theoretical and numerical evidence that these concepts are valid, a hardware demonstration is desirable.

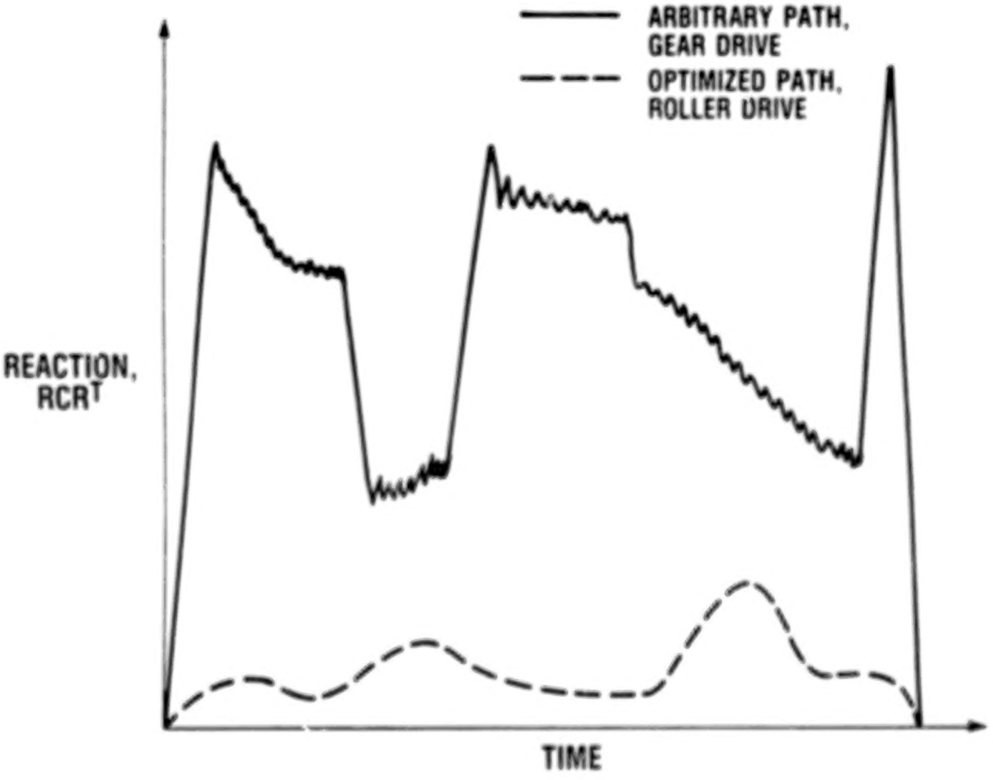

CD-88-31729

MICROGRAVITY MANIPULATOR DEMONSTRATOR
LABORATORY SETUP

The Microgravity Manipulator Demonstration will contain four main elements:

(1) A 4-DOF robotic arm utilizing traction-driven joints. These joints are expected to cause minimum vibration and have insignificant backlash.

(2) Data processing hardware based on VME bus architecture employing Motorola 68020 processors to implement arm control. In addition to providing closed-loop position and velocity control, processing capability will be available for path-optimization programs. Control software will be made as modular as possible to facilitate parallel processing. The bus architecture will allow future expansion through addition of processor or data acquisition boards.

(3) Optimization strategies that will select the best trajectory through joint space for a required end effector path in order to have minimum base reaction. These algorithms will be interchangeable modules in the control software to allow easy switching of optimization methods.

(4) A base reaction measurement system that will allow quantitative determination of the differences in reaction levels between optimized and unoptimized trajectories.

This demonstration will contribute valuable test data for developers of path optimization strategies, provide experience with programming techniques for integrating position control and trajectory optimization, and leave a reaction measurement test bed that will be useful to future microgravity robotics research.

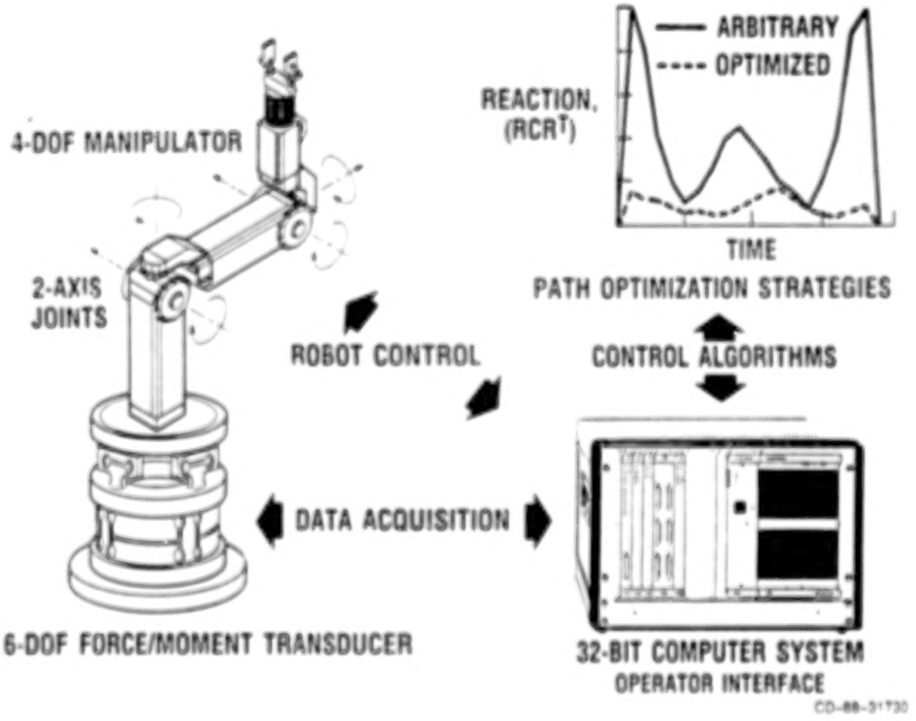
ARBITRARY
OPTIMIZED
REACTION, (RCR^T)
TIME
PATH OPTIMIZATION STRATEGIES
4-DOF MANIPULATOR
2-AXIS JOINTS
ROBOT CONTROL
CONTROL ALGORITHMS
DATA ACQUISITION
6-DOF FORCE/MOMENT TRANSDUCER
32-BIT COMPUTER SYSTEM
OPERATOR INTERFACE
CD-88-31730

POSTER PRESENTATION

OBJECTIVES

The Microgravity Manipulator Demonstration is being developed in order to facilitate assessment of hardware, software, and theoretical approaches to providing a manipulation capability for space microgravity experimentation.

The demonstration will provide quantitative evaluation of strategies for limiting manipulator base reactions and allow Lewis personnel to develop a knowledge base of experience with robotic controls for reduction of base reactions. Increased practical experience in this field is essential to the implementation of reaction-limited robotics in space.

The demonstration will also provide the opportunity to evaluate traction-driven robot joints.

- **DEMONSTRATE (PROOF OF CONCEPT) PATH OPTIMIZATION FOR LIMITING REACTIONS DUE TO MANIPULATOR MOTION**
- **DEVELOP AND EVALUATE CONTROL PROGRAMS FOR MICROGRAVITY MANIPULATORS**
- **EVALUATE TRACTION DRIVE JOINT TECHNOLOGY**

CD-88-31731

APPROACH

The test rig must be able to provide all capabilities required to meet the objectives stated previously. This will require

(1) A multi-DOF robot arm

(2) Software implementing optimization strategies to reduce base reactions

(3) A data processing facility capable of providing full control of the arm, managing data acquisition, and running optimization programs under test

(4) A modular approach to control software that will allow easy substitution of different strategies for accomplishing the objectives of robot control

(5) A means of measuring the reactions at the base of the robot in order to evaluate the success of the reaction-limiting scheme

- **MULTI-DOF MANIPULATOR ARM UTILIZING 2-DOF TRACTION JOINTS**
- **STRATEGY TO OPTIMIZE JOINT TRAJECTORIES TO MINIMIZE BASE REACTIONS**
- **HIGH-SPEED, 32-BIT, MULTIPROCESSOR CONTROL HARDWARE**
- **MODULAR CONTROL SOFTWARE**
- **MEASUREMENT OF BASE REACTIONS**

CD-88-31734

LABORATORY SETUP

The Microgravity Manipulator Demonstration will contain four main elements:

(1) A 4-DOF robotic arm using traction-driven joints. These joints are expected to cause minimum vibration and have insignificant backlash.

(2) Data processing hardware based on VME bus architecture employing Motorola 68020 processors to implement arm control. In addition to providing closed-loop position and velocity control, processing capability will be available for path-optimization programs. Control software will be made as modular as possible to facilitate parallel processing. The bus architecture will allow future expansion through addition of processor or data acquisition boards.

(3) Optimization strategies that will select the best trajectory through joint space for a required end effector path in order to have minimum base reaction. These algorithms will be interchangeable modules in the control software to allow easy switching of optimization methods.

(4) A base reaction measurement system that will allow quantitative determination of the differences in reaction levels between optimized and unoptimized trajectories.

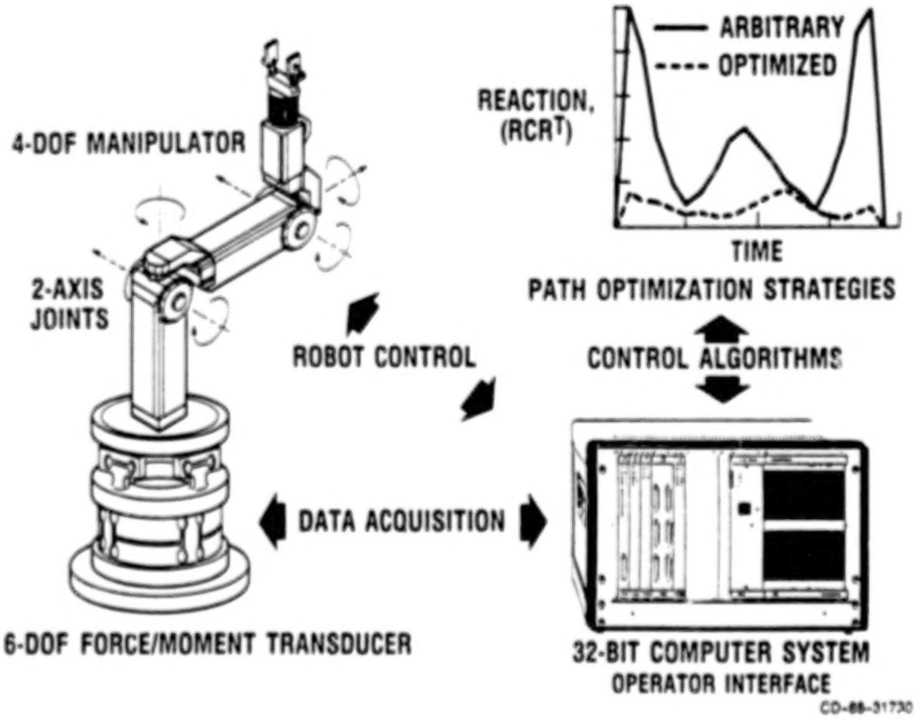
4-DOF MANIPULATOR
2-AXIS JOINTS
ROBOT CONTROL
REACTION, (RCR^T)
ARBITRARY
OPTIMIZED
TIME
PATH OPTIMIZATION STRATEGIES
CONTROL ALGORITHMS
DATA ACQUISITION
6-DOF FORCE/MOMENT TRANSDUCER
32-BIT COMPUTER SYSTEM
OPERATOR INTERFACE
CD-88-31730

TEST PLAN

Once the control system is satisfactorily debugged, strategies for minimization of base reactions will be evaluated by executing point-to-point motions of the end effector using standard and optimized trajectories in the joint space. The measured base reactions will be compared to determine the extent to which dynamic forces are mitigated.

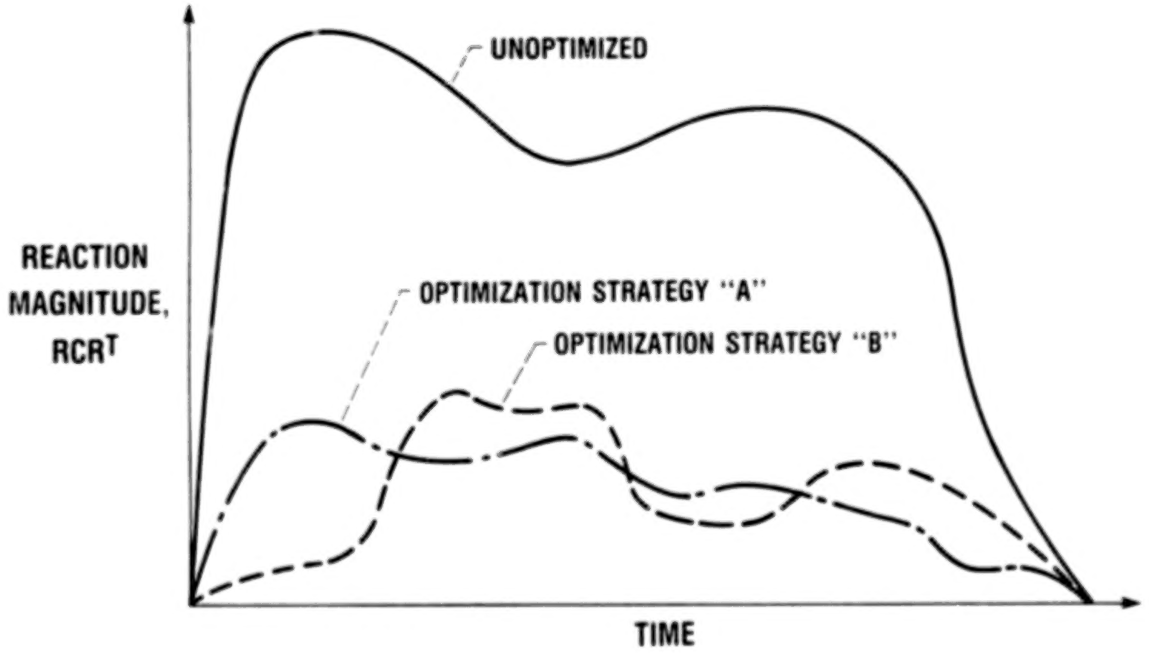

CD-88-31733

BASE REACTION MEASUREMENT - PERSPECTIVE

Until researchers became interested in experiments that take advantage of the low acceleration levels available in on-orbit spacecraft, there was no particular concern over the possible effects of small accelerations due to forces imparted by experiments or associated manipulators. Designers of the EURECA space platform discovered that they wanted to know the characteristics of the acceleration caused by each experiment that would fly on EURECA, so that they could asses the effects on other experiments. They were not able to develop a suitable 6-DOF force-moment transducer, however, so they recorded vibration levels at the attachment points of each experiment and calculated the forces using their knowledge of the dynamics of the experiment frame and the supporting structure. This was not an accurate method because of the estimation involved in determining the dynamic characteristics of the structures.

Some 6-DOF transducers have been developed that are apparently suitable for dynamic measurement of robot base reactions to the desired accuracy. The direct measurement of reactions is preferable and will be used in the demonstration.

- **SMALL SPACECRAFT ACCELERATIONS NOT A MAJOR CONCERN UNTIL THE ADVENT OF μG EXPERIMENTS**
- **REDUCING SOURCES OF FORCE IMPROVES μG ENVIRONMENT**
- **HOW CAN WE MEASURE SMALL DYNAMIC FORCES?**
  - **ACCELEROMETERS—REQUIRE PRECISE KNOWLEDGE OF DYNAMIC OF TEST ARTICLE AND SUPPORTING STRUCTURE**
  - **DIRECT MEASUREMENT OF FORCE USING 6-DOF TRANSDUCER**

CD-88-31732

SIX-DOF TRANSDUCER CONSTRUCTION

The construction of a 6-DOF transducer involves constructing a structure with predictable stiffness to forces applied at the attachment point and then instrumenting it to determine the strain or displacement in enough (six minimum) directions to fully determine the load.

Strut-type transducers attempt to resolve all forces and moments into purely axial loads in struts supporting an attachment flange (load application point).

One popular type of robust transducer uses eight flexures to measure the horizontal and vertical forces in perpendicular planes. This type may be stiff and strong but will have more crosstalk than a strut-type transducer.

Any shape of flexure may be used, as long as at least six orthogonal components of displacement can be measured with sufficient resolution. The previous types of fixtures are successful because they contain areas of high enough strains to allow use of electrical resistance strain gages.

High-precision displacement measurement techniques may present opportunities to use unconventional flexure designs.

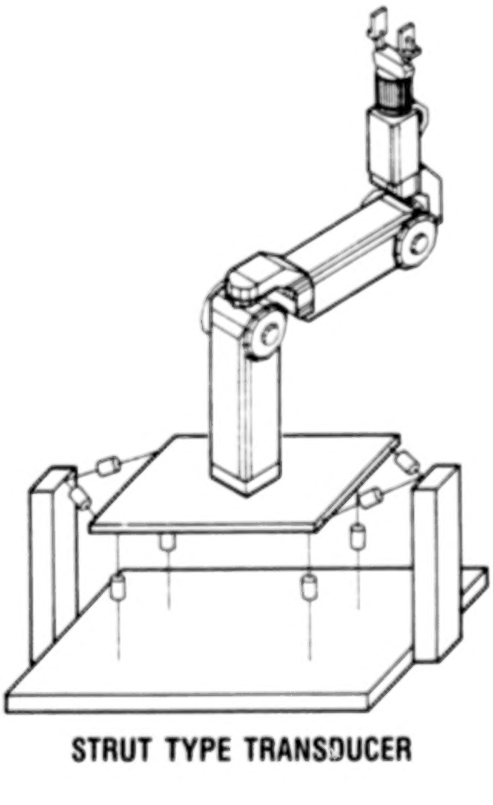

STRUT TYPE TRANSDUCER

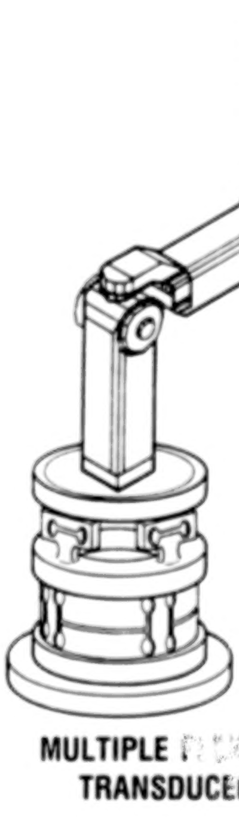

MULTIPLE FLEXURE TRANSDUCER

CD-88-31735

BASE REACTION MEASUREMENT - DATA REDUCTION

Measurement of forces arising from the motions of the manipulator and its payload are complicated in an earth-bound laboratory by the presence of static loads due to gravity. In the case of a manipulator, the static moments in the plane of the floor (M_x and M_y) are determined by a nonlinear function of the joint angles. This static component of the measured load must be subtracted from the total measured reaction:

$$R_t(t,\theta) = R_d(t) + R_s(\theta)$$

where $R_s(\theta)$ must be known for all possible points in the joint space.

The interpolation error caused by using a lookup table with a reasonable number of points (<10 000) will be excessive, so we need to develop an equation for the $R_s(\theta)$. This equation is a function of θ, having as parameters the mass distribution of the arm segments. We will eliminate having to estimate the mass distributions by fitting an equation of the proper form to experimental data.

The present demonstration does not include real-time feedback of reaction, but this may be possible if processing resources are sufficient.

- STATIC BASE FORCES DUE TO GRAVITY MUST BE IGNORED
- GRAVITY MOMENT IS A NONLINEAR FUNCTION OF JOINT ANGLES
- NEED TO KNOW GRAVITY MOMENT AT ALL POINTS IN JOINT SPACE
  - LOOKUP TABLE IS IMPRACTICAL
  - PARAMETERS IN EQUATIONS CANNOT BE EXACTLY DETERMINED ANALYTICALLY
  - ANSWER: USE PARAMETER IDENTIFICATION TECHNIQUES
- EQUATIONS ARE COMPUTATION INTENSIVE...
  REAL-TIME REACTION FEEDBACK MAY REQUIRE ADDITIONAL PROCESSOR

CD-88-31736

CONCLUSIONS AND BENEFITS

This demonstration will provide proof of concepts that will reduce robot base reactions by optimizing joint trajectory. Additionally, it will contribute experience with controls and hardware for microgravity manipulation to a knowledge base that will benefit designers of hardware for space experiments.

The force measurement system and computer system will be available after the 4-DOF demonstration for research using other types of manipulators.

- **KNOWLEDGE BASE WILL BENEFIT DESIGNERS WHO REQUIRE REACTION LIMITATION**
- **FORCE MEASUREMENT SYSTEM AND CONTROL DATA FACILITY WILL BE AVAILABLE TO TEST FUTURE MANIPULATORS AND ACTUATORS**

CD-88-31737

N88-23243

ACCURATE POSITIONING OF LONG, FLEXIBLE ARM'S*

Michael J. Malachowski
CCE-Robotics
Berkeley, CA 94709

ABSTRACT

An articulated robotic manipulator (ARM) system is being designed for space applications. It will be physically lightweight, slender, and flexible compared to typical ground-based robot systems. When manipulating unknown masses with long flexible segments, it is difficult, using standard means, to accurately determine the position of the end tips of these ARM's. The problem is how to quickly and accurately position long, flexible ARM's.

This presentation summarizes the work being done on a concept utilizing an infinitely stiff laser beam for position reference. The laser beam is projected along the segments of the ARM, and the position is sensed by the beam rider modules (BRM) mounted on the distal ends of the segments. The BRM concept is the heart of the system. It utilizes a combination of lateral displacements, and rotational and distance measurement sensors. These determine the relative position of the two ends of the segments with respect to each other in six degrees of freedom. The BRM measurement devices contain microprocessor controlled data acquisition and active positioning components. We use an indirect adaptive controller which senses this information to accurately control the position of the ARM.

The goal of the project is to design a space rated sensor, control, and manipulator assembly. This ARM will have a 10-m reach and will be capable of positioning payloads of up to 100 kg with millimeteric accuracy.

PRECEDING PAGE BLANK NOT FILMED

---

*Work performed under NASA Contract NAS3-25197.

OVERVIEW

LASER BEAM RIGID BODY POSITIONING CONCEPT

There are numerous uses for articulated robotic manipulators (ARM's) with long reaches and large load carrying capacities. The difficulty is that any material beam with length L will bend when a perpendicular force is applied at the end. This will displace the end tip by an amount d from its expected position.

When manipulating an ARM, there are two ways of dealing with this problem. The first is to make the beam so stiff that, for the forces involved, the value d is less than the positioning accuracy required. Therefore, d can be ignored. The difficulty with this approach is that a massive beam is required to obtain this rigidity. The second approach is to calculate the value of d for any particular displacement force. In general, such calculations are difficult and dependent upon the value of the payload mass. This method works best when the payload is kept constant.

We circumvent these problems by using a perfectly straight, infinitely rigid laser light reference beam. We measure in real time the displacement vector d between the segment end tip and the laser reference beam.

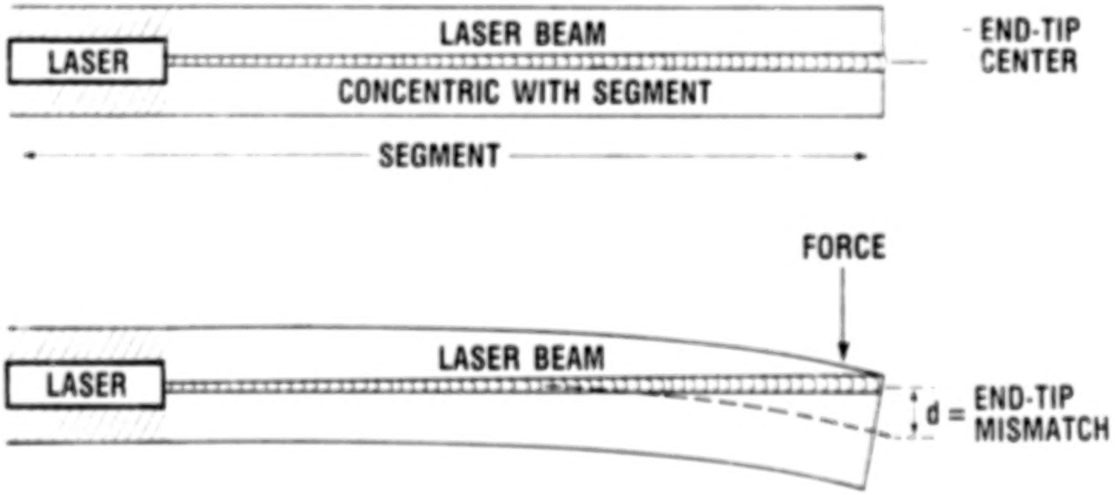

CD-88-31921

ARM CONFIGURATION

From this concept we have designed a two-segment ARM. The shoulder articulation rotates and elevates. Concentric with the shoulder is a beam positioning unit which moves simularly. Both of these are independently attached to the base reference point. BRM1 provides the vector position of the elbow with respect to the base reference point.

The rotation of the elbow articulation is monitored by a high-resolution encoder. This information is used to define the elbow laser reference point for the second segment. BRM2 provides the vector position of the wrist with respect to the elbow reference point.

A series of vector coordinate transformations is used to provide the position of the wrist end tip with respect to the base reference point. Thus, we are able to accurately specify the wrist end-tip position in real time.

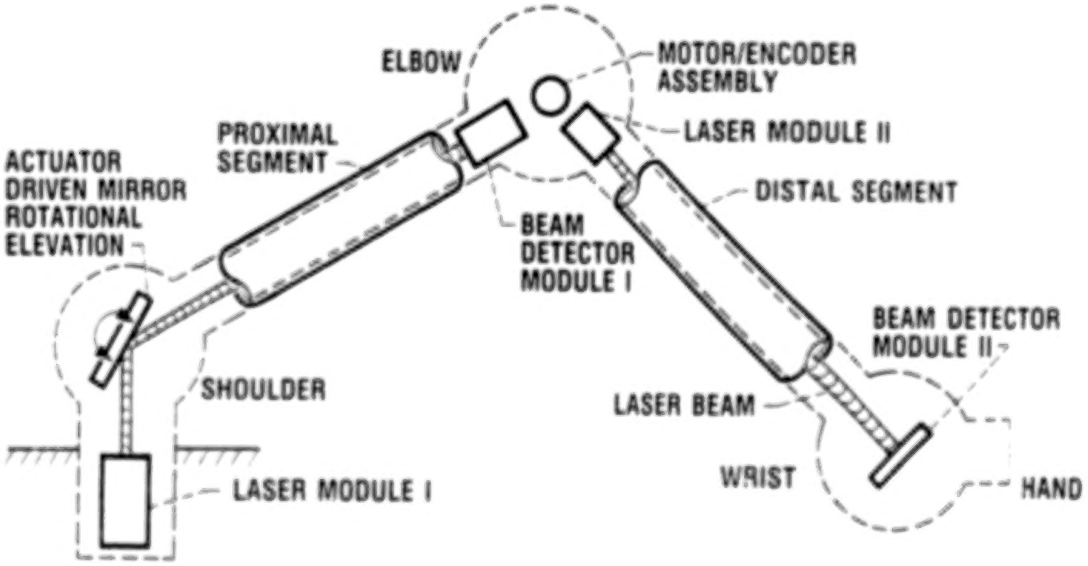
ELBOW
MOTOR/ENCODER ASSEMBLY
LASER MODULE II
PROXIMAL SEGMENT
ACTUATOR DRIVEN MIRROR ROTATIONAL ELEVATION
DISTAL SEGMENT
BEAM DETECTOR MODULE I
BEAM DETECTOR MODULE II
SHOULDER
LASER BEAM
LASER MODULE I
WRIST
HAND

CD-88-31922

INDIRECT ADAPTIVE CONTROL SCHEME

The end-tip position information serves two functions. The first function is to dynamically control the behavior of the ARM. An indirect adaptive controller is used to monitor the end-tip positions. Using the d vector information, it stimulates the actuators which force the ARM to behave in a predictable manner. The second function is to define points in the work envelopes such that the ARM can move the payload from one position to another. Such movement can be either point to point or along a predefined path.

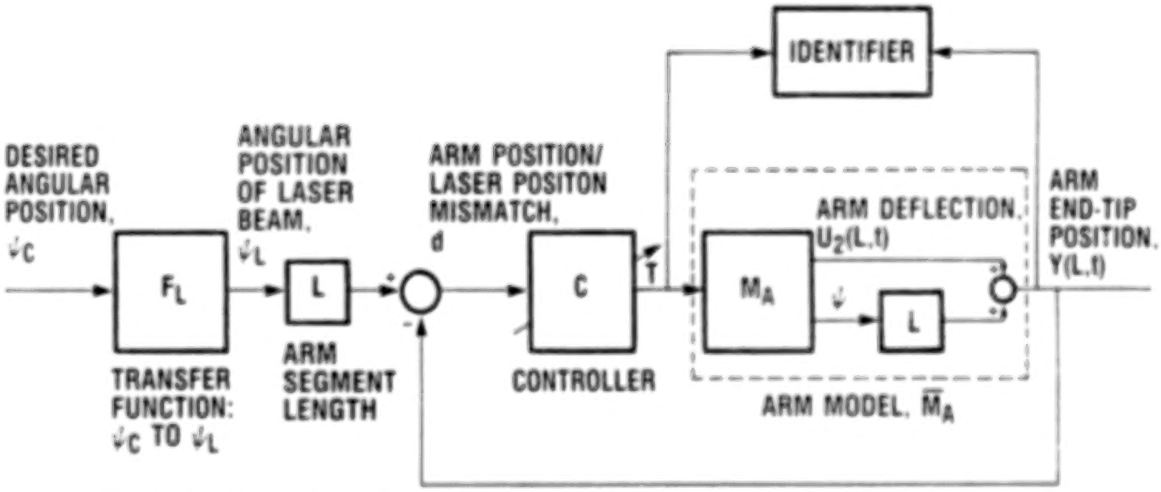
IDENTIFIER
DESIRED ANGULAR POSITION, ψ_C
F_L
TRANSFER FUNCTION: ψ_C TO ψ_L
ANGULAR POSITION OF LASER BEAM, ψ_L
L
ARM SEGMENT LENGTH
+
-
ARM POSITION/ LASER POSITON MISMATCH, d
C
CONTROLLER
T
M_A
ARM DEFLECTION, $U_2(L,t)$
ψ
L
+
+
ARM MODEL, $\overline{M}_A$
ARM END-TIP POSITION, Y(L,t)

CONTROL INPUT: TORQUE T APPLIED TO BASE OF ARM

OUTPUTS TO BE CONTROLLED:
1. POSITION OF ARM END TIP
2. DEFLECTION OF ARM END TIP

- LASER MEASURES ARM DEFLECTION AT END TIP
- TORQUE MEASURED (KNOWN) AT ARM BASE
- THESE TWO MEASUREMENTS USED TO FINE TUNE ARM MODEL WHICH IS USED TO FINE TUNE ARM CONTROLLER

CD-88-31935

POSTER PRESENTATION

LASER BEAM RIGID BODY POSITIONING CONCEPT

Assume a physical cantilever segment of length L. A force F perpendicular to the central axis of the segment will cause a displacement d. The magnitude of d is proportional to F and to the "stiffness" of the segment. Typically, robotic manipulators use short stiff segments to minimize d, preferably to a point where it can be neglected during operation. A long segment can be defined as a segment which has a value of d that becomes significant during normal operation and, therefore, cannot be neglected. Since, in general, the prediction or calculation of d is difficult, accurate positioning of long, flexible segments in real time is difficult. Our concept utilizes the fact that a light beam is perfectly rigid. Thus, the light beam serves as an axis of absolute reference. The value d is the distance between the light beam and the segment's distal end-tip position. Since, by using our methods, we can measure this value in "real time," accurate positioning of long, flexible segments becomes feasible.

Real time is the sampling frequency required to observe the effects of induced modal contributions. Currently, we are conducting experiments to determine the validity of our modal analytical model. Preliminary calculations indicate that contributions beyond the first three modes are negligible.

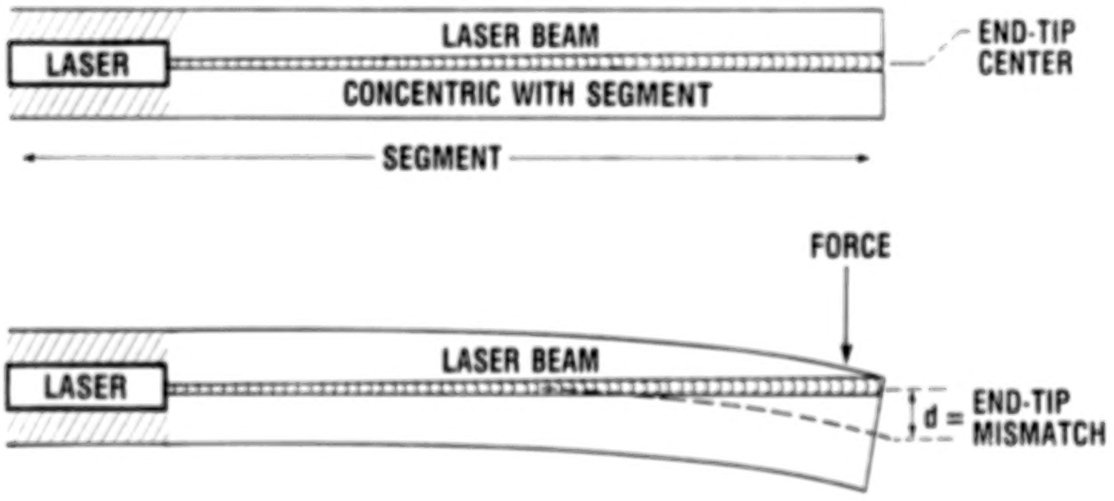

- LASER BEAM IS NORMALLY CONCENTRIC WITH SEGMENT
- APPLIED FORCE DISTORTS SEGMENT AND CAUSES END-TIP MISMATCH d

CD-88-31924

BEAM RIDER MODULE DEFINES SIX DEGREES OF FREEDOM

A two-segment ARM configuration maximizes the work space envelope. To accurately position the wrist end-tip platform of such an ARM in space requires the definition of six degrees of freedom. Although a variety of coordinate systems will meet this criterion, the one we choose is based upon our laser reference beam. A first point is determined by the values X_1, Y_1, and Z. A second point along the beam is defined by X_2 and Y_2. The angular value of rotation, about the Z-axis, defines the sixth degree of freedom. Together these values are used to uniquely specify the positions of the beam rider module (BRM) on the laser reference beam. It is the purpose of the BRM to determine the mismatch between the laser reference beam and the segment end tip, the vector d. This value is then used to accurately position the ARM.

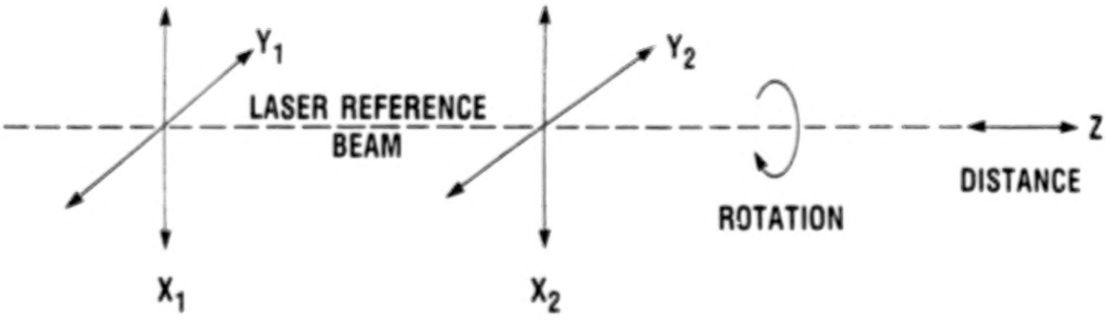

- FIVE LINEAR DEGREES OF FREEDOM
- ONE ROTATIONAL DEGREE OF FREEDOM

CD-88-31925

X-Y DETECTOR CONFIGURATIONS

Four planar detectors were selected for evaluations. The first is the quadrant detector, with and without a central orifice. In operation, analog circuitry is used to detect beam movement; the detector is physically translated such that the laser reference beam is kept centered in the quadrant. The amount of translation correlates to the X or Y values of the coordinate system. The second is the rectangular matrix detector. Digital circuitry is used to process the detector information and provide an X-Y coordinate of the beam spot. Significant amounts of digital signal processor (DSP) is required for this configuration; it was determined that this detector would be feasible only at very low (30 Hz) frequencies. The third is the annular matrix. This schema requires significant DSP, as does the rectangular matrix, and is not, generally, commercially available. Fourth is the lateral effects diode. This detector uses analog circuitry to rapidly provide an X and Y value. It appears to have sufficient resolution for our purposes. The major drawbacks are its high cost and its lack of linearity.

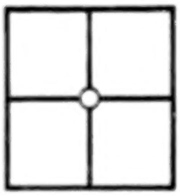

QUADRANT DETECTOR ANALOG
2 × 2

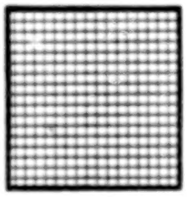

RECTANGULAR MATRIX DIGITAL
500 × 500

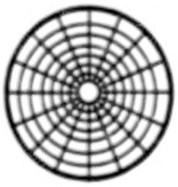

ANNULAR MATRIX DIGITAL
200 × 200

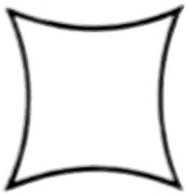

LATERAL EFFECTS ANALOG
2000 × 2000

- **DIFFERENT DETECTORS HAVE DIFFERENT RESOLUTIONS**
- **DETECTORS REQUIRE ANALOG OR DIGITAL PROCESSING**

CD-88-31926

LATERAL EFFECTS DIODE

The output of the lateral effects diode is run through a multistage analog signal processor. The first stage isolates the diode from the processor. Ideally, only the magnitude of the charge produced by the light beam is sampled. This is because any current flow decreases the resolution of the detector. Resolutions are on the order of 1 part in 2000 of the length of the detectors. The outputs from the four edges are added, subtracted, and divided in such a manner that ±X and ±Y locations of the beam are represented by the output voltages from the processor. The frequency response of the system is limited by capacitance factors, which depend upon the size of the diode. Responses on the order of hundreds of kilohertz should be possible.

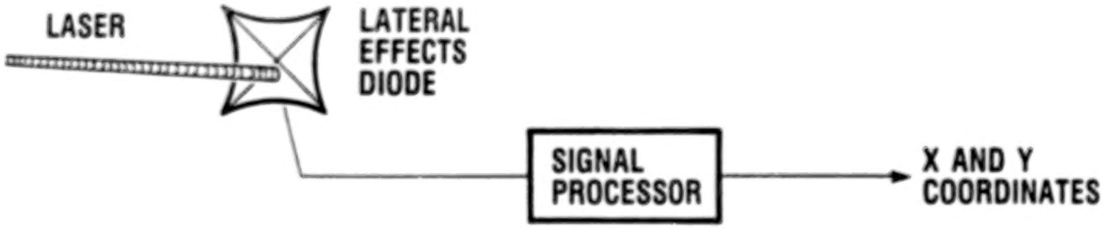

- SIGNAL FROM LATERAL EFFECTS DIODE CONVERTED TO X AND Y COORDINATES
- THIS INFORMATION USED BY INDIRECT ADAPTIVE CONTROLLER TO POSITION ARM

CD-88-31927

NONMOVING, FOUR-DEGREE-OF-FREEDOM DEFINING SCHEMA

A BRM using the lateral effect (LE) diodes would use a beam splitter to partition the beam's energy between detectors. Variation on this scheme can be used to define further degrees of freedom. For example, using a retroflector in the location of LE diode 2 would result in a laser beam retracing the path of the original beam for use with a laser interferometer. The reflected portion of this beam would be used to excite LE diode 2 and, therefore, provide information on coordinates X_2 and Y_2.

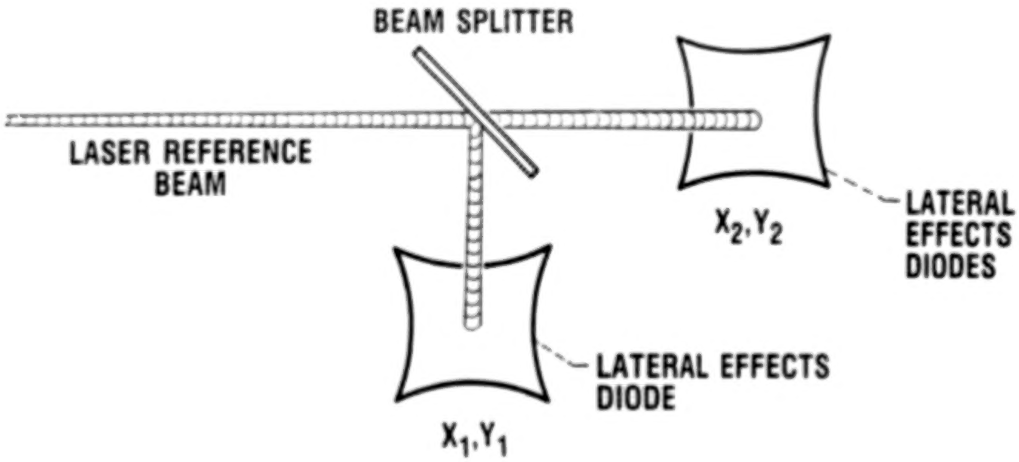
BEAM SPLITTER
LASER REFERENCE BEAM
X_2,Y_2
LATERAL EFFECTS DIODES
LATERAL EFFECTS DIODE
X_1,Y_1

- **DETECTOR ASSEMBLIES ATTACHED TO SEGMENT**
- **DEFLECTION OF SEGMENT CAUSES CHANGE IN POSITION OF LASER BEAM ON DIODE**

CD-88-31928

ACTIVE POSITIONING QUADRANT DETECTOR

A BRM can be made by using a pair of quadrant detectors and a retroflector. The BR assembly fits within the segment and is translated in the X_1,Y_1 and X_2,Y_2 directions. The beam is retroflected back down the tube. When the segment is displaced, the beam moves from the detector centers. The unbalanced output signal produced is used in a feedback loop to drive a motor and reposition the diodes. The detector and associated circuitry is analog and therefore has a high frequency response. The difficulty is in the design of a motor with matching high frequency response characteristics.

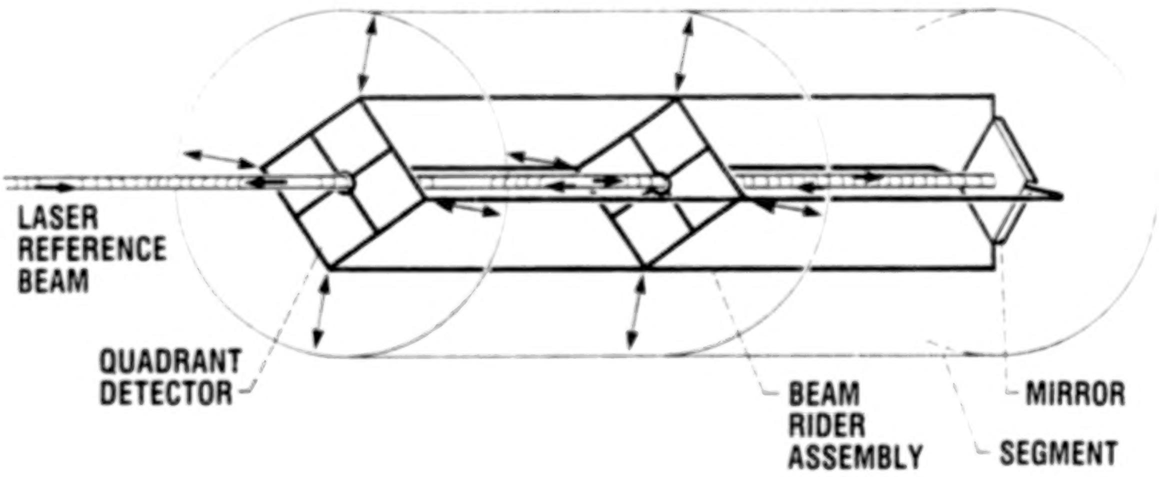

- BEAM RIDER ASSEMBLY FITS INSIDE SEGMENT
- ASSEMBLY HOLDS QUADRANT DETECTORS AND MIRRORS ASSEMBLY
- LINEAR MOTORS BETWEEN ASSEMBLY AND SEGMENT POSITION ASSEMBLY TO REMAIN COLINEAR WITH LASER REFERENCE BEAM

CD-88-31929

ACTIVE POSITIONING LINEAR MOTOR

A linear actuator, such as a voice coil, was determined to be a good candidate for the BRM because of its high frequency response. The major drawback of the voice coil actuator is that it has insufficient linear travel. To extend the travel, we designed an actuator which has serial sets of coils. Sequential or simultaneous excitations of the coils provide the desired linear travel. The coil driver can drive 256 coils with a positive or negative current. The value of the current in each coil is set by a multiplexing unit which addresses each coil uniquely by using an 8-bit code. The drive value is stored until reset. The wave from generator determines which value is placed on which address line. The wave form can be generated by a computer and represents a standing wave. The most appropriate standing wave to promote the desired movement is generated and sent to the linear actuator. The centering of the quadrant detector terminates the movement.

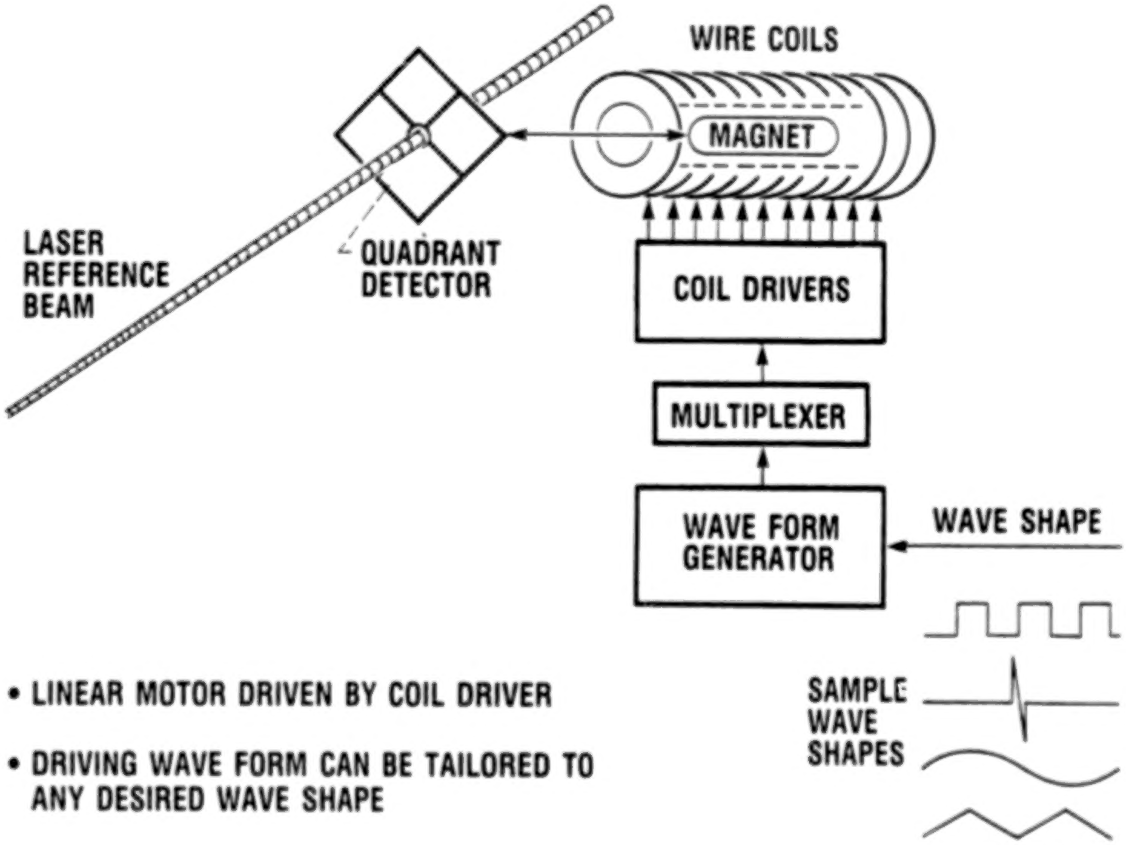
WIRE COILS
MAGNET
LASER REFERENCE BEAM
QUADRANT DETECTOR
COIL DRIVERS
MULTIPLEXER
WAVE FORM GENERATOR
WAVE SHAPE
SAMPLE WAVE SHAPES
CD-88-31930

- LINEAR MOTOR DRIVEN BY COIL DRIVER
- DRIVING WAVE FORM CAN BE TAILORED TO ANY DESIRED WAVE SHAPE

DISTANCE MEASURING EQUIPMENT - LASER INTERFEROMETER

A laser interferometer is being used as our distance measuring equipment. However, because this instrument measures incremental rather than absolute distance, an initialization is required prior to operation. During operation the incident reference beam and the return beam enter the interferometer. The interference fringes produced by changes in distance are counted and used to indicate the distance traveled. Alternative schemes using time of flight and resonant cavity length mode measurement are also under consideration.

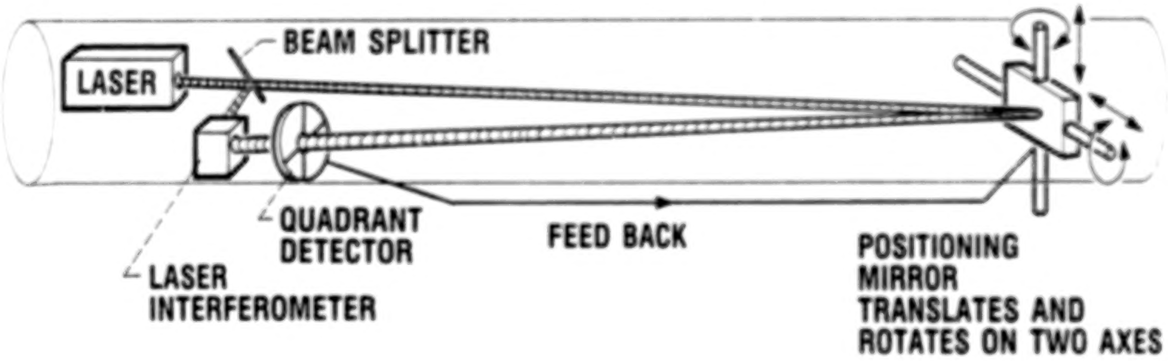
LASER
BEAM SPLITTER
QUADRANT DETECTOR
LASER INTERFEROMETER
FEED BACK
POSITIONING MIRROR TRANSLATES AND ROTATES ON TWO AXES

- QUADRANT DETECTOR SENDS FEEDBACK TO POSITIONING MIRROR TO ASSURE CORRECT POSITIONING OF BEAM ON INTERFEROMETER
- LASER INTERFEROMETER DETERMINES TOTAL DISTANCE TRAVELED BY LASER
- RESULT IS ACCURATE DETECTION OF ANY CHANGE IN LENGTH OF ARM DUE TO APPLIED LOAD OR OTHER EFFECTS

CD-88-31931

ROTATIONAL MEASURING EQUIPMENT - BEAM POLARIZATION

The rotational measurement equipment (RME) will make use of the polarized laser beam. An analyzer on the distal portion of the segment is used to analyze the beam. As an analyzer rotates around the reference beam towards 90°, the magnitude of the transmitted beam is reduced towards extinction. The RME module uses a detector to monitor beam intensity. The detector and analyzer are mounted on a motor encoder unit. The motor is controlled by detector output in such a manner that it rotates to provide maximum output. The required amount of rotation is measured by the encoder. This value can then be used for positioning the ARM.

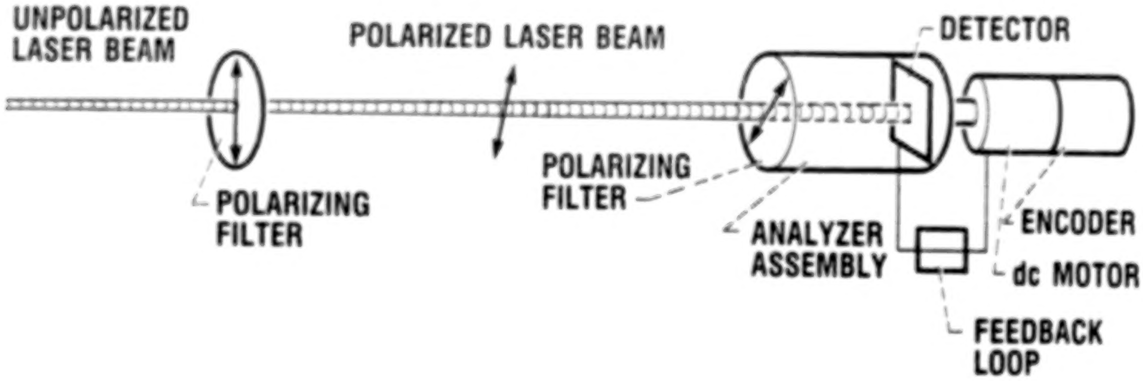
UNPOLARIZED LASER BEAM
POLARIZED LASER BEAM
DETECTOR
POLARIZING FILTER
POLARIZING FILTER
ANALYZER ASSEMBLY
ENCODER
dc MOTOR
FEEDBACK LOOP

- ARM ROTATION DETECTED USING POLARIZING FILTERS
- dc MOTOR ROTATES ANALYZER ASSEMBLY UNTIL DETECTOR READS MAXIMUM INTENSITY

CD-88-31932

ACTIVE BEAM RETROFLECTOR ASSEMBLY

The use of a conventional interferometer setup requires the reflection of the incident beam back to the interferometer. If only a linear movement along the Z-axis is allowed, a corner cube or retroflector may be used. However, because in our application lateral displacement of the distal segment is possible, an active positioning device is required to keep the reflected laser beam aimed at the interferometer. A quadrant detector with a central orifice is placed in front of the interferometer. The output of the detector is used to drive the mirror mover angularly and correctly center the beam. When the angular movement exceeds a limit value, the mirror is translated. This arrangement allows the use of this schema for large values of d.

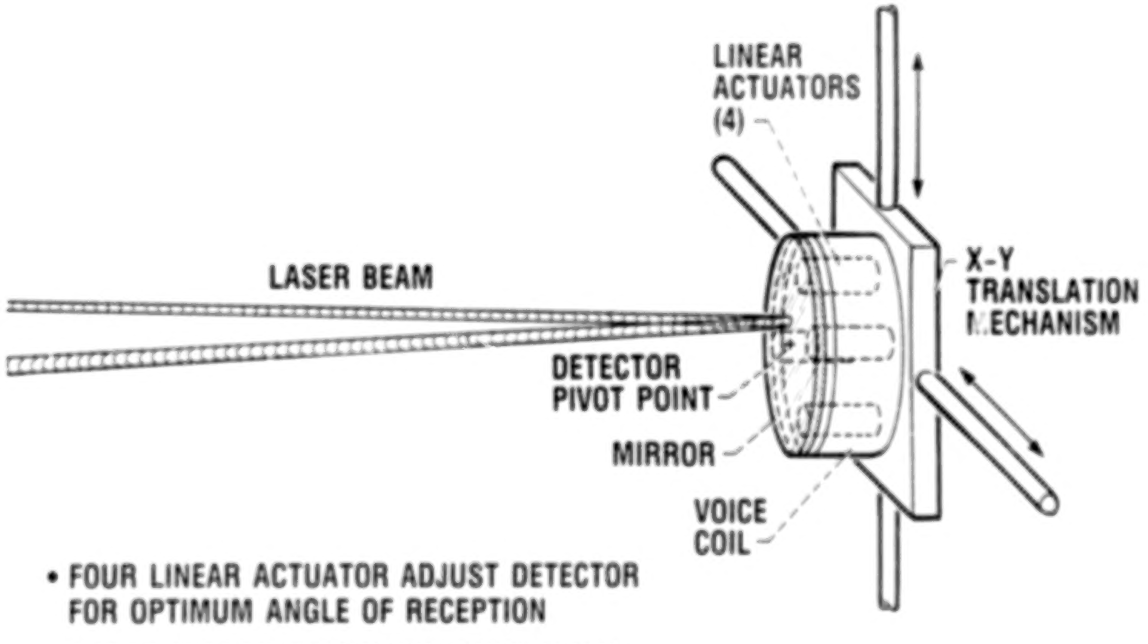

- FOUR LINEAR ACTUATOR ADJUST DETECTOR FOR OPTIMUM ANGLE OF RECEPTION
- ENTIRE MIRROR POSITIONING MECHANISM MAY TRANSLATE IN X AND Y DIRECTIONS

CD-88-31433

ARM CONFIGURATION

The ARM consists of two articulations, two segments, and a wrist platform. The shoulder articulation rotates about two axes and is connected to the elbow by the proximal segment. The elbow rotates on one axis and is connected to the wrist by the distal segment. The hand, manipulator, or end effectors mount on the wrist platform. Because of temperature changes, the segments in our current design will change length as materials expand or contract. Our concepts are compatible with future designs which would use extensible segments.

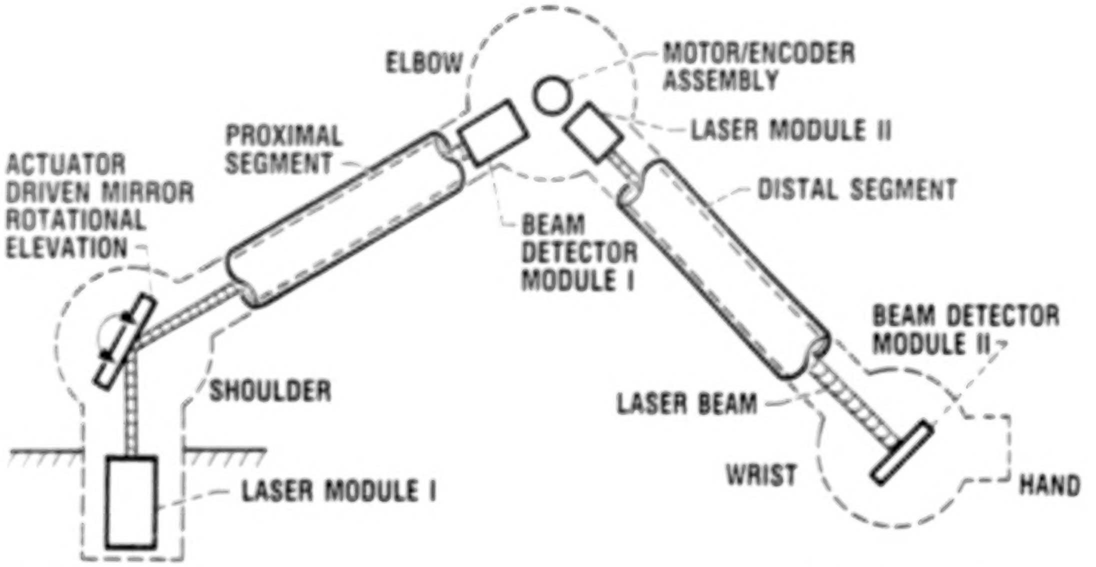
ELBOW
MOTOR/ENCODER ASSEMBLY
PROXIMAL SEGMENT
LASER MODULE II
ACTUATOR DRIVEN MIRROR ROTATIONAL ELEVATION
DISTAL SEGMENT
BEAM DETECTOR MODULE I
BEAM DETECTOR MODULE II
SHOULDER
LASER BEAM
WRIST
HAND
LASER MODULE I

FEATURES:
- LASER BEAM IS "INFINITE STIFFNESS" REFERENCE FOR FLEXIBLE STRUCTURE
- DETECTORS AND MIRROR DRIVES UNDER MICROPROCESSOR CONTROL TO TRACK ARM DEFLECTIONS

IMPACT:
- LOCATION OF END ARM IS KNOWN WITHIN 1 mm AT 10 m RADIUS
- POSITION, VELOCITY, ACCELERATION, AND FORCE OUTPUTS FOR ARM CONTROL AND REAL-TIME TRAJECTORY MANAGEMENT

CD-88-31934

INDIRECT ADAPTIVE CONTROL SCHEME

In order to design a controller for a system, one must have an accurate model of the system. In the case of the ARM, we assume that its model consists of a finite number of linear, ordinary differential equations. The driving term, or input, to this model is torque applied to the base of the ARM, and the response, or output, is the end-tip position of the ARM. We will employ an identifier to determine the number of modes which must be included in the model and the model parameters (e.g., damping coefficients) required. The identifier takes input (torque) and output (end-tip position) measurements and uses those to estimate the values of the coefficients in the differential equations which compose the model. From the model the actual controller is constructed. The controller variables become functions of the identifier's ARM parameter estimates; as the identifier obtains better estimates of the ARM's parameters the controller becomes more finely tuned to the ARM. Any changes in the ARM's characteristics (e.g., a change in arm segment material compliance due to heating or cooling) will be sensed by the identifier. The identifier then changes the corresponding variables in the in-line controller. This provides continuous smooth operation of the overall system. An identifier linked to an in-line controller is referred to as an indirect adaptive control scheme.

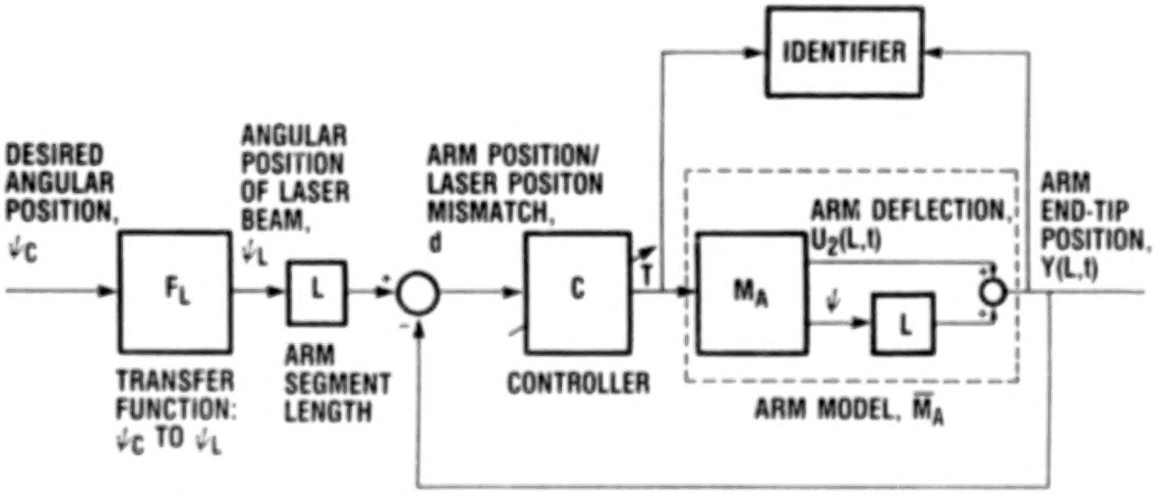
IDENTIFIER
DESIRED ANGULAR POSITION, ψ_C
F_L
TRANSFER FUNCTION: ψ_C TO ψ_L
ANGULAR POSITION OF LASER BEAM, ψ_L
L
ARM SEGMENT LENGTH
+
−
ARM POSITION/ LASER POSITON MISMATCH, d
C
CONTROLLER
T
M_A
ARM DEFLECTION, $U_2(L,t)$
ψ
L
+
+
ARM MODEL, $\overline{M}_A$
ARM END-TIP POSITION, Y(L,t)

CONTROL INPUT: TORQUE T APPLIED TO BASE OF ARM

OUTPUTS TO BE CONTROLLED: 1. POSITION OF ARM END TIP
2. DEFLECTION OF ARM END TIP

- LASER MEASURES ARM DEFLECTION AT END TIP
- TORQUE MEASURED (KNOWN) AT ARM BASE
- THESE TWO MEASUREMENTS USED TO FINE TUNE ARM MODEL WHICH IS USED TO FINE TUNE ARM CONTROLLER

CD-88-31935

AEROELASTICITY

SESSION OVERVIEW

Louis J. Kiraly
Structural Dynamics Branch
NASA Lewis Research Center

The first two papers in this session deal with aeroelastic methods and unsteady aerodynamics of turborotors and propfans. The first paper presents development of aeroelastic analysis methods, excluding mistuning, and validates the methods by comparing theoretical and experimental results. The second paper addresses the development of two-dimensional and three-dimensional time marching transonic potential flow methods for propfans. The third paper presents comprehensive wind tunnel data on propfan aeroelasticity. The fourth paper presents some preliminary ideas on forced response analysis being developed for turbomachinery. The fifth and sixth papers deal with nonlinear aerodynamics applicable to stall flutter analysis. The fifth paper presents reduced order models for nonlinear dynamics. The sixth paper applies viscous flow (Navier-Stokes) equations to stall flutter analysis.

AEROELASTICITY

SESSION OVERVIEW
- L.J. KIRALY, CHIEF, STRUCTURAL DYNAMICS BRANCH, NASA

DEVELOPMENT OF AEROELASTIC ANALYSIS METHODS FOR TURBOROTORS AND PROPFANS—INCLUDING MISTUNING
- K.R.V. KAZA, STRUCTURAL DYNAMICS BRANCH, NASA

2-D AND 3-D TIME MARCHING TRANSONIC POTENTIAL FLOW METHODS FOR PROPFANS
- M.H. WILLIAMS, PURDUE UNIVERSITY, WEST LAFAYETTE, IN

PROPFAN MODEL WIND TUNNEL AEROELASTIC RESEARCH RESULTS
- O. MEHMED, STRUCTURAL DYNAMICS BRANCH, NASA

AERODYNAMIC FORCED RESPONSE ANALYSIS OF TURBOMACHINERY
- T.E. SMITH, STRUCTURAL DYNAMICS BRANCH, SVERDRUP

REDUCED ORDER MODELS FOR NONLINEAR AERODYNAMICS
- A.J. MAHAJAN, E.H. DOWELL, AND D.B. BLISS, DUKE UNIVERSITY, DURHAM, NC

APPLICATION OF NAVIER-STOKES ANALYSIS TO STALL FLUTTER
- J.C. WU, R. SRIVASTAVA, AND L.N. SANKER, GEORGIA INSTITUTE OF TECHNOLOGY, ATLANTA, GA

CD-88-33276

N88-23244

DEVELOPMENT OF AEROELASTIC ANALYSIS METHODS FOR TURBOROTORS AND PROPFANS - INCLUDING MISTUNING

Krishna Rao V. Kaza
Structural Dynamics Branch
NASA Lewis Research Center

INTRODUCTION

The NASA Lewis aeroelastic research program is focused on unstalled and stalled flutter, forced response, and whirl flutter of turborotors and propfans. The basic research effort was started 6 years ago as a continuation of the ATE (Aeroelasticity of Turbine Engines) Program. The objectives of the effort are to understand the physical phenomena of cascade flutter and response including blade mistuning (also called detuning or mode localization). By starting with simple aeroelastic models and then progressively improving the models, aeroelastic prediction capability has been significantly improved and the role of mistuning has become well understood.

While this basic research effort was in progress, a propfan wind tunnel model (the SR-5, with 10 titanium blades) fluttered unexpectedly during a performance test. The basic aeroelastic research program was then redirected and focused on propfans in an effort to understand the physics of the instability phenomenon and to develop required analysis methods. The redirected program has been supplemented by a balanced experimental effort. The experiments have been specifically designed to clarify the physics of flutter, to guide the development of analytical models, and to provide quality data for validating the analysis methods. The unique features of propfan blades, such as their significant blade sweep and twist and their thinness and low aspect ratio, put additional demands on basic technology disciplines, such as two-dimensional and three-dimensional steady and unsteady aerodynamics in subsonic, transonic, and supersonic flow regimes; structural dynamics modeling of composite blades; geometric nonlinear theory of elasticity; linear and nonlinear Coriolis effects; and passive and active control of flutter and response. Furthermore the aeroelastic models with their refined aerodynamic and structural models have imposed additional demands on computer power (speed and memory). New analytical models in unsteady aerodynamics, structural dynamics, and aeroelasticity have been conceived that exploit the capabilities of the Cray-XMP supercomputer. Some of these models have been completed and some are in progress. These new models have been incorporated in a general-purpose computer program, ASTROP (Aeroelastic STability and Response Of Propulsion Systems). A part of the ASTROP program has been validated by comparing theoretical and experimental results for single-rotation (SR) propfans. More recently the ASTROP code has been extended to calculate the forced response of propfan blades in yawed flow, including blade mistuning.

This presentation briefly reviews the aeroelastic models employed in the basic research effort, describes the focused propfan aeroelastic program, and presents an overview of the ASTROP code. It also outlines the flutter and forced-response models employed in ASTROP, presents predicted results from these models, and validates the models by comparing predicted and measured data.

Future research in aeroelasticity will include more emphasis on computational aeroelasticity with two- and three-dimensional full velocity potential models and Euler and Navier-Stokes aerodynamic models to clarify transonic flow effects, on dynamic stall, and on the reverse thrust effects of both single-rotation and counterrotation propfans and turborotors. This effort will be supplemented with balanced wind tunnel tests to validate the new methods.

TYPICAL SECTION FLUTTER AND RESPONSE MODEL (MISER2)

A research program was begun about 6 years ago to improve the basic understanding of blade mistuning effects on aeroelastic stability and response and to explore the possibility of using mistuning as a passive response control. This program was started with simplified aeroelastic models, and the models were progressively improved. The first aeroelastic model (Kaza and Kielb, 1982; Kielb and Kaza, 1983; and Busby et al., 1985) was based on a two-degrees-of-freedom structural dynamic model with plunging and pitching motion of each blade and arbitrary frequency mistuning and on four two-dimensional cascade aerodynamic models. The results from this aeroelastic model showed that the bending and torsion coupling has a significant effect on cascade flutter and that frequency mistuning has a beneficial effect on flutter in all the flow regimes addressed and has either a beneficial or adverse effect on forced response. Furthermore these simple models were used as benchmarks for checking more complicated subsequent models.

- **STRUCTURAL DYNAMICS MODEL**
  - **PLUNGING AND PITCHING MOTION OF EACH BLADE**
  - **ARBITRARY FREQUENCY MISTUNING**

- **TWO-DIMENSIONAL UNSTEADY CASCADE AERODYNAMIC MODELS**
  - **INCOMPRESSIBLE FLOW (WHITEHEAD, 1960)**
  - **SUBSONIC FLOW (SMITH, 1973; RAO AND JONES, 1975)**
  - **SUPERSONIC FLOW (ADAMCZYK AND GOLDSTEIN, 1978)**
  - **SUPERSONIC FLOW WITH SHOCKS (GOLDSTEIN, BRAUN, ADAMCZYK, 1977)**

- **SOLUTION METHOD—FREQUENCY DOMAIN METHOD**

CD-88-31788

BLADED-DISK FLUTTER MODEL

This model is designed to account for the effects of structural coupling between the blades and the elastic, inertial, and aerodynamic coupling between the bending and torsional motions of each individual blade on the vibration and flutter characteristics of mistuned bladed-disk assemblies. These objectives are accomplished in two phases (Kaza and Kielb, 1984 and 1985). Each blade is represented by an Euler-Bernoulli beam with normal modes of a nonrotating beam. The disk is represented by a circular plate. The structural dynamic model is obtained by a component-mode synthesis approach. The generalized aerodynamic loads are obtained from two-dimensional theory in a stripwise fashion. The parametric results showed that the beneficial effect of frequency mistuning on flutter is unaffected by either the structural coupling between the blades or the additional bending and torsion coupling of each individual blade. Also, it was identified that the pretwist introduces strong coupling between the disk bending and blade chordwise motions.

- **STRUCTURAL DYNAMIC MODEL**
  - **BEAM NONROTATING MODES FOR EACH BLADE**
  - **PLATE MODES FOR DISK**
  - **COMPONENT MODE SYNTHESIS**
  - **FREQUENCY MISTUNING**

- **AERODYNAMIC MODEL**
  - **STRIPWISE APPROACH**
  - **TWO-DIMENSIONAL SUBSONIC AND SUPERSONIC CASCADE THEORY**

- **SOLUTION METHOD—FREQUENCY DOMAIN SOLUTION**

CD-88-31789

WHY FOCUSED PROPFAN AEROELASTIC RESEARCH?

Flutter occurred unexpectedly during a performance test on the SR-5 wind tunnel model, a single-rotation model with 10 titanium blades. This flutter was not predicted before the test by the existing helicopter blade flutter analysis code. Because of the unique features of the propfans listed below, it was decided that the existing aeroelastic technology for conventional propellers, turbofans, or helicopters was not adequate. It was also recognized that developing new aeroelastic methods requires new models in basic disciplines such as two-dimensional and three-dimensional, steady and unsteady (stalled and unstalled) aerodynamics in subsonic, transonic, and supersonic flow regimes and modeling of composite blades and tailored experiments to guide the analytical model development and to validate the theory.

- THIN BLADES (FLEXIBLE), CENTRIFUGAL LOADS (LARGE DEFLECTIONS)—GEOMETRIC NONLINEAR THEORY OF ELASTICITY AND CORIOLIS FORCES
- SUBSONIC, TRANSONIC, AND POSSIBLY SUPERSONIC MACH NUMBERS; LOW ASPECT RATIO; AND LARGE SWEEP—THREE-DIMENSIONAL STEADY AND UNSTEADY AERODYNAMIC THEORY
- HIGH SWEEP AND TWIST—COUPLED BLADE VIBRATORY BENDING AND TORSION MODES AND STRUCTURAL COUPLING BETWEEN BLADES
- 8 TO 10 BLADES—AERODYNAMIC COUPLING BETWEEN BLADES (CASCADE EFFECTS)
- COUPLING BETWEEN AFT AND REAR ROTORS
  - THREE-DIMENSIONAL STEADY AND UNSTEADY AERODYNAMIC THEORY
  - TIME DOMAIN AEROELASTIC MODEL

CD-88-31790

IDEALIZED SWEPT-BEAM AEROELASTIC MODEL FOR PROPFANS

The main purpose of the beam model was to predict the flutter speed of the SR-5 wind tunnel model and to clarify the mechanism of the flutter phenomenon. For expeditious results the beam model (Kaza and Kielb, 1984) was modified to account for blade sweep in an approximate manner as shown in the left-hand graph below. Since the unsteady aerodynamic models for swept blades were not available at that time, the two-dimensional cascade aerodynamic theory was modified to account for blade sweep by using similarity laws. The disk is assumed to be rigid. The predicted flutter boundary is compared with the measured one in the right-hand graph. The measured and calculated flutter boundary trends and flutter frequencies are in agreement (Mehmed et al., 1982). Although not shown in the figure, the observed flutter mode and the measured interblade phase angle agree well with the theory. But the analytical results depend on the users' judgment in selecting effective blade sweep and blade elastic axis position. However, this model was very useful in conducting parametric studies to clarify the flutter mechanism.

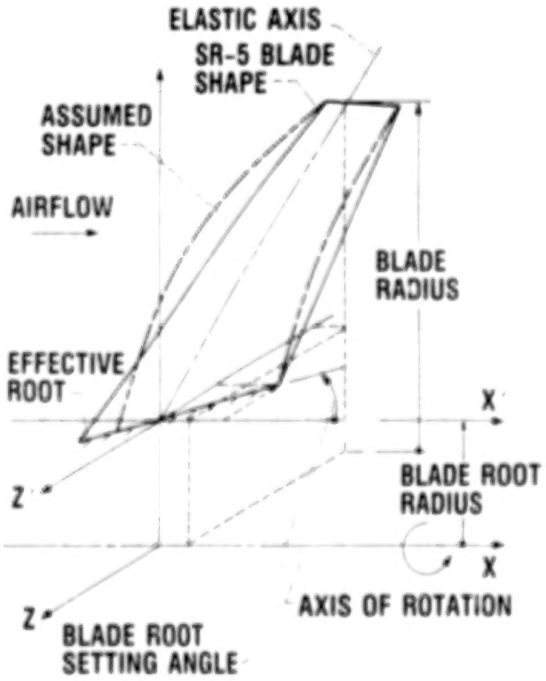
ELASTIC AXIS
SR-5 BLADE SHAPE
ASSUMED SHAPE
AIRFLOW
BLADE RADIUS
EFFECTIVE ROOT
X'
Z'
BLADE ROOT RADIUS
X
AXIS OF ROTATION
Z
BLADE ROOT SETTING ANGLE

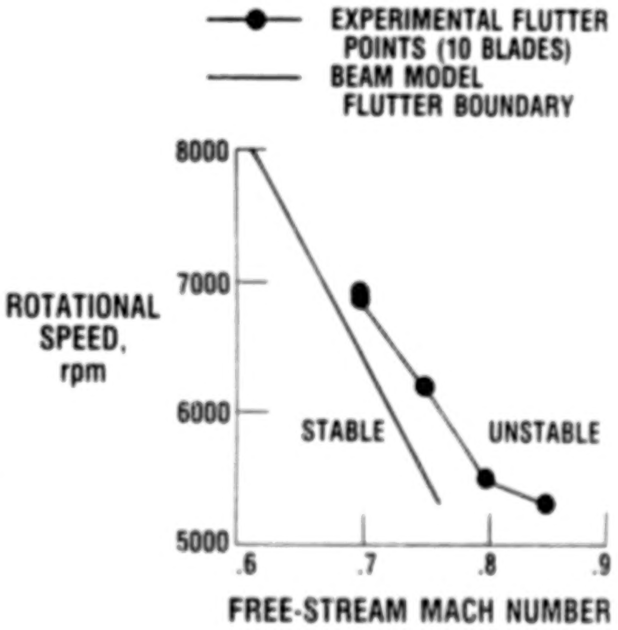

CD-88-31791

AEROELASTIC STABILITY AND RESPONSE OF PROPULSION SYSTEMS (ASTROP)

The preliminary investigation (both experimental and theoretical) of the SR-5 flutter clearly demonstrated that more refined aeroelastic prediction methods are needed so that propfans can be designed for maximum efficiency and safety. At the same time these methods should have the flexibility to incorporate new and future models in basic disciplines and have the capability to analyze new propfan concepts. With this in mind we have begun the development of a comprehensive aeroelastic program, ASTROP, as shown below. The current status of the various modules in the program is also shown. In all the ASTROP structural dynamic models the Coriolis forces are neglected because these forces were shown by Subrahmanyam et al. (1986) to have negligible effect on vibration for thin blades. The first module, ASTROP2, and the subsonic flutter (with and without mistuning) portion of second module, ASTROP3, have been completed and validated (Kaza et al., 1987a and 1987b). Extensive parametric results, which are believed to be useful for propfan designers, are also presented in these references.

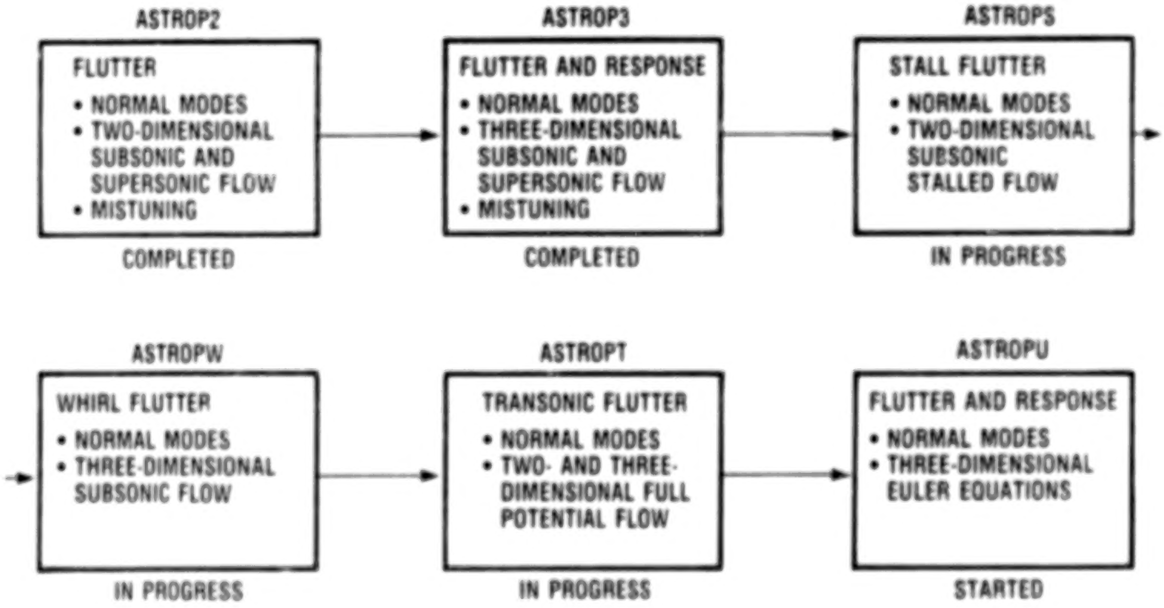
ASTROP2
FLUTTER
• NORMAL MODES
• TWO-DIMENSIONAL SUBSONIC AND SUPERSONIC FLOW
• MISTUNING
COMPLETED
ASTROP3
FLUTTER AND RESPONSE
• NORMAL MODES
• THREE-DIMENSIONAL SUBSONIC AND SUPERSONIC FLOW
• MISTUNING
COMPLETED
ASTROPS
STALL FLUTTER
• NORMAL MODES
• TWO-DIMENSIONAL SUBSONIC STALLED FLOW
IN PROGRESS
ASTROPW
WHIRL FLUTTER
• NORMAL MODES
• THREE-DIMENSIONAL SUBSONIC FLOW
IN PROGRESS
ASTROPT
TRANSONIC FLUTTER
• NORMAL MODES
• TWO- AND THREE-DIMENSIONAL FULL POTENTIAL FLOW
IN PROGRESS
ASTROPU
FLUTTER AND RESPONSE
• NORMAL MODES
• THREE-DIMENSIONAL EULER EQUATIONS
STARTED

CD-88-31792

APPLICATION OF ASTROP3 CODE FOR INVESTIGATING FLUTTER OF A COMPOSITE SR PROPFAN MODEL

The ASTROP3 code uses three-dimensional subsonic steady and unsteady cascade aerodynamics (Williams and Hwang, 1986) and a NASTRAN finite element model to represent the blade structure. The equivalent anisotropic material properties for each finite element are generated by using a preprocessor code, COBSTRAN, developed by Chamis (1981). The effect of centrifugal loads and steady-state airloads on the steady-state geometry of a composite wind tunnel model (SR3C-X2) blade is shown in the left-hand graph. The aerodynamic cascade effects (or the effect of blade number) on the eigenvalues are shown in the right-hand graph. Both centrifugal loads and aerodynamic loads untwist the blades, and this untwist increases with rotational speed. It is evident that the cascade effect is very significant on the real part of the eigenvalue and hence on stability.

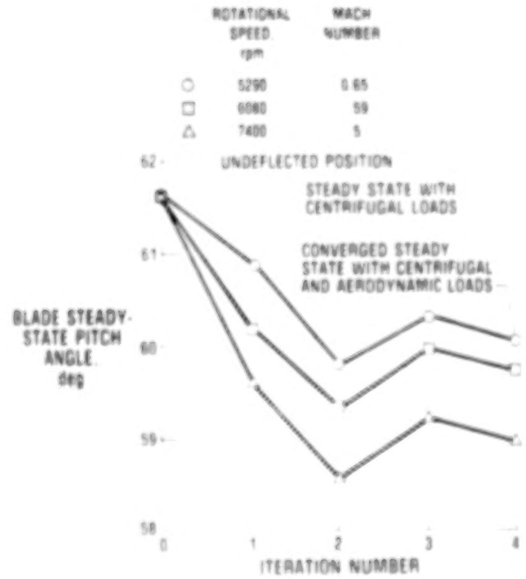

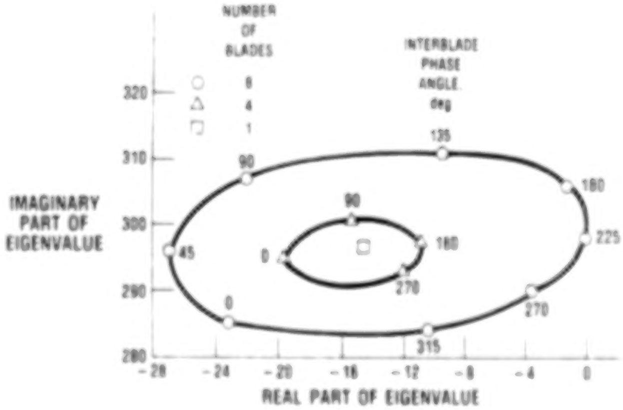

CD-86-21793

COMPARISON OF MEASURED AND CALCULATED FLUTTER BOUNDARIES FOR SR3C-X2 PROPFAN MODEL

Theoretical flutter results obtained from the ASTROP3 code have been correlated in the graph below with flutter data on a wind tunnel propfan model, SR3C-X2, with composite blades (Mehmed and Kaza, 1986). Theoretical results include the effects of centrifugal loads and steady-state airloads. The theory does reasonably well in predicting flutter speeds and boundary slopes. However, the difference between the calculated and measured flutter Mach numbers is greater for the four-blade case than for the eight-blade case. This implies that the theory may be overcorrecting for aerodynamic cascade effects with four blades. Calculated interblade phase angles at flutter (not shown) also compared well with measured values. However, calculated flutter frequencies were about 8 percent higher than measured.

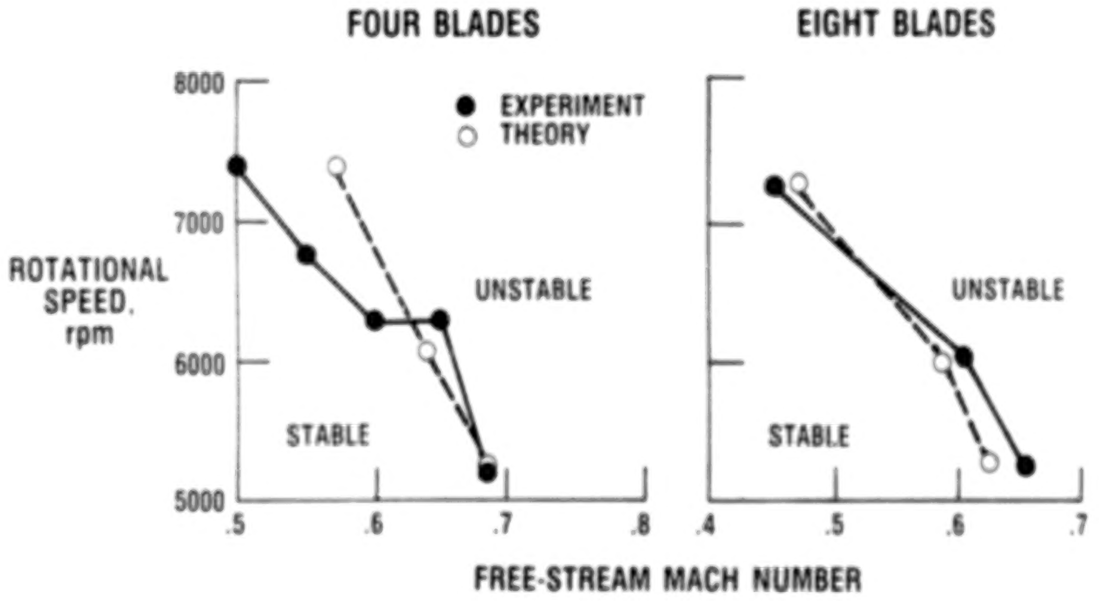

CD-88-31794

EVALUATION OF TWO-DIMENSIONAL UNSTEADY AERODYNAMIC THEORY FOR PROPFAN FLUTTER PREDICTION

So that the validity of two-dimensional aerodynamic theory and the associated sweep correction could be assessed, the real part of the eigenvalue of the critical mode was calculated by using both ASTROP2 and ASTROP3. The results are compared in the graph below, which also shows the measured flutter Mach number. The two-dimensional theory is shown to be less accurate than the three-dimensional theory in predicting flutter Mach number for this case. Correlative studies (not shown) of measured and calculated flutter boundaries were also conducted by varying Mach number, blade sweep, rotational speed, and blade setting angle. The correlation varied from poor to good. The expected conservative nature of the two-dimensional theory sometimes did not prevail, possibly because of the arbitrary nature of the reference line employed in the strip method and the associated sweep correction.

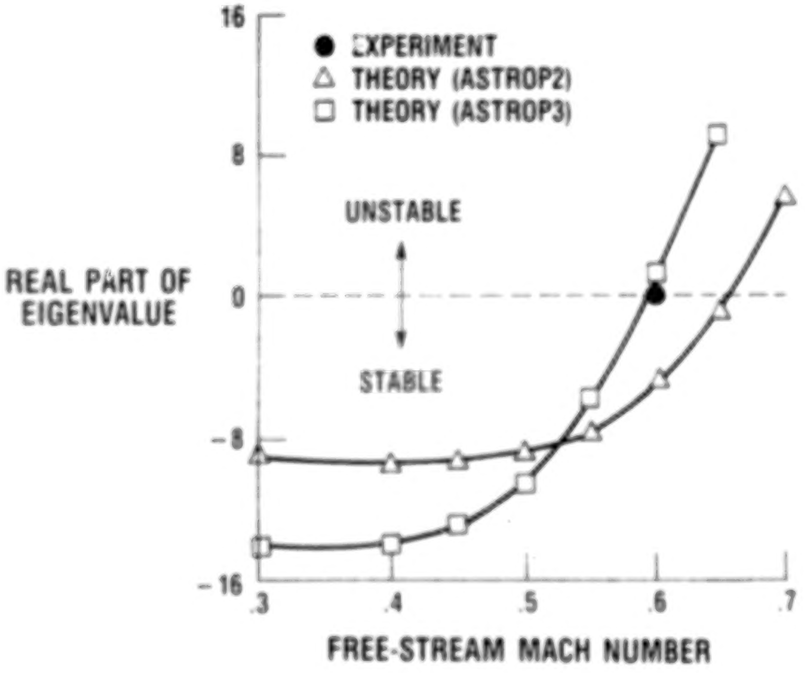

CD-88-31796

PROPFAN BLADE MISTUNING MODELS

Blade mistuning affects vibration, flutter, and forced response of turbomachinery rotors and so is a current research topic. Its effects on propfan flutter were investigated analytically and experimentally. Schematics of an eight-blade mistuned rotor used in formulating the analytical model and blade ply directions used in constructing the wind tunnel model are shown below. The analytical model, which is more general than the wind tunnel model, is based on the normal modes of a rotating composite blade and on subsonic unsteady lifting-surface aerodynamic theory. The natural frequencies and mode shapes of the SR3C-X2 and X3 model blades differed because of the ply angle variations between the blades. The first-mode frequencies of both blades were very close and insensitive to ply angles. However, the average second-mode frequency of the SR3C-3 blade was about 12 percent higher than that of the -X2 blade. More details can be found in Kaza et al. (1987b).

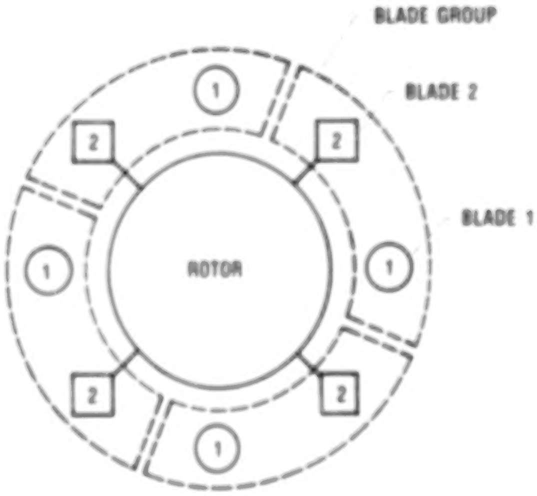
BLADE GROUP
BLADE 2
BLADE 1
ROTOR
1
2
1
2
1
1
2
2

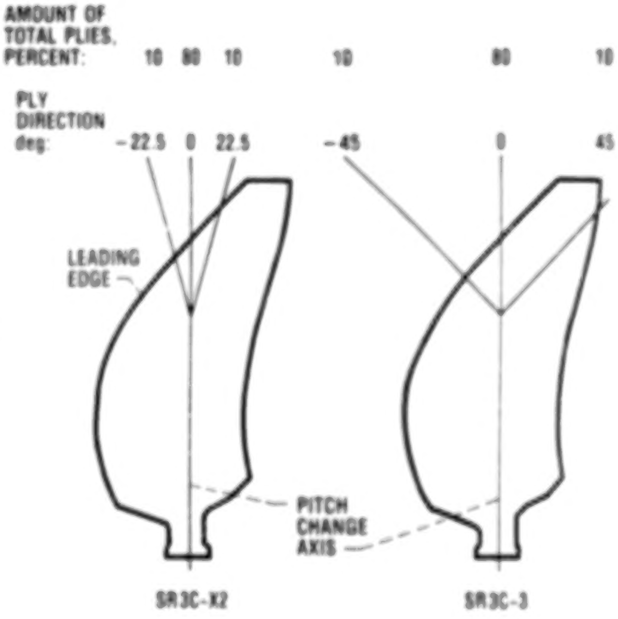
AMOUNT OF TOTAL PLIES, PERCENT:
10
80
10
10
80
10
PLY DIRECTION deg:
−22.5
0
22.5
−45
0
45
LEADING EDGE
PITCH CHANGE AXIS
SR3C-X2
SR3C-3

CD-88-31796

COMPARISON OF MEASURED AND CALCULATED FLUTTER BOUNDARIES FOR TUNED AND MISTUNED PROPFAN MODELS

Measured and calculated results for the tuned rotor SR3C-X2 and the mistuned rotor SR3C-X2/SR3C-3 are compared in the figure. The calculations for each rotor were made with the calculated modes and frequencies, except that the measured second-mode frequency was substituted for the calculated one. The calculated flutter Mach numbers for the SR3C-X2 were lower than the measured ones for all rotational speeds. The agreement would be better if the effects of steady airloads and structural damping were included in the calculations. The agreement of the mixed rotor is better but would become unconservative if steady airloads and structural damping were included in the theory. However, the overall agreement between theory and experiment is more than satisfactory. Finally the comparison of flutter boundaries for the SR3C-X2 and SR3C-3 propfans shows that a laminated composite propfan can be tailored to optimize its flutter speed by selecting the proper ply angles.

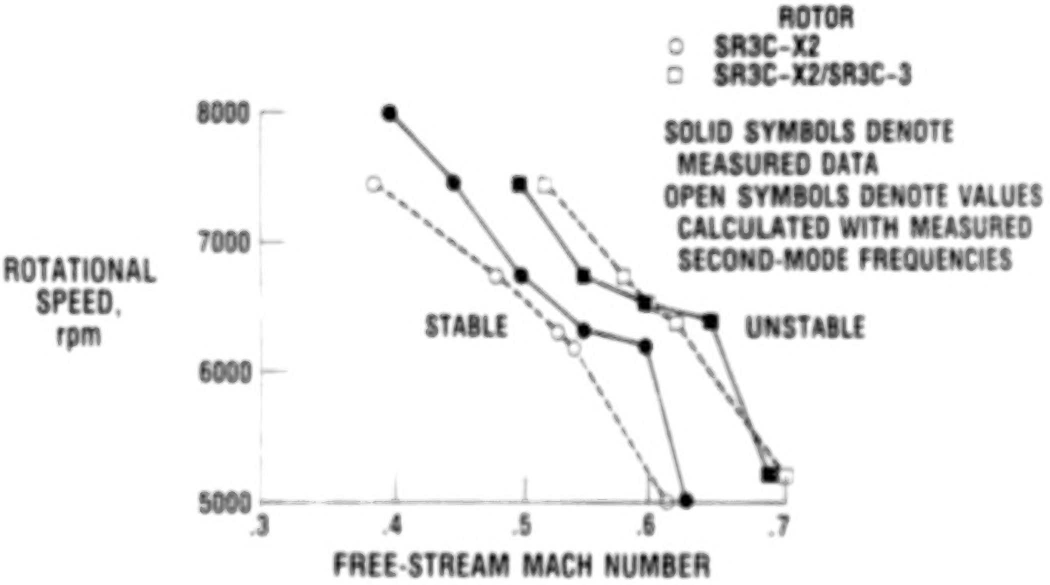

CD-88-31791

ORIGINAL PAGE IS
OF POOR QUALITY

COMPARISON OF MEASURED AND CALCULATED VIBRATORY STRESS AMPLITUDES OF A PROPFAN MODEL

A new feature of the ASTROP3 code that has just been completed (Kaza et al., 1988) is the capability to perform a modal forced-response vibration analysis that includes structural and aerodynamic mistuning of aerodynamically excited propfans. The figure depicts a single-rotation, advanced propfan wind tunnel model (the SR-5 with 10 metallic blades) operating in a generally uniform, steady inflow field and inclined at a small angle with respect to the axis of rotation. Although the absolute inflow field is constant, rotating the propfan results in velocities with oscillatory components relative to the blades. Under such conditions ASTROP3 is able to determine the oscillatory loading distributions over the propfan blades at various excitation frequencies and to calculate the vibratory displacements and stresses of the propfan. The figure shows measured and calculated one-per-revolution vibratory stress amplitudes for the SR-5 blade. The correlation between theory and experiment is very good.

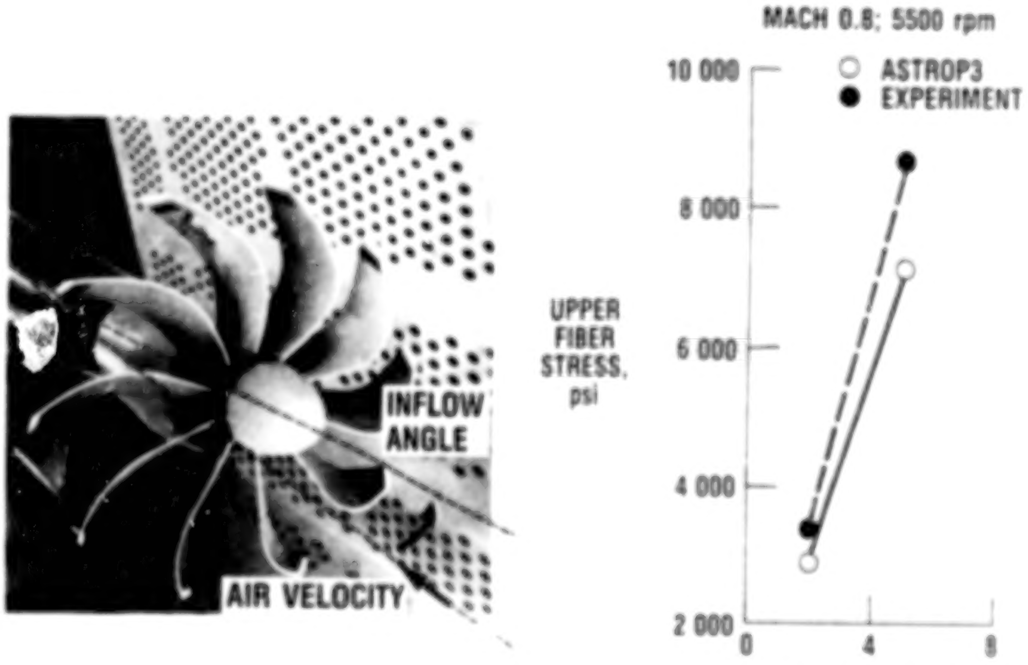

CD-88-31798

COMPARISON OF MEASURED AND CALCULATED FLUTTER BOUNDARIES OF SR-5 WIND TUNNEL MODEL

Another new feature of the ASTROP3 code that is in development is the capability to calculate flutter when the helical Mach number of the flow is supersonic. The aerodynamic code was developed by M.H. Williams of Purdue University (personal communication). This new feature of ASTROP3 is being evaluated by applying it to the SR-5 wind tunnel model since the helical flutter Mach number at the tip is near unity, or above, for most of the data. Measured and calculated flutter Mach numbers are shown for three rotational speeds at a blade setting angle of 69.3° at the three-quarter radius. The calculated mean angle of attack of the blade is also shown. The experimental flutter Mach number range was 0.86 to 0.96, with the mean angle varying from 3.07° to 11.57°. The difference between the calculated and measured flutter Mach numbers increased with increasing mean angle of attack. The maximum difference between theory and experiment was 16.7 percent at 6800 rpm. This is not surprising because a blade with substantial sweep and mean angle of attack is operating in transonic flow. Even though the blade is thin, this kind of a disagreement is expected because of the "transonic dip" (drop in flutter Mach number) phenomenon associated with substantial blade sweep. To shed further light on the transonic dip phenomenon for thin airfoils, a further investigation has been conducted (Srivastava, et al., 1988).

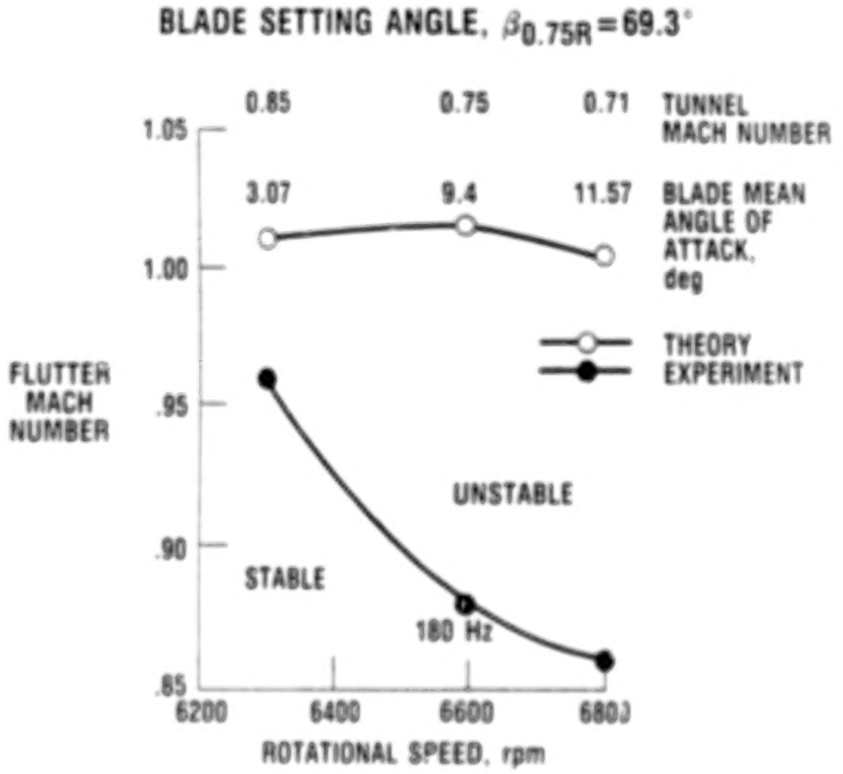

REFERENCES

Adamczyk, J.J., and Goldstein, M.E., 1978, "Unsteady Flow in Supersonic Cascade With Subsonic Leading-Edge Locus," AIAA Journal, Vol. 16, No. 12, Dec. 1978, pp. 1248-1254.

Busby, B.C., Kaza, K.R.V., and Kieth, T., 1985, "The Effects of Strong Shock Loading on Coupled Bending-Torsion Flutter of Tuned and Mistuned Cascades," Presented at the Tenth Biennial ASME Design Engineering Conference and Exhibit on Mechanical Vibration and Noise, Cincinnati, OH, Sept. 10-13, ASME Fluid-Structure Interaction and Aerodynamic Damping, E.H. Dowell and M.K. Au-Yang, eds., pp. 93-108.

Chamis, C.C., 1981, "Integrated Analysis of Engine Structures," NASA TM-82713.

Goldstein, M.E., Braun, W., and Adamczyk, J.J., 1977, "Unsteady Flow in a Supersonic Cascade With Strong In-Passage Shocks," Journal of Fluid Mechanics, Vol. 83, Part 3, pp. 569-604.

Kaza, K.R.V., and Kielb, R.E., 1982, "Flutter and Response of a Mistuned Cascade in Incompressible Flow," AIAA Journal, Vol. 20, No. 8, Aug., pp. 1120-1127.

Kaza, K.R.V., and Kielb, R.E., 1984, "Flutter and Response of Turbofan Rotors With Mistuned Blades,"AIAA Journal, Vol. 22, No. 11, Nov., pp. 1618-1625.

Kaza, K.R.V., and Kielb, R.E., 1985: "Vibration and Flutter of Mistuned Bladed-Disk Assemblies," Journal of Propulsion and Power, AIAA, Vol. 1, No. 5, Sept.-Oct., pp. 336-344.

Kaza, K.R.V., et al., 1987a, "Analytical Flutter Investigation of a Composite Propfan Model," AIAA Paper No. 87-0738 (NASA TM-88944).

Kaza, K.R.V., et al., 1987b, "Analytical and Experimental Flutter Investigation of Mistuning in Propfan Flutter," AIAA Paper No. 87-0739 (NASA TM-88959).

Kaza, K.R.V., Williams, M.H., Mehmed, O., and Narayanan, G.V., 1988, "Forced Response of Metallic and Composite Propfan Models in Yawed-Flow," AIAA/ASME/ASEE/SAE 24th Joint Propulsion Conference and Exhibit, Boston, MA, July 11-14.

Kielb, R.E., and Kaza, K.R.V., 1983, "Aeroelastic Characteristics of Cascade of Mistuned Blades in Subsonic and Supersonic Flows," Journal of Vibration, Stress and Reliability in Design, Vol. 105, pp. 1120-1127.

Mehmed, O., et al., 1982, "Bending-Torsion Flutter of a Highly Swept Advanced Turboprop," NASA TM-82975.

Mehmed, O., and Kaza, K.R.V., 1986, "Experimental Classical Flutter Results of a Composite Advanced Turboprop Model," NASA TM-88972.

Rao, B.M., and Jones, W.P., 1975, "Unsteady Airloads for a Cascade of Staggered Blades in Subsonic Flow," 46th Propulsion Energetic Review Meeting, Monterey, California.

Smith, S.N., 1973, "Discrete Frequency Sound Generation in Axial Flow Turbomachines," R&M No. 3709, British Aeronautical Research Council.

Srivastava, R., Reddy, T.S.R., and Kaza, K.R.V., 1988, "The Effects of Thickness and Shape, Viscosity and Rotation on Transonic Flutter Dip Phenomena," AIAA 29th Structures, Structural Dynamics and Materials Conference, April 18-20, Williamsburg, VA.

Subrahmanyam, K.B., et al., 1986, "Nonlinear Bending-Torsional Vibration and Stability of Rotating, Pretwisted, Preconed Blades Including Coriolis Effects," NASA TM-87207.

Whitehead, D.S., 1960, "Force and Moment Coefficients for Vibrating Airfoils in Cascades," R&M 3254, British Aeronautical Research Council.

Williams, M.H., and Hwang, C., 1986, "Three-Dimensional Unsteady Aerodynamics and Aeroelastic Response of Advanced Turboprops," AIAA 27th Structures, Structural Dynamics and Materials Conference, Part 2, NY, pp. 116-124.

N88-23245

2-D AND 3-D TIME MARCHING TRANSONIC POTENTIAL FLOW METHOD FOR PROPFANS

Marc H. Williams
School of Aeronautics and Astronautics
Purdue University
West Lafayette, IN

ABSTRACT

Prediction of aeroelastic behavior is possible only if adequate methods are available for the prediction of the unsteady aerodynamic loads that result from vibration and/or inflow disturbances. The aerodynamic analysis of propfans is complicated by several factors: the inherent three dimensionality of the flow field; the presence of strong compressibility effects at cruise Mach numbers; the importance of aerodynamic coupling between blades; and the inherently unsteady interactions between a rotor and the rest of the vehicle (e.g. the wing, nascelle, pylon or a second counter-rotating blade row.)

Previous work under this grant has led to the development of a general three-dimensional lifting surface code based on linear small disturbance theory and the assumption of simple harmonic fields (Williams and Hwang, 1986) While this method has proven to be successful in predicting propfan flutter (Kaza et. al., 1987a,b), it is restricted to single rotation configurations and does not include the effects of transonic nonlinearities.

Therefore recent efforts have concentrated on the development of aerodynamic tools for the analysis of rotors at transonic speeds, and of configurations involving relative rotation. Basically three distinct approaches have been taken: (1) extension of the lifting surface method of Williams and Hwang (1986) to relative rotation; (2) development of a time marching linear potential method for counter rotation; and (3) development of 2 and 3 dimensional finite volume potential flow schemes for single rotation. Results from each of these approaches will be described.

---

ork done under NASA Grant NAG3-499; monitor: K.R.V. Kaza.

Propeller Velocity Field Predictions

The lifting surface method described in Williams and Hwang (1986) has been modified to give the velocity field surrounding a rotor. A detailed validation study was made using extensive LDV measurements taken by Sundar and Sullivan (1986) on a low speed 2 bladed propeller. The figure shows the configuration and the predicted and measured radial velocities at a station one radius downstream from the tip. The agreement is excellent, even near the tip vortex cores. The slight phase shift is thought to be due to the neglect of vortex roll-up in the mathematical model.

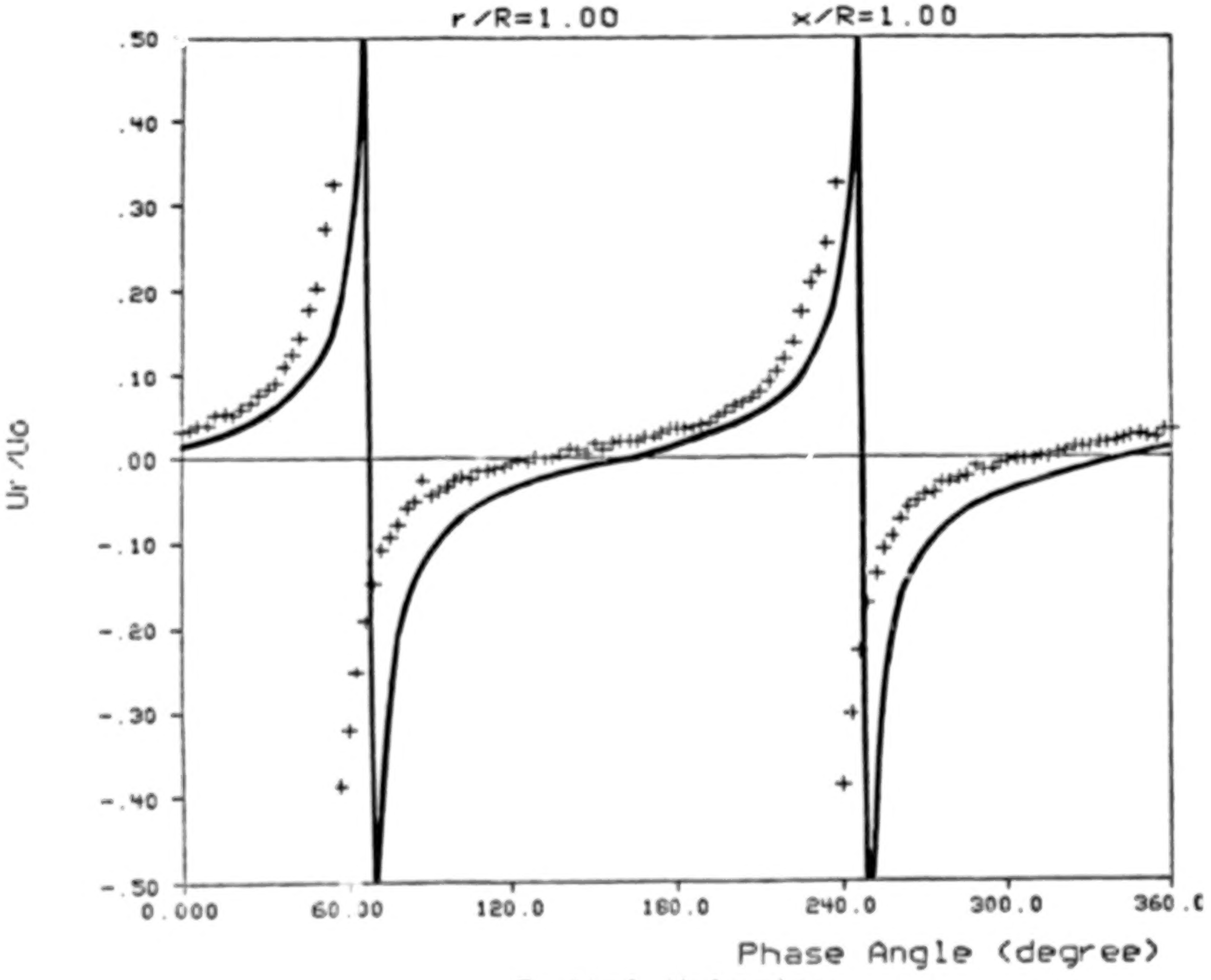

Radial Velocity

Wing Prop Interaction

The lifting surface method has been used to predict the unsteady loads on a tractor mounted wing-prop system. In this figure, the first three harmonics of the spanwise loading on the wing are shown (the wing is at zero incidence.) The zeroth harmonic agrees reasonably well with measured mean loads, though unsteady experimental data is not available for the higher harmonics.

We plan to apply this scheme to the prediction of generalized forces for aeroelastic flutter and forced response analysis with relative rotation.

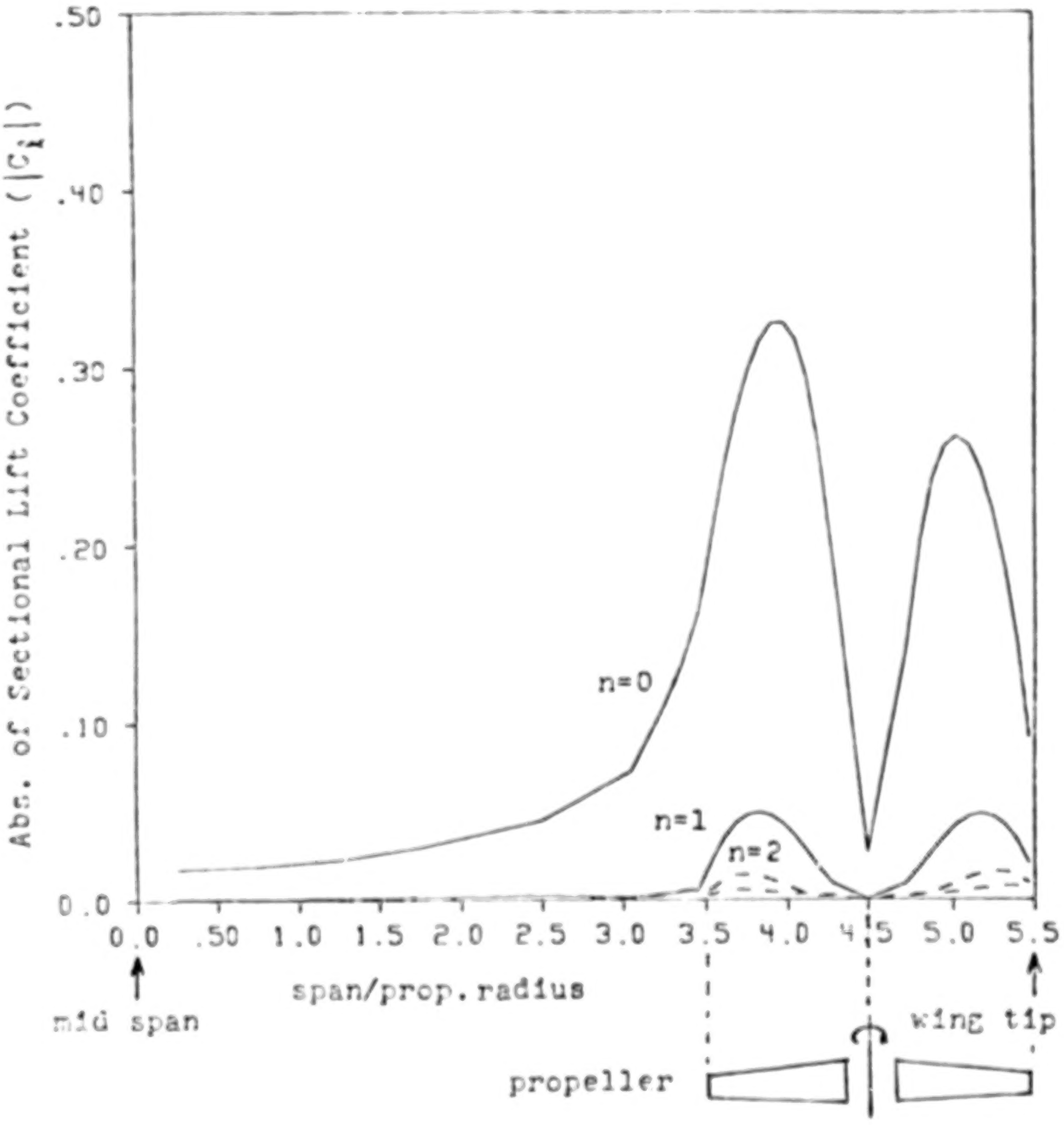

Sectional Lift Coefficients along Wing Span
Induced by Loads on the Propeller in front

Time Marching Linearized Counter Rotation Analysis

A time marching panel method was developed, Chen and Williams (1987), to study the unsteady loads on counter rotating propellers. Substantial unsteady load fluctuations were found on both the front and rear blade rows. These fluctuations were not well predicted by a quasi-steady analysis (Lesieutre and Sullivan, 1986), though the mean loads agree. Details are in Chen (1987).

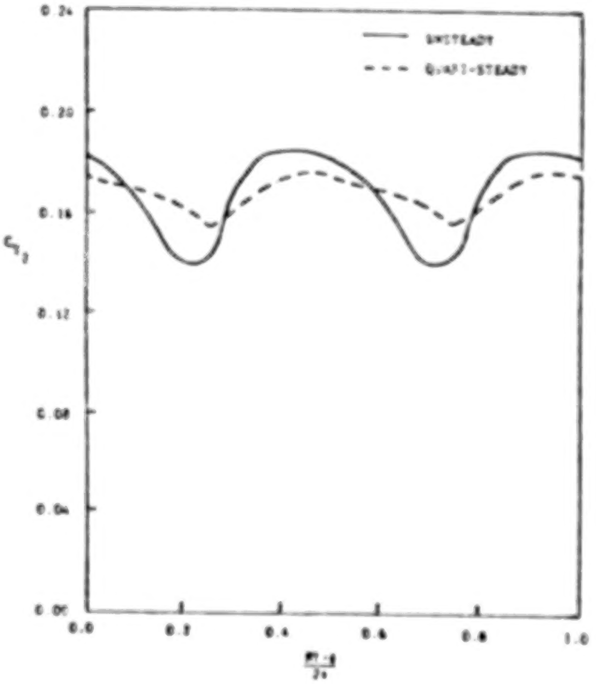

Unsteady thrust loading on rear rotor
($\beta_{3/4}$ = 41.34°, N_B = 4 x 4, J = 1.633, SR2)

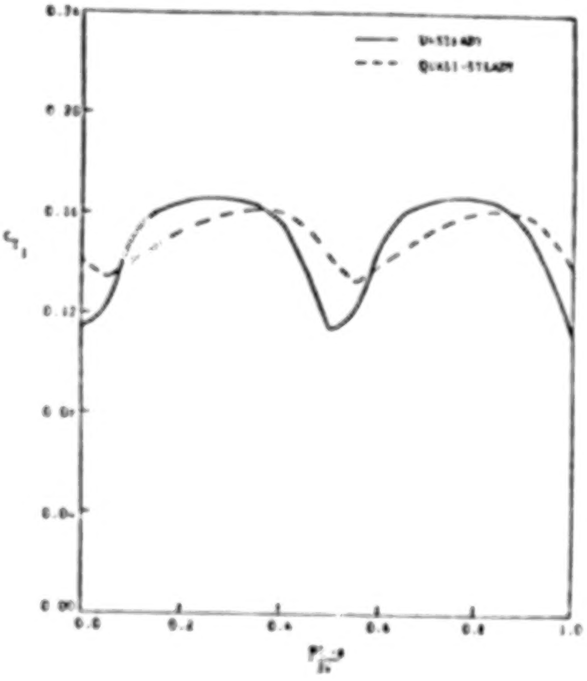

Unsteady thrust loading on front rotor
($\beta_{3/4}$ = 41.34°, N_B = 4 x 4, J = 1.633, SR2)

2-D Transonic Cascade Analysis

A 2-D time marching method has been developed using a finite volume discretization of the nonlinear potential flow equation. The scheme is an extension of the work by Shankar et. al. (1985) to cascades. The method captures shockwaves, as indicated in the figure below. Verdon (1982) used a very fine grid near the shock for better resolution, while our shock is smeared by the course grid.

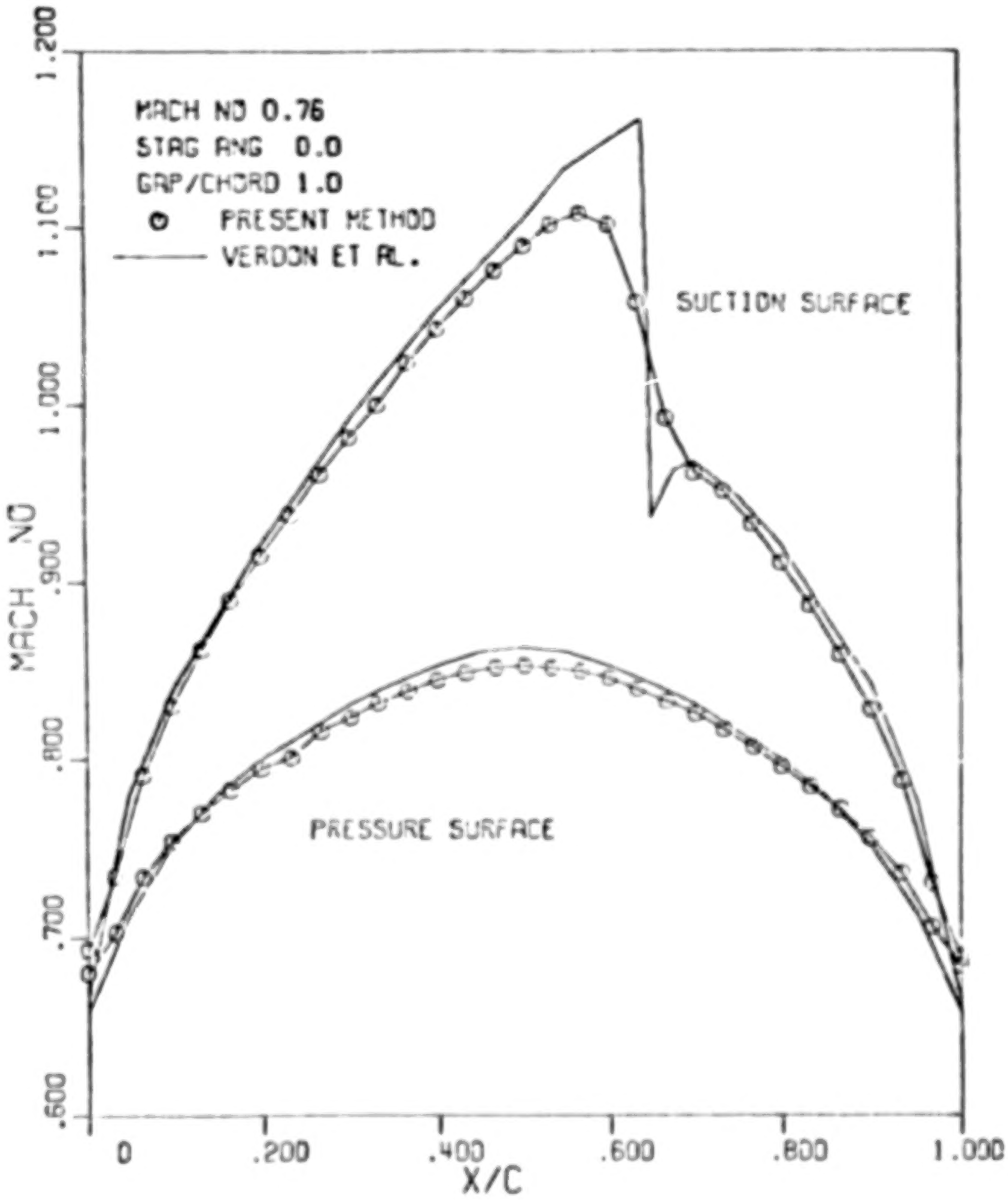

Local Mach number distributions of unstaggered half-circular-arc cascade in supercritical flow.

Interblade Phasing and Multiple Passage

The time marching scheme uses a time shearing method described by Giles (1987) to account for interblade phase lag. This can require modeling more than one passage. The calculation shown below used two passages, because of the large interblade phase angle. To avoid this a method is being developed to allow arbitrary phase angles in a single passage model.

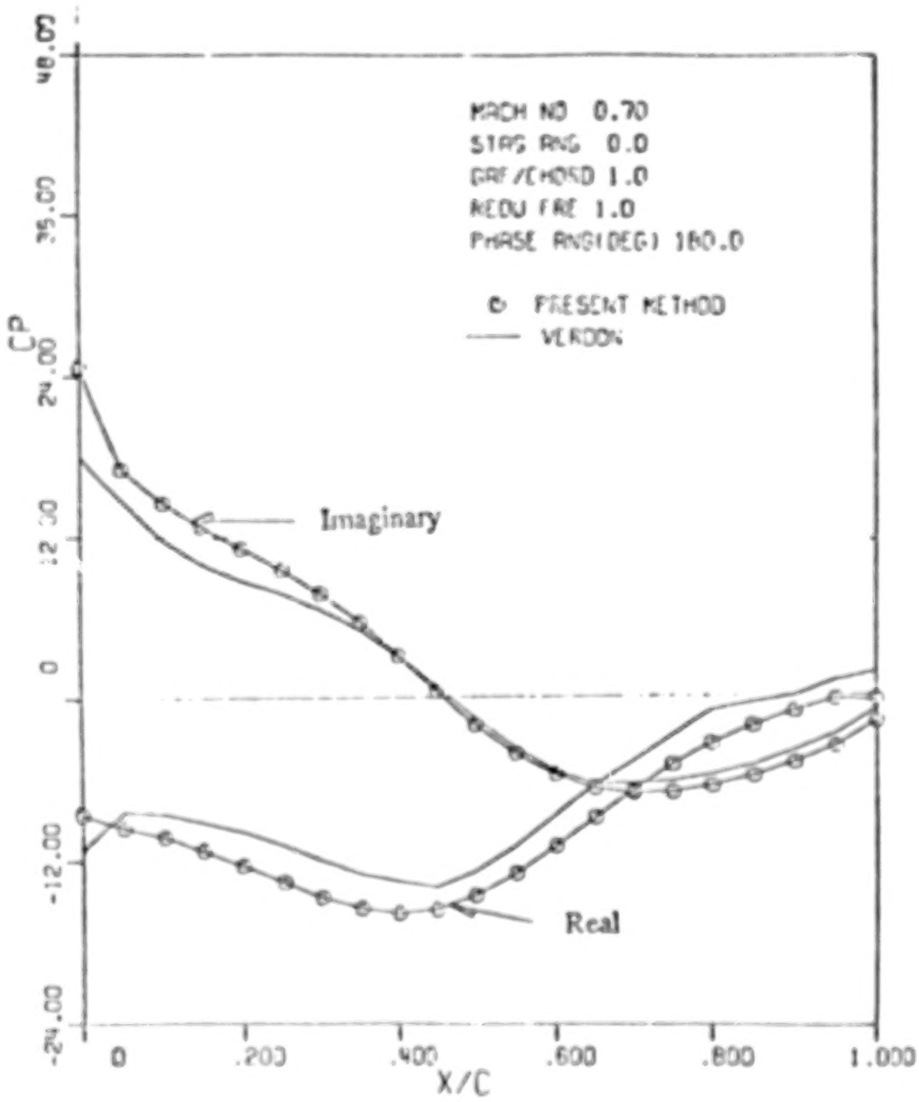

Unsteady pressure distributions due to out-of-phase torsional motion

for unstaggered half-circular-arc cascade.

Supersonic Cascades

The full potential analysis can be used at both subsonic and supersonic speeds. Shown below is the steady upper surface pressure distribution on a semi-circular arc blade at Mach 1.3, with a comparison to linear theory. This cascade has a subsonic leading edge. Some minor code modifications (in progress) are required to allow supersonic leading edges.

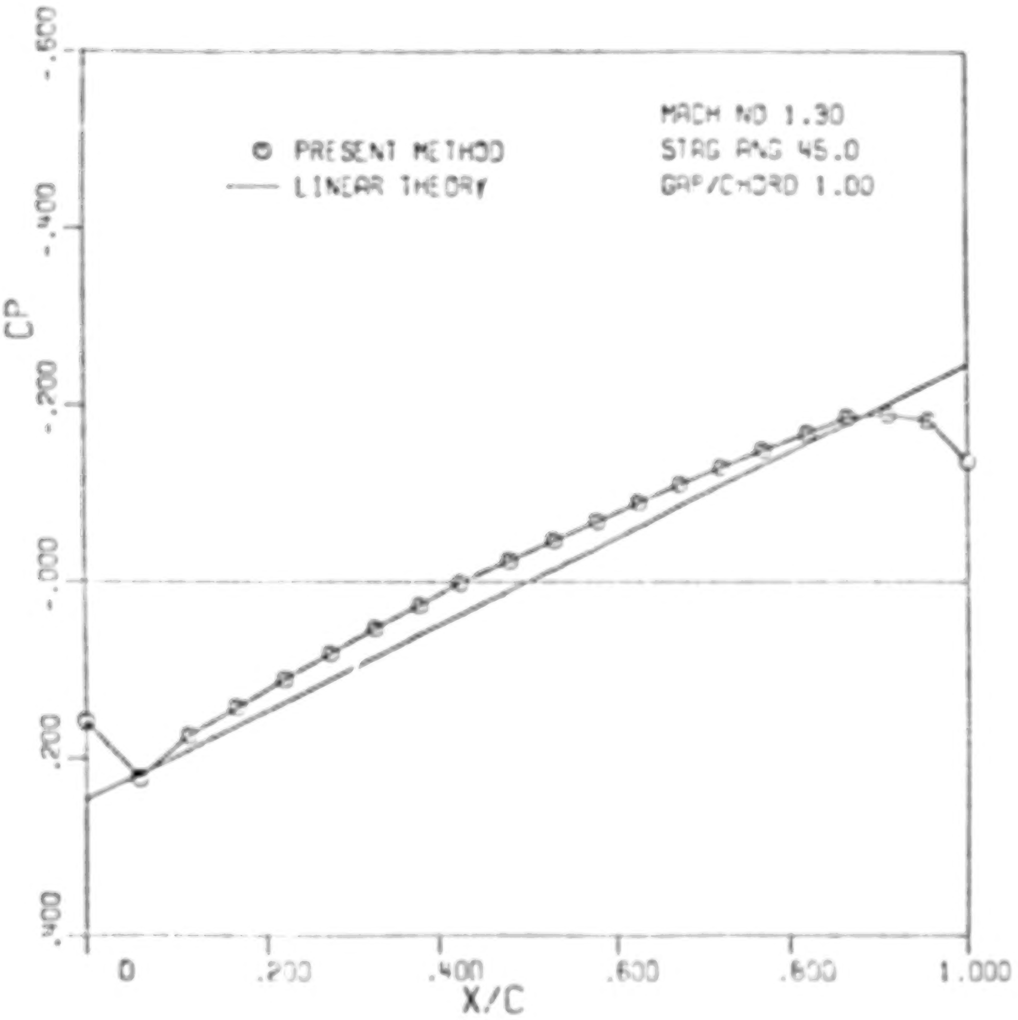

Comparison of surface pressure distributions.

Three Dimensional Full Potential Analysis

The time marching algorithm described for cascades has been implemented in three dimensions as well. Results have been obtained for relatively simple configurations. The case shown below is a rotating helical channel with a uniform axial flow. A constriction is placed in the channel to simulate a rotating blade, and the resulting steady pressure distribution is plotted at three spanwise locations. The analysis is now being extended to realistic rotor geometries. The code uses a fully moving grid network, so application to vibrating blades should be straightforward.

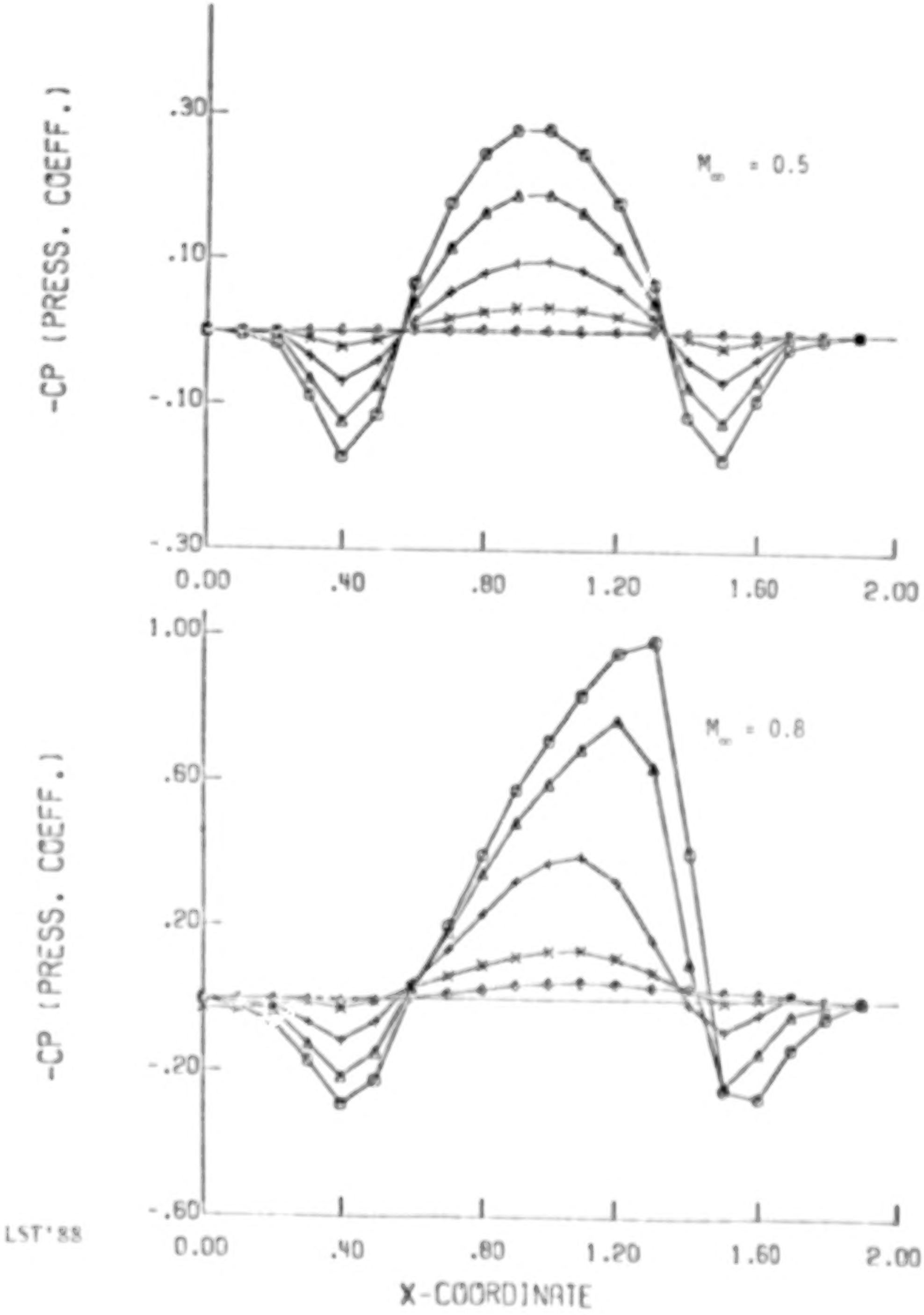

References

Chen, S.H.; Williams, M.H., 1987, "A Panel Method for Counter-rotating Propfans," AIAA paper 87-1890.

Chen, S.H., 1987, Ph.D. Thesis, Purdue University.

Giles, M. B., 1987, "Calculation of Unsteady Wake/Rotor Interactions," AIAA paper 87-0006.

Kaza, K.R.V., Mehmed, O., Narayanan, E., and Murthy, D.V., 1987a, "Analytical Flutter Investigation of a Composite Propfan Model," AIAA paper 87-0738.

Kaza, K.R.V., Williams, M.H., Mehmed, O., and Moss, L.E., 1987b, "Analytical and Experimental Investigation of Mistuning on Advanced Propfan Flutter," AIAA paper 87-0739.

Sundar, R.M. and Sullivan, J.P., 1986, "An Experimental Investigation of Propeller Wakes Using a Laser Doppler Velocimeter," AIAA paper 86-0080.

Shankar, V., Ide, H. and Gorski, J., 1985, "A Fast, Time Accurate Full Potential Scheme," AIAA paper 85-1512.

Verdon, J.M. and Caspar, J.R., 1982, "Development of a Linear Aerodynamic Analysis of Unsteady Transonic Cascades," NASA CR 168038.

④

N88-23246

PROPFAN MODEL WIND TUNNEL AEROELASTIC RESEARCH RESULTS

Oral Mehmed
Structural Dynamics Branch
NASA Lewis Research Center

ABSTRACT

The propfan offers the excellent propulsive efficiency of the conventional turboprop, but extended out to flight speeds from Mach 0.7 to 0.8. It is the thinness and sweep of propfan blades which provide the aeroacoustic gains of the propfan over lower sweep conventional turboprops. The aeroacoustic requirements of propfans also have resulted in twisted blades of low aspect ratio and high solidity, operating in high subsonic and transonic flow conditions. Then, the structural requirements of propfans have resulted in blades made of composite materials. All these characteristics make the structural design of propfans more complex than that of conventional propellers. To develop reliable technology for the structural design of these advanced propellers NASA has been conducting both experimental and analytical research in aeroelastics. This research is addressing the unconventional structural and aerodynamic characteristics of advanced propellers and is being used to improve existing and develop new aeroelastic analyses.

This short article will describe some of the single rotation propfan model wind tunnel aeroelastic findings from the experimental part of this research program. These findings include results for unstalled or classical flutter, blade response from separated flow excitations, and blade response from aerodynamic excitations at angled inflow conditions. A more comprehensive and detailed explanation of the experimental results that are given in this article can be found in the references.

PRECEDING PAGE BLANK NOT FILMED

④

PROPFAN AEROELASTIC TECHNOLOGY DEVELOPMENT

The development of propfan aeroelastic technology is being accomplished by developing theoretically based design methods and conducting propfan model experiments. As shown schematically on top, this combination is being used successfully to verify that reliable propfan design methods are developed. The research areas being investigated include flutter and aerodynamic forced excitation. The bottom figure illustrates the flight conditions where these phenomena usually are of concern. For separated flow excitations, it is at zero and low flight speeds, at operating conditions of high forward and reverse thrust. For unstalled or classical flutter, it is at high flight speeds. Whereas, for forced excitations due to angled inflow and the other sources shown, it is at both low and high flight speeds.

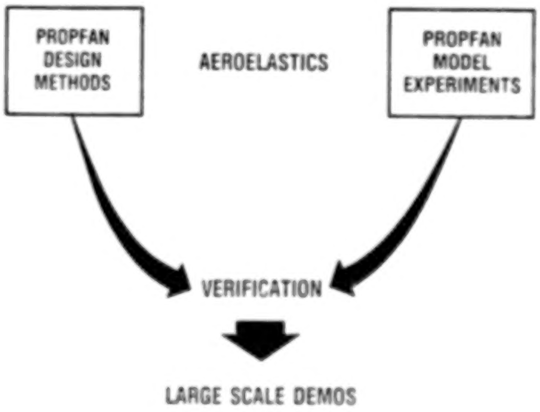

CD-88-32987

AEROELASTIC RESEARCH AREAS

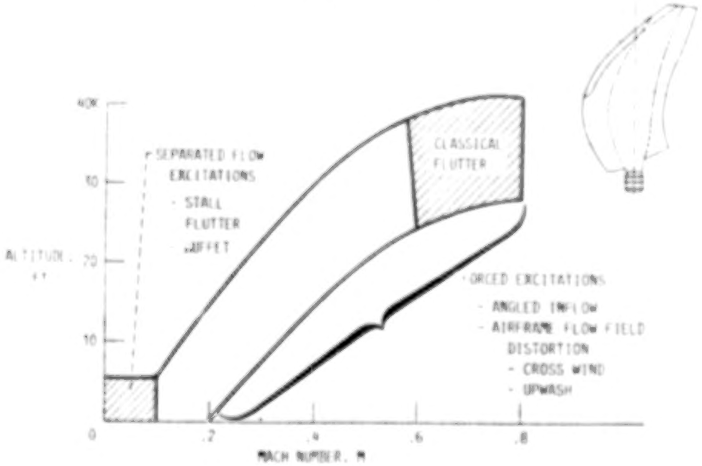

CD-88-32988

C-4

ORIGINAL PAGE IS
OF POOR QUALITY

PROPFAN MODELS USED FOR AEROELASTIC EXPERIMENTS

Aeroelastic research experiments were started in 1981 with single rotation (SR) propfan models. Shown below are some of the blade shapes that have been used and wind tunnel installation photos of two of the models. All the models are of two foot rotor diameter. The SR2, SR3, and SR5 blades are made of metal, and have 0, 45, and 60 degrees of geometric tip sweep, respectively. The SR2C and the SR3C blades have the same geometry as the corresponding metal blades but are made of graphite/epoxy material. More will be said about the SR3C blades on the next page. The SR7A blade is the first aeroelastic propfan model to be designed and tested. It has the same structural dynamics and aerodynamics as a nine foot diameter propfan demo blade that was flight tested in April, 1987. The SR7A blade consists of a metal spar, for the blade shank and core, and a composite shell over the spar. This construction is similar to that of the nine foot demo blade. All together we have competed about 1000 hours of wind tunnel aeroelastic SR model tests.

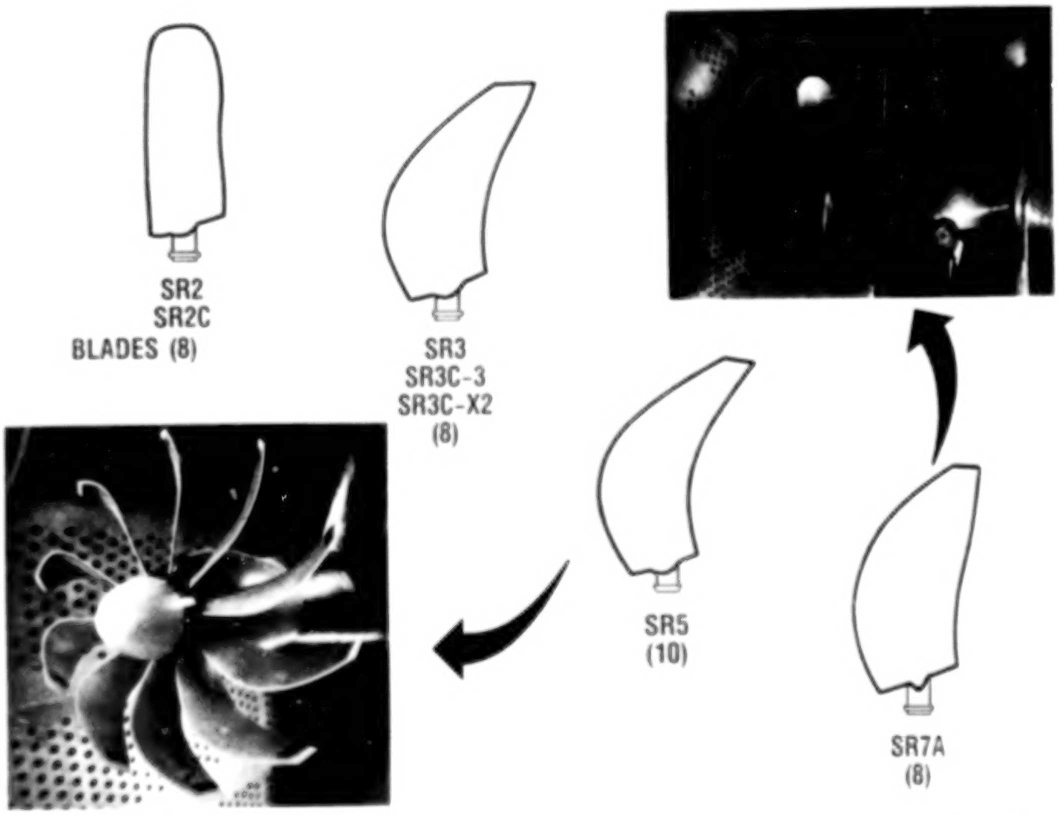

CD-88-32989

TAILORED AEROELASTIC DESIGN WITH COMPOSITE MATERIAL

The SR3C-X2 blade was designed to flutter and the SR3C-3 blade was designed to be stable. The use of composite material for the blade construction made these tailored aeroelastic designs possible. Both blades are made from a layered buildup of graphite/epoxy unidirectional tape or ply material. The two models are identical except for the orientation of some of the plys. The figure illustrates how the blades differed in construction. The ply fiber direction variation provided a difference in stiffness and mode shapes between the blades. Both models were wind tunnel tested and performed as designed. Some of these test results are given on the following pages.

SR3C BLADE SHAPE

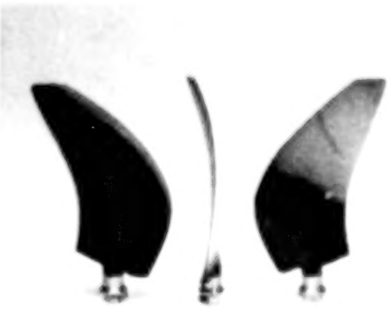

PLY DIRECTIONS

MODEL	PLY DIRECTION	PERCENT TOTAL PLYS
SR3C-3	0°	80
	±45°	20
SR3C-X2	0°	80
	±22½°	20

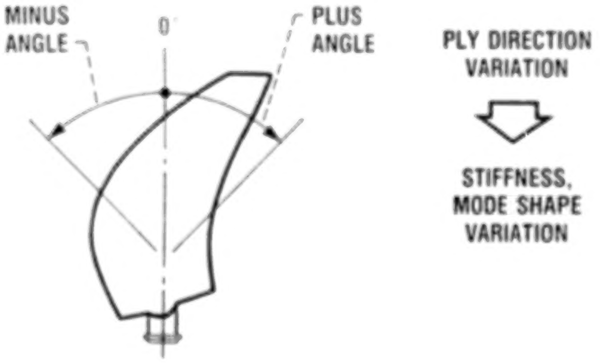

CD-88-32990

ORIGINAL PAGE IS
OF POOR QUALITY

ORIGINAL PAGE IS
OF POOR QUALITY

SR5 MODEL FLUTTER CHARACTERISTICS

The first experience with propfan unstalled (classical) flutter occurred unexpectedly at the Lewis 8 x 6 - Foot Wind Tunnel with the highly swept SR5 model. No flutter was experienced with the less swept SR2 and SR3 models during similar aerodynamic tests previously completed. When the flutter was discovered it was not understood. So the SR5 test was then redirected to investigate what type of flutter was occurring and what factors were causing the blade to flutter. Strobed video pictures taken during flutter showed a coupled bending and torsion motion occurring. At flutter the blade strain gage signals indicated the blades locked into a system mode, vibrating at a common frequency and with a common phase angle between blades. From the measured flutter conditions, shown in the figure on the left, the following is observed. A decrease in stability occurred both with an increase in blade number and an increase in blade pitch angle. The flutter occurred at relative tip Mach numbers of about one, and at conditions of both high and low blade loading, including windmilling. The test data and analytical studies led to the conclusion that it was classical flutter, and that the aerodynamic coupling between blades, known as cascade effects, and blade sweep had to be included in propfan flutter analysis. The figure on the right shows the measured flutter frequency variation with rotational speed. The measured flutter frequencies fell very close to the predicted first natural blade mode frequencies.

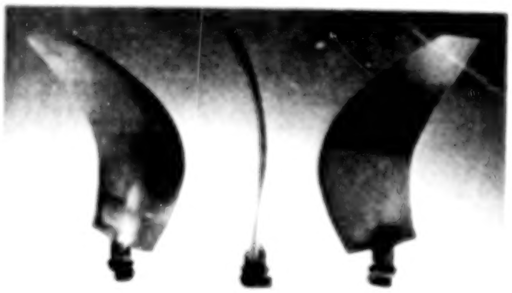

MEASURED FLUTTER CONDITIONS

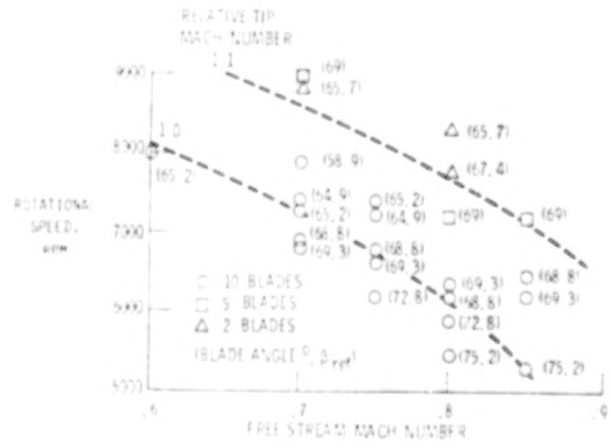

MEASURED FLUTTER FREQUENCY

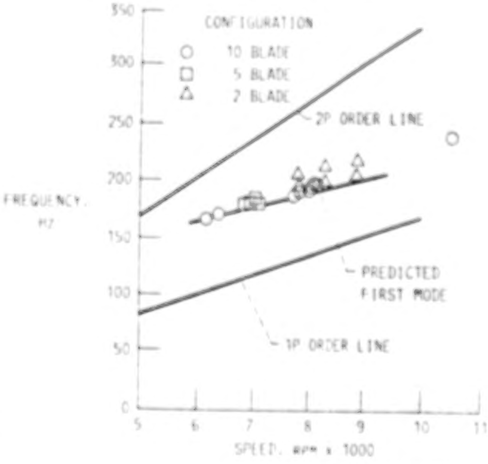

CD-88-32991

SR3C-X2 MODEL FLUTTER CHARACTERISTICS

After the SR5 flutter experiment another flutter experiment was planned and conducted to validate new flutter analyses that had been developed (Mehmed, 1982; Elchuri, 1983; Turnburg, 1983) at NASA and industry. The SR3C-X2 model, described earlier, was intentionally designed to flutter at subsonic relative velocities for this experiment. The figures below give some of the measured flutter results. The trends shown in the top and lower left figures agree with those found with SR5. That is, a decrease in stability occurs with an increase in blade number and with increasing blade angle. Note, as with SR5, the flutter here also occurred at the windmilling condition. Not shown, but reported by Mehmed and Kaza (1986), the flutter occurred at relative tip Mach numbers between 0.77 and 0.86 with eight blades, and between 0.80 and 0.90 with four blades. The lower right figure shows the flutter frequency for SR3C-X2 was between the predicted first two blade natural modes. It was seen on the previous page that the SR5 flutter frequency was much closer to the first natural blade mode. This difference is due to the larger blade-to-air mass ratio of SR5 than SR3C-X2, 115 and 33, respectively. The flutter data from the SR3C-X2 model provided validation of and confidence in the classical flutter analyses developed for propfans after the SR5 flutter experiment.

MEASURED FLUTTER CONDITIONS

OPEN SYMBOLS DENOTE 4 BLADES IN ROTOR
CLOSED SYMBOLS DENOTE 8 BLADES IN ROTOR

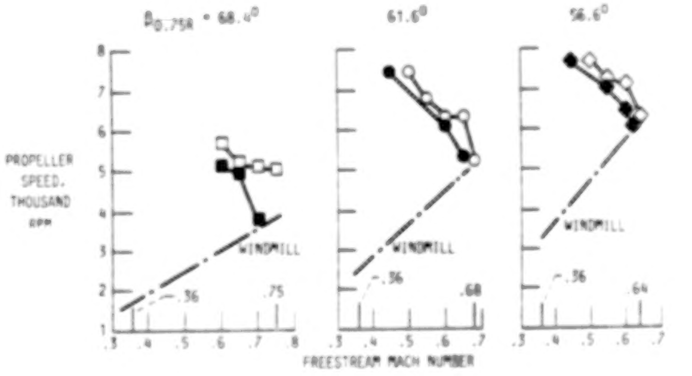

CD-88-32002

MEASURED FLUTTER CONDITIONS
8 BLADES IN ROTOR

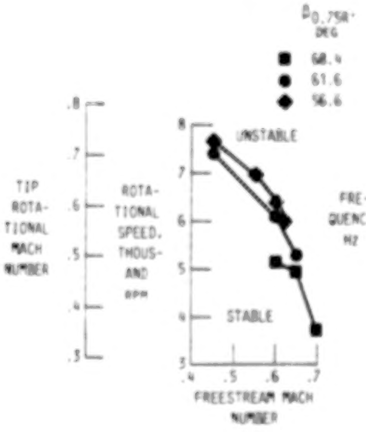

MEASURED FLUTTER FREQUENCIES
8 BLADES IN ROTOR

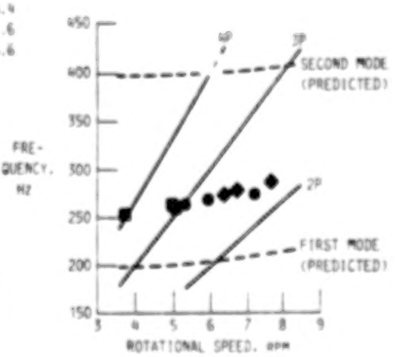

CD-88-32003

CLASSICAL FLUTTER - PERSPECTIVE

The classical flutter phenomenon discovered with a very highly swept propfan model, SR5, was fortuitous. It led to the development of reliable classical flutter analyses for propfans. Both the SR7 aeroelastic model and the large scale demo propfan have been operated without flutter, as indicated in the chart. Another flutter experiment with a counter rotation (CR) model has recently been completed at Lewis, and will help the development of flutter analyses for CR propfans.

CLASSICAL FLUTTER-PERSPECTIVE

- DISCOVERED WITH SR5
- NEWLY DEVELOPED FLUTTER ANALYSES VERIFIED WITH SR3C-X2 AND SR3C-3
- SR7 AEROELASTIC MODEL (2-FT DIAMETER) CLEARED TO 0.9 MACH AT LEWIS
- SR7 DEMO BLADE (9-FT DIAMETER) CLEARED TO 0.83 MACH AT MODANE AND TO 0.89 MACH AT 28,000 FT IN FLIGHT
- FLUTTER EXPERIMENT WITH A CR MODEL COMPLETED AT LEWIS (DEC. 1987)
  - TO INVESTIGATE THE IMPORTANCE OF ROTOR INTERACTIONS ON CLASSICAL FLUTTER

CD-88-32994

PROPFAN BLADE VIBRATIONS IN RESPONSE TO SEPARATED FLOW AT ZERO FORWARD VELOCITY

The figures below display vibratory response strain gage data for three propfan models of different sweep. The excitations are from separated flow excitations and critical speeds. The test conditions are zero forward velocity, zero thrust axis tilt, and a blade setting angle of 32 degrees. The left and right figures show bending stress data measured at blade locations inboard and near the tip, respectively. Also, data from two different facilities are compared in each figure. It is seen that the straight blade model (SR2) has the largest response, the next higher sweep model (SR3) has a lower response, and the most highly swept model (SR5) has the lowest response. This trend agrees at both blade measurement locations. The data from the two facilities shows good consistency.

PROPFAN BLADE VIBRATIONS IN RESPONSE TO SEPARATED FLOW AT ZERO FORWARD VELOCITY

Mach no. = 0, no tilt, $\beta_{ref} \sim 32°$

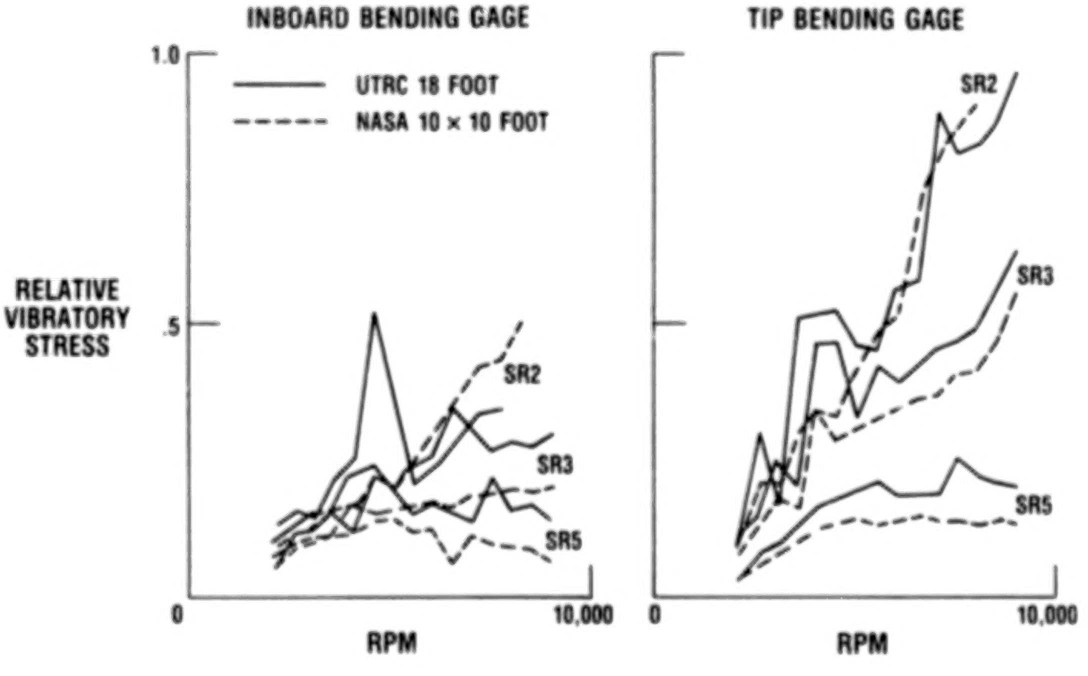

CD-88-32995

PROPFAN BLADE VIBRATIONS IN RESPONSE TO SEPARATED FLOW WITH FORWARD VELOCITY

This figure is similar to the one on the previous page, except it shows the effect of forward velocity on blade vibratory response. The figure compares the blade response at forward velocities of 0 and 0.1 Mach, for a blade setting angle of 36 degrees. It is seen at both velocity conditions that the swept blades have a lower vibratory response than the straight blades, and that a significant decrease in blade stress occurs with forward velocity. This is expected, since forward velocity causes a decrease in the blade angle of attack and a corresponding decrease in separated flow.

PROPFAN BLADE VIBRATIONS IN RESPONSE TO SEPARATED FLOW WITH FORWARD VELOCITY

NO TILT, $\beta_{ref} \sim 36^\circ$, NASA 10 × 10 FOOT, INBOARD BENDING GAGE

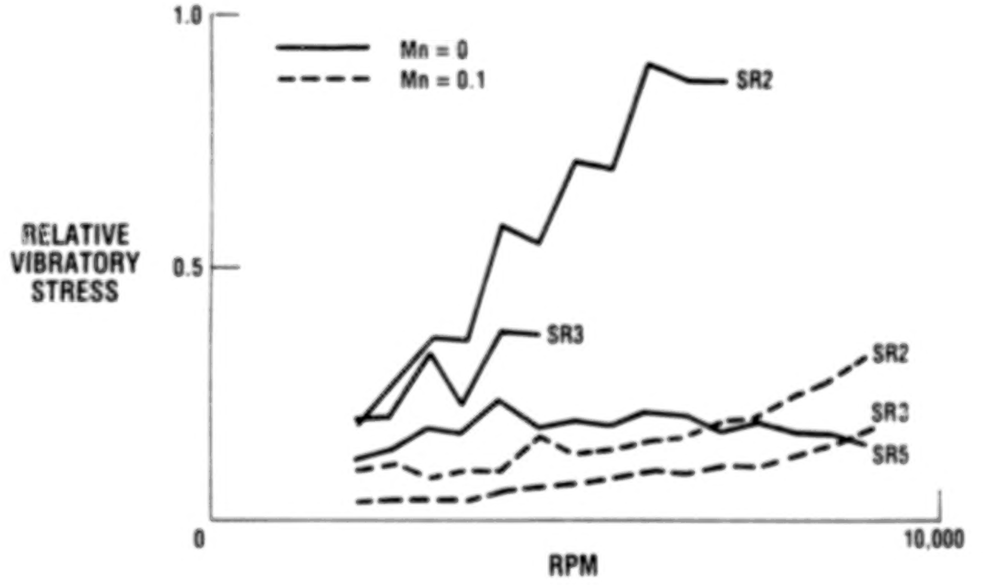

CD-88-32996

SR2C AND SR3C PROPFAN FORCED RESPONSE IN ANGLED FLOW

The figures show the measured 1P strain sensitivity variation with power coefficient for the straight SR2C and the swept SR3C-3 composite propfan models. The measurements were made with the propeller thrust axis inclined to the freestream, both in an isolated nacelle and on a wing in a tractor configuration. Strain sensitivity is defined as the amplitude of the 1P strain component per unit excitation factor. Excitation factor (E.F.) is proportional to the product of the thrust axis tilt and the freestream dynamic pressure, and the 1P strain component varies linearly with both of these parameters. The figures show that the installation on the wing causes a greater blade response than the isolated configuration. This is due to the increased angular inflow into the propeller rotor from the wing flowfield. The figures also show that the swept blade has less strain sensitivity than the straight blade at most of the operation conditions.

SR2C AND SR3C-3 PROPFAN FORCED RESPONSE IN ANGLED FLOW

ISOLATED AT NASA—LEWIS 8 × 6 FOOT
ON WING AT NASA—AMES 14 FOOT

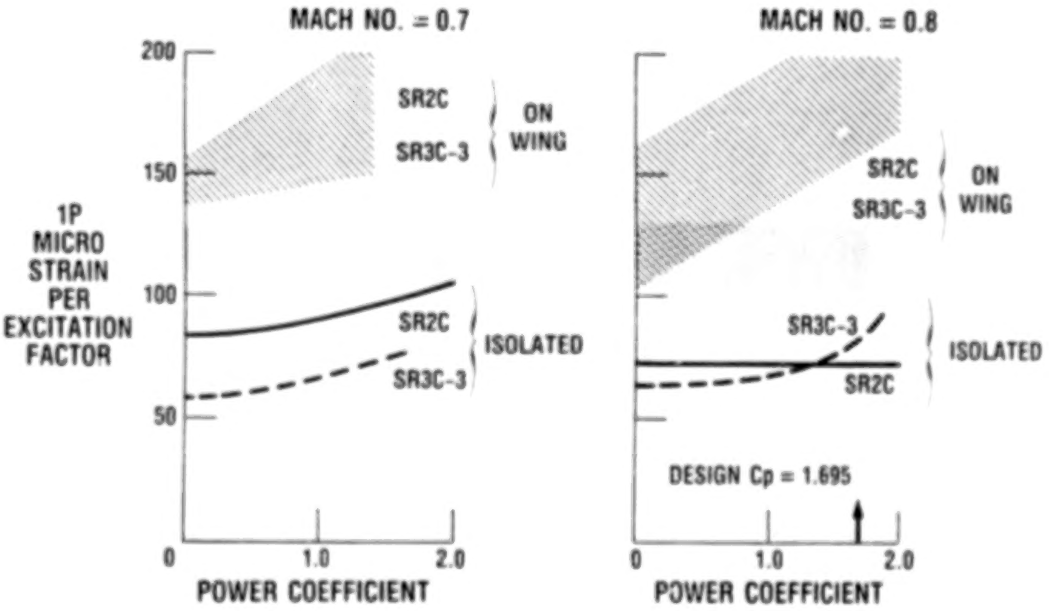

CD-88-32997

SR7A MEASURED NATURAL FREQUENCIES AND MODE SHAPES

The bench measured natural frequencies and corresponding hologram photos of the natural mode shapes of a SR7A aeroelastic model blade are shown in the figure on top. The whitest fringes represent nodes and the black fringes represent constant displacement contours. All the modes involves a coupling of the flatwise, edgewise, and torsion motion, but the mode is identified by its predominant component of motion. The measured natural frequency variation with rotational speed is shown in the bottom figure for a blade angle at 3/4R of 32 degrees. Calculated natural frequencies using MSC NASTRAN for a blade angle of 57.6 degrees are also shown. The analytical model is slightly stiffer than the actual blade for the 1E and the 2F modes, and stiffer yet for the 1T mode, but less stiff for the 1F mode at the high rpm point.

BENCH MEASURED

BLADE SERIAL NUMBER 15

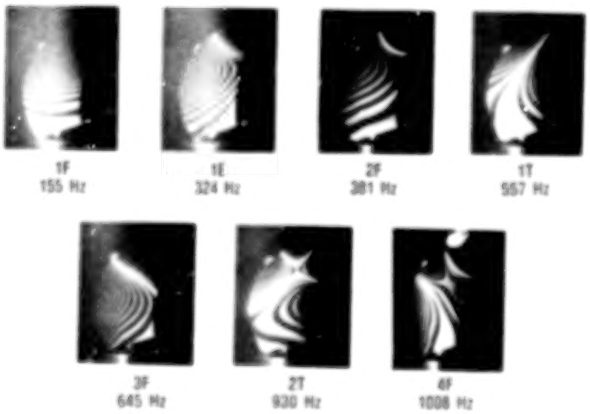

1F 155 Hz, 1E 324 Hz, 2F 381 Hz, 1T 557 Hz, 3F 645 Hz, 2T 930 Hz, 4F 1008 Hz

SR7A MEASURED NATURAL FREQUENCIES

LEWIS 9 × 15 WIND TUNNEL AND BENCH

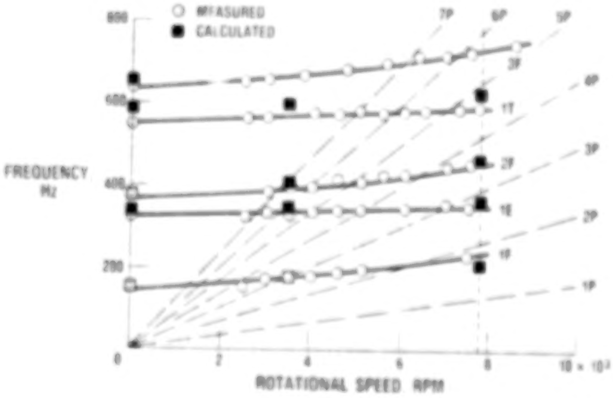

SR7A PROPFAN MODEL FORCED RESPONSE IN ANGLED INFLOW

The SR7A aeroelastic model had no classical flutter and the blade vibratory response followed expected trends. The top figure shows the total vibratory peak strain amplitude variation with shaft power for an isolated nacelle configuration. The strains show a linear increase with power for both the mid-blade and tip bending gages, except at 325 shp. These points at 325 shp are near the 1E/3P critical speed crossing and have a significant 1E amplitude component. The 1P strain is the major component of the total vibratory strain at the other conditions. The bottom figure shows the 1P vibratory strain sensitivity (defined on the previous page) with shaft power. The greatest strain sensitivity occurs at the lowest Mach number (0.6). The strain sensitivity increases with shaft power but at Mach 0.6 it falls after an initial rise.

TOTAL VIBRATORY PEAK STRAIN AMPLITUDE VARIATION WITH SHAFT POWER

SR7A PROPFAN 8 × 6 WIND TUNNEL

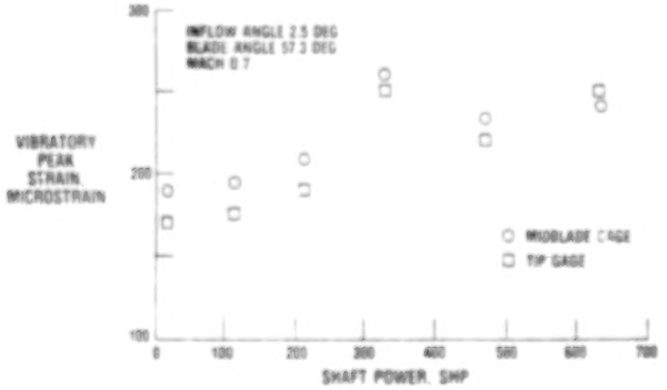

1P VIBRATORY STRAIN SENSITIVITY VARIATION WITH SHAFT POWER

SR7A PROPFAN 8 × 6 WIND TUNNEL

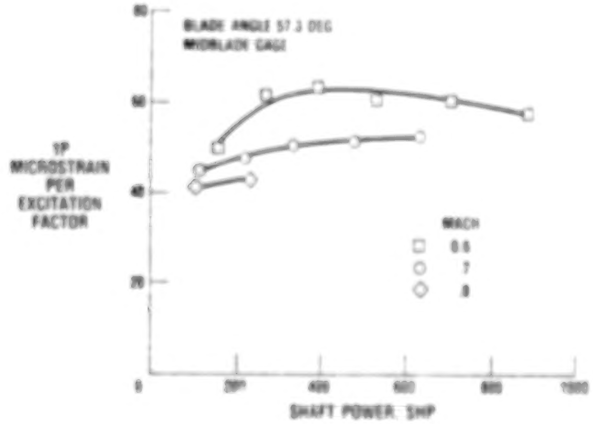

SUMMARY

The complex characteristics of propfans required the development of new aeroelastic technology for their design. To help develop this technology experiments were conducted with propfan sub-scale models. The objectives were to understand the aeroelastic phenomena of propfans, to provide a data base, and to develop and verify aeroelastic analyses. Full scale flight testing has demonstrated the successful propfan designs developed from this experimental and analytical research program.

- CLASSICAL FLUTTER
  - IS UNDERSTOOD AND CAN BE AVOIDED THROUGH DESIGN

- SEPARATED FLOW EXCITATION
  - NO STALL FLUTTER OCCURRED WITH THE SWEPT MODELS
  - HIGHER SWEEP REDUCES RESPONSE
  - FORWARD VELOCITY REDUCES RESPONSE

- FORCED EXCITATION AT ANGLED INFLOW
  - HIGHER SWEEP REDUCES RESPONSE
  - WING INSTALLATION INCREASED 1P STRAIN SENSITIVITY OVER THAT OF ISOLATED BY ABOUT TWO TIMES
  - THE 1P STRAIN SENSITIVITY INCREASED WITH SHAFT POWER IN THE BLADE DESIGN RANGE

- GENERAL
  - SWEPT BLADES EXHIBIT LESS FORCED RESPONSE THAN STRAIGHT BLADES
  - THE AEROELASTIC MODEL PERFORMED AS PREDICTED BY ANALYSES
  - COMPOSITE MATERIAL CAN BE USED TO TAILOR THE AEROELASTIC DESIGN OF PROPFANS

REFERENCES

Bansal, P.N., et al., 1985, "Analysis and Test Evaluation of the Dynamic Response and Stability of Three Advanced Turboprop Models," NASA CR-174814.

Gatzen, B.S., 1987, "Prop-Fan Recent Experimental Test Results," Aero-Propulsion Short Course, Dayton, Ohio.

Kaza, K.R.V., et al., 1987a, "Analytical Flutter Investigation of a Composite Propfan Model," NASA TM 88944.

Kaza K.R.V., et al., 1987b, "Analytical and Experimental Investigation of Mistuning in Propfan Flutter," NASA TM 88959.

Mehmed, O., et al., 1982, "Bending-Torsion Flutter of a Highly Swept Advanced Turboprop," NASA-TM 82975.

Mehmed, O., and Kaza, K.R.V., 1986, "Experimental Classical Flutter Results of a Composite Advanced Turboprop Model," NASA TM-88792.

Smith, A.F., 1985a, "Analysis and Test Evaluation of The Dynamic Stability of Three Advanced Turboprop Models at Zero Forward Speed," NASA CR-175025.

Smith, A.F., 1985b, "Analysis and Test Evaluation of The Dynamic Response and Stability Of Three Advanced Turboprop Models At Low Forward Speed," NASA CR-175026.

Smith, A.F., and Brooks, B.M., 1986a, "Dynamic Response and Stability of a Composite Propfan Model," NASA CR-179528.

Smith, A.F., 1986b, "Dynamic Response of Two Composite Prop-Fan Models On A Nacelle/Wing/Fuselage Half Model," NASA CR-179589.

N88-23247

AEROELASTIC FORCED RESPONSE ANALYSIS OF TURBOMACHINERY*

Todd E. Smith
Sverdrup Technology, Inc.
(Lewis Research Center Group)
NASA Lewis Research Center

ABSTRACT

The Structural Dynamics Branch is currently involved in the development of predictive tools for application to vibration problems within engine structures. This brief article outlines the research activity currently under way to predict the aeroelastic forced response of fan, compressor, and turbine components.

There are currently no analytical methods for predicting the forced response behavior of turbomachinery components. Traditionally, the blade Campbell diagram has been used to determine if a resonant frequency will interfere with an engine order excitation. This technique has proven very successful over the past few decades, but the push for higher stage loading and lighter engine weight raises many forced response problems. The goal of this new research is to create a system which will enable a designer to analytically predict fan, compressor, and turbine blade response due to the many inherent sources of excitation.

The Forced Response Prediction System (FREPS) is being created as an analytical tool for turbomachinery forced response. This system combines many of the traditional structural and aeroelastic system models with the more recent advanced unsteady aerodynamic models. The initial emphasis of this project is to develop methods for predicting unsteady blade loads due to flow field disturbances which result within rotating blade rows.

The use of advanced computational aerodynamic models is enabling the prediction of motion-independent airfoil unsteady loads which occur due to aerodynamic excitations. For example, the aerodynamic loads induced by viscous wake passing and downstream potential-field fluctuations can now be predicted by using these computational fluid dynamic codes.

The application of advanced unsteady aerodynamics codes also permits the prediction of the motion-dependent, unsteady blade loads which occur within complex (thick, highly cambered) blade passages. This capability allows for the estimation of the unsteady pressure field within oscillating turbine blade cascades at a variety of flow Mach numbers.

---

*Work performed on-site at the Lewis Research Center for the Structural Dynamics Branch under contract NAS3-24105.

An initial application of this predictive system is to determine the aeroelastic behavior of the space shuttle main engine (SSME) oxygen pump turbine blades. These blades have had a history of fatigue failures, and the aerodynamic loads caused by the turbine vanes, struts, and cooling jets may be contributing to the high vibratory stresses.

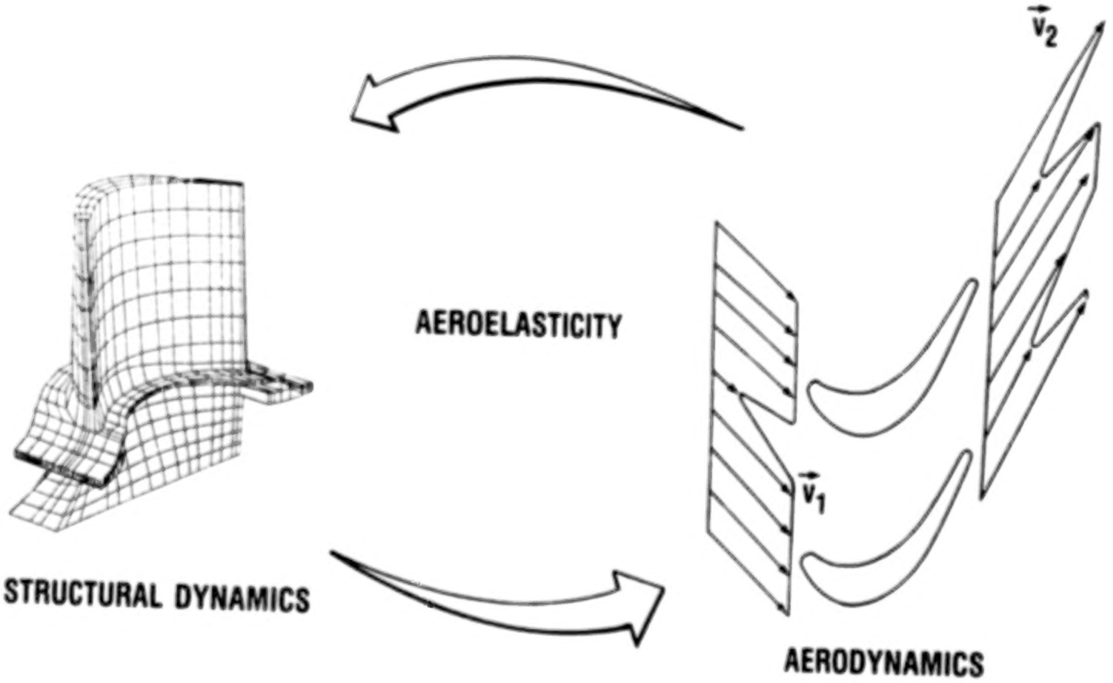
$\vec{V}_2$
AEROELASTICITY
$\vec{V}_1$
STRUCTURAL DYNAMICS
AERODYNAMICS

CD-88-31809

AEROELASTIC PHENOMENA

The aeroelastician is concerned with the manner in which elastic structures respond when placed within a flowing fluid. In particular, the stability and forced response of the structure must be determined. Stability problems are generally not encountered within turbomachinery because this is usually a constraint during initial design studies. Forced response is typically a long-term problem because there are presently no useful design tools available.

Aeroelastic stability of a structure is assured if there are no unstable self-excited vibratory modes present at the standard operating conditions. The presence of sufficient aerodynamic damping within an oscillating cascade of blades will determine if stable or unstable motion results.

The aeroelastic forced response analysis attempts to predict the manner (displacements, phase relationships) in which the structure responds to flow field disturbances.

BLADE CAMPBELL DIAGRAM

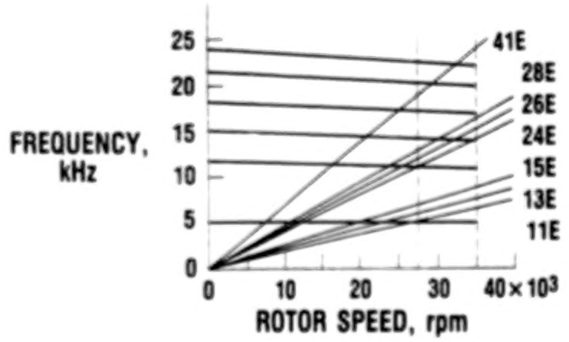

BLADE FORCED RESPONSE

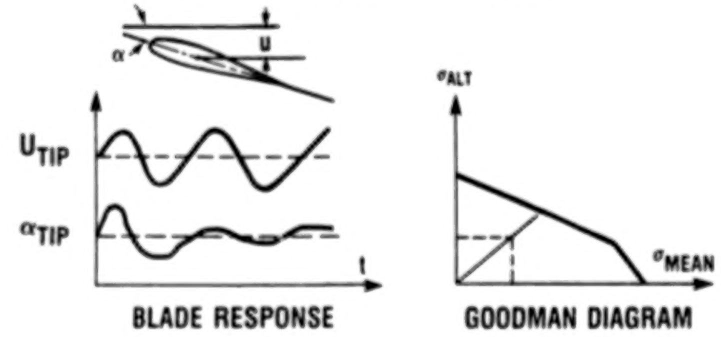

BLADE RESPONSE

GOODMAN DIAGRAM

CD-88-31810

TURBOMACHINERY FORCED RESPONSE - TRADITIONAL METHODS

The frequency-speed behavior of turbomachinery blades is customarily used to determine if a forced response problem may exist for the component. The operating line interferences with resonant blade frequencies and engine order excitations in a Campbell diagram are used to make a yes or no decision about forced response problems. An example of such a determination is demonstrated in Moss and Smith (1987). This traditional approach does not predict the actual blade response to such excitations, but it does give an indication of the possibility of having a significant blade response.

This research will provide a forced response calculation procedure which will estimate the magnitude and phase of blade motion induced by the flow field disturbances. Knowledge of the airfoil forced response may then be used to infer magnitude of vibratory stresses and fatigue characteristics through application of standard Goodman diagram techniques.

AEROELASTIC EQUATION OF MOTION

$$\underbrace{M\ddot{q} + C\dot{q} + Kq}_{\text{STRUCTURAL MODEL}} = \underbrace{A(q,t)}_{\substack{\text{MOTION-DEPENDENT}\\ \text{AERODYNAMIC}\\ \text{LOADS}}} + \underbrace{F(t)}_{\substack{\text{MOTION-INDEPENDENT}\\ \text{AERODYNAMIC}\\ \text{LOADS}}}$$

CD-88-31811

FORCED RESPONSE PREDICTION SYSTEM - FREPS

The FREPS system couples the aeroelastic equations of motion for a cascaded blade row. This system uses the aeroelastic system models developed during the last decade and the advanced aerodynamic models developed more recently.

A general aeroelastic equation of motion is presented below. This equation models the structural characteristics of the system (left-hand side) along with the forcing function (right-hand side). The structural characteristics may include structural damping, mistuning, etc. The forcing functions are due to two sources: motion-dependent forces and motion-independent, flow-induced forces.

The FREPS system uses unsteady aerodynamic analysis to predict the motion-dependent forces in complex blade passages. This system also uses empirical models and correlations to define the influence of the motion-independent aerodynamically induced loads.

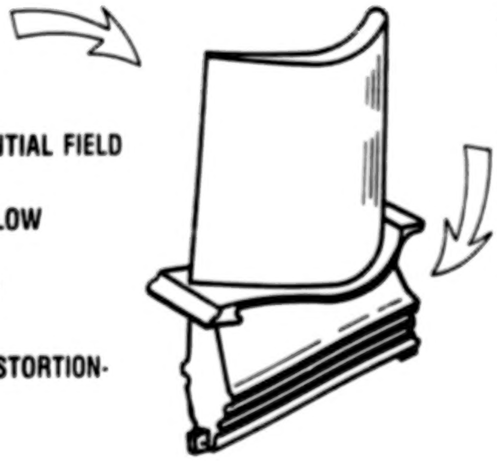

AERODYNAMIC EXCITATIONS

- UPSTREAM; VISCOUS WAKE SHEDDING
- DOWNSTREAM, POTENTIAL FIELD DISTURBANCES
- BLADE SECONDARY FLOW PHENOMENA
- COMPRESSOR SURGE/ ROTATING STALL
- INLET FLOW FIELD DISTORTION-TURBULENCE

MECHANICAL EXCITATIONS

- BLADE TIP-CASING CONTACT
- ROTOR DISK FLEXIBILITY
- SHAFT AND GEAR MESH EXCITATIONS
- FOREIGN OBJECT DAMAGE

CD-88-31812

SOURCES OF UNSTEADY BLADE LOADS

The typical rotating turbine blade is subjected to many mechanical and aerodynamic forcing functions. Mechanical vibrations may be transmitted through the supporting structures (disk, bearings, etc.) to result in unsteady blade loads.

Aerodynamic unsteadiness due to the aerodynamic interaction within a rotor-stator pair generates significant unsteady loads. Unlike the mechanical sources which may occur during specific portions of operation, the aerodynamic forcing functions are always present. This research is chiefly concerned with developing methods to estimate the effect of these aerodynamically induced unsteady loads on blade response.

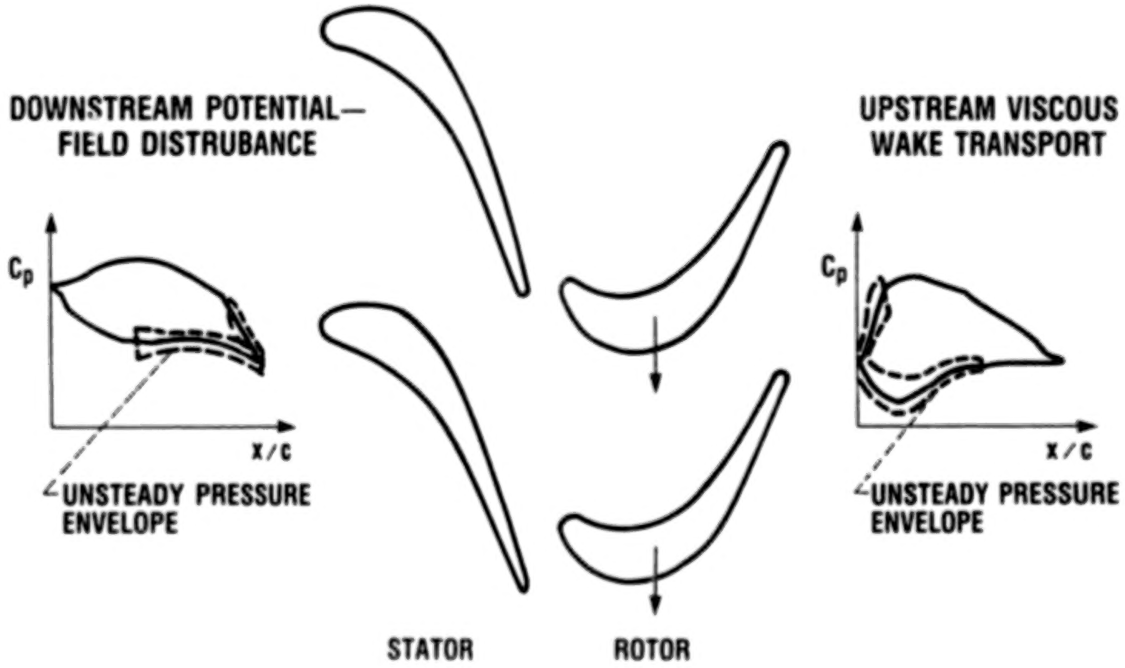
DOWNSTREAM POTENTIAL—FIELD DISTRUBANCE
UPSTREAM VISCOUS WAKE TRANSPORT
C_p
X/C
UNSTEADY PRESSURE ENVELOPE
C_p
X/C
UNSTEADY PRESSURE ENVELOPE
STATOR
ROTOR

CD-88-31813

UNSTEADINESS DUE TO AERODYNAMIC INTERACTION

The presence of adjacent rotating and stationary blade rows is inherently a source of complex, nonsteady flow conditions. Two of the more dominant aerodynamic interaction effects are due to the viscous wake shedding and the pressure-field interaction problem. A complete experimental study of these two interaction effects has been reported by Dring et al. (1982).

The upstream blade row generates a viscous wake flow disturbance which is convected downstream to a blade row moving relative to the wake. As the wake passes through the downstream blade passage, it distorts and causes unsteady surface pressures, which lead to unsteady loads. The wake shedding influence may persist far downstream within the machine.

The aft blade row represents a blockage to the primary flow field, which causes a fluctuation in the pressure field. This pressure field unsteadiness affects the flow characteristics within the upstream blade row. The influence of the pressure field interaction diminishes rapidly as the axial spacing is increased.

STEADY MEAN FLOW ANALYSIS

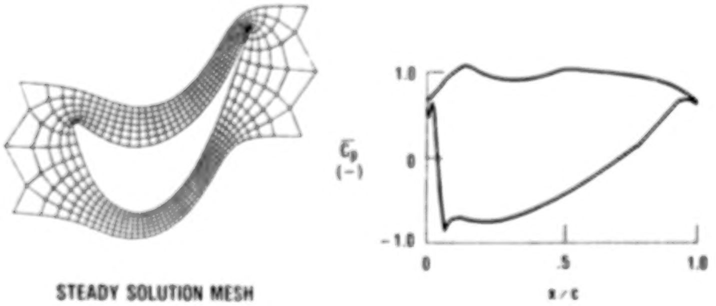

STEADY SOLUTION MESH

UNSTEADY OSCILLATORY FLOW ANALYSIS

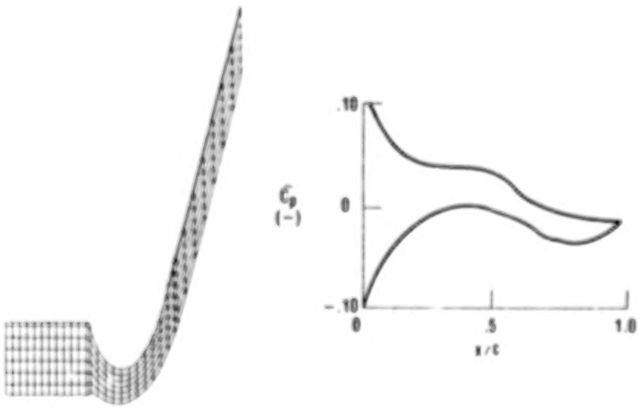

UNSTEADY SOLUTION MESH

CD 88 31629

UNSTEADY BLADE LOADS

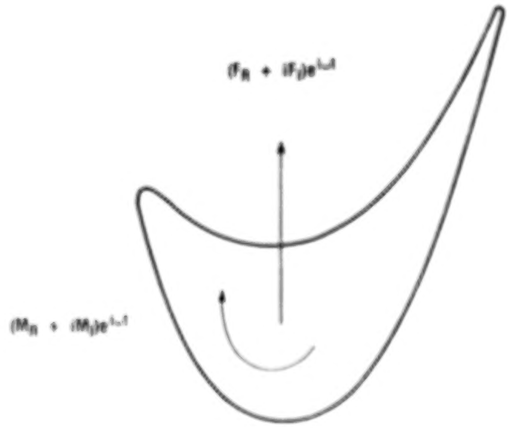

CD 88 31630

UNSTEADINESS DUE TO OSCILLATING BLADE MOTION

The traditional small-disturbance strip theories are not applicable for predicting the unsteady flow in thick, cambered turbine blade passages. Newly developed aerodynamic tools (Verdon and Caspar, 1984) are being used to predict the steady and unsteady pressures and loads caused by turbine blade airfoil oscillations. These aerodynamic models allow for the prediction of unsteady flow behavior over a range of subsonic and transonic flow conditions.

CASCADE MODEL

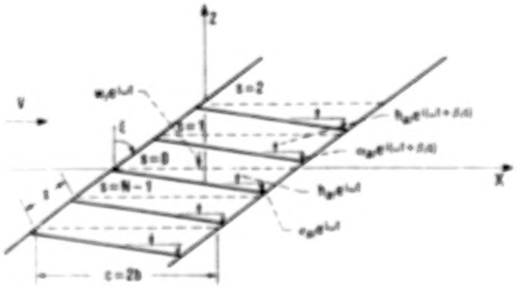
Z
V
X
s = 2
s = 1
s = 0
s = N − 1
c = 2b
ξ
s
$h_{\alpha}e^{i(\omega t+\beta_s)}$
$\alpha_{\alpha}e^{i(\omega t+\beta_s)}$
$h_{\alpha}e^{i\omega t}$
$\alpha_{\alpha}e^{i\omega t}$

FINITE ELEMENT MODAL ANALYSIS

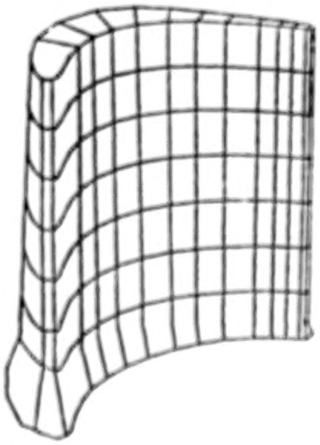

2-DOF OSCILLATOR

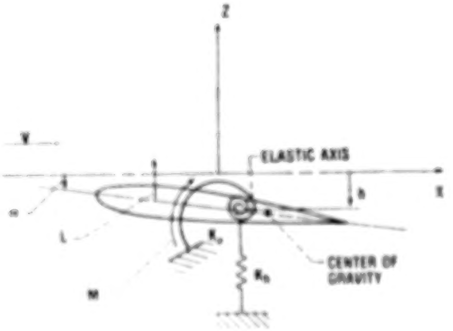
Z
V
X
ELASTIC AXIS
h
α
L
M
K_{α}
K_h
CENTER OF GRAVITY

AEROELASTIC SYSTEM MODELS

The modeling techniques for the structural response of the system to the aerodynamic excitation is based on a wide range of structural models ranging from simple two-DOF lumped parameter models, to cascaded blade models, up to highly refined finite-element modal analysis techniques. Example applications of these aercelastic models have been presented by Kielb and Kaza (1982) and Kaza et al. (1987).

- **FREPS SYSTEM COUPLES AEROELASTIC, UNSTEADY AERODYNAMIC, AND FORCING FUNCTION MODELS**
- **EMPHASIS ON DEVELOPMENT OF CORRELATIONS TO MODEL AERODYNAMIC FORCING FUNCTIONS**
- **ADVANCES IN CFD ARE REQUIRED TO BETTER MODEL AERODYNAMIC INTERACTION BETWEEN BLADE ROWS**

CD-88-?1895

SUMMARY

An introduction has been presented to the research activity under way to enable the prediction of turbomachinery aeroelastic forced response. An effort is being made to assemble a computer program (FREPS) which incorporates the aeroelastic structural models, unsteady aerodynamic models, and forcing function models. The structural and aerodynamic models are currently well developed. The forcing function models are currently at a primitive level.

A significant activity has begun to identify the forcing functions due to stator-rotor aerodynamic interaction. This is a formidable task which requires the use of advanced computational fluid dynamic programs. The results from these CFD predictions will be combined into "semiempirical" correlations which are more amenable for inclusion within the aeroelastic analysis models.

REFERENCES

Dring, R.P., Joslyn, H.D., Hardin, L.W., and Wagner, J.H., 1982, "Turbine Rotor-Stator Interaction," Journal of Engineering for Power, Vol. 104, p. 729.

Kaza, K.R.V., Mehmed, O., Narayanan, G.V., and Murthy, D.V., 1987, "Analytical Flutter Investigation of a Composite Propfan Model," AIAA Paper 87-0738, Presented at the AIAA/ASME/ASEE/AHS 28th Structures, Structural Dynamics, and Materials Conference, Monterey, CA.

Kielb, R.E., and Kaza, K.R.V., 1982, "Aeroelastic Characteristics of a Cascade of Mistuned Blades in Subsonic and Supersonic Flows," Journal of Vibration, Acoustics, Stress, and Reliability in Design, Vol. 105, p. 425.

Moss, L.A., and Smith, T.E., 1987, "SSME Single Crystal Turbine Blade Dynamics," NASA CR-179644.

Verdon, J.M., and Caspar, J.R., 1984, "A Linear Aerodynamic Analysis for Unsteady Transonic Cascades," NASA CR-3833.

N88-23248

REDUCED ORDER MODELS FOR NONLINEAR AERODYNAMICS

Aparajit J. Mahajan,
Earl H. Dowell,
and
Donald B. Bliss

Department of Mechanical Engineering
and Materials Science
Duke University
Durham, North Carolina 27706

ABSTRACT

Reduced order models are needed for reliable, accurate and efficient prediction of aerodynamic forces to analyze fluid-structure interaction problems in turbomachinery including prop fans. The phenomenological models, though efficient, require a large amount of experimental data for verification and are not always accurate. The models based on first principles of fluid mechanics, such as Navier-Stokes methods, are accurate but computationally expensive and difficult to integrate with structural mechanics models to obtain an interdisciplinary prediction capability. In the present work, a finite difference, time marching Navier-Stokes code is validated for unsteady airfoil motion by comparing with classical potential flow results. The Navier-Stokes code is then analyzed for calculation of primitive and exact estimates of eigenvalues and eigenvectors associated with fluid-airfoil interaction. A variational formulation for the Euler equations and Navier-Stokes equations will be the basis for reduction of order through an eigenvector transformation. This will help identify and exploit the relationships between the simpler phenomenological models and those based on first principles of fluid mechanics.

PRECEDING PAGE BLANK NOT FILMED

Grant : NAG3 - 724, NASA Lewis technical monitor : Dr. Krishna Rao V. Kaza

Analysis of fluid-structure interaction problems in turbomachinery requires an accurate knowledge of fluid properties and forces (Dowell, 1978). Some unique features of propfans preclude the use of existing aeroelastic technology of conventional propellers, turbofans and helicopters. The accurate and efficient prediction of aerodynamic forces in nonlinear regimes, such as separated, transonic flows, is important for aeroelastic analysis of propfans (especially stall flutter, whirl flutter).

THE NEED FOR REDUCED ORDER MODELS

-Accurate prediction of aerodynamic forces is required for aeroelastic response and flutter analysis
  -Low angles of attack - linear relationship
  -High angles of attack - nonlinear relationship
    stall and dynamic stall
    separated flow

-Theoretical Approaches
  -Methods - Navier-Stokes
    discrete vortex
    zonal methods
  -Limitations - computationally expensive
    lack of generality
    difficult to use in routine aeroelastic analysis

-Reduced Order Models
  -Methods - empirical / semi-empirical
    new methods based on first principles
  -Advantages - computationally fast
    easily used in routine aeroelastic analysis
    allow for various airfoil motions and flow conditions

The nonlinear relationship between lift (also moment) and angle of attack is modelled in various ways. The easiest and most popular way is curve-fitting experimental data with algebraic or transcendental functions which represent qualitative approximations to physical behavior. Ordinary differential equations are also used to represent the lift-angle of attack relationship. These models are derived empirically or semi-empirically and have no direct relation to first principles of fluid mechanics.

The Navier-Stokes methods and Euler methods to calculate flow over airfoils are based on finite difference and/or finite elements techniques and involve a large number of degrees of freedom, depending on the grid/elements setup. The nonlinear equations of fluid mechanics are solved with linearized solution methods, such as approximate factorization, alternate direction implicit procedure, etc. Reduction in the number of degrees of freedom can be achieved by identifying the important or dominant modes and then writing the system of equations in terms of these modes.

AD HOC MODELS

Different ways to model nonlinearity in lift and moment.

- **-corrected angle of attack methods.**
- **-time-delay methods, synthesis procedures.**
- **-ordinary differential equation methods.**

FIRST PRINCIPLE MODELS

Flow over airfoils calculated using Navier-Stokes methods or Euler methods.

Identify/recognize the important or dominant modes. Write the system of equations in terms of dominant modes.

For development of a reduced order model, a Navier-Stokes code capable of calculating unsteady, transonic and separated flows for different airfoil motions, such as pitching and plunging, was required. A finite difference, time marching code developed by Sankar and Tang (1985) was selected. This code solves the unsteady, two-dimensional Navier-Stokes equations on a body-fitted moving coordinate system in a strong conservative form using the ADI procedure. The convective terms are treated implicitly and the viscous terms are treated explicitly. The code was modified to include step change response. The results from the code for inviscid flow were in reasonable agreement with classical potential flow results.

NAVIER-STOKES CODE MATHEMATICAL FORMULATION

$$(x,y,t) \rightarrow (\xi,\eta,\tau)$$

$$\xi = \xi(x,y,t), \quad \eta = \eta(x,y,t), \quad \tau = \tau(t)$$

Transformed Navier-Stokes Equations:

$$\tilde{q}_\tau + \tilde{F}_\xi + \tilde{G}_\eta = \tilde{R}_\xi + \tilde{S}_\eta$$

where $q = (\rho, \rho u, \rho v, e)$

$$F = (\rho u, \rho u^2+p, \rho uv, u(e+p))$$

$$G = (\rho v, \rho uv, \rho v^2+p, v(e+p))$$

$$R = (0, \tau_{xx}, \tau_{xy}, R_4)$$

$$S = (0, \tau_{xy}, \tau_{yy}, S_4)$$

$$R_4 = u\,\tau_{xx} + v\,\tau_{xy} + K\,(a^2)_x$$

$$S_4 = u\,\tau_{xy} + v\,\tau_{yy} + K\,(a^2)_y$$

Variational formulations not only concentrate all of the intrinsic features of the problem (governing equations, boundary conditions, initial conditions and constraints) in a single functional, but also provide a natural means for approximation. In solid mechanics, a variational formulation is easy to obtain. However, in fluid mechanics, use of an Eulerian reference frame and the nonlinearity in the expression for conservation of momentum make a variational formulation very difficult to obtain. Extremization of an energy functional has been formulated in the literature (Oden and Reddy, 1983, Girault and Raviart, 1986, Temam, 1984) for the cases listed below. The approximate variational formulations are used in methods of weighted residuals, collocation methods, Galerkin's method, least-squares methods and semi-discrete methods.

VARIATIONAL FORMULATIONS

-Inviscid potential flow

- -incompressible flow (linear elliptic p.d.e.).
- -compressible flow
    - -subsonic (small-disturbance equation).
    - -transonic (slender body assumption).

-Euler equations

- -unsteady, compressible form.

-Navier-Stokes equations

- -Stokes' problem.
- -steady, incompressible N-S equations.
- -unsteady, incompressible N-S equations.
- -stream function-vorticity formulation.

To determine primitive modes, the airfoil is oscillated at different frequencies about several steady angles of attack with various amplitudes of oscillation. Primitive modes are amplitudes and phase differences for (ρ, ρu, ρv, e) over the entire grid. For the Euler Solution, the primitive modes are independent of oscillation amplitude, sufficiently far away from the airfoil.

To detrmine exact modes, an eigenvalue problem is formulated for the Navier-Stokes code. This eigenproblem is then solved to determine the exact eigenvalues and eigenmodes.

EIGENVALUE PROBLEM FORMULATION

$$\tilde{q}_\tau + \tilde{F}_\xi + \tilde{G}_\eta = \tilde{R}_\xi + \tilde{S}_\eta$$

$\tilde{F}, \tilde{G}, \tilde{R}, \tilde{S}$ are functions of $\tilde{q}$.

$$\begin{aligned}\tilde{q}_\tau &= -\tilde{F}_\xi - \tilde{G}_\eta + \tilde{R}_\xi + \tilde{S}_\eta \\ &= \tilde{Q}\,(\tilde{q})\end{aligned}$$

Substitute $\tilde{q} = \bar{q} + \hat{q}$

$\bar{q}$: steady state value, $\hat{q}$: small perturbation.

$$\hat{q}_\tau = \tilde{Q}\,(\bar{q}) + \frac{d\tilde{Q}}{d\tilde{q}}_{\bar{q}}\,\hat{q}$$

$$\hat{q}_\tau = \frac{d\tilde{Q}}{d\tilde{q}}_{\bar{q}}\,\hat{q}$$

Substitute $\hat{q} = q\,e^{\lambda t}$

$$\lambda\, q\, e^{\lambda\tau} = \frac{d\tilde{Q}}{d\tilde{q}}_{\bar{q}}\, q\, e^{\lambda\tau}$$

$$\lambda \{q\} = [A]\{q\}$$

A is a sparse, real, nonsymmetric matrix of order N, where
N = 4 x total number of grid points.
≈ 24000.

The state of the art software available for an eigenvalue calculation is NOT capable of storing a 24000 x 24000 matrix or utilizing the sparsity and nonsymmetry of the present problem for obtaining a solution in a reasonable computer time. A procedure was developed to exploit the sparsity of the matrix for storage and calculation purposes. A modified Lanczos recursive procedure with no reorthogonalization is used to calculate eigenvalues (Cullum and Willoughby, 1986). These eigenvalues are found to be independent of the starting vectors used in the recursion.

Below are shown preliminary results from this eigenvalue calculation for different values of explicit and implicit damping in the Navier-Stokes code for NACA 0012 airfoil at M = 0.8, α = 0 using the Euler equations. The addition of artficial damping to the governing equations in the N-S code appears to change unstable eigenvalues into stable ones. Also the N-S code was able to calculate the time history of flow over the airfoil with artificial damping, but failed without this damping.

Eigenvalues for NACA 0012 at M = 0.8, α = 0.
(Euler Solution)

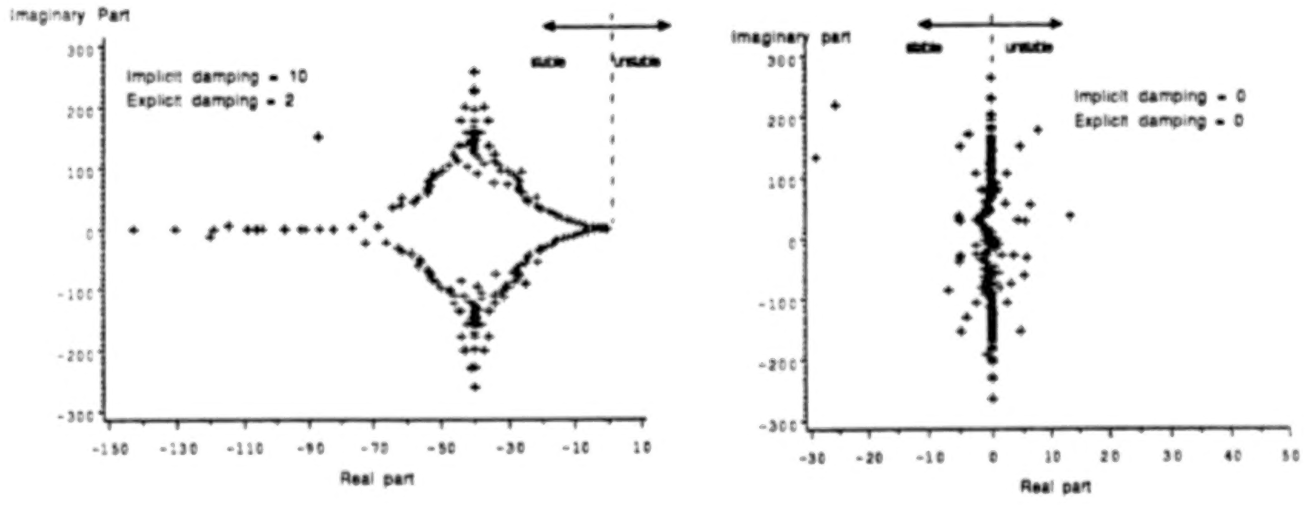

Transformation of the system from physical coordinates to modal coordinates using the classical or approximate variational formulation for flow over an airfoil can be done as shown below. The dominant eigenmodes are used for this transformation. This transformation reduces the order of the fluid-airfoil system. For example, a single modal coordinate equation can then be compared to a simple phenomenological model represented by an ordinary differential equation.

CONSTRUCTION OF REDUCED ORDER MODEL USING EIGENVALUES AND VARIATIONAL PRINCIPLE

Variational principle in physical coordinates:

$$\int [L(q)] \{\delta q\} \, dt = 0$$

Eigenvector transformation:

$$\{q\} = [E] \{a\}$$

Variational principle in modal coordinates:

$$\int [L(a)] [E] \{\delta a\} \, dt = 0$$

(set all $a_i = o$ for $i > N$)

From the preliminary results obtained in the present research effort, fluid-structure interaction problems can be analyzed using the modal behavior of the fluid. There is a strong relationship between the eigenvalues associated with the fluid and the damping present in the N-S code. Further study of eigenmodes will help understand the complex fluid-structure interaction on a modal basis and offers substantial potential for solving various other problems involving fluid forces.

SUMMARY OF RESULTS TO DATE

Survey of empirical and semi-empirical reduced order models.

Validation of N-S code for transient time responses.

Formulation of the eigenvalue problem using the finite difference code and calculation procedure for eigenvalues.

Assessment of potential for reduction of order using primitive modes and exact eigenmodes.

REFERENCES

Cullum, J. and Willoughby, R. A., "A Practical Procedure for Computing Eigenvalues of Large Sparse Nonsymmetric Matrices," Large Scale Eigenvalue Problems, J. Cullum and R. A. Willoughby, ed., Elsevier Science Publishers, New York, NY, 1986, pp. 193-240.

Dowell, E. H., "A Modern Course in Aeroelasticity," Kluwer Academic Publishers, The Netherlands, 1978.

Girault, V. and Raviart, P., "Finite Element Methods for Navier-Stokes Equations," Springer-Verlag, New York, NY, 1986.

Oden, J. T. and Reddy, J. N., "Variational Methods in Theoretical Mechanics," Springer-Verlag, New York, NY, 1983.

Sankar, N. L. and Tang, W., "Numerical Solution of Unsteady Viscous Flow Past Rotor Sections," AIAA Paper 85-0129, Jan. 1985.

Temam, R., "Navier-Stokes Equations," Elsevier Science Publishers, New York, NY, 1984.

N88-23249

APPLICATION OF NAVIER-STOKES ANALYSIS TO STALL FLUTTER*

J.C. Wu, R. Srivastava, and L.N. Sankar
Georgia Institute of Technology
Atlanta, GA

ABSTRACT

A solution procedure has been developed to investigate the two-dimensional, one- or two-degree-of-freedom flutter characteristics of arbitrary airfoils. This procedure requires a simultaneous integration in time of the solid and fluid equations of motion. The fluid equations of motion are the unsteady compressible Navier-Stokes equations, solved in a body-fitted, moving coordinate system using an approximate factorization scheme. The solid equations of motion are integrated in time using an Euler implicit scheme. Flutter is said to occur if small disturbances imposed on the airfoil attitude lead to divergent oscillatory motions at subsequent times.

The flutter characteristics of airfoils in subsonic speed at high angles of attack and airfoils in high subsonic and transonic speeds at low angles of attack are investigated. The stall flutter characteristics were also predicted using the same procedure. Results of a number of cases are included and compared with numerical and experimental data where available. The effects of mass ratio, initial perturbation, mean angle of attack, viscosity, and shape and thickness, on the flutter boundary are also investigated.

---

*This work was performed under NASA Grant NAG 3-730. The authors acknowledge Drs. K.R.V. Kaza and T.S.R. Reddy for the technical discussions and their suggestions.

GOVERNING EQUATIONS

The fluid equations of motion used in the present formulation are the compressible Navier-Stokes equations. These equations are written below in a conservative form. These are solved in a body-fitted, moving coordinate system using an appropriate factorization scheme.

$$\delta_t q + \delta_x E + \delta_y F = Re^{-1}(\delta_x R + \delta_y S)$$

WHERE

$$q = \begin{bmatrix} \rho \\ \rho u \\ \rho v \\ e \end{bmatrix}, \quad E = \begin{bmatrix} \rho u \\ \rho u^2 + P \\ \rho uv \\ u(e + P) \end{bmatrix}, \quad F = \begin{bmatrix} \rho v \\ \rho uv \\ \rho v^2 + P \\ v(e + P) \end{bmatrix}, \quad R = \begin{bmatrix} 0 \\ \tau_{xx} \\ \tau_{xy} \\ R_4 \end{bmatrix}, \quad S = \begin{bmatrix} 0 \\ \tau_{xy} \\ \tau_{yy} \\ S_4 \end{bmatrix}$$

STRUCTURAL MODEL FOR 2-DOF SYSTEM

The structural dynamic model considered is a 2-DOF (pitching and plunging motion) system. An Euler implicit scheme was used to integrate the structural governing equation. The fluid and the solid equations were simultaneously integrated in time to monitor how lift, moment, and drag vary with time.

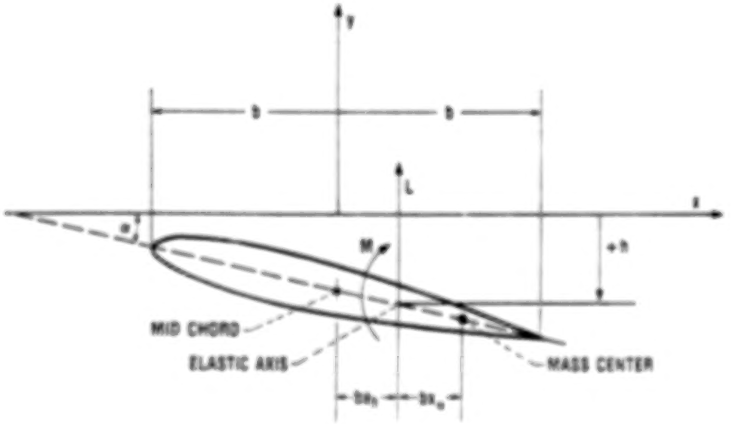
y
b
b
L
x
α
M
+h
MID CHORD
ELASTIC AXIS
MASS CENTER
ba_h
bx_α

GOVERNING EQUATION OF THE 2-DOF STRUCTURAL MODEL

$$I\ddot{\alpha} + S\ddot{h} + g_\alpha\dot{\alpha} + K_\alpha\alpha = M(t)$$

$$m\ddot{h} + S\ddot{\alpha} + g_h\dot{h} + K_h h = -L(t)$$

- EULER IMPLICIT SCHEME FOR $\dot{h}$, $\ddot{h}$, etc.

$$\dot{h} = \frac{h^{n+1} - h^n}{\Delta t}, \qquad \ddot{h} = \frac{h^{n+1} - 2h^n + h^{n-1}}{\Delta t^2}$$

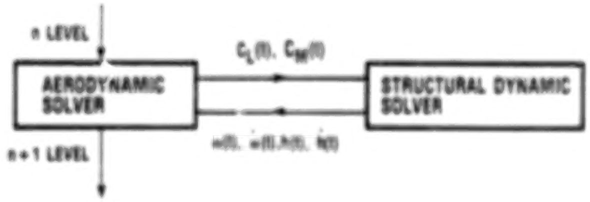
n LEVEL
$C_L(t)$, $C_M(t)$
AERODYNAMIC SOLVER
STRUCTURAL DYNAMIC SOLVER
$\alpha(t)$, $\dot{\alpha}(t)$, $h(t)$, $\dot{h}(t)$
n+1 LEVEL

COMPARISONS OF UNSTEADY AIRLOADS ON A NACA 0012 AIRFOIL EXPERIENCING DYNAMIC STALL

The present Navier-Stokes solver is able to obtain time-accurate results in highly separated flows. The lift, drag, and moment hysteresis loops are shown here and compared with experiments by McAlister et al (1982). The case is shown of a NACA 0012 airfoil oscillating in pitch with the mean angle of oscillation 15 degrees and 10 degrees of amplitude of oscillation. The solver correctly predicts (1) the near-linear increase in lift during the upstroke; (2) the dynamic stall which causes rapid variations in lift, drag, and moment alike; and (3) the post stall recovery phase of the flow during the downstroke.

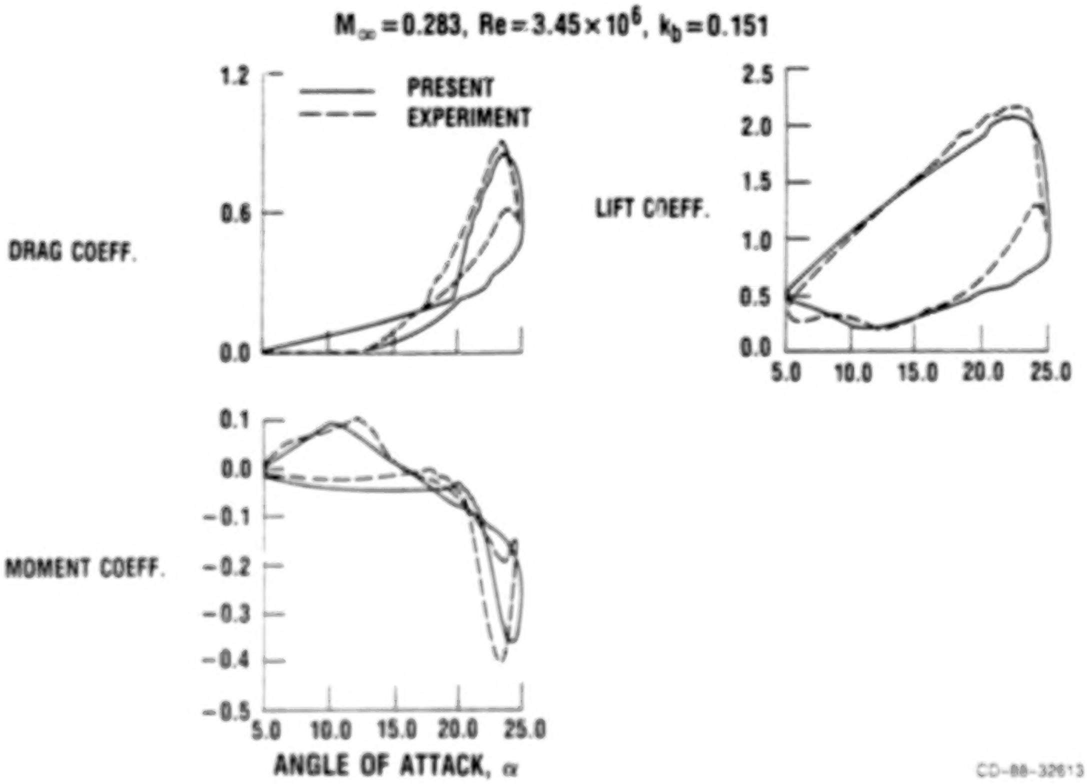
$M_\infty = 0.283$, $Re = 3.45 \times 10^6$, $k_b = 0.151$

CD-88-32613

VARIATION OF LIFT AND PITCHING MOMENT COEFFICIENT FOR PLUNGING MOTION

The present code's ability to handle unsteady, transonic flows in a time-accurate manner is illustrated in the figure below. The case is shown of a NACA 64A010 airfoil oscillating sinusoidally in plunge at a free stream Mach number of 0.8 at zero mean angle of attack. The lift and pitching moment history are plotted as a function of phase, and are compared with the Euler calculations performed by Steger (1978). Very good agreement is observed between the two solvers.

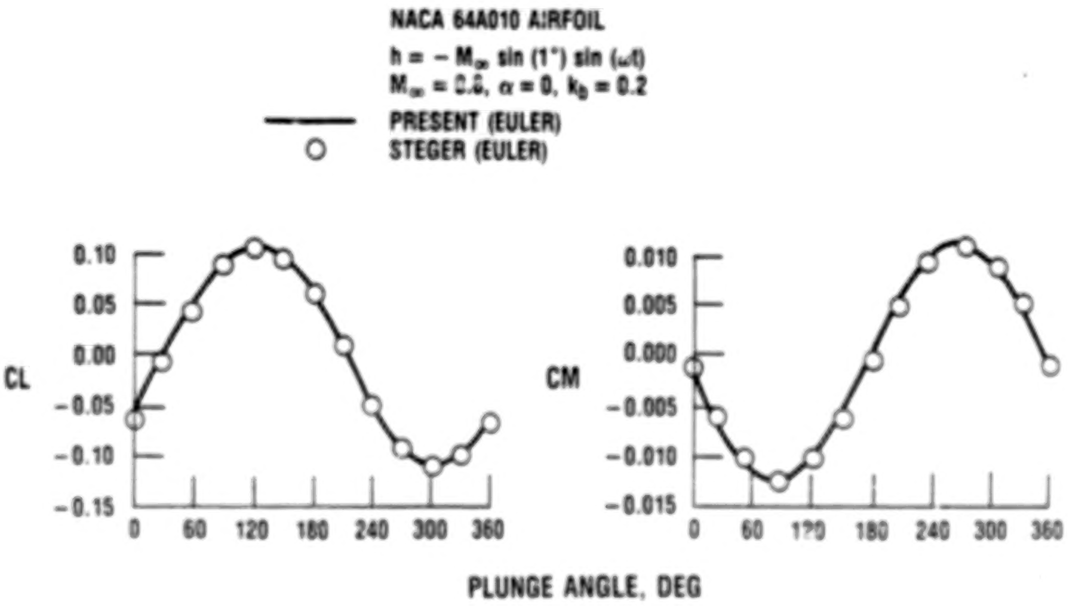

CD-88-32614

EFFECTS OF AIRFOIL-AIR MASS RATIO ON FLUTTER SPEED

The present technique for the prediction of stall flutter was validated for transonic flutter calculations where reliable numerical solutions exist. The airfoil is a NACA 64A006 airfoil at a free stream Mach number 0.85, and the flow was assumed to be inviscid. The flutter speed predicted by the present theory is plotted as a function of the airfoil-air mass ratio (Wu et al., 1987). For comparison, the results from the LTRAN2 and UTRANS2 (Ballahus, 1978) and UTRANS2 (Farr et al., 1974) codes are shown. It is seen that the Euler results agree very well with the prediction of the UTRANS2 code, while only a qualitative agreement between the present results and the LTRAN2 code could be found.

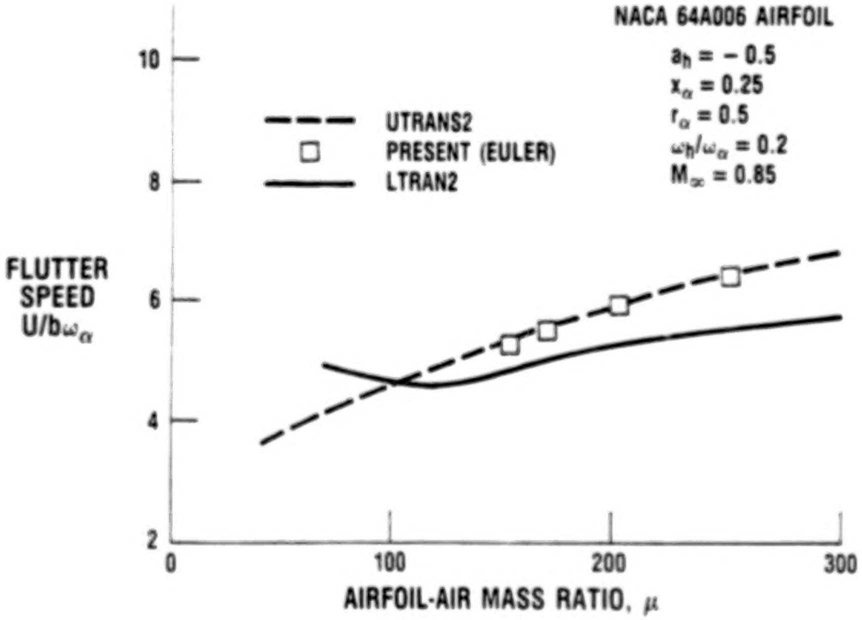

CD-88-32615

RESPONSES OF THE 2-DOF SOLID-FLUID SYSTEM AS A FUNCTION OF TIME

The following figure illustrates the time responses of a 2-DOF flutter calculation. The flow is assumed to be inviscid at free stream Mach number 0.85. A NACA 64A006 airfoil was released after the forced sinusoidal oscillation and was allowed to follow pitching and plunging motions dictated by the structural dynamic equations. By parametrically varying the airfoil air mass ratio during this phase of the calculations, it led to damped oscillations, neutral oscillations, stable oscillations, or divergent (flutter) oscillations.

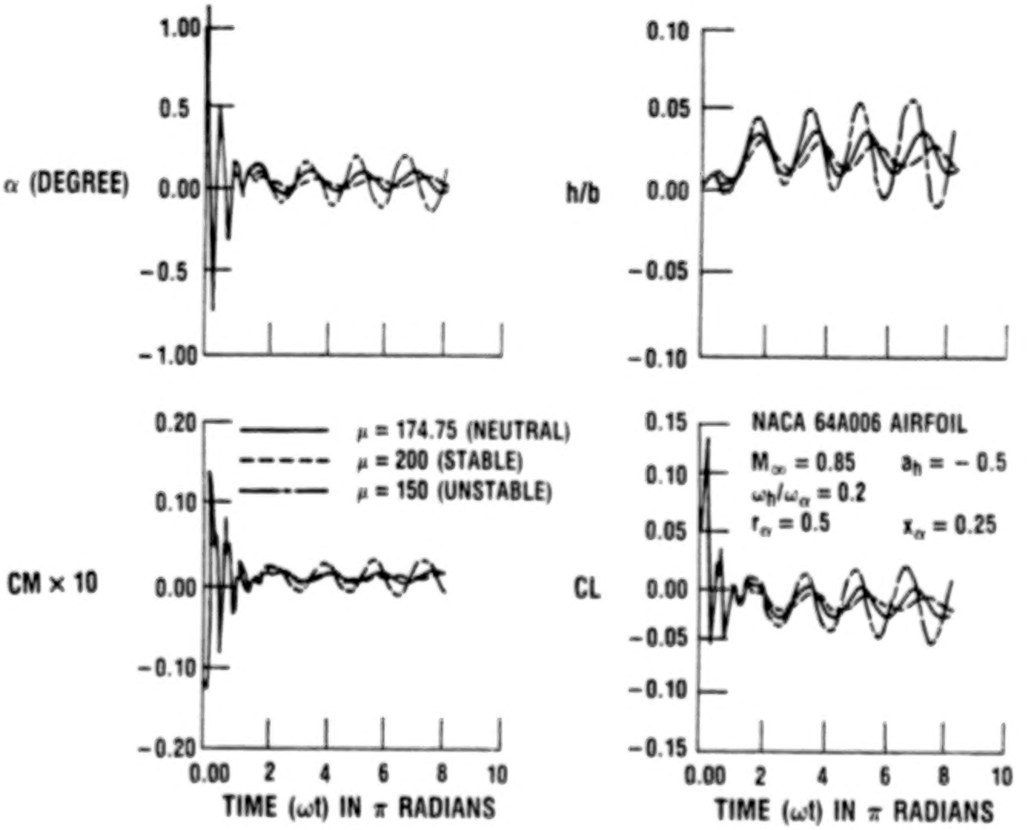

CD-88-32616

EFFECTS OF VISCOSITY ON THE TIME RESPONSE

The effect of flow viscosity on the flutter characteristics for a 2-DOF system was studied using the present solver operating in the Navier-Stokes mode. The airfoil is a NACA 64A006 airfoil at a free stream Mach number 0.85. Viscous solution corresponds to a Reynolds number of 9×10^6. The flutter boundaries predicted by the viscous and inviscid calculations were within 2 percent of each other, which means that in high Reynolds number transonic flutter studies, inviscid calculations would suffice.

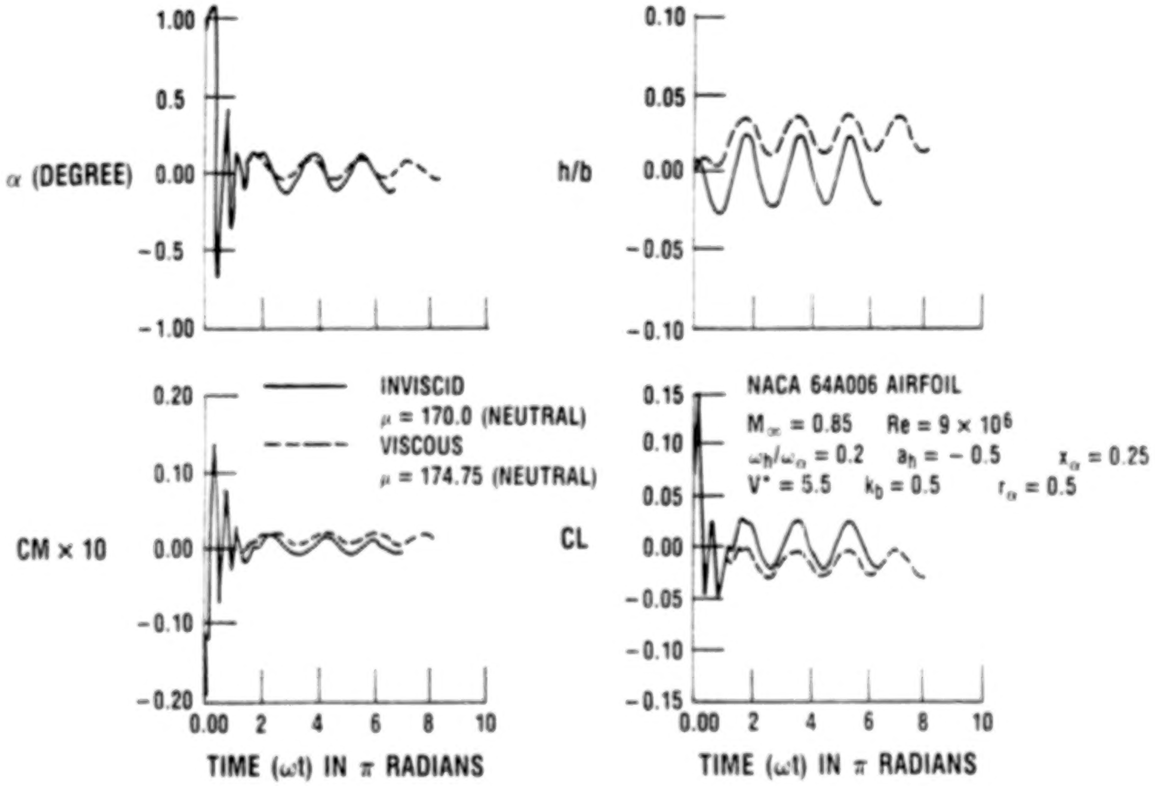

CD-88-32617

TIME RESPONSES OF A 2-DOF SYSTEM EXPERIENCING STALL FLUTTER

The stall flutter calculations are carried out using the Navier-Stokes/structural dynamics solver. The case considered was a NACA 0012 airfoil, initially subjected to a sinusoidal pitching oscillation between 5 and 25 degrees. During the downstroke, around 23.8 degrees, the airfoil was released and was allowed to follow a pitching and plunging motion dictated by the structural dynamic equations. Two dimensionless speeds V*, 4 and 8, were considered. At the lower speed, the airfoil began to undergo a damped sinusoidal oscillation and reached a stable condition eventually. The time history for the speed V* equal to 8, however, showed a rapidly growing oscillating motion indicative of dynamic stall flutter.

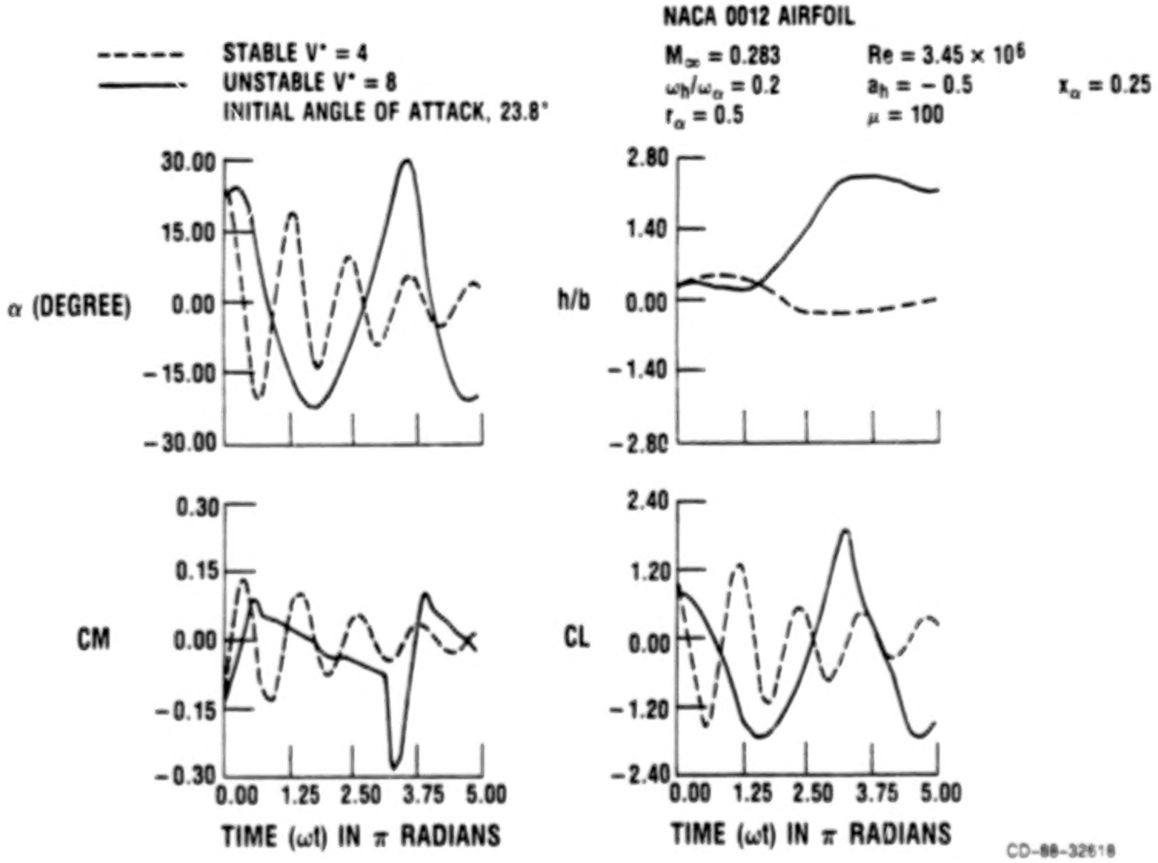

CD-88-32618

COMPARISON OF CALCULATED FLUTTER BOUNDARIES

A comparison of flutter boundaries with the boundaries obtained by various codes presented by Bendikson et al. (1987) is shown below. Two artificial viscosity models were used in the present calculations (Reddy et al., 1988). The artificial viscosity in the present code is based on pressure gradient. In model 1, the pressure gradient was scaled by a constant coefficient, whereas in model 2, it was scaled by the spectral radius.

The rotational effects of the flow behind the shock wave have strong effect on the transonic flutter speed, depending on the chordwise location of the shock. Neglecting the flow rotation effects results in predicting a higher flutter speed.

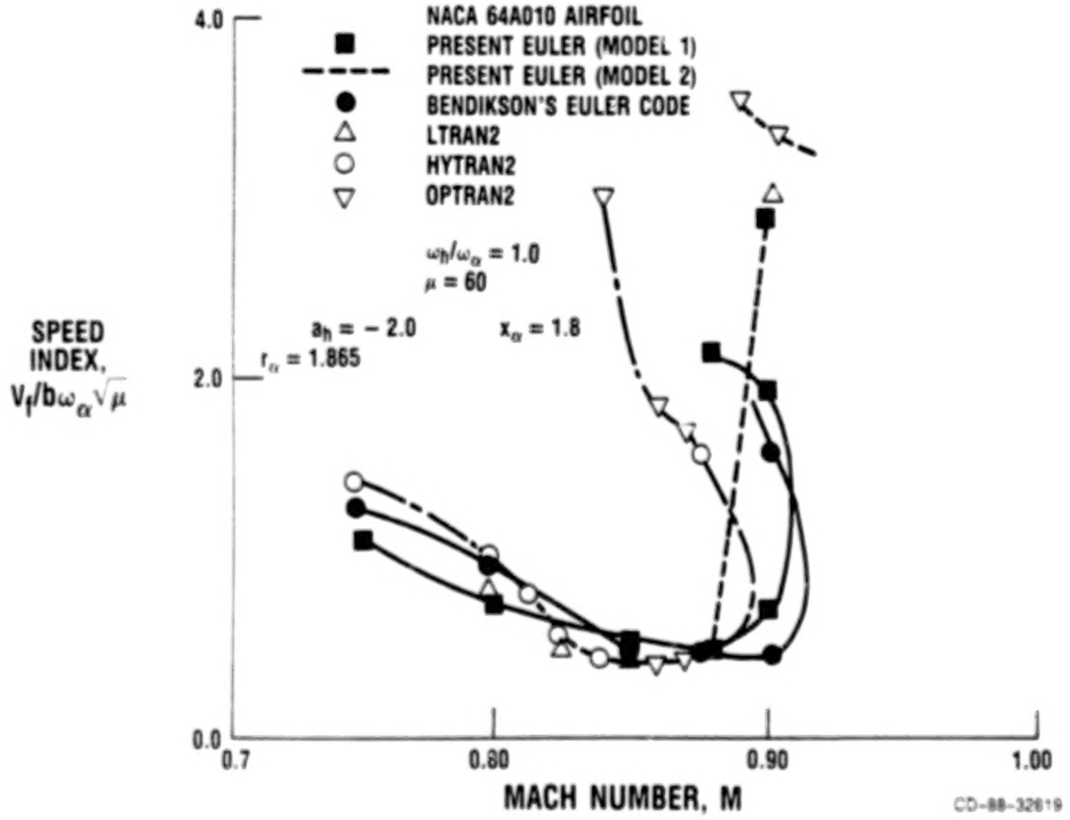

EFFECT OF MEAN ANGLE OF ATTACK, INITIAL PERTURBATION, AND VISCOSITY ON THE FLUTTER BOUNDARY

The effect of initial perturbation, mean angle of attack, and viscosity are shown in the figure below.

The effects of initial conditions, mean angle of attack, and viscosity on the minima of the transonic dip seem negligible. However, they have a significant effect away from the dip. Similar results for mean angle of attack were obtained by Edwards et al. (1983).

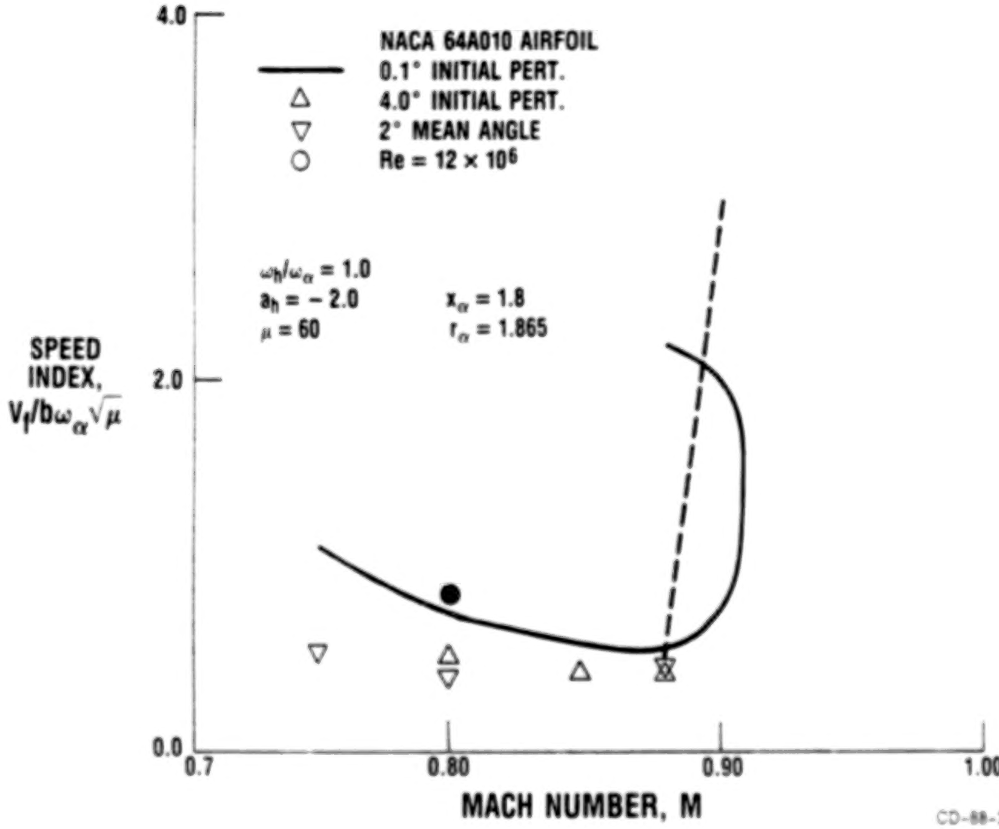

CD-88-32620

EFFECT OF AIRFOIL SHAPE AND THICKNESS ON THE FLUTTER BOUNDARY

The blade thickness and shape dictate the location and strength of shock, thereby affecting the flutter boundary. The transonic dip shifts to higher Mach numbers for symmetric airfoils with decreasing airfoil thickness to chord ratios. For very thin cambered airfoils, the transonic dip occurs at lower Mach numbers.

This effect is shown in this figure.

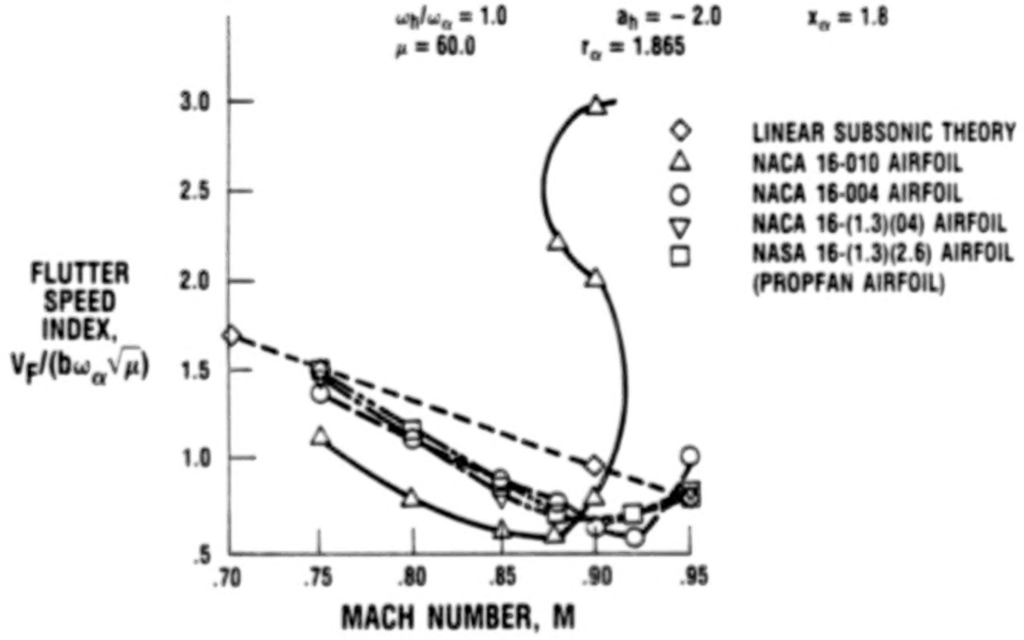

CD-88-32621

FLUTTER BOUNDARY FOR A SIMULATED SR5 TYPICAL SECTION STRUCTURAL MODEL

This figure shows the predicted flutter boundary of a simulated typical section model of an SR5 propfan blade. The flutter Mach number predicted by the present code is about 4.5 percent lower than that predicted by linear theory and experiment. This difference could be attributed to the simplified aeroelastic model used in the present analysis.

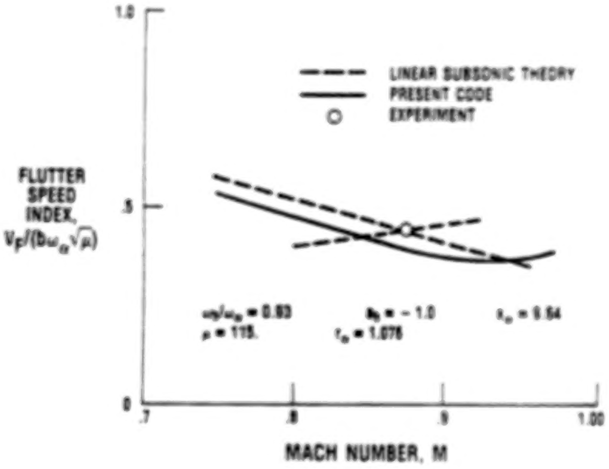

REFERENCES

Ballahus, W.F., and Goorjian, P.M., 1987, "Computation of Unsteady Transonic Flow by the Implicit Method," AIAA Journal, Vol. 16, No. 2, pp. 117-124.

Bendikson, O.O., and Kousen, K.A., 1987, "Transonic Flutter Analysis Using the Euler Equations," AIAA Paper No. 87-0911-CP.

Edwards, J.W., Bennett, R.M., Whitlow, W., Jr., and Seidel, D.A., 1983, "Time-Marching Transonic Flutter Solutions Including Angle-of-Attack Effects," Journal of Aircraft, Vol. 20, pp. 899-906.

Farr, J.L., Traci, R.M., and Albano, E.D., 1974, "Computer Programs for Calculating Small Disturbance Transonic Flows About Oscillating Airfoils," AFFDL-TR-74-135.

Reddy, T.S.R., Rivastava, R., and Kaza, K.R.V., 1988, "The Effects of Rotational Flow, Viscosity, Thickness, and Shape on Transonic Flutter Dip Phenomena," AIAA/ASME/ASCE/AHS 29th Structures, Structural Dynamics and Materials Conference.

Steger, J.L., 1978, "Implicit Finite Difference Simulation of Flow About Arbitrary Geometries," AIAA Journal, Vol. 15, No. 7.

Wu, J.C., Kaza, K.R.V., and Sankar, L. N., 1987, "A Technique for the Prediction of Airfoil Flutter Characteristics in Separated Flow," AIAA Paper No. 87-0910-CP.

COMPUTATIONAL METHODS FOR DYNAMICS

SESSION OVERVIEW

Louis J. Kiraly
Structural Dynamics Branch
NASA Lewis Research Center

Session 12 consists of four presentations related to computational methods for dynamics. In the first presentation a direct solution procedure for computing aeroelastic stability of propfans will be presented. This procedure, which is demonstrated using a tuned and mistuned assembly of propfan blades, has advantages over conventional computational methods because convergence is reached with only one-half the number of iterations.

The second presentation pertains to the characterization of stiffness and damping properties in structural connections. In this research, the process of combining substructuring methods with parameter identification procedures is developed. Improvements in connection properties are computed in terms of physical parameters so that the physical characteristics of the connections can be better understood.

The third presentation features a formulation for optimal shape design of elastic bodies. The formulation, which is based on the finite element method, relocates the body boundary nodes so that stresses and strains are minimized. The optimization executes automatically, alternating between evaluating element stress-strain levels and reshaping the body to the optimality criterion.

The final presentation addresses the forced response of propfan blades in yawed flow. In this work, forced response is computed by combining modal models of the blades with unsteady aerodynamic loads. An emphasis is placed on the method for computing resulting vibratory blade stresses.

COMPUTATIONAL METHODS FOR DYNAMICS

SESSION OVERVIEW
- L.J. KIRALY, CHIEF, STRUCTURAL DYNAMICS BRANCH, NASA

A COMPUTATIONAL PROCEDURE FOR AUTOMATED FLUTTER ANALYSIS
- D.V. MURTHY, STRUCTURAL DYNAMICS BRANCH, UNIVERSITY OF TOLEDO, TOLEDO, OH

CHARACTERIZATION OF STRUCTURAL CONNECTIONS FOR MULTICOMPONENT SYSTEMS
- C. LAWRENCE, STRUCTURAL DYNAMICS BRANCH, NASA
- A.A. HUCKELBRIDGE, CASE WESTERN RESERVE UNIVERSITY, CLEVELAND, OH

MIXED FINITE ELEMENT FORMULATION APPLIED TO SHAPE OPTIMIZATION
- H. RODRIGUES, UNIVERSITY OF MICHIGAN, ANN ARBOR, MI
- J. TAYLOR, UNIVERSITY OF MICHIGAN, ANN ARBOR, MI

MODAL FORCED RESPONSE OF PROPFANS IN YAWED FLOW
- G.V. NARAYANAN, SVERDRUP TECHNOLOGY, INC.

CD-88-33244

N88-23250

A COMPUTATIONAL PROCEDURE FOR AUTOMATED FLUTTER ANALYSIS

Durbha V. Murthy*
University of Toledo
Toledo, Ohio 43606

ABSTRACT

A direct solution procedure for computing the flutter Mach number and the flutter frequency is applied to the aeroelastic analysis of propfans. The procedure uses a finite element structural model and an unsteady aerodynamic model based on a three-dimensional, subsonic, compressible lifting-surface theory. An approximation to the Jacobian matrix that improves the efficiency of the iterative process is presented. The Jacobian matrix is indirectly approximated from approximate derivatives of the flutter matrix. Examples are used to illustrate the convergence properties. The direct solution procedure facilitates the automated flutter analysis and contributes to the efficient use of computer time as well as the analyst's time. Further details of the numerical procedure are given by Murthy and Kaza (1987).

---

*NASA Resident Research Associate.

MOTIVATION

Flutter of propfans and other types of turbomachinery blading is an important phenomenon that has generated considerable interest. Flutter prevention has been a significant factor in the design of propfan blades. Flutter prevention is also significant for turbomachinery, particularly for unshrouded blades. With the recent advances in computer technology, automated design of propfan and turbomachinery blades by using optimization techniques has become practical. Design optimization employing flutter constraints requires repeated solution of the aeroelastic equations of motion to obtain the flutter parameters as the design is updated. For the optimization to be performed in a realistic period of time an automated flutter analysis capability is essential. It is also desirable for the analysis to be computationally efficient in order to keep the central processing unit (CPU) time and the turnaround time within reasonable limits. Automated flutter analysis can also shorten the nonautomated design process by reducing the analyst's time.

WHY AUTOMATED FLUTTER ANALYSIS?

- ESSENTIAL FOR REPEATED EXECUTION OF FLUTTER ANALYSIS CODE

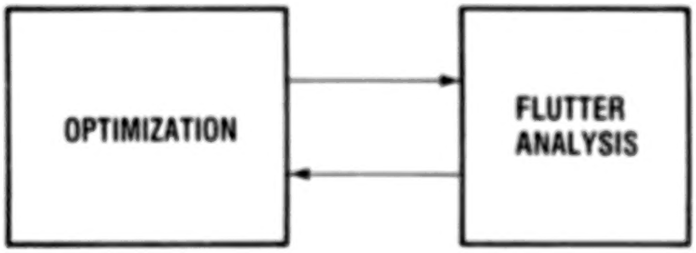

OPTIMIZATION

FLUTTER ANALYSIS

- ALSO USEFUL IN NONAUTOMATED DESIGN PROCESS

CD-88-31710

FORMULATION OF FLUTTER ANALYSIS PROBLEM

The computational procedure to be presented is applied to the analytical formulation described in detail by Kaza, et al. (1987a, 1987b). This formulation is applicable to the flutter analysis of a single-rotor propfan containing an arbitrary number of blades rotating at a fixed speed in an axial flow. The structure is modeled by finite elements. The aerodynamic model (Williams and Hwang, 1986) is based on a three-dimensional, subsonic, compressible lifting-surface theory.

For simplicity, the effect of steady deformations due to aerodynamic loads on the flutter boundary is neglected. The error introduced by ignoring the steady aerodynamic deformations is shown in Kaza, et al. (1987a) to be small enough to produce an approximate flutter point. In particular, the effect of the steady aerodynamic deformations on the flutter Mach number is not very significant. Thus the approximate flutter analysis neglecting steady aerodynamic deformations is suitable for use in design optimization procedures that require repeated efficient execution of the flutter analysis. The optimal design can be easily checked for the flutter condition by using the refined flutter analysis with steady deformations and the conventional procedure.

The propfan is assumed to have identical groups of blades symmetrically distributed about a rigid disk. The linearized aeroelastic equations of motion are then uncoupled for different intergroup phase angle modes σ_r. The flutter Mach number for the propfan is then the lowest Mach number at which one of the intergroup phase angle modes becomes unstable.

$$[M_g]\{\ddot{q}\} + [K_g]\{q\} = [A(M,\omega)]\{q\}$$

$[M_g]$	**GENERALIZED MASS MATRIX**
$[K_g]$	**GENERALIZED STIFFNESS MATRIX**
$\{q\}$	**GENERALIZED COORDINATE VECTOR**
$[A(M,\omega)]$	**GENERALIZED AERODYNAMIC MATRIX**

$[A(M,\omega)]$ IS USUALLY VALID ONLY FOR SIMPLE HARMONIC MOTION

CD-88-31711

CONVENTIONAL PROPFAN FLUTTER ANALYSIS

The conventional procedure for obtaining the flutter Mach number M_F and frequency ω_F is as follows. The aerodynamic matrix is evaluated at an assumed Mach number M_F, an assumed frequency ω_F, and an assumed interblade phase angle σ_F, and then the flutter equation is solved for all the eigenvalues ω^2. This procedure has been implemented for propfans in a program called ASTROP3. In general, these eigenvalues are complex. The real and imaginary parts of $i\omega$ represent the effective damping and frequency, respectively. The assumed frequency is varied until it is equal to the frequency corresponding to the eigenvalue with the least effective damping. This frequency matching forms the inner iteration. When this iteration reaches convergence, the Mach number is varied until the effective damping of the eigenvalue corresponding to the matched frequency is equal to zero. This forms the outer iteration. The flutter Mach number and the flutter frequency are obtained at the convergence of the outer iteration.

The conventional procedure cannot be reliably automated because it requires that the identity or ordering of the eigenvalues be preserved over a wide range of assumed frequencies and Mach numbers. Most eigensolution routines do not compute the eigenvalues in any particular order, and the sorting of eigenvalues by frequency or magnitude does not usually preserve the continuity. Loss of continuity necessitates user intervention and complicates the automated analysis. A direct solution of the flutter equation that alleviates these problems is proposed and described. It views the flutter equation as an inplicit double-eigenvalue problem.

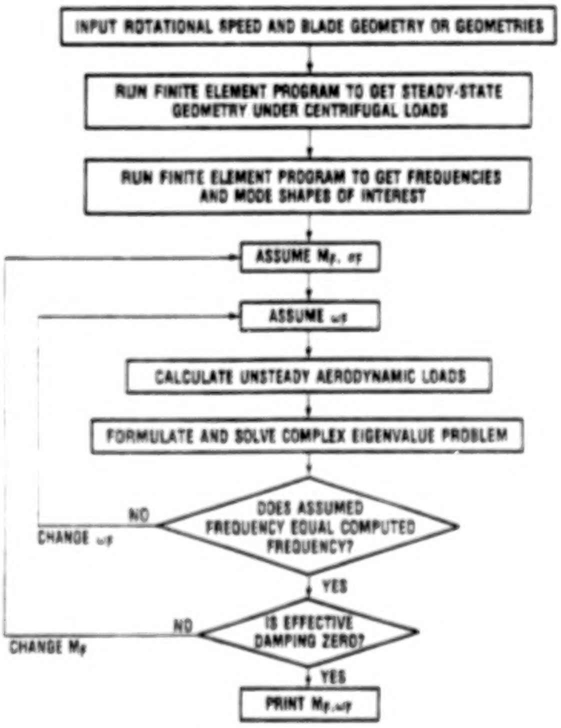
INPUT ROTATIONAL SPEED AND BLADE GEOMETRY OR GEOMETRIES
RUN FINITE ELEMENT PROGRAM TO GET STEADY-STATE GEOMETRY UNDER CENTRIFUGAL LOADS
RUN FINITE ELEMENT PROGRAM TO GET FREQUENCIES AND MODE SHAPES OF INTEREST
ASSUME M_F, σ_F
ASSUME ω_F
CALCULATE UNSTEADY AERODYNAMIC LOADS
FORMULATE AND SOLVE COMPLEX EIGENVALUE PROBLEM
DOES ASSUMED FREQUENCY EQUAL COMPUTED FREQUENCY?
NO
CHANGE ω_F
YES
IS EFFECTIVE DAMPING ZERO?
NO
CHANGE M_F
YES
PRINT M_F, ω_F

- NEEDS EIGENVALUE TRACKING AND IS THUS DIFFICULT TO AUTOMATE
- REQUIRES DOUBLE ITERATION (INNER-OUTER LOOPS)
- NEEDS AS MANY EIGENVALUES AS THERE ARE MODES

DIRECT SOLUTION OF FLUTTER EQUATION

When the dependence of the aerodynamic matrix on the assumed Mach number and frequency is considered explicitly, the flutter equation can be viewed as an implicit double-eigenvalue problem. In general, the aerodynamic matrix $[A(M_F, \omega_F]$ is a transcendental function of the assumed frequency and Mach number. Only real values of M_F and ω_F are of interest. The two eigenvalues M_F and ω_F are coupled since the aerodynamic matrix is complex.

We now have two equations in two unknowns, M_F and ω_F. These equations can be solved by any of the methods for solving a system of nonlinear equations. When they are solved for M_F and ω_F, no further iterations are required for the purpose of matching assumed and computed quantities. This procedure is illustrated below. Once M_F and ω_F are found, inverse iteration can be used to find the flutter mode.

IF M_F IS THE FLUTTER MACH NUMBER AND ω_F THE FLUTTER FREQUENCY,

$$[B]\{q_0\} = \{0\}$$

WHERE

$$[B] = -\omega_F^2[M_g] + [K_g] - [A(M_F,\omega_F)]$$

FOR A NONTRIVIAL FLUTTER MODE, WE HAVE

$$\det\{-\omega_F^2[M_g] + [K_g] - [A(M_F,\omega_F)]\} = 0$$

LET

$$\begin{aligned} D &= \det\{-\omega_F^2[M_g] + [K_g] - [A(M_F,\omega_F)]\} \\ &= D_R(M_F,\omega_F) + iD_I(M_F,\omega_F) \end{aligned}$$

WHERE D_R AND D_I ARE THE REAL AND IMAGINARY PARTS OF THE CHARACTERISTIC DETERMINANT D, RESPECTIVELY. THEN AT FLUTTER CONDITION

$$D_R(M_F,\omega_F) = 0$$

$$D_I(M_F,\omega_F) = 0$$

CD-88-31713

PROPFAN FLUTTER ANALYSIS BY DIRECT SOLUTION

In contrast to the conventional procedure the direct solution outlined here eliminates the need to track eigenvalues to determine the flutter point. In addition to this important benefit the double iteration on the complex eigensolution is replaced by a single solution of a system of two real nonlinear equations. The Mach number and frequency are varied simultaneously in this procedure rather than one at a time as in the conventional procedure. Thus the flutter Mach number and the flutter frequency are determined simultaneously.

The formulation of a transcendental double-eigenvalue problem in preference to a linear single-eigenvalue problem may seem to defeat the objective of increased efficiency, even if it is more suitable for automation. However, the price to be paid is not as great as it may seem. The transcendental eigenvalue problem needs to be solved for only one set of eigenvalues in most cases, whereas the linear eigenvalue problem has to be repeatedly solved for all the eigenvalues, which are equal in number to the number of assumed mode shapes.

The direct solution may not find the lowest flutter Mach number if more than one structural mode were to flutter in the Mach number and frequency range of interest for the selected intergroup phase angle mode. Under these circumstances one will be forced to search the entire range of interest for the roots M_F and ω_F, starting with different initial guesses. This is not amenable to an efficient automated procedure. However, it is expected that these circumstances will rarely occur for tuned or alternately mistuned propfans. This is not a major limitation for two other reasons: (1) the frequency interval in which flutter occurs is usually determined early in the design phase and (2) the search domain can be considerably reduced after a few orienting runs.

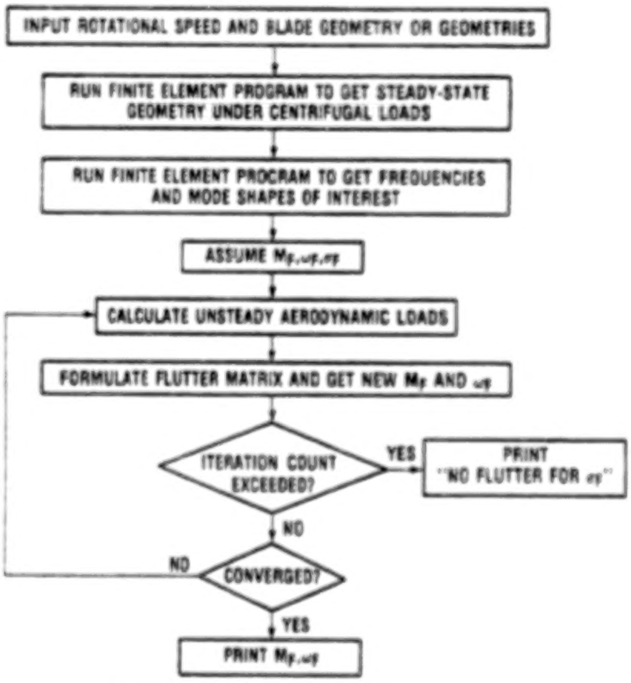
INPUT ROTATIONAL SPEED AND BLADE GEOMETRY OR GEOMETRIES
RUN FINITE ELEMENT PROGRAM TO GET STEADY-STATE GEOMETRY UNDER CENTRIFUGAL LOADS
RUN FINITE ELEMENT PROGRAM TO GET FREQUENCIES AND MODE SHAPES OF INTEREST
ASSUME M_F, ω_F, σ_F
CALCULATE UNSTEADY AERODYNAMIC LOADS
FORMULATE FLUTTER MATRIX AND GET NEW M_F AND ω_F
ITERATION COUNT EXCEEDED?
YES
PRINT "NO FLUTTER FOR σ_F"
NO
CONVERGED?
NO
YES
PRINT M_F, ω_F

- ELIMINATES EIGENVALUE TRACKING
- REQUIRES ONLY SINGLE ITERATION
- REQUIRES SOLUTION OF ONLY ONE SET OF M AND ω

CD-86-21714

NUMERICAL METHODS FOR DIRECT SOLUTION

The flutter Mach number and flutter frequency M_F and ω_F may be solved for by Newton's method. The iterative scheme for Newton's method is

$$\begin{Bmatrix} M_F \\ \omega_F \end{Bmatrix}_{(k+1)} = \begin{Bmatrix} M_F \\ \omega_F \end{Bmatrix}_{(k)} - [J_k]^{-1} \begin{Bmatrix} D_R \\ D_I \end{Bmatrix}_{(k)}$$

where k is the iteration number and $[J_K]$ is the Jacobian matrix given by

$$[J_k] = \begin{bmatrix} D_{kR,M_F} & D_{kR,\omega_F} \\ D_{kI,M_F} & D_{kI,\omega_F} \end{bmatrix}$$

The Jacobian $[J_k]$ is expensive to compute because the evaluation of the aerodynamic matrix $[A_k]$ is computationally intensive. Several quasi-Newton algorithms that approximate the Jacobian in various ways are available.

NEWTON'S METHOD:

$$\begin{Bmatrix} M_F \\ \omega_F \end{Bmatrix}_{(k+1)} = \begin{Bmatrix} M_F \\ \omega_F \end{Bmatrix}_{(k)} - [J_k]^{-1} \begin{Bmatrix} D_R \\ D_I \end{Bmatrix}_{(k)}$$

$[J_k]$ EXPENSIVE TO COMPUTE

QUASI-NEWTON METHODS:

$[J_k]$ APPROXIMATED IN VARIOUS WAYS

CD-88-31715

A BETTER QUASI-NEWTON METHOD

A quasi-Newton algorithm is proposed that is more efficient than the algorithms currently available for determining the flutter Mach number and the flutter frequency. The numerical scheme is based on the hypothesis that approximating the derivatives of the flutter matrix $[B_k]$ provides a more accurate approximation to the Jacobian matrix $[J_k]$ than directly approximating the derivatives of the characteristic determinant. The numerical scheme based on this hypothesis approaches Newton's method in its superior convergence characteristics with the same cost per iteration as the secant method.

The derivatives $[B_k]_{,M_F}$ and $[B_k]_{,\omega_F}$ of the flutter matrix are approximated by following a reasoning similar to that employed in deriving Broyden's method (Johnston, 1982). Let $\Delta M_k = M_{F(k-1)} - M_{F(k)}$ and $\Delta\omega_k = \omega_{F(k-1)} - \omega_{F(k)}$. The derivatives are approximated in the direction of the last move to satisfy

$$[B_{k-1}] = [B_k] + [B_k]_{,M_F} \cdot \Delta M_k + [B_k]_{,\omega_F} \cdot \Delta\omega_k$$

and are assumed to be unchanged in the direction orthogonal to the last move.

APPROACH

- **APPROXIMATE THE JACOBIAN INDIRECTLY BY APPROXIMATING THE DERIVATIVES OF THE FLUTTER MATRIX**
- **UPDATE THE DERIVATIVES OF THE FLUTTER MATRIX ONLY IN THE DIRECTION OF THE LAST MOVE**

RESULT

- **A QUASI-NEWTON METHOD MORE LIKE NEWTON'S METHOD THAN OTHERS**
- **THE FLUTTER MODE ALMOST A BYPRODUCT**

CD-88-31716

EFFICIENCY OF NUMERICAL PROCEDURE

The direct solution procedure was demonstrated by performing flutter boundary calculations at various rotational speeds for two propfan rotor configurations. The first configuration consisted of eight identical blades. The second configuration was an alternately mistuned rotor with eight blades.

The typical progress of iteration, for initial guesses for flutter Mach number and flutter frequency of 0.5 and 310 Hz, respectively, with the direct solution procedure and the conventional procedure, is shown in the first table. Recall that the conventional procedure relies on user interaction and judgment. The progress of iteration shown for the conventional procedure is typical. The direct solution procedure, in addition to being suitable for automation, is also more efficient as evidenced by the considerably smaller number of analysis steps. Thus both the CPU time and the analyst's time are considerably reduced by using the direct solution procedure.

The results show that a fair initial guess would converge to the "exact" flutter point after about 5 to 10 flutter matrix evaluations. The second table shows the CPU times on the Cray-XMP required to obtain the flutter boundary for good initial guesses and poor initial guesses. The CPU times for one flutter eigenvalue analysis at a given set of Mach number and assumed frequency are also shown for comparison. With a good initial guess the flutter Mach number and the flutter frequency can be obtained for two or three times the cost of a single eigenanalysis. The direct solution procedure is much less expensive in terms of CPU time as well as analyst's time than the conventional procedure, although precise comparisons have not been made.

PROGRESS OF ITERATION
(5280 rpm; BLADE SETTING ANGLE AT 0.75 RADIUS, 61.6°; $\sigma_r = 225°$)

COUNT	CONVENTIONAL PROCEDURE		DIRECT SOLUTION PROCEDURE	
	FLUTTER MACH NUMBER, M	FLUTTER FREQUENCY, ω, Hz	FLUTTER MACH NUMBER, M	FLUTTER FREQUENCY, ω, Hz
1	0.500	310.0	0.500	310.0
2	↓	267.5	.499	310.0
3	↓	268.9	.500	313.0
4	↓	268.9	.701	289.7
5	.700	268.9	.590	287.7
6	↓	299.8	.641	293.6
7	↓	298.9	.642	294.1
8	↓	298.9	.641	294.1
9	.616	286.3	[a].641	294.1
10	↓	290.1		
11	↓	290.5		
12	↓	290.4		
13	.640	292.9		
14	.640	293.9		
15	.640	294.0		
16	.641	293.9		
17	.641	294.1		
18	[a].641	294.1		

[a] Converged.

CD-88-31717

CPU TIME FOR AUTOMATED FLUTTER ANALYSIS

	EIGENSOLUTION AT A SINGLE SET OF MACH NUMBER M AND FREQUENCY ω	DIRECT SOLUTION TO FIND M_F AND ω_F	
		GOOD INITIAL GUESS[a]	POOR INITIAL GUESS[a]
	CPU TIME, SEC		
TUNED ROTOR[b]—8 BLADES; 6 MODES/BLADE; 5280 rpm; $\sigma_r = 225°$	4.332	10.356 ($M = 0.70$; $\omega = 310$ Hz)	22.146 ($M = 0.45$; $\omega = 340$ Hz)
MISTUNED ROTOR[c]—8 BLADES; 4 GROUPS; TWO MODES/BLADE; 5190 rpm; $\sigma_r = 90°$	10.020	22.084 ($M = 0.65$; $\omega = 310$ Hz)	31.970 ($M = 0.5$; $\omega = 340$ Hz)

[a] INITIAL GUESSES ARE GIVEN IN PARENTHESES.
[b] "EXACT" $M_F = 0.641$ AND "EXACT" $\omega_F = 294$ Hz.
[c] "EXACT" $M_F = 0.718$ AND "EXACT" $\omega_F = 285$ Hz.

CD-88-31718

ACCURACY OF JACOBIAN

So that the accuracy of the approximate Jacobian could be judged, the nonlinear equations were solved by Newton's method, by the present numerical procedure, and by alternative quasi-Newton methods such as the multipoint secant method (implemented in IMSL routine ZSCNT), the modified Powell algorithm (implemented in IMSL routine ZSPOW), and Broyden's method (Johnston, 1982). For the cases tested, the present procedure outperformed all three alternative methods in terms of efficiency. Even though the characteristic determinant D_k is never calculated in the present procedure, the variation of the absolute value of D_k with each iteration is shown in the graph so that the procedure can be compared with Newton's method and the multipoint secant method. For these cases, the "exact" flutter Mach number was 0.641, the "exact" flutter frequency was 294 Hz, and the initial values for M_F and ω_F were 0.65 and 330 Hz, respectively. The determinant value has been scaled so that $1.0 \leq D_0 \leq 10.0$, where D_0 is the characteristic determinant at the beginning of iteration. The iteration history for the current numerical procedure closely resembles that for Newton's method, indicating the accuracy of the approximation proposed here for the Jacobian matrix. In contrast, the secant approximation for the Jacobian matrix requires almost double the number of iterations.

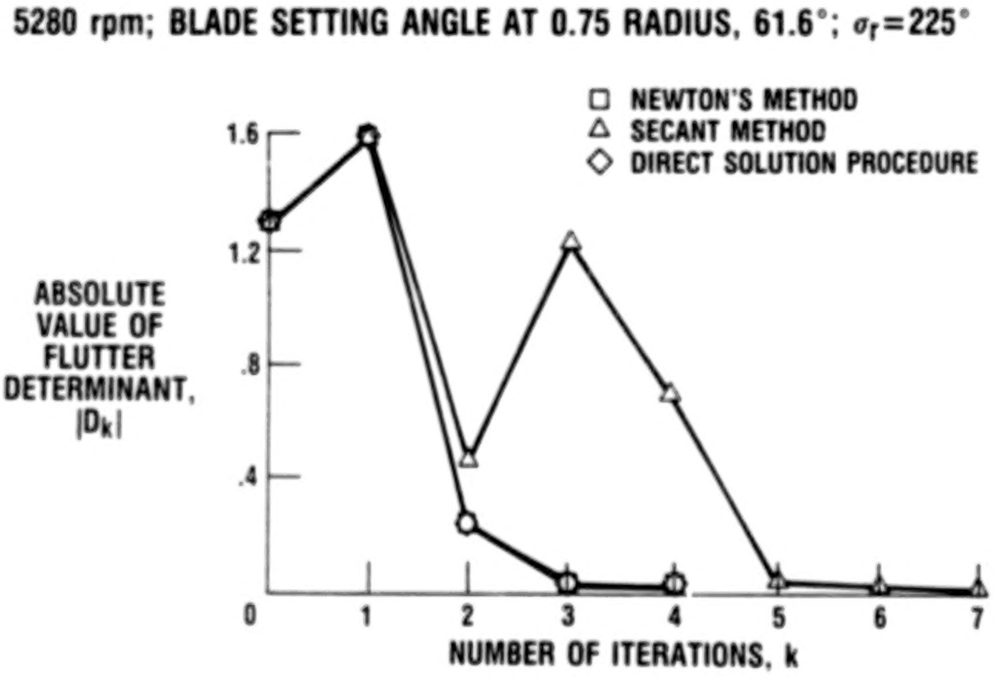
5280 rpm; BLADE SETTING ANGLE AT 0.75 RADIUS, 61.6°; σ_r=225°

CD-88-31719

RANGE OF CONVERGENCE

The range of convergence is an important factor in any iterative procedure since it has an important effect on how closely the initial solution must approximate the final solution. The graph on the left shows the number of flutter matrix evaluations required for convergence; the initial guesses for M_F are varied and the initial guess for ω_F is fixed at 310 Hz. The range of Mach number convergence is from 0.2 to 0.8. The graph on the right similarly shows the number of flutter matrix evaluations required for convergence; the initial guess for M_F is fixed at 0.65 and the initial guesses for ω_F are varied. The frequency range of convergence with the direct solution procedure, 230 to 350 Hz, is slightly larger than that with the secant method. From these graphs it can be stated that the present procedure has a large range of convergence.

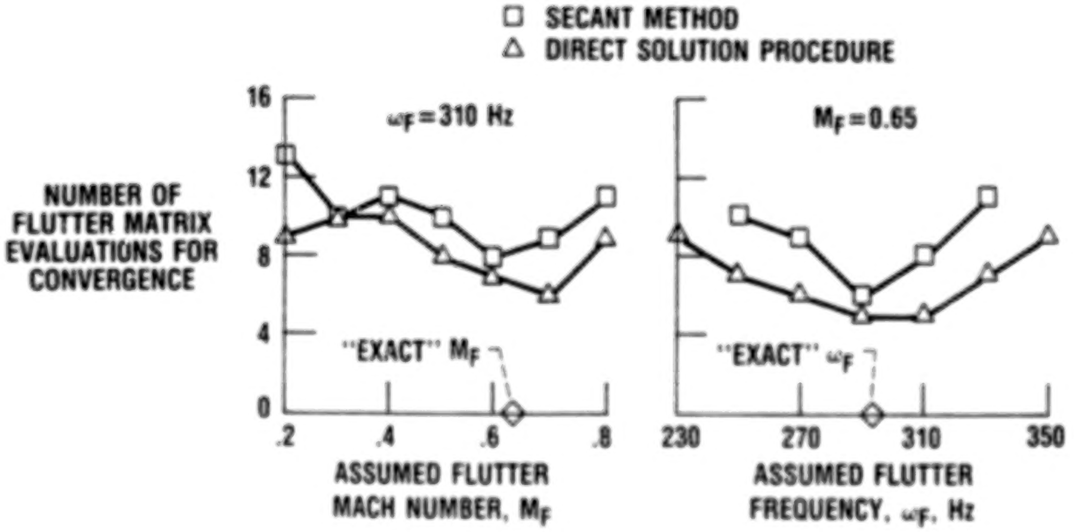

CD-88-31720

SUMMARY

A direct solution of the equations of motion is demonstrated to be a reliable automated flutter analysis procedure if steady aerodynamic deformations are ignored. The direct solution procedure replaces the inner-outer iteration loop of the conventional procedure by a single iteration loop. A numerical procedure, based on an accurate and efficient approximation to the Jacobian matrix, is presented. The procedure is straightforward in concept, and results for test cases show good convergence properties. Since the procedure is iterative, it is particularly suitable for design optimization. As the optimal design is evolved, the flutter solution is expected to change incrementally from design to design, so that the previous solution provides good estimates for the current solution.

- DEVELOPED A QUASI-NEWTON METHOD FOR DETERMINANT ITERATION
- AUTOMATED THE PROPFAN FLUTTER ANALYSIS BY DIRECT SOLUTION
- DEMONSTRATED GOOD CONVERGENCE AND EFFICIENCY OF DIRECT SOLUTION METHOD WITH ADVANCED AERODYNAMIC MODEL

CD-88-31721

REFERENCES

Johnston, R.L., 1982, "Numerical Methods: A Software Approach," John Wiley & Sons, New York, pp. 189-192.

Kaza, K.R.V., et al., 1987a, "Analytical Flutter Investigation of a Composite Propfan Model," 28th Structures, Structural Dynamics and Materials Conference, Part 2A, AIAA, pp. 84-97, NASA TM-88944.

Kaza, K.R.V., et al., 1987b, "Analytical and Experimental Investigation of Mistuning on Propfan Flutter," 28th Structures, Structural Dynamics and Materials Conference, Part 2A, AIAA, pp. 98-110, NASA TM-88959.

Murthy, D.V. and Kaza, K.R.V., 1987, "A Computational Procedure for Automated Flutter Analysis", NASA TM-100171.

Williams, M.H. and Hwang, C.C., 1986, "Three Dimensional Unsteady Aerodynamics and Aeroelastic Response of Advanced Turboprops," 27th Structures, Structural Dynamics and Materials Conference, Part 2, AIAA, pp. 116-124.

N88-23251

CHARACTERIZATION OF STRUCTURAL CONNECTIONS FOR MULTICOMPONENT SYSTEMS

Charles Lawrence and Arthur A. Huckelbridge*
Structural Dynamics Branch
NASA Lewis Research Center

ABSTRACT

The inability to adequately model connections has limited the ability to predict overall system dynamic response. Connections between structural components are often mechanically complex and difficult to model analytically. Improved analytical models for connections are needed to improve system dynamic predictions. This research explores combining component mode synthesis methods for coupling structural components with parameter identification procedures for improving the analytical modeling of the connections (Hucklebridge, 1987; and Lawrence, 1988). Improvements in the connection stiffness and damping properties are computed in terms of physical stiffness and damping parameters, so the physical characteristics of the connections can be better understood, in addition to providing improved input for the system model.

---

*Case Western Reserve University.

OBJECTIVES AND APPROACH

Analytical models of structural systems do not normally produce characteristics that agree with those obtained from experiments. The discrepancy can often be attributed to structural properties such as connection damping and stiffness, which are extremely difficult to characterize, while their influence on structural response predictions is profound.

OBJECTIVE

- DEVELOP IMPROVED ANALYTICAL MODELS FOR STRUCTURAL CONNECTIONS
- IDENTIFY CONNECTION STIFFNESS AND DAMPING PROPERTIES FROM SYSTEM MODAL DATA
- DETERMINE CONNECTION PROPERTIES IN TERMS OF PHYSICAL PARAMETERS
- USE SUBSTRUCTURING METHODS FOR MODELING EFFICIENCY AND INCORPORATION OF MODAL COMPONENTS

APPROACH

- DEVELOP COUPLED SYSTEM EQUATIONS FROM "MIXED" SUBSTRUCTURES
- OBTAIN BOTH PREDICTED AND MEASURED MODAL DATA FOR SYSTEM
- MINIMIZE DIFFERENCE BETWEEN MEASURED AND PREDICTED SYSTEM CHARACTERISTICS BY OPTIMAL SELECTION OF CONNECTION PARAMETERS

CD-88-31843

JOINT STIFFNESS EFFECTS ON DISPLACEMENTS

The effect of connection flexibility on steady-state displacements, and frequencies and mode shapes, was assessed for the GE-A7-B4 advanced propfan blade. Results indicate that connection flexibility is significant, and in order to insure accuracy, connection flexibility must be precisely characterized.

ORIGINAL PAGE IS
OF POOR QUALITY

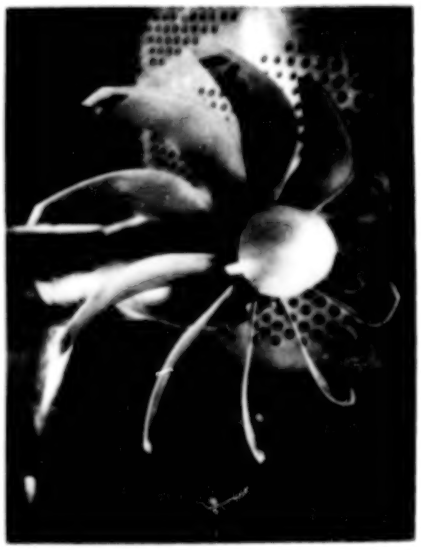

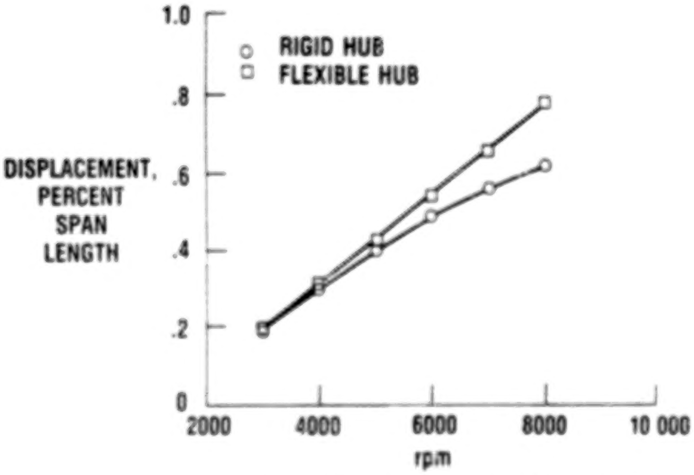

GE-A7-B4 LEADING EDGE TIP DISPLACEMENTS. RIGID HUB VERSUS FLEXIBLE HUB

CD 88 31844

COMPONENT COUPLING

The approach used for developing the coupled system equations of motion used component models represented through the use of finite elements or with modal data. Component modal data may be obtained from experiment or from a reduced finite-element model. Once the system equations of motion are constructed, they can be used to predict the system frequencies and mode shapes. These modal data are then used in conjunction with the experimentally measured modal parameters to identify the connection properties.

U^I	**DISPLACEMENT DEGREES OF FREEDOM (DOF) FOR COMPONENT I**
U^{II}	**DISPLACEMENT DOF FOR COMPONENT II**
U^C	**DISPLACEMENT DOF FOR CONNECTION**
b	**BOUNDARY DOF**

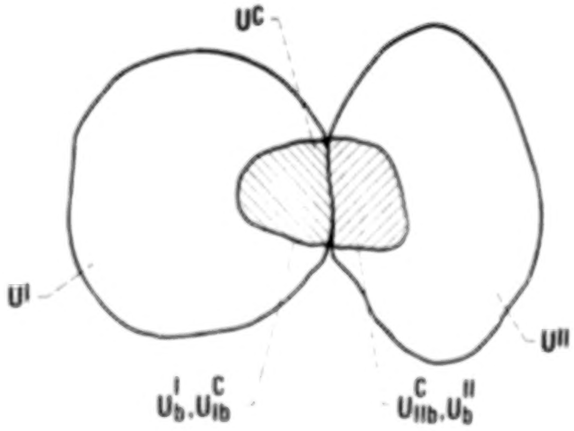

CD 88 31845

PARAMETER IDENTIFICATION PROCEDURE

Parameter identification methods that incorporate optimization strategies can be classified into three groups: least squares, weighted least squares, and Bayesian estimation. With the least squares method, the set of parameters that minimizes the difference between the measured and predicted response is computed. The weighted least squares method incorporates a weight, indicating the relative confidence in the measured data. The Bayesian method permits specification of the randomness of the connection parameters as well as the confidence in the measured data.

THE WEIGHTED SQUARED DIFFERENCE BETWEEN THE PREDICTED AND MEASURED CHARACTERISTICS IS

$$\{F\} = [W]\left(\{\bar{C}\} - \{C\}\right)^{2}$$

SETTING THE DERIVATIVE TO ZERO AND EXPANDING THE PREDICTED SYSTEM CHARACTERISTICS IN A TAYLOR SERIES, THE CONNECTION PROPERTIES ARE SOLVED FOR ITERATIVELY FROM

$$\{r\} = \{r\}_{EST} + \left([S]^{T}[W][S]\right)^{-1}[S]^{T}[W]\left(\{\bar{C}\} - \{C\}_{EST}\right)$$

$\{\bar{C}\}$, $\{C\}$	**MEASURED AND COMPUTED SYSTEM FREQUENCIES AND MODE SHAPES**
$[W]$	**WEIGHTING MATRIX**
$[S]$	$\partial\{C\}/\partial\{r\}$
$\{r\}$	**CONNECTION STIFFNESSES AND DAMPING**

CD-88-31846

SYSTEM DYNAMICS PARAMETER IDENTIFICATION PROGRAM

A general FORTRAN computer code was developed for incorporating the component coupling and parameter identification procedures. Components are represented by fixed or free interface modes and can include residual flexibilities. Coupling is through flexible or rigid connections. Damping is added to the system through the use of viscous dampers. The experimental data used for the parameter identification include complex eigenvalues (frequency and damping) and mode shape values.

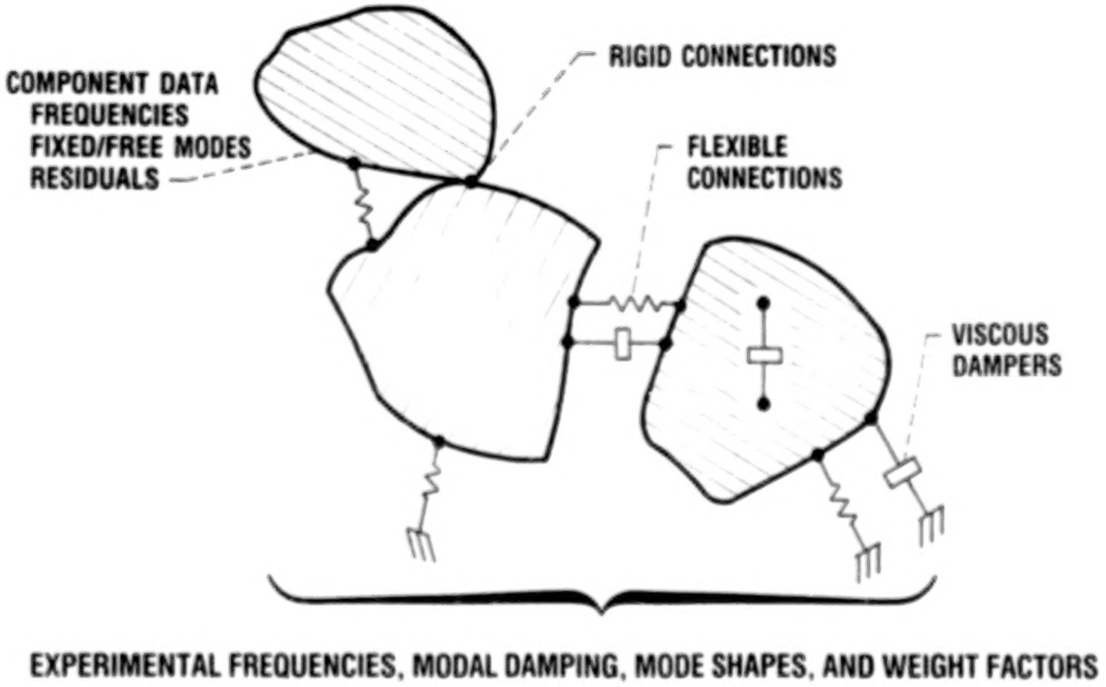
COMPONENT DATA
FREQUENCIES
FIXED/FREE MODES
RESIDUALS
RIGID CONNECTIONS
FLEXIBLE CONNECTIONS
VISCOUS DAMPERS
EXPERIMENTAL FREQUENCIES, MODAL DAMPING, MODE SHAPES, AND WEIGHT FACTORS

CD 88 31847

ROTATING STRUCTURAL DYNAMICS RIG

The rotating structural dynamics (RSD) rig at NASA Lewis was used to evaluate the component coupling and parameter identification algorithms. The RSD rig, which was designed to simulate actual engine structures, is used to study active rotor control and system dynamics (component interaction) problems. The rig components, although considerably simpler than a real turbine engine's compounds, were scaled to simulate an actual engine's structural dynamics response characteristics.

ORIGINAL PAGE IS
OF POOR QUALITY

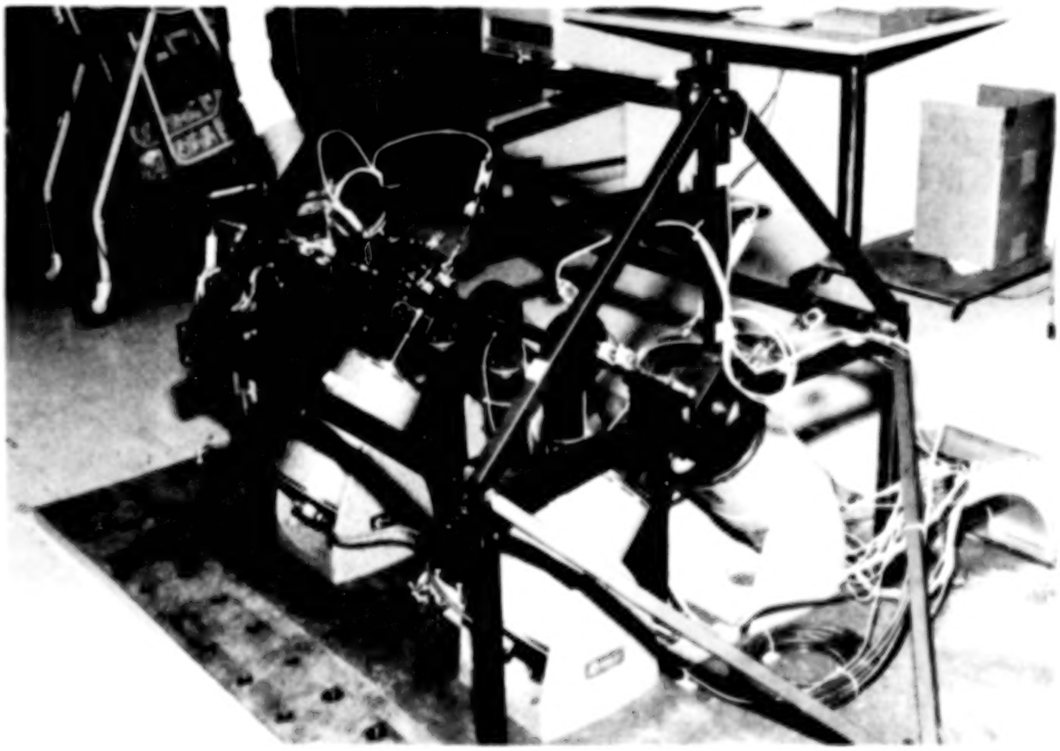

CD 88 31848

PARTITIONING OF SYSTEM

The objective of the parameter identification was to determine the stiffnesses of the bearing support that connects each end of the rotor to the support frame. To accomplish this, the RSD rig was divided into two components: the rotor support frame, and the rotor.

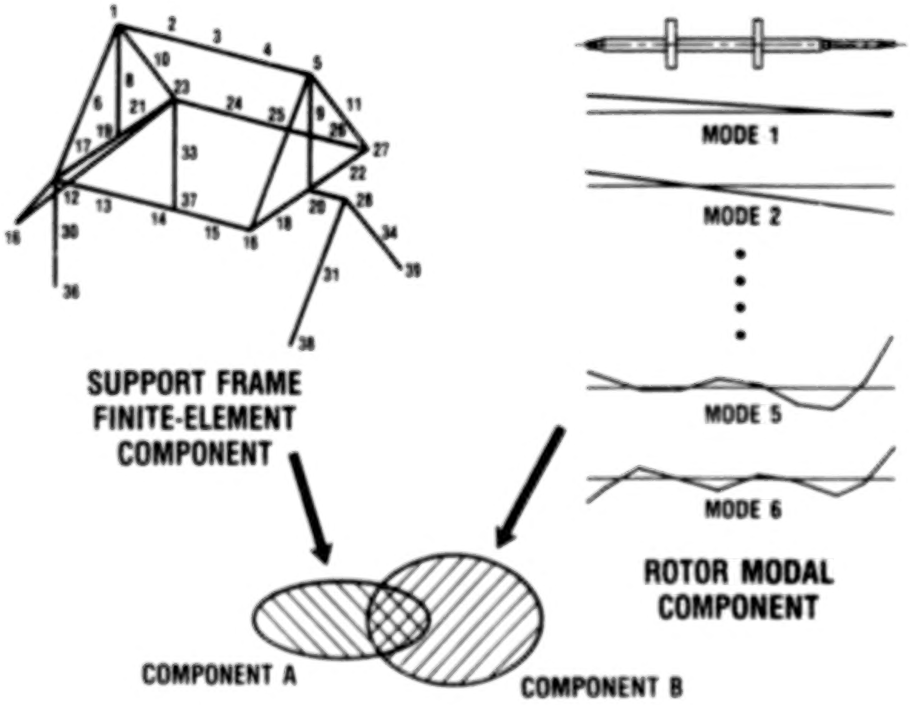
1
2
3
4
5
10
8
6
21
23
24
25
9
11
26
27
17
19
33
22
12
13
37
14
15
16
18
20
28
34
16
30
31
39
36
38
SUPPORT FRAME
FINITE-ELEMENT
COMPONENT
MODE 1
MODE 2
MODE 5
MODE 6
ROTOR MODAL
COMPONENT
COMPONENT A
COMPONENT B

CD-88-31849

COUPLED SYSTEM ANALYSIS

The coupled system frequencies are plotted along with the measured frequencies. The predicted frequencies were computed for different values of bearing support stiffness to determine the effect that the supports have on the system frequencies. When three system frequencies are used, the cage stiffness is identified as 5750 lb/in. This value is in good agreement with the measured stiffness of 5050 lb/in.

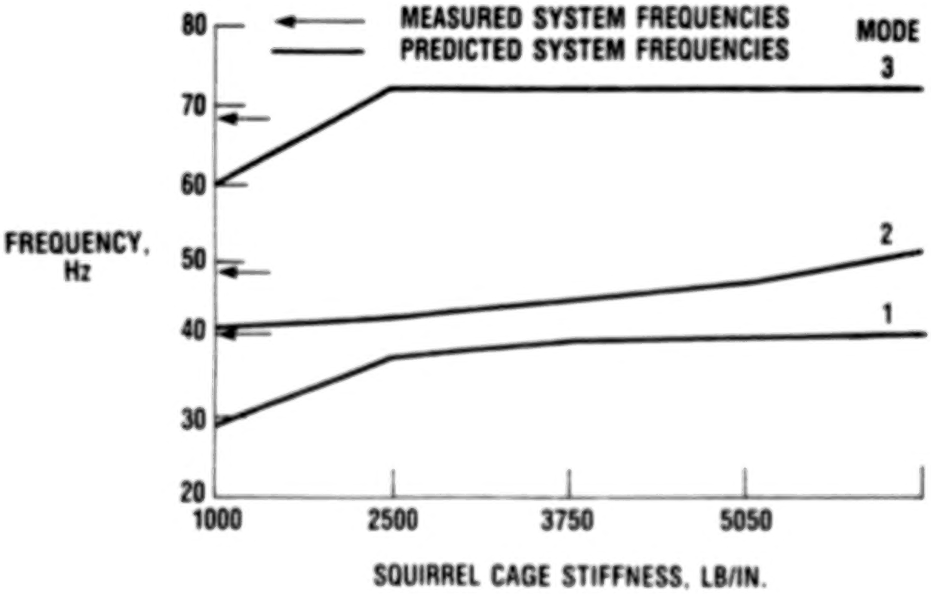

CD 88 31850

DAMPED COUPLED SYSTEM

This sample problem is presented to demonstrate identification of connection damping. For this problem a finite-element model was used to generate simulated experimental data. The model consists of three planar elastic beams connected at their ends with revolute (pinned) connections. Each of the connections is connected to ground by linear, translational springs and viscous dampers.

THREE COMPONENT COUPLED SYSTEM ($EI = 10^5$, $\rho = 0.10$, $\Delta L = 1.0$)

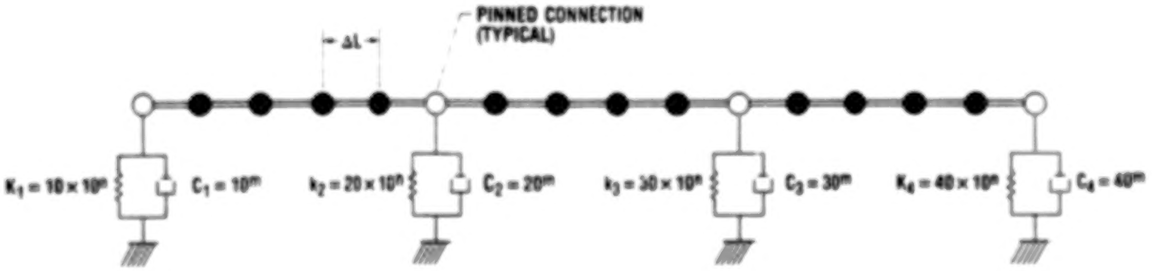
PINNED CONNECTION (TYPICAL)
ΔL
$K_1 = 10 \times 10^n$
$C_1 = 10^m$
$k_2 = 20 \times 10^n$
$C_2 = 20^m$
$k_3 = 30 \times 10^n$
$C_3 = 30^m$
$K_4 = 40 \times 10^n$
$C_4 = 40^m$

CD-88-31851

DIFFERENCES BETWEEN COMPUTED AND EXPERIMENTAL PROPERTIES

Damping and stiffness connection properties were identified for a range of damping levels. The flatness of the curves demonstrates the insensitivity of the identified connection stiffness and damping to the level of damping. Even near critical damping, the properties are computed accurately.

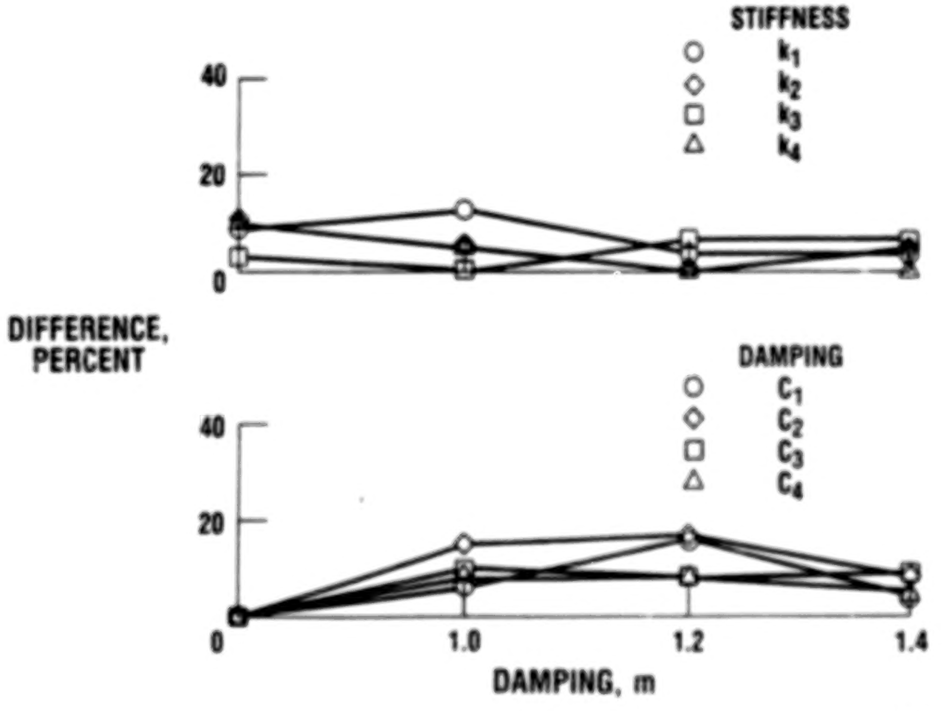

CD-88-31852

ASSESSMENT OF EXPERIMENTAL ERROR

A Monte Carlo simulation was used to assess the accuracy of the parameter identification for various degrees of experimental error. Plots displaying the probability of achieving a precision level are shown below. As the deviation in the measured data increases, the probability of achieving a given level of precision decreases.

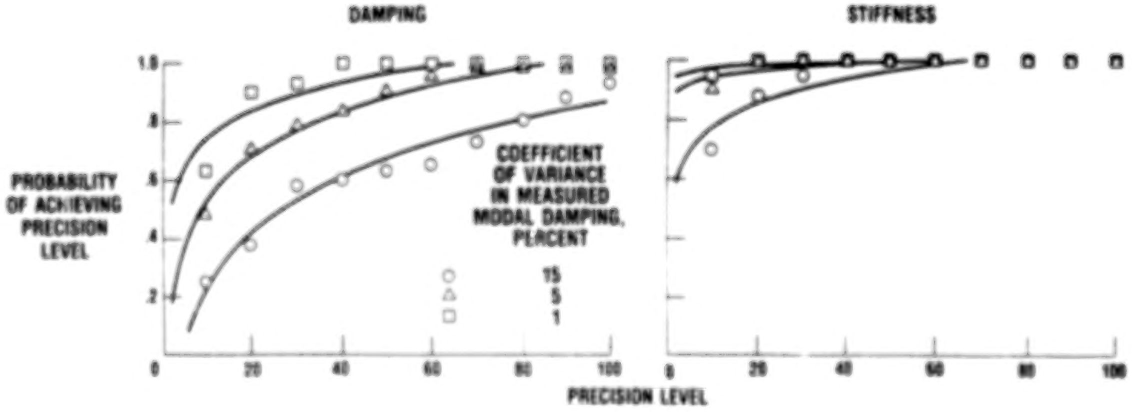

CD-88-31853

THREE-COMPONENT SYSTEM WITH FRICTION DAMPING

The connections in many structural systems contain nonlinearities such as friction. For multidegree of freedom systems it is virtually impossible to identify and characterize all the complexities that can exist in the connections. Often, a simplifying assumption is made that the connection damping can be adequately described by linear viscous dampers even though other types of damping exist in the connection.

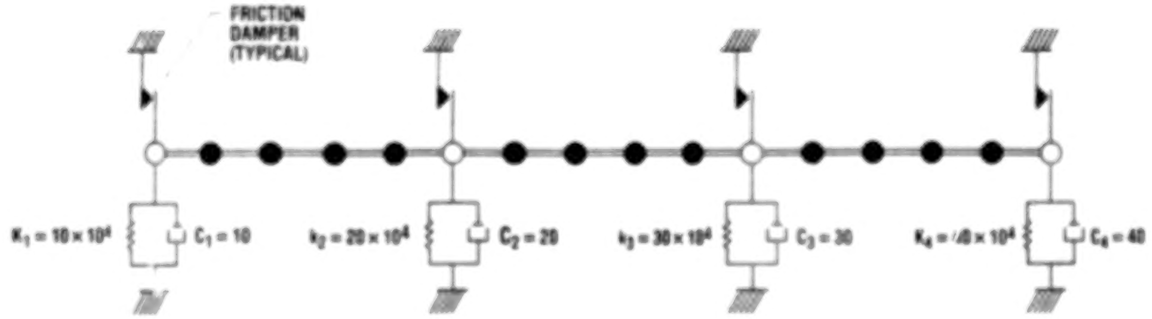
FRICTION DAMPER (TYPICAL)
$K_1 = 10 \times 10^4$
$C_1 = 10$
$k_2 = 20 \times 10^4$
$C_2 = 20$
$k_3 = 30 \times 10^4$
$C_3 = 30$
$K_4 = 40 \times 10^4$
$C_4 = 40$

CD-88-31894

EVALUATION OF VISCOUS DAMPING MODEL

Equivalent viscous damping ratios were computed for various levels of friction damping. The performance of the identified models was assessed by comparing transient responses of the identified models to those from the experimental models. The responses from the identified and experimental models were evaluated by comparing peak response, settling time, and RMS error.

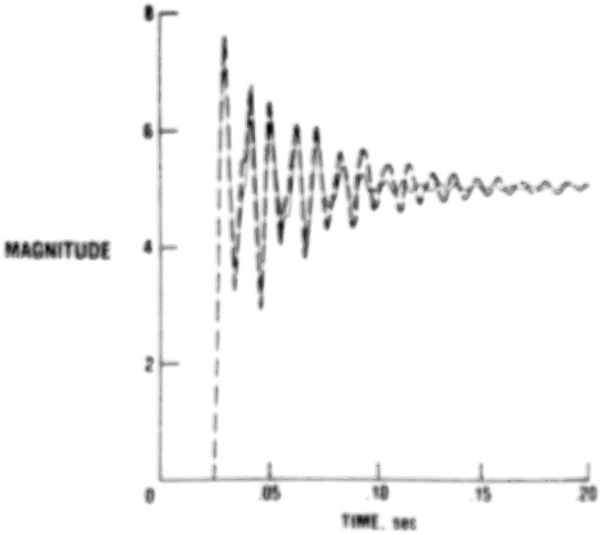

TRANSIENT RESPONSE

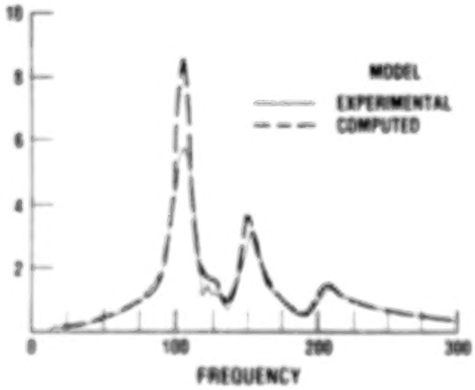

FREQUENCY RESPONSE

CD-88-31855

SUMMARY AND CONCLUSIONS

Identification of structural dynamic systems is effectively performed by combining substructuring methods with parameter identification techniques. When substructuring methods, such as component mode synthesis, are used, the complexity of the identification problem is greatly reduced. Components and intercomponent structural connection properties are identified and evaluated independently, thus drastically decreasing the magnitude of the identification problem.

- IDENTIFICATION OF STANDARD CONNECTION IS EFFECTIVELY PERFORMED BY COMBINING SUBSTRUCTURING METHODS WITH PARAMETERS IDENTIFICATION TECHNIQUES
- MODAL TEST DATA ARE EFFECTIVE FOR IDENTIFYING STIFFNESS AND DAMPING PROPERTIES OF COMPONENT CONNECTIONS.
- THE PARAMETER IDENTIFICATION IS IMPROVED WHEN THE QUALITY AND QUANTITY OF EXPERIMENTAL DATA ARE INCREASED.
- SMALL AMOUNTS OF NONLINEARITY CAN BE APPROXIMATED WITH VISCOUSLY DAMPED MODELS.

CD-88-31856

REFERENCES

Hucklebridge, A.A., and Lawrence, C., 1987, "Identification of Structural Interface Characteristics Using Component Mode Synthesis," ASME Vibrations Conference, Boston, MA, NASA TM-88960.

Lawrence, C., and Hucklebridge, A.A., 1988, "Characterization of Damped Structural Connections for Multi-Component Systems," NASA TM-100801.

N88-23252

Mixed Finite Element Formulation Applied to Shape Optimization

by

Helder Rodrigues, John E. Taylor, and Noboru Kikuchi

The University of Michigan
Ann Arbor, MI 48109

ABSTRACT

This study is concerned with development of a variational formulation and a procedure for computational solution for the shape optimal design of a two-dimensional linear elastic body, using a mixed finite element discretization. Shape optimal design is a problem that has interested many researchers in the last fifteen years. The subject has been surveyed in a number of review articles, see e.g. Haftka and Grandhi [11].

Zienkiewicz and Campbell [see , e.g. 12], were among the first to approach this problem using finite element methods. Subsequently this method has been applied widely to problems in shape optimal design[see, e.g.2,3,13- 15] , but only with mixed success. The finite element method based on the displacement formulation has two main disadvantages, (1) the increase of finite element error that results from mesh distortion during shape redesign, and (2) in some situations, a lack of sufficient precision in the prediction of stresses and strains at the boundary and internal nodes. There are some methods one can consider to overcome these difficulties. Some investigators have applied the Boundary Element Method[see, e.g.16 - 18]. While the BEM has proved to be very useful and looks promising in certain applications of shape optimal design, for problems that require numerous evaluations of state variables in the domain (objective function = $\max_{\mathbf{x}\in\Omega}F(\mathbf{u},\varepsilon)$, for example) the BEM loses some of its advantages, also at the current stage of development it lacks the generality provided by FEM in structural analysis. Within the FEM applications, the domain method [see, e.g. 19], where sensitivity expressions are defined in terms of domain integrals rather than boundary integrals (thereby avoiding the evaluation of state variables at the boundary), provides for improved accuracy in the numerical calculation of sensitivities. Also recently, Haber proposed an Eulerian - Lagrangian formulation based on the mutual Reissner energy [see, e.g. 20], where the shape optimization problem can be formulated in an arbitrary initial domain as a means to overcome the difficulties inherited from shape redesign .

In this work another approach is considered. With the development of automatic mesh generation and optimization techniques[see, e.g.7] the first of the cited disadvantages of FEM is avoided. Mixed finite element methods[see, e.g.8] that may provide for accurate computation of stresses and strains at the element nodes appears to be a natural approach to resolve the other difficulty. These considerations are brought together in the developments reported here, to demonstrate a more effective approach to the overall treatment of shape optimal design.

EXAMPLES OF SHAPE OPTIMIZATION PROBLEMS

For simplicity let us consider plane linearly elastic structures to find the optimal shape using the mixed finite element formulation together with an automatic mesh generation method based on the elliptic differential equations. Two model problems shown in the figure are solved by the present method to demonstrate its effectiveness. It is noted that the fillet optimal shape design problem (Model B) is a standard one, but is one of the most difficult problems because of sharp design change at the left edge of the design boundary.

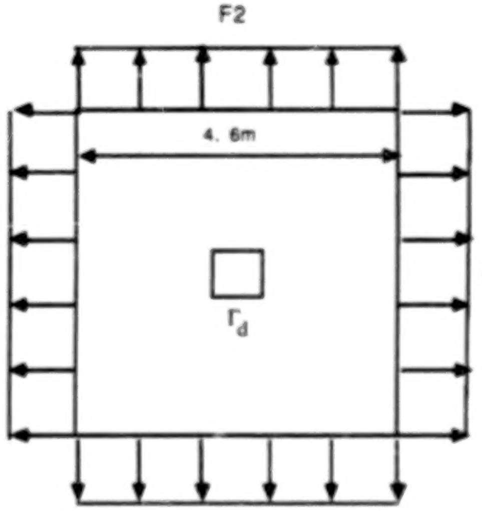

Model A

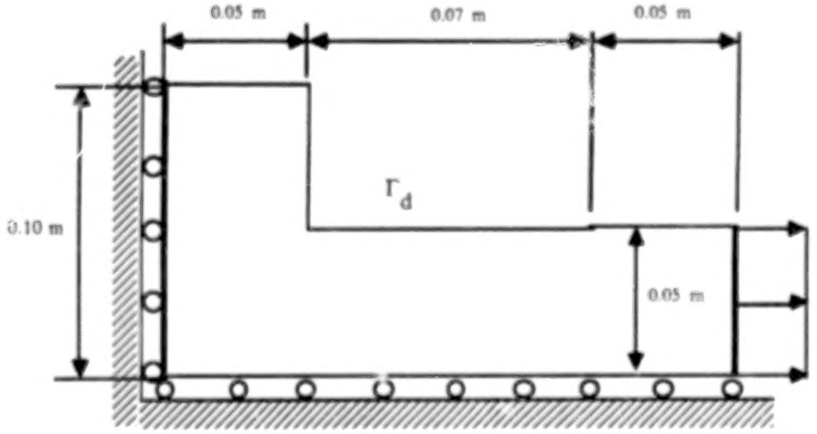

Model B

DIFFICULTIES OF SHAPE OPTIMIZATION PROBLEMS

The difficulty of the shape optimization problem is large design changes lead to significant changes of the corresponding finite element model of the structure during an optimization process. If the final, that is, optimal shape is known, it is possible to set the initial finite element model very close to the optimum. In this case, design change does not imply large change of finite element models, and then it is possible to avoid distorted finite elements which yield significant approximation errors and sometimes even negative values of the Jacobian of the isoparametric transformation. It is natural that the optimal shape is not known *a priori*, and then it is necessary to establish a shape optimization method to deal with large design change. Finite element approximation errors are strongly dependent upon the size and shape of finite elements. Errors are generally very large in regions where stresses are rapidly varying. In most shape optimization problems, stresses are varying rapidly at the end points of the design boundary where shape also changes rapidly. Furthermore, if shape change is large, this almost automatically yields distortion of finite elements, i.e. generation of unnecessary approximation errors. Figure (a) shows the distribution of finite element approximation error in a similar problem to Model A, while Figure (b) indicates a pathology in shape optimization.

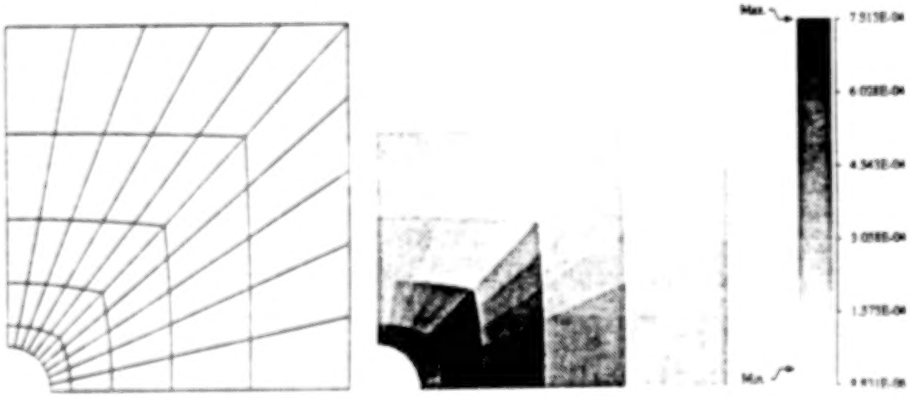

(a) Finite Element Approximation Error Distribution

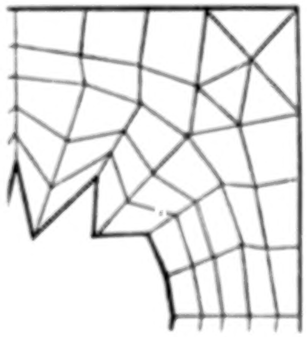

(b) Oscillation of the Design Boundary (by. C. Fleury)

FORMULATION OF THE DESIGN PROBLEM

The optimal shape design problem is defined by minimizing the maximum value of a local criterion $F(\mathbf{u},\varepsilon)$ stated by the displacement **u** and the linearized strain tensor ε, subject to the state equations which represent equilibrium, constitutive relation, and boundary conditions. Here D represents the design variable to describe the shape of the design boundary.

$$\mathrm{Min}_D \quad \mathrm{Max}_{\mathbf{x}\in\Omega} \quad F(\mathbf{u}(\mathbf{x}),\varepsilon(\mathbf{x}))$$

subject to

the resource constraint $\int_{\Omega} d\Omega - A \leq 0$

the equilibrium equations $\mathrm{div}\,\Sigma + \mathbf{f} = \mathbf{0}, \quad \Sigma = \Sigma^T \quad \text{in } \Omega$

the strain - displacement relations $\varepsilon = \frac{1}{2}(\nabla\mathbf{u} + \mathbf{u}\nabla) \quad \text{in } \Omega$

the stress - strain relation $\Sigma = \Xi : \varepsilon \quad \text{in } \Omega$

the traction boundary condition $\mathbf{n}\,\Sigma = \mathbf{t} \quad \text{on } \Gamma_t$

the displacement boundary condition $\mathbf{u} = \mathbf{0} \quad \text{on } \Gamma_u$

MIXED FINITE ELEMENT FORMULATION

If the displacement method is applied in finite element analysis, strain and stress components are computed at each Gaussian integration point to form element stiffness matrices and load vectors. However, values of stress components must be obtained at the nodes on the design boundary for the shape optimization problems. Thus an extrapolation method must be introduced to obtain nodal values of stress components. For example, if the least squares method is applied to obtain nodal values, it cannot provide sufficiently accurate values in the region that stress gradient is high. Furthermore, it becomes very inaccurate if distorted irregular finite elements exist in a finite element model. To avoid such problems, we here apply a mixed formulation that computes nodal values of displacements, strains, and stresses, directly without applying an extrapolation method.

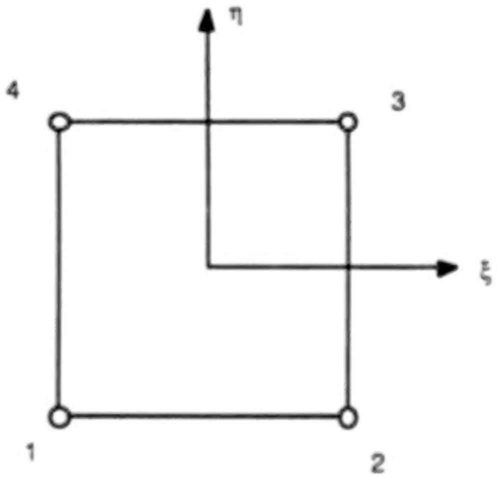

QUAD4

8 degrees of freedom per node $\{u_x, u_y, \varepsilon_{xx}, \varepsilon_{yy}, \gamma_{xy}, \sigma_{xx}, \sigma_{yy}, \sigma_{xy}\}^T$

$$u_x = \sum_{\alpha=1}^{4} u_{x\alpha} N_\alpha(\xi,\eta), \text{ etc}$$

$$\varepsilon_{xx} = \sum_{\alpha=1}^{4} \varepsilon_{xx\alpha} N_\alpha(\xi,\eta), \text{ etc}$$

$$\sigma_{xx} = \sum_{\alpha=1}^{4} \sigma_{xx\alpha} N_\alpha(\xi,\eta), \text{ etc}$$

$$N_\alpha(\xi,\eta) = \frac{1}{4}(1+\xi_\alpha\xi)(1+\eta_\alpha\eta), \quad \alpha=1,\ldots,4$$

OPTIMALITY CONDITIONS

Transferring the original shape optimization problem to the upper-bound formulation $\mathrm{Min}_D\, \beta$ subject to the above constraints and the additional one $F(\mathbf{u},\varepsilon) - \beta \leq 0$ in Ω, the Lagrange multiplier method implies the necessary condition for optimality as shown in below.

Equilibrium Equations

$$\int_{\Omega} \{\frac{1}{2}(\nabla\delta\mathbf{v}+\delta\mathbf{v}\nabla):\Sigma - \delta\mathbf{v}.\mathbf{f}\}d\Omega \;-\; \int_{\Gamma_t} \delta\mathbf{v}.\mathbf{t}\, d\Gamma$$

$$+ \int_{\Omega} [\delta\mathbf{e}:(\Xi\varepsilon - \Sigma) + \delta T:\{\frac{1}{2}(\nabla\mathbf{u}+\mathbf{u}\nabla) - \varepsilon\}]d\Omega = 0, \quad \mathbf{u}=\mathbf{0} \quad \text{on } \Gamma_u.$$

Adjoint Problems

$$\int_{\Omega} \{\frac{1}{2}(\nabla\mathbf{v}+\mathbf{v}\nabla):\delta\Sigma + \lambda(\frac{\partial F}{\partial\delta\varepsilon}:\delta\varepsilon + \frac{\partial F}{\partial\mathbf{u}}.\delta\mathbf{u})\}d\Omega$$

$$+ \int_{\Omega} \mathbf{e}:(\Xi:\delta\varepsilon - \delta\Sigma) + T:(\frac{1}{2}(\nabla\delta\mathbf{u}+\delta\mathbf{u}\nabla) - \delta\varepsilon)\}\, d\Omega = 0$$

Optimality Condition due to Variation by Shape Change

$$\int_{\Gamma_d} (\Sigma:\mathbf{e}+ \Lambda)(\theta.\mathbf{n})\, d\Gamma = 0, \quad \Lambda(\int_{\Omega} d\Omega - A) = 0, \quad 0\leq\Lambda, \quad \int_{\Omega} d\Omega - A \leq 0$$

Normality Condition

$$\int_{\Omega} \lambda\, d\Omega = 1, \quad \lambda(F(\mathbf{u},\varepsilon) - \beta) = 0, \quad 0\leq\lambda, \quad F(\mathbf{u},\varepsilon) - \beta\leq 0, \quad \text{in } \Omega$$

SOLUTION PROCEDURE : OPTIMIZATION ALGORITHM

Solution procedure for the shape optimization is described in the following flow chart.

Program Flow Chart

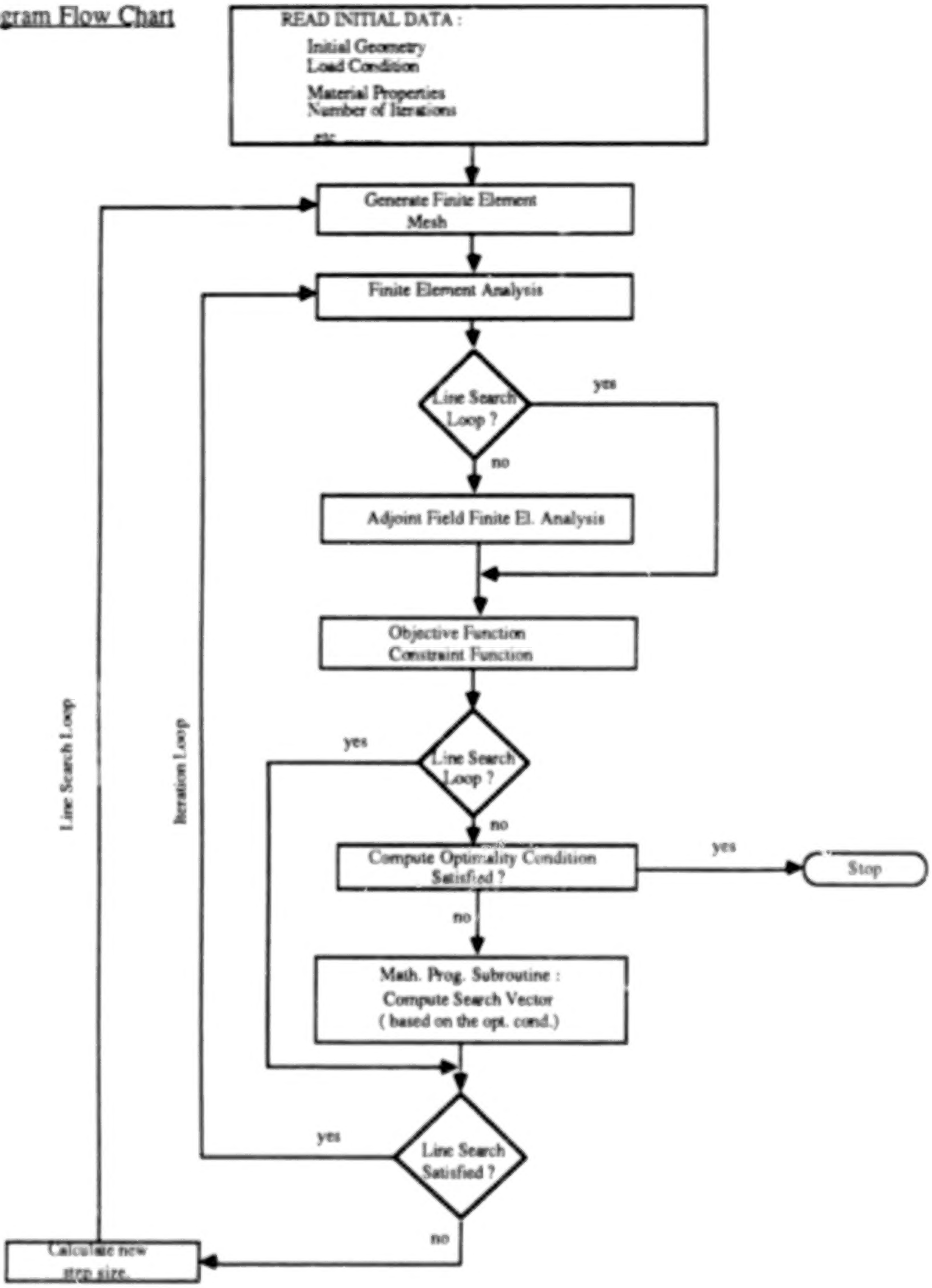
READ INITIAL DATA :
Initial Geometry
Load Condition
Material Properties
Number of Iterations
etc.
Generate Finite Element Mesh
Finite Element Analysis
Line Search Loop ?
yes
no
Adjoint Field Finite El. Analysis
Objective Function
Constraint Function
Line Search Loop ?
yes
no
Compute Optimality Condition Satisfied ?
yes
Stop
no
Math. Prog. Subroutine :
Compute Search Vector
(based on the opt. cond.)
Line Search Satisfied ?
yes
no
Calculate new step size.
Line Search Loop
Iteration Loop

MESH GENERATION METHOD : ELLIPTIC MESH GENERATOR

At each design iteration, a new finite element mesh is reconstructed using the elliptic mesh generation method. In most of shape optimization practice, finite element meshes are not regenerated, but are modified during the optimization process. Because of the method applied for modification of the initial finite element mesh, unnecessary element distortion is, in general, generated in each iteration. Element distortion can become so large it can actually destroy accuracy of the finite element approximations, and then yield unsatisfactory results in shape optimization. To avoid this difficulty, it is better to regenerate a finite element mesh at each design stage despite of expense required. Here the elliptic mesh generation method is used that generates almost orthogonal meshes using only the data of the boundary of the domain occupied by a structure. If the boundary is represented by a set of spline curves, it is possible to represent the design boundary by several spline functions defined by the location θ_α, $\alpha=1,...,\alpha_{max}$, of the so-called control points without loss of generality.

Elliptic Mesh Generation Method

$$\nabla(\mathbf{D}\nabla\xi) = -P(\xi,\eta) \quad \text{and} \quad \nabla(\mathbf{D}\nabla\eta) = -Q(\xi,\eta)$$

where $\nabla = \mathbf{i}\frac{\partial}{\partial x} + \mathbf{j}\frac{\partial}{\partial y}$, (x,y) are the physical coordinates, and (ξ,η) are the mesh coordinates.

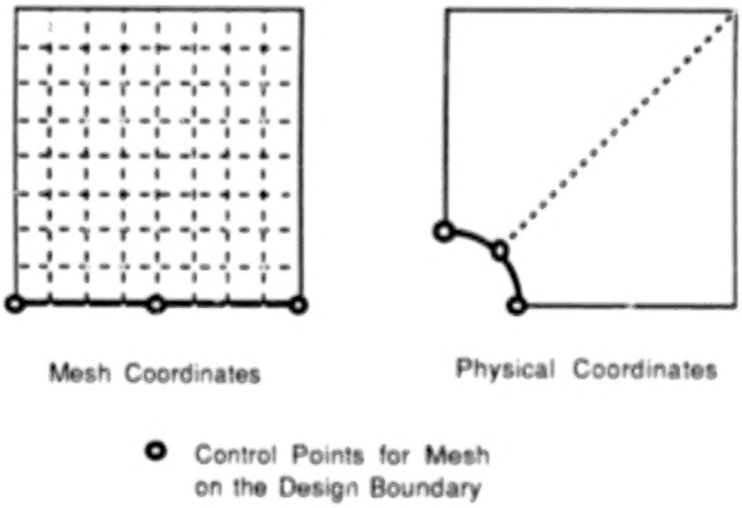

EXAMPLE : MODEL A

Model Problem A is to find the optimally shaped hole in a biaxially loaded linearly elastic thin plate. Starting from a rectangular hole, the optimal shape of the hole is obtained for the loading condition which yields an elliptic hole as the optimum. Applying the symmetry condition, only a quarter part of the plate is discretized by 110 QUAD4 elements together with 11 control points on the design boundary for shape optimization. The minimum admissible area of the hole prescribed by the user is restricted to $A=0.16m^2$. Iteration history and the optimal shape are given in the figure. The first three redesigns rapidly reduce the maximum value of the von Mises equivalent stress from 6.6 to 3.3, while the optimum obtained after 23 iterations is about 2.8.

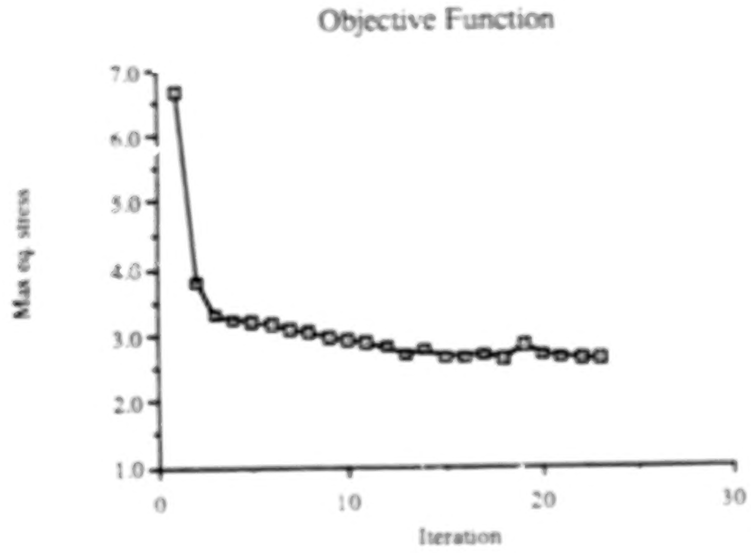

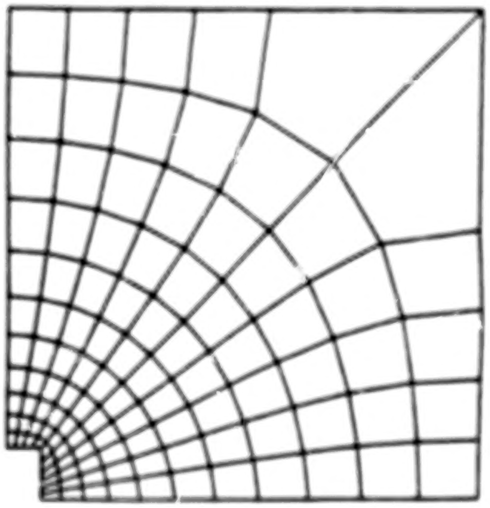

Iteration 1

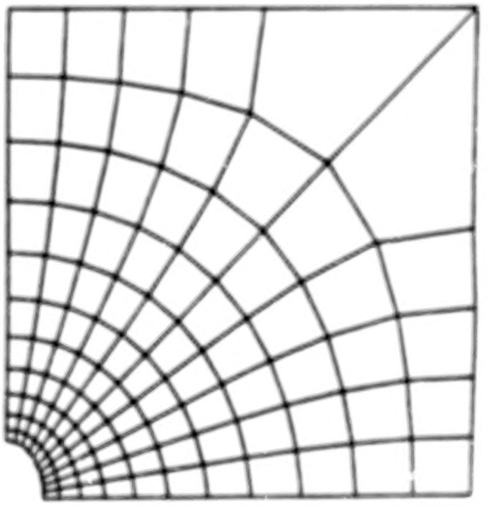

Iteration 23

EXAMPLE : MODEL B

For finding the optimal shape for a linearly elastic fillet, the domain is discretized by 126 QUAD4 elements together with 14 control points on the design boundary. In this case, the objective function F is the von Mises equivalent stress. Assuming that the maximum allowable area of the fillet is restricted to $A=1.135 \times 10^{-2} m^2$, an optimal shape is obtained. The maximum value of the equivalent stress becomes very stable after 15 design iterations, and its minimum is achieved at the 24th iteration. This means that optimization and finite element remeshing is performed 24 times. First 10 iterations give rapid reduction of the maximum value of the stress. The maximum von Mises stress in the final fillet obtained is less than half of the maximum stress of the initial structure.

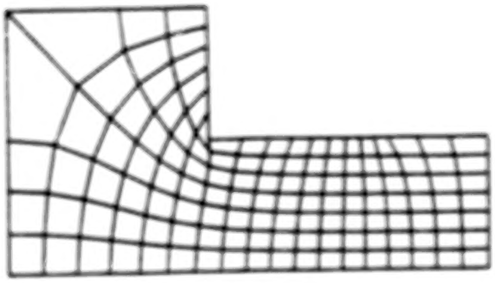

Iteration 1

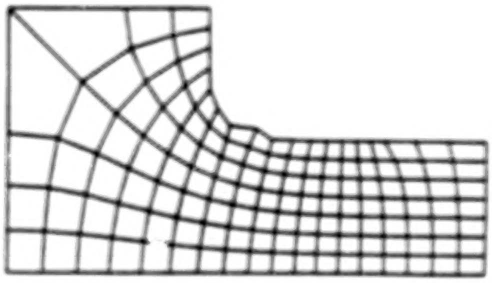

Iteration 3

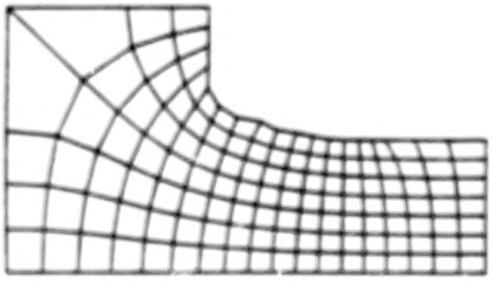

Iteration 11

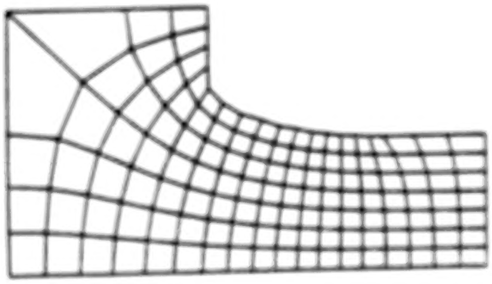

Iteration 24

FINAL REMARKS

The development presented introduces a general form of mixed formulation for the optimal shape design problem, and the associated optimality conditions are easily obtained without resorting to highly elaborate mathematical developments. Also the physical significance of the adjoint problem comes out to be clearly defined with this formulation.

In the examples presented, an elliptical automatic mesh generator assuring an orthogonal finite element mesh at the domain boundary [see, e.g. 7] was used at each shape redesign . Although this procedure might seem to be computationally a very expensive procedure, actually it guarantees a good accuracy for the discrete model with an increase on computational time of less than 5% of the actual time required for the finite element analysis.

The numerical examples presented demonstrates the stability of the procedure. Problems commonly encountered in shape optimization arising from the development of instabilities in the design boundary definition were largely avoided. As is to be expected, however, this improvement is accomplished at the expense of the increase in cost of computation as compared to the simple displacement formulation.

SHAPE OPTIMIZATION

1. **Mixed Finite Element Methods for Analysis**
2. **Automatic Remeshing Scheme by Elliptic Mesh Generation Methods**
3. **Optimality Conditions are Obtained by the Upper Bound Method**
4. **Demonstration by Numerical Examples**

REFERENCES

[1] - Taylor , J. E. and Bendsoe , M. P. (1984) , " An Interpretation for Min - Max Structural Design Problems Including a Method for Relaxing Constraints , " Int . J. Solids and Structures , Vol. 20 , No. 4 , pp . 301 - 314 .

[2] - Chung , K. Y. (1985) , " Shape Optimization and Free Boundary Value Problem Problems With Grid Adaptation , " Ph. D. Thesis , The University of Michigan, Ann Arbor , Michigan.

[3] - Na , M. S. , Kikuchi , N. and Taylor J. E. (1983) , " Optimal Modification of Shape for Two - Dimensional Elastic Bodies , " J. Struct. Mech. , 11 (1) , pp. 111 - 135 .

[4] - Cea , J. (1981) , " Problems of Shape Optimal Design , " Optimization of Distributed Parameter Structures Vol. II (eds. Haug , E. J. and Cea, J.), Sijthoff and Noordhoff .

[5] - Haug , E. J. , Choi , K. K. , and Komkov , V. (1986) , " Design Sensitivity Analysis of Structural Systems ," Academic Press .

[6] - Zolesio, J.P. (1981) , " Material Derivative (or Speed) Method for Shape Optimization, " Optimization of Distributed Parameter Structures Vol. II (eds. Haug , E. J. and Cea, J), Sijthoff and Noordhoff .

[7] - Kikuchi , N. (1986) , " Adaptive Grid - Design Methods For Finite Element Analisys , " Comp. Meth. Appl . Mech. Engrg. , " Vol. 55 , pp . 129 - 160

[8] - Atluri, S. N. , Gallagher, R. N. and Zienkiewicz, O. C. (eds.) (1983) ,
" Hybrid and Mixed Finite Element Methods, " Wiley .

[9] - Washizu , K. (1983) , " Variational Methods in Elasticity and Plasticity, " Pergamon Press.

[10] - Pshenichny, B. N. and Danilin, Yu. M. (1978), " Numerical Methods in Extremal Problems, " Mir Publishers .

[11] - Haftka, R.T. and Grandhi, R. V. (1986), "Structural Shape Optimization - a survey ," Comp. Meth. Appl . Mech. Engrg. , " Vol. 57 , pp . 91- 106 .

[12] - Zienkiewicz , O. C. and Campbell , J. S. (1973), " Shape Optimization and Sequential Linear Programming " , Optimum Structural Design (eds. Gallagher , R. H. and Zienkiewicz , O. C.) , Wiley , London.

[13] - Yang, R. J. , Choi, K. K. and Haug, E. J. (1985), " Numerical Considerations in Structural Component Shape Optimization ," ASME J. of Mechanisms , Transmissions and Automation in Design , Vol. 107 , pp 334 - 339 .

[14] - Dems, K. and Mroz, Z. (1978), " Multiparameter Structural Shape Optimization, by the Finite Element Method ," Int. J. Num. Meth. Engrg., Vol. 13 , pp. 247 - 263.

[15] - Braibant , V. and Fleury, C. (1984) , " Shape Optimal Design Using B-splines ," Comp. Meth. Appl. Mech. Engrg., Vol. 44, pp. 247 - 267 .

[16] - Eizadian, D. and Trompette, P. (1985) , " Shape Optimization of Bidimensional Structures by the Boundary Element Method, CAD/CAM, Robotics and Automation Conference, Tucson, Arizona

[17] - Mota Soares , C. A. , Rodrigues , H. C. and Choi , K. K. (1984) , " Shape Optimal Structural Design Using Boundary Elements and Minimum Compliance Techniques" , ASME J. of Mechanisms , Transmissions and Automation in Design , Vol. 106 , pp 518 - 523 .

[18] - Burczynsky, T. and Adamczyk, T. (1985), "The Boundary Element Formulation for Multiparameter Shape Optimization," Appl. Mathematical Modelling , 9 , pp. 195 - 200

[19] - Choi, K. K. and Seong, H. G.(1986) " A Domain Method for Shape Design Sensitivity Analysis of Built -Up Structures, " Comp. Meth. Appl . Mech. Engrg. , " Vol. 57, pp 1 - 15

[20] - Haber, R. B. (1986), "Application of the Eulerian Lagrangian Kinematic Description to Structural Shape Design, " Computer Aided Optimal Design: Structural and Mechanical Systems," (ed. Mota Soares, C. A.), NATO ASI Series, Series F : Computer and Systems Sciences, Vol. 27, Spinger - Verlag.

N88-23253

MODAL FORCED RESPONSE OF PROPFANS IN YAWED FLOW*

G.V. Narayanan
Sverdrup Technology, Inc.
(Lewis Research Center Group)
NASA Lewis Research Center

ABSTRACT

This research is part of the ongoing NASA Lewis aeroelastic research program on propfans. A modal forced response method for propfans in yawed flow is presented here. This capability now exists in the Aeroelastic Stability and Response of Propfan (ASTROP3) code that has been developed at NASA Lewis.

The ASTROP3 code by Kaza et al. (1987) uses three-dimensional steady and unsteady cascade aerodynamics by Williams and Hwang (1986) and a NASTRAN finite element model to represent the blade structure. In addition, many utility programs exist in ASTROP3 that help in both the preprocessing of the NASTRAN model and the postprocessing of modal response results. This presentation will highlight the postprocessing work that computes the blade vibratory displacements and stresses in yawed flow.

Code validation for obtaining the blade vibratory displacements and stresses using this method was done successfully by comparing one-per-rev measured blade vibratory stresses and calculated values for two single-rotation propfan models. Data from the SR5 model with 10 blades and SR3 model with 8 blades are used for the code validation. The correlation between theory and experiment is good.

ORIGINAL PAGE IS
OF POOR QUALITY

PRECEDING PAGE BLANK NOT FILMED

---

*Work performed on-site at the Lewis Research Center for the Structural Dynamics Branch.

INTRODUCTION

The presentation will give a description of the propfan models and outline a method of calculating modal forced response of propfans in yawed flow. In particular, the discussion will be on the postprocessing routines developed and implemented for computing vibratory displacements and stresses in ASTROP3. In addition, the comparison of measured and calculated stresses for the SR5 and SR3 propfan models will be presented for selected cases.

- PROPFAN MODEL DESCRIPTION
- MODAL FORCED RESPONSE METHOD IN ASTROP3
- POSTPROCESSING ROUTINES
- COMPARISON OF MEASURED AND CALCULATED RESULTS

CD-88-[illegible]

ORIGINAL PAGE IS
OF POOR QUALITY

PROBLEM DEFINITION

The models considered for analyses are the SR5 propfan with 10 blades and the SR3 propfan with 8 blades. In both these propfans, the blades are made of titanium. The SR5 propfan installation in the Lewis 8- by 6-foot wind tunnel is shown below at the left. For these propfans, the given parameters in the analysis are the inflow angle, the rotor speed, the wind tunnel velocity of air, and the blade pitch setting angle. The blade vibratory displacements and stresses are solved for in the analysis.

SR5 PROPFAN

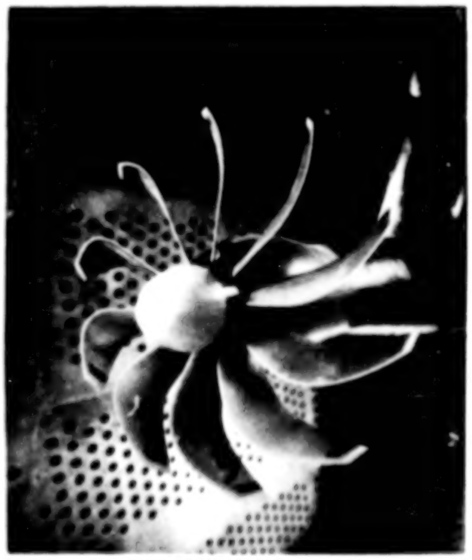

CD-88-32832

PROBLEM DEFINITION
MODELS

MODELS
- SR5 (10 BLADES)
- SR3 (8 BLADES)
- TITANIUM

GIVEN PARAMETERS
- INFLOW ANGLE
- ROTOR SPEED
- TUNNEL VELOCITY
- BLADE PITCH SETTING ANGLE

CALCULATED PARAMETERS
- BLADE VIBRATORY DISPLACEMENTS AND STRESSES

CD-88-32831

FLOWCHART OF MODAL FORCED RESPONSE ANALYSIS

The modal forced response analysis consists of eight steps, as shown in the blocks below. In step 1, finite element analysis is used to obtain steady-state deflections and the differential stiffness matrix (Lawrence and Kielb, 1984). In step 2, the differential stiffness matrix generated in step 1 is used to determine the blade natural frequencies and mode shapes in the deformed state. In step 3, the generalized equations of motion are formulated for the system. In step 4, the calculation of the airloads distribution over the rotating blades inclined at a unit yaw angle is done (Williams and Hwang, 1986). In step 5, the solution of the generalized coordinate values for the given operating conditions is obtained. These values are referred to as modal participation factors. In steps 6 and 7, the physical displacements and finite element stresses are retrieved by appropriate modal summation using modal participation factors. Lastly, in step 8, the finite element stresses are transformed into normal and shear stresses along the measured blade strain gage directions. Steps 1 through 5 have been discussed by Kaza et al. (1988). Steps 6 through 8 will be discussed in detail in this presentation.

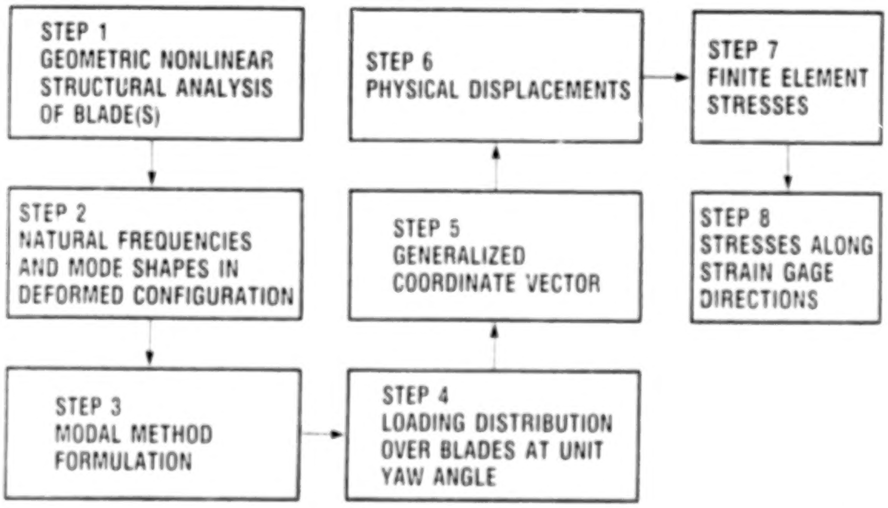
STEP 1
GEOMETRIC NONLINEAR STRUCTURAL ANALYSIS OF BLADE(S)
STEP 6
PHYSICAL DISPLACEMENTS
STEP 7
FINITE ELEMENT STRESSES
STEP 2
NATURAL FREQUENCIES AND MODE SHAPES IN DEFORMED CONFIGURATION
STEP 5
GENERALIZED COORDINATE VECTOR
STEP 8
STRESSES ALONG STRAIN GAGE DIRECTIONS
STEP 3
MODAL METHOD FORMULATION
STEP 4
LOADING DISTRIBUTION OVER BLADES AT UNIT YAW ANGLE

CD-88-32932

COORDINATE SYSTEMS

The global coordinate system used in ASTROP3 is shown at the left. The global X-axis is along the propeller thrust axis. The blade plane of rotation is the Y-Z plane. The physical displacements along X-, Y-, and Z-axes are represented by u, v, and w, respectively. A typical triangular finite element is shown on the blade at the left. The stresses on the finite element are in the local element coordinate system. This is shown in the figure on the right. Normal and shear element stresses in the local x- and y-axes directions are represented by σ_{xx}, σ_{yy}, and τ, respectively.

GLOBAL COORDINATE SYSTEM

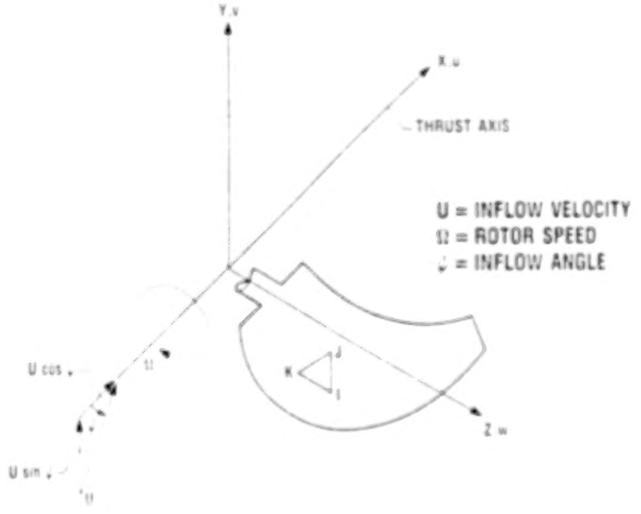
Y,v
X,u
THRUST AXIS
U = INFLOW VELOCITY
Ω = ROTOR SPEED
ψ = INFLOW ANGLE
U cos ψ
Ω
K
J
I
Z,w
U sin ψ
U
CD-88-32933

LOCAL ELEMENT COORDINATE SYSTEM

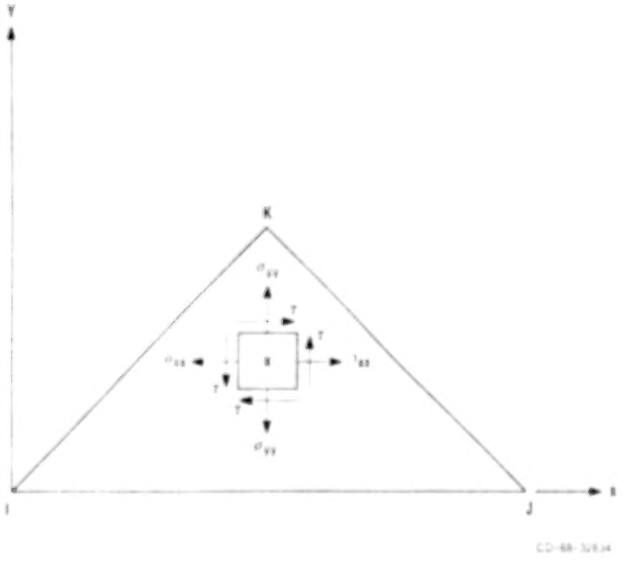
Y
K
σyy
τ
τ
σxx
x
σxx
τ
τ
σyy
I
J
x
CD-88-32934

PHYSICAL DISPLACEMENT

The physical displacements on the blade can be obtained by appropriate summation of the modal displacements using participation factors $\{(q_j), j=1,NM\}$ as modal weights. The summations of the modal displacements are written in mathematical form below. A routine called TOTAD exists in ASTROP3 that performs this set of calculations. Depending on the need, one can obtain either amplitude or phase of physical displacement at a grid, or both of these values.

PHYSICAL DISPLACEMENTS ON BLADE

$$u_i = \sum_{j=1}^{NM} q_j u_{ij}$$

$$v_i = \sum_{j=1}^{NM} q_j v_{ij}$$

$$w_i = \sum_{j=1}^{NM} q_j w_{ij}$$

WHERE i = GRID NUMBER AND j = MODE NUMBER

CD-88-32835

PARAMETERS

NM	NUMBER OF MODES
q_j	GENERALIZED COORDINATE VALUES FOR MODE j
(u_{ij}, v_{ij}, w_{ij})	MODAL DISPLACEMENT VECTOR AT GRID i FOR MODE j

CD-88-32836

ELEMENT STRESS

Similar to physical displacements, the element stresses on the blade can be obtained by appropriate summation of the modal stresses using participation factors $\{(q_j), j=1,NM\}$ as modal weights. The summations of the modal stresses are written in mathematical form below. A routine called CESTRS exists in ASTROP3 that performs this set of calculations. An associated routine, called RDSTRS, has been developed to read the modal stresses on the blade for all modes.

ELEMENT STRESSES ON BLADE

$$(\sigma_{xx})^E = \sum_{j=1}^{NM} q_j \, (\sigma_{xx})_j^E$$

$$(\sigma_{yy})^E = \sum_{j=1}^{NM} q_j \, (\sigma_{yy})_j^E$$

$$(\tau)^E = \sum_{j=1}^{NM} q_j \, (\tau)_j^E$$

WHERE j = MODE NUMBER AND E = ELEMENT NUMBER

CD-88-[illegible]

PARAMETERS

NM	NUMBER OF MODES
q_j	GENERALIZED COORDINATE VALUES FOR MODE j
$(\sigma_{xx})_j^E$, $(\sigma_{yy})_j^E$, $(\tau)_j^E$	MODAL STRESSES ON FINITE ELEMENT E FOR MODE j

CD-88-[illegible]

CALCULATED ELEMENT AVERAGE STRESS IN GAGE DIRECTION

Let g represent a uniaxial strain gage located on the blade in a direction that makes angle θ^g with the global Y-axis. The figures below show the element stress and gage directions. It can be noted that the gage location may not coincide with the centroid of any of the finite elements of the blade. In such a case, the finite elements surrounding gage g are identified from the geometry of the blade. For the element surrounding gage g, element stresses are transformed to be in the gage direction. The stress transformation relations are also given below. These transformed stresses are used to compute an element average stress in the gage direction. A routine called GAGEST exists in ASTROP3 that performs the computation of normal and shear stresses in strain gage directions. The stress averaging of the calculated element stresses in the strain gage direction is done in ASTROP3 by CESTRS routine.

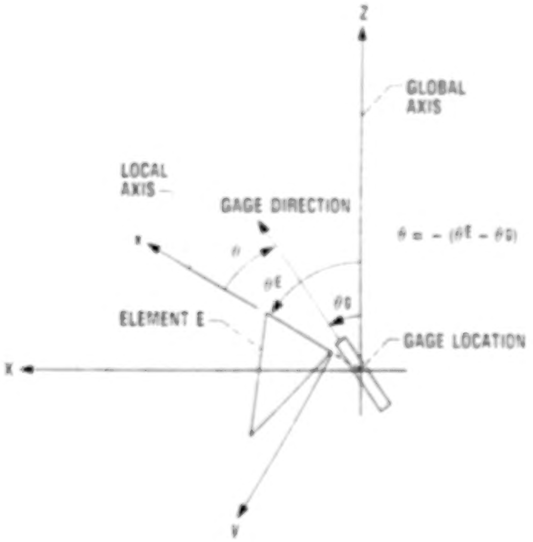

WHERE θ = ANGLE BETWEEN ELEMENT x-AXIS AND GAGE DIRECTION

ELEMENT STRESS IN STRAIN GAGE DIRECTIONS

$$(\sigma_n)^E_T = \frac{(\sigma_{xx})^E + (\sigma_{yy})^E}{2} + \frac{(\sigma_{xx})^E - (\sigma_{yy})^E}{2} \cos(2\theta) + (\tau)^E \sin(2\theta)$$

$$(\tau)^E_T = \frac{(\sigma_{xx})^E - (\sigma_{yy})^E}{2} \sin(2\theta) - (\tau)^E \cos(2\theta)$$

AVERAGE ELEMENT STRESS IN GAGE DIRECTION

$$(\sigma_n)^g = \frac{1}{(NE)} \sum_{E=1}^{NE} (\sigma_n)^E_T$$

$$(\tau)^g = \frac{1}{(NE)} \sum_{E=1}^{NE} (\tau)^E_T$$

WHERE NE = NUMBER OF ELEMENTS SURROUNDING GAGE g

COMPARISON OF MEASURED AND CALCULATED STRESSES

For the SR5 propfan model, the normal stresses on an inboard strain gage for two inflow angles are used for comparison of measured and calculated stresses. Also, the calculated stresses for four strain gages are compared with experimental values for the SR3 propfan model. The calculated values for SR5 are lower than the experimental values by 20 to 50 percent, whereas the calculated values for SR3 are higher than the experimental values by 10 to 50 percent except for strain gage 2.

SR5 PROPFAN

(MACH = 0.36, rpm = 6000, $\beta_{3/4R} = 60.8$)

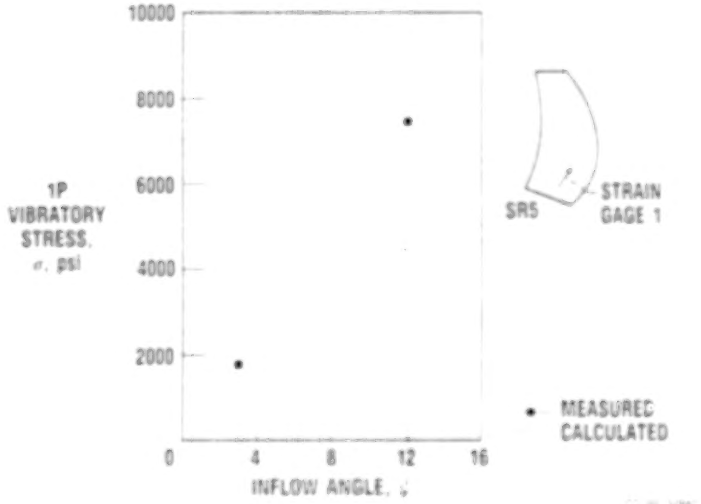

SR3 PROPFAN

(MACH = 0.353, rpm = 8000, $\beta_{3/4R} = 48.9$, ψ = 8°)

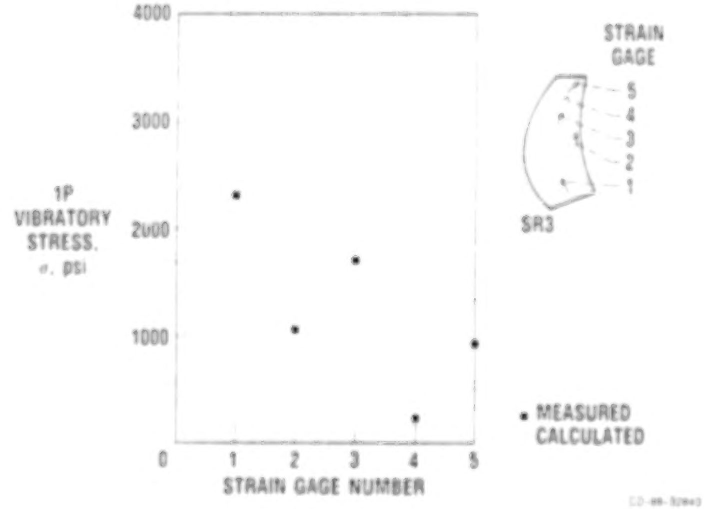

SUMMARY

A method for the computation of vibratory displacements and stresses for propfans in yawed flow is presented. This capability now exists in ASTROP3.

- MODAL FORCED RESPONSE ANALYSIS FOR PROPFANS IN YAWED FLOW DEVELOPED
- USES 3-D STEADY AND UNSTEADY CASCADE AERODYNAMICS
- CALCULATES BLADE VIBRATORY DISPLACEMENTS AND STRESSES
- PART OF ASTROP3 CODE

REFERENCES

Kaza, K.R.V. et al., 1987, "Analytical Flutter Investigation of a Composite Propfan Model," AIAA Paper No. 87-0738, NASA TM-88944.

Kaza, K.R.V. et al., 1988, "Forced Response of Metallic and Composite Propfan Models in Yawed-Flow," AIAA/ASME/ASEE/SAE 24th Joint Propulsion Conference and Exhibit, Boston, Massachusetts, July 11-14, 1988.

Lawrence, C., and Kielb, R.E., 1984, "Nonlinear Displacement Analysis of Advanced Propeller Structures using NASTRAN," NASA TM-83737.

Williams, M.H., and Hwang, C., 1986, "Three-dimensional Unsteady Aerodynamics and Aeroelastic Response of Advanced Turboprops," AIAA 27th Structures, Structural Dynamics and Materials Conference, Part 2, New York, pp. 116-124.

STRUCTURAL DYNAMICS CODE APPLICATIONS

SESSION OVERVIEW

Krishna Rao V. Kaza
Structrual Dynamics Branch
NASA Lewis Research Center

The first two presenters of this session have applied aeroelastic codes for stability analyses. The first paper deals with the stability analysis of an advanced, large-scale propfan. A computer code based on three-dimensional, subsonic, unsteady, lifting surface aerodynamic theory is used to examine the propfan's stability at a cruise condition of Mach 0.8 and 1700 rpm. The second paper presents a flutter analysis of the NASA Lewis supersonic through-flow fan. Lane's formulation of unsteady pressure distribution on an oscillating two-dimensional flat plate cascade in supersonic axial flow was developed into a computer code and incorporated with an existing aeroelastic code for the analysis. The last presenter will describe the development of a methodology for the analysis of stall flutter of propfans and its implementation within an aeroelasticity code. This stall flutter analysis uses empirical dynamic stall aerodynamic models and a finite element structural model. Calculated results are correlated with a propfan model's stall flutter data.

TYPES OF AEROELASTICITY PROBLEMS STUDIED

- STABILITY OF A LARGE-SCALE PROPFAN (AUGUST)
- SUPERSONIC AXIAL FLOW FAN FLUTTER (RAMSEY)
- STALL FLUTTER ANALYSIS OF PROPFANS (REDDY)

CD-88-32626

STRUCTURAL DYNAMICS CODE APPLICATIONS

This session has two papers dealing in the dynamic characterization of rotating blades and one paper involving computational methods. The first presenter will discuss predicting blade natural frequencies of single crystal turbopump blades in order to find possible critical engine order excitations. The second presenter will discuss a code restructuring program called Parafrase that aids in the optimization of codes for implementation with parallel processing machines. The last presenter will describe techniques used for the nonlinear analysis of rotating flexible blades with MSC/NASTRAN.

GENERAL DYNAMIC PROBLEMS STUDIED

- SSME SINGLE-CRYSTAL TURBINE BLADE DYNAMICS (MOSS)
- PARAFRASE RESTRUCTURING OF FORTRAN CODE FOR PARALLEL PROCESSING (WADHWA)
- ANALYSIS OF ROTATING FLEXIBLE BLADES USING MSC/NASTRAN (ERNST)

CD-88-32627

N88-23254

VIBRATION AND FLUTTER ANALYSIS OF THE SR-7L LARGE-SCALE PROPFAN

Richard August*
Sverdrup Technology, Inc
(Lewis Research Center Group)
NASA Lewis Research Center

ABSTRACT

One of the major research and technology programs at NASA Lewis Research Center is the Advanced Turboprop Program. The goal of this effort is the development of turboprop (also known as propfan) propulsion systems that would have significant gains in fuel economy over turbofans without sacrificing aircraft performance. An important phase of this program is the Large-Scale Advance Propfan Program (LAP). This program involves the development and both ground and flight testing of a complete eight-bladed, 2.7-m- (9-ft-) diameter rotor system.

The SR-7L advanced turboprop blade used in the LAP program is designed for a Mach number of 0.80 at an altitude of 10.7 km (35 000 ft). It uses a number of unique design features, such as thin, highly swept and twisted, composite material blades of low aspect ratio and high disc solidity, to improve propeller performance. Recent research efforts at Lewis have focused on these properties, particularly with respect to improved structural modeling and aeroelastic analysis of the bladed propfan assemblies. Some areas where new analytical techniques have been implemented include composite blade modeling, nonlinear displacement analysis, and three-dimensional, aeroelastic analysis.

This paper presents a structural and aeroelastic analysis of the SR-7L advanced turboprop incorporating the aforementioned techniques. Analyses were conducted for selected cases at different blade pitch angles, blade support conditions, rotational speeds, free-stream Mach numbers, and number of blades. A finite element model of the final blade design was used to determine the blade's vibration behavior and its sensitivity to support stiffness. A computer code recently developed at Lewis, which was based on three-dimensional, subsonic, unsteady lifting surface aerodynamic theory, was used for the aeroelastic analysis to examine the blade's stability at a cruise condition of Mach 0.8 at 1700 rpm. The results showed that the calculated frequencies and mode shapes obtained with this model agreed well with the published experimental data and that the blade is stable for that operating point.

---

*Work performed on-site at the Lewis Research Center for the Structural Dynamics Branch.

SR-7L FLUTTER ANALYSIS DESCRIPTION

The analysis procedure consisted of using the blade's finite element model to obtain the vibration characteristics at the design rotational speed and then conducting aeroelastic studies to determine unstalled flutter stability at the design condition. The finite element code MSC/NASTRAN was used extensively to calculate the vibration characteristics of the blade using techniques suggested by Lawrence et al. (1984, 1987). The calculated frequencies and mode shapes were then used in conjunction with the computer program ASTROP (Aeroelastic STability and Response Of Propulsion Systems), a recently developed modal flutter code, for the aeroelastic stability studies (Kaza, 1987).

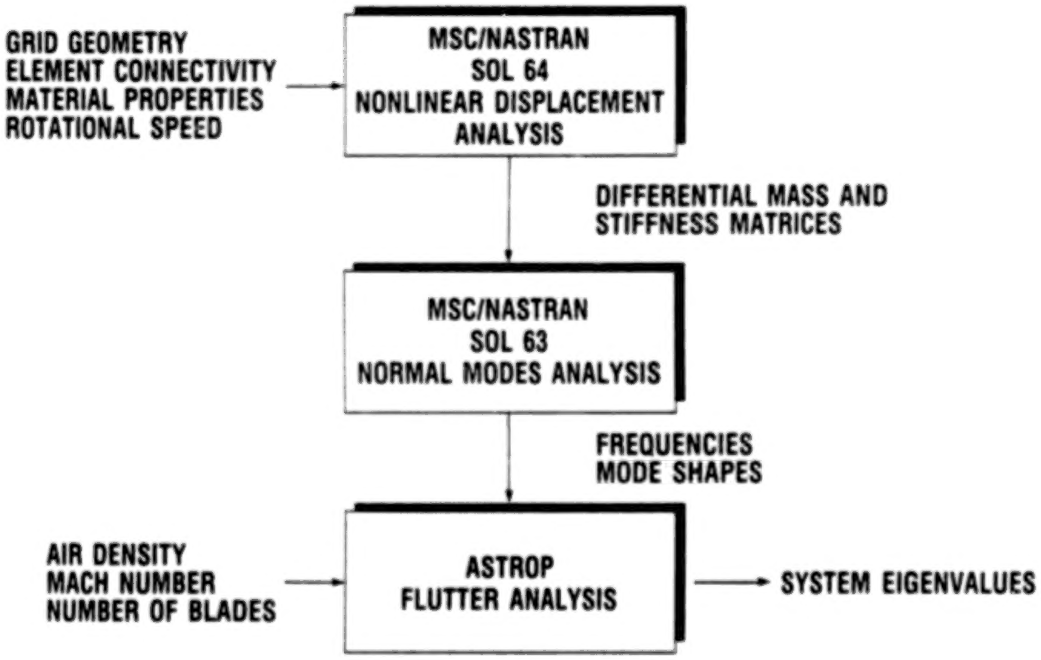
GRID GEOMETRY
ELEMENT CONNECTIVITY
MATERIAL PROPERTIES
ROTATIONAL SPEED
MSC/NASTRAN
SOL 64
NONLINEAR DISPLACEMENT ANALYSIS
DIFFERENTIAL MASS AND STIFFNESS MATRICES
MSC/NASTRAN
SOL 63
NORMAL MODES ANALYSIS
FREQUENCIES
MODE SHAPES
AIR DENSITY
MACH NUMBER
NUMBER OF BLADES
ASTROP
FLUTTER ANALYSIS
SYSTEM EIGENVALUES

CD-88-32302

SR-7L FINITE ELEMENT MODEL DESCRIPTION

The NASTRAN finite element model used in this study is based on the final SR-7L design. The blade geometry and airfoil data were obtained from the engineering design drawings. The composite material properties were calculated by a micromechanics approach using available fiber and matrix properties obtained from actual testing of the material. Shell, adhesive, spar, and shell filler material were combined using the composite blade structure analysis (COBSTRAN) program to produce monolithic shell elements (Aiello and Chi, 1987). The finite element model has 261 nodes, 449 triangular shell elements (NASTRAN element CTRIA3), and 5 bar elements (NASTRAN element CBAR). Bar elements were used to model the blade shank. Multipoint constraint cards that couple the displacement of prescribed gird points were used to define the shank-blade interface. The blade constraints were modeled by using spring elements attached to the base of the blade shank. A total of four degrees of freedom for the shank base were allowed: translation along the pitch change axis, bending rotations in and out of the plane of rotation, and rotation about the blade's pitch change axis. The blade shank was completely fixed for translation out of the plane of rotation and normal to the blade's rotation vector and pitch change axis (Chou, S., 1986, "SR-7L Turboprop Blade Finite Element Model," Sverdrup internal communication).

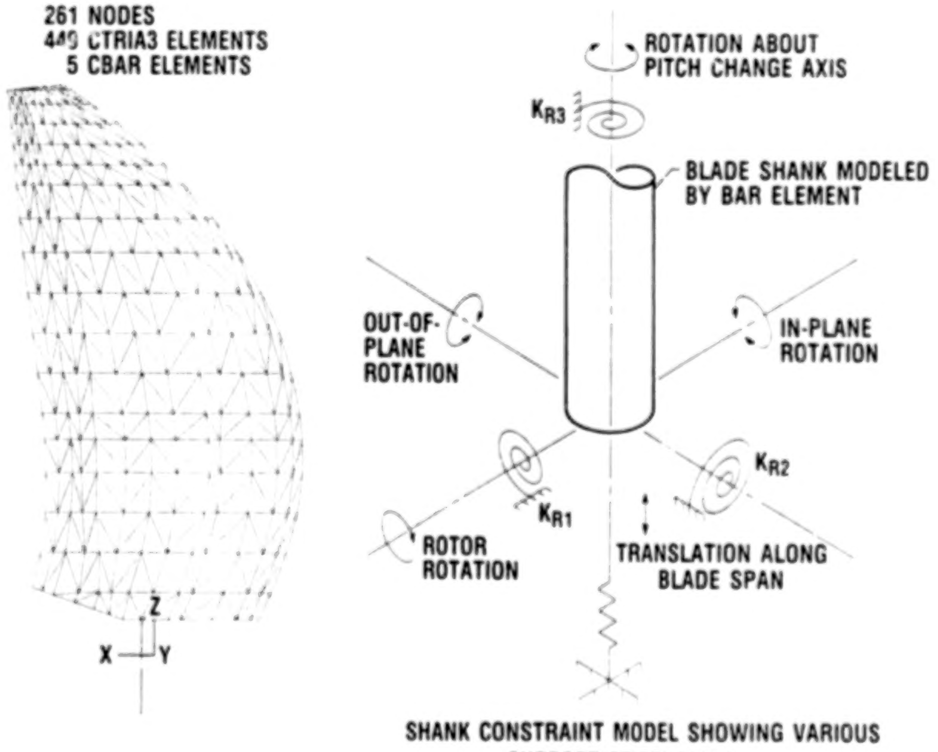
261 NODES
449 CTRIA3 ELEMENTS
5 CBAR ELEMENTS
Z
X
Y
ROTATION ABOUT PITCH CHANGE AXIS
K_{R3}
BLADE SHANK MODELED BY BAR ELEMENT
OUT-OF-PLANE ROTATION
IN-PLANE ROTATION
K_{R2}
K_{R1}
ROTOR ROTATION
TRANSLATION ALONG BLADE SPAN

SHANK CONSTRAINT MODEL SHOWING VARIOUS SUPPORT STIFFNESSES, K_R.

CD-88-32303

SR-7L CALCULATED MODE SHAPES AND FREQUENCIES

Since aeroelastic analyses are sensitive to blade frequencies and mode shapes, it is important that the blade finite element model and analysis accurately reflect the blade's modal characteristics. To establish the validity of the finite element blade model, it was necessary to show that calculated frequencies agreed well with experimental values. Consequently, frequencies and corresponding mode shapes were calculated at 1200 rpm over a range of blade setting angles from 35° to 60°, and were compared with those given by Turnberg (1986 handout of SR-7L test results distributed at the Advanced Turboprop Workshop, NASA Lewis Research Center). It should be noted that the calculated frequencies do not include the effect of steady airloads.

The blade's first mode is seen to be predominantly a first bending mode with no nodal lines and fairly evenly spaced contours in the upper half of the blade. The second mode is predominantly a first edgewise mode, with most of the motion occurring near the tip in the chordwise direction. The third mode can be classified as the second bending mode since there is a generally chordwise nodal line near the tip. The fourth mode can be classified as the first torsion mode since there is a midchord nodal line.

CONTOUR PLOTS

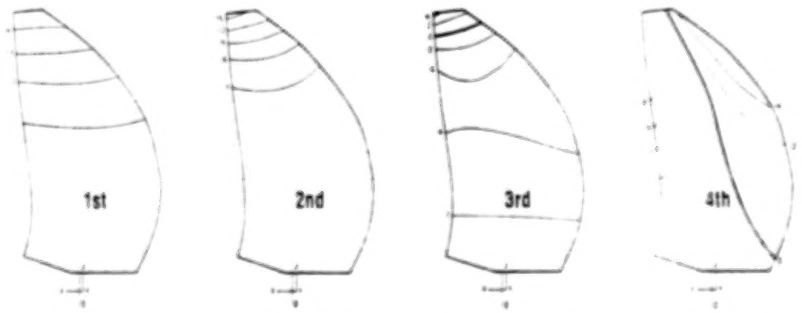

FIRST BENDING 38.10 Hz | FIRST EDGEWISE 86.89 Hz | SECOND BENDING 101.0 Hz | FIRST TORSION 160.9 Hz

CD-88-32304

"ANIMATED" MODE SHAPES

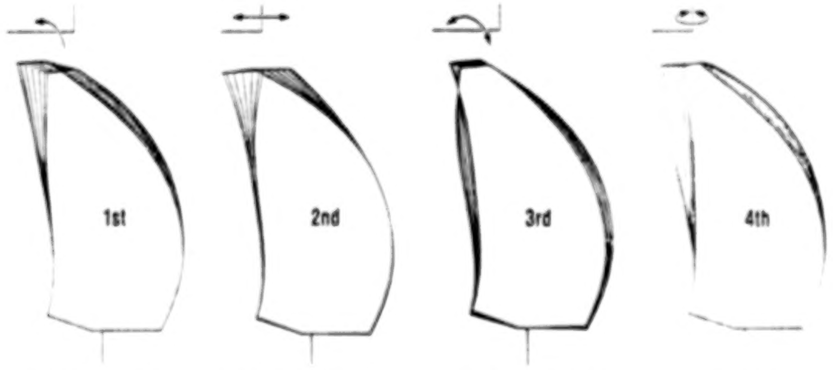

FIRST BENDING | FIRST EDGEWISE | SECOND BENDING | FIRST TORSION

CD-88-32305

ACCURACY OF CALCULATED SR-7L FREQUENCIES

A comparison of the measured and calculated frequencies shows that there is very good agreement for the first mode (i.e., first bending) over the entire range of blade setting angles. A comparison of the fourth mode frequencies (i.e., first torsion) similarly shows acceptable agreement. However, there is not a good match on the second mode, first edgewise, nor on the third mode, second bending. For both cases, the calculated frequencies were higher than the measured frequencies.

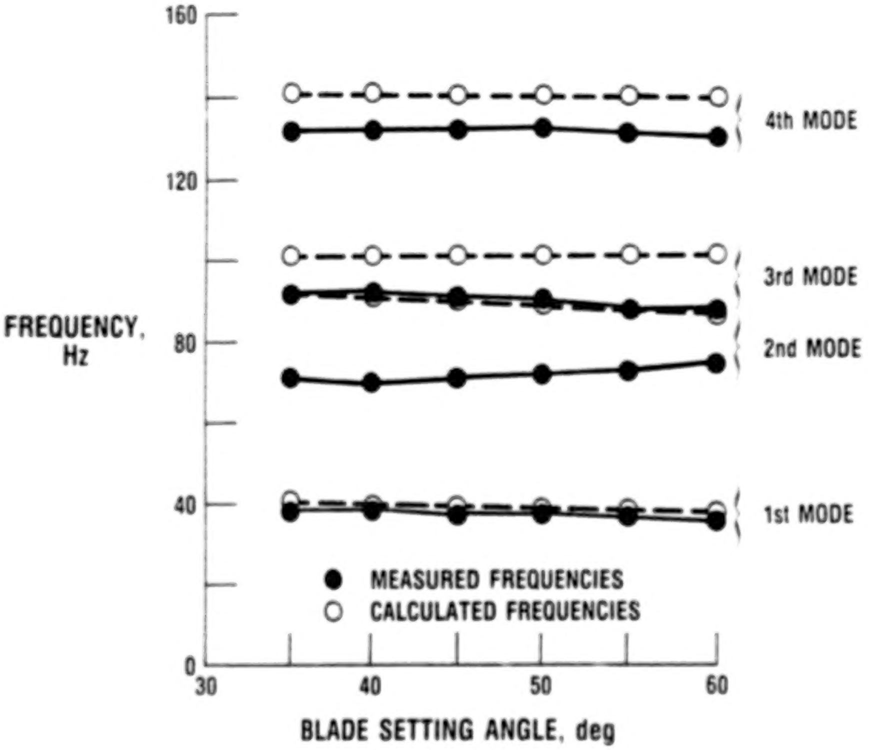

CD-88-32306

SR-7L CALCULATED FREQUENCIES VERSUS SUPPORT STIFFNESS

The values suggested by Sullivan et al. (1987) for the original model of the blade support stiffnesses were used to make parametric runs to examine the effect of varying these stiffnesses on natural frequencies and mode shapes. Each stiffness value was varied individually while the other values were held constant. Variation of the in-plane bending rotation support stiffness K_{R1} had little effect. The first two modes did have noticeable changes, but only over three orders of magnitude of stiffness changes. The pitching axis support stiffness K_{R3} and spanwise translational support stiffness had virtually no effect on the frequencies. However, the out-of-plane bending rotation support stiffness K_{R2} greatly affected the frequency values for the first edgewise mode. Frequencies for the first and second bending modes and for the first torsional modes were relatively unaffected. The edgewise mode could be selected to be the second, third, or fourth mode, depending on the out-of-plane bending stiffness value.

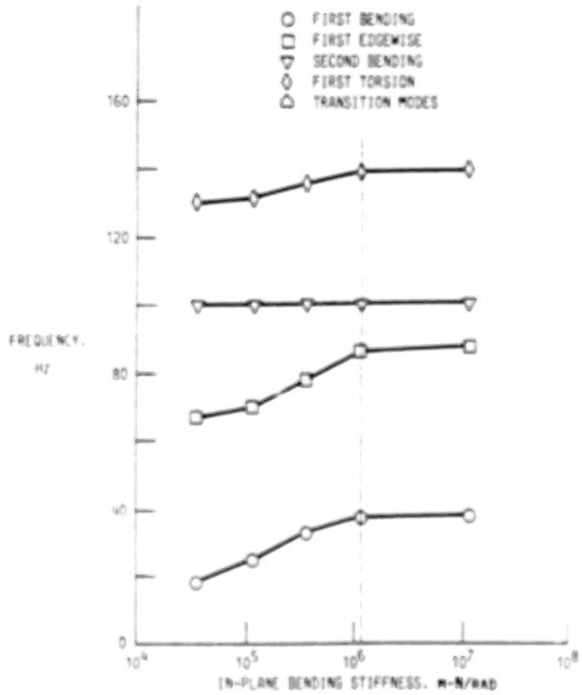

CD-88-32308

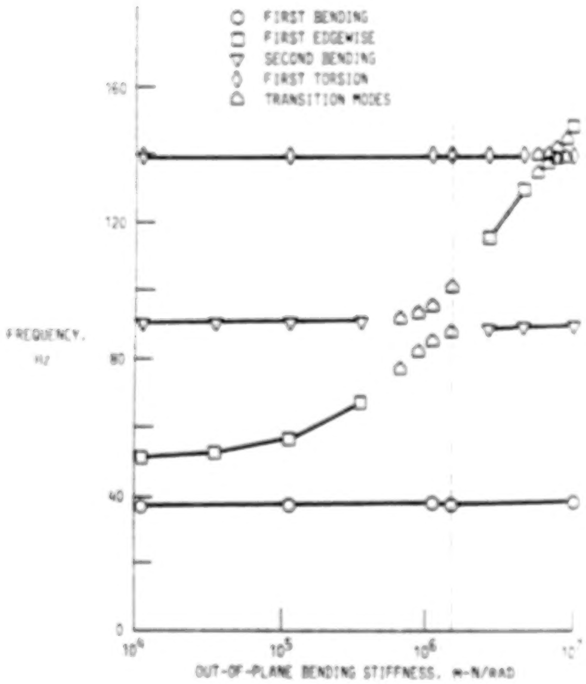

CD-88-32307

SR-7L BLADE MODAL DISPLACEMENTS VERSUS SUPPORT STIFFNESS

Examining the three-quarters radius chord modal displacement as viewed down the blade span helps characterize the mode shape. For relatively low values of K_{R2}, the second mode is clearly the first edgewise mode since the motion is nearly all in the chordwise direction. The first and third modes can be characterized as the first and second bending modes from the amount of blade normal displacements. The second mode from the first crossover region (K_{R2} = 1.514x10^6 m-N/rad) still has a fair degree of chordwise motion, although the leading edge area does have a some blade normal motion. Note that the third mode now also contains a degree of chordwise motion. At the second crossover region (K_{R2} = 1.13x10^8 m-N/rad), the second mode can be classified a bending mode because of the predominate blade normal displacements. The third mode is clearly the first torsional mode, whereas the fourth mode appears to be the first edgewise mode because of the chordwise motion at the leading edge.

The originally suggested values for K_{R2} cause the second and third modes to occur in a transition region between the first edgewise and second bending modes. This helps to account for the difference between the experimental and calculated second and third mode frequencies. The experimental edgewise mode is much lower than the calculated one, reflecting that mode's strong sensitivity to the support stiffness. The narrow range of values for the calculated second and third modes, and even for the experimental third mode, also illustrate the effect of the support stiffness within the crossover region.

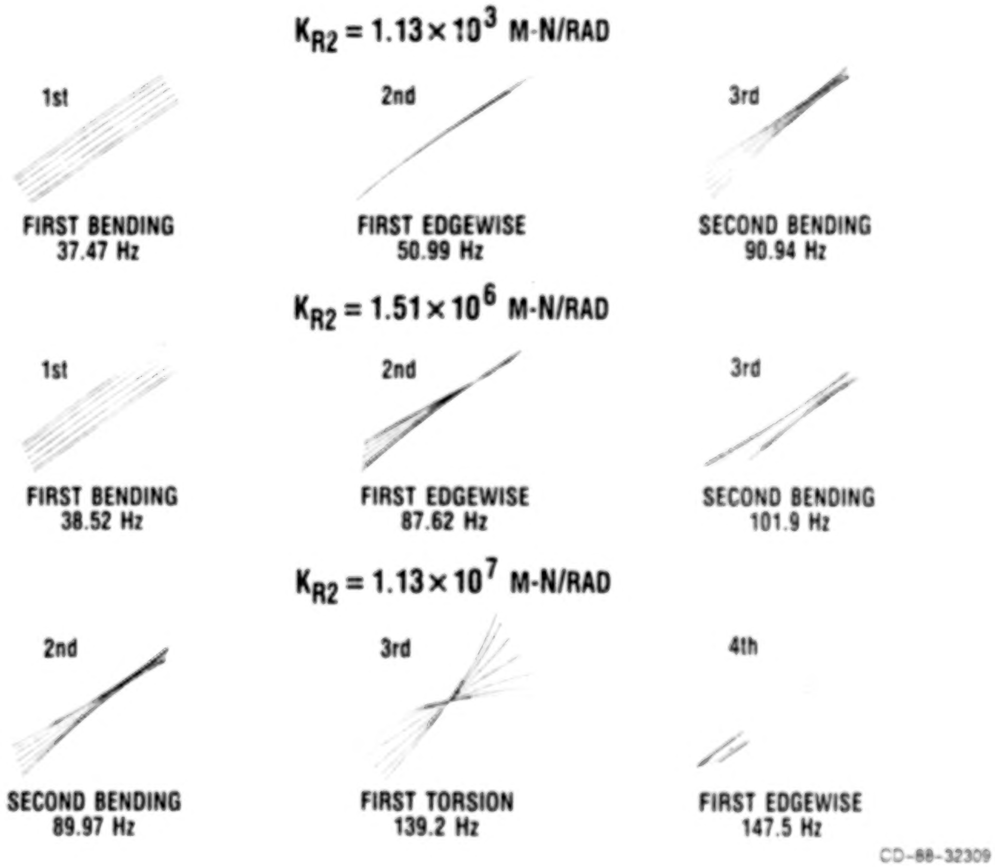

$K_{R2} = 1.13 \times 10^3$ M-N/RAD

1st — FIRST BENDING 37.47 Hz

2nd — FIRST EDGEWISE 50.99 Hz

3rd — SECOND BENDING 90.94 Hz

$K_{R2} = 1.51 \times 10^6$ M-N/RAD

1st — FIRST BENDING 38.52 Hz

2nd — FIRST EDGEWISE 87.62 Hz

3rd — SECOND BENDING 101.9 Hz

$K_{R2} = 1.13 \times 10^7$ M-N/RAD

2nd — SECOND BENDING 89.97 Hz

3rd — FIRST TORSION 139.2 Hz

4th — FIRST EDGEWISE 147.5 Hz

CD-88-32309

SR-7L CALCULATED FREQUENCIES VERSUS TUNED SUPPORT

From the parametric studies, values for the support stiffnesses were selected so that a "tuned support" model was developed. This was done in an attempt to give the best overall agreement between the calculated and measured frequencies. It was decided to try to soften the support stiffnesses since the edgewise, second bending, and torsional frequencies were too high. The value of K_{R1} was chosen at 4.52×10^5 m-N/rad because this seemed to be the minimum value above which there were very little changes in the blade frequencies. The value of K_{R2} was chosen slightly lower at 9.04×10^5 m-N/rad because this was the value that gave the best agreement with the experimental edgewise mode without greatly affecting the other three modes. Since the K_{R3} value seemed to have very little effect on the frequencies, it was purposely chosen to be very low (1.13×10^2 m-N/rad). The effect of the softer support springs are immediately evident. The first mode frequencies are slightly lower. However, the second, third, and fourth modes show much better agreement than before, especially near the operational blade setting angle of 58°.

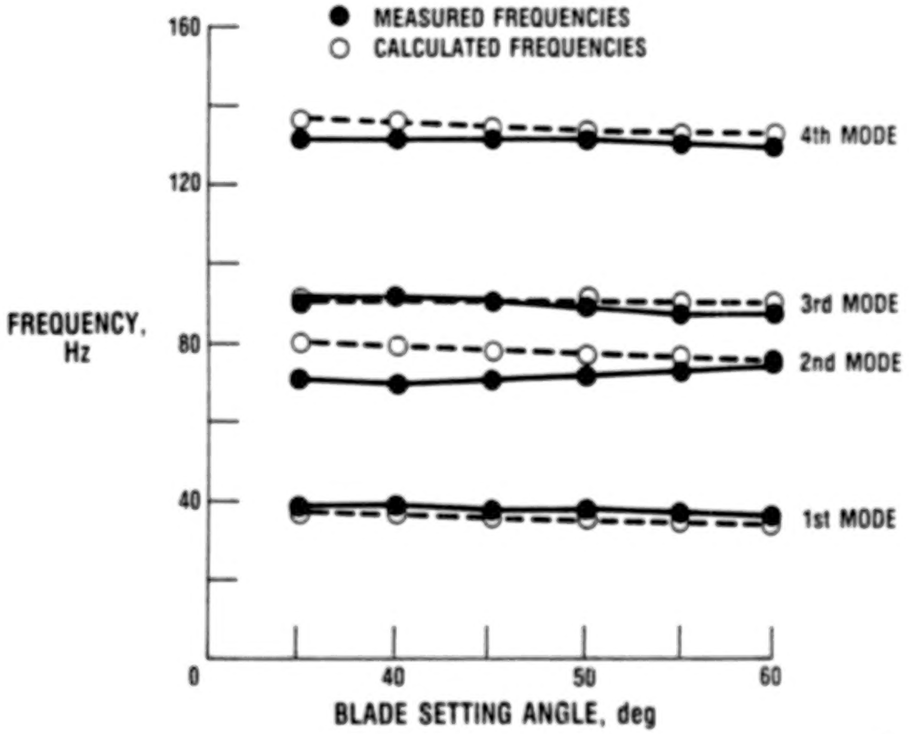

CD-88-32310

SR-7L CALCULATED FREQUENCIES VERSUS DESIGN SPEED

Parametric studies using the two models were done to examine the effect of rotating speed on natural frequencies for the two models. Because of the softer support, frequencies for the tuned model are generally slightly lower (<10 percent) than for the original model. For the three modes that most affect flutter, first torsion and first and second bending, there is generally better agreement between calculated and measured results at the design speed (1700 rpm) using the original model. Conversely, at 1200 rpm, the tuned, softer support showed better agreement.

A possible explanation for the difference is that at the higher speed the blade shank had seated itself better, resulting in a stiffer support. This is supported by the fact that the measured frequencies showed a greater degree of change between the two test speeds than the frequencies calculated by either of the finite element models. This type of nonlinear support would be impossible to model accurately over a wide range of speeds using linear spring elements.

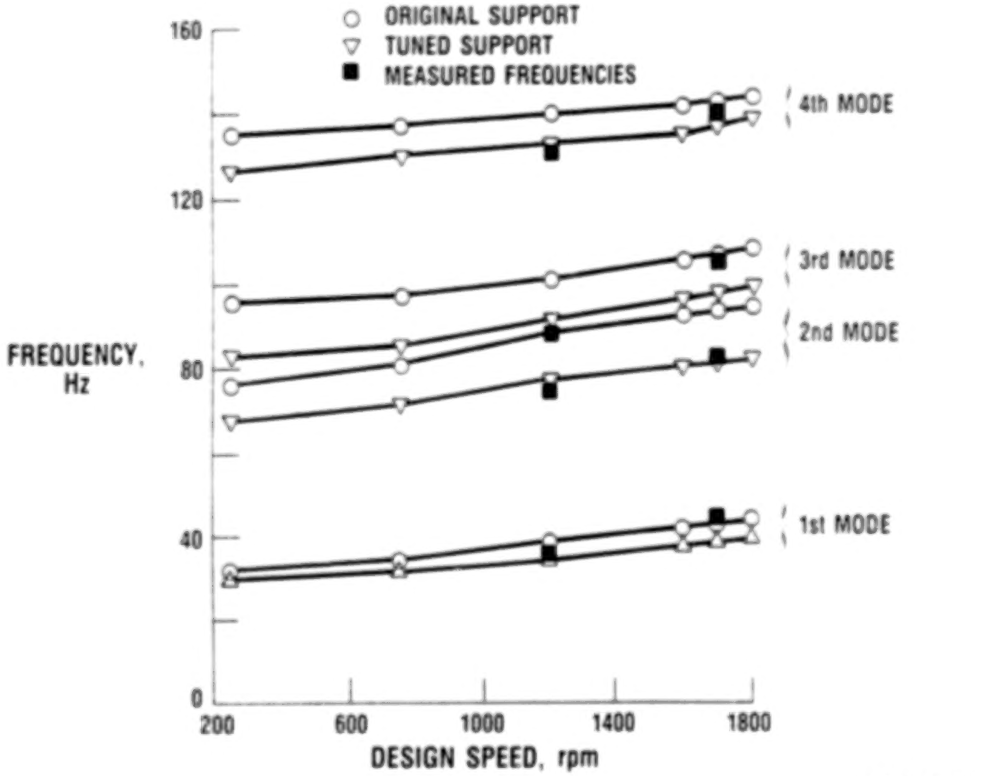

SR-7L FLUTTER CURVES

The modal flutter code ASTROP3 was used to calculate the aerodynamic damping. This code is a normal mode analysis method that was developed for the analysis of propulsion blading. It is based on three-dimensional, subsonic (the Mach number of relative flow is less than unity), unsteady aerodynamics as described by Williams and Hwang (1986). However, for the SR-7L configuration at a design free-stream Mach number of 0.80 and a rotational speed of 1700 rpm, the Mach number of relative flow at the tip is greater than one. To calculate the unsteady aerodynamics for supersonic Mach numbers, Kaza et al. (1987) have further extended the aerodynamic model.

The cascade aeroelastic stability is determined by solving the eigenvalue problem for the dynamic system. System damping and damped frequency are represented by the real and imaginary parts of the complex eigenvalue, respectively. Flutter occurs when the real part of the eigenvalue is greater than zero. Aerodynamic damping at the design speed is predicted as a function of free-stream Mach number. Aerodynamic damping values for free-stream Mach numbers greater than 0.8 were also calculated and included so that the available flutter margin for the SR-7L propfan could be estimated. The values shown are for the most unstable SR-7L interblade phase angles for both the original and tuned support condition, respectively. The blade was stable for both cases at the design point of Mach 0.8 and 1700 rpm at an altitude of 10.66 km (35 000 ft). There was also very little difference in the most unstable interblade phase angle identified. The predicted values are considered to be conservative, since neither material nor friction damping due to the hub constraint has been included in the analysis. Additional system damping would only have a stabilizing effect. From these results, it is concluded that the SR-7L propfan is free from flutter at the design point.

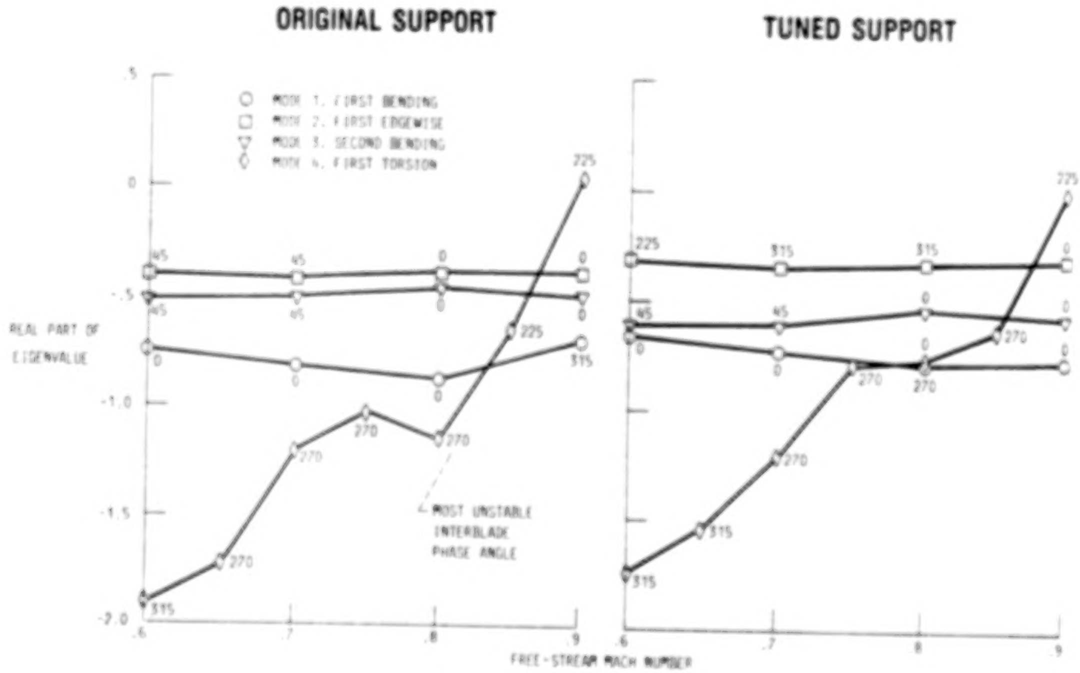

CD-88-32312

COMPARISON WITH A TWO-DIMENSIONAL AEROELASTIC CODE

The ASTROP3 damping ratio results for the original stiffness model were compared with those given by Hirschbein et al. (1987). That study used a modal flutter aerocode solver, ACA, available in COSMIC/NASTRAN. The ACA code utilizes the two-dimensional, subsonic cascade aerodynamic theory of Jones and Rao applied in a strip theory manner (Elchuri et al.,1985). The calculated damping values are qualitatively similar: the first mode being much more stable than either the second or third modes, and the third mode showing the least damping. A direct comparison of the values for the critical damping cannot be made because of differences in the aerodynamic theories used, as well as two slightly different blade designs. The finite element blade model used by Hirschbein is based on a preliminary blade design and has higher third and fourth mode (second bending and first torsion) frequencies, 111.6 and 160.7 Hz versus 97.9 and 137.0 Hz, respectively, than the final blade design.

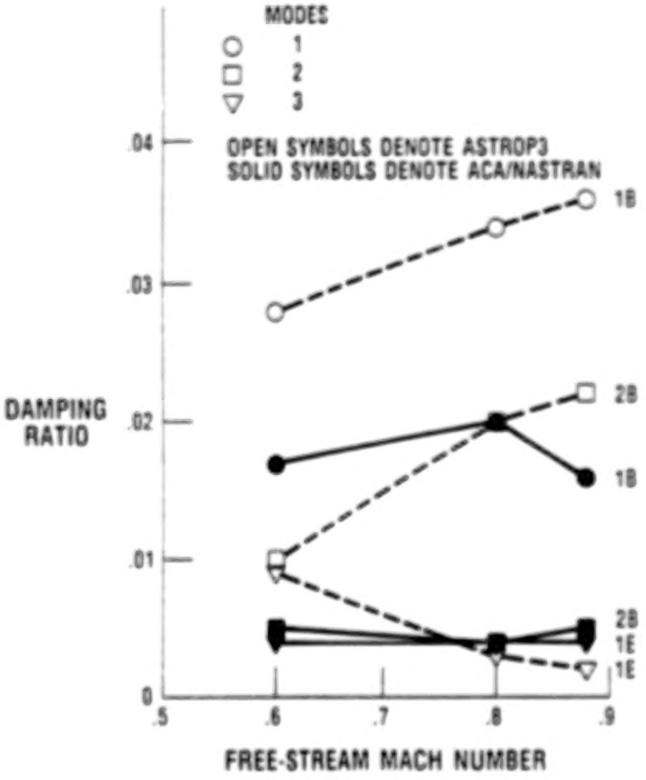

CD-88-32313

CASCADE EFFECTS ON SR-7L STABILITY

To illustrate the effects of cascade aerodynamics on flutter, parametric studies were made varying the number of blades in the propfan assembly. The effect of the number of blades on modal damping is significant, with the first and third mode aerodynamic damping decreasing by 25 and 16 percent, respectively. The destabilizing influence of the cascade effect is demonstrated as the least stable interblade phase angle shifts to the right with increased blading. The critical frequency is also reduced with increased blading.

AT DESIGN POINT

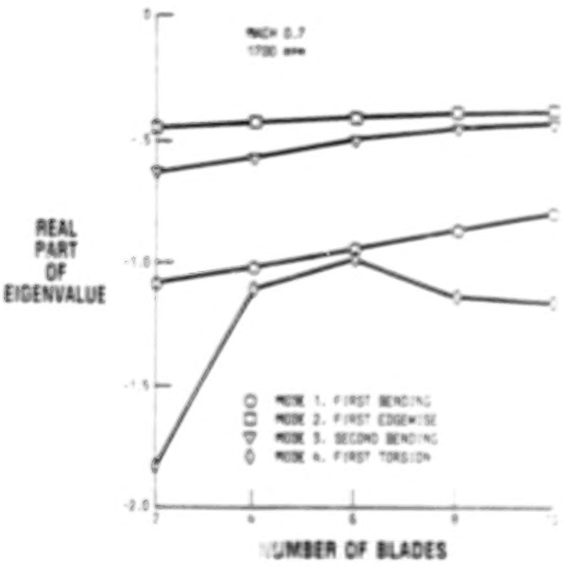

CD-88-32014

MODE-1 ROOT LOCUS PLOT WITH CASCADE EFFECTS

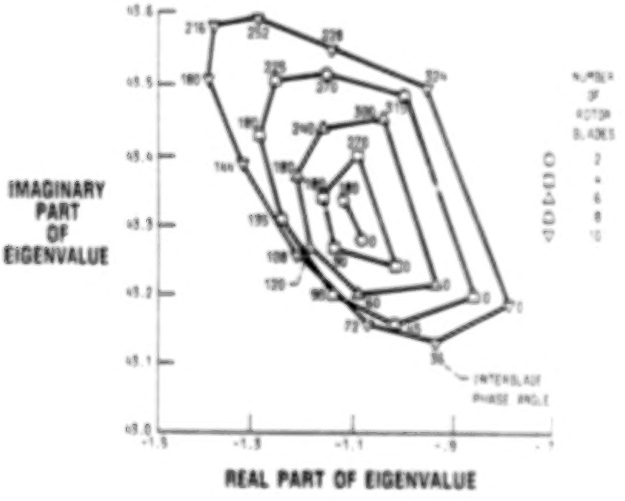

CD-88-32015

SUMMARY OF RESULTS

1. Bending and torsional frequencies were generally insensitive to the support stiffness used. However, the blade edgewise frequencies were particularly sensitive to the out-of-plane support stiffness used.

2. With the exception of the edgewise mode, there was generally good agreement between calculated and experimental frequencies at the design speed. From the available test information, it appeared as if the blade hub constraint stiffness acted in a nonlinear manner with respect to rotational speed. This made it difficult to model the blade constraint condition with linear spring elements over a wide range of speeds.

3. The blade was stable at its design point of Mach 0.8 and 1700 rpm at an altitude of 10.66 km (35 000 ft). The analysis did not consider any structural damping, which would have a beneficial effect on stability.

4. Some components of the blade support stiffness values had little effect on the calculated aerodynamic damping. This would imply that modeling efforts should be concentrated most on matching the in-plane and out-of-plane bending stiffnesses and obtaining reasonably close values (within 10 percent) for the bending and torsional modes.

5. Cascade effects were found to be considerable at the design point for configurations from 2 to 10 blades, although an increase in the number of blades from 8 to 10 did not cause an instability for the configuration analyzed.

REFERENCES

Aiello, R.A., and Chi, S., 1987, "Advanced Composite Turboprops: Modeling, Structural and Dynamic Analyses," ASME Paper 87-GT-78.

Elchuri, V., et al., 1985, "NASTRAN Documentation for Flutter Analysis of Advanced Turbopropellers," NASA CR-167927.

Hirschbein, M., et al., 1987, "Structural and Aeroelastic Analysis of the SR7L Propfan," NASA TM-86877.

Kaza, K.R.V., et al., 1987, "Analytical Flutter Investigation of a Composite Propfan Model," AIAA Paper 87-0738.

Lawrence, C., and Kielb, R.E., 1984, "Nonlinear Displacement Analysis of Advanced Propeller Structures Using NASTRAN," NASA TM-82727.

Lawrence, C., et al., 1987, "A NASTRAN Primer for the Analysis of Rotating Flexible Blades," NASA TM-89861.

Sullivan, W.E., Turnberg, J.E., and Violette, J.A., 1987, "Large-Scale Advanced Propfan (LAP) Blade Design," NASA CR-174790.

Williams, M.H., and Hwang, C., 1986, "Three-Dimensional Unsteady Aerodynamics and Aeroelastic Response of Advanced Turboprops," AIAA 27th Structures, Structural Dynamics, and Materials Conference, AIAA Paper 86-0846, vol. 2, NY, pp. 116-124.

N88-23255

SUPERSONIC AXIAL-FLOW FAN FLUTTER

John K. Ramsey
Structural Dynamics Branch
NASA Lewis Research Center

ABSTRACT

The development of a supersonic axial-flow compressor has been the subject of a limited amount of research over the past 32 years (Ferri, 1956; Klapproth, 1961; and Savage et al., 1961). During the middle 1970's a supersonic axial-flow compressor was constructed, but it encountered a blade failure before reaching its design point (Breugelmans, 1975). Many reached the conclusion that the supersonic axial-flow compressor was a very difficult, if not practically impossible, design problem. However, recent renewed interest in supersonic and hypersonic flight vehicles have rekindled interest in the supersonic axial-flow fan. For example, a research project to design, build, and conduct experiments on a single-stage supersonic axial-flow fan is now underway at the NASA Lewis Research Center (Schmidt et al., 1987; and Wood et al., 1987).

Although past experimentation on this type of compressor has been rather sparse, some useful analytical technology has been developed. One example is in the area of aeroelastic stability. Since the aeroelastic stability of the NASA supersonic through-flow fan was a concern, an analytical capability was needed to predict the unsteady aerodynamic loading. Consequently, a computer code based on Lane's (1957) formulation was developed for the case of supersonic axial flow (Ramsey and Kielb, 1987). This presentation will discuss this code and its application to the flutter analysis of the NASA Lewis supersonic through-flow fan.

The flutter analysis was performed by incorporating this code into an existing aeroelastic code and applying it to the NASA blade. The analysis (Kielb and Ramsey, 1988) predicted the blades to be unstable at supersonic relative velocities. As a consequence, the rotor blades were redesigned by reducing the aspect ratio to bring the through-flow fan into the stable operating range.

UNSTEADY AERODYNAMIC MODEL

Lane's (1957) formulation for the unsteady pressure distribution was used to calculate the unsteady aerodynamic loads. This formulation considers a cascade of two-dimensional flat plates with arbitrary stagger (provided the locus of blade leading edges is located ahead of the Mach lines) and arbitrary inter-blade phase angle. The upper figure shows the cascade geometry, and the lower figure defines the airfoil unsteady pressure distribution.

CASCADE GEOMETRY

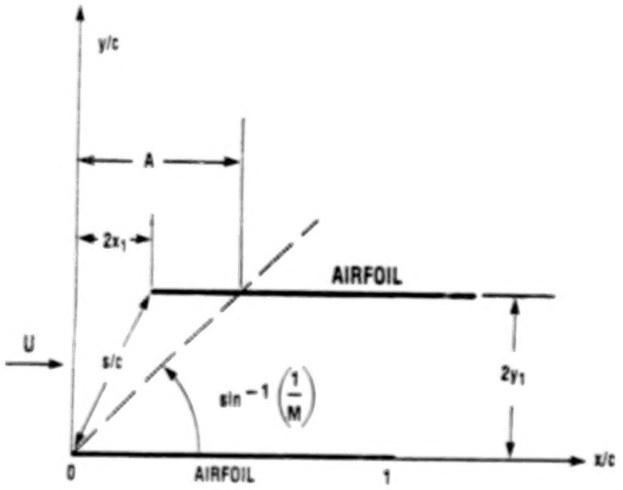

CD-86-32906

UNSTEADY PRESSURE

$$P_-(x,t) - P_+(x,t) = 2\rho U^2 T(x) e^{i\omega t}$$

$$T(x) = -B^{-1}(\partial/\partial x + iK) \left\{ \int_0^x \alpha(\zeta) e^{-i\kappa M(x-\zeta)} \right.$$

$$\times \left[e^{-i\Omega} \sum_{n=0}^{\infty} J_0 \left\{ \kappa \sqrt{(x + 2x_1 - \zeta)^2 - (1+2n)^2 A^2} \right\} 1[x + 2x_1 - \zeta - (1-2n)A] \right.$$

$$+ e^{i\Omega} \sum_{n=0}^{\infty} J_0 \left\{ \kappa \sqrt{(x - 2x_1 - \zeta)^2 - A^2(1+2n)^2} \right\} 1[x - 2x_1 - \zeta - (1+2n)A]$$

$$\left. \left. - \sum_{n=0}^{\infty} \epsilon_n J_0 \left\{ \kappa \sqrt{(x-\zeta)^2 - 4n^2 A^2} \right\} 1[x - \zeta - 2nA] \right] d\zeta \right\}$$

WHERE $\Omega = \sigma + 2\kappa M x_1$, $\kappa = KM/B^2$, and $A = 2By_1$

CD-86-33267

COMPUTER CODE VERIFICATION - PITCHING MOTION

The pressure distribution and lift and moment coefficients due to torsional motion were compared with Nagashima and Whitehead's (1977) published results. Close agreement can be seen.

PRESSURE DIFFERENCE
(M = 2.5, s/c = 1.0, STAGGER ANGLE = 60°, K = 1.0, x_0 = 0.5)

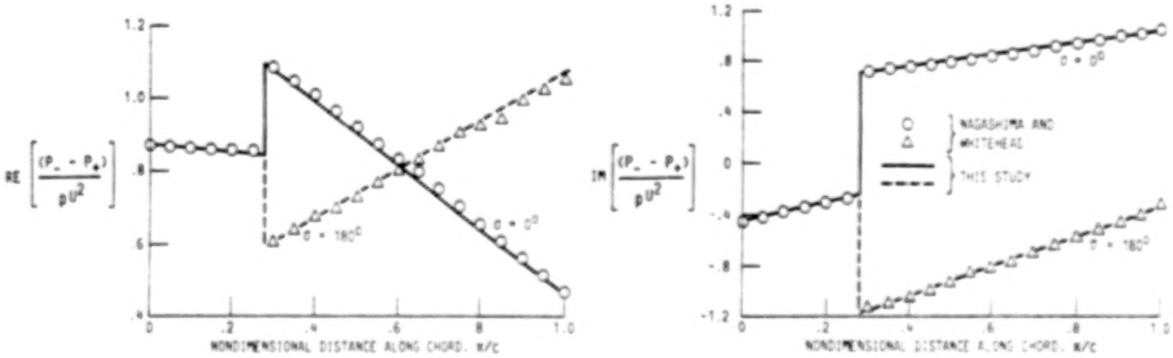

CD-88-32907

MOMENT COEFFICIENT
(M = 1.2, s/c = 1.0, STAGGER ANGLE = 0°, x_0 = 0.5)

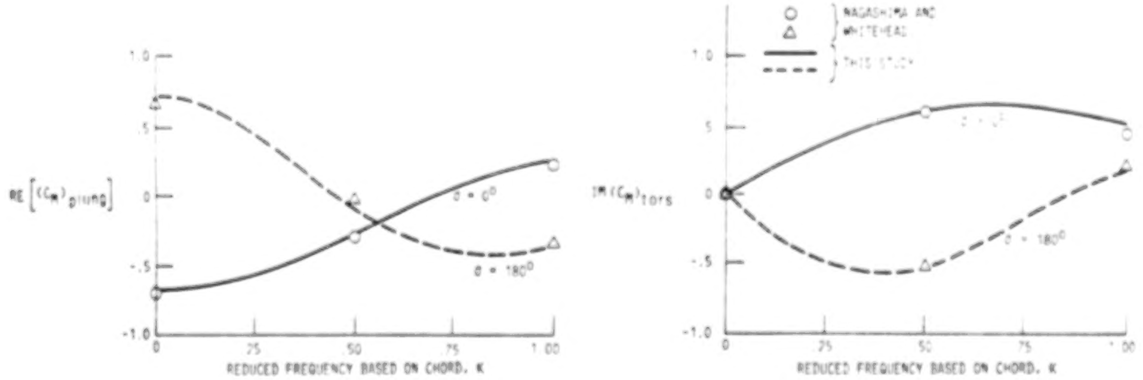

CD-88-32908

COMPUTER CODE VERIFICATION - PLUNGING MOTION

It would have been ideal to compare the lift and moment plunging coefficients with those of Nishiyama and Kikuchi (1973). However, it was felt that the published graphs were too small to accurately digitize. Therefore, the plunging coefficients obtained from this code were compared to those of Jordan (1953) for an isolated airfoil in supersonic axial flow. Close agreement can be seen.

LIFT COEFFICIENT

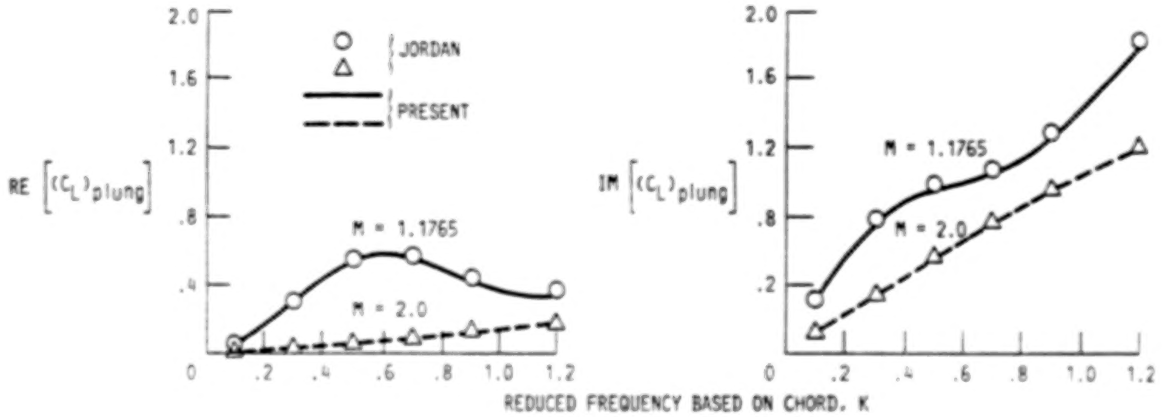

CD-88-32909

MOMENT COEFFICIENT

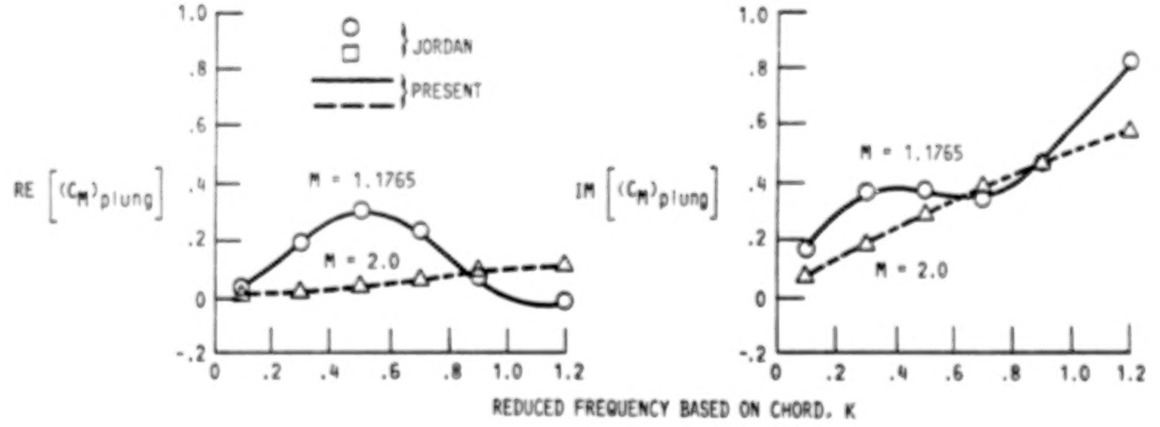

CD-88-32910

STRUCTURAL MODEL

The classical typical section is used to model the structure. Each airfoil is assumed to be a two-degree-of-freedom oscillator supported by bending and torsional springs. The airfoil is assumed to be rigid in the chordwise direction. Coupling between bending and torsional motions is modeled through the offset distance between the center of gravity and the "elastic axis."

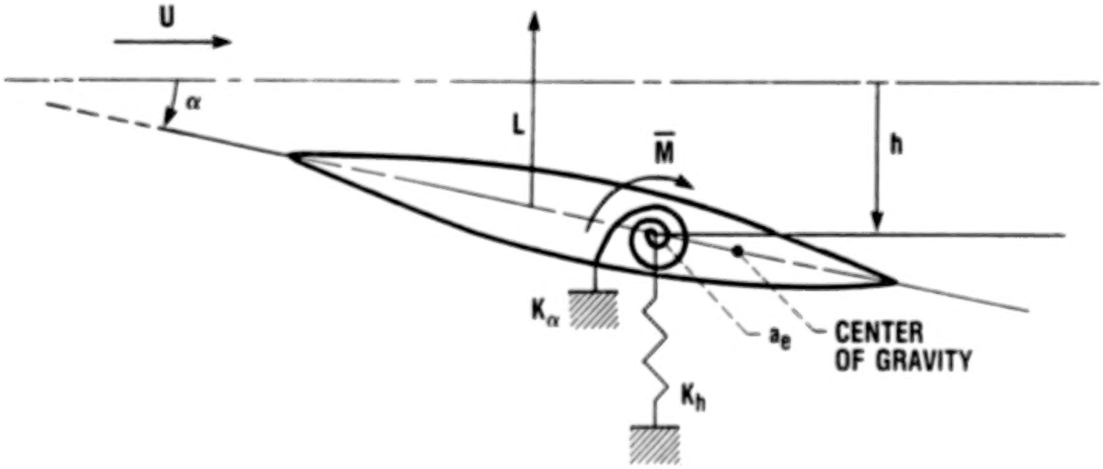
U
α
L
$\overline{M}$
h
K_α
a_e
CENTER OF GRAVITY
K_h

CD-88-32911

ORIGINAL DESIGN - 73.3-PERCENT SPAN

The NASA blade is much higher in solidity and lower in stagger angle than typical fan stages. However, the airfoil cross section is similar to that of conventional fan blades. The first mode is primarily bending, and the second mode is primarily torsion. The physical properties of the 73.3-percent span location were chosen as being representative and were used in the flutter analysis.

NUMBER OF BLADES	**58**
MASS RATIO	**456.2**
RADIUS OF GYRATION (MIDCHORD)	**0.431**
STAGGER ANGLE, deg	**28**
SOLIDITY	**3.215**
AT DESIGN POINT	
AXIAL MACH NUMBER	**2.300**
RELATIVE MACH NUMBER	**2.606**
REDUCED FREQUENCY (BENDING MODE)	**0.376**
REDUCED FREQUENCY (TORSION MODE)	**0.663**

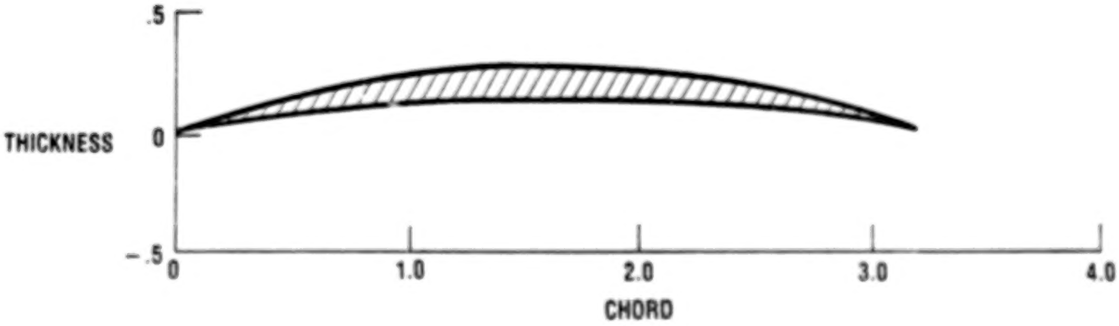

CD-88-32912

FLUTTER ANALYSIS

The flutter analysis was performed by incorporating this unsteady aerodynamic code into an existing aeroelastic code that solves the stability problem. The aeroelastic code was then applied to the NASA through-flow fan blade (Kielb and Ramsey, 1988). The analysis predicted that the through-flow fan would be torsionally unstable at supersonic relative velocities. As a result, the blade aspect ratio was reduced in the final design to bring the rotor into the stable operating range.

TORSIONAL FLUTTER

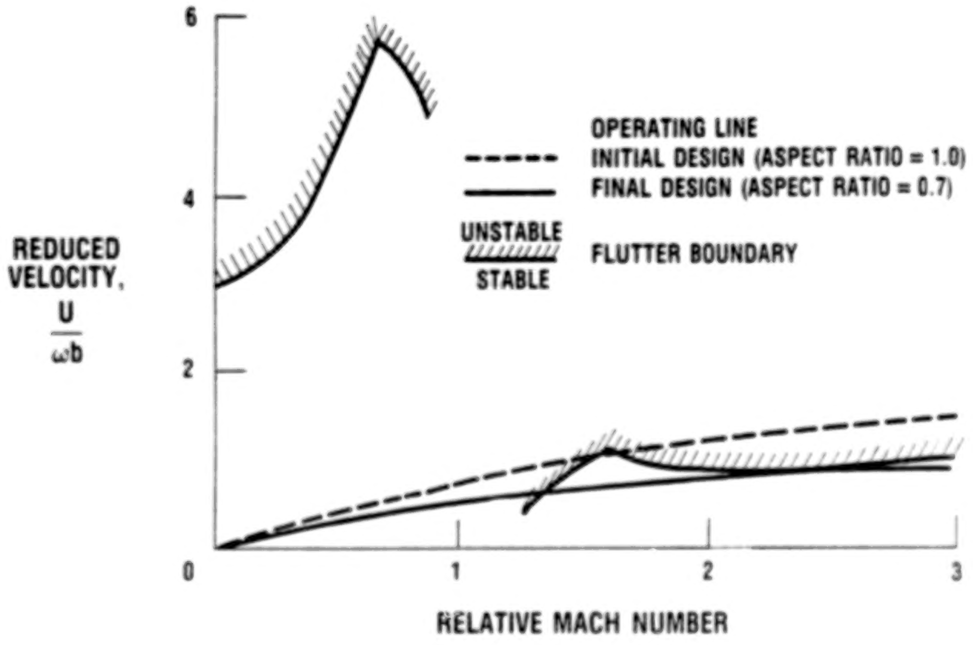

CD-88-32913

SUMMARY

Lane's (1957) analytical formulation, of the unsteady pressure distribution on an oscillating two-dimensional flat plate cascade in supersonic axial flow, has been developed into a computer code. This unsteady aerodynamic code has shown good agreement with other published data. This code has also been incorporated into an existing aeroelastic code to analyze the NASA Lewis supersonic through-flow fan design. A more sophisticated aerodynamic model that takes into account blade camber and/or thickness is being considered as a follow-on to this work.

- **LANE'S (1957) FORMULATION HAS BEEN DEVELOPED INTO AN UNSTEADY AERODYNAMIC CODE**
- **THE UNSTEADY AERODYNAMIC CODE HAS SHOWN GOOD AGREEMENT WITH PREVIOUSLY PUBLISHED DATA**
- **THE UNSTEADY AERODYNAMIC CODE HAS BEEN INCORPORATED INTO AN AEROELASTIC CODE**
- **AN UNSTEADY AERODYNAMIC MODEL THAT INCLUDES THICKNESS AND/OR CAMBER EFFECTS IS BEING CONSIDERED FOR FUTURE WORK**

CD-88-32914

APPENDIX - SYMBOLS

A	$2By_1$
a_0	speed of sound
a_e	elastic axis position
B	$\sqrt{M^2 - 1}$
b	semi-chord
c	chord
$(C_L)_{plung}$	lift coefficient due to plunging motion
$(C_L)_{tors}$	lift coefficient due to pitching motion
$(C_M)_{plung}$	moment coefficient due to plunging motion
$(C_M)_{tors}$	moment coefficient due to pitching motion
h	plunging displacement
i	imaginary unit
IM( )	imaginary part of ( )
J_0	Bessel function of the first kind of order 0
K	reduced frequency based on chord, $\omega c/U$
K_h	bending stiffness
K_α	torsional stiffness
L	aerodynamic lift
M	Mach number
$\bar{M}$	aerodynamic moment
P_-	pressure on lower surface of airfoil
P_+	pressure on upper surface of airfoil
RE( )	real part of ( )
s	blade spacing
t	time
U	free-stream velocity
x	streamwise coordinate

x_0	x/c coordinate of pitching axis with respect to the leading edge
y	transverse coordinate
α	complex amplitude of incidence
ϵ_n	$\epsilon_n = 1$ if $n = 0$; $\epsilon_n = 2$ if $n \geq 1$
ζ	dummy variable of integration
κ	$KM/B^2 = \omega c/B^2 a_0$
ρ	air density at free stream
σ	interblade phase angle
Υ	complex amplitude of dimensionless pressure difference
Ω	$\sigma + 2\kappa M x_1$
ω	angular frequency
$1[\ ]$	unit step function

REFERENCES

Breugelmans, F.A.E., 1975, "The Supersonic Axial Inlet Component in a Compressor," ASME paper 75-GT-26.

Ferri, A., 1956, "Problems Related to Matching Turbojet Engine Requirements to Inlet Performance as a Function of Flight Mach Number and Angle of Attack," Air Intake Problems in Supersonic Propulsion, J. Fabri, Ed., Agardograph No. 27, AGARD, France.

Jordan, P.F., 1953, "Aerodynamic Flutter Coefficients for Subsonic, Sonic and Supersonic Flow (Linear Two-Dimensional Theory)," ARC-R&M-2932.

Kielb, R.E., and Ramsey J.K., 1988, "Flutter of a Fan Blade in Supersonic Axial Flow," 33rd ASME International Gas Turbine and Aero Engine Conference and Exposition, Amsterdam, The Netherlands. ASME Paper 88-GT-78.

Klapproth, J.F., 1961, "A Review of Supersonic Compressor Development," J. Eng. Power, Vol. 83, No. 3, pp. 258-268.

Lane, F., 1957, "Supersonic Flow Past an Oscillating Cascade with Supersonic Leading-Edge Locus," J. Aeronaut. Sci., Vol. 24, No. 1, pp. 65-66.

Nagashima, T., and Whitehead, D.S., 1977, "Linearized Supersonic Unsteady Flow in Cascades," ARC-R&M-3811.

Nishiyama, T., and Kikuchi, M., 1973, "Theoretical Analysis for Unsteady Characteristics of Oscillating Cascade Aerofoils in Supersonic Flows," The Technology Reports of the Tohoku University, Vol. 38, No. 2, pp. 565-597.

Ramsey J.K., and Kielb R.E., 1987, "A Computer Program For Calculating Unsteady Aerodynamic Coefficients for Cascades in Supersonic Axial Flow," NASA TM-100204.

Savage, M., Boxer, E., and Erwin, J.R., 1961, "Resume of Compressor Research at the NACA Langley Laboratory," J. Eng. Power, Vol. 83, pp. 269-285.

Schmidt, J.F., et al., 1987, "Supersonic Through-Flow Fan Design," AIAA-87-1746, (NASA-TM 88908).

Wood, J.R., et al., 1987, "Application of Advanced Computational Codes in the Design of an Experiment for a Supersonic Throughflow Fan Rotor," ASME Paper 87-GT-160, (NASA-TM 88915).

N88-23256

STALL FLUTTER ANALYSIS OF PROPFANS

T.S.R. Reddy*
Structural Dynamics Branch
NASA Lewis Reasearch Center

ABSTRACT

Stall flutter is a self-excited limit cycle oscillation triggered by separation of flow during part of every cycle of oscillation. Under takeoff conditions, the propfan blades may operate at high angles of attack and have the potential to stall flutter. The aerodynamic phenomenon associated with an airfoil oscillating into and out of stall is called dynamic stall. The forces generated in dynamic stall are an order of magnitude greater than the forces in separated flow with no vibration.

The present research is aimed at developing methods for the analysis of stall flutter of propfans and the computer implementation of these methods in the general purpose computer program, ASTROP - Aeroelastic STability and Response Of Propulsion systems.

Prediction of forces during dynamic stall has been a continuing research effort. The methods vary from solving the basic equations of fluid mechanics (purely theoretical) to fitting the analysis to direct measurement (empirical). The empirical methods take less time to implement and are able to quantitatively produce the dynamic stall effects. However, they require extensive experimentation and data before a model is developed. In addition, they do not provide any information about the physics of the flow. On the other hand, the purely theoretical methods are computationally expensive and not preferred for preliminary design work.

This report briefly reviews the dynamic stall analysis methods, and presents the application of two empirical models to the stall flutter analysis and correlation with experimental data of a propfan.

PRECEDING PAGE BLANK NOT FILMED

---

*(The University of Toledo, Department of Mechanical Engineering, Toledo, Ohio 43606) and NASA Resident Research Associate.

PURPOSE

To obtain maximum aerodynamic and acoustic performance, the trend in high speed propeller design has been toward thin, swept blades. These new designs are called propfans. A research program to establish the required technology for successful design of propfans is in progress at the NASA Lewis Research Center. Analysis of stall flutter, that may occur at takeoff conditions, is part of this research program. This involves the evaluation of the stall flutter analysis methods for propfans and the development of new analysis methods.

PURPOSE

- ★ *THICK AIRFOILS*
- ★ *4 STRAIGHT BLADES*
- ★ *LIGHT DISK LOADING (10-15 SHP/D^2)*
- ★ *2-D, SUBSONIC, ISOLATED AERO*
- ★ *HIGH AR BLADES-BEAM BEHAVIOR*
- ★ *EMPIRICAL MODELS*

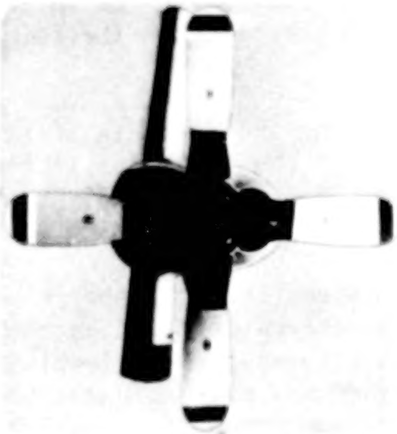

MACH 0.6 DESIGN

ATP TECHNOLOGY

MACH 0.8 DESIGN

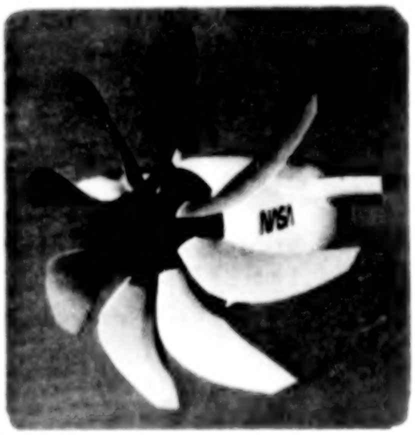

- ★ *8-10 SWEPT, VERY THIN BLADES*
- ★ *HIGH DISK LOADING (30-40 SHP/D^2)*
- ★ *3-D, TRANSONIC, CASCADE AERO, AREA-RULED SPINNER & CONTOURED NACELLE*
- ★ *LOW AR BLADES-PLATE DYNAMICS*
- ★ *EMPIRICAL TO CFD MODELS*

CD-88-32756

ORIGINAL PAGE IS
OF POOR QUALITY

OBJECTIVES

The objectives of the research are to (1) develop stall flutter analysis methods for propfans, (2) verify the analyses with experimental data, and (3) implement the analyses in the general purpose aeroelastic analysis program ASTROP - Aeroelastic STability and Response of Propulsion systems.

- **DEVELOP STALL FLUTTER ANALYSIS METHODS FOR PROPFANS**
- **CORRELATE WITH EXPERIMENTAL DATA**
- **IMPLEMENT IN ASTROP CODE**

CD-88-32757

TYPES OF STATIC STALL

Three types of static stall or separation under static conditions have been identified (McCullough and Gault, 1951). They are (1) the trailing edge stall, (2) leading edge stall, and (3) thin airfoil stall. In trailing edge stall the boundary layer separation progresses gradually forward from the trailing edge and there is a gradual loss of lift. Leading edge stall is identified by the burst of the leading edge separation bubble when the stall angle is reached and is associated with sudden loss of lift. In the thin-airfoil stall, a separation bubble originates near the leading edge and elongates as the angle of attack is increased. This type of stall is associated with gradual loss of lift. These three types of stall occur for airfoils with thickness-to-chord ratios (t/c) greater than 0.15, 0.09 to 0.15, and less than 0.09 respectively. Propfans have airfoils in the t/c range of 0.02 to 0.04, and hence are assumed to exhibit thin airfoil stall.

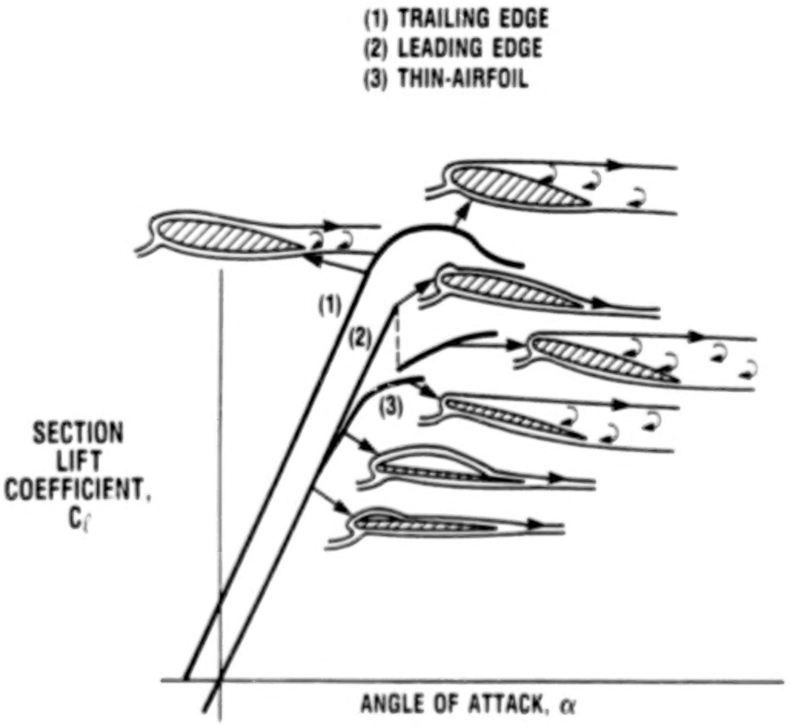

CD-88-32758

DYNAMIC STALL EVENTS ON AN OSCILLATING AIRFOIL

Dynamic stall refers to the aerodynamic phenomena of an airfoil oscillating into and out of stall. The predominant feature (McCroskey, 1981) is the shedding of a vortex-like disturbance from the leading edge, which alters the chordwise pressure distribution. This vortex moves downstream at about 35 to 40 percent of free stream velocity. The unsteady forces due to the passage of this vortex are much greater than the corresponding static values.

ORIGINAL PAGE IS
OF POOR QUALITY

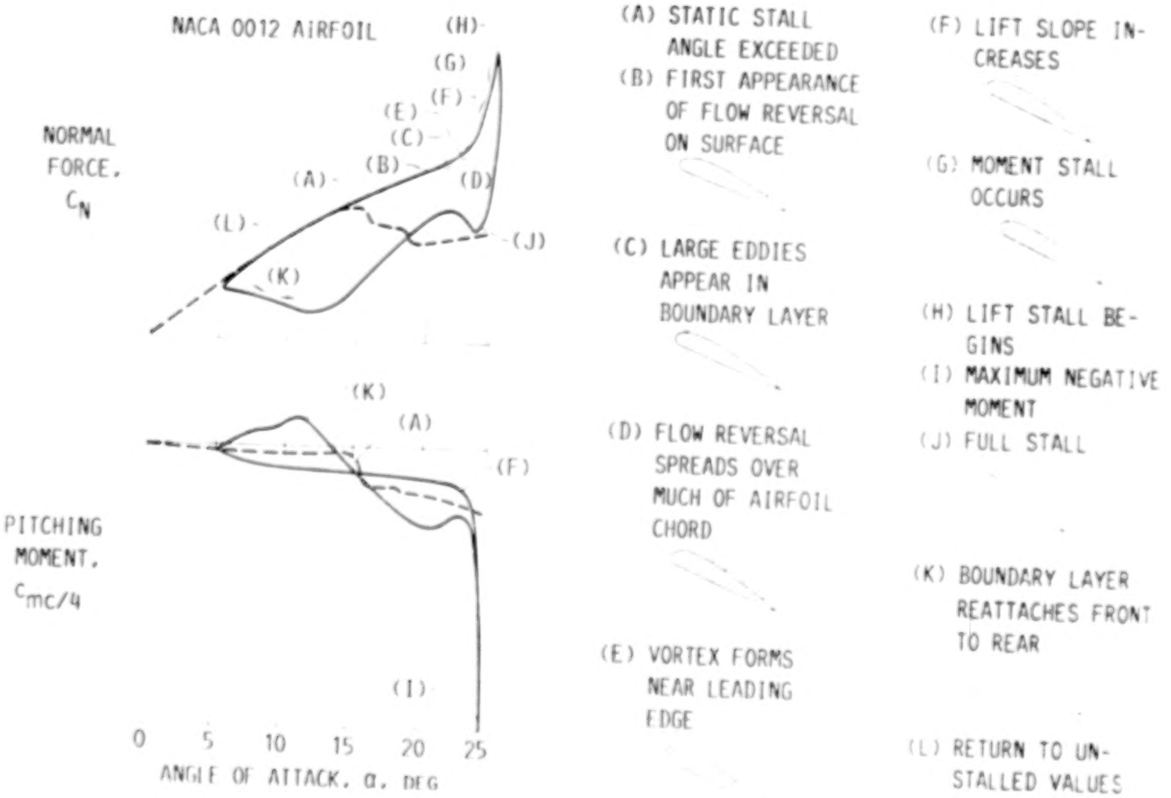

CD-88-32759

IMPORTANT EFFECTS OF DYNAMIC STALL

Three important effects resulting from dynamic stall are (1) flow separation is delayed to an angle beyond the static stall angle (stall delay); (2) the forces and moments are an order of magnitude larger than the static values (overshoot); (3) the variation of the forces versus angle of attack shows hysteresis. Stall flutter, a self-excited limit cycle oscillation can occur if hysteresis leads to negative damping. The magnitude of these effects depend on the airfoil shape, Mach number, and Reynold's number of the flow over the airfoil and on amplitude and frequency of oscillation.

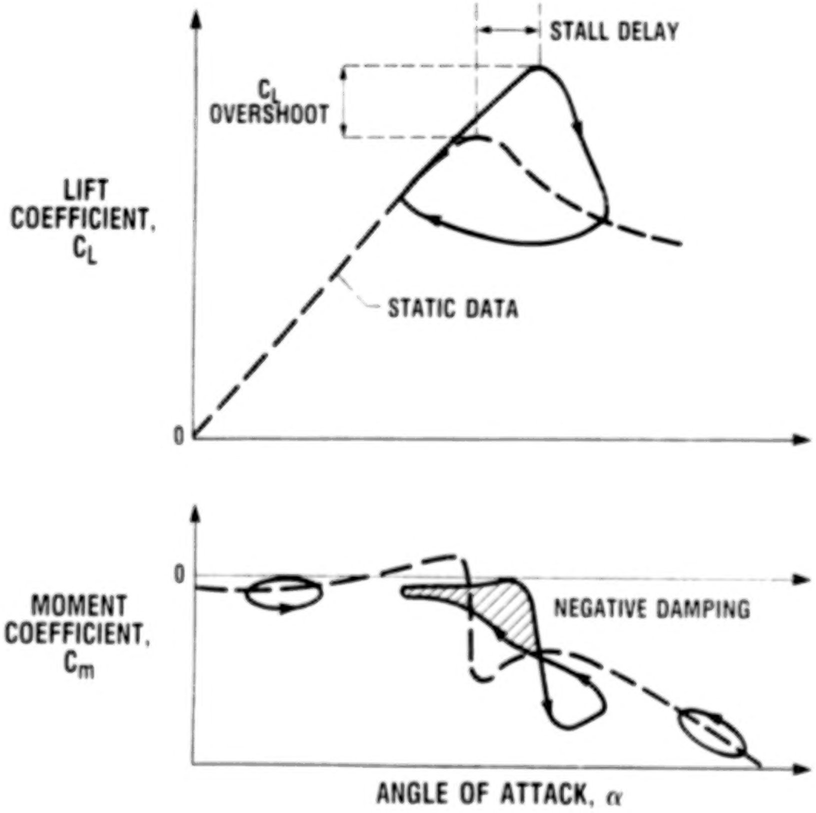

CD-88-32760

STALL FLUTTER ANALYSIS METHODS

Two components are needed to analyze stall flutter--an aerodynamic stall model and a structural model. The aerodynamic models available to analyze dynamic stall vary from solving the basic fluid mechanics equations to fitting analysis to experimental data (Reddy and Kaza, 1987). The Navier-Stokes Solvers (NSS), vortex methods, and zonal methods attempt to solve the fluid mechanics equations in their fundamental form by numerical techniques with varying degrees of simplifications and assumptions. These models require a significant amount of computer time. In the empirical models an analytical fit is attempted to approximately reproduce wind tunnel data. The empirical models take less computer time and can be used in a routine aeroelastic analysis though they are not able to give the complete picture of the flow. The structural models vary from a two-degree-of-freedom typical section model to a finite element model with a large number of degrees of freedom.

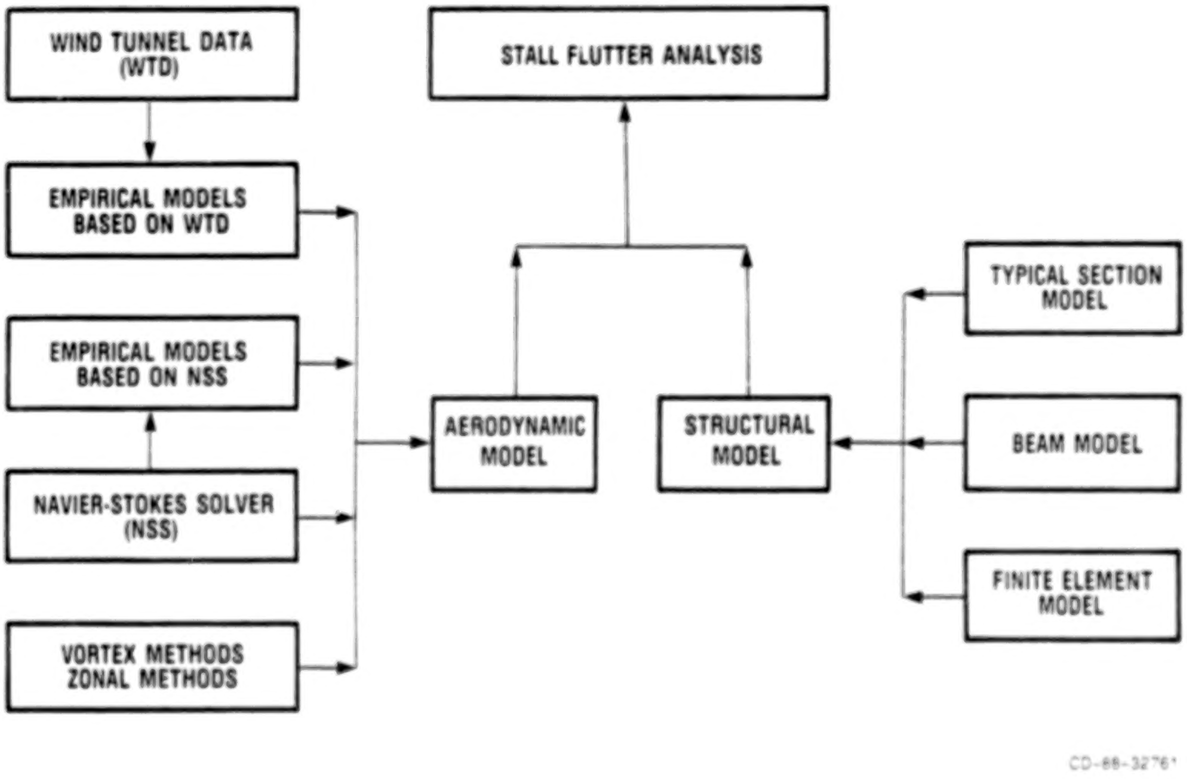
WIND TUNNEL DATA (WTD)
STALL FLUTTER ANALYSIS
EMPIRICAL MODELS BASED ON WTD
TYPICAL SECTION MODEL
EMPIRICAL MODELS BASED ON NSS
AERODYNAMIC MODEL
STRUCTURAL MODEL
BEAM MODEL
NAVIER-STOKES SOLVER (NSS)
FINITE ELEMENT MODEL
VORTEX METHODS ZONAL METHODS
CD-88-32761

SR2 PROPFAN MODEL

A propfan model SR2 exhibited stall flutter type behavior at static thrust condition in wind tunnel testing (Smith, 1985). This propfan has 8 unswept metallic blades with NACA 16 series airfoils for 45 percent of the span and NACA 65 series airfoils for 37 percent of the span. The thickness ratio (t/b), twist (Δβ), design lift coefficient (C_{LD}), and planform (b/D) distribution are established to provide for high efficiency.

VARIATION OF PROPELLER DESIGN PARAMETERS WITH BLADE RADIUS FOR THE UNSWEPT SR-2 PROPELLER

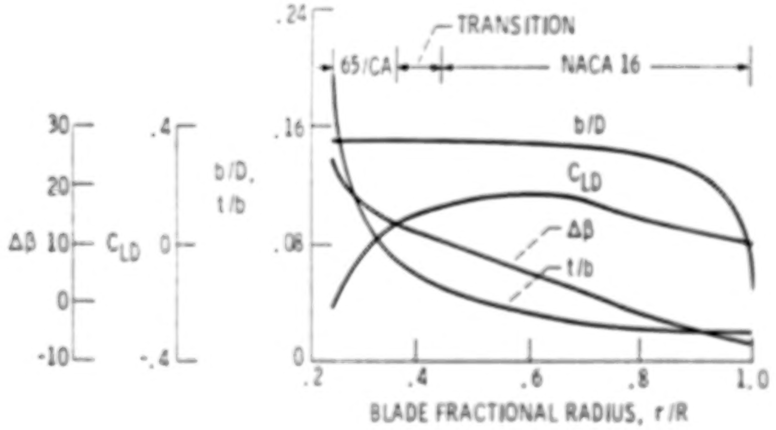

SR-2 PROPFAN, 8 BLADES, 0° SWEEP

CD-88-32762

APPROACH

Two empirical aerodynamic stall models, model A and B, and a finite element structural model were selected to analyze the SR2 propfan stall flutter. Model A uses fewer parameters in modeling the dynamic stall than does model B. A single blade is considered for the analysis. Normal mode analysis is used in formulating the governing equations of motion. The aerodynamic forces are calculated at a selected number of stations (strips) and integrated to obtain the total generalized forces on the blade. Combined momentum-blade element theory is used to calculate the induced velocity.

AERO-DYNAMIC MODEL: STRIP THEORY WITH EMPIRICAL DYNAMIC STALL MODELS

- MODEL A (GORMONT, 1973): TWO PARAMETERS GIVEN AS FUNCTION OF MACH NUMBER AND AIRFOIL THICKNESS TO CHORD RATIO.
- MODEL B (GANGWANI, 1983): ANALYTICAL FIT WITH 24 PARAMETERS

STRUCTURAL MODEL

- FINITE ELEMENT STRUCTURAL MODEL

SOLUTION METHOD

- INTEGRATION IN TIME

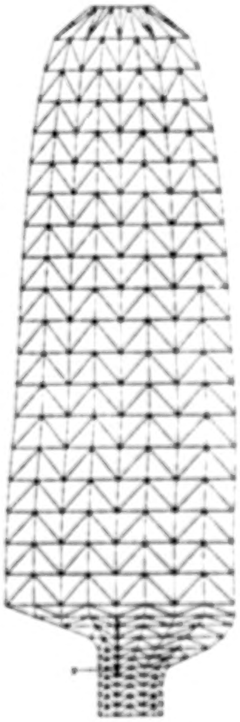

FINITE ELEMENT STRUCTURAL MODEL

CD-88-32763

CALCULATED NATURAL FREQUENCIES AND MODE SHAPES

The variation of the calculated first four natural frequencies with rotational speed is shown in the diagram below. The COSMIC NASTRAN program with triangular elements (CTRIA2) was used for the analysis. The first two calculated natural frequencies agreed well with the measured bench values whereas the third and fourth showed about 8 to 13 percent error. The frequencies show the effect of centrifugal force, the effect being higher for first, second, and forth modes than for third mode. The first four mode shapes calculated with blade setting angle, β, equal to 56.77°, using COSMIC- NASTRAN, showed that the first mode is 1st bending, the second mode is second bending, the third mode is 1st torsion mode and the fourth mode is third bending.

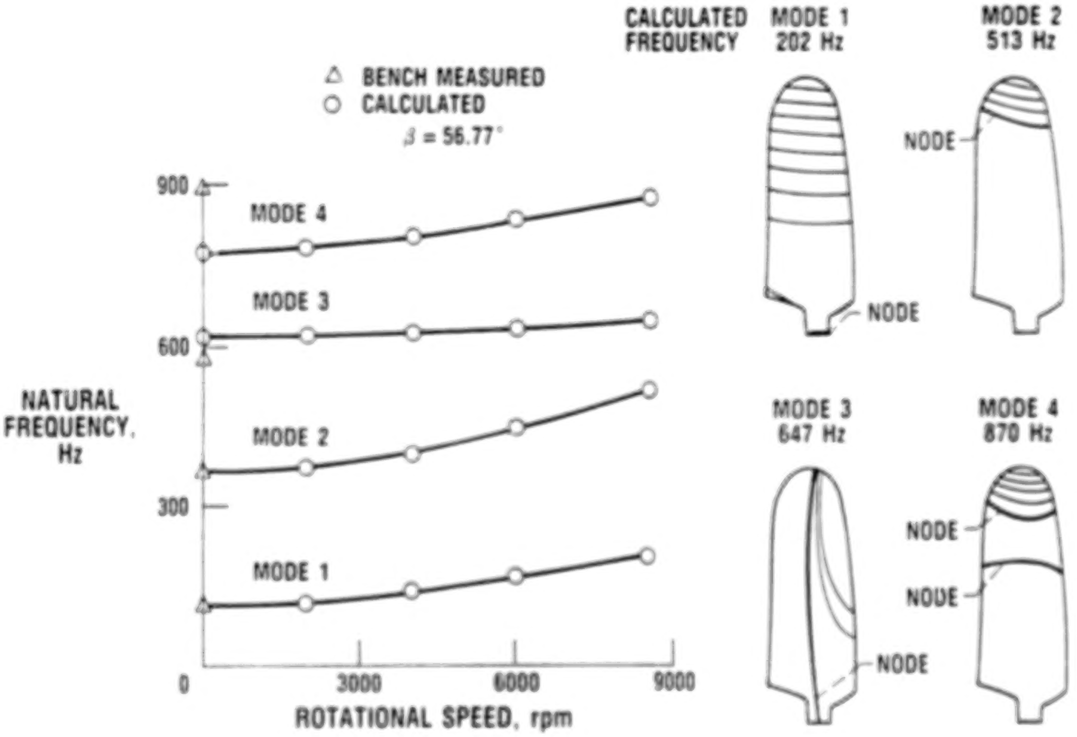

CD-86-32764

STALL FLUTTER RESPONSE WITH DYNAMIC STALL MODEL A

The operating condition considered for the analysis is 8500 rpm at zero free stream velocity, that is static thrust condition. Four modes are used in the analysis.

The figure on the right shows the variation of the first normal coordinate with time. The response shows that the first normal coordinate, which is predominantly bending, is converging to a steady value for the three setting angles considered (20, 25, and 30), thereby indicating stable oscillations. The response of the second and fourth normal coordinates showed stable oscillations.

The response of the third normal coordinate, (shown on the left) which is predominantly torsion, shows a converging trend for β = 20°. A limit cycle oscillation is predicted at β = 25°, and a diverging oscillation at β = 30°. The calculated frequency of the limit cycle oscillation is 617 Hz. This is qualitatively in agreement with the experimental data which showed a very high response at β = 31.8° at a frequency of 600 Hz.

The analysis indicated that the stall flutter response for this propfan is essentially a single degree of freedom response, since the modes are uncoupled.

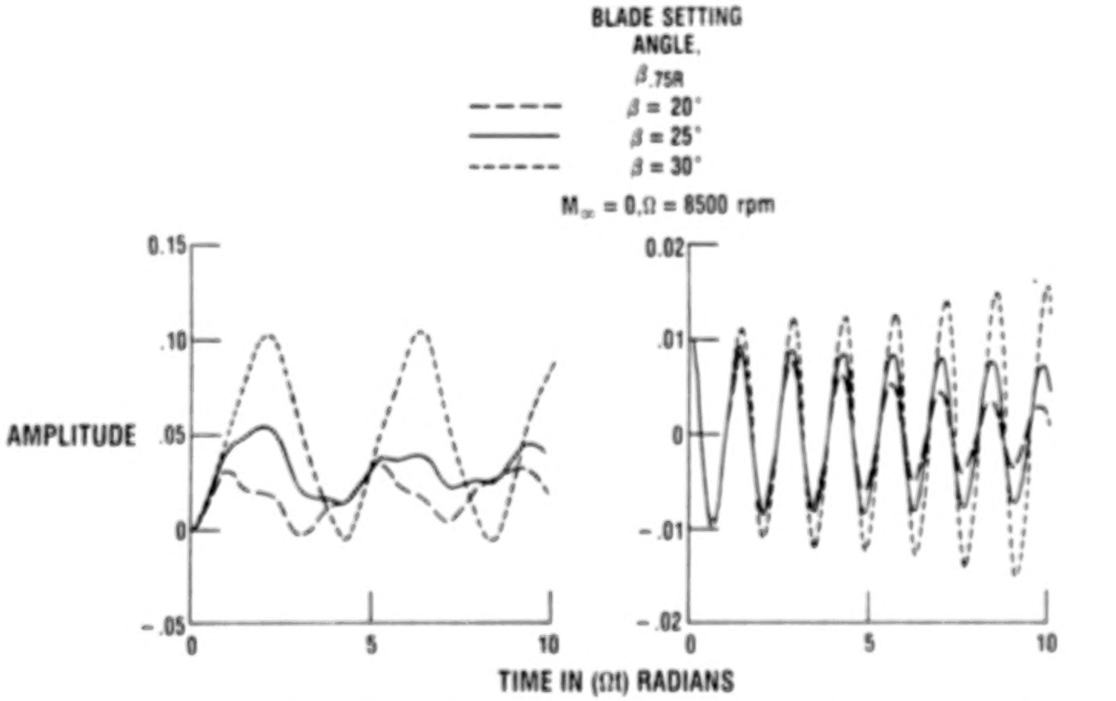

RESPONSE OF THE FIRST NORMAL MODE   RESPONSE OF THE THIRD NORMAL MODE

CD-88-32765

COMPARISON OF THE RESPONSE OF DYNAMIC STALL MODELS A AND B

The response calculated from the dynamic stall models, model A and model B, is compared next. The rotational speed is 8500 and the setting angle is 20°. Free stream velocity is zero. Both the models predicted the same type of response.

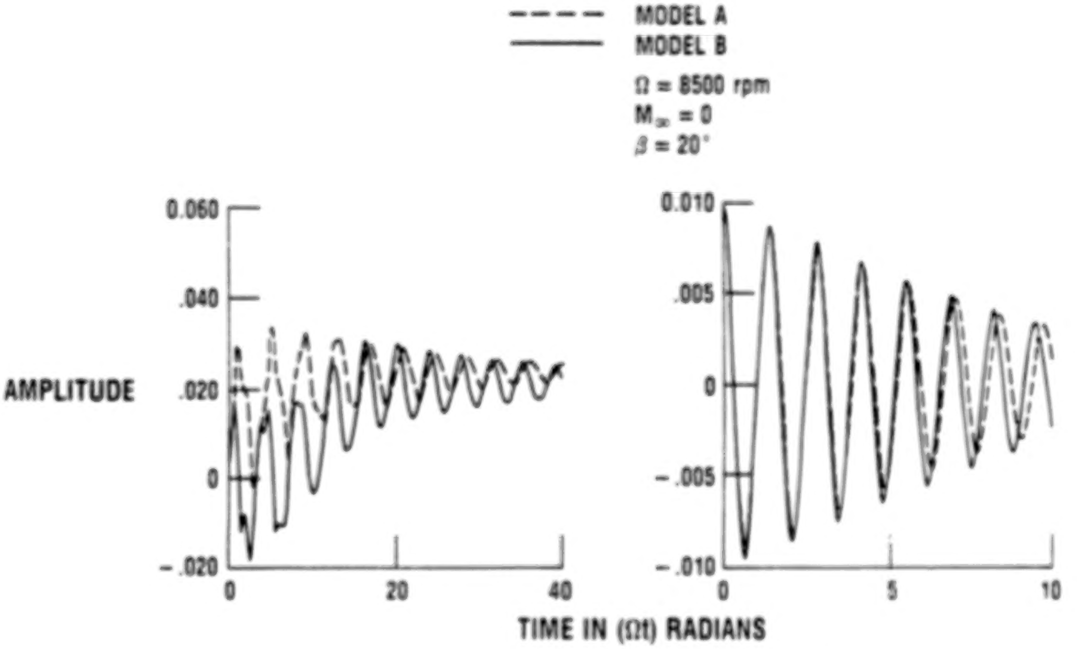

RESPONSE OF THE FIRST NORMAL MODE

RESPONSE OF THE THIRD NORMAL MODE

CD-88-32766

STALL FLUTTER RESPONSE WITH DYNAMIC STALL MODEL A

The operating condition considered for the analysis is 8500 rpm at zero free stream velocity, that is static thrust condition. Four modes are used in the analysis.

The figure on the right shows the variation of the first normal coordinate with time. The response shows that the first normal coordinate, which is predominantly bending, is converging to a steady value for the three setting angles considered (20, 25, and 30), thereby indicating stable oscillations. The response of the second and fourth normal coordinates showed stable oscillations.

The response of the third normal coordinate, (shown on the left) which is predominantly torsion, shows a converging trend for $\beta = 20°$. A limit cycle oscillation is predicted at $\beta = 25°$, and a diverging oscillation at $\beta = 30°$. The calculated frequency of the limit cycle oscillation is 617 Hz. This is qualitatively in agreement with the experimental data which showed a very high response at $\beta = 31.8°$ at a frequency of 600 Hz.

The analysis indicated that the stall flutter response for this propfan is essentially a single degree of freedom response, since the modes are uncoupled.

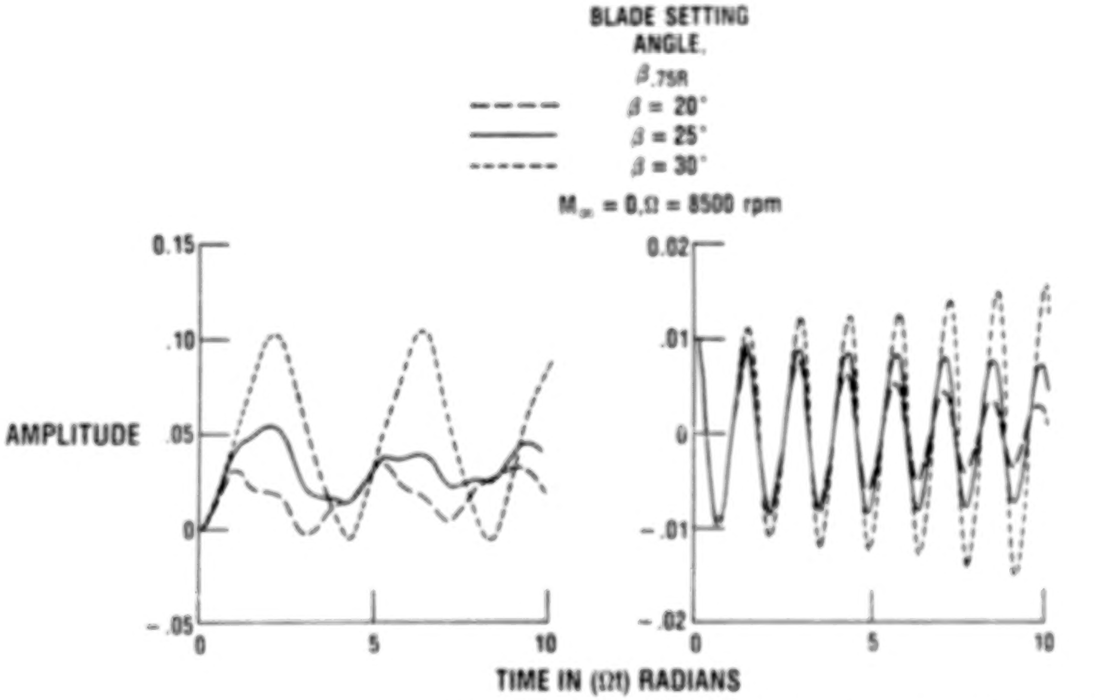

RESPONSE OF THE FIRST NORMAL MODE RESPONSE OF THE THIRD NORMAL MODE

CD-86-32765

④

COMPARISON OF THE RESPONSE OF DYNAMIC STALL MODELS A AND B

The response calculated from the dynamic stall models, model A and model B, is compared next. The rotational speed is 8500 and the setting angle is 20°. Free stream velocity is zero. Both the models predicted the same type of response.

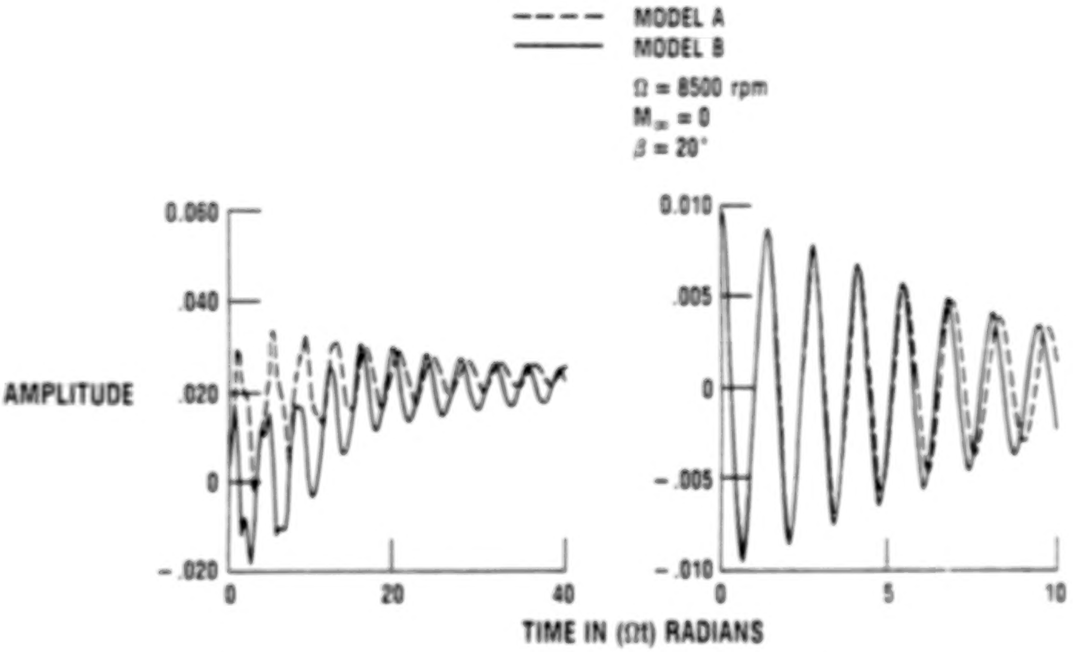

RESPONSE OF THE FIRST NORMAL MODE RESPONSE OF THE THIRD NORMAL MODE

CD-88-32766

④

LOGARITHMIC DECREMENT COMPARISON

A study of the variation of logarithmic decrement with the blade pitch angle as predicted by both the dynamic stall models showed that both models predict the same type of behavior. However, it is seen that model B predicts the stall angle at a higher value than that predicted by model A.

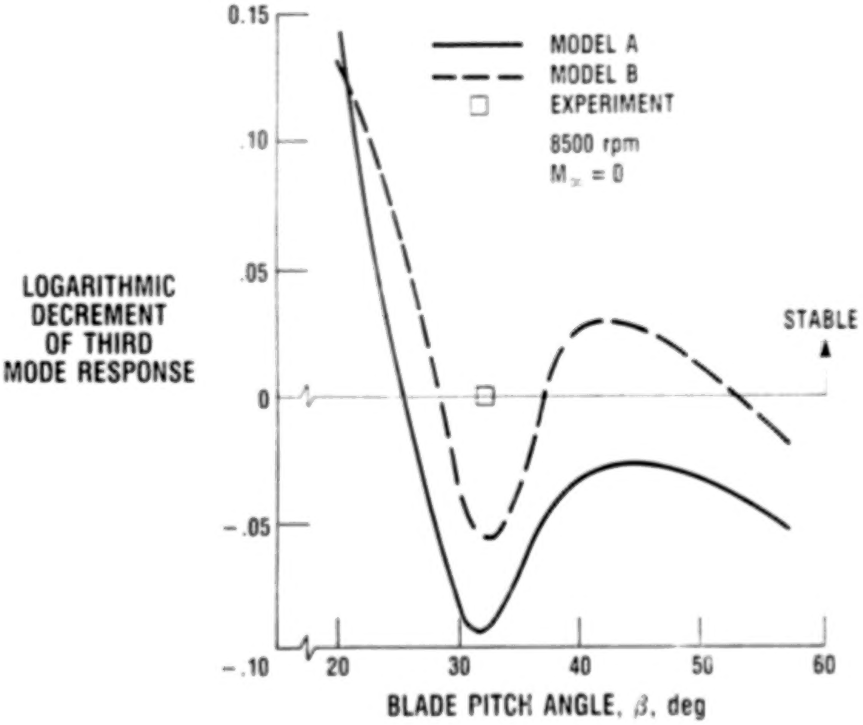

CD-88-32767

SUMMARY

The two empirical dynamic stall models employed in the stall flutter analysis of the SR2 propfan predicted the setting angle, mode, and the frequency as that observed in the experiment. However, they failed to give any detail of the flow at the dynamic stall condtions. A comparison of the response obtained with three empirical models, not presented here, showed that the response depends on the empirical model used. A computational fluid dynamics approach is planned to better understand the physics of the flow and the dynamic stall phenomenon of propfan airfoils.

- **ONLY QUALITATIVE PREDICTION POSSIBLE WITH EMPIRICAL MODELS.**
- **PREDICTED RESPONSE SENSITIVE TO EMPIRICAL MODEL**
- **RANGE OF VALIDITY OF EMPIRICAL MODELS RESTRICTED BY THE EXPERIMENTAL DATA USED TO DEVELOP THE MODEL**
- **COMPUTATIONAL FLUID DYNAMICS (CFD) APPROACHES ARE REQUIRED TO PREDICT PHYSICS OF FLOW AND DYNAMIC STALL PHENOMENON OF PROPFAN AIRFOILS**

CD-88-32766

REFERENCES

Gangwani, S.T., 1983, "Synthesized Airfoil Data Method for Prediction of Dynamic Stall and Unsteady Airloads," NASA CR 3672.

Gormont, R.E., 1973, "A Mathematical Model of Unsteady Aerodynamics and Radial Flow for Application to Helicopter Rotors," USAAMRDL TR -72-67.

McCroskey, W.J., 1981, "The Phenomenon of Dynamic Stall," NASA TM-81264.

McCullough, G.B., and Gault, D.E., 1951," Examples of Three Representative Types of Airfoil Section Stall at Low Speed," NACA TN-2502.

Reddy, T.S.R., and Kaza, K.R.V., 1987," A Comparative Study of Some Dynamic Stall Models," NASA TM-88917.

Reddy, T.S.R., and Kaza, K.R.V., 1988," Stall Flutter Analysis of an Unswept Propfan Blade with Semi-Empirical Dynamic Stall Models," NASA TM (to be published).

Smith, A.F., 1985, "Analysis and Test Evaluation of the Dynamic Stability of Three Advanced Turboprop Models at zero Forward Speeds," NASA CR-175025.

N88-23257

SSME SINGLE-CRYSTAL TURBINE BLADE DYNAMICS

Larry A. Moss*
Sverdrup Technology, Inc.
(Lewis Research Center Group)
NASA Lewis Research Center

ABSTRACT

There are many concerns surrounding the current directionally solidified (DS) blades for the first-stage rotor of the space shuttle main engine (SSME) high-pressure fuel turbopump (HPFTP). The blades' design life goal of 55 launches is not being met. The blade life has been shortened primarily by fatigue cracking. One method of lengthening blade life is by substituting single-crystal (SC) material. Past experience and current applications in commercial and military aviation have shown the feasibility of using SC material.

Research was conducted at Lewis to predict the SC blade natural frequencies and to find possible critical engine-order excitations. The effort was both experimental and analytical. Experiments were used to validate the analytical procedures. Bench experiments for SC blades at different crystal orientations were conducted to determine their nonrotating natural frequencies and mode shapes. These results were compared with the analytical results to confirm the validity of the MSC/NASTRAN model.

The analytical effort examined the blades' dynamic characteristics with respect to crystal orientations under typical operating conditions. Additional investigations attempted to determine the crystal orientation that would most effectively avoid critical engine-order excitations.

The conclusions developed from the analyses and tests were as follows:

1. The MSC/NASTRAN blade model successfully predicts the nonrotating natural frequencies and mode shapes of the SC blades.

2. From a dynamics viewpoint the SC blade is an improvement over the DS blade. No new engine-order interferences were introduced with the material substitution.

3. The engine-order interferences of the SC blades can be minimized by changing the crystal orientation.

---

*Work performed on-site at the Lewis Research Center for the Structural Dynamics Branch.

PRECEDING PAGE BLANK NOT FILMED

SSME HIGH-PRESSURE FUEL TURBOPUMP AND FIRST-STAGE TURBINE BLADE

Sixty-three blades are mounted within the first-stage rotor of the SSME high-pressure fuel turbopump (HPFTP), as shown below. The mounted blades have a tip diameter of approximately 11 in. The blade consists of four sections; airfoil, platform, shank, and fir tree. The airfoil is highly cambered and the cross section is nearly constant along the slightly twisted blade span. The four-lobed fir tree section mates with the rotor.

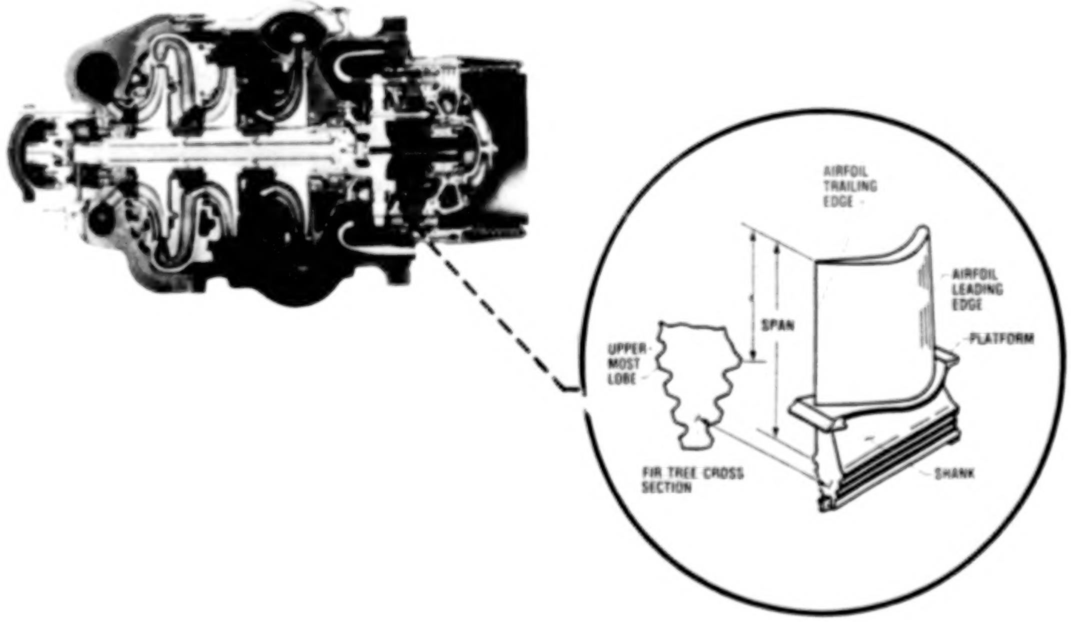
AIRFOIL TRAILING EDGE
AIRFOIL LEADING EDGE
SPAN
PLATFORM
UPPER-MOST LOBE
FIR TREE CROSS SECTION
SHANK

CD-88-31885

MATERIAL ORIENTATION OF SINGLE-CRYSTAL BLADE

The SC material orientation is determined from Laue x-ray diffraction techniques. Polar projections of the material's ‹111› axis are developed. The ‹111› axis is referenced within the HPFTP blade according to its projected rotation and tilt angles. The tilt angle is referenced according to the ‹111› axis projection on the X-Y plane of the blade. Positive rotation is measured counterclockwise from the blade chord (leading edge to trailing edge) with respect to the trailing edge, as shown below.

A cylindrical coordinate system was defined to specify the crystal orientation in the blade analyses. The variation in the single-crystal orientation was accommodated by supplying the appropriate direction cosines for the material coordinate system.

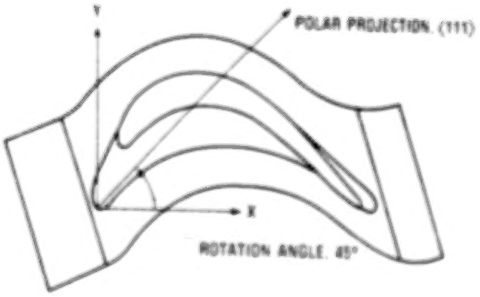
Y
POLAR PROJECTION, ⟨111⟩
X
ROTATION ANGLE, 45°

TOP VIEW

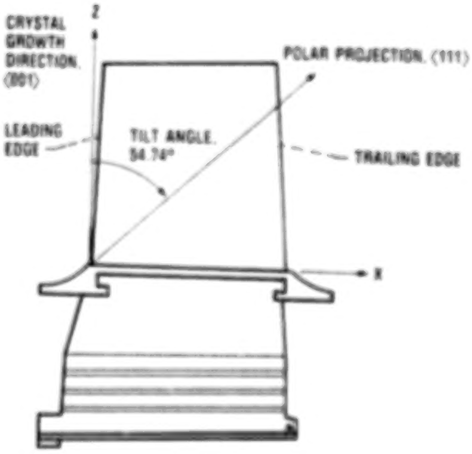
CRYSTAL GROWTH DIRECTION, ⟨001⟩
Z
POLAR PROJECTION, ⟨111⟩
LEADING EDGE
TILT ANGLE, 54.74°
TRAILING EDGE
X

CD-86-31886

EXPERIMENTAL FREQUENCIES AND MODE SHAPES

The blade attachment to the actual rotor was simulated by brazing the SC blades in a stainless steel mounting block as shown in the photograph. Each blade tested had a different crystal orientation. The tests were conducted at nonrotating, room-temperature conditions. Two experimental methods were used to identify the modal frequencies and to approximate the mode shapes of the SC blades. These methods involved a modal analyzer and interferometry. Experimental modal frequencies between 0 and 25 000 Hz determined from the modal analyzer are shown in the graph. Mode shapes determined by interferometry are shown in a later figure.

MODAL ANALYZER

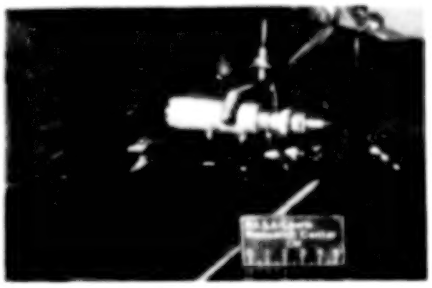

EXPERIMENTAL MODAL FREQUENCIES

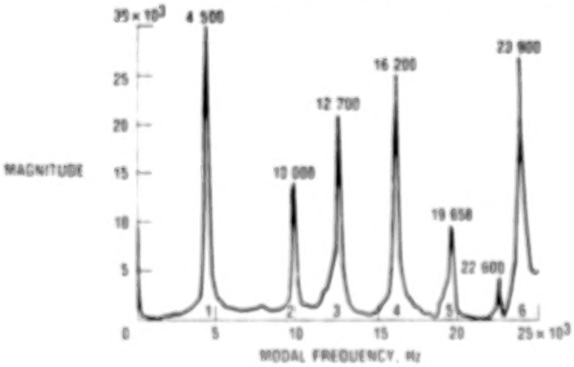

CD-88-31887

MSC/NASTRAN FINITE ELEMENT MODEL

MSC/NASTRAN was used to perform the analysis (Joseph, 1981). The finite element model shown below consists of 1025 solid eight-node hexahedron elements with three degrees of freedom per node. The base of the blade was fully constrained at the center of its uppermost fir tree attachment lobe. The in-disk span length was defined from this attachment point to the blade tip. The in-disk span length was assumed to simulate the blade's span length under actual rotor conditions.

A geometric nonlinear, large-displacement, static analysis was used to determine the steady-state displacements of the blade under centrifugal and thermal loading. Then a normal modes analysis was performed on the geometry to estimate the blade's natural frequencies and mode shapes.

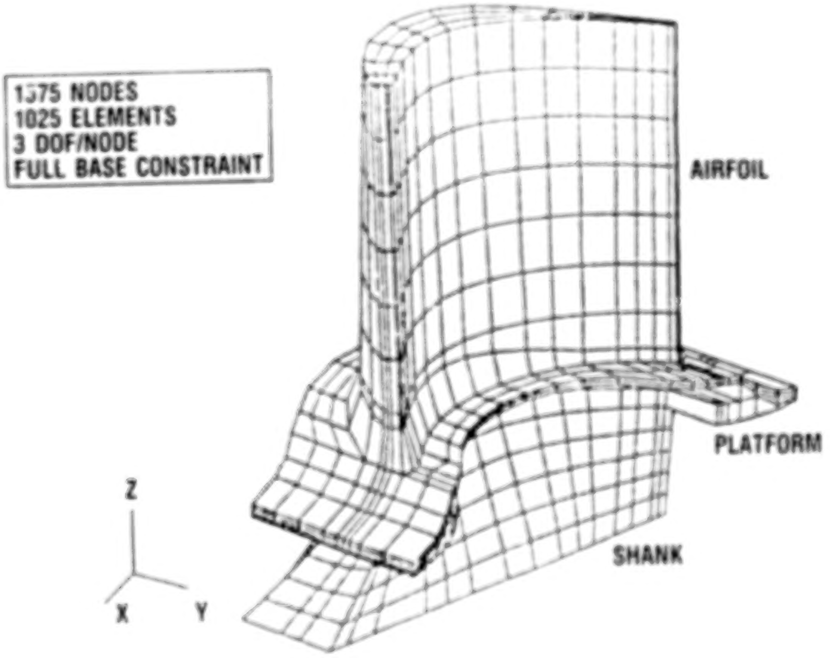

CD-88-31888

EXPERIMENTAL AND ANALYTICAL FREQUENCIES AND MODE SHAPES

The experimental mode shapes and frequencies for one SC orientation blade are shown below. Even though these modes are not pure beam modes, they can be classified by using beam terminology. Mode 1 proved to be first bending in the flatwise direction. Modes 2 and 3 were difficult to distinguish. The two modes appear similar because of the blade's high camber. Data from the modal analyzer indicated mode 2 to be first torsion and mode 3 to be bending in the edgewise direction. Mode 4 was second bending. Mode 5 appeared to be the lyre mode, and mode 6 (not shown) was a tip mode.

The analytical results from the same blade had excellent agreement with the interferometry results, shown below. The first five mode shapes duplicated the holograms. The modal frequencies were within 6 percent of the experimental results.

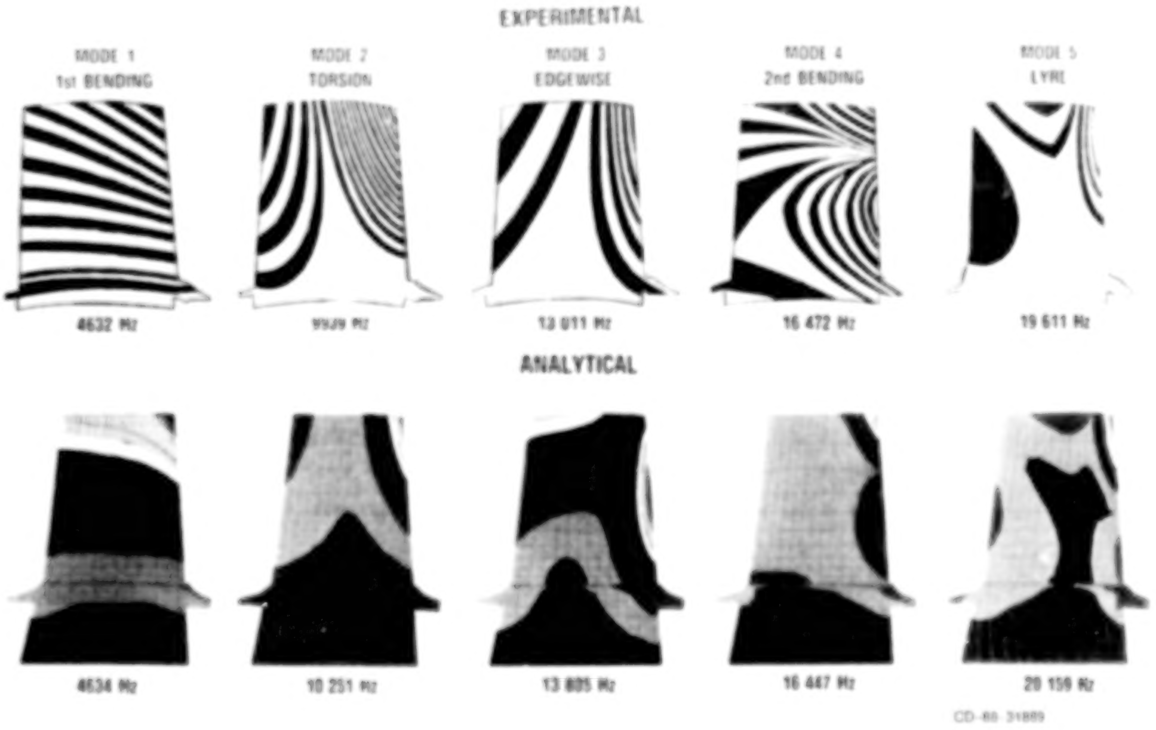
EXPERIMENTAL
MODE 1
1st BENDING
MODE 2
TORSION
MODE 3
EDGEWISE
MODE 4
2nd BENDING
MODE 5
LYRE
4632 Hz
9939 Hz
13 011 Hz
16 472 Hz
19 611 Hz
ANALYTICAL
4634 Hz
10 251 Hz
13 805 Hz
16 447 Hz
20 159 Hz
CD-80-31889

ORIGINAL PAGE IS
OF POOR QUALITY

PARAMETRIC STUDY OF CRYSTAL ORIENTATION

A parametric study was performed on the SC blades to investigate the effect of crystal orientation on the blades' natural frequencies. The figure graphically represents frequency as a function of rotation angle for three distinct tilt angles. The effects of crystal orientations on the nonrotating first blade mode are shown. The analyses of SC material were conducted at both nonrotating room-temperature conditions and operating conditions.

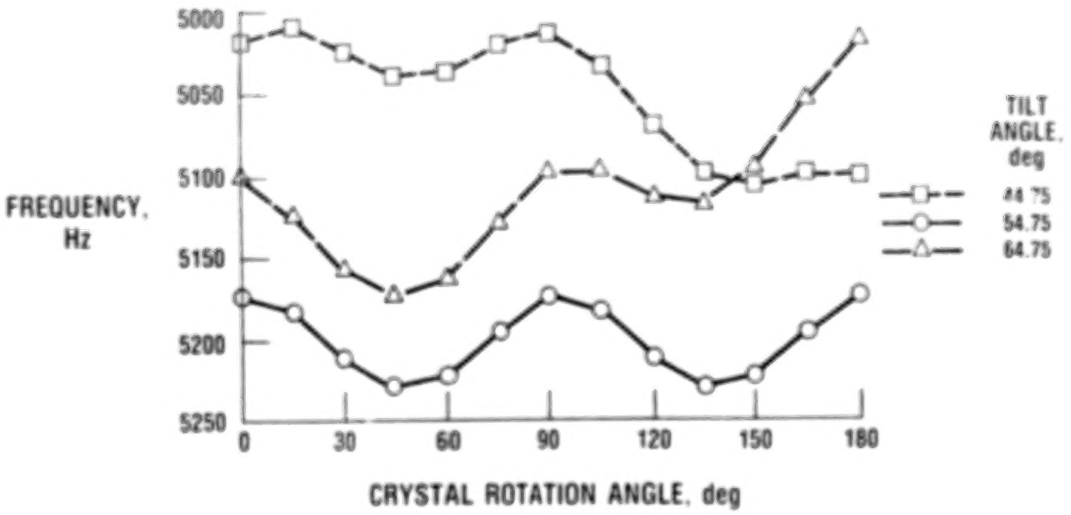

CD 88 31890

CAMPBELL DIAGRAM

Attempts were made to find an orientation that would eliminate or minimize the critical engine-order excitations. The Campbell diagram below shows that orienting the <111> axis in the chordwise direction (90° tilt angle) reduced the number of critical excitations when compared with the DS blade. This is a beneficial effect of SC blading.

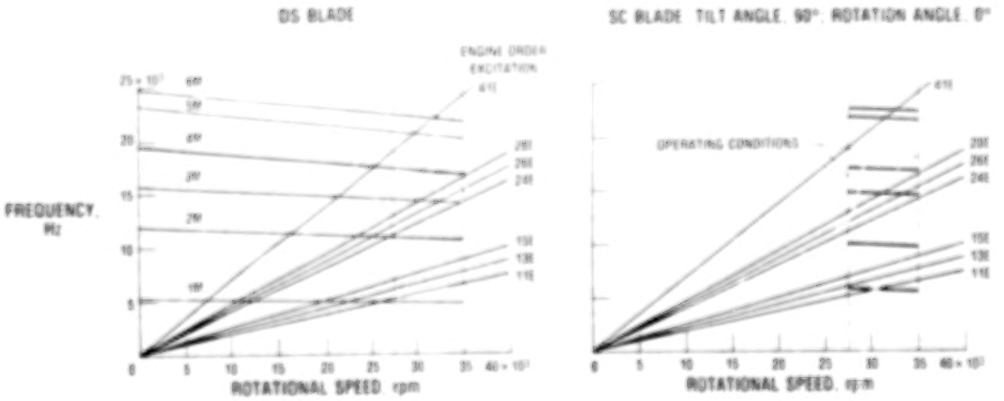

CD-88-31891

SUMMARY

An MSC/NASTRAN finite element blade model successfully determined the natural blade modes of single-crystal SSME turbopump blades. The SC blade dynamic characteristics were further analyzed with respect to crystal orientation under typical operating conditions. From a dynamics viewpoint the SC blade was an improvement over the DS blade. No new engine-order interferences were introduced with the material substitution. Additional studies proved that the engine-order interferences can be minimized by changing the blades' crystal orientation.

- **SC BLADES' NATURAL MODES WERE PREDICTED BY MSC/NASTRAN.**
- **NO NEW ENGINE-ORDER INTERFERENCES WERE INTRODUCED WITH THE SC MATERIAL SUBSTITUTION.**
- **BLADE INTERFERENCES WERE MINIMIZED BY OPTIMUM SC ORIENTATIONS.**

CD-89-31892

BIBLIOGRAPHY

Bowen, K., Nagy, P., and Parr, R.A., 1986, "The Evaluation of Single Crystal Superalloys for Turbopump Blades in the SSME," AIAA Paper 86-1477.

Dreshfield, R.L., and Parr, R.A., 1987, "Application of Single Crystal Superalloys for Earth-to-Orbit Propulsion Systems," AIAA Paper 87-1976, (NASA TM-89877).

Joseph, J.A., ed., 1981, "MSC/NASTRAN Application Manual," MacNeal-Schwendler.

Moss, L.A., and Smith, T.E., 1987, "SSME Single Crystal Turbine Blade Dynamics," NASA CR-179644.

N88-23258

PARAFRASE RESTRUCTURING OF FORTRAN CODE FOR PARALLEL PROCESSING*

Atul Wadhwa
Sverdrup Technology, Inc.
(Lewis Research Center Group)
NASA Lewis Research Center

ABSTRACT

Because of the existence of large and cumbersome computer codes, there is a need to find new and more efficient ways of performing structural computations. Today, there is a heavy emphasis on emerging parallel processing methods. A research effort is in progress at NASA Lewis to develop these methods to reduce time and cost of program execution. Restructuring FORTRAN codes to take advantage of parallel processing architecture is a part of this effort. An automatic code restructurer, Parafrase, is used to meet this effort. Parafrase, developed at the University of Illinois, transforms a FORTRAN code, subroutine by subroutine, into a parallel code for a vector and/or shared-memory multiprocessor system. Parafrase is not a compiler; it transforms a code and provides information for a vector or concurrent process.

Parafrase uses a data dependency to reveal parallelism among instructions. The data dependency test distinguishes between recurrences and statements that can be directly vectorized or parallelized. A number of transformations are required to build a data dependency graph.

The purpose of this presentation is to give an overview of the Parafrase restructuring approach. Specifically, key aspects of the Parafrase program (such as data dependence tests and machine-dependent transformations) will be discussed.

---

*Work performed on-site at the Lewis Research Center for the Structural Dynamics Branch.

ELEMENTS OF PARALLEL PROCESSING

Some current computer software packages written in sequential codes (i.e., existing FORTRAN) have an undesirable turnaround time. Parallel processing can minimize execution time by employing vector or concurrent events in the computing process. The most common terms characterizing parallel processing are vector and multiprocessing.

In vector processing a loop can be vectorized if each statement of the loop can be executed for the entire index set of the loop before executing the next statement and producing the same result. Multiprocessing refers to a system with two or more processors. There are basically two types of multiprocessing systems, a shared-memory system and a message-passing system. In the shared-memory system, all the processors exchange information through the shared-memory; while in the message-passing system, each processor has its own private memory, and each can communicate and synchronize with others through some network connection.

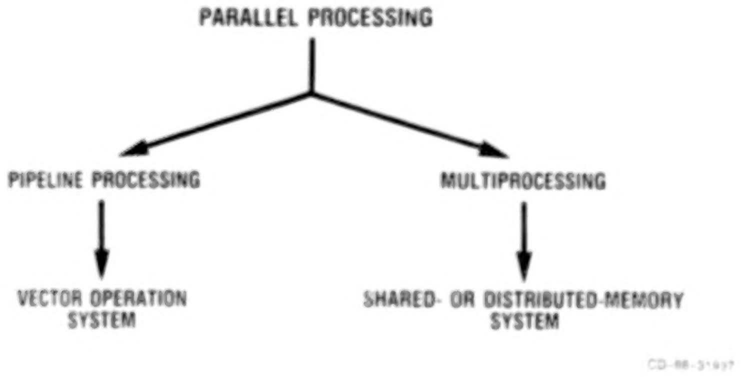
PARALLEL PROCESSING
PIPELINE PROCESSING
MULTIPROCESSING
VECTOR OPERATION SYSTEM
SHARED- OR DISTRIBUTED-MEMORY SYSTEM
CD-88-31937

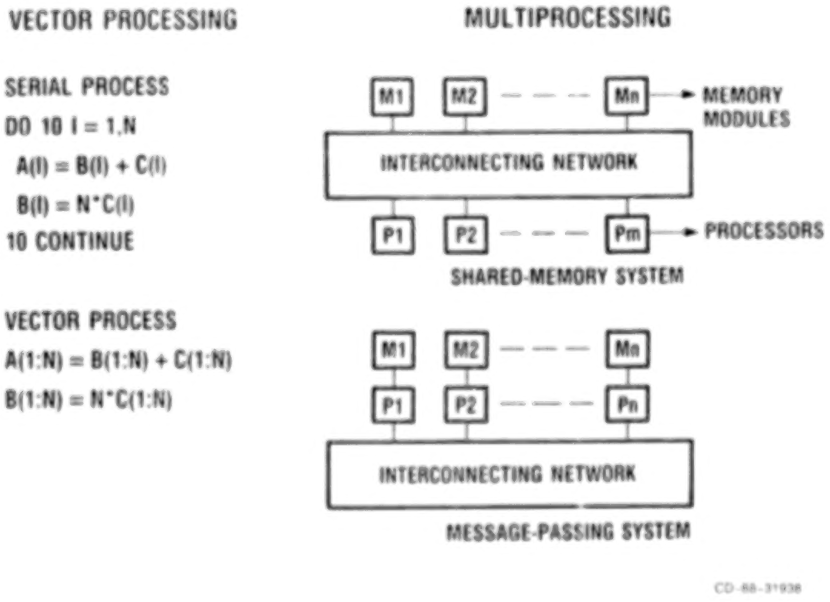
VECTOR PROCESSING
MULTIPROCESSING

SERIAL PROCESS

```
DO 10 I = 1,N
 A(I) = B(I) + C(I)
 B(I) = N*C(I)
10 CONTINUE
```

VECTOR PROCESS

```
A(1:N) = B(1:N) + C(1:N)
B(1:N) = N*C(1:N)
```

M1
M2
Mn
MEMORY MODULES
INTERCONNECTING NETWORK
P1
P2
Pm
PROCESSORS
SHARED-MEMORY SYSTEM
M1
M2
Mn
P1
P2
Pn
INTERCONNECTING NETWORK
MESSAGE-PASSING SYSTEM
CD-88-31938

PARAFRASE: AN AUTOMATIC CODE RESTRUCTURER

Parafrase is a restructuring tool that transforms a code, subroutine by subroutine, to take advantage of the parallelism available in a particular machine (Kuck et al., 1984). Parafrase accepts an input program in FORTRAN, analyzes its data dependency, then targets the detected parallelism on vector processor (Single Execution Array (SEA)) or multiprocessor (Multiple Execution Scalar (MES)). To determine if a loop can be parallelized, Parafrase builds a graph of the data dependencies; the nodes represent program statements and the edges represent data and control dependencies. Parafrase output is useful in analyzing and evaluating parallel programs.

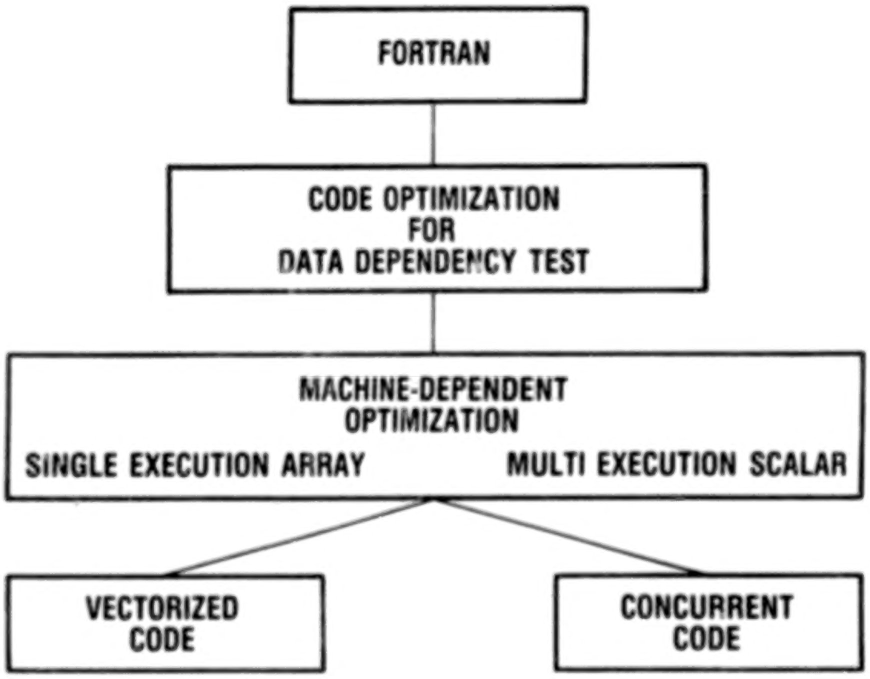
FORTRAN
CODE OPTIMIZATION FOR DATA DEPENDENCY TEST
MACHINE-DEPENDENT OPTIMIZATION
SINGLE EXECUTION ARRAY
MULTI EXECUTION SCALAR
VECTORIZED CODE
CONCURRENT CODE

CD-88-31939

DATA DEPENDENCY TEST

Detecting parallelism in a code requires data dependency testing, which reveals information about data computation and use in the program. The data dependency test determines whether or not a statement uses a value that was computed on previous iteration. There are four types of dependencies: flow, antidependence, output dependence, and control dependence (Wolfe, 1982). These dependencies must be considered to detect recurrences.

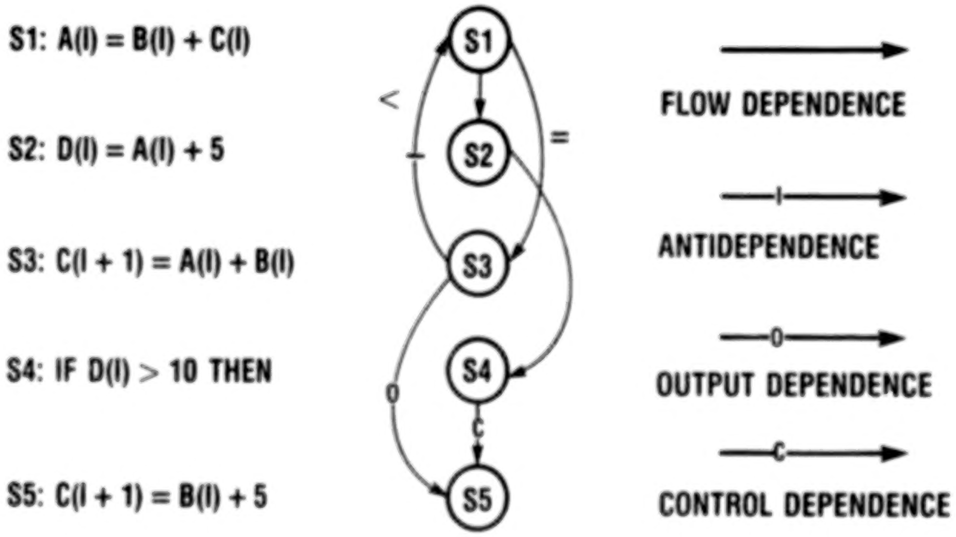
S1: A(I) = B(I) + C(I)
S2: D(I) = A(I) + 5
S3: C(I + 1) = A(I) + B(I)
S4: IF D(I) > 10 THEN
S5: C(I + 1) = B(I) + 5
S1
S2
S3
S4
S5
<
=
0
c
FLOW DEPENDENCE
ANTIDEPENDENCE
OUTPUT DEPENDENCE
CONTROL DEPENDENCE

CD-88-31940

TRANSFORMATION FOR DATA DEPENDENCE TEST

Parafrase uses a data dependency test to detect parallelism. A number of machine-independent passes are required to build an effective data dependency graph. Some of the important passes are as follows: DO loop normalization, induction variable substitution, statement forward substitution, and dead-code elimination.

A NUMBER OF TRANSFORMATIONS ARE REQUIRED TO BUILD A DATA DEPENDENCY GRAPH. THESE TRANSFORMATIONS ARE MACHINE-INDEPENDENT TRANSFORMATIONS. SOME OF THE IMPORTANT PASSES ARE

1. **DO-LOOP NORMALIZATION**
2. **INDUCTION VARIABLE SUBSTITUTION**
3. **STATEMENT FORWARD SUBSTITUTION**
4. **DEAD-CODE ELIMINATION**

CD-88-31941

DO LOOP NORMALIZATION

The first of machine-independent passes is the DO-loop normalization (Polychronopolus, 1986). A DO loop normalization transforms loops in such a way that the induction variables of each loop increase by one, starting from one, to some upper bound. Every old induction variable within the loop is replaced by the new induction variable.

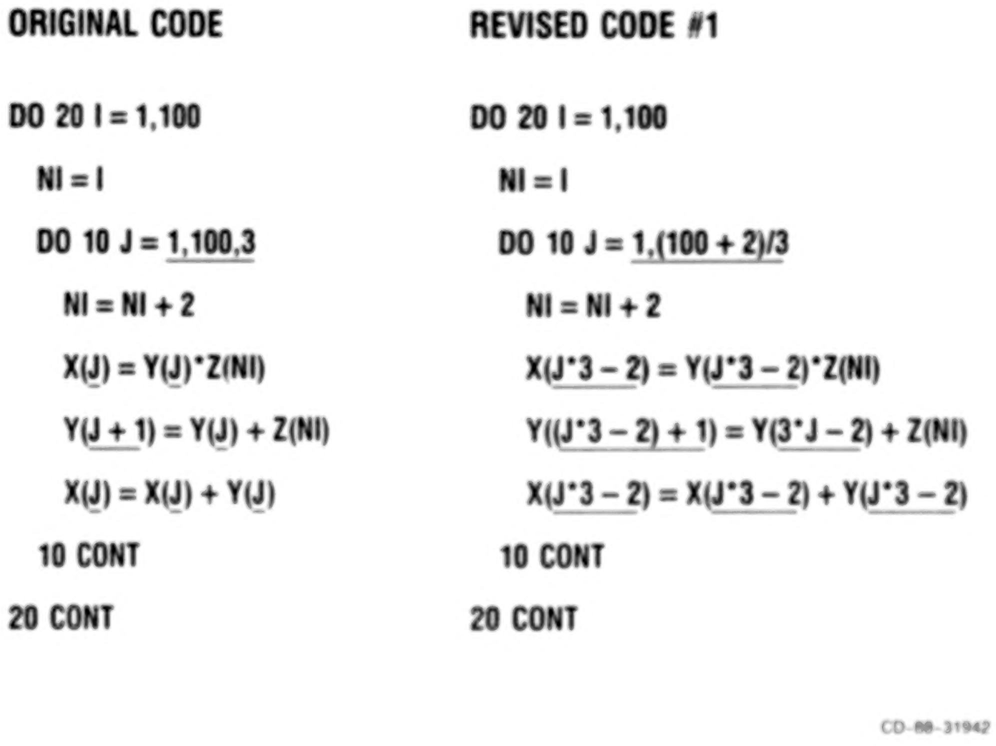

```
ORIGINAL CODE                  REVISED CODE #1

DO 20 I = 1,100                DO 20 I = 1,100
  NI = I                         NI = I
  DO 10 J = 1,100,3              DO 10 J = 1,(100 + 2)/3
    NI = NI + 2                    NI = NI + 2
    X(J) = Y(J)*Z(NI)              X(J*3 – 2) = Y(J*3 – 2)*Z(NI)
    Y(J + 1) = Y(J) + Z(NI)        Y((J*3 – 2) + 1) = Y(3*J – 2) + Z(NI)
    X(J) = X(J) + Y(J)             X(J*3 – 2) = X(J*3 – 2) + Y(J*3 – 2)
  10 CONT                        10 CONT
20 CONT                        20 CONT
```

CD-88-31942

INDUCTION VARIABLE SUBSTITUTION

Induction variables are used inside loops to simplify subscripts to linear functions of loop index variables. Detection and elimination of these variables reduce the number of operations. This transformation may also allow vectorization and parallelization of the loop, which would have been impossible because of the dependence cycle (when two statements are closely coupled). The discovery of induction variables is required since the data dependency test needs the array subscripts to be in terms of the loop index variables.

REVISED CODE #1

```
DO 20 I = 1,100
  NI = I
  DO 10 J = 1,(100 + 2)/3
    NI = NI + 2
    X(J*3 – 2) = Y(J*3 – 2)*Z(NI)
    Y((J*3 – 2) + 1) = Y(3*J – 2) + Z(NI)
    X(J*3 – 2) = X(J*3 – 2) + Y(J*3 – 2)
  10 CONT
20 CONT
```

REVISED CODE #2

```
DO 20 I = 1,100
  NI = I
  DO 10 J = 1,(100 + 2)/3
    NI = I + 2*J
    X(J*3 – 2) = Y(J*3 – 2)*Z(NI)
    Y((J*3 – 2) + 1) = Y(3*J – 2) + Z(NI)
    X(J*3 – 2) = X(J*3 – 2) + Y(J*3 – 2)
  10 CONT
20 CONT
```

CD-88-31943

STATEMENT FORWARD SUBSTITUTION

A statement forward substitution replaces integer expressions and constants into subscripts. A scalar variable that is assigned a value, and is used in a subscript, is replaced by an expression. The statement forward substitution eliminates the need for compiler or user temporaries. This transformation provides more information for the data dependency test.

REVISED CODE #2

```
DO 20 I = 1,100
  NI = I
  DO 10 J = 1,(100 + 2)/3
    NI = I + 2*J
    X(J*3 – 2) = Y(J*3 – 2)*Z(NI)
    Y((J*3 – 2) + 1) = Y(3*J – 2) + Z(NI)
    X(J*3 – 2) = X(J*3 – 2) + Y(J*3 – 2)
  10 CONT
20 CONT
```

REVISED CODE #3

```
DO 20 I = 1,100
  NI = I
  DO 10 J = 1,(100 + 2)/3
    NI = I + 2*J
    X(J*3 – 2) = Y(J*3 – 2)*Z(I + 2*J)
    Y((J*3 – 2) + 1) = Y(3*J – 2) + Z(I + 2*J)
    X(J*3 – 2) = X(J*3 – 2) + Y(J*3 – 2)
  10 CONT
20 CONT
```

CD-88-31944

DEAD-CODE ELIMINATION

The dead-code elimination removes the statements whose output is never used. This transformation reduces the number of computations by eliminating unnecessary calculations. These transformations convert as many subscripts as possible to a linear function of DO loop induction variables.

REVISED CODE #3

```
DO 20 I = 1,100
  NI = I
  DO 10 J = 1,(100 + 2)/3
    NI = I + 2*J
    X(J*3 – 2) = Y(J*3 – 2)*Z(I + 2*J)
    Y((J*3 – 2) + 1) = Y(3*J – 2) + Z(I + 2*J)
    X(J*3 – 2) = X(J*3 – 2) + Y(J*3 – 2)
  10 CONT
20 CONT
```

REVISED CODE #4

```
DO 20 I = 1,100
  DO 10 J = 1,(100 + 2)/3
    X(J*3 – 2) = Y(J*3 – 2)*Z(I + 2*J)
    Y((J*3 – 2) + 1) = Y(3*J – 2) + Z(I + 2*J)
    X(J*3 – 2) = X(J*3 – 1) + Y(J*3 – 2)
  10 CONT
20 CONT
```

CD-88-31945

VECTORIZATION AND PARALLELIZATION

After building the data dependency graph, Parafrase starts restructuring a code from serial to parallel form. If the data dependency relation prevents loop vectorization or parallelization, then several machine-dependent transformations on the loop would be attempted. Loop interchanging and loop fission are two of the important passes.

AFTER BUILDING A DATA DEPENDENCY GRAPH, PARAFRASE STARTS TO RESTRUCTURE THE PROGRAM FROM SERIAL TO PARALLEL FORM. FOR THESE TRANSFORMATIONS A NUMBER OF PASSES ARE TARGETED FOR A VECTOR (SINGLE EXECUTION ARRAY) OR A MULTIPROCESSOR (MULTI-EXECUTION SCALAR) SYSTEM. TWO OF THESE PASSES ARE AS FOLLOWS:

1. **LOOP INTERCHANGING**
2. **LOOP FISSION**
    - **a) INSIDE-OUT LOOP DISTRIBUTION**
    - **b) DO-LOOP SPREADING**

CD-88-31850

LOOP INTERCHANGING

The first transformation is loop interchanging, a switching of inner and outer loops. Loop interchanging may be used to vectorize the inner loop or to parallelize the outer loop. Loop interchanging is impossible when two or more statements of the loop are dependent with "<" and ">" directions.

REVISED CODE #4

```
DO 20 I = 1,100
  DO 10 J = 1,(100 + 2)/3
    X(J*3 - 2) = Y(J*3 - 2)*Z(I + 2*J)
    Y((J*3 - 2) + 1) = Y(3*J - 2) + Z(I + 2*J)
    X(J*3 - 2) = X(J*3 - 1) + Y(J*3 - 2)
  10 CONT
20 CONT
```

REVISED CODE #5

```
DO 10 J = 1,102/3
  DO 20 I = 1,100
    X(J*3 - 2) = Y(J*3 - 2)*Z(i + 2*J)
    Y((J*3 - 2) + 1) = Y(3*J - 2) + Z(I + 2*J)
    X(J*3 - 2) = X(J*3 - 1) + Y(J*3 - 2)
20 CONT
10 CONT
```

CD 88 31951

INSIDE-OUT LOOP DISTRIBUTION

Some loops can be divided into two or more loops, a process known as loop fission. If the statement forward substitution does not remove the data dependence cycle, then the loop fission may be allowed to vectorize or parallelize a part of the loop. Inside-out loop distribution is used for the case of the vector operation machine (Allen and Kennedy, 1982), and Doall Loop Distribution is used for the multiprocess machine.

REVISED CODE #4

```
DO 20 I = 1,100
  DO 10 J = 1,(100 + 2)/3
    X(J*3 - 2) = Y(J*3 - 2)*Z(I + 2*J)
    Y((J*3 - 2) + 1) = Y(3*J - 2) + Z(I + 2*J)
    X(J*3 - 2) = X(J*3 - 2) + Y(J*3 - 2)
  10 CONT
20 CONT
```

FINAL REVISED VECTOR CODE

```
DO 20 J = 1,100
  DO 10 I = 1,102/3
    X(J*3 - 2) = Y(J*3 - 2)*Z(I + 2*J)
10 CONT
  DO 10 J = 1,102/3
    Y((J*3 - 2) + 1) = Y(3*J - 2) + Z(I + 2*J)
    X(J*3 - 2) = X(J*3 - 1) + Y(J*3 - 2)
20 CONT
10 CONT
```

CD 88 31953

DOALL LOOP DISTRIBUTION

Doall loop distribution for a multiprocessor machine is a spreading of the loop iteration across multiple processors. This transformation detects if each loop iteration can be executed independently of the others.

REVISED CODE #5

```
DO 10 J = 1,102/3
  DO 20 I = 1,100
    X(J*3 - 2) = Y(J*3 - 2)*Z(I + 2*J)
    Y((J*3 - 2) + 1) = Y(3*J - 2) + Z(I + 2*J)
    X(J*3 - 2) = X(J*3 - 1) + Y(J*3 - 2)
  10 CONT
20 CONT
```

FINAL REVISED CONCURRENT CODE

```
DOALL 30 J = 1,102/3
  DO 10 I = 1,100
    X(J*3 - 2) = Y(J*3 - 2)*Z(I + 2*J)
    X(J*3 - 2) = X(J*3 - 1) + Y(J*3 - 2)
10 CONT
30 CONT
DOALL 30 J = 1,102/3
  DO 20 I = 1,100
    Y((J*3 - 2) + 1) = Y(3*J - 2) + Z(I + 2*J)
20 CONT
30 CONT
```

CD 88 31965

APPLICATION

Parafrase was used to restructure a rotor dynamics SOLVE subroutine, as well as initialization INIT subroutine. The estimate of speedup values has been computed by Parafrase. The restructured subroutines were executed on CFT, a CRAY compiler, which detected more vector operations than the original code.

SPEEDUP COMPARED WITH NUMBER OF VECTOR PROCESSORS

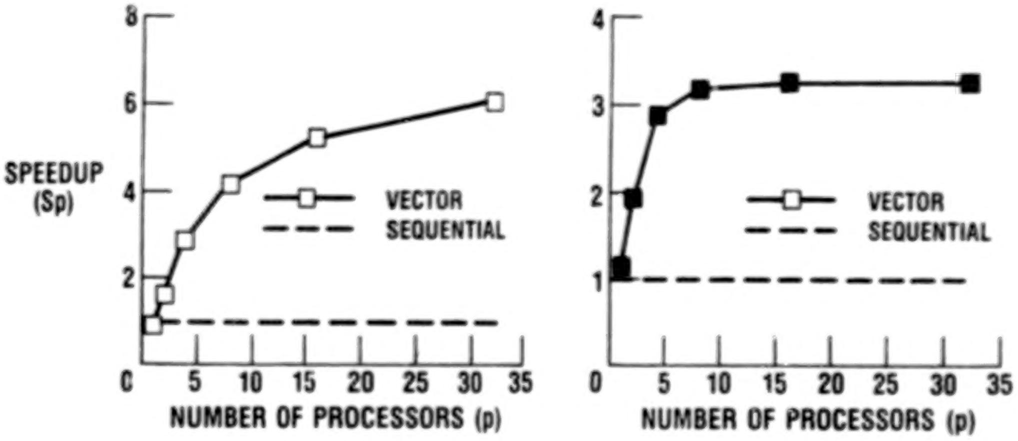

ROTOR RUB DYNAMICS
(SOLVE ROUTINE)

ROTOR RUB DYNAMICS
(INIT ROUTINE)

CD-88-31957

SPEEDUP COMPARED WITH NUMBER OF MULTIPROCESSORS

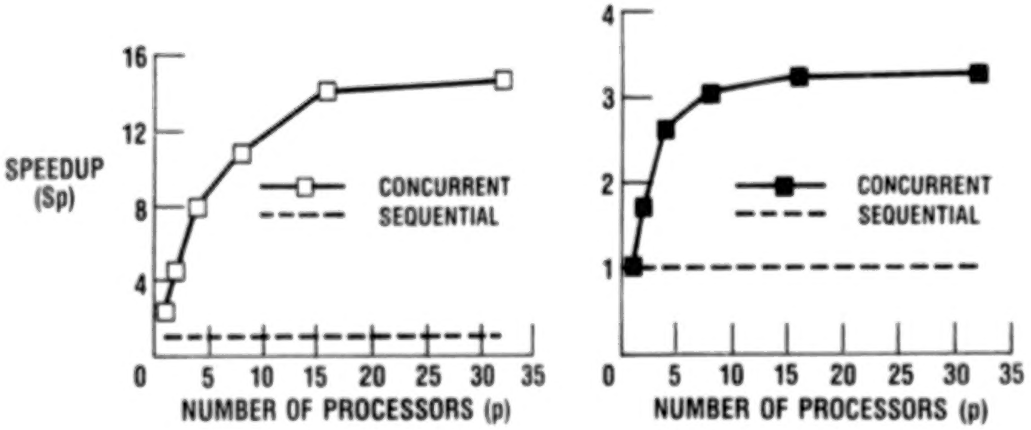

ROTOR RUB DYNAMICS
(SOLVE ROUTINE)

ROTOR RUB DYNAMICS
(INIT ROUTINE)

CD-88-31958

SPEEDUP OF A RESTRUCTURED CODE

Kuck, et al., has applied Parafrase to EISPACK subroutines, an eigenvalue/eigenvector conjecture. After restructuring them, Parafrase calculated the speedup values of subroutines.

SPEEDUP VALUES OBTAINED BY KUCK'S GROUP ON EISPAK

SUBROUTINE NAME	NUMBER OF PROCESSORS, 32	NUMBER OF PROCESSORS, 256	NUMBER OF PROCESSORS, 2048
ELMBAK	31.9	242.0	668.0
ELMHES	31.7	33.6	33.6
ETRAN	29.3	71.3	84.5
TRED1	31.0	235.0	240.0
TRED2	18.3	36.5	39.5
CBABK2	30.0	53.5	57.4
COMBAK	31.9	248.5	721.0
CORTB	32.0	254.0	1250.0
CORTH	32.0	252.0	501.0
BANDV	31.0	98.0	98.0

CD-88-31959

SUMMARY

Most existing code compilers take advantage of parallel processing, but don't perform code restructuring. To achieve effective and efficient use of parallel processing architecture, existing codes have to be restructured. Parafrase is a FORTRAN code-restructuring tool. It is not a compiler. It produces information for vector or shared-memory processing systems. Parafrase has been applied to subroutines of the Rotor Rub Dynamics code. The restructured output code has been executed on a CRAY compiler, which found more vector operations than the original code.

- **TO ACHIEVE FAST EXECUTION, RESTRUCTURING OF A SEQUENTIAL CODE IS NEEDED FOR PARALLEL PROCESSING**
- **PARAFRASE CAN BE USED AS A RESTRUCTURING TOOL**
- **PARAFRASE OPTIMIZES A CODE FOR THE DATA DEPENDENCY TEST**
- **THE OUTPUT OF PARAFRASE CAN BE MODIFIED FOR VECTOR OR SHARED-MEMORY ARCHITECTURE**

CD-88-31956

REFERENCES

Allen, J.R., and Kennedy, K., 1982, PFC: A Program to Convert Fortran to Parallel Form, Report MASC-TR82-6. Rice Univ., Houston Texas.

Kuck, D.J. et al., 1984, "The Effect of Program Restructuring, Algorithm Change, and Architecture Choice on Program Performance," *Proceedings of the 1984 International Conference on Parallel Processing*, R.M. Keller, ed., IEEE, New York, pp. 129-138.

Kuck, D.J., 1978, *The Structure of Computers and Computations*, John Wiley and Sons, New York.

Leu, J.S., Agrawal, D.P., and Mauney, J., 1987, "Modeling of Parallel Software for Efficient Computation-Communication Overlap," to be published.

Midkiff, S.P., and Padua, D.A., 1986, "Compiler Generated Synchronization for Loops," *Proceedings of the 1986 International Conference on Parallel Processing*, K. Hwang, S.M. Jacobs, and E.E. Swartzlander, eds., IEEE, New York, pp. 544-551.

Padua, D.A., Kuck, D.J., and Lawrie, D.H., 1980, "High-Speed Multiprocessors and Compilation Techniques," *IEEE Transaction on Computers*, Vol. 29, No. 9, pp. 763-776.

Polychronopolus, C.D., and Banerjee, U., 1986, "Speedup Bounds and Processor Allocation of Parallel Programs on Multiprocessor Systems," *Proceedings of the 1986 International Conference on Parallel Processing*, K. Hwang, S.M. Jacobs, and E.E. Swartzlander, eds., IEEE, New York, pp. 554-551.

Wolfe, M.J., 1982, "Optimizing Supercompilers for Supercomputers," Ph.D. Thesis, University of Illinois at Urbana-Champaign, Illinois.

N88-23259

ANALYSIS OF ROTATING FLEXIBLE BLADES USING MSC/NASTRAN

Michael A. Ernst
Structural Dynamics Branch
NASA Lewis Research Center

ABSTRACT

This presentation gives an overview of the use of MSC/NASTRAN in the analysis of rotating flexible blades (Lawrence, et al., 1987). The geometrically nonlinear analysis using NASTRAN Solution Sequence 64 is discussed along with the determination of frequencies and mode shapes using Solution Sequence 63. Items unique to rotating blade analyses, such as setting angle, centrifugal softening effects, and hub flexibility, are emphasized.

PRECEDING PAGE BLANK NOT FILMED

PROPFAN

Because of the potential for very high propulsive efficiency at cruise speeds up to Mach 0.8, advanced forms of the propeller, called propfans, are being seriously considered for aircraft propulsion. To obtain maximum aerodynamic and acoustic performance, the trend in advanced high speed propeller design has been toward thin, swept blades of complicated structural design. A research program to establish the required technology for successful design of propfans is in progress at the NASA Lewis Research Center (Mikkelson, et al, 1984 and Strack, et al, 1981).

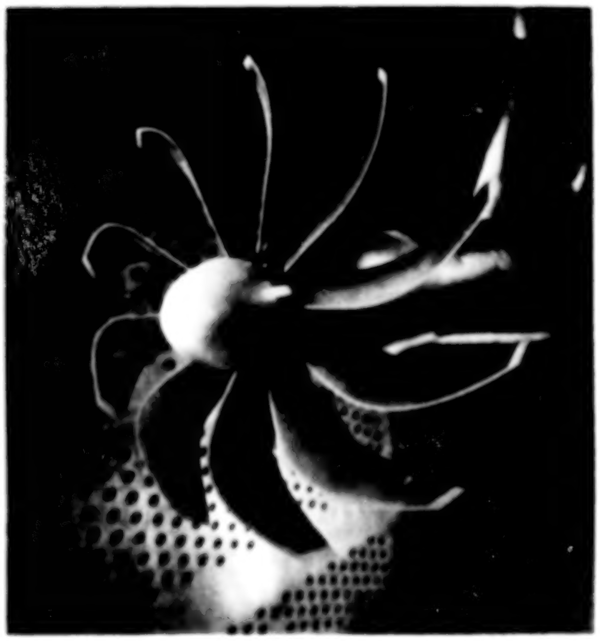

CD 88 32814

ORIGINAL PAGE IS
OF POOR QUALITY

STRUCTURAL MODEL

Part of the Advanced Turboprop Program effort is to understand and predict the structural and dynamic behavior of these blades. The analysis of rotating flexible blades, such as compressor and turboprop blades, often requires complex procedures, including geometrically nonlinear (large-displacement) analysis and frequency and mode shape determination. In performing these analyses, and in modeling the complex geometries and material properties of the blades, finite element (F.E.) computer programs typically are used.

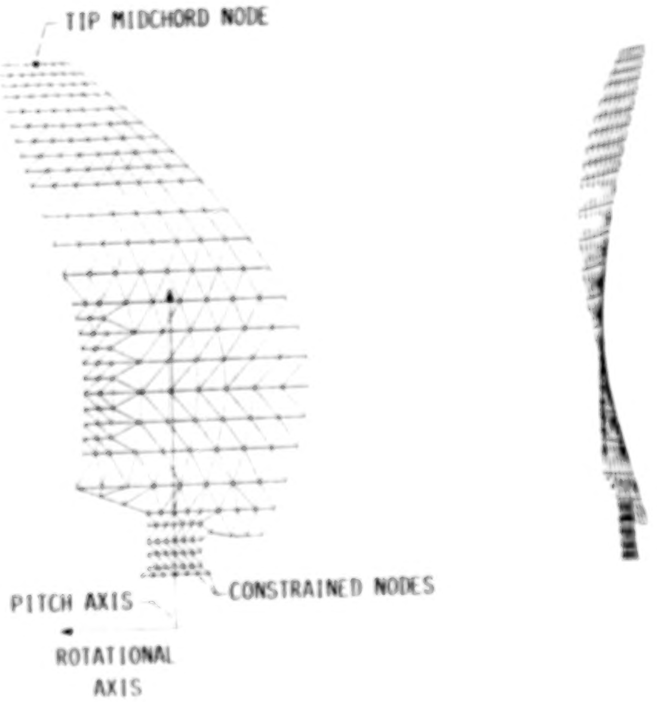
TIP MIDCHORD NODE
PITCH AXIS
CONSTRAINED NODES
ROTATIONAL AXIS

CD 88 32815

OBJECTIVE

The objectives in performing such analyses include the prediction of steady-state deflections and stresses under centrifugal forces, the generation of data for constructing Campbell diagrams (plots of frequency with respect to rotational speed), and the provision of modal data for use in flutter calculations.

- STRUCTURAL ANALYSIS OF TURBOPROP BLADES
  - STEADY-STATE DISPLACEMENTS
  - FREQUENCIES
  - MODE SHAPES

CD-88-32816

APPROACH

NASTRAN is particularly well-suited to this purpose because of its ability to compute steady-state displacements with its geometrically nonlinear analysis capabilities, and to use those results for subsequent normal-modes analyses (McCormick, 1983).

- **FINITE ELEMENT ANALYSIS USING NASTRAN**
    - **STEADY-STATE DISPLACEMENT (SOLUTION SEQUENCE 64)**
    - **EIGENSOLUTION (SOLUTION SEQUENCE 63)**

CD-88-32817

PROCEDURE

The computation of steady-state displacements, frequencies, and mode shapes of flexible rotating blades requires that two NASTRAN Solution sequences be run. First, a large-displacement analysis is run using NASTRAN Solution Sequence 64. This solution sequence performs a large-displacement analysis on the rotating blade, computes steady-state displacements and stresses, and then stores the blade final stiffness and mass matrices in a database. Following the large-displacement analysis, the frequencies and mode shapes are computed using Solution Sequence 63. This solution sequence computes the modal parameters from the final mass and stiffness matrices which were computed during the Solution 64 run (Lawrence, et al, 1987).

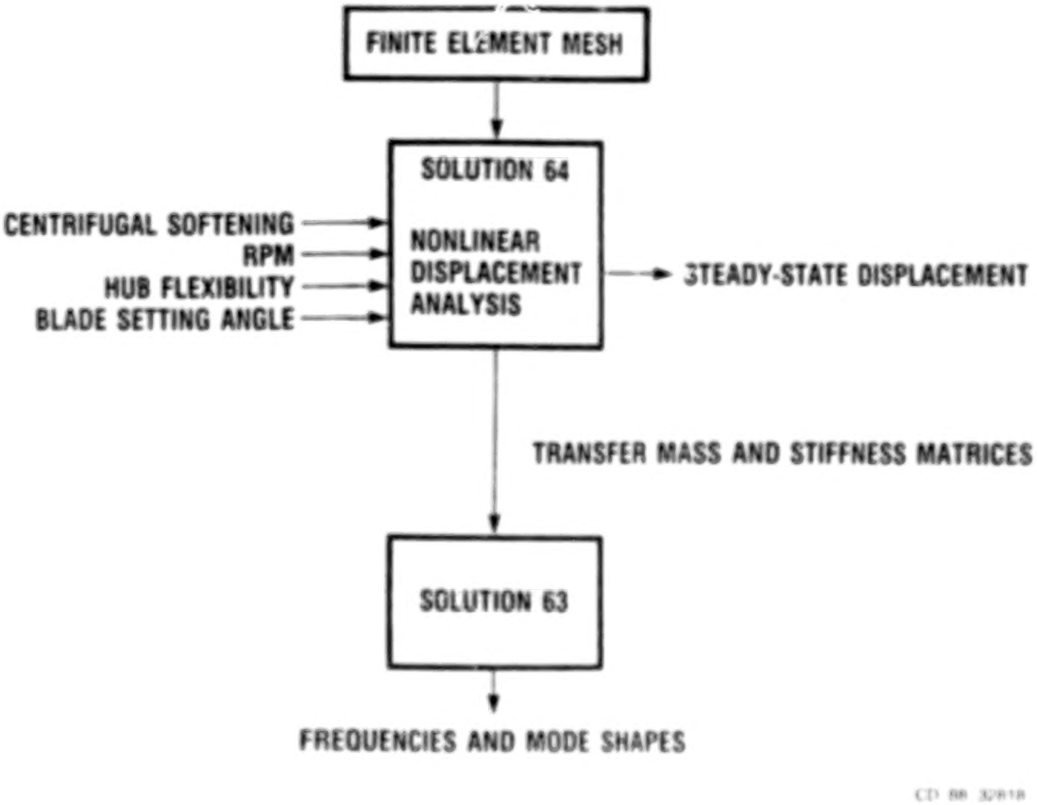
FINITE ELEMENT MESH
SOLUTION 64
CENTRIFUGAL SOFTENING
RPM
HUB FLEXIBILITY
BLADE SETTING ANGLE
NONLINEAR DISPLACEMENT ANALYSIS
STEADY-STATE DISPLACEMENT
TRANSFER MASS AND STIFFNESS MATRICES
SOLUTION 63
FREQUENCIES AND MODE SHAPES
CD 88 32818

TYPICAL NONLINEAR DEFLECTION CURVE FOR FLEXIBLE BLADE

Experience has shown that a large-displacement analysis is required because the blades are relatively flexible and normally deflect considerably under centrifugal forces (Lawrence and Kielb, 1984).

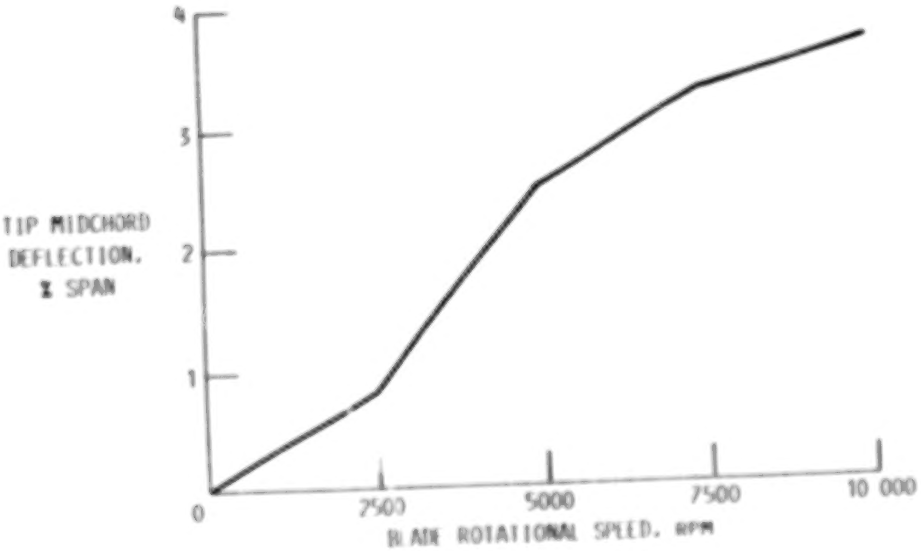

TYPICAL FLEXIBLE BLADE CAMPBELL DIAGRAM

A typical plot demonstrating the variation in natural frequencies with rotational speed is shown.

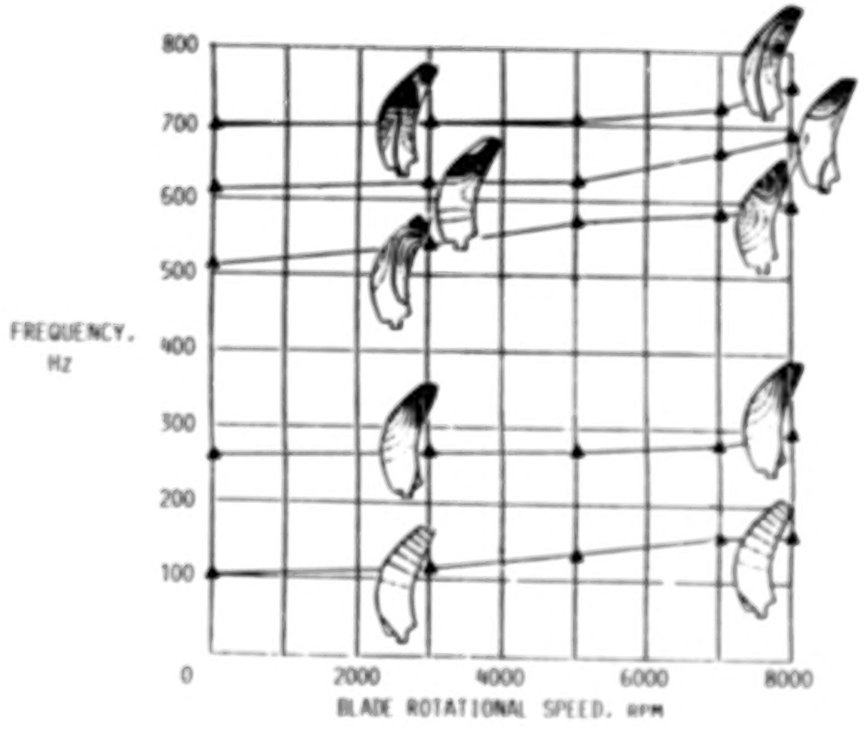

CD-88-32820

CENTRIFUGAL SOFTENING

When performing the large-displacement analysis, NASTRAN will automatically consider the increment in load by updating the centrifugal loads based on the deformed position of the blade. Although this approach will work for the large-displacement analysis, the softening terms must still be inserted into the stiffness matrix when a subsequent normal-modes analysis is performed. If the softening term $-\Omega^2 M$ is not included in the stiffness matrix that is transferred from the Solution 64 to the Solution 63 analysis, the frequencies will be computed incorrectly.

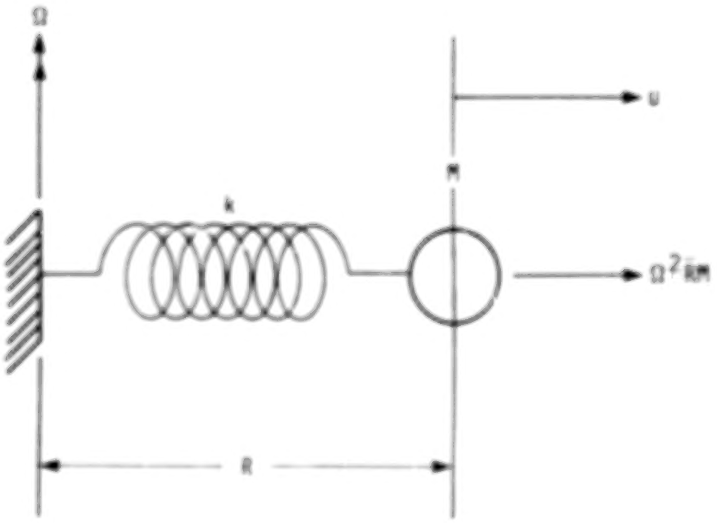

$$ku = \Omega^2 \bar{R} M$$
$$ku = \Omega^2 (R + u) M$$
$$(k - \Omega^2 M) u = \Omega^2 R M$$

CD 88 32821

EFFECT ON NATURAL FREQUENCIES DUE TO CENTRIFUGAL SOFTENING

To demonstrate the effect that the softening terms have on the natural frequencies, a steel plate (6 in. by 2 in. by 0.10 in.) was analyzed. In this figure, two sets of frequencies are plotted; one for the plate lying in the plane of rotation, and the other lying perpendicular to the plane of rotation. For the latter case the softening terms have a significant effect on the plate's first bending mode frequency. This is understandable since both the softening terms and the bending mode motion are in the plane of rotation. For actual blades, which have more complexity in their geometries than the steel plate, the centrifugal softening will have some influence on all of the modes, and therefore, will need to be included in all of the normal-modes analyses.

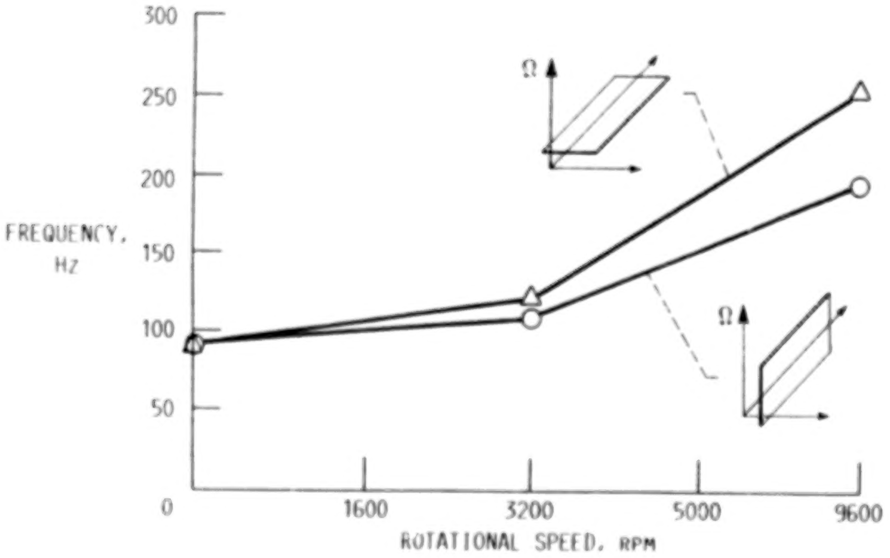

CD 88 32822

ALTERING BLADE SETTING ANGLE

To obtain the steady-state displacements, frequencies, and mode shapes when the blade is rotating at a new speed, both the large-displacement and normal-modes analysis need to be rerun. In addition to changing the blade rotational speed, the blade setting angle generally has to be adjusted. To implement a change in the setting angle, the entire blade can be rotated by defining the blade geometry in a new coordinate system via the CORD2R card.

INPUT DATA CARD CORD2R

(McCORMICK, 1983)

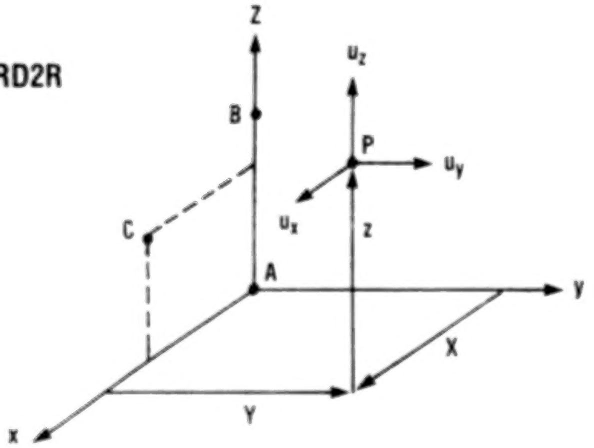

FORMAT

1	2	3	4	5	6	7	8	9	10
CORD2R	CID	RID	AI	A2	A3	B1	B2	B3	ABC
CORD2R	3	17	−2.9	1.0	0.0	3.6	0.0	1.0	123

+BC	C1	C2	C3						
+23	5.2	1.0	−2.9						

CD 88 32823

HUB FLEXIBILITY

Ernst and Lawrence, 1987, have shown that base flexibility can have a significant effect on steady-state displacements, frequencies, and mode shapes. The blade chosen for their study was the 0.175 scale model of the GE-A7-B4, shown below. A series of nonlinear static and dynamic analyses were conducted on the blade for both rigid and flexible hub configurations. Results indicated that hub flexibility is significant in the nonlinear static and dynamic analyses of the GE-A7-B4, and that in order to insure accuracy in analyses of other blades, hub flexibility should always be considered.

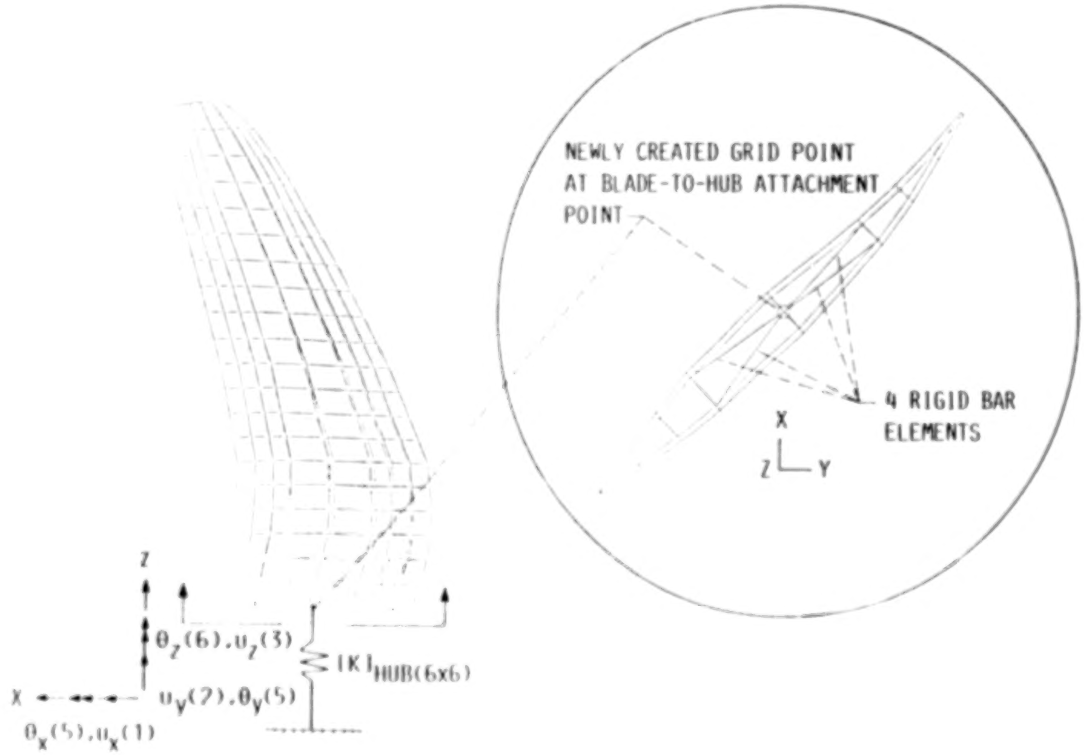
NEWLY CREATED GRID POINT AT BLADE-TO-HUB ATTACHMENT POINT
4 RIGID BAR ELEMENTS
X
Z
Y
Z
$\theta_Z(6), u_Z(3)$
$[K]_{HUB(6x6)}$
X
$u_Y(2), \theta_Y(5)$
$\theta_X(5), u_X(1)$

CD 88 32824

EFFECT OF HUB FLEXIBILITY ON LEADING-EDGE TIP DISPLACEMENTS

The figure below presents the magnitude of leading-edge tip displacements versus rotational speed for the 2-ft diameter GE-A7-B4 blade model, with both rigid and flexible hubs. At low rpm, the flexible hub has little effect on the static displacement. However, at greater than 4000 rpm, the influence of the flexible hub becomes notable.

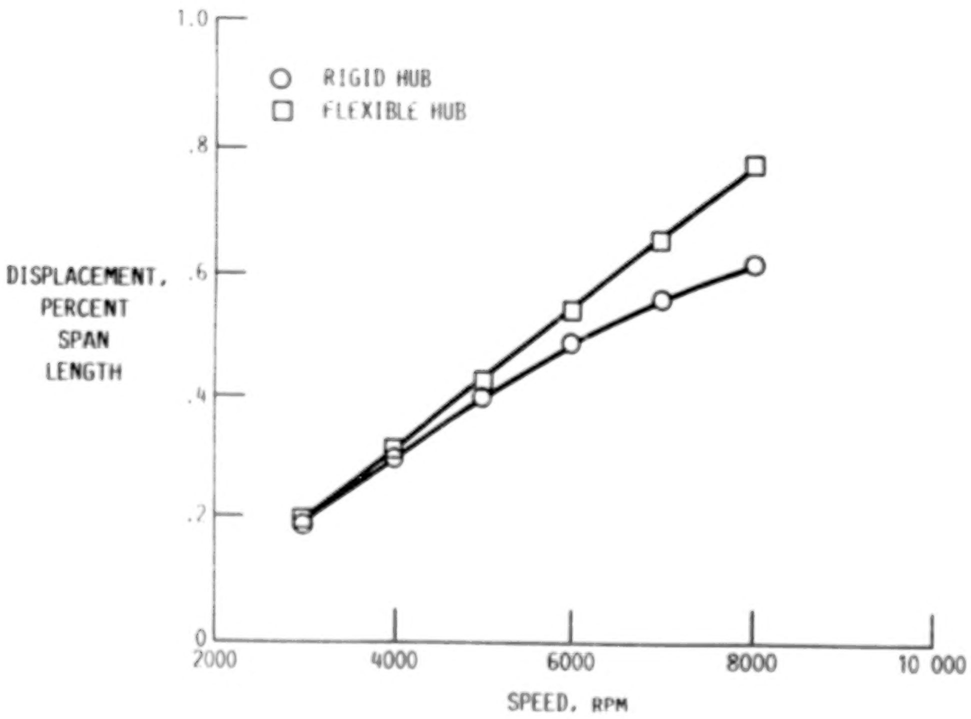

CD-88-32825

EFFECT OF HUB FLEXIBILITY ON MODAL FREQUENCIES

The figure below presents the first bending, second bending, first torsional, and third bending eigenvalues for the 2-ft diameter GE-A7-B4 blade model at various rpm, in both rigid hub and flexible hub configurations. Although the first bending and first torsional frequencies seem to be unaffected by the flexible hub, there is an appreciable discrepancy between the flexible hub and the rigid hub configurations relating to the second bending and third bending frequencies. Also, the first edgewise mode was seen between the second bending and first torsional modes of the flexible hub, whereas the first edgewise mode was not seen for the rigid hub in lower frequency range.

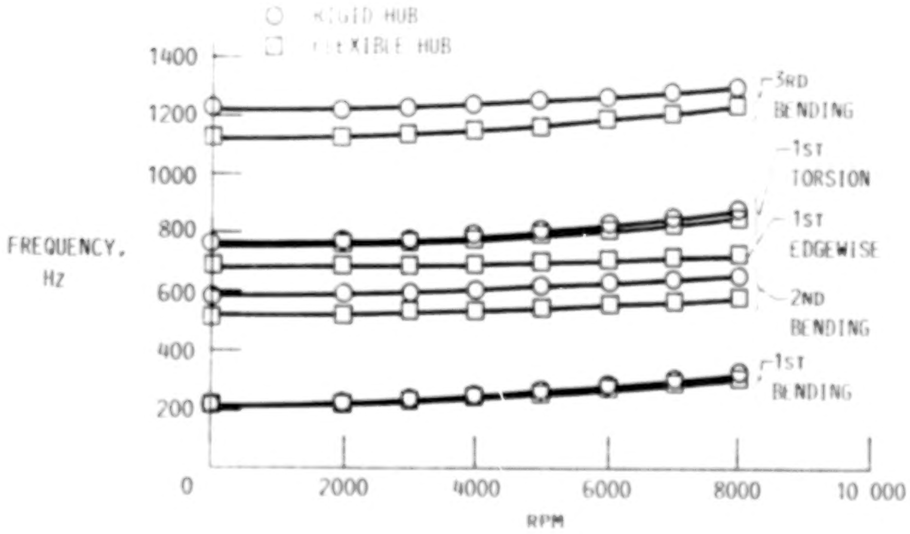

CD-86-32826

SUMMARY

NASTRAN is a valuable tool in the large-displacement and dynamic analyses of Propfan blades. However, in order to insure accurate results, the user must account for the following: an updated global stiffness matrix with the appropriate centrifugal softening terms before proceeding with the Solution 63 dynamic analysis; a proper blade setting angle for each of the respective rotational speeds at which the blade is being analyzed; and the effects due to hub flexibility.

NASTRAN IS AN EFFECTIVE TOOL FOR THE ANALYSIS OF PROPFAN BLADES.

CENTRIFUGAL SOFTENING TERMS ARE IMPORTANT IN THE STIFFNESS MATRIX OF NASTRAN'S SOLUTION SEQUENCE 63.

PROPFAN BLADES NEED TO BE MODELED WITH THE APPROPRIATE BLADE SETTING ANGLE.

IN ORDER TO INSURE ACCURACY IN THE ANALYSES OF PROPFAN BLADES, HUB FLEXIBILITY SHOULD ALWAYS BE CONSIDERED.

REFERENCES

Ernst, M.A.; Lawrence, C., 1987: "Hub Flexibility Effects on Propfan Vibration." NASA TM-89900.

Lawrence, C.; Aiello, R.A.; Ernst, M.A.; McGee, O.G., 1987: "A NASTRAN Primer for the Analysis of Rotating Flexible Blades." NASA TM-89861.

Lawrence, C.; Kielb, R.E., 1984: "Nonlinear Displacement Analysis of Advanced Propeller Structures Using NASTRAN." NASA TM-83737.

McCormick, C.W., ed., 1983: MSC/NASTRAN User's Manual, Vol. I, MacNeal-Schwendler.

Mikkelson, D.C.; Mitchell, G.A.; and Bober, L.J., 1984: "Summary of Recent NASA Propeller Research." NASA TM-83733.

Strack, W.C., et al., 1981: "Technology and Benefits of Aircraft Counter Rotation Propellers." NASA TM-82983.

APPENDIX

CONTENTS TO VOLUMES 2 and 3

④

CONTENTS TO VOLUME 2

CONSTITUTIVE MODELS AND EXPERIMENTAL CAPABILITIES

Session Overview 2-1
Robert L. Thompson, NASA Lewis Research Center

High-Temperature Combustor Liner Tests in Structural Component Response Test Facility 2-5
Paul E. Moorhead, NASA Lewis Research Center

Life Assessment of Combustor Liner Using Unified Constitutive Models 2-15
M.T. Tong, Sverdrup Technology, Inc., Lewis Research Center Group, and R.L. Thompson, NASA Lewis Research Center

Experiments Investigating Advanced Materials Under Thermomechanical Loading 2-27
Paul A. Bartolotta, NASA Lewis Research Center

Biaxial Experiments Supporting the Development of Constitutive Theories for Advanced High-Temperature Materials 2-37
J.R. Ellis, NASA Lewis Research Center

Unified Constitutive Model Development for Metal Matrix Composites at High Temperature 2-49
D.N. Robinson, University of Akron

Unified Constitutive Model for Single Crystal Deformation Behavior with Applications 2-57
K.P. Walker, Engineering Science Software, Inc., T.G. Meyer, Pratt & Whitney, and E.H. Jordan, University of Connecticut

Finite Element (MARC) Solution Technologies for Viscoplastic Analyses 2-73
V.K. Arya, National Research Council, and Robert L. Thompson, NASA Lewis Research Center

STRUCTURAL MECHANICS CODES

Session Overview 2-81
Christos C. Chamis, NASA Lewis Research Center

The Composite Blade Structural Analyzer (COBSTRAN) 2-83
Robert A. Aiello, NASA Lewis Research Center

Features and Applications of the Integrated Composites Analyzer (ICAN) Code 2-99
C.A. Ginty, NASA Lewis Research Center

Three-Dimensional Inelastic Approximate Analysis Code (MOMM) 2-113
Jeffrey P. Meister, Sverdrup Technology, Inc., Lewis Research Center Group

Specialty Three-Dimensional Finite Element Analysis Codes 2-123
Joseph J. Lackney, Sverdrup Technology, Inc., Lewis Research Center Group

④

MHOST: An Efficient Finite Element Program for Inelastic Analysis of Solids and Structures 2-131
S. Nakazawa, MARC Analysis Research Corp.
METCAN - the Metal Matrix Composite Analyzer 2-141
Dale A. Hopkins, NASA Lewis Research Center, and
Pappu L.N. Murthy, Cleveland State University
Computational Simulation Methods for Composite Fracture Mechanics . . . 2-157
Pappu L.N. Murthy, Cleveland State University

STRUCTURAL OPTIMIZATION

Session Overview 2-171
Robert H. Johns, NASA Lewis Research Center
Probabilistic Structural Analysis Computer Code (NESSUS) 2-173
Michael C. Shiao, Sverdrup Technology, Inc., Lewis Research Center Group
Structural Tailoring of High-Speed Turbine Blades(SSME/STAEBL) 2-183
Robert Rubinstein, Sverdrup Technology, Inc., Lewis Research Center Group
Computational Structural Mechanics for Engine Structures 2-189
Christos C. Chamis, NASA Lewis Research Center
Structural Tailoring of Advanced Turboprops 2-205
K.W. Brown, Pratt & Whitney, and Dale A. Hopkins, NASA Lewis Research Center
Advanced Probabilistic Methods for Quantifying the Effects of Various Uncertainties in Structural Response 2-219
Vinod K. Nagpal, Sverdrup Technology, Inc.

STRUCTURAL MECHANICS CODE APPLICATIONS

Session Overview 2-233
Robert H. Johns, NASA Lewis Research Center
Impact Damage in Composite Laminates 2-235
Joseph E. Grady, NASA Lewis Research Center
Thermostructural Analysis of Simulated Cowl Lips 2-245
Matthew E. Melis, NASA Lewis Research Center
Thermal-Structural Analyses of Space Shuttle Main Engine (SSME) Hot Section Components 2-255
Ali Abdul-Aziz, Sverdrup Technology, Inc., Lewis Research Center Group, and Robert L. Thompson, NASA Lewis Research Center
Structural Analyses of Engine Wall Cooling Concepts and Materials . . . 2-265
Albert Kaufman, Sverdrup Technology, Inc., Lewis Research Center Group
Structural Assessment of a Space Station Solar Dynamic Heat Receiver Thermal Energy Storage Canister 2-281
R.L. Thompson and T.W. Kerslake, NASA Lewis Research Center, and M.T. Tong, Sverdrup Technology, Inc., Lewis Research Center Group
An Efficient Mindlin Finite Strip Plate Element Based on Assumed Strain Distribution 2-295
Abhisak Chulya, Institute for Computational Mechanics in Propulsion, and Robert L. Thompson, NASA Lewis Research Center

CONTENTS TO VOLUME 3

CERAMIC COMPONENT RELIABILITY

Session Overview 3-1
John P. Gyekenyesi, NASA Lewis Research Center
Monolithic Ceramic Analysis Using the SCARE Program 3-5
Jane M. Manderscheid, NASA Lewis Research Center
Whisker-Reinforced Ceramic Composites for Heat Engine Components 3-21
Stephen F. Duffy, Cleveland State University
Continuous Fiber Ceramic Matrix Composites for Heat Engine Components 3-41
David E. Tripp, Cleveland State University

NONDESTRUCTIVE EVALUATION

Session Overview 3-63
Alex Vary, NASA Lewis Research Center
Nondestructive Evaluation by Acousto-Ultrasonics 3-67
Harold E. Kautz, NASA Lewis Research Center
Characterization of Sintered SiC by Using NDE 3-79
George Y. Baaklini, NASA Lewis Research Center
Systems for Ultrasonic Scanning, Analysis, and Imagery 3-93
David B. Stang, Sverdrup Technology, Inc., Lewis Research Center Group, Edward R. Generazio, NASA Lewis Research Center, and Steve Abe, Cleveland State University
Flaw Characterization in Structural Ceramics Using Scanning Laser Acoustic Microscopy 3-107
Don J. Roth, NASA Lewis Research Center
Nondestructive Evaluation of Sintered Ceramics 3-123
George Y. Baaklini, Stanley J. Klima, and William A. Sanders, NASA Lewis Research Center

FRACTURE MECHANICS

Session Overview 3-135
John L. Shannon, Jr., NASA Lewis Research Center
Fracture Technology for Brittle Materials 3-141
Jonathan A. Salem, NASA Lewis Research Center
Mode II Fracture Mechanics 3-149
Robert J. Buzzard, NASA Lewis Research Center, and Louis Ghosn, Cleveland State University
In Situ Fatigue Loading Stage Inside Scanning Electron Microscope . . . 3-161
Jack A. Telesman, NASA Lewis Research Center, Peter Kantzos, Case Western Reserve University, and David N. Brewer, U.S. Army Aviation Research and Technology Activity - AVSCOM

Grain Boundary Oxidation and Low-Cycle Fatigue at Elevated Temperatures 3-173
H.W. Liu and Y. Oshida, Syracuse University
Elevated Temperature Crack Growth 3-187
K.S. Kim, R.H. Van Stone, S.N. Malik, and J.H. Laflen, General Electric Co.

FATIGUE AND DAMAGE

Session Overview 3-199
Marvin H. Hirschberg, NASA Lewis Research Center
Cumulative Fatigue Damage Models 3-201
Michael A. McGaw, NASA Lewis Research Center
Fatigue Damage Mapping 3-213
Darrell Socie, University of Illinois at Urbana-Champaign
Bithermal Fatigue: A Simplified Alternative to Thermomechanical Fatigue 3-221
Michael J. Verrilli, NASA Lewis Research Center
Life Prediction Modeling Based on Strainrange Partitioning 3-231
Gary R. Halford, NASA Lewis Research Center
Life Prediction Modeling Based on Cyclic Damage Accumulation 3-245
Richard S. Nelson, Pratt & Whitney
Fatigue Damage Modeling for Coated Single Crystal Superalloys 3-259
David M. Nissley, Pratt & Whitney
Life and Reliability of Rotating Disks 3-271
Erwin V. Zaretsky, NASA Lewis Research Center, and Todd E. Smith and Richard August, Sverdrup Technology, Inc., Lewis Research Center Group

WIND TURBINES

Large-Scale Wind Turbine Structures 3-285
David A. Spera, NASA Lewis Research Center

HOST

Aircraft Engine Hot Section Technology - An Overview of the HOST Project 3-299
Daniel E. Sokolowski, NASA Lewis Research Center
Research Sensors 3-323
David R. Englund, NASA Lewis Research Center
HOST Combustion R&T Overview 3-337
Raymond E. Gaugler and James D. Holdeman, NASA Lewis Research Center
Review and Assessment of the HOST Turbine Heat Transfer Program 3-349
Herbert J. Gladden, NASA Lewis Research Center

NASA
National Aeronautics and Space Administration

Report Documentation Page

1. Report No.
NASA CP-3003

2. Government Accession No.

3. Recipient's Catalog No.

4. Title and Subtitle
Lewis Structures Technology – 1988

5. Report Date
May 1988

6. Performing Organization Code

7. Author(s)

8. Performing Organization Report No.
E-3970

10. Work Unit No.
505-63-1B

9. Performing Organization Name and Address
National Aeronautics and Space Administration
Lewis Research Center
Cleveland, Ohio 44135-3191

11. Contract or Grant No.

13. Type of Report and Period Covered
Technical Paper

12. Sponsoring Agency Name and Address
National Aeronautics and Space Administration
Washington, D.C. 20546-0001

14. Sponsoring Agency Code

15. Supplementary Notes

16. Abstract

A Symposium and Exposition entitled Lewis Structures Technology – 1988 (LST '88), sponsored by the Structures Division of the NASA Lewis Research Center, was held May 24 and 25, 1988, in Cleveland, Ohio. The charter of the Structures Division is to perform and disseminate results of research conducted in support of aerospace engine structures. These results have a wide range of applicability to practitioners of structural engineering mechanics beyond the aerospace arena. The specific purpose of the symposium was to familiarize the engineering structures community with the depth and range of research performed by the division and its academic and industrial partners. The more significant results of the division's research efforts were presented in 14 overviews and 83 technical presentations. The complete text of each presentation is included in this volume. Sessions covered vibration control, fracture mechanics, ceramic component reliability, parallel computing, nondestructive evaluation, constitutive models and experimental capabilities, dynamic systems, fatigue and damage, wind turbines, hot section technology (HOST), aeroelasticity, structural mechanics codes, computational methods for dynamics, structural optimization, and applications of structural dynamics, and structural mechanics computer codes.

17. Key Words (Suggested by Author(s))
Engine structures, Structures mechanics, Structural dynamics, Structural optimization, Structural durability, Fatigue(metals), Fracture mechanics, Nondestructive evaluation, Aeroelasticity, Parallel computing, Cyclic constitutive models, Wind turbines, HOST

18. Distribution Statement
Unclassified – Unlimited
Subject Category 39

19. Security Classif. (of this report)
Unclassified

20. Security Classif. (of this page)
Unclassified

21. No. of pages

22. Price*

END

DATE

FILMED

AUG 10 1988